

Dissertation zur Erlangung des Doktorgrades
der Fakultät für Chemie und Pharmazie
der Ludwig-Maximilians-Universität München

Transmission Electron Microscopy
and X-Ray Diffraction –
Joint Characterization of
Nitride Networks and Thermoelectric Tellurides

Lukas Neudert

aus

Memmingen, Deutschland

2017

Erklärung

Diese Dissertation wurde im Sinne von §7 der Promotionsordnung vom 28. November 2011 von Herrn Prof. Dr. Wolfgang Schnick betreut.

Eidesstattliche Erklärung

Diese Dissertation wurde eigenständig und ohne unerlaubte Hilfe erarbeitet.

München, 22.11.2017

.....

(Lukas Neudert)

Dissertation eingereicht am

23.11.2017

1. Gutachter:

Prof. Dr. Wolfgang Schnick

2. Gutachter:

Prof. Dr. Oliver Oeckler

Mündliche Prüfung am

20.12.2017

*Für Benedikt,
Elisabeth und Christian*

„An jeder Sache etwas zu sehen was noch niemand gesehen und woran noch niemand gedacht hat.“

Georg Christoph Lichtenberg, J 1248 / 1363

&

“Wo alle dasselbe denken, wird nicht viel gedacht.”

Karl Valentin

Acknowledgments

I would like to thank Prof. Dr. Wolfgang Schnick and Prof. Dr. Oliver Oeckler for the opportunity to prepare my doctoral thesis in both groups and on diverse questions of solid-state chemistry by the means of transmission electron microscopy. I want to thank them for their review and for their sharing of knowledge as an important step towards the publications and unpublished results presented in this dissertation. Constructive advice and conceptual input have been kept in balance. Furthermore, I would like to thank Prof. Dr. Oliver Oeckler for his constructive guidance in encouraging my scientific work and my mind since I started my research in solid-state chemistry. I am grateful that I have had the chance to present my results and those of both groups at national and international conferences. I want to thank Prof. Dr. Wolfgang Schnick and Prof. Dr. Oliver Oeckler for taking the time to be my referees.

I would like to thank Prof. Dr. Lena Daumann, Prof. Dr. Konstantin Karaghiosoff, Prof. Dr. Hans-Christian Böttcher, and Prof. Dr. Joost Wintterlin for the evaluation of my thesis and for participating in the examiners committee during the oral defense.

I would also like to thank Prof. Dr. Thomas Bein and the *NIM* community for generously allowing me to use the microscopes.

My special thanks go to Dr. Markus Döblinger and Dr. Steffen Schmidt for the time-consuming training on different electron microscopes and the inspiring discussions on several TEM challenges. Furthermore, I would like thank Dr. Constantin Hoch and Dr. Thomas Bräuniger for their constant support, not only on professional issues.

I would like to express my gratitude to all my collaboration partners, Dr. Christine Poesl, Dr. Dominik Baumann, Dr. Alexey Marchuk, Dr. Dajana Durach, Frank Heinke, Peter Schultz, Stefan Schwarzmüller, Simon Kloß, Fabian Keßler, Markus Nentwig and Jonas Häusler who made it possible for me to work on a variety of challenges. Together, we achieved great results in solid-state chemistry.

I am thankful to Dr. Gavin B. M. Vaughan and Dr. Jonathan Wright (both at ESRF, Grenoble) as well as Dr. Philipp Urban and Dr. Simon Welzmler for their help during the synchrotron measurements. Thanks go to scientists of the Lumileds Development Center in Aachen for luminescence measurements. I would like to thank all members of Prof. Schnick's, Prof. Oeckler's, Prof. Johrendt's, Prof. Lotsch's and Dr. Hoch's groups at the LMU Munich and the University of Leipzig for their support and for creating a constructive working atmosphere.

Furthermore, I like to thank Christian Minke, Thomas Miller and Wolfgang Wünschheim for their help with SEM measurements, temperature-dependent powder X-ray diffraction measurements and IT-related topics. Special thanks go to Olga Lorenz for her engagement in organizational duties.

My deep gratitude goes to Robin Niklaus, Christian Maak, Lucien Eisenburger, Eugenia Elzer and Christine Poesl, my fellow PhD students of lab D2.100, who became friends of mine. I am grateful to all my colleagues of both, Prof. Schnick's and Prof. Oeckler's, groups for the cordial reception in their midst and their support not only in scientific questions.

I want to thank Dr. Tobias Rosenthal, who inspired me for electron microscopy and Dr. Thorsten Schröder for the exciting time in the laboratory. Big thanks go to my student trainees Kim Novacek, Matthias Grotevent, Lucien Eisenburger, Manuel Scheel und Siliva Schmitzer for their interest in science and engagement in my research context.

In addition, I want to thank my close friends for their motivation and for the support I received.

My greatest thanks go to my family Elisabeth, Benedikt and Christian Neudert for their constant encouragement and ongoing support. I am extremely grateful to have a father, who is more than an idol to me.

Table of Contents

1 Introduction	1
1.1 Expectations of the combination of electron microscopy and X-ray diffraction	1
1.2 Method diversity in transmission electron microscopy	2
1.3 TEM at atomic resolution.....	3
1.4 Electron diffraction compared to X-ray diffraction.....	9
1.5 Efficient crystallographic approach to the determination of new crystal structures	11
1.6 References.....	12
2 New Oxonitridosilicate Structures Determined by a Combination of Electron Microscopy and Synchrotron X-ray Diffraction	16
2.1 Overview	16
2.2 $\text{La}_3\text{BaSi}_5\text{N}_9\text{O}_2\text{:Ce}^{3+}$ – A yellow phosphor with an unprecedented tetrahedra network; structure investigated by combination of electron microscopy and synchrotron X-ray diffraction	18
2.2.1 Introduction.....	18
2.2.2 Experimental	19
2.2.3 Results and discussion.....	21
2.2.3.1 Synthesis and chemical analysis.....	21
2.2.3.2 Single-crystal structure analysis	22
2.2.3.3 Bond-valence sum calculations	27
2.2.3.4 Electron microscopy	27
2.2.3.5 Luminescence	29
2.2.4 Conclusion	30
2.2.5 References.....	31
2.2.6 Supporting Information.....	34
2.3 Highly Symmetric AB_2 Framework Related to Tridymite in the Disordered Nitridosilicate $\text{La}_{24}\text{Sr}_{14-7x}[\text{Si}_{36}\text{N}_{72}](\text{O}_{1-x}\text{F}_x)_{14}$ ($x = 0.849$).....	39
2.3.1 Introduction.....	39

2.3.2 Results and Discussion	41
2.3.2.1 Synthesis and sample characterization	41
2.3.2.2 Structure determination.....	42
2.3.2.3 Structure description.....	45
2.3.3 Conclusion	48
2.3.4 Experimental Section.....	49
2.3.5 Supporting Information.....	53
3 Complex crystal structures of (oxo)nitridophosphates elucidated by transmission electron microscopy	60
3.1 Overview	60
3.2 CaMg₂P₆O₃N₁₀ – A Quinary Oxonitridophosphate with an Unprecedented Tetrahedra Network Structure type	62
3.2.1 Introduction.....	62
3.2.2 Results and Discussion	63
3.2.2.1 Synthesis.....	63
3.2.2.2 Structure determination.....	64
3.2.2.3 Structure description.....	67
3.2.2.4 Bond-valence sum calculations	71
3.2.2.5 Lattice-energy calculations (MAPLE)	72
3.2.3 Conclusion	73
3.2.4 Experimental section.....	73
3.2.5 References.....	76
3.2.6 Supporting Information.....	79
3.3 Puzzling Intergrowth in Cerium Nitridophosphate Unraveled by Joint Venture of Aberration-Corrected Scanning Transmission Electron Microscopy and Synchrotron Diffraction.....	82
3.3.1 Introduction.....	82
3.3.2 Experimental Details	84
3.3.3 Results and Discussion	87
3.3.3.1 Preparation and Chemical Analysis	87
3.3.3.2 Determination of the Average Structure	89

3.3.3.3 Description of the Average Structure.....	91
3.3.3.4 Transmission Electron Microscopy.....	94
3.3.3.5 Superstructure Determined from Synchrotron Data	98
3.3.3.6 (3+2)D Superspace Description	100
3.3.3.7 Superstructure Discussion	102
3.3.3.8 Optical Properties.....	103
3.3.3.9 Magnetic Properties	104
3.3.4 Conclusion	105
3.3.5 References.....	106
3.3.6 Supporting Information.....	109
3.4 An unusual nitride network of aluminum-centered octahedra and phosphorus- centered tetrahedra and structure determination from microcrystalline samples	132
3.4.1 Introduction.....	132
3.4.2 Results and discussion.....	133
3.4.3 Conclusion	139
3.4.4 References.....	140
3.4.5 Supporting Information.....	142
4 Structure-property relations of tin and indium containing tellurides	152
4.1 Overview	152
4.2 Structural variations in indium tin tellurides and their thermoelectric properties ..	155
4.2.1 Introduction.....	155
4.2.2 Experimental Section.....	157
4.2.3 Results and Discussion	159
4.2.3.1 Composition and average structure of quenched and slowly cooled phases.....	159
4.2.3.2 Thermal behavior of quenched phases	163
4.2.3.3 Influence of the composition on the nanostructure.....	163
4.2.3.4 Thermoelectric properties.....	166
4.2.4 Conclusion	168
4.2.5 References.....	168
4.2.6 Supporting Information.....	171

4.3 Structural Complexity and Thermoelectric Properties of Quaternary and Quinary Tellurides ($(\text{Ge}_x\text{Sn}_{1-x})_{0.8}(\text{In}_y\text{Sb}_{1-y})_{0.13}\text{Te}$ with $0 \leq x, y \leq 1$)	182
4.3.1 Introduction.....	182
4.3.2 Results and Discussion	184
4.3.2.1 Sample characterization and average crystal structures	184
4.3.2.2 Element distribution in quinary phases with layered structures determined by resonant X-ray diffraction	187
4.3.2.3 TEM study of $(\text{Ge}_x\text{Sn}_{1-x})_{0.8}(\text{In}_y\text{Sb}_{1-y})_{0.13}\text{Te}$	190
4.3.2.4 Temperature-dependent behavior and thermoelectric properties.....	193
4.3.3 Conclusions.....	194
4.3.4 Experimental Section.....	195
4.3.5 References.....	198
4.3.6 Supporting Information.....	200
5 Using electron microscopy for the elucidation of new crystal structures.....	213
5.1 Intergrowth of luminescent oxonitridosilicates with complex crystal structures	213
5.2 Phase identification and unit-cell parameter of new oxonitridophosphates	217
5.3 Formation of Superstructures in Tellurides	218
6 Conclusion and Outlook	222
6.1 Complex oxonitridosilicate and oxonitridophosphate frameworks.....	222
6.2 Tin and indium containing tellurides.....	225
7 Summary.....	227
A Miscellaneous	234
A 1 List of Publications	234
A 1.1 Part of this thesis.....	234
A 1.2 Other Publications.....	238
A 2 Conference contributions.....	240
B Deposited Crystallographic Data	244
C Curriculum Vitae.....	245

1 Introduction

1.1 Expectations of the combination of electron microscopy and X-ray diffraction

Compounds which structurally can only be pre-characterized, e.g. with powder X-ray diffraction, remain unpublished. Due to the absence of a structure model, they impede scientific considerations and assessments, which can be fundamental for solving problems or further research. Frequent problems that prevent complete structure refinement are either heterogeneous products or too small single crystals. Even structural features in small domains that elude characterization due to the relatively long coherence length of conventional X-rays with respect to crystallographic relevant dimensions, are among the challenges. Researchers of solid-state materials are seeking effective solutions to obtain crystal structures from structurally difficult-to-characterize samples. Thus, new approaches to enable unequivocal structural statements at state-of-the-art levels of precision are required.

Present X-ray diffraction for structure determination is a relatively fully developed method at the edge of physical limits given by the nature of X-rays.^{1,2} The methods of electron microscopy are not that fully developed, partially because of the more complex interaction of electrons with matter. However, electron microscopy can fill gaps left open by X-ray structure determination. It is common for a combination of methods to deliver the scientific breakthrough, as has been shown by providing structure models by combined electron microscopy and X-ray powder diffraction on oxides or zeolites.³ Furthermore, different combinations of methods including both X-ray diffraction and electron microscopy will be presented in this thesis in order to obtain access to the structures of new (oxo)nitridosilicates, (oxo)nitridophosphates and tellurides. Challenges with respect to structure elucidation of the latter compounds can be as versatile as their compositional variations and have to be solved during their characterization.

This thesis presents solutions for various problems of structure determination on different solids delivered by no less versatile contributions of electron microscopy. The main objectives of this thesis are the discovery and structural characterization of solids in cases where individual methods for structure determination are limited. The objective of direct observation and the explanation of structural features, like intergrown domains or superstructures, by imaging at atomic scale is pursued. Because of combined chemical and structural information on different length scales provided by electron microscopy, a better understanding of structure-property relations is expected.

1.2 Method diversity in transmission electron microscopy

The understanding of matter and its properties, irrespective of whether it is inorganic, organic or biological, correlates with its macroscopic, microscopic or even atomic structure. For solid-state science, homogeneous samples as well as crystal-structure determinations are requirements to understand and explain structure-property relations as the first step towards the prediction of materials with application. As the structural diversity and complexity of modern materials continuously expand, their structural elucidation can often require different methods or combinations of different methods. In ideal cases, this conceptual approach leads to the exploration of new materials by their targeted synthesis.

Since Max Knoll and Ernst Ruska invented the transmission electron microscope⁴ in the 1930s, it was possible to beat the resolution limit in common light microscopy, which is approximately half the wavelength of the light used. The wavelength of fast electrons is much shorter than that of visible light exemplarily shown for an acceleration voltage of 1000 kV the wavelength of an electron is $\lambda_{\text{electron}} \approx 0.00087$ nm. The invention of the transmission electron microscope was awarded with the Nobel Prize for Physics in 1986.⁵ Due to its fast wide-ranging developments, electron microscopy in general became a crucial tool for fundamental research on a broad range of materials, not only hard matter. As one of the ongoing developments, cryo-electron microscopy was also awarded with the Nobel Prize in chemistry in 2017.⁶ A modern transmission electron microscope (TEM) can combine imaging methods, diffraction techniques and spectroscopy, all at possibly atomic resolution in just one instrument (Fig. 1).^{7,8}

Well established techniques like bright-field imaging (BF), high resolution transmission microscopy (HRTEM), selected area electron diffraction (SAED) and convergent beam electron diffraction (CBED) as well as scanning transmission electron microscopy (STEM) with different detectors, can be combined with energy dispersive X-ray spectroscopy (EDX) or electron energy loss spectroscopy (EELS).⁹⁻¹³ This synergism of methods made it possible to discover structure-property relations more easily in metals, ceramics, and more recently in biomolecules and semiconductors.¹⁴ The fast and intensive progression of TEM on the one hand indicates the interest and the demands for TEM and underlines on the second hand, its effectiveness of answering recent questions of natural scientists. Modern methods like electron crystallography,¹⁵ electron tomography,¹⁶ electron holography,¹⁷ direct atom counting¹⁸ and electron microscopy under environmental conditions^{19,20} are pushing into the field of electron microscopy and become more common in the community of physicists, chemists and biologists. Further improvements like energy filters^{21,22} or spherical-aberration probe correctors and image correctors, respectively enhance the possible resolution limit in (S)TEM down to sub-Angstrom range.²³⁻²⁶ These advantages have to be considered in regards to the relatively large effort

of operating a TEM and the special sample requirements like vacuum- and electron-beam stability as well as electron transparency.

The broad range of experimental possibilities in TEM leads to popular applications in solid-state chemistry. Major issues in materials science like structure determination, real-structure elucidation and chemical analysis both on length scales from Å to mm can be discussed on the basis of data obtained from electron microscopes.

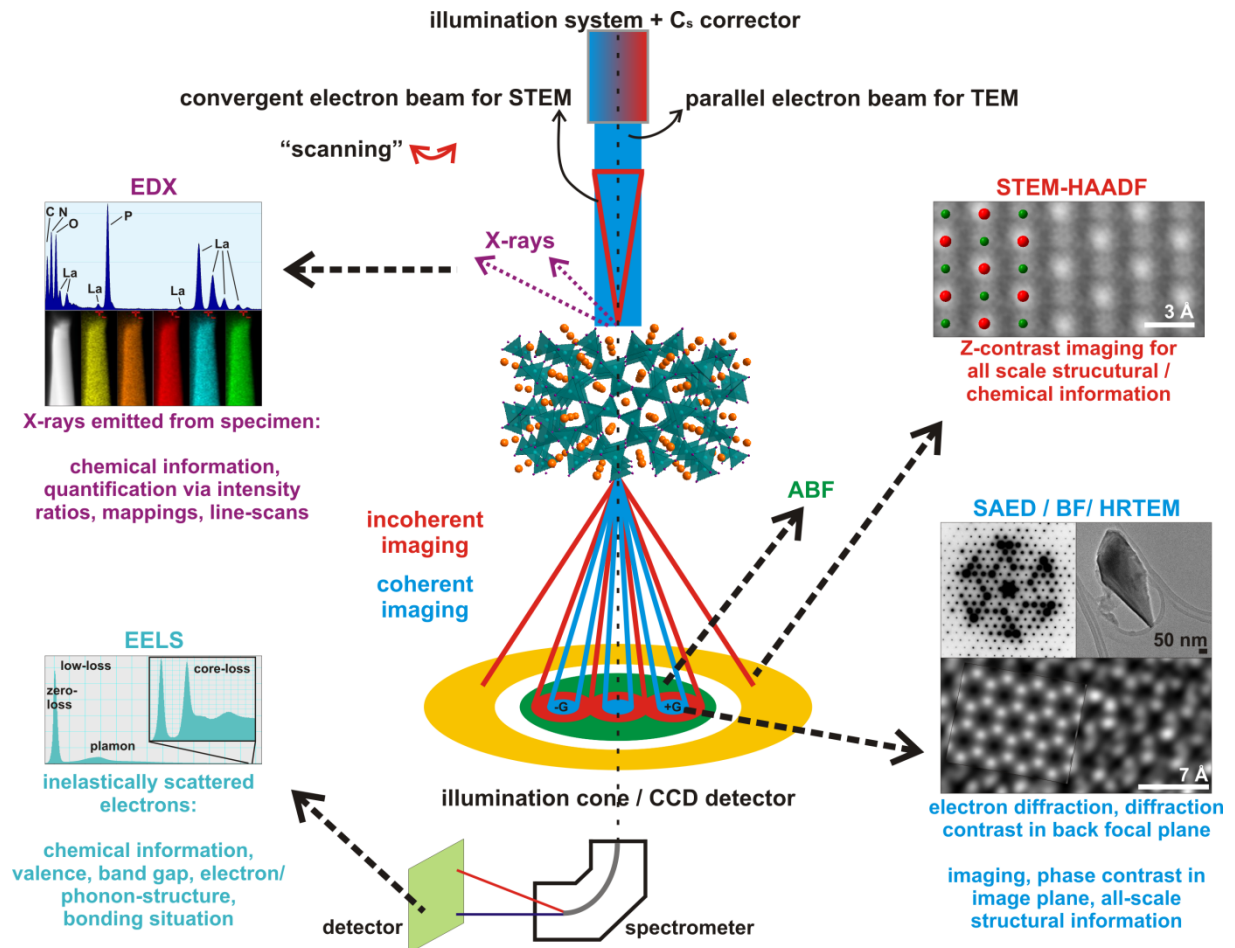


Figure 1: Selected interactions of electrons with matter and their methodical applications for (scanning) TEM micro analytic, which are relevant for this thesis.

1.3 TEM at atomic resolution

The main setup of a TEM consists of an illumination, an image-formation and an image-recording system, both in a sealed unit held under ultra-high vacuum (Fig. 2 left). Moreover, the intermediate lenses allow the change between imaging and diffraction mode. In general, the theoretical point resolution (d_{theo}) is based on the Rayleigh criterion $d_{theo} = 0.61\lambda/nsin\alpha$ with λ as wavelength of electrons, n the refractive index and α as the half-opening angle of the objective. Lens imperfections, non-uniform magnetic fields and distortions have a strong impact on the experimental point

resolution ($d_{real} = d_s + d_c$). The resulting spherical ($d_s = C_s \alpha^3$) and chromatic ($d_c = C_c \alpha \Delta E / E_0$) aberrations, astigmatism or irregular magnification lower the point resolution significantly (spherical aberration coefficient C_s , chromatic aberration coefficient C_c and the energy spread of electron source $\Delta E / E_0$). A conventional TEM operating with e.g. 200 kV acceleration voltage yields a typical point resolution in imaging mode in the range of 2.4 Å. Under ideal conditions and with the additional use of spherical aberration correction the values of d_{real} can be improved to 1.4 Å.²⁷ Since the interactions between electron beams and crystalline matter are very complex, approximations are needed to simplify the description of theoretical considerations (Fig. 2 right). The phase-object approximation defines that during passing through crystalline matter the plane electron wave function ($\Psi_0(xy)$, z is neglected due to ultra thin crystals) is undulated representing the potential distribution of the crystal projection by changed phases ($\Psi_{ex}(xy) = \exp[-i\sigma N_z \rho(xy)]$ with the electrostatic potential $\rho(xy)$, the number of periods N_z and the interaction constant σ). Varied interaction of the electron wave with unmodified amplitude interacts differently with various atoms. The weak-phase-object approximation is valid for very thin crystals ($|\sigma N_z \rho(xy)| \ll 1$) and can be written as $\Psi_{ex}(xy) = 1 - i\sigma N_z \rho(xy)$. The amplitude of the exiting wave Ψ_{ex} after the objective lens is proportional to the amplitude of the structure factors F of the atoms while the phase of Ψ_{ex} is shifted by -90° ($X(hk) - \frac{1}{2}\pi$) with respect to the phase of F (with F for each reflection: $F(hkl) = \sum_{\text{Atome } i \text{ in EZ}} f_i \left(\frac{\sin\theta}{\lambda} \right) e^{2\pi i (hx_i + ky_i + lz_i)}$ with the atomic scattering factor f_i). The propagating electron waves are conjoined by the objective lens to form an image onto the image plane. The Fourier transform (FT) of the image plane is located at the back focal plane. Without any shift the wave function in the image plane $\Psi_{im}(xy)$ is the same as the exit wave $\Psi_{ex}(xy)$ after the sample. In an ideal case and in focus the intensity distribution would be $I_{im}(xy) = \Psi_{im}(xy) \cdot \Psi_{im}^*(xy) = 1$ thus, constant. However, an image with phase contrast can be recorded by defocusing the objective lens. Amplitude contrast is a mixture of amplitude and phase changes based on different absorption and can be described by $I_{im}(xy) = \Psi_{im}(xy) \cdot \Psi_{im}^*(xy) = \exp[-2\mu(xy)]$ with μ as absorption coefficient. In the image plane, all electron waves interfere with each other and are imaged on the screen by the intermediate and projection lenses. The recorded intensity in a HRTEM image is the square root of the amplitude Ψ_{im} . The phase of the electron wave is lost. However, the phase of the structure factor is preserved in the image and from its Fourier transformation it is possible to extract the phase information of the structure factors directly. To summarize it in easy words, for HRTEM imaging transmitted and scattered electrons are used to create an interference image.^{28,29} HRTEM can support a challenging crystal structure determination because features in sub-Å range are imaged directly.^{30,31} Local structural information obtained from HRTEM micrographs taken at *Scherzer* defocus are close to the projected potential of the atoms in a thin crystal. Doubly scattered electrons (F^{II}) do not contribute significantly to the intensity ($I_{image}(hk)$) of an image at *Scherzer* defocus since the cosine term becomes nearly zero when the phase shift ($X(hk)$) of the objective lens is close to

$\pm 90^\circ$. The mathematical description is $I_{\text{image}}(hk) = D(hk)[2F^I(hk)\sin X(hk) - F^{II}(hk)\cos X(hk)]$ with $D(hk)$ as the envelope function of the contrast transfer function. While in reality, the phase shifts due to the objective lens are not exactly $\pm 90^\circ$ over the whole resolution range, the objective lens applies different influence on single and doubly scattered electrons. Thus, doubly scattered electrons cannot be separated perfectly. The contributions to the intensities in the recorded HRTEM image are described by the envelope function of the contrast transfer function, which is included in the Fourier transform of the HRTEM image.

It is obvious that HRTEM achieves qualitative structural information at atomic resolution, e.g. lattice imperfections or the atomic structure at grain boundaries in ZnO or stacking faults in graphene layers.^{32,33} An image corrector improves the HRTEM data significantly. Further quantitative structural information from HRTEM micrographs not taken at *Scherzer* defocus can only be interpreted unambiguously with a defocus series matching corresponding simulations.^{34,35}

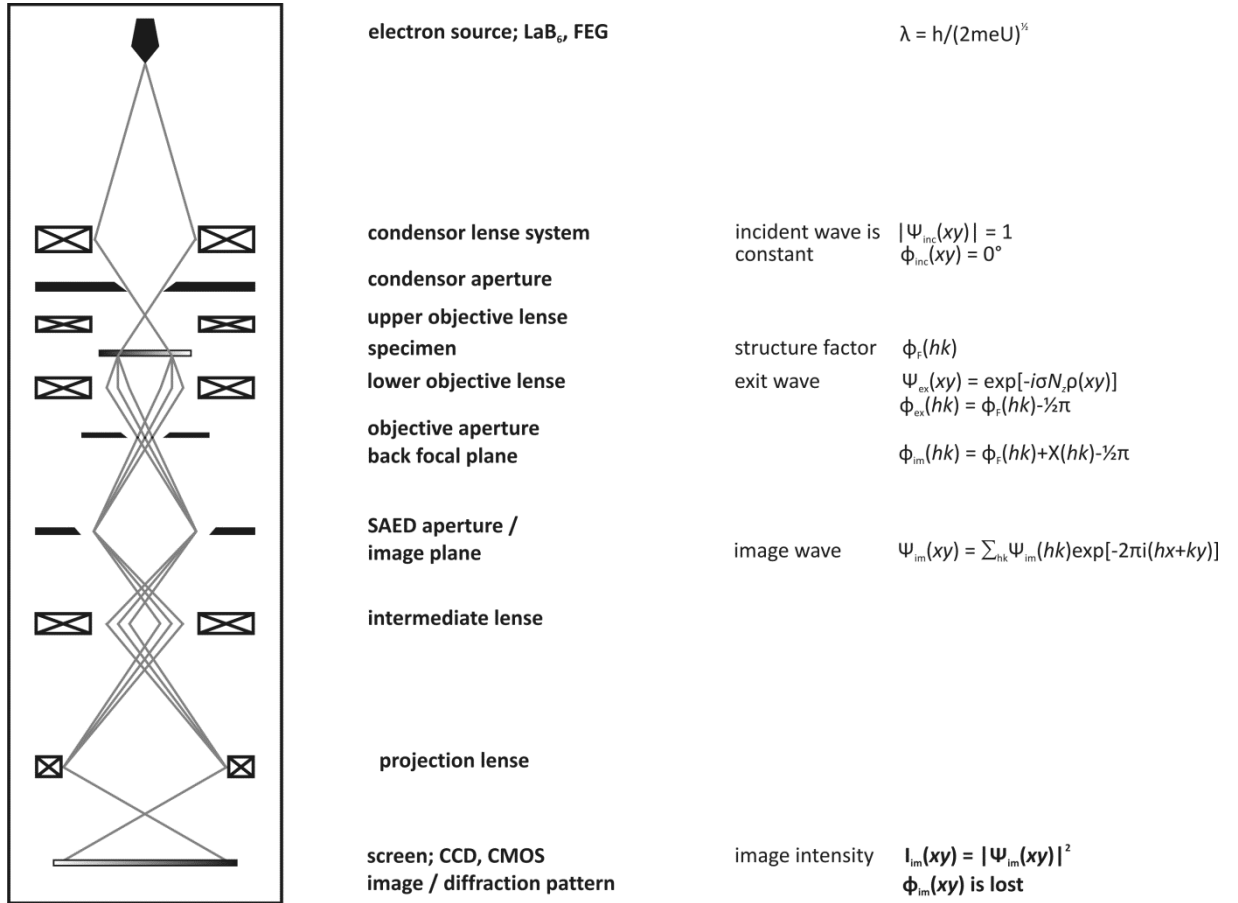


Figure 2: Simplified setup of a transmission electron microscope and corresponding terms and their relations (inspired by a similar representation in ref. 28 and 29). With h being Planck's constant, m and e the relativistic mass and charge of one electron, U the accelerating voltage, σ the interaction constant, $\rho(xy)$ electrostatic potential distribution, N_z the number of passed periods, F the structure factor and $X(xy)$ the phase shift due to objective lens.

The understanding of the exit wave function and the development of image simulation software using the multislice algorithm are one basis of state-of-the-art software for HRTEM evaluation.³⁶ The multislice algorithm converts the interaction of the electron waves with the sample into following interactions with each of the constructed thin slices. The Fast Fourier Transform (FFT) greatly improves computing time used in the software (J)EMS.^{37,38} Such calculated HRTEM images and corresponding experimental images are compared to evaluate the match with potential structure models. The power of HRTEM can be illustrated exemplarily by the characterization of ordering phenomena in silicates or chalcogenides, exemplarily shown for a new polymorph of luminescent $\text{SrSi}_2\text{O}_2\text{N}_2\text{:Eu}^{2+}$ or superstructures in $\text{A}_2\text{In}_{12}\text{Q}_{19}$ ($\text{A} = \text{K, TI, NH}_4$; $\text{Q} = \text{Se, Te}$) and $\text{Ge}_{3.25}\text{Sn}_{1.10}\text{Sb}_{1.10}\text{Te}_6$.³⁹⁻⁴¹ The latter compound classes will be of interest later on in this thesis. For investigations of real-structure effects different methods of conventional transmission electron microscopy (CTEM) are essential, e.g. when the influences of defect concentrations, detection of nanocrystalline precipitate, temperature depending structural changes or the characterization of metastable phases is of interest.^{42,43} Further current examples are gallium tellurides, silver-rich Ag_2Se or germanium antimony tellurides (GST).⁴⁴⁻⁴⁶ HRTEM illustrate differently pronounced vacancy ordering affected by chemical variations in GST (Fig. 3a) as well as the average structure of Ni_3GeTe_2 matches corresponding simulation (Fig. 3b).

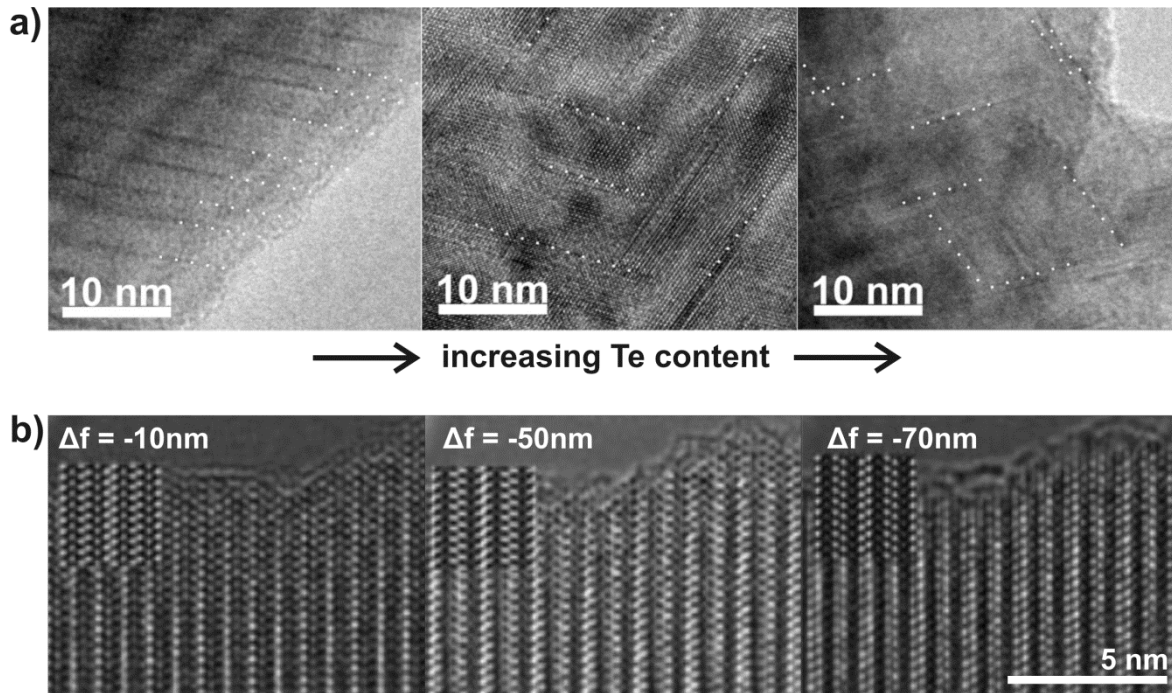


Figure 3: a) HRTEM images of germanium antimony tellurides, showing the influences of various Te content on the characteristics of differently pronounced defect layers. Adapted from *Rosenthal et. al.*⁴⁷ b) HRTEM defocus series viewed long [100] zone axis of Ni_3GeTe_2 and simulations of the average structure inserted. Adapted from *Deiseroth et. al.*⁴⁸

Another frequently used method for reaching atomic resolution is scanning transmission electron microscopy (STEM). Such images obtained from STEM on modern microscopes provide direct interpretable Z-contrast. To achieve elemental contrast at sub-Å resolution field emission guns (FEG), an additional C_s corrector, and finally, high-angle annular dark field (HAADF) detectors are crucial.⁴⁹ Although the requirements for atomic resolved STEM to the microscope and the specimen (electron-beam stability, drift) are higher than in CTEM, STEM data is easier to interpret because different contrast is directly interpretable. STEM-(HA)ADF imaging is close to perfect incoherent imaging and one is not confronted with the phase problem.⁵⁰ During STEM, an image is formed by scanning the specimen and simultaneously detecting the intensity of scattered electrons which is a function of the scanned probe position (xy). The intensity I_{HAADF} in Z-contrast images can be simply described as $I_{\text{HAADF}}(xy) = |P(xy)|^2 \otimes O(xy)$, where the square root of the point spread function $P(xy)$ is convoluted (\otimes) with the object function $O(xy)$. The latter is proportional to the number of atoms in a column and to their atomic weight. Thus, the potential of the projected crystal structure is imaged.⁵¹ This offers structural and chemical information at the same time and different contrast can be directly assigned to different element columns (Fig. 4). Thus, real-structure effects can be correlated with possible structure models. Z-contrast and phase contrast images were used to exemplarily characterize $\text{SrTiO}_3/\text{LaAlO}_3$ interfaces or to directly observe the occupancy of interstitial sites in Ge crystals.^{52,53} Annular bright field images of YH_2 illustrate both Y^{2+} and H^- ions with different contrast.⁵⁴ In monolayers even the elements B, C and N could be differentiated directly by Z-contrast STEM using a cold field emission source operated at 60 kV accelerating voltage.⁵⁵ Information at atomic resolution about the cations in silicate minerals like *orthopyroxene*, *augite* and *cronstedtite* were obtained by C_s -corrected STEM imaging.⁵⁶

In non-ideal cases spectroscopy like EDX line scans or mappings can help with the element assignment. In combination with STEM-HAADF, coordinates of (heavy) atoms can be obtained. EDX is based on fast electrons that excite core electrons of the atoms. Subsequently, electrons of upper shells close this gap and a specific amount of energy is released as X-rays, which can be detected as a function of their energy. Usually, EDX delivers information about the chemical composition with spatial resolution of a few nm⁵⁷ while EELS has improved spatial resolution down to an atomic scale. The principle of EELS is a magnetic prism spreading out the energy distribution of inelastically scattered electrons detecting the local density of states. EEL spectrometers attached underneath the conventional detectors have an energy resolution of usually 1 eV and even 0.1 eV if a monochromator is used. For instance, EELS combined with STEM images, taken at certain energy losses provides elemental maps of $\text{Bi}_{0.5}\text{Sr}_{0.5}\text{MnO}_3$.⁵⁸

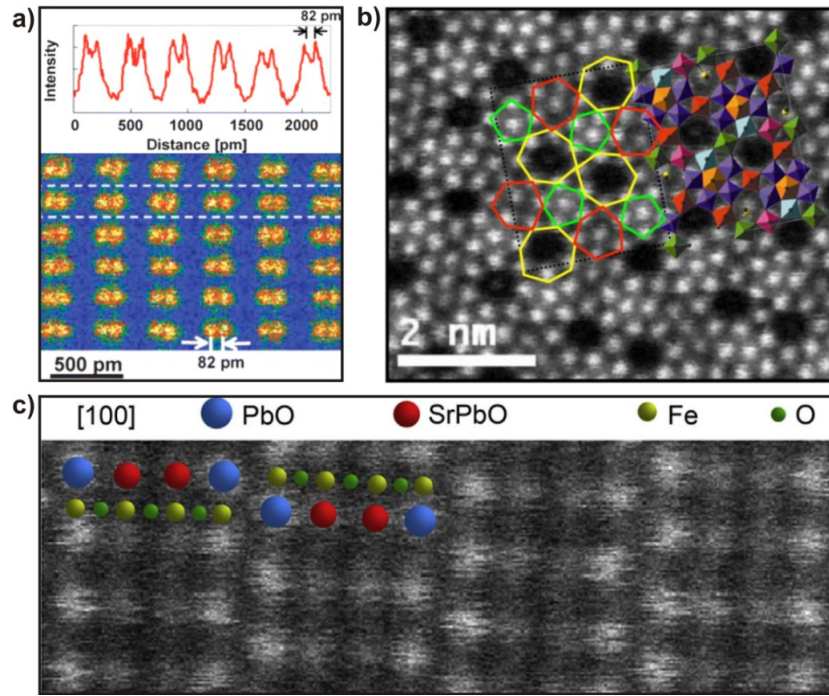


Figure 4: Experimental high-resolution STEM-HAADF images: Ge[112] crystal with intensity profile for the dumbbells of Ge atoms resolving the peak-to-peak distance of 82 pm (a, colored). Complex MoVTenbO catalyst material with structure projections overlaid showing sites in channels partially occupied with Te atoms (b). $\text{Pb}_{1.2}\text{Sr}_{0.8}\text{Fe}_2\text{O}_5$ crystal viewed along [100], element assignment based on different contrast intensities and crystal simulation (c). Adapted from *Sawade et. al.*,⁵⁹ *Pyrz et. al.*⁶⁰ and *Martinez et. al.*⁶¹

EEL spectra can be divided into three different regions: First, the zero-loss peak, whose intensity in relation to the intensity of the whole spectrum gives the sample thickness. Second, the analysis of the low-loss region contains information about the general valence states by the onset of electron loss as well as mechanical properties like elastic, bulk and shear modulus that correlated with the square of the plasmon energy. Third, the high-loss region with its element-specific edges yields the chemical analysis as well as the oxidation state of certain elements judged from chemical shift and from near-edge fine structure of the edges as fingerprints. EELS gives further structural information of solids based on the fine structure of the edges. Structural analysis like the local environment or coordination can be determined with the help of the extended energy loss fine structure.⁶²⁻⁶⁴ The significance of both analytic methods EDX and EELS depend on the quality of microscope components and the sample thickness, which is the thinner the better. In ideal cases, detection of a few or even single atoms is possible. Radiation damage in relation to signal intensity is a crucial problem one has to deal with using scanning electron beams to probe the sample. The relation between accelerating voltage, beam damage, sample drift, signal intensity and illumination as well as collecting time has to be considered in order to get the best information out of a sample.

1.4 Electron diffraction compared to X-ray diffraction

The kinematical scattering theory is the theoretical background of X-ray structure determination (XRD), which is the most important method for crystal-structure elucidation. Therefore, the majority of known crystal structures are based on X-ray data. However, XRD can hardly be used for structure determination if only nanocrystalline or heterogeneous samples are present. X-rays have one major disadvantage: Their interaction with matter is quite weak because they only interact with the electrons of the atoms and thus, X-rays detect the electron density distribution. In contrast, electrons detect the electrostatic potential distribution, which can be described as a three-dimensional function with its maxima in the atoms nuclei. The beam of charged electrons in a TEM interacts with both the electrons and the electric field of the nuclei, resulting in a very strong interaction with matter. Thus, crystals investigated with electrons can be several orders of magnitudes smaller than with X-rays. Few unit cells (about 20) can be theoretically enough for structural analysis with TEM.^{65,66} For example, coherent nano-area electron diffraction was applied to 4 nm Au particles and 1 nm carbon nanotubes.⁶⁷ Single crystals and domains with a size down to 20 nm were investigated with SAED or nanobeam-electron diffraction in order to determine crystallographic relations between intergrown domains (Fig. 5).⁶⁸

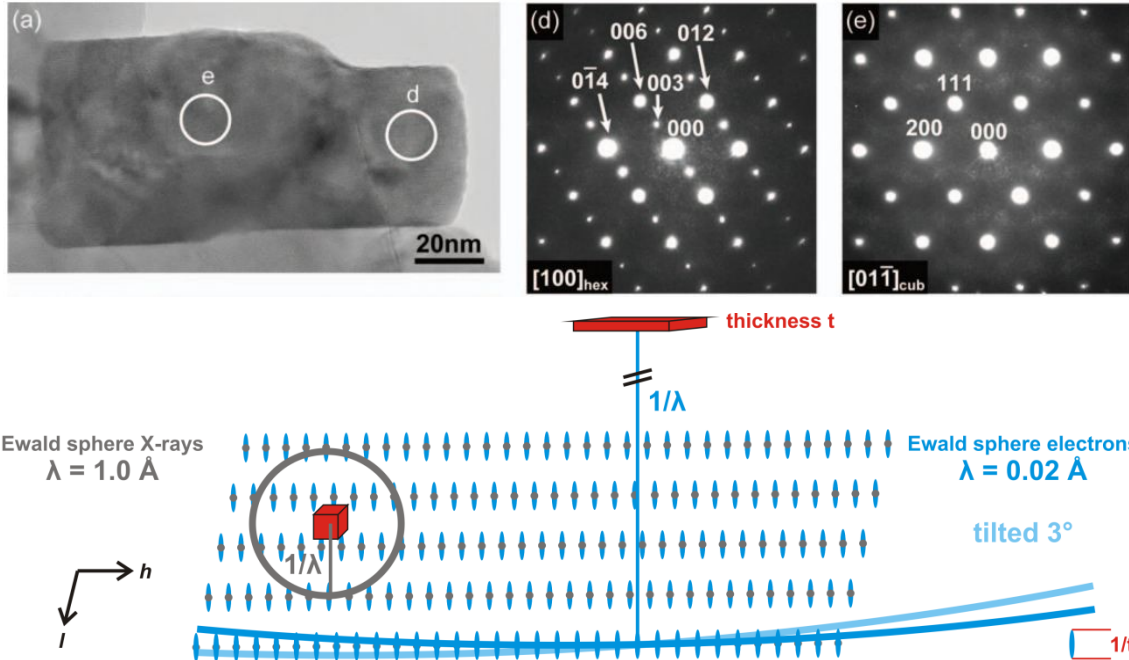


Figure 5: Top: BF image of a $\text{Li}_{1.2}\text{Mn}_{0.4}\text{Fe}_{0.4}\text{O}_2$ particle and corresponding electron diffraction pattern of the regions d and e, showing different metrics and thus different structure models. Adapted from Kikkawa *et. al.*⁶⁸ Bottom: *Ewald* construction for X-rays (grey) and electrons (blue) in comparison.

Due to the short wavelengths of electrons, the *Ewald* sphere has a large radius and many reflections of the zero-order Laue zone are excited in electron diffraction patterns taken along a zone axis.

Because of the thin areas transmitted by electrons, the reflections show a “cigar-like” shape. With SAED, more information can be collected in one single orientated diffraction pattern than in a single X-ray diffraction pattern using monochromatic X-rays (Fig. 5 bottom).

Since the kinematical approximation only applies to a maximum sample thickness of a few nm dynamic scattering occurs with thicker samples. Because of multiple scattering (*Renninger* effect) and inelastic scattering electrons undergo complicated interactions with matter and thus, electron diffraction data is not as easy to interpret as X-ray data.⁶⁹⁻⁷² The reflection intensities $I(hkl)$ of electron diffraction depend mostly on the structure factor for electrons $F(hkl)$ and can be described by the following relations: $I_{\text{kinematic}}(hkl) \sim |F(hkl)|^2$ and $I_{\text{dynamic}}(hkl) \sim |F(hkl)|$.⁷³ The phases are lost and a crystal structure cannot be determined directly from the diffraction intensities. The loss of the phase information in an electron diffraction experiments can be compensated by HRTEM, so that crystal structures can be refined with electron diffraction data (neglecting dynamic effects) reaching an accuracy of 0.02 Å as exemplarily reported for $\text{Ti}_{11}\text{Se}_4$.^{74,75}

To minimize dynamic scattering one has to use either ultra thin areas for SAED or precession electron diffraction (PED). The latter reduces dynamic diffraction effects as well as the influence of slight misorientation of the sample. Only a few reflections are excited simultaneously and the reflections are successively scanned by the off-axis beam. Thus, the possibility of multiple scattering is reduced.^{76,77} Recording a PED pattern involves scanning (above the sample) de-scanning (underneath the sample) of the tilted and diffracted beams, respectively. The final diffraction pattern is the sum of a set of continuous electron-diffraction patterns. Precession frequency and precession angle can be varied in order to obtain best results. PED data with large precession angles ($\approx 4^\circ$) show more reflections at high diffraction angles than SAED as well as reflections of the zeroth and first Laue zone. Combined with the more kinematical nature of the reflections, this can be advantageous for structure determination using electron diffraction data.^{78,79} Beyond the qualitative analysis of electron diffraction, electron crystallography or CTEM combined with other methods of structure elucidation yield more quantitative structural analysis of electron-diffraction data, exemplarily shown for modulated $\text{Sr}_{1.4}\text{Ta}_{0.6}\text{O}_{2.9}$.^{80,81}

1.5 Efficient crystallographic approach to the determination of new crystal structures

During explorative synthesis, single-phase samples are often missing and frequently only small quantities of the product can be obtained, especially using the high-pressure multianvil technique.⁸² It is also conceivable that heterostructured products with precipitates at a length scale of only a few nm in a matrix with different composition can be obtained. In such cases, the structure determination using conventional X-ray methods is usually impossible. Here, the combination of TEM and microdiffraction with synchrotron radiation⁸³ is an appropriate approach for the structure determination.^{84,85} Thus, crystallographic challenges on micro- to nanoscale crystallites from inhomogeneous samples can be remedied with reasonable effort and with the high precision and accuracy analogous to structure determination of macroscopic single crystals. Structure determination by means of powder diffraction requires homogeneous samples and often does not provide enough data to determine complex structures. Smallest sample quantities (a few mg) are sufficient for TEM pre-characterization on powder or grounded bulk samples. EDX is used to examine the chemical composition and SAED is used to determine the metrics and lattice parameters. Subsequently, the lattice parameters can be compared with databases, to check if the investigated crystals are new compounds. In favorable cases, additional HRTEM and STEM-HAADF images recorded on aberration corrected TEM yield direct structure information. The *Single-Particle Diagnose Approach*⁸⁶ can be enhanced by electron microscopy. With the latter, new phases are easily identified and characterized. Due to modern X-ray optics, synchrotron beams with high intensity and brilliance can be focused. Hence, it was possible to develop a setup for the data collection of the pre-characterized microcrystals of the new phases located on the TEM grids. The collected datasets provide at least the accuracy of common X-ray structure determinations on large single crystals using laboratory diffractometers.⁸⁴ After structure solution and refinement with the synchrotron data, HRTEM simulations or STEM-HAADF images can confirm the obtained crystal structures, independently of the corresponding X-ray data. Compared to X-ray single-crystal structure determination, electron crystallography is limited in data quality because of dynamic scattering effects, detection of different crystal volume during tilting, beam damage or excitation error. In contrast to classical electron crystallography,⁸⁷ however, modern electron diffraction tomography realizes diffraction-data acquisition of micro- or nanocrystals by tilting incrementally around an arbitrary axis automatically. Within kinematical approximations, the 3D electron data sets can be analyzed mostly similar to X-ray single-crystal data. To collect the correct reflection intensities between the tilting of the crystal in large steps of $\sim 5^\circ$, different approaches of electron diffraction can improve data acquisition.

Automated diffraction tomography (ADT)⁸⁸⁻⁹¹ uses the precession technique and stepwise data acquisition. In rotation electron diffraction (RED),^{92,93} the electron beam is tilted in very small steps ($\sim 0.05^\circ$) for each diffraction pattern. Furthermore, electron diffraction data can be collected continuously during beam tilting (integration over $\approx 1^\circ$ beam sweep).^{94,95} Both methods can yield the same quality of structure solution and refinement⁹⁶ and can be enhanced by combination with other methods of structure determination like powder X-ray diffraction.⁹⁷⁻⁹⁹

1.6 References

- 1 J. Miao, T. Ishikawa, I. K. Robinson, M. M. Murnane, *Science* **2015**, *348*, 530.
- 2 J. Li, J. Sun, *Acc. Chem. Res.* **2017**, *50*, 2737.
- 3 X. Zou, S. Hovmöller, *Acta Crystallogr. Sect. A* **2008**, *64*, 149.
- 4 M. Knoll, E. Ruska, *Z. Phys.* **1932**, *78*, 318.
- 5 E. Ruska, *Angew. Chem.* **1987**, *99*, 611; *Angew. Chem. Int. Ed. Engl.* **1987**, *26*, 595.
- 6 D. Cressey, E. Callaway, *Nature* **2017**, *550*, 167.
- 7 D. A. Muller, *Nat. Mater.* **2009**, *8*, 263.
- 8 M. A. O'Keefe, C. J. D. Hetherington, Y. C. Wang, E. C. Nelson, J. H. Turner, C. Kisielowski, J. -O. Malm, R. Mueller, J. Ringnalda, M. Pan, A. Thust, *Ultramicroscopy* **2001**, *89*, 215.
- 9 F. H. Li, *Phys. Status Solidi A* **2010**, *207*, 2639.
- 10 A. J. Papworth, M. Watanabe, D. B. Williams, *Ultramicroscopy* **2001**, *88*, 265.
- 11 P. D. Nellist, S. J. Pennycook, *Adv. Imag. Elect. Phys.* **2000**, *113*, 147.
- 12 C. Colliex, P. Trebbia, *Ultramicroscopy* **1982**, *9*, 259.
- 13 L. E. Thomas, *Ultramicroscopy* **1985**, *18*, 173.
- 14 D. E. Newbury, D. B. Williams, *Acta Mater.* **2000**, *48*, 323.
- 15 W. Mertin, *Angew. Chem.* **1997**, *109*, 46; *Angew. Chem. Int. Ed.* **1997**, *36*, 46.
- 16 P. Ercius, O. Alaidi, M. J. Rames, G. Ren, *Adv. Mater.* **2015**, *27*, 5638.
- 17 H. Lichte, M. Lehmann, *Rep. Prog. Phys.* **2008**, *71*, 016102.
- 18 A. B. Yankovich, B. Berkels, W. Dahmen, P. Binev, S. I. Sanchez, S. A. Bradley, A. Li, I. Szlufarska, P. M. Voyles *Nat. Commun.* **2014**, *5*, 1.
- 19 J. R. Jinschek, S. Helveg, *Micron* **2012**, *43*, 1156.
- 20 J. F. Creemer, S. Helveg, G. H. Hoveling, S. Ullmann, A. M. Molenbroek, P. M. Sarro, H. W. Zandbergen, *Ultramicroscopy* **2008**, *108*, 993.
- 21 L. Reimer, I. Fromm, C. Hülk, R. Rennekamp, *Microsc. Microanal. Microstruct.* **1992**, *3*, 141.
- 22 L. Reimer, *Mater. T. JIM* **1998**, *39*, 873.
- 23 M. Haider, H. Rose, S. Uhlemann, E. Schwan, B. Kabius, K. Urban, *Ultramicroscopy* **1998**, *75*, 53.
- 24 S. Uhlemann, M. Haider, *Ultramicroscopy* **1998**, *72*, 109.
- 25 A. V. Crewe, D. B. Salzman, *Ultramicroscopy* **1982**, *9*, 373.

- 26 P. D. Nellist, B. C. McCallum, J. M. Rodenburg, *Nature* **1995**, 374, 630.
- 27 M. Haider, S. Uhlemann, E. Schwan, H. Rose, B. Kabius, K. Urban, *Nature* **1998**, 392, 768.
- 28 X. Zou, *Microsc. Res. Techniq.* **1999**, 46, 202.
- 29 X. Zou, S. Hovmöller, P. Oleynikov, *Electron Crystallography, Electron Microscopy and Electron Diffraction*, Oxford University Press, Oxford, Great Britain, **2011**.
- 30 F. Phillipp, *Mater. T. JIM* **1998**, 39, 888.
- 31 D. J. Smith, *Micron* **2012**, 43, 504.
- 32 Y. Sato, T. Yamamoto, Y. Ikuhara, *J. Am. Ceram. Soc.* **2007**, 90, 337.
- 33 J. H. Warner, M. H. Rummeli, T. Gemming, B. Büchner, G. A. D. Briggs, *Nano Lett.* **2009**, 9, 102.
- 34 A. Thust, W. M. J. Coene, M. Op de Beeck, D. Van Dyck, *Ultramicroscopy* **1996**, 64, 211.
- 35 L. Houben, A. Thust, K. Urban, *Ultramicroscopy* **2006**, 106, 200.
- 36 S. Kret, P. Rutherana, A. Rosenauer, D. Gerthsen, *Phys. Stat. Sol. B* **2001**, 227, 247.
- 37 E. J. Kirkland, *Acta Cryst.* **2016**, A72, 1.
- 38 a) P. A. Stadelmann, *Ultramicroscopy* **1987**, 21, 131. b) Stadelmann, P. A., JEMS, version 3.3425, CIME–EPFL, Switzerland, **2008**.
- 39 M. Seibald, T. Rosenthal, O. Oeckler, C. Maak, A. Tucks, P. J. Schmidt, D. Wiechert, W. Schnick, *Chem. Mater.* **2013**, 25, 1852.
- 40 L. Kienle, M. Schlosser, M. J. Manos, C. D. Malliakas, V. Duppel, C. Reiner, H.-J. Deiseroth, M. G. Kanatzidis, K. Kelm, A. Simon, *Eur. J. Inorg. Chem.* **2010**, 367.
- 41 T. Rosenthal, S. Welzmler, L. Neudert, P. Urban, A. Fitch, O. Oeckler, *J. Solid State Chem.* **2014**, 219, 108.
- 42 Z. Xu, Y. Bando, W. Wang, X. Bai, D. Golberg, *ACS Nano* **2010**, 4, 2515.
- 43 Z. L. Wang, *Adv. Mater.* **2003**, 15, 1497.
- 44 L. Kienle, V. Duppel, A. Simon, H. J. Deiseroth, *Z. Anorg. Allg. Chem.* **2003**, 629, 1412.
- 45 L. Kienle, V. Duppel, B. Mogwitz, J. Janek, M. v. Kreutzbruck, A. Leineweber, A. Simon, *Cryst. Growth Des.* **2011**, 11, 2412.
- 46 M. N. Schneider, P. Urban, A. Leineweber, M. Döblinger, O. Oeckler, *Phys. Rev. B* **2010**, 81, 184102.
- 47 T. Rosenthal, M. N. Schneider, C. Stiewe, M. Döblinger, O. Oeckler, *Chem. Mater.* **2011**, 23, 4349.
- 48 H. -J. Deiseroth, K. Aleksandrov, C. Reiner, L. Kienle, R. K. Kremer, *Eur. J. Inorg. Chem.* **2006**, 1561.
- 49 M. P. Oxley, A. R. Lupini, S. J. Pennycook, *Rep. Prog. Phys.* **2017**, 80, 026101.
- 50 P. D. Nellist, S. J. Pennycook, *J. Microsc.* **1998**, 190, 159.
- 51 X. Sang, K. Du, M. Zhuo, H. Ye, *Micron* **2009**, 40, 247.
- 52 C. L. Jia, S. B. Mi, M. Faley, U. Poppe, J. Schubert, K. Urban, *Phys. Rev. B* **2009**, 79, 081405.
- 53 D. Alloyeau, B. Freitag, S. Dag, L. W. Wang, C. Kisielowski, *Phys. Rev. B* **2009**, 80, 014114.
- 54 R. Ishikawa, E. Okunishi, H. Sawada, Y. Kondo, F. Hosokawa, E. Abe, *Nat. Mater.* **2011**, 10, 278.
- 55 O. L. Krivanek, M. F. Chrisholm, V. Nicolosi, T. J. Pennycook, G. J. Corbin, N. Dellby, M. F. Murfitt, C. S. Own, Z. S. Szilagy, M. O. Oxely, S. T. Pantelides, S. J. Pennycook, *Nature* **2010**, 464, 271.
- 56 T. Kogure, E. Okunishi, *J. Electron. Microsc.* **2010**, 59, 263.
- 57 J. J. Friel, C. E. Lyman, *Microsc. Microanal.* **2006**, 12, 2.

- 58 M. Bosman, V. J. Keast, J. L. García-Munoz, A. J. D'Alfonso, S. D. Findlay, L. J. Allen, *Phys. Rev. B* **2007**, *99*, 086102.
- 59 H. Sawade, Y. Tanishiro, N. Ohashi, T. Tomita, F. Hosokawa, T. Kaneyama, Y. Kondo, K. Takayanagi, *J. Electron. Microsc.* **2009**, *58*, 357.
- 60 W. D. Pyrz, D. A. Blom, T. Vogt, D. J. Buttrey, *Angew. Chem.* **2008**, *120*, 2830; *Angew. Chem. Int. Ed.* **2008**, *47*, 2788.
- 61 G. T. Martinez, A. Rosenauer, A. De Backer, J. Verbeek, S. Van Aert, *Ultramicroscopy* **2014**, *137*, 12.
- 62 R. F. Egerton, *Rep. Prog. Phys.* **2009**, *72*, 016502.
- 63 R. Brydson, H. Sauer, W. Engel, E. Zeitler, *Microsc. Microanal. M.* **1991**, *2*, 159.
- 64 A. Altay, C. B. Carter, P. Rulis, W.-Y. Ching, I. Arslan, M. A. Gülgün, *J. Solid State Chem.* **2010**, *183*, 1776.
- 65 J. L. Sun, Z. B. He, S. Hovmöller, X. D. Zou, F. Gramm, C. Baerlocher, L. B. McCusker, *Z. Kristallogr.* **2010**, *225*, 77.
- 66 L. B. McCusker, C. Baerlocher, *Z. Kristallogr.* **2013**, *228*, 1.
- 67 J. M. Zou, M. Gao, J. Tao, B. Q. Li, R. Twesten, A. Petrov, *Microsc. Techniq.* **2004**, *64*, 347.
- 68 J. Kikkawa, T. Akita, M. Tabuchi, M. Shikano, K. Tatsumi, M. Kohyama, *J. Appl. Phys.* **2008**, *103*, 104911.
- 69 R. D. Twesten, J. M. Gibson, *Ultramicroscopy* **1994**, *53*, 223.
- 70 P. A. Midgley, A. S. Eggeman, *IUCrJ* **2015**, *2*, 126.
- 71 D. L. Dorset, *Acta Crystallogr. Sect. B* **1996**, *52*, 753.
- 72 J. Jansen, D. Tang, H. W. Zandbergen, H. Schenk, *Acta Crystallogr. Sect. A* **1998**, *54*, 91.
- 73 V. V. Klechkovskaya, R. M. Imanov, *Crystallogr. Rep.* **2001**, *46*, 534.
- 74 S. Hovmöller, X. Zou, *Cryst. Res. Technol.* **2011**, *46*, 535.
- 75 T. E. Weirich, R. Ramlau, A. Simon, S. Hovmöller, X. Zou, *Nature* **1996**, *382*, 144.
- 76 R. Vincent, P. A. Midgley, *Ultramicroscopy* **1994**, *53*, 271.
- 77 M. Gemmi, S. Nicolopoulos, *Ultramicroscopy* **2007**, *107*, 483.
- 78 L. Palatinus, D. Jacob, P. Cuvillier, M. Klementová, W. Sinkler, L. D. Marks, *Acta Crystallogr. Sect. A* **2013**, *69*, 171.
- 79 C. S. Own, L. D. Marks, W. Sinkler, *Acta Crystallogr. Sect. A* **2006**, *62*, 434.
- 80 D. L. Dorset, *Ultramicroscopy* **2007**, *107*, 453.
- 81 M. T. Caldes, P. Deniard, X. D. Zou, R. Marchand, N. Diot, R. Brec, *Micron* **2001**, *32*, 497.
- 82 H. Huppertz, *Z. Kristallogr.* **2004**, *219*, 330.
- 83 G. B. M. Vaughan, J. P. Wright, A. Bytchkov, M. Rossat, H. Gleyzolle, I. Snigireva, A. Snigirev, *J. Synchrotron Rad.* **2011**, *18*, 125.
- 84 F. Fahrnbauer, T. Rosenthal, T. Schmutzler, G. Wagner, G. B. M. Vaughan, J. P. Wright, O. Oeckler, *Angew. Chem.* **2015**, *127*, 10158; *Angew. Chem. Int. Ed.* **2015**, *54*, 10020.
- 85 F. Heinke, R. Meyer, G. Wagner, O. Oeckler, *Z. Anorg. Allg. Chem.* **2015**, *641*, 192.
- 86 N. Hirosaki, T. Takeda, S. Funahashi, R. J. Xie, *Chem. Mater.* **2014**, *26*, 4280.
- 87 X. Zou, A. Hovmöller, S. Hovmöller, *Ultramicroscopy* **2004**, *98*, 187.
- 88 U. Kolb, T. Gorelik, C. Kübel, M. T. Otten, D. Hubert, *Ultramicroscopy* **2007**, *107*, 507.
- 89 U. Kolb, T. Gorelik, M. T. Otten, *Ultramicroscopy* **2008**, *108*, 763.

- 90 E. Mugnaioli, T. Gorelik, U. Kolb, *Ultramicroscopy* **2009**, 109, 758.
- 91 U. Kolb, E. Mugnaioli, T. E. Gorelik, *Cryst. Res. Technol.* **2011**, 46, 542.
- 92 D. Zang, P. Oleynikov, S. Hovmöller, X. Zou, *Z. Kristallogr.* **2010**, 225, 94.
- 93 W. Wan, J. Sun, J. Su, S. Hovmöller, X. Zou, *J. Appl. Crystallogr.* **2013**, 46, 1863.
- 94 B. L. Nannenga, D. Shi, A. G. W. Leslie, T. Gonen, *Nat. Methods* **2014**, 11, 927.
- 95 B. L. Nannenga, T. Gonen, *Curr. Opin. Struc. Biol.* **2014**, 27, 24.
- 96 M. Gemmi, P. Oleynikov, *Z. Kristallogr.* **2013**, 228, 51.
- 97 T. Willhammar, X. Zou, *Z. Kristallogr.* **2013**, 228, 11.
- 98 A. S. Eggemann, J. S. Barnard, P. A. Midgley, *Z. Kristallogr.* **2013**, 228, 43.
- 99 Y. Yun, X. Zou, S. Hovmöller, W. Wan, *IUCrJ* **2015**, 2, 267.

2 New Oxonitridosilicate Structures Determined by a Combination of Electron Microscopy and Synchrotron X-ray Diffraction

2.1 Overview

Research on energy-saving materials is one of the key issues of modern solid-state chemistry. High energy-saving potential is required in the field of luminescence, because worldwide nearly $\frac{1}{4}$ of the energy consumption is due to lighting. Great advances have been achieved by further developing phosphors for state-of-the-art LEDs in order to efficiently convert electrical power into light.¹⁻³ Recently, narrow band red-emitting phosphors for warm-white emission of phosphor-converting LEDs or green phosphors for backlighting in screens are of particular interest.⁴⁻⁷ Prerequisites for applicable luminescent materials are chemical and thermal stability, transparency, rigid frameworks to suppress electron-phonon coupling, and for narrowband phosphors, high symmetry of the activator-ion (mainly Eu^{2+} or Ce^{3+}) coordination. These properties are often realized in (oxo)nitridosilicates. They encompass a wide variety of structures related to the diversity of oxosilicate tetrahedra structures.⁸⁻¹⁰ The maximum degree of condensation (κ = centers of tetrahedra : anions of tetrahedra framework = $n(\text{Si}) : n(\text{O}) = 0.5$) represented by SiO_2 in 3D oxosilicate networks can be exceeded with the introduction of N to extend the structural diversity.

Stable (oxo)nitridosilicates are predominantly synthesized at temperatures $> 1000^\circ\text{C}$. Using reactive starting materials like “ $\text{Si}(\text{NH})_2$ ” combined with rare-earth hydrides, metal diimides and metal halogenides is a feasible route to obtain new luminescent phases.^{11,12} The advantage of this synthesis strategy is the easy accessibility of new phases. The disadvantage, however, is that the products are often heterogeneous and frequently microcrystalline, and consist of a variety of elements that are difficult to distinguish with X-ray and electron methods (e.g. N/O/F, Ba/La). In addition, crystallographic phenomena like coherently intergrown domains or twinning can render common structure determination challenging or make it even impossible. Complementary, the combination of TEM and X-ray methods often provided the breakthrough to a final structure model and to an interpretation of corresponding properties. Luminescent oxonitridosilicates are good examples for such relations. Thus, the existence of monoclinic stacking of $\text{SrSi}_2\text{O}_2\text{N}_2\cdot\text{Eu}^{2+}$ was elucidated by TEM. The structural comparison with the triclinic polymorph referred to the different coordination of Eu^{2+} , explain the shift between the two corresponding emission wavelengths of the two phases.¹³ In the case of $\text{Sr}_{0.25}\text{Ba}_{0.75}\text{Si}_2\text{O}_2\text{N}_2$, HRTEM images showed the short-range ordering of cations proving different structure types in intergrown domains compared to pure $\text{BaSi}_2\text{O}_2\text{N}_2$. Corrugated metal atom layers turned out to be relevant for the unexpected blue luminescence of $\text{Sr}_{0.25}\text{Ba}_{0.75}\text{Si}_2\text{O}_2\text{N}_2\cdot\text{Eu}^{2+}$.¹⁴

Diffuse scattering in powder diffraction and SAED patterns of $\text{Sr}_{0.5}\text{Ba}_{0.5}\text{Si}_2\text{O}_2\text{N}_2$ was explained by small antiphase domains coupled with twin domains.¹⁵ The real-structure effects, which are very pronounced in $\text{SrSi}_2\text{O}_2\text{N}_2\text{:Eu}^{2+}$ and $\text{BaSi}_2\text{O}_2\text{N}_2\text{:Eu}^{2+}$, can influence luminescence properties significantly.^{16,17} For further breakthroughs in the field of luminescence, new compounds and their exact structure analysis using TEM are important in order to be able to derive and, in ideal cases predict, structure-property relations.

References

- 1 S. Schmiechen, H. Schneider, P. Wagatha, C. Hecht, P. J. Schmidt, W. Schnick, *Chem. Mater.* **2014**, *26*, 2712.
- 2 R. Mueller-Mach, G. Mueller, M. R. Krames, H. A. Höpfe, F. Stadler, W. Schnick, T. Juestel, P. Schmidt, *Phys. Status Solidi (a)* **2005**, *202*, 1727.
- 3 P. Pust, V. Weiler, C. Hecht, A. Tücks, A. S. Wochnik, A. -K. Henß, D. Wiechert, C. Scheu, P.J. Schmidt, W. Schnick, *Nat. Mater.* **2014**, *13*, 891.
- 4 P. F. Smet, A. B. Parmentier, D. Poelman, *J. Electrochem. Soc.* **2011**, *158*, 37.
- 5 R. -J. Xie, N. Hirotsaki, *Sci. Technol. Adv. Mat.* **2007**, *8*, 588.
- 6 L. Wang, X. Wang, T. Kohsei, K. -I. Yoshimura, M. Izumi, N. Hirotsaki, R. -J. Xie, *Opt. Express* **2015**, *23*, 249252.
- 7 Y. Fukuda, N. Matsuda, A. Okada, I. Mitsuishi, *Jpn. J. Appl. Phys.* **2012**, *51*, 122101.
- 8 H. Huppertz, W. Schnick, *Angew. Chem.* **1996**, *108*, 2115.
- 9 M. Zeuner, S. Pagano, W. Schnick, *Angew. Chem.* **2011**, *123*, 7898; *Angew. Chem., Int. Ed.* **2011**, *50*, 7754.
- 10 C. Feldmann, *Z. Anorg. Allg. Chem.* **2012**, *638*, 2169.
- 11 W. Schnick, H. Huppertz, *Chem. Eur. J.* **1997**, *3*, 679.
- 12 D. Durach, Dissertation, Ludwig-Maximilians-University Munich, **2016**.
- 13 M. Seibald, T. Rosenthal, O. Oeckler, C. Maak, A. M. Tücks, P. J. Schmidt, D. Wiechert, W. Schnick, *Chem. Mater.* **2013**, *25*, 1852.
- 14 M. Seibald, T. Rosenthal, O. Oeckler, F. Farnbauer, A. Tücks, P. J. Schmidt, W. Schnick, *Chem. Eur. J.* **2012**, *18*, 13446.
- 15 M. Seibald, O. Oeckler, V.R. Celinski, P.J. Schmidt, A. Tücks, W. Schnick, *Solid State Sci.* **2011**, *13*, 1769.
- 16 O. Oeckler, F. Stadler, T. Rosenthal, W. Schnick, *Solid State Sci.* **2007**, *9*, 205.
- 17 J. A. Kechele, O. Oeckler, F. Stadler, W. Schnick, *Solid State Sci.* **2009**, *11*, 537.

2.2 $\text{La}_3\text{BaSi}_5\text{N}_9\text{O}_2\text{:Ce}^{3+}$ – A yellow phosphor with an unprecedented tetrahedra network; structure investigated by combination of electron microscopy and synchrotron X-ray diffraction

Dajana Durach, Lukas Neudert, Peter J. Schmidt, Oliver Oeckler and Wolfgang Schnick

Chem. Mater. **2015**, 27, 4832.

Reprinted with permission from *Chemistry of Materials*. Copyright 2015 ASC Publications.

Abstract

Due to the relationship between structure and luminescence properties, detailed crystal structure determination for microcrystalline phosphors is necessary for a profound understanding of materials properties. The yellow phosphor $\text{La}_3\text{BaSi}_5\text{N}_9\text{O}_2\text{:Ce}^{3+}$ ($\lambda_{\text{max}} = 578 \text{ nm}$; $\text{fwhm} \sim 4700 \text{ cm}^{-1}$) was characterized by a combination of transmission electron microscopy (TEM) and synchrotron microfocus diffraction as only agglomerates of crystals with a maximum size of a few μm could be obtained yet. $\text{La}_3\text{BaSi}_5\text{N}_9\text{O}_2\text{:Ce}^{3+}$ was synthesized from LaF_3 , $\text{La}(\text{NH}_2)_3$, BaH_2 , $\text{Si}(\text{NH})_2$, and CeF_3 in a radio frequency furnace. It crystallizes in space group $Pmn2_1$ (no. 31) with $a = 9.5505(8)$, $b = 19.0778(16)$, $c = 12.1134(9) \text{ \AA}$, and $Z = 8$. Its interrupted three-dimensional tetrahedra network contains *zehner* and *dreier* rings of vertex-sharing SiN_4 and SiN_2O_2 tetrahedra. The crystal structure was confirmed by high-resolution TEM and Z-contrast scanning TEM. The element distribution was derived by bond-valence sum calculations. The infrared spectrum proves the absence of N–H bonds.

2.2.1 Introduction

In 2014, the Nobel Prize in Physics was awarded to Akasaki, Amano, and Nakamura “for the invention of efficient blue light-emitting diodes which has enabled bright and energy-saving white light sources”.¹ This emphasizes the importance of light-emitting diodes (LEDs) which are typically combined with luminescent materials to phosphor converted pc-LEDs that produce white light. Owing to their excellent properties such as long lifetime, energy efficiency, small volume, and environmental compatibility, they convince as light source now and in the future.^{2–5} Presently, most white-light pc-LEDs are produced by combining a blue primary (In,Ga)N LED chip with yellow-emitting $(\text{Y,Gd})_3(\text{Al,Ga})_5\text{O}_{12}\text{:Ce}^{3+}$ (YAG:Ce³⁺). This phosphor shows a broad yellow emission and excellent chemical and thermal stability. However, this combination yields only cool-white light.^{6,7} In order to achieve warm-white light for general lighting, a multiphosphor approach is necessary, which

combines at least two phosphors, e.g. a broadband green–yellow with an orange–red emitting one.⁸ As nitridoaluminates and nitridosilicates can be thermally and chemically inert due to their highly condensed structures, they turned out to be excellent phosphors. Moreover, they have partially covalent bonds between the activator (dopant) and N, which leads to red-shifted photoluminescence (nephelauxetic effect). Thus, Eu²⁺-doped nitridoaluminates and nitridosilicates such as (Ba,Sr)₂Si₅N₈:Eu²⁺ 9-12 or (Ca,Sr)SiAlN₃:Eu²⁺ 13-16 are applied as red emitting component in commercially available warm-white pc-LEDs.^{8,17} Owing to the nephelauxetic effect, the luminescence of nitridosilicates is shifted to warmer color temperatures. Thus, Ce³⁺-doped nitridosilicates have great potential for application in warm-white pc-LEDs based on a single-phosphor approach (1pc-LEDs). An outstanding example for this is (La,Ca)₃Si₆N₁₁:Ce³⁺.¹⁸ White 1pc-LEDs using this phosphor emit in the 2600–3800 K color temperature range and show good thermal stability.

The continuous development of new solid-state lighting technologies and devices and a growing demand motivate the search for new nitridosilicate phosphors. However, structure elucidation of such new phosphors often proved difficult and time-consuming, and either large single crystals or phase-pure samples were usually necessary. Commonly, a single-particle-diagnosis approach is used, which enables the determination of luminescence and crystal structures of rather small single crystals up to 10 µm.¹⁹ Yet, many explorative syntheses lead to inhomogeneous and microcrystalline products with crystal size below a few µm. Consequently, structure characterization with conventional single-crystal X-ray diffraction is no longer possible. Here, we apply an approach that combines transmission electron microscopy (TEM) and synchrotron microfocus diffraction. This method allows for the analysis of particles with a volume even smaller than 1 µm³ and furthermore provides the possibility of analyzing the same particle by TEM and X-ray diffraction.²⁰ In contrast to structure determination by electron crystallography, e.g. with automated electron diffraction tomography (ADT) or rotation electron diffraction (RED),²¹⁻²⁵ this method allows a much more accurate determination of bond lengths, mixed occupancies and displacement parameters. Data acquired with microfocused synchrotron radiation yielded the crystal structure of the novel yellow phosphor La₃BaSi₅N₉O₂:Ce³⁺ discussed in this contribution.

2.2.2 Experimental

Synthesis

For the synthesis of La₃BaSi₅N₉O₂:Ce³⁺ (with 2 mol % Ce), 0.15 mmol (29.8 mg) of LaF₃ (Sigma–Aldrich, 99.99%), 0.17 mmol (31 mg) of La(NH₂)₃,²⁶ 0.48 mmol (66.8 mg) of BaH₂ (Materion, 99.7%), 0.55 mmol (32.2 mg) of Si(NH)₂,²⁷ and 0.006 mmol (1.2 mg) of CeF₃ as dopant (Alfa Aesar, 99.99%) were mixed in an agate mortar and filled into a tungsten crucible. These steps were performed under

argon atmosphere in a glovebox (Unilab, MBraun, Garching; O₂ < 1 ppm; H₂O < 1 ppm). Subsequently, the crucible was placed in a water-cooled silica glass reactor of a radio frequency furnace (type AXIO 10/450, maximal electrical output 10 kW, Hüttinger Elektronik, Freiburg),²⁸ heated under N₂-atmosphere to 1600 °C within 1 h, maintained at that temperature for 10 h, then cooled to 900 °C in 44 h, and finally quenched to room temperature by switching off the furnace. The reaction yielded an inhomogeneous sample with small aggregates of yellow crystals with a maximum size of a few μm (Figure S1), which show yellow luminescence after excitation with blue light. Moreover the crystals have high air and water stability. Contact with air and water over several hours does not lead to a decomposition of the crystals.

Electron microscopy

For scanning electron microscopy (SEM), a JSM 6500F instrument (JEOL) with a Si/Li energy-dispersive X-ray (EDX) detector (Oxford Instruments, model 7418) was used. EDX spectra were collected with an accelerating voltage of 12 kV. In order to ensure electrical conductivity on the sample surface, it was coated with carbon by means of an electron beam evaporator (BAL-TEC MED 020, Bal Tec AG).

For TEM investigations, the crushed polycrystalline aggregates of La₃BaSi₅N₉O₂:Ce³⁺ were dispersed in absolute ethanol and drop-cast on copper finder grids coated with a holey carbon film (S166-2, Plano GmbH, Germany). The grids were fixed on double-tilt holders. Selected area electron diffraction (SAED), high resolution TEM (HRTEM), scanning TEM using a high-angle annular dark-field detector (STEM-HAADF), and EDX measurements were acquired on a Titan 80-300 (FEI, USA) with a field emission gun operated at 300 kV, equipped with a TEM TOPS 30 EDX spectrometer (EDAX, Germany). Images were recorded using an UltraScan 1000 camera (Gatan, USA, resolution: 2k × 2k). Further SAED and EDX measurements were done on a Jeol 2010 (Jeol, Germany) with a thermal emitter operated at 200 keV, equipped with an EDAX Apollo XLT EDX detector (EDAX Germany) and a TemCam F216 camera (TVIPS, Germany, resolution: 2k × 2k). HRTEM and SAED data were evaluated using the programs Digital Micrograph²⁹ (including Fourier filtering of the HRTEM images) and JEMS.³⁰ EDX data were processed with ES Vision³¹ and EDAX TEAM.³²

Single-crystal X-ray diffraction

The X-ray diffraction data of La₃BaSi₅N₉O₂:Ce³⁺ were collected at beamline ID11 of the ESRF in Grenoble (Ge(111) double-crystal monochromator, Frelon CCD detector)³³ with a wavelength of λ = 0.33510 Å. The beam was focused to 4.5 μm in horizontal direction and 0.5 μm in vertical direction with a beryllium lens system.³⁴ A single-crystalline tip (ca. 1 μm · 0.5 μm) of a crystallite was centered in the beam with the help of the fluorescence signal.

Diffraction data were indexed with SMART³⁵ and integrated with SAINT.³⁶ Scaling and absorption correction were done with SADABS.³⁷ In addition, a correction for the incomplete absorption in the CCD phosphor was applied.³⁸ The structure was solved by direct methods (SHELXS) and refined by full matrix least-squares methods (SHELXL).³⁹

Powder X-ray diffraction

Powder diffraction data were collected with a STOE STADI P diffractometer (Mo-K α_1 radiation, λ = 0.70930 Å, Ge(111) monochromator, MYTHEN 1K detector) in Debye–Scherrer geometry. Simulated powder diffraction patterns were calculated using the WinXPOW program package⁴⁰ on the basis of the single-crystal structure data. Rietveld refinement was performed by using TOPAS-Academic.⁴¹

Luminescence

The luminescence was analyzed with a luminescence microscope, consisting of a HORIBA Fluoromax4 spectrofluorimeter system attached to an Olympus BX51 microscope via fiber optics. Using an excitation wavelength of 440 nm with a spectral width of 10 nm, the emission spectra were measured between 460 and 780 nm with 2 nm step size. This spectral range was also used for color point calculations. Excitation spectra were measured between 385 and 520 nm with 2 nm step size.

FTIR spectroscopy

The Fourier transform infrared spectrum (FTIR) spectrum of La₃BaSi₅N₉O₂:Ce³⁺ was recorded using a KBr pellet with a Spectrum BX II spectrometer (PerkinElmer, Waltham MA, USA).

2.2.3 Results and discussion

2.2.3.1 Synthesis and chemical analysis

The synthesis is probably based on the decomposition of BaH₂ (decomposition at 675 °C),⁴² and its reaction with LaF₃ to BaF₂, which resublimates at the reactor wall of the radio frequency furnace. Subsequently, the remaining Ba reacts with the dopant and the precursors La(NH₂)₃ and Si(NH)₂ to La₃BaSi₅N₉O₂:Ce³⁺. The incorporated O supposedly originates from contamination of commercially acquired starting materials. La₃BaSi₅N₉O₂:Ce³⁺ forms small yellow crystals, whose size could not be increased so far by variation of synthesis conditions.

The sum formula obtained from single-crystal structure refinement and bond-valence sum calculations is corroborated by SEM-EDX analyses as the measurements result in an average composition of $\text{La}_{3.00(17)}\text{Ba}_{0.49(4)}\text{Si}_{4.4(2)}\text{N}_{12.0(4)}\text{O}_{2.34(11)}$ (sum formula normalized according to the La content; four measurements on different crystals; unusually large errors are due to La/Ba line overlap and the simultaneous presence of light and very heavy elements). Although Ce was not detected by EDX, its presence is proven unequivocally by luminescence measurements.

2.2.3.2 Single-crystal structure analysis

As only agglomerates with low scattering intensity of the crystals could be separated, their characterization was not possible with conventional single-crystal X-ray diffraction. As no phase-pure sample could be obtained and the powder pattern suggested a novel compound with a very complex structure, crystal-structure determination by means of powder X-ray diffraction was also not feasible. As the product shows interesting luminescence properties, it was investigated by a combination of TEM and synchrotron microfocus diffraction. Therefore, the agglomerates were crushed in order to obtain small single crystals which were then dispersed on a TEM grid. An appropriate tip of a crystallite of $\text{La}_3\text{BaSi}_5\text{N}_9\text{O}_2\text{:Ce}^{3+}$ was selected by means of EDX and SAED (Figure 1).

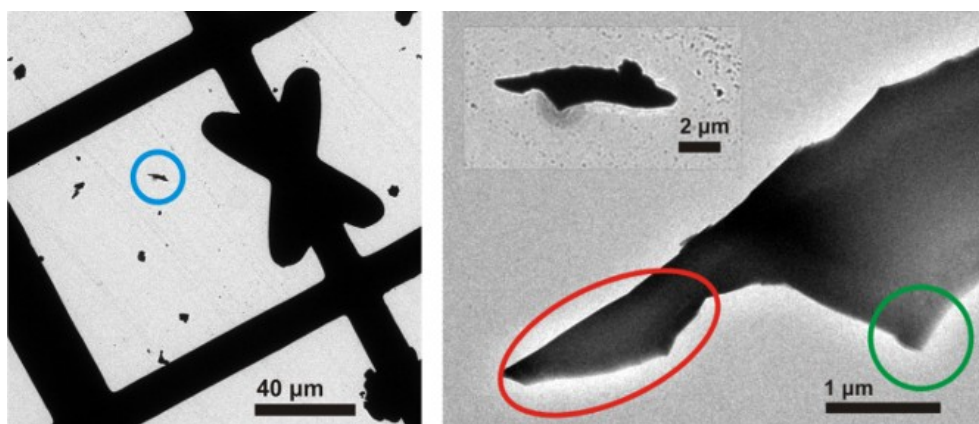


Fig 1: Bright-field image of the selected crystal (blue circle) and investigated areas of the microcrystal; green: for TEM, red: for microfocused synchrotron beam.

Indexing of the SAED patterns (Figure 2) leads to orthorhombic metrics with so far unknown lattice parameters ($a = 10.37$, $b = 19.1$, $c = 12.21$ Å). Further electron diffraction patterns along $[100]$, $[010]$, and $[001]$ confirm the orthorhombic metrics of $\text{La}_3\text{BaSi}_5\text{N}_9\text{O}_2$ and the reflection condition $h0l$: $h + l = 2n$ for a (010) n -glide plane is fulfilled.

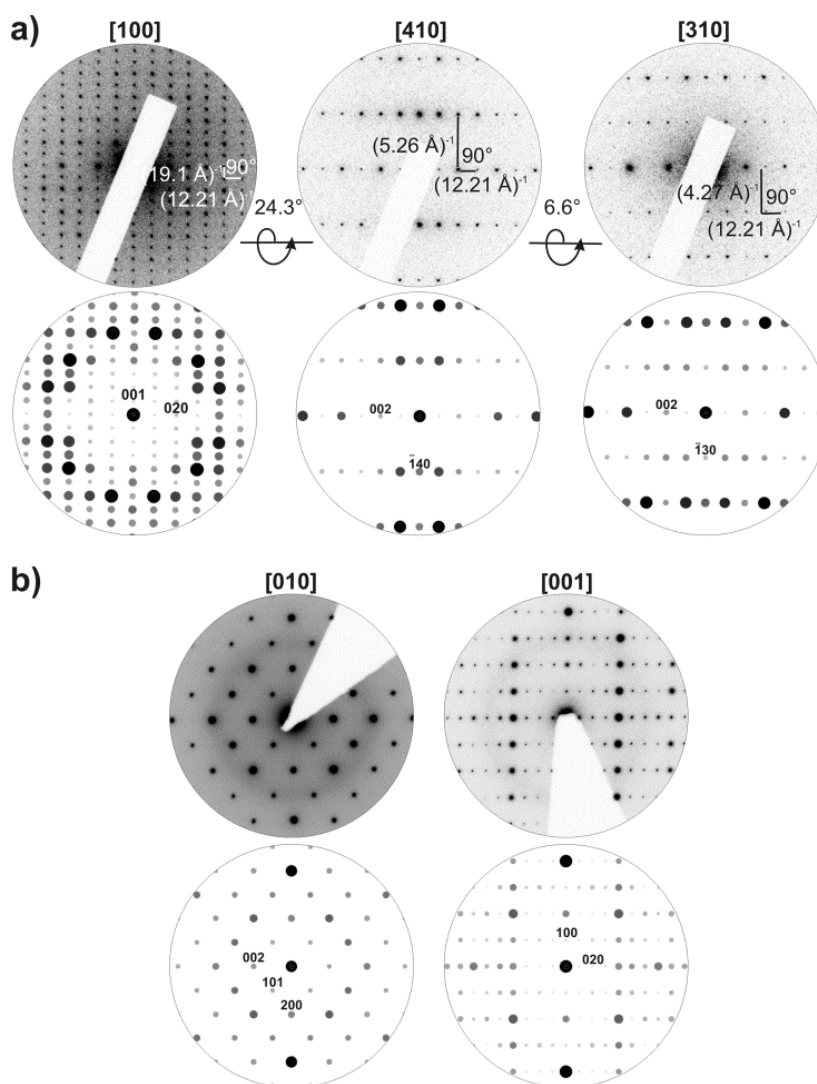


Fig. 2: (a) SAED tilt series (maximum deviation between experimental and simulated tilt angles 1.5°) of the $\text{La}_3\text{BaSi}_5\text{N}_9\text{O}_2\text{:Ce}^{3+}$ microcrystal investigated by synchrotron radiation; experimental SAED pattern with some highlighted $1/d$ -values (top), simulated SAED patterns with selected reflections labeled with indices (bottom, selected reflections labeled with indices, kinematical intensities according to the final structure model), (b) experimental SAED patterns along $[010]$ and $[001]$ obtained from thin regions of different crystallites of $\text{La}_3\text{BaSi}_5\text{N}_9\text{O}_2\text{:Ce}^{3+}$ (top) and corresponding, simulated SAED patterns (bottom, selected reflections are labeled with indices).

Consequently, the selected crystal was investigated by microfocused radiation. The crystal structure was solved and refined in space group $Pmn2_1$. Inversion twinning had to be taken into account. The crystallographic data are summarized in Table 1, and the atomic parameters are given in the Supporting Information (Tables S1, S2).⁴³ Due to its insignificant contribution to the scattering density, Ce^{3+} was neglected in the refinement of the crystal structure as well as for bond-valence sum calculations (BVS) (Tables S3, S4). The distribution of La and Ba as well as of N and O is based on BVS calculations and EDX measurements and is explained in detail in the chapter on BVS calculations below.

Tab. 1: Crystallographic data of the single-crystal structure determination of $\text{La}_3\text{BaSi}_5\text{N}_9\text{O}_2$.

formula	$\text{La}_3\text{BaSi}_5\text{N}_9\text{O}_2$
crystal system	orthorhombic
space group	$Pmn2_1$ (no. 31)
lattice parameters / Å	$a = 9.5505(8)$, $b = 19.0778(16)$, $c = 12.1134(9)$
cell volume / Å ³	2207.1(3)
formula units per unit cell	8
density / g·cm ⁻³	5.132
μ / mm ⁻¹	2.045
T / K	298(2)
radiation / Å	synchrotron ($\lambda = 0.3351$)
F(000)	3008
ϑ range / °	$1.4 \leq \vartheta \leq 12.9$
independent reflections	5514 [$R_{\text{int}} = 0.0518$]
refined parameters	296
twin ratio	0.51(8)/ 0.49
goodness of fit	1.036
$R1$ (all data / for $F^2 > 2\sigma(F^2)$)	0.0357 / 0.0343
$wR2$ (all data / for $F^2 > 2\sigma(F^2)$)	0.0859 / 0.0848
$\Delta\rho_{\text{max}}$, $\Delta\rho_{\text{min}}$ (e·Å ⁻³)	1.841, -1.777

$\text{La}_3\text{BaSi}_5\text{N}_9\text{O}_2$ is characterized by a three-dimensional network of vertex-sharing Q^4 - and Q^2 -type $\text{SiN}_4/\text{SiN}_2\text{O}_2$ tetrahedra in the ratio of $Q^4/Q^2 = 4/1$ (Figure 3a). This leads to a degree of condensation $\kappa = n(\text{Si}):n(\text{N},\text{O}) = 0.45$. In the network, there are singly bridging $\text{N}^{[2]}$ atoms and terminal $\text{O}^{[1]}$ atoms. The absence of N–H groups was confirmed by FTIR spectroscopy (Figure S3). The SiN_4 tetrahedra form *sechser* rings, which are condensed to *zehner* rings. These *zehner* rings are interconnected by *dreier* rings, which are composed of two SiN_4 and one SiN_2O_2 tetrahedra (Figure 3a, 3c, 3d).^{44,45} Thus, although nitridosilicates with $\kappa < 0.5$ usually tend to form layered or less-condensed structures,⁴⁵ an interrupted three-dimensional network with *zehner* ring channels along [100] is formed (Figure 3b). An interrupted tetrahedra framework based on a degree of condensation smaller than 0.5 was also observed for $\text{M}_7\text{Si}_6\text{N}_{15}$ (M = La, Ce, Pr).⁴⁶ The unique topology of the network^{47,48} of $\text{La}_3\text{BaSi}_5\text{N}_9\text{O}_2$, keeping the 2-coordinated nodes forming the *dreier* rings, is represented by the point symbol $\{3.6^3.7^2\}_2\{3\}\{6^6\}_2$.

The Si–N [1.670(10)–1.773(8) Å] and Si–O [1.647(14)–1.709(14) Å] distances are in good agreement with comparable compounds, such as $\text{Sr}_2\text{Si}_5\text{N}_8$ [1.653(9)–1.786(5) Å]⁴⁹ and $\text{Pr}_2\text{Si}_2\text{O}_7$ [1.519–1.712 Å]⁵⁰ as well as with the sum of the ionic radii.⁵¹

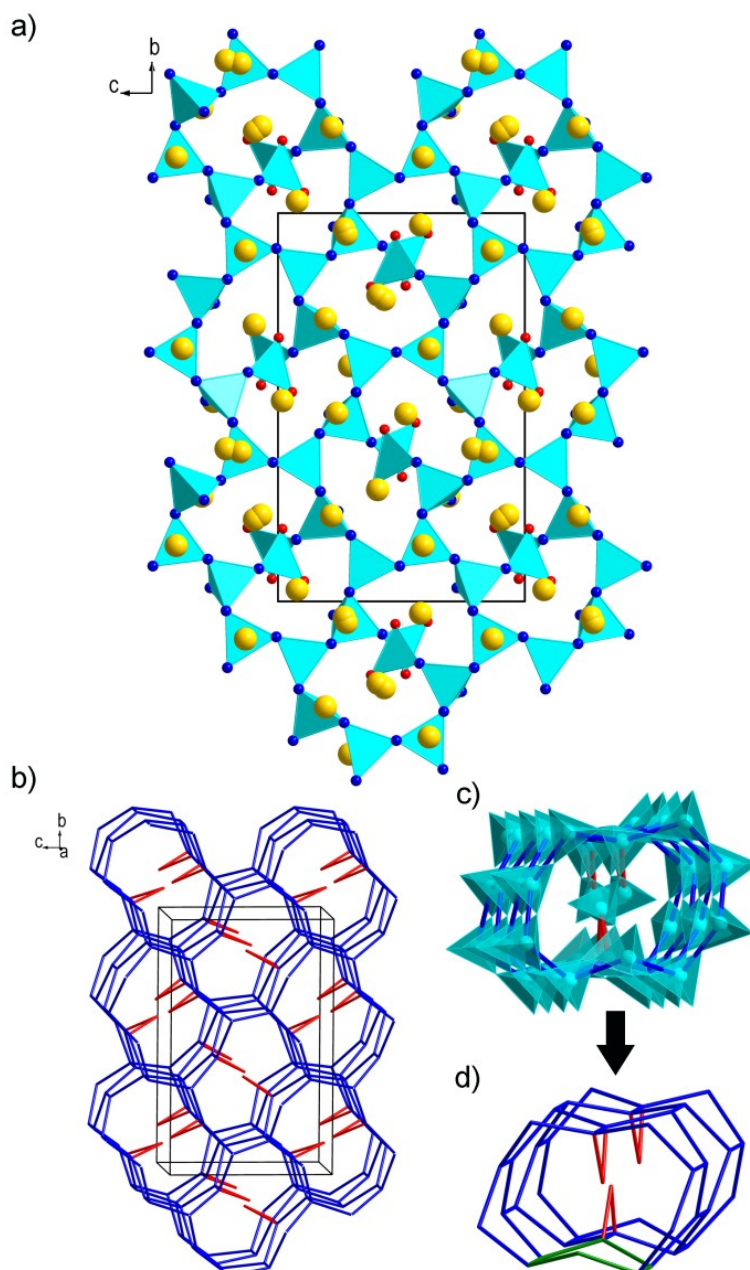


Fig. 3: (a) Structure of $\text{La}_3\text{BaSi}_5\text{N}_9\text{O}_2$ in projection along [100] with $\text{SiN}_4/\text{SiN}_2\text{O}_2$ tetrahedra (turquoise), N atoms (blue), O atoms (red), and La/Ba atoms (yellow), unit cell outlined in black; (b) topological representation of $\text{La}_3\text{BaSi}_5\text{N}_9\text{O}_2$, *zehner* rings are represented by blue and *dreier* rings by red lines. Each connecting line represents a Si–N–Si bond; (c,d) detailed representation of *zehner* rings (blue), which are condensed with *sechser* (d: green) and *dreier* (red) rings.

The crystal structure contains 12 crystallographically independent heavy-atom sites. Bond-valence sum calculations (see below and Tables S3, S4) suggest that all positions are mixed occupied with La and Ba. The sites La3/Ba3, La5/Ba5, and La9/Ba9 were described with split positions (each containing

La and Ba) with site occupation factors of 0.755(17): 0.244(17), 0.213(17): 0.286(17), and 0.039(2): 0.460(2), respectively. In order to maintain a charge neutral formula, the site occupation factors were fixed to ratios of 0.750:0.250, 0.215:0.285, and 0.040:0.460, respectively (see chapter on BVS calculations below). La1/Ba1–La4/Ba4, La5B/Ba5B, La7/Ba7, La10/Ba10, and La11/Ba11 are 8-fold coordinated by N^{3-} and O^{2-} . The sites La8/Ba8 and La9A/Ba9A are 8-fold coordinated by N^{3-} . For the sites La5A/Ba5A, La6/Ba6, La9B/Ba9B, and La12/Ba12 a coordination with nine anions is observed, whereas La6/Ba6, La9B/Ba9B, and La12/Ba12 are exclusively surrounded by N^{3-} and La5A/Ba5A is surrounded by N^{3-} and O^{2-} . All cations coordination spheres correspond to nonregular polyhedra (Figure 4). The bond lengths of La/Ba–N [2.419(12)–3.22(2) Å] and La/Ba–O [2.40(2)–2.908(19) Å] correspond to those in other lanthanum and barium compounds as well as to the sum of the ionic radii.^{51–54} A Rietveld refinement based on powder X-ray diffraction data (Figure S2) shows that the sample is composed of 93% $\text{La}_3\text{BaSi}_5\text{N}_9\text{O}_2$ and 7% LaSi_3N_5 . In addition, there are a few weak reflections which cannot be ascribed to any known compound. The refinement also confirms the structure determined by single-crystal structure analysis.

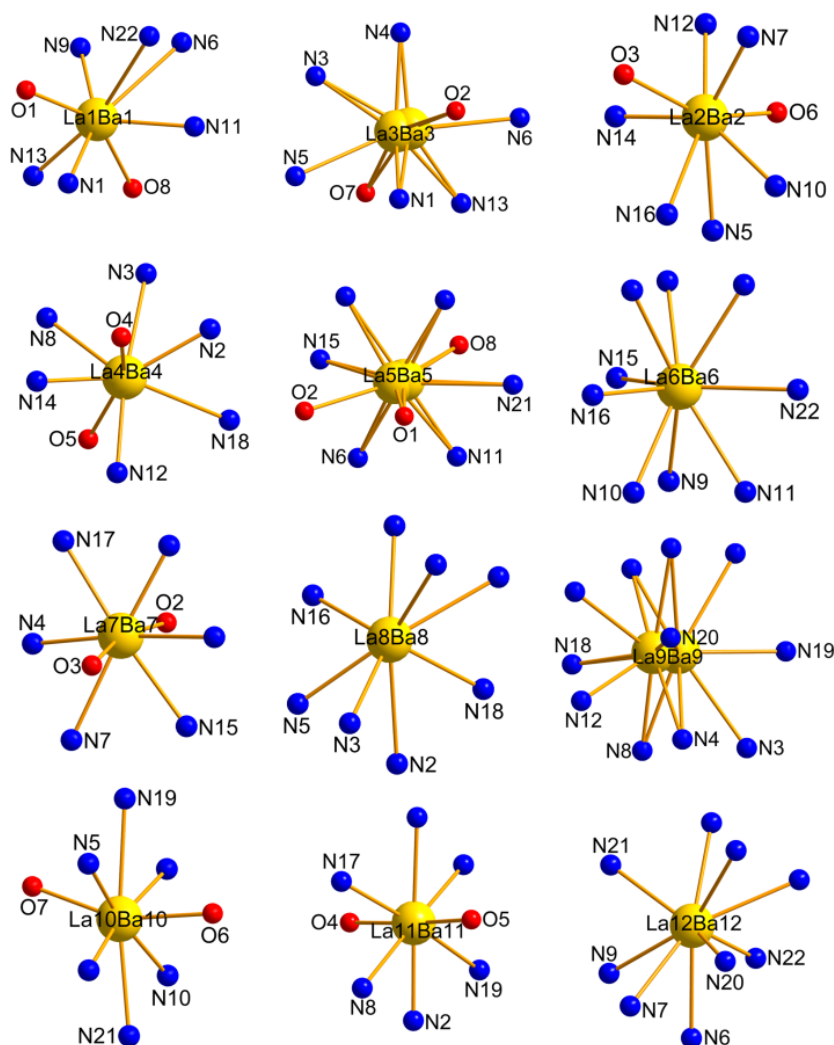


Fig. 4: Coordination spheres of the heavy-atom sites in $\text{La}_3\text{BaSi}_5\text{N}_9\text{O}_2$.

2.2.3.3 Bond-valence sum calculations

Due to the very similar scattering factors of La and Ba, it is impossible to distinguish these atoms by X-ray diffraction. The same is true concerning the differentiation between N and O. Moreover, charge neutrality could be maintained by arbitrary exchange of LaO and BaN units. Thus, BVS calculations were performed to determine the cation site occupancies.⁵⁵ The calculations were based on the fact that terminal anion positions would preferentially be occupied by O rather than by N (Pauling's rules),⁵⁶ whereas all other light-atom sites were assumed to be occupied by N. The validity of this assumption is corroborated by EDX measurements, which leads to a comparable ratio of N and O. On the basis of this assumption, the BVS of the cations were determined (Table S3, S4). Thereby, the BVS of each heavy atom site was determined for La as well as for Ba. Optimizing the weighted average BVS for each site so that it corresponds to the site valence⁵⁵ yielded to the relative occupation of the heavy-atom sites. This calculation led to a sum formula with 0.14 negative excess charges. These were evenly distributed over all heavy atoms sites by adjusting the site occupancies in order to achieve a neutral formula. The negligible deviation between the refined and fixed site occupation factors as well as between the oxidation states and the BVS of the heavy atom sites that was achieved by this strategy confirms that the structure model is consistent (Table S4). Additionally, the La/Ba ratio is also corroborated by EDX measurements.

2.2.3.4 Electron microscopy

Simulations of HRTEM images along [001] based on the structure model of $\text{La}_3\text{BaSi}_5\text{N}_9\text{O}_2$ obtained by X-ray structure refinement are consistent with the experimental images (Figure 5).

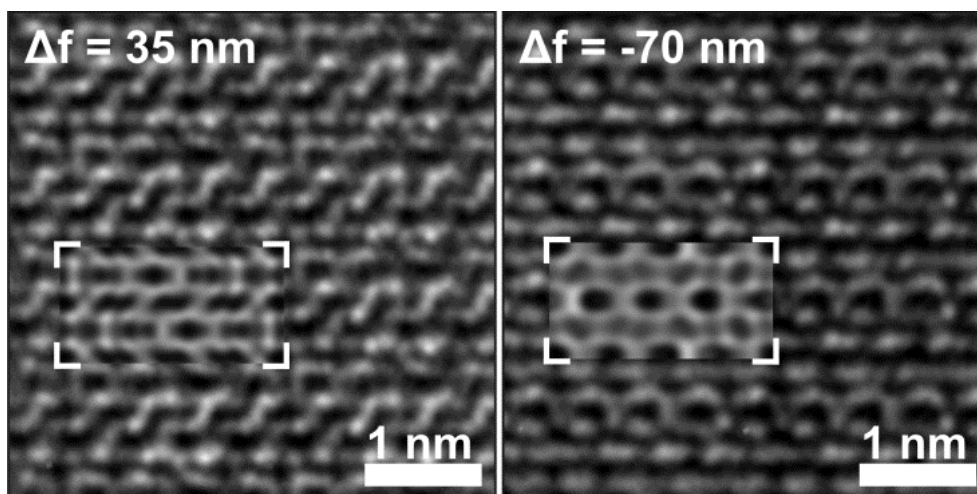


Fig. 5: Fourier filtered HRTEM images along [001] with different defocus values Δf , insets: simulated images in the size of one unit cell (multislice method,³⁰ $C_s = 0.6$ nm, spread of focus = 3.6 nm, beam semiconvergence = 25 mrad, layer thickness ~ 25 nm).

This is supported by STEM-HAADF images along [001]. Real structure effects were also observed, e.g. an antiphase boundary along $\langle 010 \rangle$ specified by an antiphase vector $p = 1/4b$ (Figure 6). Due to the large difference of the atomic numbers in $\text{La}_3\text{BaSi}_5\text{N}_9\text{O}_2$, only the heavy atoms La and Ba are visible in STEM-HAADF images.

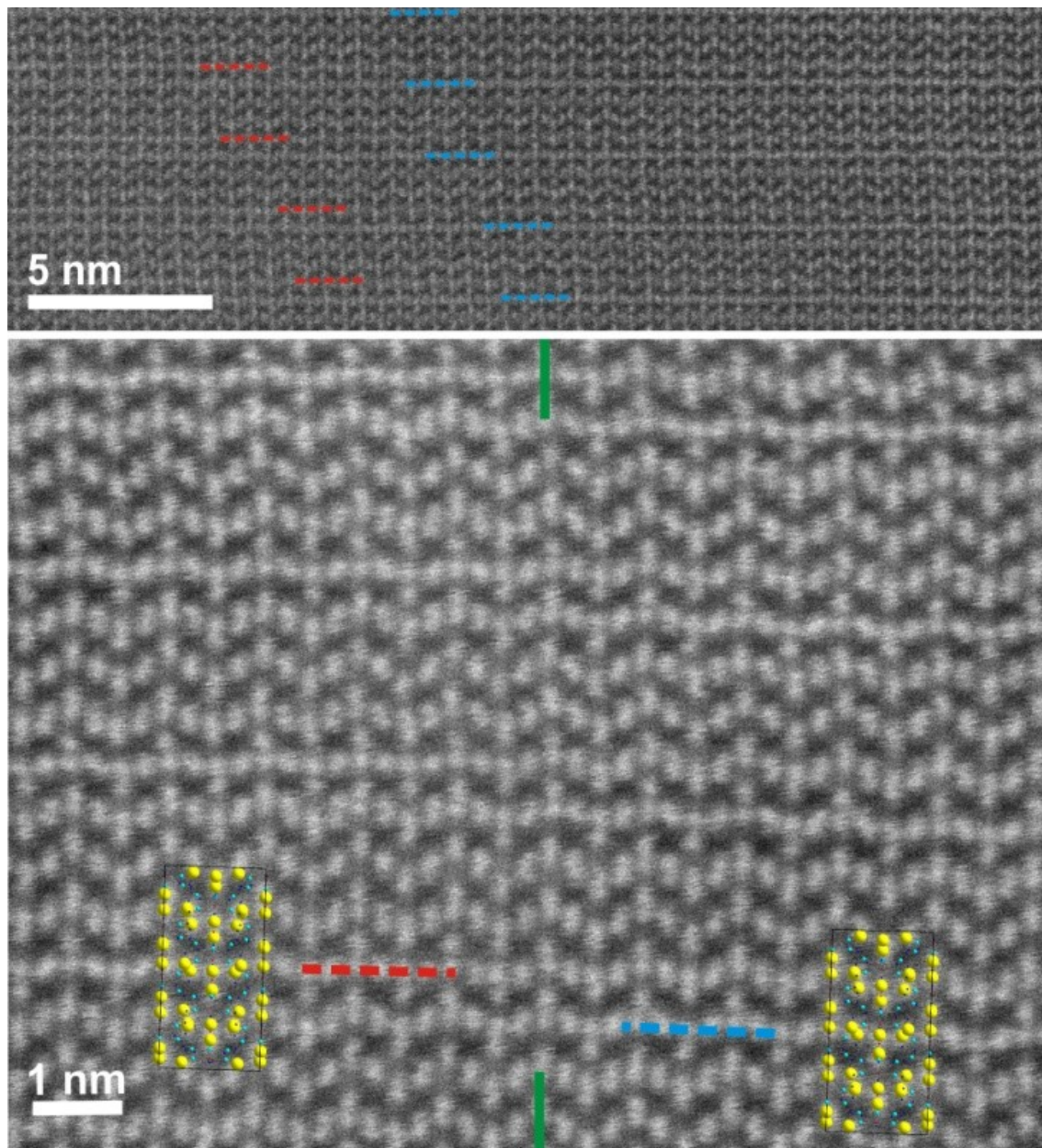


Fig. 6: STEM-HAADF images along [001] at different magnifications with structure projections (unit cell contents) of $\text{La}_3\text{BaSi}_5\text{N}_9\text{O}_2$, antiphase boundary highlighted with green lines and domain positions visualized by red and blue lined.

2.2.3.5 Luminescence

Luminescence measurements were performed on isolated aggregates of $\text{La}_3\text{BaSi}_5\text{N}_9\text{O}_2:\text{Ce}^{3+}$ (2 mol % Ce^{3+} , nominal composition). All particles show comparable yellow emission under irradiation with blue light. Exemplary emission and excitation spectra are depicted in Figure 7. Excitation at 440 nm yields an emission spectrum with the characteristic broadband emission of the $5d-4f$ transition of Ce^{3+} . The emission band peaks at 578 nm with a fwhm of ~ 167.4 nm (~ 4700 cm^{-1}) and CIE (Commission Internationale de l'Éclairage) color coordinates of $x = 0.464$ and $y = 0.493$. The excitation spectrum shows a broad band with maximum intensity at approximately 385–455 nm, thus the material can be excited very well by blue light as originating from a (Ga,In) N-LED.

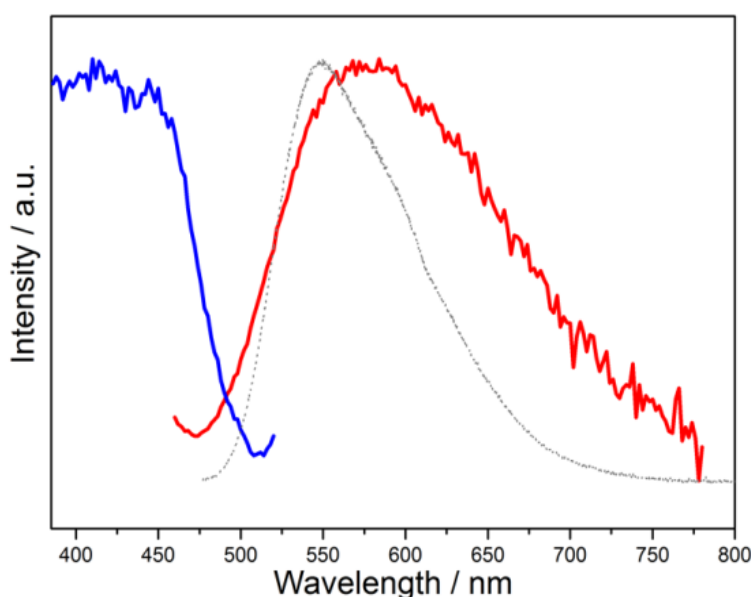


Fig. 7: Excitation (blue) and emission (red) spectra of $\text{La}_3\text{BaSi}_5\text{N}_9\text{O}_2:\text{Ce}^{3+}$ in comparison to the emission of a $\text{YAG}:\text{Ce}^{3+}$ sample (gray).

Emissions comparable to $\text{La}_3\text{BaSi}_5\text{N}_9\text{O}_2:\text{Ce}^{3+}$ are also observed by other industrially applied LED phosphor materials such as $(\text{La,Ca})_3\text{Si}_6\text{N}_{11}:\text{Ce}^{3+}$ ($\lambda_{\text{em}} = 577\text{--}581$ nm; fwhm ~ 3800 cm^{-1}),¹⁸ $\text{CaAlSiN}_3:\text{Ce}^{3+}$ ($\lambda_{\text{em}} = 580$ nm; fwhm ~ 3900 cm^{-1}),⁵⁷ and $\text{YAG}:\text{Ce}^{3+}$ ($\lambda_{\text{em}} = 550\text{--}570$ nm; fwhm ~ 3700 cm^{-1}).⁵⁸ These compounds as well as $\text{La}_3\text{BaSi}_5\text{N}_9\text{O}_2:\text{Ce}^{3+}$ show a relatively broad emission with double band shape as the $4f^1$ ground state configuration of Ce^{3+} yields two levels separated by approximately 2000 cm^{-1} .⁵⁹ Compared to the emission of $\text{YAG}:\text{Ce}^{3+}$ (Figure 7, $\lambda_{\text{em}} = 550$ nm; fwhm ~ 2994 cm^{-1} , $x = 0.432$ and $y = 0.549$) $\text{La}_3\text{BaSi}_5\text{N}_9\text{O}_2:\text{Ce}^{3+}$ shows a red-shifted and a markedly broader emission, so that a broader color range can be covered. Both aspects lead to a warmer color temperature under excitation with blue light. The warmer color temperature is also proven by the CIE diagram (Figure 8). The color coordinates of $\text{La}_3\text{BaSi}_5\text{N}_9\text{O}_2:\text{Ce}^{3+}$ and $\text{YAG}:\text{Ce}^{3+}$ are positioned in the yellow spectral range. The combination with a 450 nm InGaN LED yields white 1pc-LEDs, whereas the

combination with $\text{La}_3\text{BaSi}_5\text{N}_9\text{O}_2:\text{Ce}^{3+}$ leads to a crossing of the blackbody curve at a warmer correlated color temperature (~ 4000 K) than that with $\text{YAG}:\text{Ce}^{3+}$ (~ 10000 K). The broad emission spectrum of $\text{La}_3\text{BaSi}_5\text{N}_9\text{O}_2:\text{Ce}^{3+}$ most likely originates from the superposition of light emitted from multiple chemically different sites.⁶⁰ Moreover the asymmetric coordination of the sites might increase the width of the emission, as asymmetric dopant site environment leads to stronger structural relaxation around the activator in its excited state and consequently to a broad, red-shifted emission.⁶⁰ Since $\text{La}_3\text{BaSi}_5\text{N}_9\text{O}_2:\text{Ce}^{3+}$ shows a large number of different substitutable sites, which are additionally asymmetrically coordinated (Figure 4), its host lattice is especially suitable for broad band emission.

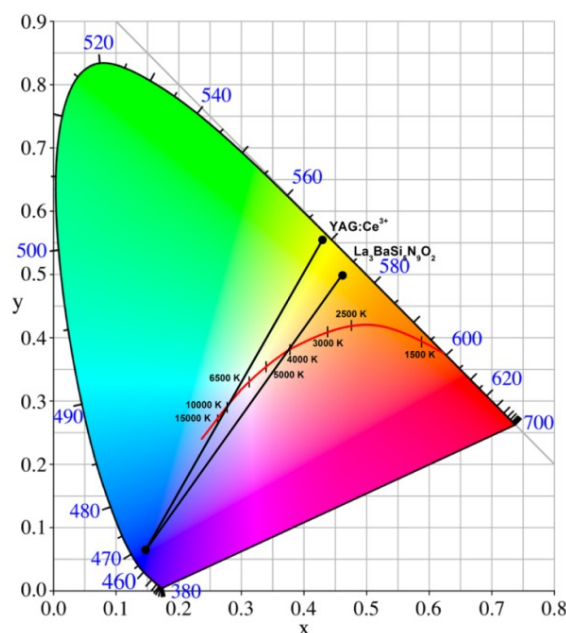


Fig. 8: CIE 1931 chromaticity diagram showing the color coordinates of $\text{La}_3\text{BaSi}_5\text{N}_9\text{O}_2:\text{Ce}^{3+}$ and the $\text{YAG}:\text{Ce}^{3+}$ sample.

2.2.4 Conclusion

The lanthanum barium nitridosilicate $\text{La}_3\text{BaSi}_5\text{N}_9\text{O}_2:\text{Ce}^{3+}$ could be obtained from reactive starting materials. It exhibits a new type of interrupted tetrahedra network and shows intense yellow emission under irradiation of blue light. Compared to $\text{YAG}:\text{Ce}^{3+}$, the emission yields a warmer color temperature. This synthesis approach might offer an intriguing way to new lanthanum nitridosilicates, which might have potential as phosphors for pc-LEDs.

By combination of TEM and synchrotron microfocus diffraction, it was possible to analyze the small crystals of $\text{La}_3\text{BaSi}_5\text{N}_9\text{O}_2:\text{Ce}^{3+}$, which occur as aggregates of crystals with a maximum size of only a few μm . Compared with other methods for micro- or nanocrystal analysis like ADT and RED, this approach allows for a precise structure refinement, which e.g. clearly reveals split positions and

renders data suitable for BVS calculations. Consequently, this method is a powerful tool for the analysis of single particles of new promising phosphors, even with complicated structures not accessible by powder X-ray diffraction or conventional single-crystal measurements. With a detailed knowledge of their structures, it might be possible to draw conclusions about the relation between structures and properties which is necessary for a systematic tuning of the luminescence properties. Moreover, the information on the crystal structures could probably accelerate the development of syntheses to phase-pure samples. Both aspects could help to push forward the research of phosphor materials for LEDs.

2.2.5 References

- 1 J. Heber, *Nat. Phys.* **2014**, *10*, 791.
- 2 E. F. Schubert, J. -K. Kim, *Science* **2005**, *308*, 1274.
- 3 M. S. Shur, A. Zukauskas, *Proc. IEEE* **2005**, *93*, 1691.
- 4 Y. Narukawa, J. Narita, T. Sakamoto, T. Yamada, H. Narimatsu, M. Sano, T. Mukai, *Phys. Status Solidi A* **2007**, *204*, 2087.
- 5 J. Y. Tsao, M. E. Coltrin, M. H. Crawford, J. A. Simmons, *Proc. IEEE* **2010**, *98*, 1162.
- 6 A. A. Setlur, *Electrochem. Soc. Interf.* **2009**, *18*, 32.
- 7 D. J. Robbins, *T J. Electrochem. Soc.* **1979**, *126*, 1550.
- 8 M. Zeuner, S. Pagano, W. Schnick, *Angew. Chem.* **2011**, *123*, 7898; *Angew. Chem., Int. Ed.* **2011**, *50*, 7754.
- 9 R. Müller-Mach, G. Müller, M. R. Krames, H. A. Höppe, F. Stadler, W. Schnick, T. Jüstel, P. Schmidt, *Phys. Status Solidi A* **2005**, *202*, 1727.
- 10 Y. Q. Li, J. E. J. van Steen, J. W. H. van Krevel, G. Botty, A. C. A. Delsing, F. J. DiSalvo, G. de With, H. T. Hintzen, *J. Alloys Compd.* **2006**, *417*, 273.
- 11 M. R. Krames, G. O. Müller, R. B. Müller-Mach, H.-H. Bechtel, P. J. Schmidt, *WO 2010131133A1*, **2010**.
- 12 H. A. Höppe, H. Lutz, P. Morys, W. Schnick, A. Seilmeier, *J. Phys. Chem. Solids*, **2000**, *61*, 2001.
- 13 R. -J. Xie, N. Hirotsaki, K. Sakuma, Y. Yamamoto, M. Mitomo, *Appl. Phys. Lett.* **2004**, *84*, 5404.
- 14 R. -J. Xie, N. Hirotsaki, M. Mitomo, Y. Yamamoto, T. Suehiro, K. Sakuma, *J. Phys. Chem. B* **2004**, *108*, 12027.
- 15 K. Uheda, N. Hirotsaki, H. Yamamoto, *Phys. Status Solidi A* **2006**, *203*, 2712.
- 16 K. Uheda, N. Hirotsaki, Y. Yamamoto, A. Naito, T. Nakajima, H. Yamamoto, *Electrochem. Solid-State Lett.* **2006**, *9*, H22.
- 17 S. Schmichen, P. Pust, P. J. Schmidt, W. Schnick, *Nachr. Chem.* **2014**, *62*, 847.
- 18 T. Suehiro, N. Hirotsaki, R. -J. Xie, *Appl. Mater. Interfaces*, **2011**, *3*, 811.
- 19 N. Hirotsaki, T. Takeda, S. Funahashi, R. -J. Xie, *Chem. Mater.* **2014**, *26*, 4280.

- 20 F. Fahrnbauer, T. Rosenthal, T. Schmutzler, G. Wagner, G. Vaughan, J. Wright, O. Oeckler, *Angew. Chem.* **2015**, 127, 10158; *Angew. Chem. Int. Ed.*, 2015, **54**, 10020.
- 21 U. Kolb, T. Gorelik, C. Kübel, M. T. Otten, D. Hubert, *Ultramicroscopy* **2007**, 107, 507.
- 22 U. Kolb, T. Gorelik, M. T. Otten, *Ultramicroscopy* **2008**, 108, 763.
- 23 E. Mugnaioli, T. Gorelik, U. Kolb, *Ultramicroscopy* **2009**, 109, 758.
- 24 U. Kolb, E. Mugnaioli, T. Gorelik, *Cryst. Res. Technol.* **2011**, 46 542.
- 25 D. Zhang, P. Oleynikov, S. Hovmöller, X. Zou, Z. Kristallogr. **2010**, 225, 94.
- 26 C. Hadenfeldt, B. Gieger, H. Jacobs, Z. Anorg. Allg. Chem. **1974**, 410, 104.
- 27 H. Lange, G. Wötting, G. Winter, *Angew. Chem.* **1991**, 103, 1625; *Angew. Chem. Int. Ed.* **1991**, 30, 1579.
- 28 W. Schnick, H. Huppertz, R. Lauterbach, *J. Mater Chem.* **1999**, 9, 289.
- 29 Digital Micrograph, v3.6.1, *Gatan Software Team*, Pleasanton, USA, **1999**.
- 30 Stadelmann, P. A., *JEMS*, v3.3425U2008, CIME-EPFL, Switzerland, **1999 – 2008**.
- 31 ES Vision, v4.0.164, *Emispec Systems Inc.*, Tempe, USA, **1994 – 2002**.
- 32 TEAM, v3.4.1, *EDAX AMETEK*, Wiesbaden, Germany, **2013**.
- 33 J. C. Labiche, O. Mathon, S. Pascarelli, M. A. Newton, G. G. Ferre, C. Curfs, G. Vaughan, A. Homs, D. F. Carreiras, *Rev. Sci. Instrum.* **2007**, 78, 091301.
- 34 G. Vaughan, J. P. Wright, A. Bytchkov, C. Curfs, C. Grundlach, M. Orlova, L. Erra, H. Gleyzolle, T. Buslaps, A. Götz, G. Suchet, S. Petitdemange, M. Rossat, L. Margulies, W. Ludwig, A. Snigirey, I. Snigireva, H. O. Sorensen, E. M. Lauridsen, U. L. Olsen, J. Oddershede, H. F. Poulsen, *Science* **2010**, 457.
- 35 J. L. Chambers, K. L. Smith, M. R. Pressprich, Z. Jin, *SMART*, v.5.059, *Bruker AXS*, Madison, USA, 1997–98.
- 36 Bruker AXS, *SAINT*, v. 6.36A, Madison, USA, **1997–2002**.
- 37 G. M. Sheldrick, *SADABS*, v. 2: *Multi-Scan Absorption Correction*; *Bruker-AXS: WA*, **2012**.
- 38 G. Wu, B. L. Rodrigues, P. Coppens, *J. Appl. Crystallogr.* **2002**, 35, 356.
- 39 G. M. Sheldrick, *Acta Crystallogr., Sect. A* **2008**, 64, 112.
- 40 Stoe & Cie GmbH, *WINXPOW*, v. 2.21; Darmstadt, Germany, **2007**.
- 41 A. Coelho, *TOPAS*, v. 4.1, *Coelho Software*; **2007**.
- 42 W. Grochala, P. Edwards, *Chem. Rev.* **2004**, 104, 1283.
- 43 Further details of the crystal structure investigation can be obtained from the Fachinformations-Zentrum Karlsruhe, 76344 Eggenstein-Leopoldshafen, Germany (fax: (+49)7247–808–666; e-mail: crysdata@fiz-karlsruhe.de) on quoting the depository number CSD– 429510.
- 44 F. Liebau, Springer: Berlin, **1985**.
- 45 The term *dreier* (*sechser*, *zehner*) ring was coined by Liebau and is derived from the German word “dreier” (“sechser”, “zehner”); a *dreier* (*sechser*, *vierer*) ring comprised three (six, ten) tetrahedra centers.
- 46 C. Schmolke, O. Oeckler, D. Bichler, D. Johrendt, W. Schnick, *Chem. Eur. J.* **2009**, 15, 9215
- 47 V. A. Blatov, M. O’Keeffe, D. M. Proserpio, *Cryst. Eng. Comm.* **2010**, 12, 44.
- 48 V. A. Blatov, *IUCr Comp. Comm Newsletter* **2006**, 7, 4.

- 49 T. Schlieper, W. Milius, W. Schnick, *Z. Anorg. Allg. Chem.* **1995**, 621, 1380.
- 50 J. Feschle, *Z. Kristallogr.* **1971**, 133, 364.
- 51 R. D. Shannon, *Acta Crystallogr. Sect. A.* **1976**, 32, 751.
- 52 C. Schmolke, S. Lupart, W. Schnick, *Solid State Sci.* **2009**, 11, 305.
- 53 H. Katscher, G. Bissert, F. Liebau, *Z. Kristallogr.* **1973**, 137, 146.
- 54 A. C. Tas, M. Akinc, *J. Am. Ceram. Soc.* **1994**, 77, 2968.
- 55 A. S. Wills, *VaList*, v. 4.0.7; University College London: UK, 2010.
- 56 P. E. D. Morgan, *J. Mater. Sci.* **1986**, 21, 4305.
- 57 Y. Q. Li, N. Hirosaki, R.-J. Xie, T. Takeda, M. Mitomo, *Mater. Chem. Mater.* **2008**, 20, 6704.
- 58 T. Moriguchi, Y. Noguchi, K. Sakanao, Y. Shimizu, *US 5998925 A*, **1997**.
- 59 G. Blasse, B. C. Grabmaier, Springer: Berlin; Heidelberg, NY, **1994**.
- 60 A. Meijerink G. Blasse, *J. Lumin.* **1989**, 43, 283.

2.2.6 Supporting Information

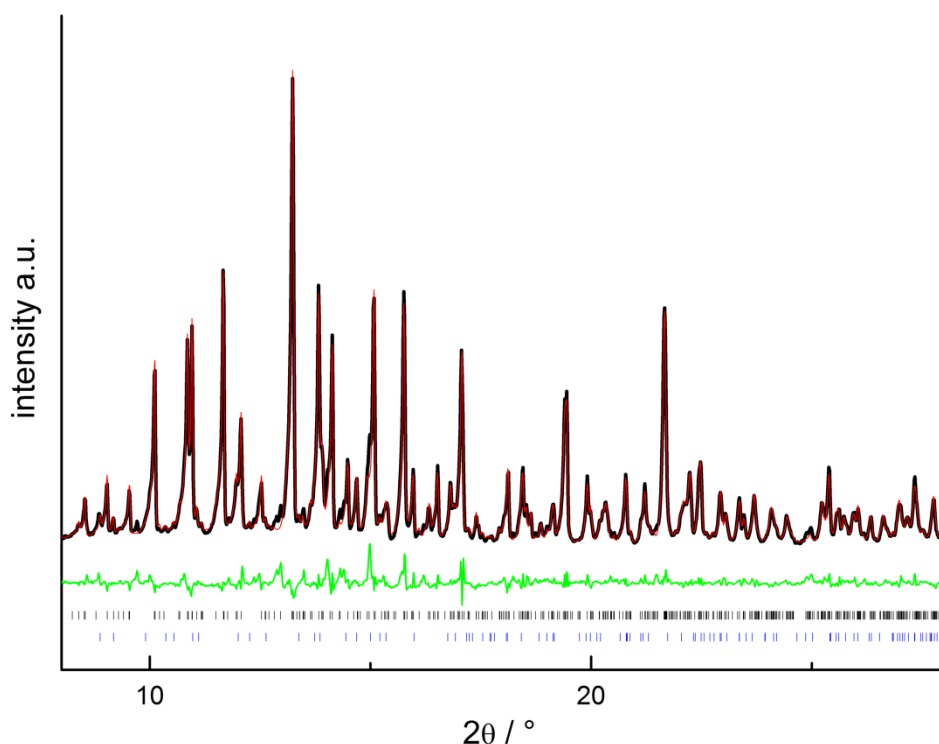


Fig. S1: Characteristic section of the Rietveld profile fit for a sample of $\text{La}_3\text{BaSi}_5\text{N}_9\text{O}_2$: observed (black line) and calculated (red line) powder diffraction pattern as well as position of Bragg reflections (black: $\text{La}_3\text{BaSi}_5\text{N}_9\text{O}_2$ (93%), blue: LaSi_3N_5 (7%)) and difference profile (green line).

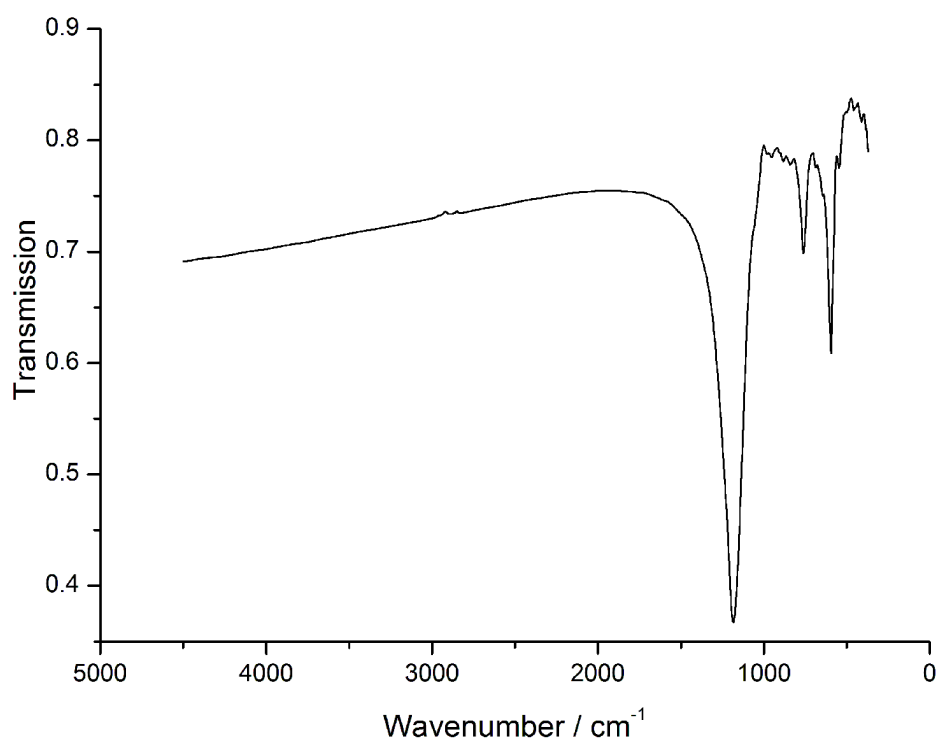


Fig. S2: IR spectrum of the sample whose powder pattern is shown in Figure S1.

2.2 $\text{La}_3\text{BaSi}_5\text{N}_9\text{O}_2\text{:Ce}^{3+}$ – A yellow phosphor with an unprecedented tetrahedra network; structure investigated by combination of electron microscopy and synchrotron X-ray diffraction

Table S3: Atomic coordinates, site occupancies and isotropic (for O/N) or equivalent isotropic atomic displacement parameters (for Si/La/Ba) of $\text{La}_3\text{BaSi}_5\text{N}_9\text{O}_2$ (in \AA^2) with standard deviations in parentheses.

atom		x	y	z	$U_{\text{iso}}/U_{\text{eq}}$	s.o.f.
La1	4b	0.22420(8)	0.03047(4)	0.92256(6)	0.00950(16)	0.9144
Ba1	4b	0.22420(8)	0.03047(4)	0.92256(6)	0.00950(16)	0.0856
La2	4b	0.22608(7)	0.28788(3)	0.59655(6)	0.00728(15)	0.9544
Ba2	4b	0.22608(7)	0.28788(3)	0.59655(6)	0.00728(15)	0.0456
La3A	4b	0.2717(2)	0.21079(9)	0.09552(13)	0.0113(3)	0.5433
Ba3A	4b	0.2717(2)	0.21079(9)	0.09552(13)	0.0113(3)	0.2067
La3B	4b	0.2725(8)	0.2223(4)	0.0692(5)	0.0113(3)	0.1936
Ba3B	4b	0.2725(8)	0.2223(4)	0.0692(5)	0.0113(3)	0.0564
La4	4b	0.27890(8)	0.48297(4)	0.48236(6)	0.00865(16)	0.9044
Ba4	4b	0.27890(8)	0.48297(4)	0.48236(6)	0.00865(16)	0.0956
La5A	2a	0	0.0542(6)	0.2231(14)	0.0071(10)	0.3459
Ba5A	2a	0	0.0542(6)	0.2231(14)	0.0071(10)	0.0841
La5B	2a	0	0.0402(4)	0.2316(10)	0.0071(10)	0.4585
Ba5B	2a	0	0.0402(4)	0.2316(10)	0.0071(10)	0.1115
La6	2a	0	0.09669(6)	0.63200(9)	0.0115(2)	0.2344
Ba6	2a	0	0.09669(6)	0.63200(9)	0.0115(2)	0.7656
La7	2a	0	0.27154(5)	0.30800(8)	0.0092(2)	0.8344
Ba7	2a	0	0.27154(5)	0.30800(8)	0.0092(2)	0.1656
La8	2a	0	0.34883(5)	0.88810(12)	0.0175(3)	0.4544
Ba8	2a	0	0.34883(5)	0.88810(12)	0.0175(3)	0.5456
La9A	2a	0	0.6070(7)	0.7095(16)	0.0141(3)	0.0403
Ba9A	2a	0	0.6070(7)	0.7095(16)	0.0141(3)	0.0396
La9B	2a	0	0.61423(6)	0.65333(12)	0.0141(3)	0.1788
Ba9B	2a	0	0.61423(6)	0.65333(12)	0.0141(3)	0.7412
La10	2a	0	0.77904(5)	0.28360(8)	0.0097(2)	0.8244
Ba10	2a	0	0.77904(5)	0.28360(8)	0.0097(2)	0.1756
La11	2a	0	0.51509(5)	0.26193(8)	0.00816(19)	0.9344
Ba11	2a	0	0.51509(5)	0.26193(8)	0.00816(19)	0.0656
La12	2a	0	0.85597(5)	0.91257(8)	0.00748(19)	0.6744
Ba12	2a	0	0.85597(5)	0.91257(8)	0.00748(19)	0.3256
Si1	4b	0.1636(3)	0.20837(14)	0.8093(2)	0.0050(5)	1
Si2	4b	0.1757(3)	0.38100(15)	0.1514(2)	0.0051(5)	1
Si3	4b	0.1769(3)	0.64476(14)	0.3985(3)	0.0053(5)	1
Si4	4b	0.1808(3)	0.14229(14)	0.4051(3)	0.0053(5)	1
Si5	4b	0.3227(3)	0.09717(15)	0.6405(3)	0.0050(5)	1
Si6	4b	0.3359(3)	0.29008(15)	0.3446(3)	0.0058(5)	1
Si7	4b	0.3368(3)	0.53404(14)	0.2322(3)	0.0047(5)	1
Si8	4b	0.3377(3)	0.05057(15)	0.2084(2)	0.0054(5)	1
Si9	2a	0	0.1457(2)	0.0003(4)	0.0073(8)	1
Si10	2a	0	0.4030(2)	0.5446(3)	0.0049(8)	1
Si11	2a	0	0.6385(2)	0.0144(3)	0.0056(8)	1
Si12	2a	0	0.8995(2)	0.5091(4)	0.0088(8)	1
N1	4b	0.1479(11)	0.1594(5)	0.9263(8)	0.0099(18)	1
N2	4b	0.2275(10)	0.5678(5)	0.3317(8)	0.0080(17)	1
N3	4b	0.2315(14)	0.3581(7)	0.0208(12)	0.025(3)	1
N4	4b	0.2360(10)	0.3120(5)	0.2323(9)	0.0092(18)	1
N5	4b	0.2401(12)	0.7167(5)	0.3283(10)	0.013(2)	1
N6	4b	0.2425(14)	0.1089(7)	0.2843(11)	0.023(2)	1
N7	4b	0.2472(11)	0.2257(5)	0.4161(9)	0.0106(18)	1
N8	4b	0.2491(11)	0.4614(5)	0.1836(9)	0.012(2)	1
N9	4b	0.2552(11)	0.0912(5)	0.5071(8)	0.0093(18)	1
N10	4b	0.2583(11)	0.1707(5)	0.7051(9)	0.0098(18)	1
N11	4b	0.2646(11)	0.0242(5)	0.7107(9)	0.0110(19)	1
N12	4b	0.3496(11)	0.3583(5)	0.4388(8)	0.0094(18)	1
N13	4b	0.3520(10)	0.0843(5)	0.0779(8)	0.0100(18)	1
N14	4b	0.3537(10)	0.5900(5)	0.1222(8)	0.0088(17)	1
N15	2a	0	0.1423(7)	0.4073(13)	0.013(3)	1
N16	2a	0	0.2321(7)	0.7564(12)	0.013(3)	1
N17	2a	0	0.3861(7)	0.1695(13)	0.014(3)	1
N18	2a	0	0.4830(6)	0.7935(11)	0.007(2)	1
N19	2a	0	0.6470(8)	0.4111(15)	0.020(3)	1
N20	2a	0	0.7388(6)	0.7994(11)	0.006(2)	1
N21	2a	0	0.8956(7)	0.1313(13)	0.014(3)	1
N22	2a	0	0.9648(7)	0.7753(13)	0.013(3)	1
O1	2a	0	0.0582(6)	0.0247(10)	0.012(2)	1
O2	2a	0	0.1899(7)	0.1230(11)	0.021(3)	1
O3	2a	0	0.3211(6)	0.4971(10)	0.011(2)	1
O4	2a	0	0.4607(7)	0.4436(12)	0.019(3)	1
O5	2a	0	0.5571(6)	0.0686(10)	0.011(2)	1
O6	2a	0	0.6995(6)	0.1159(10)	0.015(2)	1
O7	2a	0	0.8132(7)	0.4828(12)	0.019(3)	1
O8	2a	0	0.9477(8)	0.3948(13)	0.027(3)	1

Table S4: Anisotropic displacement parameters (U_{ij} , in \AA^2) (for Si/La/Ba) of $\text{La}_3\text{BaSi}_5\text{N}_9\text{O}_2$.

atom	U_{11}	U_{22}	U_{33}	U_{23}	U_{13}	U_{12}
La1	0.0085(4)	0.0110(3)	0.0089(3)	-0.0012(3)	-0.0003(3)	0.0007(2)
Ba1	0.0085(4)	0.0110(3)	0.0089(3)	-0.0012(3)	-0.0003(3)	0.0007(2)
La2	0.0081(3)	0.0089(3)	0.0049(3)	0.0015(2)	0.0010(3)	0.0014(2)
Ba2	0.0081(3)	0.0089(3)	0.0049(3)	0.0015(2)	0.0010(3)	0.0014(2)
La3A	0.0110(4)	0.0119(8)	0.0110(9)	-0.0043(5)	-0.0013(7)	0.0023(5)
Ba3A	0.0110(4)	0.0119(8)	0.0110(9)	-0.0043(5)	-0.0013(7)	0.0023(5)
La3B	0.0110(4)	0.0119(8)	0.0110(9)	-0.0043(5)	-0.0013(7)	0.0023(5)
Ba3B	0.0110(4)	0.0119(8)	0.0110(9)	-0.0043(5)	-0.0013(7)	0.0023(5)
La4	0.0089(3)	0.0099(3)	0.0072(3)	0.0033(2)	0.0002(3)	0.0005(2)
Ba4	0.0089(3)	0.0099(3)	0.0072(3)	0.0033(2)	0.0002(3)	0.0005(2)
La5A	0.0041(5)	0.011(3) 0	0.0068(18)	-0.001(2)	0	0
Ba5A	0.0041(5)	0.011(3) 0	0.0068(18)	-0.001(2)	0	0
La5B	0.0041(5)	0.011(3) 0	0.0068(18)	-0.001(2)	0	0
Ba5B	0.0041(5)	0.011(3) 0	0.0068(18)	-0.001(2)	0	0
La6	0.0071(5)	0.0163(5)	0.0110(4)	0.0022(4)	0	0
Ba6	0.0071(5)	0.0163(5)	0.0110(4)	0.0022(4)	0	0
La7	0.0047(5)	0.0133(4)	0.0095(4)	0.0048(4)	0	0
Ba7	0.0047(5)	0.0133(4)	0.0095(4)	0.0048(4)	0	0
La8	0.0064(5)	0.0105(4)	0.0356(7)	-0.0039(4)	0	0
Ba8	0.0064(5)	0.0105(4)	0.0356(7)	-0.0039(4)	0	0
La9A	0.0066(6)	0.0130(5)	0.0226(7)	-0.0018(5)	0	0
Ba9A	0.0066(6)	0.0130(5)	0.0226(7)	-0.0018(5)	0	0
La9B	0.0066(6)	0.0130(5)	0.0226(7)	-0.0018(5)	0	0
Ba9B	0.0066(6)	0.0130(5)	0.0226(7)	-0.0018(5)	0	0
La10	0.0039(5)	0.0160(4)	0.0091(4)	0.0001(3)	0	0
Ba10	0.0039(5)	0.0160(4)	0.0091(4)	0.0001(3)	0	0
La11	0.0049(4)	0.0131(4)	0.0065(4)	0.0024(3)	0	0
Ba11	0.0049(4)	0.0131(4)	0.0065(4)	0.0024(3)	0	0
La12	0.0050(5)	0.0098(4)	0.0076(4)	-0.0018(3)	0	0
Ba12	0.0050(5)	0.0098(4)	0.0076(4)	-0.0018(3)	0	0
Si1	0.0037(14)	0.0070(12)	0.0043(12)	0.0000(10)	-0.0004(11)	-0.0009(9)
Si2	0.0028(14)	0.0088(12)	0.0038(13)	0.0007(9)	-0.0004(10)	-0.0001(10)
Si3	0.0043(14)	0.0073(12)	0.0042(13)	-0.0004(9)	-0.0007(11)	0.0009(10)
Si4	0.0039(14)	0.0065(11)	0.0056(13)	-0.0003(9)	-0.0001(11)	0.0004(10)
Si5	0.0033(13)	0.0073(11)	0.0042(12)	0.0009(10)	0.0011(11)	-0.0006(9)
Si6	0.0047(14)	0.0080(12)	0.0046(12)	0.0008(9)	-0.0007(11)	-0.0010(10)
Si7	0.0045(14)	0.0049(11)	0.0048(12)	0.0014(9)	0.0006(11)	-0.0001(9)
Si8	0.0056(15)	0.0069(12)	0.0037(12)	-0.0003(9)	0.0002(10)	-0.0001(10)
Si9	0.006(2)	0.0115(18)	0.0047(18)	0.0014(14)	0	0
Si10	0.002(2)	0.0092(18)	0.0033(17)	-0.0009(14)	0	0.
Si11	0.005(2)	0.0068(17)	0.0048(18)	-0.0010(14)	0	0
Si12	0.005(2)	0.017(2)	0.0044(18)	-0.0017(15)	0	0

Table S5: Bond-valence sums for the anions and Si in $\text{La}_3\text{BaSi}_5\text{N}_9\text{O}_2$.

atom	BVS	oxidation state	atom	BVS	oxidation state	atom	BVS	oxidation state
Si1	4.05	4	N3	2.79	3	N17	2.85	3
Si2	4.02	4	N4	2.99	3	N18	2.52	3
Si3	4.03	4	N5	2.96	3	N19	2.62	3
Si4	4.07	4	N6	2.68	3	N20	2.62	3
Si5	4.02	4	N7	3.05	3	N21	2.72	3
Si6	3.93	4	N8	2.94	3	N22	2.56	3
Si7	3.95	4	N9	3.05	3	O1	1.87	2
Si8	3.95	4	N10	3.05	3	O2	1.46	2
Si9	3.80	4	N11	2.86	3	O3	2.10	2
Si10	4.03	4	N12	2.98	3	O4	1.94	2
Si11	3.78	4	N13	3.19	3	O5	2.24	2
Si12	4.08	4	N14	3.27	3	O6	1.84	2
N1	3.00	3	N15	2.72	3	O7	1.75	2
N2	3.18	3	N16	2.71	3	O8	1.57	2

Table S6: Bond-valence sums for the heavy atom sites in $\text{La}_3\text{BaSi}_5\text{N}_9\text{O}_2$.

atom	BVS	oxidation state	s.o.f.	weighted average BVS	weighted average oxidation state
La1	2.76	3	0.91	2.92	2.91
Ba1	4.60	2	0.09		
La2	2.86	3	0.95	2.96	2.95
Ba2	4.77	2	0.05		
La3A	2.30	3	0.54	2.04	2.16
Ba3A	3.81	2	0.21		
La3B	2.40	3	0.19	0.69	0.69
Ba3B	3.97	2	0.06		
La4	2.72	3	0.90	2.90	2.90
Ba4	4.52	2	0.10		
La5A	2.48	3	0.35	1.20	1.21
Ba5A	4.04	2	0.08		
La5B	2.47	3	0.46	1.59	1.60
Ba5B	4.06	2	0.11		
La6	1.41	3	0.23	2.23	2.23
Ba6	2.48	2	0.77		
La7	2.56	3	0.83	2.84	2.83
Ba7	4.23	2	0.17		
La8	1.73	3	0.45	2.46	2.45
Ba8	3.05	2	0.55		
La9A	1.79	3	0.04	0.21	0.20
Ba9A	3.16	2	0.04		
La9B	1.36	3	0.18	2.02	2.02
Ba9B	2.39	2	0.74		
La10	2.54	3	0.82	2.83	2.82
Ba10	4.15	2	0.18		
La11	2.82	3	0.93	2.94	2.93
Ba11	4.57	2	0.07		
La12	2.13	3	0.67	2.66	2.67
Ba12	3.75	2	0.33		

2.3 Highly Symmetric AB₂ Framework Related to Tridymite in the Disordered Nitridosilicate $\text{La}_{24}\text{Sr}_{14-7x}[\text{Si}_{36}\text{N}_{72}](\text{O}_{1-x}\text{F}_x)_{14}$ ($x = 0.849$)

Lukas Neudert, Dajana Durach, Felix Fahrnbauer, Gavin B. M. Vaughan, Wolfgang Schnick and Oliver Oeckler

Inorg. Chem. **2017**, 56, 13070.

Reprinted with permission from *Inorganic Chemistry*. Copyright 2017 ASC Publications.

Abstract

$\text{La}_{24}\text{Sr}_{14-7x}[\text{Si}_{36}\text{N}_{72}](\text{O}_{1-x}\text{F}_x)_{14}$ with $x = 0.489$ was obtained as a microcrystalline product by metathesis at 1500 °C in a radio-frequency furnace starting from $\text{Si}(\text{NH})_2$, $\text{La}(\text{NH}_2)_3$, SrH_2 , LaF_3 , and CeF_3 . The structure of the new nitridosilicate oxide fluoride was determined by combining transmission electron microscopy (TEM) and single-crystal X-ray diffraction using a microfocused synchrotron beam. The structure model with pronounced disorder [$P6_3/mmc$, $Z = 1$, $a = 16.2065(3)$, $c = 9.4165(1)$ Å, $R_1(\text{obs}) = 0.0436$] was confirmed by electron diffraction and aberration-corrected Z-contrast scanning TEM. The highly symmetric AB₂ framework, which was theoretically predicted but not yet realized, consists of all-side vertex-sharing SiN_4 tetrahedra that form channels along [001] filled with La, Sr, O, and F atoms. The connectivity pattern is related to that of tridymite. X-ray spectroscopy and bond-valence-sum calculations were further taken into account for assignment of the N, O, and F atoms.

2.3.1 Introduction

Starting from the great variety of oxosilicates found in nature, research on (oxo)nitridosilicates at the end of the last century was motivated by extending the fundamental knowledge of structural chemistry and possible applications.¹⁻³ Variation of the atomic ratio N:O permits, in principle, greater structural variety than that for conventional metal oxosilicates. Using the elements Si, N, and O for the building of 3D structures, a nearly infinite number of unique frameworks is theoretically possible. Even with the constraint of forming only AB₂ networks, i.e., such as with the number of O and N atoms being twice that of Si atoms or other tetrahedral centers, an enormous structural diversity has been predicted, although only a very small fraction of theoretically possible structures has been realized experimentally.^{4,5} Because most AB₂ frameworks correspond to 3D networks of linked polyhedra with a 1:2 ratio of polyhedra centers and bridging atoms, the crystal chemistry of (nitrido)silicates is predestined to feature such structures. SiO_2 as a prominent representative

crystallizes in many structure types as a function of the temperature or pressure. Among these, the tridymite structure type⁶ shows hexagonal channels. Related aluminosilicate networks such as that of megakalsilite (KAlSiO_4)^{7,8} as well as isostructural compounds exhibit channels filled with different metal ions.^{9,10} Such frameworks can be characterized by formal decomposition into layers of *sechser* rings, which may differ with respect to the orientation of the tetrahedra in these layers. (Oxo)nitridosilicates often favor quite unique framework structures. Several of these exhibit promising properties like zeolite-like behavior (e.g., porosity, ion exchange, or absorption) and second harmonic generation or may serve as host lattices for Eu^{2+} and Ce^{3+} dopants in luminescence materials.¹¹⁻¹⁶ Charge neutrality can be achieved by varying the atom types in the framework, e.g., O/N or Al/Si, or by varying the cations and anions in the structural cavities (e.g., Sr/La or O/F). This enables many options of improving the properties.^{17,18} Typical (oxo)nitridosilicates form rigid, highly condensed tetrahedral networks with a degree of condensation $\kappa = n(\text{Si}):n(\text{N/O}) \geq 0.5$ and high symmetry; this leads to high physical and chemical resistance.¹⁹⁻²³

The synthesis of heterogeneous samples with a number of uncharacterized new compounds represents the starting point for the *Single-Particle-Diagnosis Approach*.²⁴ This strategy is suitable for the discovery of new compounds, especially in complex systems such as the above-mentioned materials with intriguing properties. The precise elucidation of the crystal structures of the different phases is often the crucial step toward targeted synthesis and further property tuning of the corresponding pure compounds. (Oxo)nitridosilicates have frequently been synthesized by high-temperature metathesis, which has the drawback that a high variety of elements are usually present in the starting materials as well as in the products. In the case of, e.g., N/O/F or Ba/La, it is difficult to exactly assign atom types by X-ray diffraction. This impedes targeted attempts to obtain certain compositions, and multiphase products are frequently obtained. Subsequent structural characterization of such inhomogeneous and often microcrystalline oxonitridosilicates is demanding or even impossible using conventional X-ray methods. It has been shown that in such cases the combination of transmission electron microscopy (TEM) and synchrotron microfocus diffraction can deliver accurate structure data.²⁵⁻²⁹ For example, Z-contrast scanning TEM (STEM) and selected-area electron diffraction (SAED) have enabled structure determination of zeolite-like networks.³⁰⁻³² Furthermore, complex crystallographic phenomena like diffuse scattering, the presence of intergrown domains, or pseudomeroheredral twinning were observed for highly efficient luminescent (oxo)nitridosilicates and analyzed using a combination of TEM and X-ray methods.³³⁻³⁸

Here we report on a highly symmetrical crystal structure derived from microfocus synchrotron and TEM data of the microcrystalline nitridosilicate oxide fluoride $\text{La}_{24}\text{Sr}_{14-7x}[\text{Si}_{36}\text{N}_{72}](\text{O}_{1-x}\text{F}_x)_{14}$, which was obtained as part of a multiphase product. This approach may open an efficient pathway to compounds with potentially intriguing properties.

2.3.2 Results and Discussion

2.3.2.1 Synthesis and sample characterization

$\text{La}_{24}\text{Sr}_{14-7x}[\text{Si}_{36}\text{N}_{72}](\text{O}_{1-x}\text{F}_x)_{14}$ was synthesized by high-temperature metathesis starting from reactive N-rich materials $\text{Si}(\text{NH})_2$ and $\text{La}(\text{NH}_2)_3$ combined with LaF_3 and an excess of SrH_2 . Decomposition of the hydrides and subsequent formation of SrF_2 and H_2 are the driving forces of this reaction type.²⁵ Colorless needle-shaped $\text{La}_{24}\text{Sr}_{14-7x}[\text{Si}_{36}\text{N}_{72}](\text{O}_{1-x}\text{F}_x)_{14}$ crystals with maximum lengths of a few microns (Figure 1, right) were obtained as agglomerates in a multiphase sample (Figure 1, left) and are stable to air and moisture. With respect to the La content, ca. 1.4 atom % Ce^{3+} doping was applied, yet no luminescence was observed. The incorporated O may originate from commercially acquired starting materials. Further details of the synthesis are given in the Experimental Section.

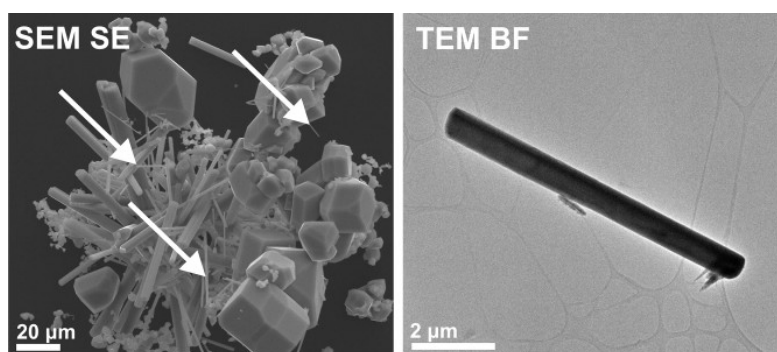


Figure 1. Representative crystals of $\text{La}_{24}\text{Sr}_{14-7x}[\text{Si}_{36}\text{N}_{72}](\text{O}_{1-x}\text{F}_x)_{14}$: (left) SEM image with agglomerates highlighted by white arrows and (right) TEM bright-field image showing an individual needlelike crystal.

TEM and scanning electron microscopy (SEM) EDX analyses of $\text{La}_{24}\text{Sr}_{14-7x}[\text{Si}_{36}\text{N}_{72}](\text{O}_{1-x}\text{F}_x)_{14}$ show no elements other than Sr, La, Ce, Si, N, O, and F. With the exception of O, whose amount appears too high because of the typical surface oxidation in nitrides, the average EDX results for $\text{La}_{20(2)}\text{Sr}_{9(2)}\text{Si}_{30(2)}\text{N}_{69(8)}\text{O}_{18(2)}\text{F}_{9(2)}$ (normalized for optimal comparability; for details, see Table S1) are in accordance with values calculated from the sum formula $\text{La}_{24}\text{Sr}_{10.58}\text{Si}_{36}\text{N}_{72}\text{O}_{7.16}\text{F}_{6.84}$ (as obtained by structure refinement based on synchrotron X-ray data) within experimental error. The Ce content was not quantified, but traces of Ce were detected in the EDX spectra (Figure S1). The very small needle-shaped crystals in an inhomogeneous sample preclude more precise chemical analysis. As expected from the synthesis conditions, the IR spectrum exhibits no valence modes between 2600 and 3250 cm^{-1} , indicating the absence of $-\text{OH}$ and $-\text{NH}$ groups (Figure S2). The presence of the element combinations La/Sr and N/O/F combined with vacancies on the cation sites may lead to solid solutions without compromising the charge neutrality. Taking into account the vacancies on the Sr sites, the crystal structure determination (see below) yields the sum formula $\text{La}_{24}\text{Sr}_{14-7x}[\text{Si}_{36}\text{N}_{72}](\text{O}_{1-x}\text{F}_x)_{14}$, where x was refined as 0.489 but may, in principle, vary between 0 and 1.

Thus, the compound with $x = 0.489$, i.e., $\text{La}_{24}\text{Sr}_{10.58}\text{Si}_{36}\text{N}_{72}\text{O}_{7.16}\text{F}_{6.84}$, can be interpreted as one possible variant. Assuming mixed and/or vacancy-containing Sr and La sites would suggest the formula $\text{La}_{24-y}\text{Sr}_{14-x}[\text{Si}_{36}\text{N}_{72}](\text{O}_{1-x/7-y/14}\text{F}_{x/7+y/14})_{14}$ with $x/7 + y/14 \leq 1$. Further degrees of freedom may result from variations of the N/O/F ratio. Several TEM investigations of many crystals suggest different N/O/F and La/Sr ratios; however, these were not investigated in detail. Hypothetical chemical variations without changing the framework and the metrics could inspire further substitution experiments. Powder X-ray diffraction (PXRD) reveals the presence of the title compound and probably one major side phase (Figure S3). The side phase is an unknown lanthanum–strontium oxonitridosilicate (TEM-EDX; La:Si:N:O \approx 14:8:26:43:11) whose structure could not yet be solved. This corresponds to the more isometric crystals in Figure 1.

2.3.2.2 Structure determination

Because the maximal volume of the $\text{La}_{24}\text{Sr}_{14-7x}[\text{Si}_{36}\text{N}_{72}](\text{O}_{1-x}\text{F}_x)_{14}$ needles is only about $50 \mu\text{m}^3$ and structure solution with PXRD was impeded by side phases, data were collected using a microfocused synchrotron beam. The crystal structure was solved and refined in space group $P6_3/mmc$ (Table 1), yielding an AB₂ framework with channels filled with F and O. Because of the lack of scattering contrast between La and Ce, the latter was neglected in the refinement. Parts of the crystallographic data are shown in Tables S2 and S3. Further details on the structure analysis can be obtained from the Fachinformationszentrum Karlsruhe, Eggenstein-Leopoldshafen, Germany (fax +49-7247-808-666; e-mail crysdata@fiz-karlsruhe.de) upon quoting the depository number CSD 432688.

The structure refinement, especially with respect to the cation distribution, is characterized by the fact that the ratio of charge and electron count, i.e., scattering power, is the same for La^{3+} ($3/54 = 0.0556$) and Sr^{2+} ($2/36 = 0.0556$). Taking possible cation vacancies into account, the refinement thus directly yields the total charge on the respective positions but gives no information on the atomic ratio La/Sr. As an initial step, the total scattering density on each of the six cation positions was determined assuming either La, Sr, or mixed occupancy; as expected, the results did not differ significantly. The scattering density on positions La1, La2, and La3 corresponds to full occupancy of La. Taking into account the chemical composition as determined by EDX, the remaining positions are likely to be occupied exclusively by Sr. Following this assumption, positions Sr4 and Sr5 turned out to be fully occupied, whereas the refined occupancy of the split position Sr6 is 14.6%. The resulting atomic ratio La:Si of 2.26 is quite close to the value 2.27 determined by EDX. Complementary bond-valence-sum (BVS) calculations approximately match this cation assignment (Table S4).³⁹ Because $\text{La}_{24}\text{Sr}_{10.58}[\text{Si}_{36}\text{N}_{72}]\text{O}_{7.16}\text{F}_{6.84}$ is transparent, charge neutrality was assured by constraints. In accordance with chemical analysis (see the section on the synthesis and sample characterization), which shows significantly more N than O; the N atoms were assigned to the bridging atoms in the framework,

covering the majority of the required negative charge. The assignment of the anions was further based on Pauling's rules and comparisons to other nitridosilicate oxides/fluorides.⁴⁰⁻⁴² For the remaining two independent anion sites in the channels, full occupancy was found. Matching the charge neutrality, a fixed mixed occupancy with O and F of $\approx 1:1$ was assumed because O and F cannot be accurately distinguished by X-ray diffraction. The final structure model yields meaningful interatomic distances and displacement parameters, and the assignments of all atoms are approximately consistent with BVS calculations (Table S4).

Table 2. Crystallographic Data and X-ray Structure Determination of $\text{La}_{24}\text{Sr}_{14-7x}[\text{Si}_{36}\text{N}_{72}](\text{O}_{1-x}\text{F}_x)_{14}$ with $x = 0.489$.

Formula	$\text{La}_{24}\text{Sr}_{10.58}\text{Si}_{36}\text{N}_{72}\text{O}_{7.16}\text{F}_{6.84}$
Molar weight (in g/mol)	6525.69
Space group	$P6_3/mmc$ (no. 194)
Lattice parameters (in Å)	$a = 16.2065(3)$ $c = 9.4165(1)$
Cell volume (in Å ³)	2141.90(8)
Formula unit per unit cell	1
X-ray density (in g·cm ⁻³)	5.059
F(000)	2897.0
Absorption coefficient (in mm ⁻¹)	4.361
Resolution d_{\min} (in Å)	0.75
Wavelength (in Å)	0.41300 (synchrotron, ID11, ESRF)
Total no. of reflections / independent reflections	19029 / 1034
$R_{\text{int}} / R_{\sigma}$	0.0439 / 0.0151
Refined parameters / restraints	87 / 0
R_1 / wR_2 (all data)	0.0443 / 0.1293
R_1 / wR_2 ($F^2 > 2\sigma(F^2)$)	0.0436 / 0.1287
Goodness of fit	1.663
$\Delta\rho_{\max} / \Delta\rho_{\min}$ (in e / Å ⁻³)	+4.74 / -1.68

Because the structure determination was not straightforward, TEM was performed in order to rule out the occurrence of a superstructure or twinning and to confirm the final structure model. The SAED tilt series confirms the hexagonal metrics with $a = 16.24$ Å and $c = 9.44$ Å and no detectable superstructure reflections. In accordance with Laue class $6/mmm$, the SAED pattern along zone axis [110] shows $mm2$ symmetry, and the reflection intensities approximately match those of the corresponding kinematical simulations (see Figure 2).

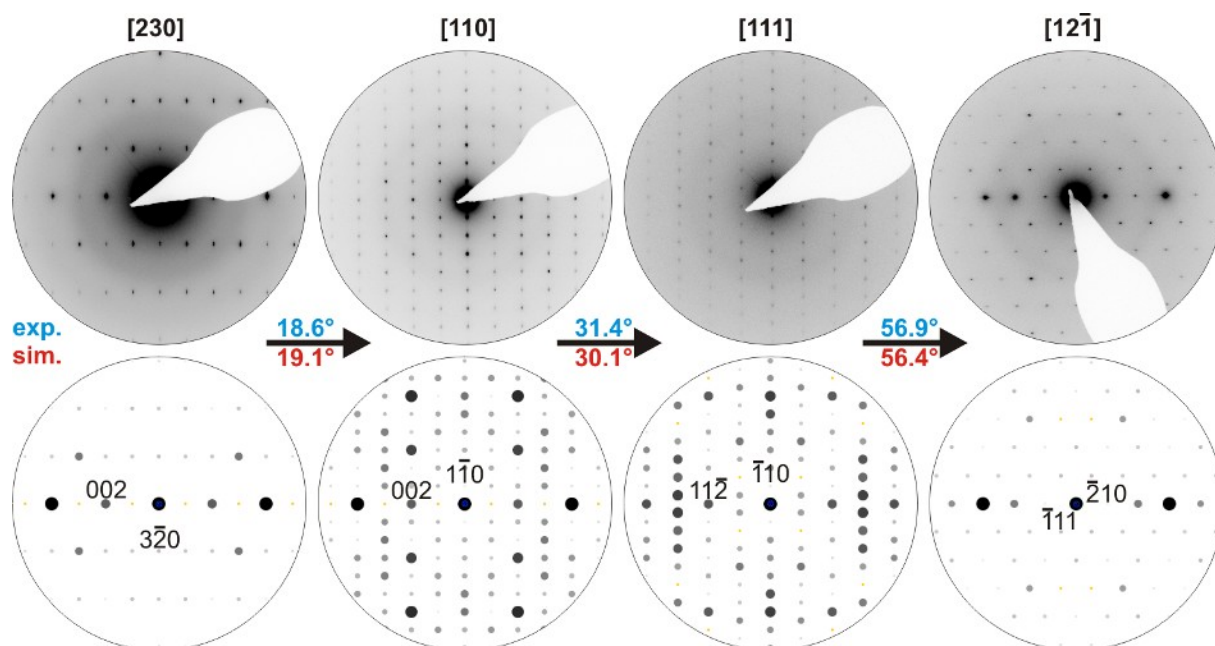


Figure 2. SAED tilt series of a representative crystallite with experimental patterns (top) and tilt angles (blue) as well as simulated patterns (bottom) and tilt angles (red) based on the refined structure model from X-ray data. Selected reflections are labeled with indices.

STEM using a high-angle annular dark field (HAADF) detector yielded the projected heavy-atom positions along the $[100]$ and $[101]$ zone axes (Figure 3 and enlarged and unfiltered in Figure S4), confirming the cation positions of the structure model. An additional weak diffuse scattering intensity was observed in various SAED patterns (Figure S5) along different zone axes. Because of the similar ionic radii of both La^{3+} and Sr^{2+} , it seems likely that these diffuse intensities are associated with cation disorder.

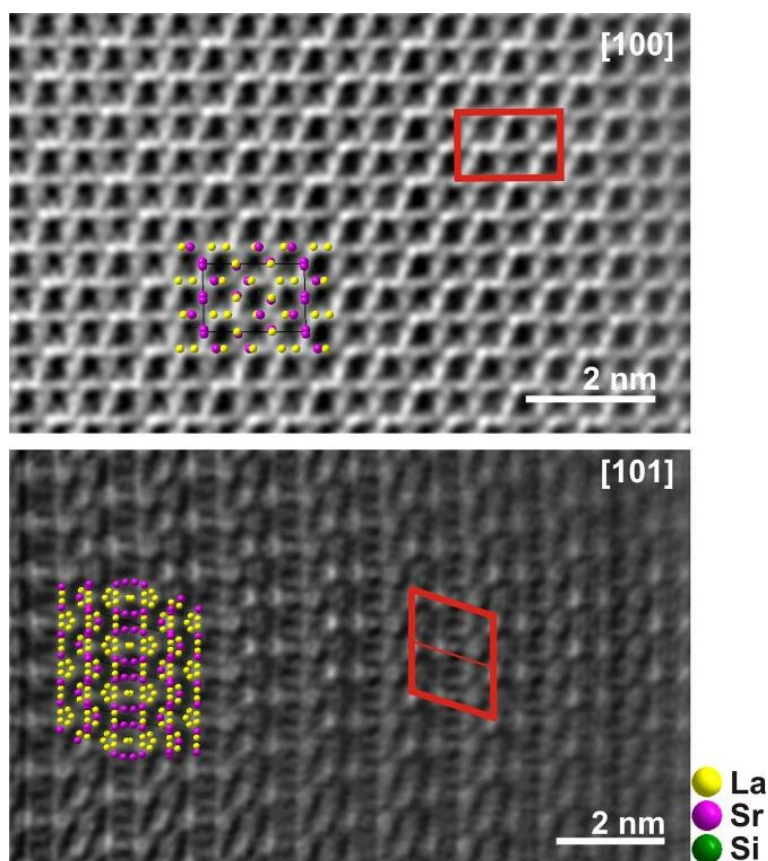


Figure 3. Fourier-filtered Z-contrast STEM-HAADF images along the [100] (top) and [101] (bottom) zone axes of $\text{La}_{24}\text{Sr}_{14-7x}[\text{Si}_{36}\text{N}_{72}](\text{O}_{1-x}\text{F}_x)_{14}$. The unit cell is highlighted in red with a colored overlay of heavy atoms.

2.3.2.3 Structure description

$\text{La}_{24}\text{Sr}_{14-7x}[\text{Si}_{36}\text{N}_{72}](\text{O}_{1-x}\text{F}_x)_{14}$ exhibits a highly condensed SiN_4 tetrahedral framework with $\kappa = n(\text{Si}):n(\text{N}) = 0.5$ (Figure 4). All SiN_4 tetrahedra are corner-sharing Q^4 -type ones so that the framework itself corresponds to an AB₂ type. The crystal structure can be simplified to $\text{M}_{38}[\text{Si}_{36}\text{N}_{72}]\text{X}_{14}$ with $\text{M} = \text{La}, \text{Sr}$, and \square and $\text{X} = \text{O}$ and F , highlighting the AB₂-type framework more clearly. This framework has been experimentally realized for the first time. It matches type 194_3_3914 (Figure S6) of the over 2 million theoretical unique frameworks deposited in the hypothetical zeolite database.⁴ The framework can be derived from the tridymite structure. The connectivity pattern is comparable; however, the tetrahedra within each layer perpendicular to [001] are differently oriented (Figure S7; various orientations of tetrahedra, pointing up or down). Another related pattern is known from the mineral megakalsilite.⁴³ According to the nomenclature introduced by Liebau, the framework of the title compound consists of *vierer* and *sechser* rings (Figure 5a,b; light blue, green, and red).^{44,45} The *vierer* rings are oriented along all (110) face diagonals, and the *sechser* rings form channels parallel to [001], filled with Sr, La, O, and F. Similar to nitrides crystallizing in the UCr_4C_4 structure type,⁴⁶ the framework of $\text{La}_{24}\text{Sr}_{14-7x}[\text{Si}_{36}\text{N}_{72}](\text{O}_{1-x}\text{F}_x)_{14}$ can act as a starting point for further experiments realizing

a solid-solution series based on different substitutions. Finding a rigid and stable network is therefore fundamental for the targeted design of new materials.¹⁹

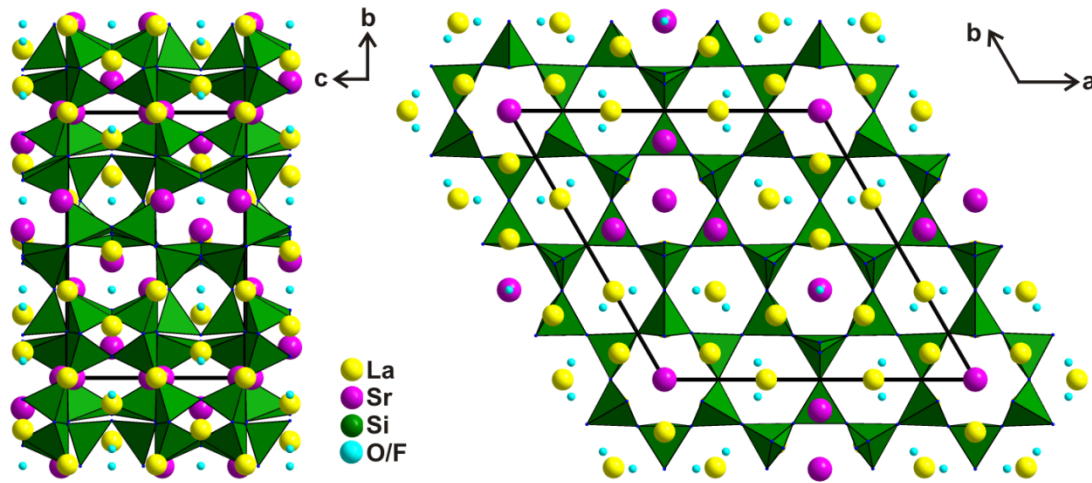


Figure 4. Crystal structure of $La_{24}Sr_{14-7x}[Si_{36}N_{72}](O_{1-x}F_x)_{14}$ along [100] (left) and [001] (right). SiN_4 tetrahedra are in green, La in yellow, Sr in pink, and O/F in cyan.

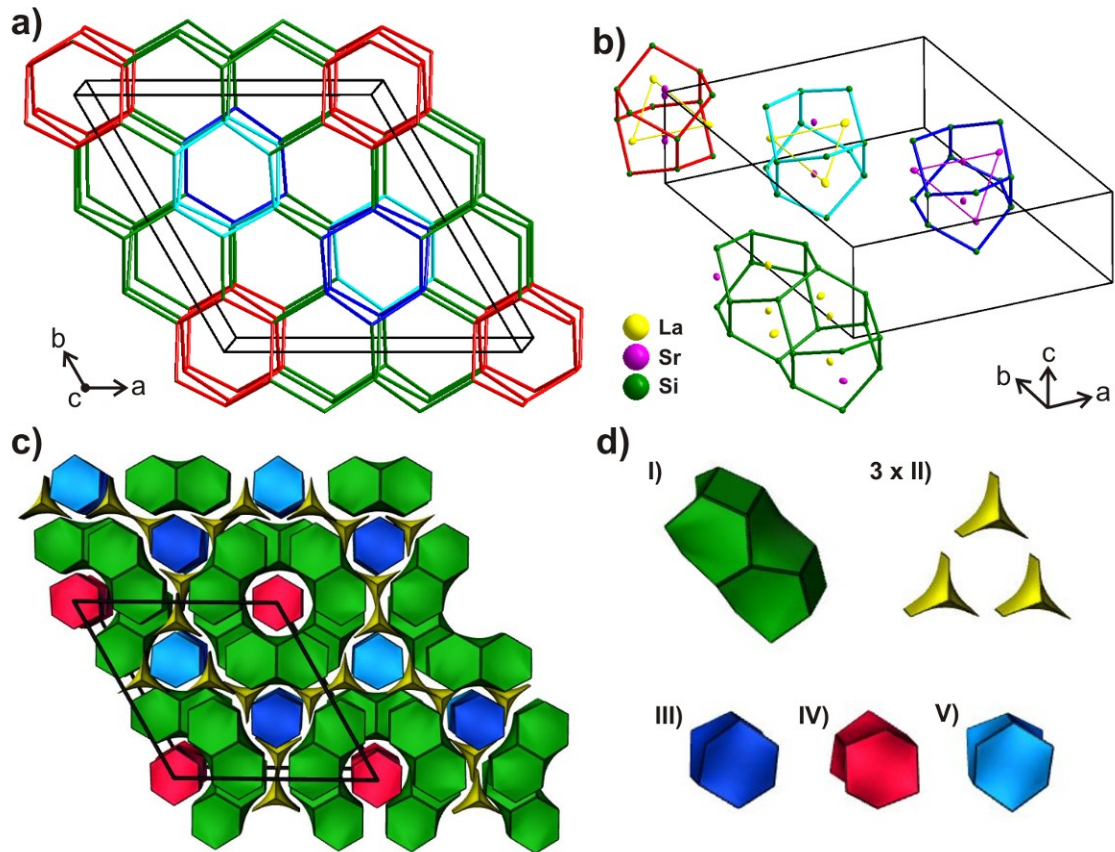


Figure 5. (a) Network topology of $La_{24}Sr_{14-7x}[Si_{36}N_{72}](O_{1-x}F_x)_{14}$. Each line represents a Si–N–Si bond. (b) Different types of tiles with incorporated cations highlighted in green, blue, light blue, and red. (c) Whole tiling viewed along [001] represented by (d) different polyhedra in green, blue, light blue, and red.

The Si–Si connection pattern yielded the network topology and the related *natural tiling* with the point symbol $(4.6^5)_2.6^6$ (Figure 5a).^{47–51} The Si–Si network consists of three vertices; Si1 with point symbol 6^6 and Si2 and Si3, both with point symbol 4.6^5 . The tiles' faces consist of *locally strong rings* (built up from Si–Si adjacencies), which are characterized in Table 2 and Figure 5c,d, representing the cavities in the structure. The tiles include rings of a distorted boat configuration (tile I), a regular boat configuration (tile II), and a chair conformation (tiles III–V). Although tiles III–V look similar, they differ in their orientation as well as in their centroids and volume. The cations La2, La3, and Sr4 form triangles at the level of $1/4c$ and $3/4c$ within tiles III–V (Figure 5b). Without reducing the symmetry, mixing the occupancy of the cations forming the triangles is theoretically possible. The split positions of Sr6 is oriented parallel to [001] at heights $00^{1/2}$ and 000, respectively. The mixed occupied anion sites O9/F9 are arranged circularly at a level of $1/4c$ around tile IV, whereas O8/F8 is within tile IV linearly coordinated by Sr. Because $\text{La}_{24}\text{Sr}_{14-7x}[\text{Si}_{36}\text{N}_{72}](\text{O}_{1-x}\text{F}_x)_{14}$ crystallizes in space group $P6_3/mmc$, the highest possible hexagonal symmetry is present in both the crystal structure and its natural tiling. This is also true for tridymite.

Table 2. Characterization of Different Tiles in $\text{La}_{24}\text{Sr}_{14-7x}[\text{Si}_{36}\text{N}_{72}](\text{O}_{1-x}\text{F}_x)_{14}$.

tile (color code)	face symbol	centroid	volume in Å ³	incorporated cations (occupancy)
I (green)	$[4^2.6^8]$	(0.833, 0.167, 0.250)	245.243	La1(1) La2 (1) La3 (1) Sr4 (1)
II (yellow)	$[6^3]$	(0.887, 0.443, 0.750)	25.404	-
III (blue)	$[6^5]$	(0.333, 0.667, 0.750)	93.505	Sr5 (1)
IV (red)	$[6^5]$	(0.000, 0.000, 0.750)	85.285	Sr6 (0.146)
V (light blue)	$[6^5]$	(0.333, 0.667, 0.250)	86.788	Sr5 (1)

As is typical for Sr-, Ba-, and Ln-containing (oxo)nitridosilicates, the cations show high coordination numbers (Figure 6, La1^[8], La2^[8], La3^[9], Sr4^[9], Sr5^[10], and Sr6^[9]). The Si–N bond lengths (see Table S12) range between 1.670(6) and 1.742(6) Å and correspond to typical values in (oxo)nitridosilicates.^{52–54} The same applies for the La–N [2.496(6)–2.758(1) Å] and Sr–N [2.737(3)–3.050(2) Å] bond lengths (Table S5), corresponding to other lanthanum or strontium nitridosilicates like LaSi_3N_5 , $\text{La}_3\text{Si}_6\text{N}_{11}$, and $\text{La}_2\text{Si}_3\text{N}_4\text{O}_3$ or $\text{SrYbSi}_4\text{N}_7$, $\text{SrSi}_7\text{N}_{10}$, and SrSiN_2 .^{55–60} The Si–N–Si bond angles in $\text{La}_{24}\text{Sr}_{14-7x}[\text{Si}_{36}\text{N}_{72}](\text{O}_{1-x}\text{F}_x)_{14}$ with $x = 0.489$ also match typical values.^{61–63}

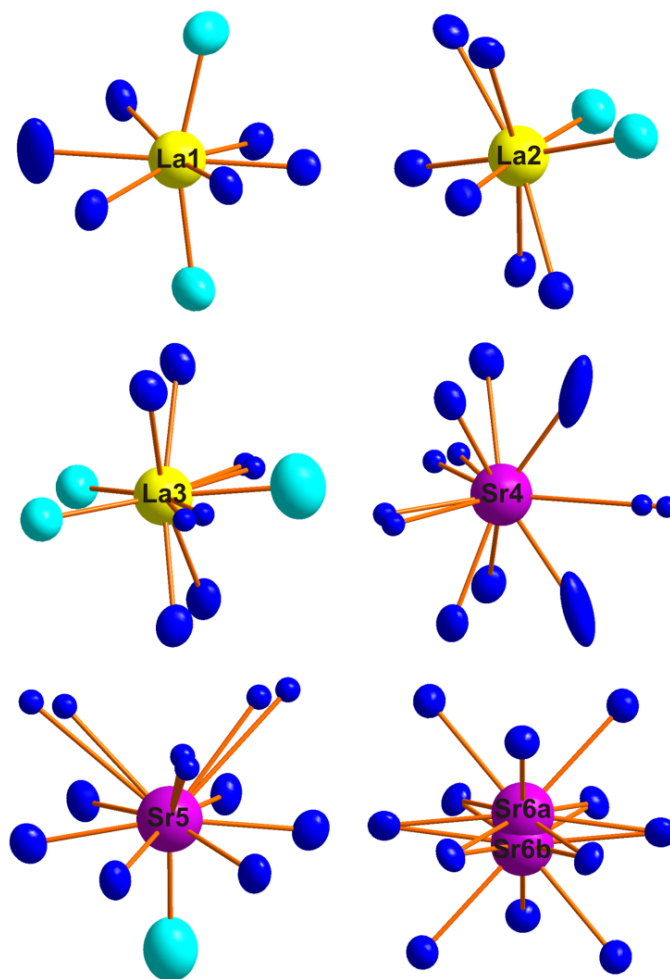


Figure 6. Coordination spheres of La (yellow) and Sr (magenta) sites in $\text{La}_{24}\text{Sr}_{14-7x}[\text{Si}_{36}\text{N}_{72}](\text{O}_{1-x}\text{F}_x)_{14}$, with N in blue and mixed O/F sites in cyan (ellipsoids with 90% probability). Because N5 is part of the SiN_4 tetrahedra containing the split positions N6A/B, N5 has prolate displacement parameters within the coordination sphere of La1 and Sr4.

2.3.3 Conclusion

Challenges occurring during the phase characterization of nitridosilicates obtained from high-temperature metathesis were overcome by the combination of TEM and single-crystal diffraction using a microfocused synchrotron beam. The latter is well suited to provide accurate X-ray data for the structure determination of single crystals with small scattering volume. Concerning its structural classification and tiling, the structure determination of $\text{La}_{24}\text{Sr}_{14-7x}[\text{Si}_{36}\text{N}_{72}](\text{O}_{1-x}\text{F}_x)_{14}$ with $x = 0.489$ revealed a predicted AB₂ framework topology that is experimentally observed for the first time. It is related but not isostructural to that of tridymite. Electron diffraction and Z-contrast STEM images confirmed the structure model. The approach applied here enables an efficient pathway to the discovery of new compounds with promising structural features.

The highly symmetric structure of $La_{24}Sr_{14-7x}[Si_{36}N_{72}](O_{1-x}F_x)_{14}$ shows channels filled with La, Sr, O, and F atoms, and because of the cavities, it might be suitable for ion exchange of La^{3+} or Sr^{2+} with other cations like Na^+ , Ca^{2+} , or lanthanides, especially Eu^{2+} , in combination with a changed O:F ratio. The recently described ion exchange in metal halide melts can be one possible strategy for realizing this issue, while retaining the framework.⁶⁴ Further substitution experiments (e.g., with Si/Al) open structural and chemical variations, and the latter can have a positive influence for the discovery of prospective solid solutions. Thus, new SiALON host lattices for activator ions with regard to luminescent materials can be obtained. Therefore, the presence of F is beneficial because of an enhanced tuning ability.¹⁷ In combination with different metal cations, it may be an appropriate approach to stimulate luminescence of the title compound or a corresponding SiALON.

2.3.4 Experimental Section

Synthesis of $La_{2.26x}Sr_x[Si_{36}N_{72}]O_{0.675x}F_{0.645x}$

$Si(NH)_2$ (53.4 mg, 0.919 mmol, synthesized according to Winter),⁶⁵ SrH_2 (64.1 mg, 0.7 mmol), LaF_3 (30.5 mg, 0.156 mmol), and CeF_3 (0.9 mg, 4.566 μ mol) were added to $La(NH_2)_3$ (30.2 mg, 0.162 mmol, synthesized according to Jacobs).⁶⁶ The mixture was ground and filled in a tungsten crucible, which was placed in a radio-frequency furnace (Typ AXIO 10/450, Hüttinger Elektronik, Freiburg, Germany).⁶⁷ Inert gas conditions prevented the presence of O_2 and moisture. The following temperature program was used: heating to 1500 °C in 1 h, dwelling for 10 h, cooling to 900 °C in 2 days, and finally quenching to room temperature by switching off the furnace. The reaction yielded an inhomogeneous air- and moisture-stable product. Small amounts of the title compound were also obtained in other reactions without CeF_3 , which proves that Ce is not necessary to stabilize it.

Single-crystal X-ray diffraction

Single-crystals were separated under a light microscope and mounted on Kapton foil holders (20 μ m micromount, MiTeGen, Ithaca). X-ray diffraction data were obtained at the ID11 beamline (ESRF Grenoble) at a wavelength of 0.41300 Å (Si(111) double-crystal monochromator) using a Frelon2k CCD detector.⁶⁸ Indexing, integration and scaling as well as semi-empirical absorption correction were done with CrysAlis.⁶⁹ Structure solution and refinement were done with SHELX.⁷⁰

Electron microscopy

SEM was done with a Zeiss LEO 1530 microscope (Zeiss, Jena, Germany) and a JEOL JSM 6500F microscope (JEOL, Freising, Germany), both equipped with an energy-dispersive X-ray (EDX) INCA system (model 7418, Oxford Instruments, Oxford, U.K.) and with a Dualbeam Helios Nanolab G3UC

(FEI, USA, Hillsboro, OR) with a field-emission gun (operating at 20 kV) and an X-Max80 SDD EDX detector (Oxford Instruments). The product was fixed on a conductive adhesive film coated with C. For TEM, small amounts of the product were ground in absolute ethanol and drop-cast on Cu grids with a holey C film (S166-2, Plano GmbH, Wetzlar, Germany). The TEM experiments were performed on a Titan Themis 60-300 (FEI, USA) operated at a 300 kV acceleration voltage and equipped with an X-FEG monochromator, C_s corrector, and windowless four-quadrant Super-X EDX detector (acquisition time 45 s). The TEM images were recorded using a 4K × 4K Ceta CMOS camera (FEI, USA). The following software was used for data evaluation: Digital Micrograph and ProcessDiffraction7 (geometric calculations for SAED), JEMS (SAED simulations), and ES Vision (evaluation of EDX spectra).⁷¹⁻⁷⁴

FTIR spectroscopy

FTIR spectra were recorded on a PerkinElmer Spectrum BXII spectrometer using KBr pellets.

2.3.5 References

- 1 J. Lang, Y. Laurent, M. Maunaye, R. Marchand, *Prog. Crystal Growth Ch.* **1979**, 2, 207.
- 2 F. J. DiSalvo, S. J. Clarke, *Curr. Opin. Solid St. M.* **1996**, 1, 241.
- 3 W. Schnick, *Angew. Chem. Int. Ed.* **1993**, 32, 806.
- 4 a) M. M. J. Treacy, I. Rivin, E. Balkovsky, K. H. Randall, M. D. Foster, *Micropor. Mesopor. Mater.* **2004**, 74, 121-132; b) M. D. Foster, M. M. J. Treacy, J. B. Higgins, I. Rivin, E. Balkovsky, K. H. Randall, *J. Appl. Crystallogr.* **2005**, 38, 1028; c) M. D. Foster, M. M. J. Treacy, Database of Hypothetical Zeolite Structures: <http://www.hypotheticalzeolites.net>.
- 5 D. Baumann, S. J. Sedlmaier, W. Schnick, *Angew. Chem.* **2012**, 124, 4785; *Angew. Chem., Int. Ed.* **2012**, 51, 4707.
- 6 R. E. Gibbs, *Proc. R. Soc. London, Ser. A* **1926**, 113, 351.
- 7 W. A. Dollase, W. P. Freeborn, *Am. Mineral.* **1977**, 62, 336.
- 8 V. Kahlenberg, R. X. Fischer, J. B. Parise, *J. Solid State Chem.* **2000**, 154, 612.
- 9 M. J. Buerger, *Am. Mineral.* **1954**, 39, 600.
- 10 F. W. Karau, L. Seyfarth, O. Oeckler, J. Senker, K. Landskrin, W. Schnick, *Chem. -Eur. J.* **2007**, 13, 6841.
- 11 M. Zeuner, S. Pagano, W. Schnick, *Angew. Chem.* **2011**, 123, 7898; *Angew. Chem., Int. Ed.* **2011**, 50, 7754.
- 12 W. Schnick, *Int. J. Inorg. Mater.* **2001**, 3, 1267.
- 13 R. -J. Xie, N. Hirotsaki, Y. Li, Takeda, T. *Materials* **2010**, 3, 3777.
- 14 W. Schnick, H. Huppertz, *Chem. Eur. J.* **1997**, 3, 679.
- 15 H. Lutz, S. Joosten, J. Hoffmann, P. Lehmeier, A. Seilmeier, H. A. Höppe, W. Schnick, *J. Phys. Chem. Solids* **2004**, 65, 1285.

- 16 A. J. D. Barnes, T. J. Prior, M. G. Francesconi, *Chem. Commun.* **2007**, 4638.
- 17 K. Horky, W. Schnick, *Chem. Mater.* **2017**, 29, 4590.
- 18 V. Bachmann, C. Ronda, O. Oeckler, W. Schnick, A. Meijerink, *Chem. Mater.* **2009**, 21, 316.
- 19 P. Pust, V. Weiler, C. Hecht, A. Tücks, A. S. Wochnik, A.-K. Henß, D. Wiechert, C. Scheu, P. J. Schmidt, W. Schnick, *Nat. Mater.* **2014**, 13, 891.
- 20 S. Schmiechen, P. Strobel, C. Hecht, T. Reith, M. Siegert, P. J. Schmidt, H. Huppertz, D. Wiechert, W. Schnick, *Chem. Mater.* **2015**, 17, 3242.
- 21 T. Suehiro, N. Hirosaki, R. -J. Xie, *ACS Appl. Mater. Interfaces* **2011**, 3, 811.
- 22 V. Bachmann, T. Juestel, A. Meijerink, C. Ronda, P. J. Schmidt, *J. Lumin.* **2006**, 121, 441.
- 23 G. Li, C. C. Lin, W. T. Chen, M. S. Molokeev, V. V. Atuchin, C. Y. Chiang, W. Zhou, C. W. Wang, W. H. Li, H. S. Sheu, T. S. Chan, C. Ma, R. S. P. Liu, *Chem. Mater.* **2014**, 26, 2991.
- 24 N. Hirosaki, T. Takeda, S. Funahashi, R. -J. Xie, *Chem. Mater.* **2014**, 26, 4280.
- 25 D. Durach, L. Neudert, P. J. Schmidt, O. Oeckler, W. Schnick, *Chem. Mater.* **2015**, 27, 4832.
- 26 F. Fahrnbauer, T. Rosenthal, T. Schmutzler, G. Wagner, G. B. M. Vaughan, J. P. Wright, O. Oeckler, *Angew. Chem.* **2015**, 127, 10158; *Angew. Chem. Int. Ed.* **2015**, 54, 10020.
- 27 R. Paria Sena, A. A. Babaryk, S. Khainakov, S. Garcia-Granda, N.S. Slobodyanik, G. A. van Tendeloo, M. Abakumov, J. Hadermann, *Dalton Trans.* **2016**, 45, 973.
- 28 T. Kogure, E. Okunishi, *J. Electron Microsc.* **2010**, 59, 263.
- 29 R. Huang, T. Mizoguchi, K. Sugiura, H. Ohta, K. Koumoto, T. Hirayama, Y. Ikuhara, *Appl. Phys. Lett.* **2008**, 93, 181907.
- 30 S. J. Sedlmaier, M. Döblinger, O. Oeckler, J. Weber, J. Schmedt auf der Günne, W. Schnick, *J. Am. Chem. Soc.* **2011**, 133, 12069.
- 31 S. Correll, O. Oeckler, N. Stock, W. Schnick, *Angew. Chem.* **2003**, 115, 3674; *Angew. Chem., Int. Ed.* **2003**, 42, 3549.
- 32 S. Pagano, O. Oeckler, T. Schröder, W. Schnick, *Eur. J. Inorg. Chem.* **2009**, 2678.
- 33 O. Oeckler, F. Stadler, T. Rosenthal, W. Schnick, *Solid State Sci.* **2007**, 9, 205.
- 34 J. A. Kechele, O. Oeckler, F. Stadler, W. Schnick, *Solid State Sci.* **2009**, 11, 537.
- 35 M. Seibald, T. Rosenthal, O. Oeckler, C. Maak, A. M. Tücks, P. J. Schmidt, D. Wiechert, W. Schnick, *Chem. Mater.* **2013**, 25, 1852.
- 36 M. Seibald, T. Rosenthal, O. Oeckler, F. Farnbauer, A. Tücks, P. J. Schmidt, W. Schnick, *Chem. Eur. J.* **2012**, 18, 13446.
- 37 M. Seibald, O. Oeckler, V. R. Celinski, P. J. Schmidt, A. Tücks, W. Schnick, *Solid State Sci.* **2011**, 13, 1769.
- 38 M. Seibald, T. Rosenthal, O. Oeckler, W. Schnick, *Crit. Rev. Solid State Mater. Sci.* **2014**, 39, 215.
- 39 Wills, A. S. *Valist, version 4.0.7*, University College London, UK, **2010**.
- 40 P. E. D. Morgan, *J. Mater. Sci.* **1986**, 21, 4305.
- 41 D. Durach, W. Schnick, *Eur. J. Inorg. Chem.* **2015**, 4095.
- 42 D. Durach, W. Schnick, *Z. Anorg. Allg. Chem.* **2016**, 101.

- 43 A. P. Khomyakov, G. N. Nechelyustov, E. Sokolova, E. Bonaccorsi, S. Merlino, M. Pasero,
Canadian Mineral. **2002**, *40*, 961.
- 44 Liebau, F. *Structural Chemistry of Silicates*; Springer, Berlin, Germany, **1985**.
- 45 The term *vierer* (*sechser*) ring was imprinted by Liebau and is derived from the German numeral “vier”
 (“sechs”). A *vierer* (*sechser*) ring consist of four (six) tetrahedra centers.
- 46 R. K. Behrens, W. Jeitschko, *Monatsh. Chem.* **1987**, *118*, 43.
- 47 V. A. Blatov, A. P. Shevchenko, D. M. Prosperio, *Cryst. Growth Des.* **2014**, *14*, 3576.
- 48 O. Delgado-Friedrichs, M. O’Keeffe, *J. Solid State Chem.* **2005**, *178*, 2480.
- 49 V. A. Blatov, M. O’Keeffe, D. M. Proserpio *Cryst. Eng. Comm.* **2010**, *12*, 44.
- 50 V. A. Blatov, O. Delgado-Friedrichs, M. O’Keeffe, D. M. Proserpio *Acta Crystallogr. Sect. A Found.*
Crystallogr. **2007**, *A63*, 418.
- 51 O. Delgado-Friedrichs, M. O’Keeffe, O. M. Yaghi, *Acta Crystallogr. Sect. A* **2002**, *A59*, 22.
- 52 C. Schmolke, D. Bichler, D. Johrendt, W. Schnick, *Solid. State Sci.* **2009**, *11*, 389.
- 53 C. Schmolke, S. Lupart, W. Schnick, *Solid. State Sci.* **2009**, *11*, 305.
- 54 T. Schlieper, W. Milius, W. Schnick, *Z. Anorg. Allg. Chem.* **1995**, *621*, 1380.
- 55 Z. Inoue, T. Sawada, K. Ohsumi, M. Mitomo, R. Sadanaga, *Acta Crystallogr. Sect. A* **1981**, *37*, C154a.
- 56 M. Woike, W. Jeitschko, *Inorg. Chem.* **1995**, *34*, 5105.
- 57 R. Marchand, A. Jayaweera, P. Verdier, J. C. R. Lang, *Seances Acad. Sci. (Ser. C)* **1976**, *283*, 675.
- 58 H. Huppertz, W. Schnick, *Z. Anorg. Allg. Chem.* **1997**, *623*, 212.
- 59 G. Pilet, H. A. Höpfe, W. Schnick, S. Esmaeilzadeh, *Solid State Sci.* **2005**, *7*, 391.
- 60 Z. A. Gal, P. M. Mallinson, H. J. Orchard, S. J. Clarke, *Inorg. Chem.* **2004**, *43*, 3998.
- 61 F. Monteverde, G. Celotti, *J. Eur. Ceram. Soc.* **2002**, *22*, 721.
- 62 W. H. Zachariasen, *Z. Kristallogr.* **1930**, *73*, 1.
- 63 D. W. J. Cruickshank, H. Lynton, G. A. Barclay, *Acta Crystallogr.* **1962**, *15*, 491.
- 64 P. Bielec, W. Schnick, *Angew. Chem.* **2017**, *129*, 4888; *Angew. Chem. Int. Ed.* **2017**, *56*, 4810.
- 65 H. Lange, G. Wotting, G. Winter, *Angew. Chem.* **1991**, *103*, 1625; *Angew. Chem., Int. Ed.* **1991**, *30*,
 1579.
- 66 B. Gieger, H. Jacobs, C. Hadenfeldt, *Z. Anorg. Allg. Chem.* **1974**, *410*, 104.
- 67 W. Schnick, H. Huppertz, R. Lauterbach, *J. Mater. Chem.* **1999**, *9*, 289.
- 68 J. C. Labiche, O. Mathon, S. Pascarelli, M. A. Newton, G. G. Ferre, C. Curfs, G. Vaughan, A. Homs,
 D. F. Carreiras, *Rev. Sci. Instrum.* **2007**, *78*, 091301.
- 69 CrysAlisPro, version 1.171.38.41, Rigaku Oxford Diffraction, Great Britain, **2015**.
- 70 G. M. Sheldrick, *Acta Crystallogr. Sect. A* **2008**, *64*, 112.
- 71 Digital Micrograph, version 3.6.1, Gatan, USA, **1999**.
- 72 J. L. Lábár, *Ultramicroscopy* **2005**, *103*, 237.
- 73 Stadelmann, P. A., JEMS, version 3.3425, CIME–EPFL, Switzerland, **2008**.
- 74 ES Vision, version 4.0.164, Emispec Systems Inc., USA, **2002**.

2.3.5 Supporting Information

Table S1. EDX analyses of four different microcrystals (three measurements points each) of $\text{La}_{24}\text{Sr}_{14-7x}[\text{Si}_{36}\text{N}_{72}](\text{O}_{1-x}\text{F}_x)_{14}$, variance in parentheses.

	K1	K2	K3	K4	Ø
N(K)	49(2)	38(2)	43.5(9)	46(1)	44(5)
O(K)	11(3)	16(1)	10.9(6)	12(2)	12(2)
F(K)	6.7(3)	5.7(2)	6.0(2)	6.1(1)	6(1)
Si(K)	18(2)	20.2(2)	20.1(4)	18.1(6)	19(1)
Sr(L)	4.6(2)	6.8(1)	6.0(3)	5.8(7)	6(1)
La(L)	11.2(4)	13.7(3)	13.5(7)	12.0(5)	13(1)

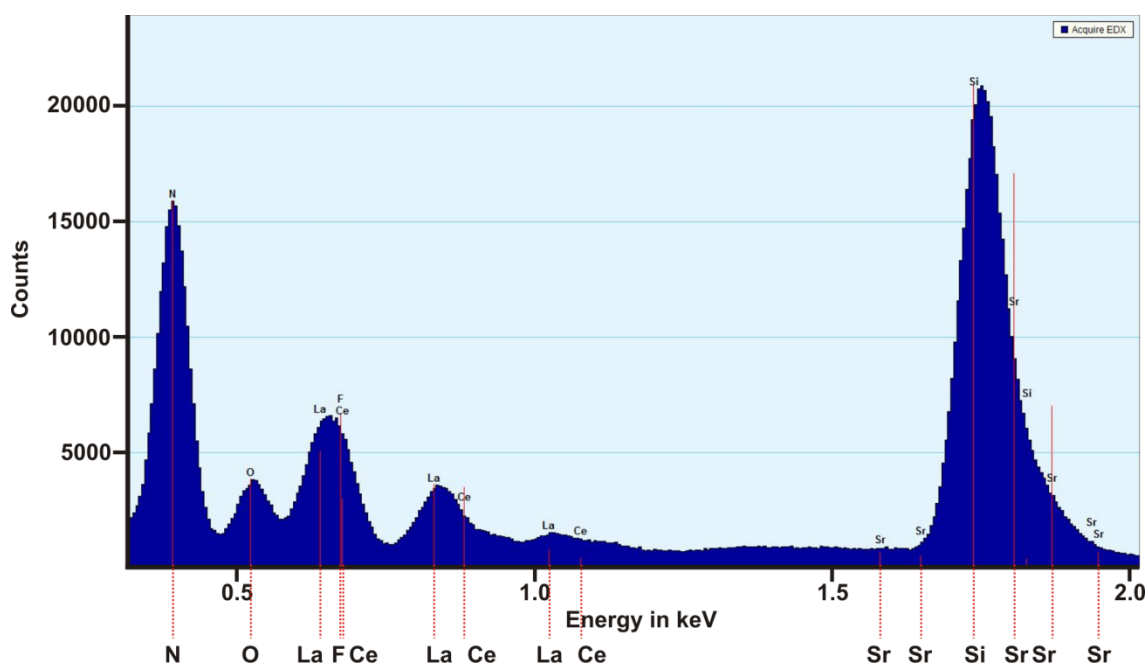


Figure S2. Representative EDX spectrum of $\text{La}_{24}\text{Sr}_{14-7x}[\text{Si}_{36}\text{N}_{72}](\text{O}_{1-x}\text{F}_x)_{14}$ doped with Ce. The presence of elements including Ce is observed.

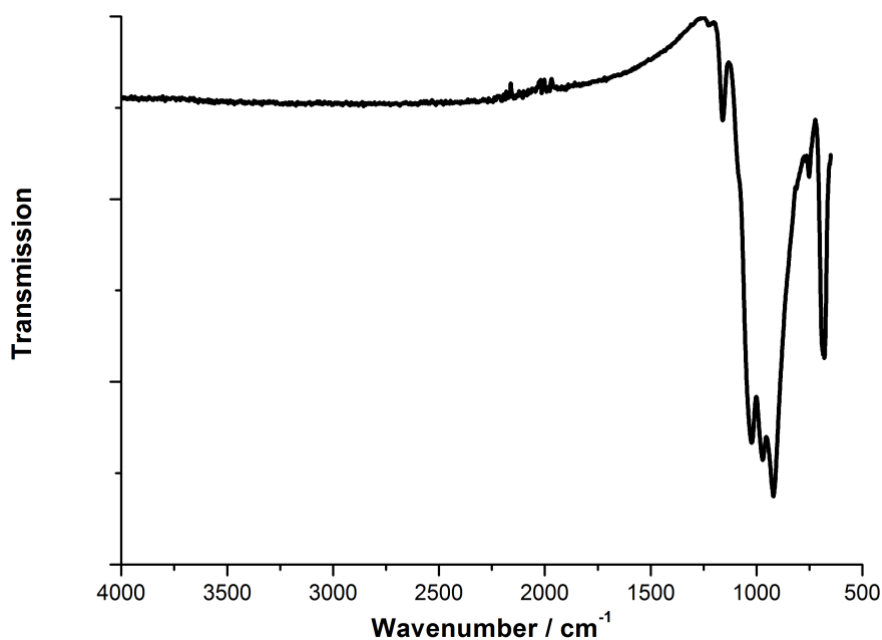


Figure S2. FTIR spectrum of $\text{La}_{24}\text{Sr}_{14-7x}[\text{Si}_{36}\text{N}_{72}](\text{O}_{1-x}\text{F}_x)_{14}$.

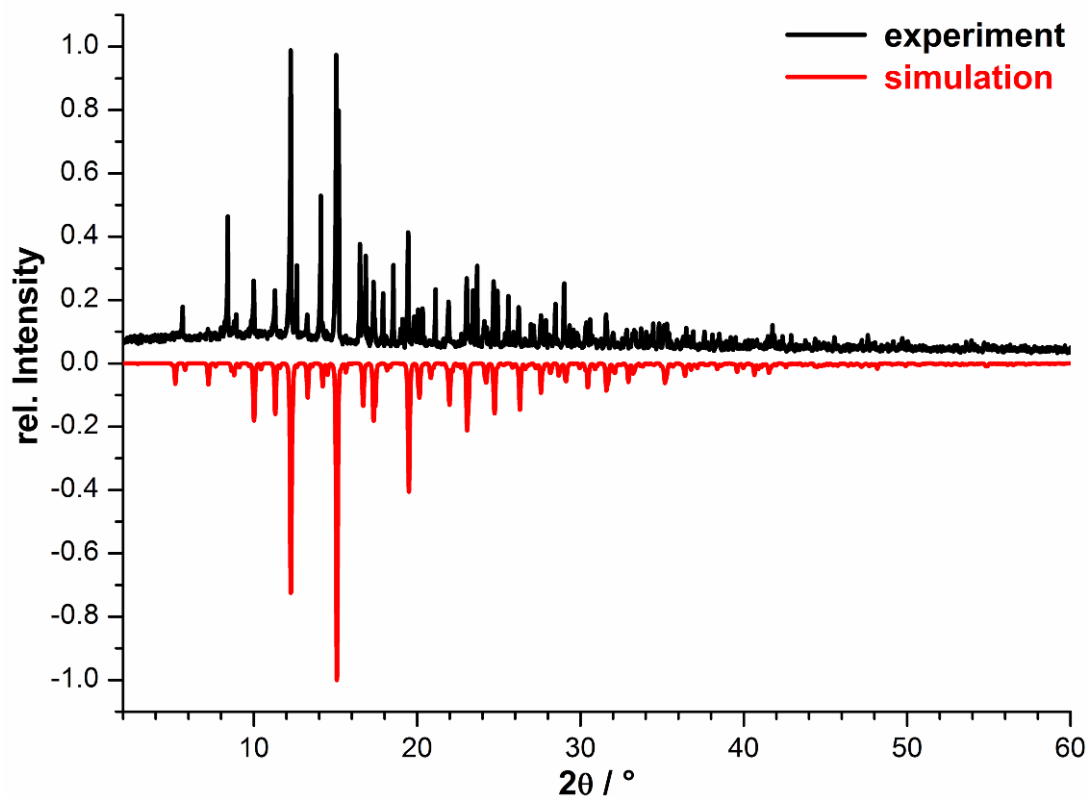


Figure S3. Experimental PXRD pattern of a typical reaction product (black) compared to one calculated from the single-crystal data of $\text{La}_{24}\text{Sr}_{14-7x}[\text{Si}_{36}\text{N}_{72}](\text{O}_{1-x}\text{F}_x)_{14}$ (red). Misfits concerning reflection intensities may come from preferred orientation, which was not taken into account. Further unexplained reflections originate from an unknown phase.

Table S2. Atom coordinates, isotropic displacement parameters (in Å²) of $La_{24}Sr_{14-7x}[Si_{36}N_{72}](O_{1-x}F_x)_{14}$ ($x = 0.489$) with estimated standard deviations in parentheses.

atom	Wyckoff site	x	y	z	U_{eq}	s. o. f.
La1	12i	0.32734(3)	0	0	0.0258(3)	1
La2	6h	0.90248(3)	0.80496(6)	¼	0.0252(3)	1
La3	6h	0.76114(3)	0.52229(7)	¼	0.0313(3)	1
Sr4	6h	0.44259(4)	0.88519(8)	¼	0.0205(3)	1
Sr5	4f	⅓	⅓	0.03377(18)	0.0227(3)	1
Sr6	4e	0	0	0.0339(10)	0.029(4)	0.146(6)
Si1	12k	0.55493(8)	0.10987(15)	0.0737(2)	0.0178(5)	1
Si2	12k	0.10638(8)	0.21277(15)	0.0858(2)	0.0159(5)	1
Si3	12k	0.22639(8)	0.45278(16)	0.0864(2)	0.0167(4)	1
N1	12k	0.1666(2)	0.3331(4)	0.0726(8)	0.0210(14)	1
N2	6h	0.0806(3)	0.1613(7)	¼	0.0186(17)	1
N3	12i	0.1733(4)	0	0	0.0164(13)	1
N4	24l	0.4956(4)	0.1638(4)	0.0054(5)	0.0207(12)	1
N5	6g	½	0	0	0.048(4)	1
N6A	6h	0.5685(5)	0.1369(10)	¼	0.009(2)	0.75(3)
N6B	6h	0.5482(16)	0.096(3)	¼	0.009(2)	0.25(3)
N7A	6h	0.2553(4)	0.5106(8)	¼	0.011(2)	0.76(2)
N7B	6h	0.2301(14)	0.460(3)	¼	0.011(2)	0.24(2)
O8 / F8	2d	⅓	⅓	¾	0.053(5)	0.5114 / 0.4885
O9 / F9	12j	0.3319(4)	0.0636(5)	¼	0.0322(13)	0.5114 / 0.4885

Table S3. Anisotropic displacement parameters (in Å²) of $La_{24}Sr_{14-7x}[Si_{36}N_{72}](O_{1-x}F_x)_{14}$ ($x = 0.489$) with standard deviation in parentheses.

Atom	U_{11}	U_{22}	U_{33}	U_{23}	U_{13}	U_{12}
La1	0.0184(3)	0.0192(3)	0.0400(4)	0.0064(2)	0.00321(10)	0.00962(17)
La2	0.0239(3)	0.0357(5)	0.0201(4)	0	0	0.0178(2)
La3	0.0320(4)	0.0487(6)	0.0186(4)	0	0	0.0243(3)
Sr4	0.0205(4)	0.0292(5)	0.0147(5)	0	0	0.0146(3)
Sr5	0.0154(4)	0.0154(4)	0.0373(7)	0	0	0.0077(2)
Sr6	0.018(3)	0.018(3)	0.050(9)	0	0	0.0089(15)
Si1	0.0169(8)	0.0180(10)	0.0188(10)	0.0009(7)	0.0005(4)	0.0090(5)
Si2	0.0151(7)	0.0167(9)	0.0165(11)	-0.0010(7)	-0.0005(4)	0.0084(5)
Si3	0.0164(7)	0.0168(10)	0.0171(10)	0.0001(7)	0.0000(4)	0.0084(5)
N1	0.020(2)	0.017(3)	0.025(3)	0.003(2)	0.0016(11)	0.0086(16)
N2	0.019(3)	0.016(4)	0.020(4)	0	0	0.008(2)
N3	0.017(2)	0.014(3)	0.018(3)	0.006(2)	0.0029(11)	0.0068(16)
N4	0.019(3)	0.020(3)	0.027(3)	0.0026(18)	0.0025(17)	0.012(2)
N5	0.022(4)	0.022(6)	0.100(11)	-0.024(7)	-0.012(3)	0.011(3)
O8/F8	0.046(7)	0.046(7)	0.067(13)	0	0	0.023(4)
O9/F9	0.027(3)	0.037(3)	0.029(3)	0	0	0.013(3)

Table S4. Bond-valence sums for $La_{24}Sr_{14-7x}[Si_{36}N_{72}](O_{1-x}F_x)_{14}$.

	La1	La2	La3	Sr4	Sr5	Sr6	Si1	Si2	Si3
BVS	2.56	2.70	2.53	1.58	1.84	1.52	4.22	4.21	4.25
occ.	1	1	1	1	1	0.145	1	1	1
	N1	N2	N3	N4	N5	N6A/N6B	N7A/N7B	O8/F8	O9/F9
BVS	2.81	3.13	3.18	3.06	3.02	2.78/2.78	2.68/3.57	1.30/0.99	1.39/1.11
occ.	1	1	1	1	1	0.75/0.24	0.74/0.26	0.51/0.49	0.51/0.49

The bond-valence sums (BVS) for $La_{24}Sr_{14-7x}[Si_{36}N_{72}](O_{1-x}F_x)_{14}$ confirm the element assignment based on the X-ray data. The BVS of the cations sites 1-3 are significantly > 2 in contrast to the BVS of the sites 4-6, which are < 2, confirming the assignment of La and Sr, respectively. The deviations of the BVS to the oxidation numbers are < 8% for most atoms forming the AB₂ framework. Due to the short Si1-N7B distance of 1.555 Å (affected by disorder) the BVS of N7B seems too large. The mixed occupancy of O and F on the anion sites between the tetrahedral network matches the BVS between 1 and 2.

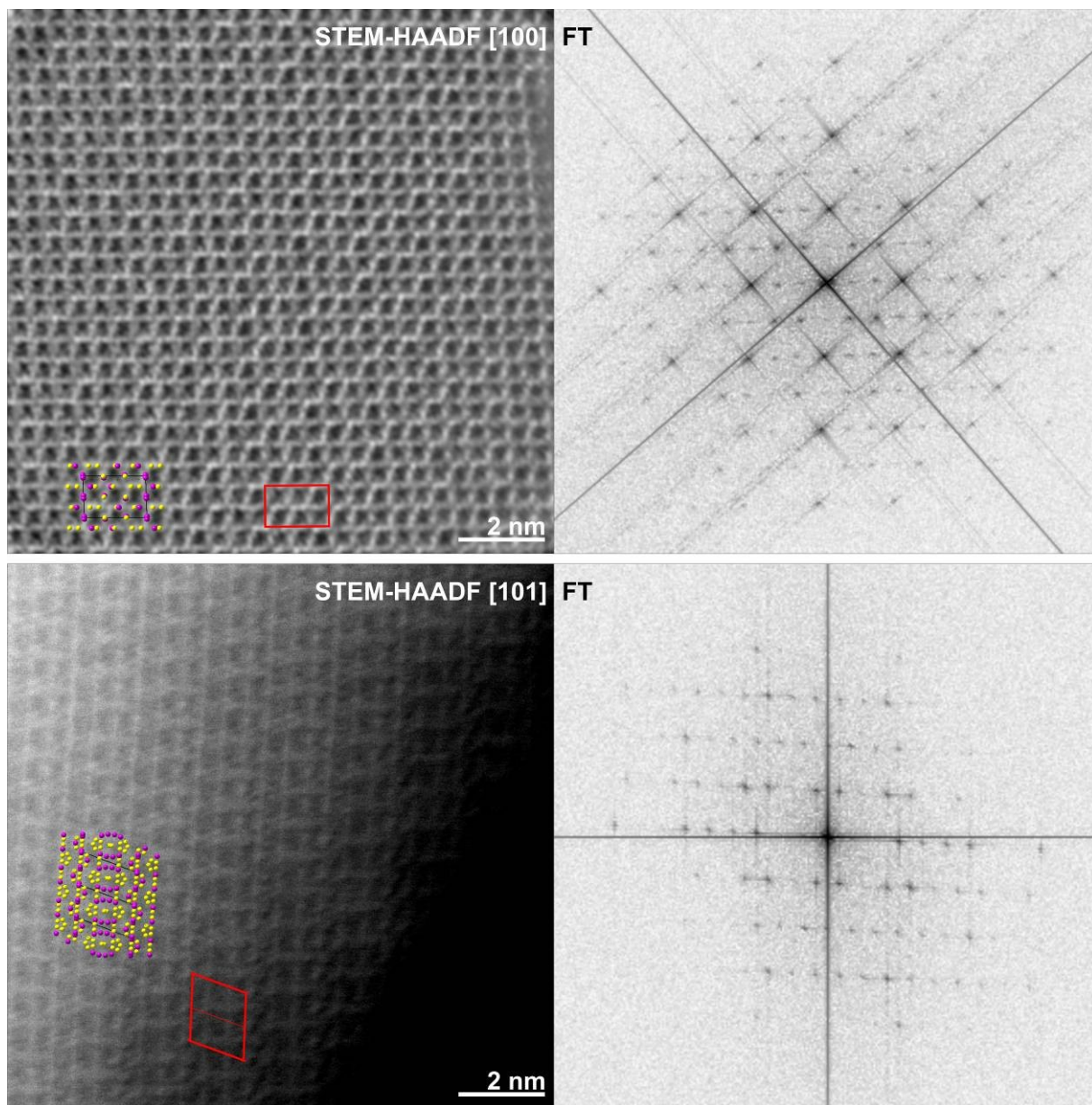


Figure S4. Enlarged STEM-HAADF micrographs (left) viewed along the zone axes [100] (top) and [101] (bottom) with corresponding Fourier transforms (right) of $La_{24}Sr_{14-7x}[Si_{36}N_{72}](O_{1-x}F_x)_{14}$. Unit cell highlighted in red, colored overlay of La^{3+} (yellow) and Sr^{2+} (pink) ions.

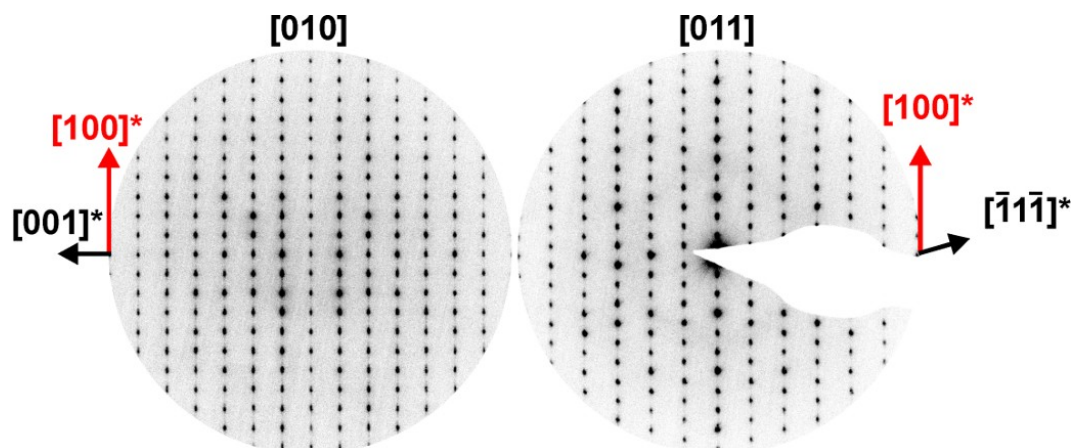


Figure S5. SAED pattern of $\text{La}_{24}\text{Sr}_{14-7x}[\text{Si}_{36}\text{N}_{72}](\text{O}_{1-x}\text{F}_x)_{14}$ showing weak diffuse intensities along $[100]$ (red arrows) observed along zone axis $[010]$ (left) and $[011]$ (right).

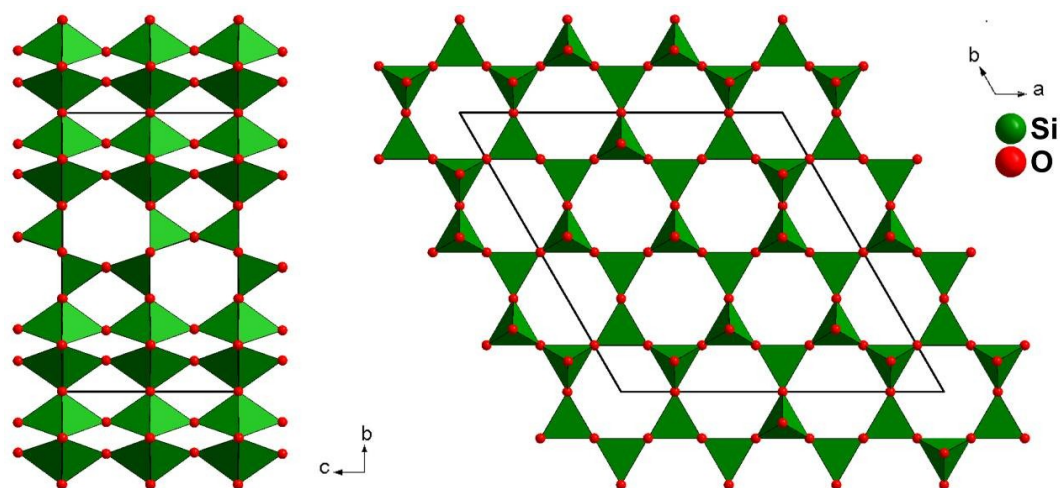


Figure S6. Calculated crystal structure of SiO_2 in the theoretical prospective unique network type 194_3_3914, listed in the hypothetical zeolite database.¹

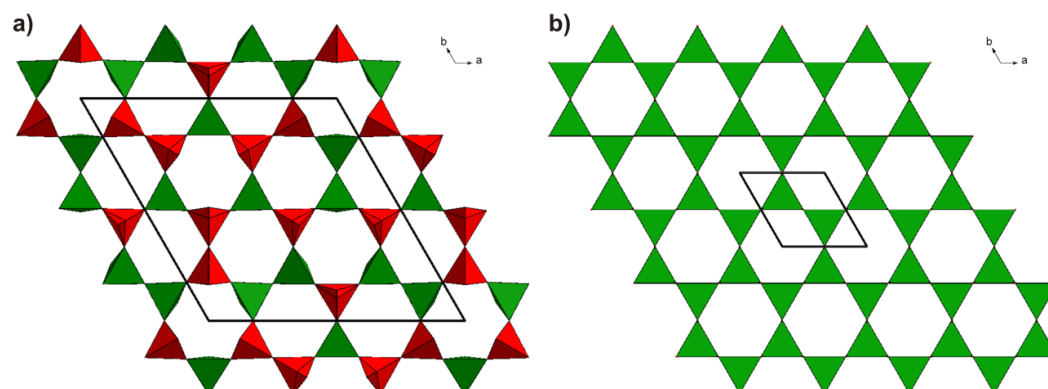


Figure S7. Orientation of the tetrahedra in $\text{La}_{24}\text{Sr}_{14-7x}[\text{Si}_{36}\text{N}_{72}](\text{O}_{1-x}\text{F}_x)_{14}$ (a) and tridymite (b) viewed along $[001]$. Tetrahedra pointing down represented in green and pointing up represented in red. Unit cells are outlined in black.

Every individual six-membered ring consist of each three up-orientated (Figure S11: red) and down-orientated (Figure S11: green) tetrahedra. Their arrangement generates *sechser* rings with either alternating up and down orientation of the tetrahedra, or one pair plus one lone tetrahedron point in the same direction within each ring.

Table S5. Bond lengths in $La_{24}Sr_{14-7x}[Si_{36}N_{72}](O_{1-x}F_x)_{14}$ ($x = 0.489$) with standard deviations in parentheses. The unrealistically short Si3-N7B distance (1.5445(65) Å) observed at the anion split position N7A/B is associated with disorder, which can be compared to the situations in $Y_2AlSiNO_5$, $NaSi_2N_3$ or Si_3N_4 .²⁻⁵

bond	length (in Å)	bond	length (in Å)
La1-N3	2.496(6)	Sr5-N4	2.785(8)
La1-N4	2.692(5)	Sr5-N7A	2.991(9)
La1-N5	2.7982(6)	Sr5-O8/F8	2.6721(17)
La1-O9/F9	2.556(3)	Sr6-N3	2.827(7)
La2-N2	2.534(3)	Si1-N4	1.716(5)
La2-N3	2.7582(10)	Si1-N5	1.691(2)
La2-O9/F9	2.538(6)	Si1-N6A	1.703(4)
La3-N4	2.687(5)	Si1-N6B	1.670 (6)
La3-N6A	2.706(8)	Si2-N1	1.694(6)
La3-O8/F8	2.6520(10)	Si2-N2	1.707 (5)
La3-O9/F9	2.634(6)	Si2-N3	1.7121(15)
Sr4-N4	2.867(5)	Si3-N1	1.685(7)
Sr4-N5	2.8528(6)	Si3-N4	1.720(5)
Sr4-N6B	2.96(5)	Si3-N7A	1.742 (6)
Sr4-N7A	2.736(3)	Si3-N7B	1.545(6)
Sr4-N7B	2.986(18)		

References

- 1 a) M. M. J. Treacy, I. Rivin, E. Balkovsky, K. H. Randall, M. D. Foster, *Microporous Mesoporous Mater.* **2004**, *74*, 121; b) M. D. Foster, M. M. J. Treacy, J. B. Higgins, I. Rivin, E. Balkovsky, K. H. Randall, *J. Appl. Crystallogr.* **2005**, *38*, 1028; c) M. D. Foster, M. M. J. Treacy, Database of Hypothetical Zeolite Structures: <http://www.hypotheticalzeolites.net>.
- 2 M. F. Gonon, J. -C. Descamps, F. Cambier, D. P. Thompson, *Mater. Sci. Forum* **2000**, *323*, 325.
- 3 H. Mengis, H. Jacobs, *Eur. J. Solid State Inorg. Chem.* **1993**, *30*, 45.
- 4 M. Billy, J. C. Labbé, A. Selvaraj, G. Rault, *Mater. Res. Bull.* **1983**, *18*, 921.
- 5 J. Schneider, F. Frey, N. Johnson, K. Laschke, Z. *Anorg. Allg. Chem.* **1994**, *209*, 328.

3 Complex crystal structures of (oxo)nitridophosphates elucidated by transmission electron microscopy

3.1 Overview

Phosphorus oxide nitride (PON) is isoelectronic to silica (SiO_2) and because of this analogy, oxonitridophosphates are closely related to silicates. Due to threefold coordinated nitrogen atoms, the variable atomic ratio N:O and the possibility of forming tetrahedra networks with a degree of condensation (κ) larger 0.5, a structural diversity at least as great as for oxosilicates is expected for oxonitridophosphates.¹⁻³ Moreover, further variability can be achieved by substitution of O^{2-} by NH^{2-} . However, relatively few (oxo)nitridophosphates and their crystal structures have been reported. Nevertheless, research on (oxo)nitridophosphates is a growing field of interest because they are discussed as innovative materials and for some (oxo)nitridophosphates promising properties have been already observed in analogy to (oxo)nitridesilicates. For instance with respect to energy saving, recently discovered (oxo)nitridophosphates have been tested as phosphors for LED lighting.^{4,5} Interesting luminescence properties were observed for Eu^{2+} -doped MP_2N_4 ($M = \text{Ca}, \text{Sr}, \text{Ba}$) and $\text{BaSr}_2\text{P}_6\text{N}_{12}$.⁶ The nitridophosphate $\text{Ba}_3\text{P}_5\text{N}_{10}\text{Br}:\text{Eu}^{2+}$ has a zeolite-like structure and with its white luminescence, it is discussed as single emitter phosphor.⁷ Based on tetrahedra networks with large cavities, further features of (oxo)nitridophosphates are ion-exchange or ion-conductivity. Li_7PN_4 and $\text{Li}_{18}\text{P}_6\text{N}_{16}$ as well as thin layers of $\text{Li}_{2.88}\text{PO}_{3.73}\text{N}_{0.14}$ are discussed as Li-ion conductors and future applications as solid electrolytes are imaginable.⁸⁻¹²

For the synthesis of (oxo)nitridophosphates predominantly extreme high-pressure and high-temperature conditions are applied, which are achieved with multianvil press or in a diamond-anvil cell. The decomposition of azides, the reaction of nitrides or metathesis are promising routes. Using these synthetic approaches, only small amounts of microcrystalline products with occasional bad crystallinity are obtained. Mineralizers like NH_4Cl or Li_2O can facilitate the formation and crystallization of metal-(oxo)nitridophosphates.¹³ In addition to the structural and functional analogy between (oxo)nitridophosphates and oxonitridosilicates, a methodical analogy for approaches for their structure determination seems sensible. Thus, TEM, as a particularly sensitive method, is ideal to contribute significantly to the structure determination. For example, ADT was used to determine the crystal structure of nanocrystalline $\text{SrP}_3\text{N}_5\text{O}$ and $\text{Ba}_6\text{P}_{12}\text{N}_{17}\text{O}_9\text{Br}_3$.^{14,15} TEM, especially electron diffraction, was an important tool for the structural elucidation of the first two zeolite-type oxonitridophosphates (NPO-framework type, for nitridophosphate one: $\text{Li}_x\text{H}_{12-x-y+z}[\text{P}_{12}\text{O}_y\text{N}_{24-y}]\text{Cl}_z$ and NPT-framework type: $\text{Ba}_{19}\text{P}_{36}\text{O}_{6+x}\text{N}_{66-x}\text{Cl}_{8+x}$ with $x = 4.54$).^{16,17}

The combination of X-ray diffraction and TEM enables the elucidation of complex oxonitridophosphate structures, exemplarily shown for the ortho-phosphate $\text{Ca}_2\text{PO}_3\text{N}$, which is an incommensurately modulated modification of the $\beta\text{-K}_2\text{SO}_4$ type.¹⁸

The structural diversity of (oxo)nitridophosphates and the wide range of potential properties not only allows unusual insights into the basic relations between structures and properties, but can also pave the way towards applications.¹⁹

References

- 1 W. Schnick, W. Schnick, *Angew. Chem.* **1993**, 105, 846; *Angew. Chem. Int. Ed. Engl.* **1993**, 32, 806.
- 2 F. J. Pucher, F. W. Karau, J. Schmedt auf der G nne, W. Schnick, *Eur. J. Inorg. Chem.* **2016**, 1497.
- 3 S. Horstmann, E. Irran, W. Schnick, *Z. Anorg. Allg. Chem.* **1998**, 624, 620.
- 4 S. Schmiechen, P. Pust, P. J. Schmidt, W. Schnick, *Nachr. Chem.* **2014**, 62, 847.
- 5 M. Zeuner, S. Pagano, W. Schnick, *Angew. Chem.* **2011**, 123, 7898; *Angew. Chem. Int. Ed.* **2011**, 50, 7754.
- 6 F. J. Pucher, A. Marchuk, P. J. Schmidt, D. Wiechert, W. Schnick, *Chem. Eur. J.* **2015**, 21, 6443.
- 7 A. Marchuk, W. Schnick, *Angew. Chem.* **2015**, 127, 2413; *Angew. Chem. Int. Ed.* **2015**, 54, 2383.
- 8 W. Schnick, J. L cke, *Solid State Ionics.* **1990**, 38, 271.
- 9 E. -M. Bertschler, C. Dietrich, J. Janek, W. Schnick, *Chem. Eur. J.* **2017**, 23, 2185.
- 10 P. Knauth, *Solid State Ionics* **2009**, 180, 911.
- 11 N. Mascaraque, J. L. G. Fierro, A. Duran, F. Munoz, *Solid State Ionics* **2013**, 233, 73.
- 12 K. Senevirathne, C. S. Day, M. D. Gross, A. Lachgar, N. A. W. Holzwarth, *Solid State Ionics* **2013**, 233, 95.
- 13 A. Marchuk, Dissertation, Ludwig-Maximilians-University, Munich, **2015**.
- 14 S. J. Sedlmaier, E. Mugnaioli, O. Oeckler, U. Kolb, W. Schnick, *Chem. Eur. J.* **2011**, 17, 11258.
- 15 E. Mugnaioli, S. J. Sedlmaier, O. Oeckler, U. Kolb, W. Schnick, *Eur. J. Inorg. Chem.* **2012**, 121.
- 16 S. J. Sedlmaier, M. D blinger, O. Oeckler, J. Weber, J. Schmedt auf der G nne, W. Schnick, *J. Am. Chem. Soc.* **2011**, 133, 12069.
- 17 S. Correll, O. Oeckler, N. Stock, W. Schnick, *Angew. Chem.* **2003**, 115, 3674; *Angew. Chem. Int. Ed.* **2003**, 42, 3549.
- 18 A. Marchuk, P. Schultz, C. Hoch, O. Oeckler, W. Schnick *Inorg. Chem.* **2016**, 55, 974.
- 19 R. Marchand, W. Schnick, N. Stock, *Adv. Inorg. Chem.* **2000**, 50, 193.

3.2 $\text{CaMg}_2\text{P}_6\text{O}_3\text{N}_{10}$ – A Quinary Oxonitridophosphate with an Unprecedented Tetrahedra Network Structure type

Alexey Marchuk, Lukas Neudert, Oliver Oeckler and Wolfgang Schnick

Eur. J. Inorg. Chem. **2014**, 3427.

Reprinted with permission from *European Journal of Inorganic Chemistry*. Copyright 2014 Wiley Online Library.

Abstract

$\text{CaMg}_2\text{P}_6\text{O}_3\text{N}_{10}$ has been synthesized starting from stoichiometric amounts of $\text{Ca}(\text{N}_3)_2$, Mg_3N_2 , P_3N_5 , and PON in a high-pressure/high-temperature reaction at 8 GPa and 1100 °C. Adding small amounts of NH_4Cl to the starting mixture afforded single crystals of $\text{CaMg}_2\text{P}_6\text{O}_3\text{N}_{10}$, which form transparent, colorless truncated octahedra. The crystal structure [space group $I4_1/acd$ (no. 142), $a = 12.494(1)$, $c = 23.797(2)$ Å, $Z = 16$] was solved and refined by single-crystal X-ray diffraction analysis and confirmed by electron diffraction and transmission electron microscopy, including HRTEM image simulations. Rietveld refinement proved the phase purity of the product. FTIR analysis confirmed the absence N–H groups in the structure. Bond valence and lattice energy calculations (MAPLE) of the title compound are discussed. The crystal structure consists of polyhedral building units constructed from vertex-sharing $\text{P}(\text{O},\text{N})_4$ tetrahedra with condensed *dreier* and *sechser* rings.

3.2.1 Introduction

Silicates form one of the most abundant, varied, and important classes of minerals, with more than 1000 representatives. More than 90 % of the earth's crust consists of silicates.¹ Their wide range of applications in the ceramics and glass industries as well as their great potential as functional materials in catalysis, microelectronics, and optical fibers make silicates nearly indispensable for everyday life.^{2,3} Their important role as luminescent materials for phosphor-converted light-emitting diodes (pc-LEDs) also emphasizes the significance of silicates in future technologies.⁴

Accordingly, the great structural variety and associated properties make structures that are analogous to silicates an attractive research target. Because PON is isoelectronic with SiO_2 , the silicate-analogous compound class of oxonitridophosphates is expected to exhibit a structural diversity similar to that of silicates. The formal partial substitution of O by N in a tetrahedral network implies significant new structural possibilities. N in oxonitridophosphates may occur as N^1 , N^2 , N^3 , or even N^4 atoms connecting up to four neighboring tetrahedral centers.^{5,6} Compared with oxonitridophosphates, the structural variety of silicates is limited to terminal O^1 or singly bridging O^2

atoms. An excellent example of the additional structural possibilities arising from the substitution of O by N in a network structure analogous to silicates is the nitridic clathrate $\text{P}_4\text{N}_4(\text{NH})_4(\text{NH}_3)$, which has been discussed as a possible gas-storage material.^{7,8} This clathrate network structure had been predicted for silicates but has been observed only in this nitride compound so far. However, compared with oxosilicates or nitridophosphates, only a few oxonitridophosphates have been synthesized so far. This is due to fundamental difficulties concerning their synthesis and the often poor crystallinity of the reaction products. Thus, the structure determination of these compounds requires a combination of different analytical methods such as X-ray diffraction, solid-state NMR spectroscopy, or electron microscopy. Nevertheless, several important representatives of the class of oxonitridophosphates have already been described. In addition to the layer compounds $\text{M}^{\text{II}}\text{P}_6\text{O}_6\text{N}_8$ ($\text{M}^{\text{II}} = \text{Sr}, \text{Ba}$),^{9,10} $\text{M}_2^{\text{I}}\text{M}_2^{\text{II}}\text{P}_3\text{O}_9\text{N}$ ($\text{M}^{\text{I}} = \text{Na}$; $\text{M}^{\text{II}} = \text{Mg}, \text{Mn}, \text{Fe}, \text{Co}$),¹¹ $\text{M}_3^{\text{I}}\text{M}^{\text{III}}\text{P}_3\text{O}_9\text{N}$ ($\text{M}^{\text{I}} = \text{Na}, \text{K}$; $\text{M}^{\text{III}} = \text{Al}, \text{Ga}, \text{In}, \text{Ti}, \text{V}, \text{Cr}, \text{Mn}, \text{Fe}$),¹² $\text{Cs}_3\text{M}_2^{\text{II}}\text{P}_6\text{O}_{17}\text{N}$ ($\text{M}^{\text{II}} = \text{Mg}, \text{Fe}, \text{Co}$),¹³ and $\text{SrP}_3\text{N}_5\text{O}$,¹⁴ the compounds $\text{Li}_x\text{H}_{12-x-y+z}[\text{P}_{12}\text{O}_y\text{N}_{24-y}]\text{X}_z$ ($\text{X} = \text{Cl}, \text{Br}$)¹⁵ and $\text{Ba}_{19}\text{P}_{36}\text{O}_{6+x}\text{N}_{66-x}\text{Cl}_{8+x}$ ¹⁶ exhibit uncommon frameworks and represent the first nitridic zeolite-like network types NPO and NPT, respectively. This suggests that the structural chemistry of oxonitridophosphates has immense potential.

In this contribution, we report on the synthesis and structural elucidation of the novel quinary oxonitridophosphate $\text{CaMg}_2\text{P}_6\text{O}_3\text{N}_{10}$ with an unprecedented tetrahedral network structure constructed from vertex-sharing $\text{P}(\text{O},\text{N})_4$ tetrahedra.

3.2.2 Results and Discussion

3.2.2.1 Synthesis

Almost all known oxonitridophosphates have been synthesized by conventional solid-state reactions.¹⁷ In contrast, the synthesis of $\text{CaMg}_2\text{P}_6\text{O}_3\text{N}_{10}$ requires high-pressure conditions. So far, only two oxonitridophosphates, namely $\text{M}^{\text{II}}\text{P}_6\text{O}_6\text{N}_8$ ($\text{M}^{\text{II}} = \text{Sr}, \text{Ba}$), have been synthesized under such high-pressure conditions.^{9,10}

$\text{CaMg}_2\text{P}_6\text{O}_3\text{N}_{10}$ was obtained by using a Walker-type multi-anvil assembly¹⁸ at 8 GPa and 1100 °C starting from stoichiometric amounts of $\text{Ca}(\text{N}_3)_2$, Mg_3N_2 , P_3N_5 , and PON [Eq. (1)]. A high N_2 partial pressure, which is available by in situ thermolysis of $\text{Ca}(\text{N}_3)_2$, prevents P_3N_5 from dissociation into elements at reaction temperatures above 1000 °C,¹⁹ under ambient pressure, P_3N_5 already dissociates into elements at temperatures above 850 °C. By adding catalytic amounts of NH_4Cl to the mixture of starting materials, colorless crystals in the form of morphologically well-developed truncated octahedra were obtained and isolated (see Figure 1). Thus, the addition of NH_4Cl as a mineralizer helps to overcome the main problem of the poor crystallization of oxonitridophosphates mentioned above.

As discussed previously, HCl, formed as an intermediate, presumably enables reversible bond cleavage and re-formation, and thus facilitates the growth of single crystals.²⁰ Detailed information on the synthesis of CaMg₂P₆O₃N₁₀ is given in the Exp. Sect.

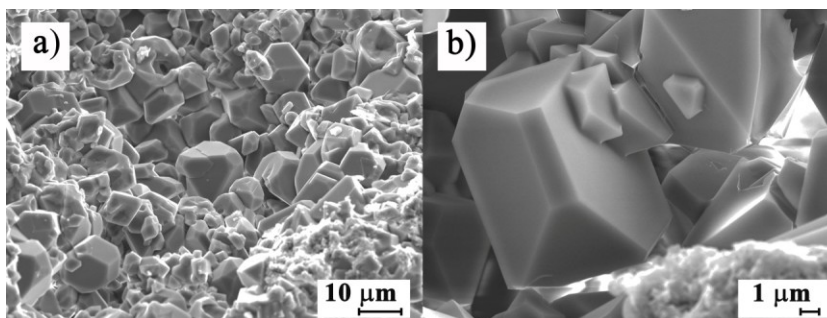
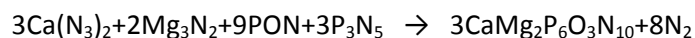


Figure 1. SEM images of crystals of CaMg₂P₆O₃N₁₀.

3.2.2.2 Structure determination

The crystal structure of CaMg₂P₆O₃N₁₀ was solved and refined from the single-crystal X-ray diffraction data in the tetragonal space group *I*4₁/*acd*. For crystal structure refinement the values of the lattice parameters obtained from the Rietveld refinement were used. It was possible to refine significant site occupancies for the mixed O/N positions. All atoms were refined anisotropically. The crystallographic data of CaMg₂P₆O₃N₁₀ are summarized in the Exp. Sect. and the atomic parameters are given in Table 1.

Because some displacement parameters and interatomic distances appeared unusual (see below), TEM investigations were performed to verify the structure derived from the X-ray diffraction data. The reflection positions and intensities of the SAED (selected area electron diffraction) patterns (Figure 2) of different crystallites of CaMg₂P₆O₃N₁₀ matched the calculated ones, which proves the tetragonal metrics, the four-fold axis (Figure 2, a), and the reflection conditions ($h + k + l = 2n$) of the body-centered Bravais lattice. Systematic absences due to glide planes (*a*, *c*, *d*) are evident in the corresponding zone-axis patterns (Figure 2, a–d).

Table 1. Atomic coordinates, isotropic displacement parameters, and occupation of crystallographic positions of $\text{CaMg}_2\text{P}_6\text{O}_3\text{N}_{10}$.^[a]

Atom		<i>x</i>	<i>Y</i>	<i>z</i>	<i>U</i> _{eq} /Å ²	Occupancy
Ca1	8 <i>a</i>	1/2	1/4	1/8	0.0086(3)	1.0
Ca2	8 <i>b</i>	1	3/4	3/8	0.0590(9)	1.0
Mg1	32 <i>g</i>	0.34412(11)	0.06404(12)	0.04286(7)	0.0128(3)	1.0
P1	32 <i>g</i>	0.60101(8)	0.02018(8)	0.08042(5)	0.0052(2)	1.0
P2	32 <i>g</i>	0.74435(8)	0.19018(8)	0.08350(4)	0.0053(2)	1.0
P3	32 <i>g</i>	0.58898(7)	0.18157(8)	-0.00049(5)	0.0053(2)	1.0
N1	32 <i>g</i>	0.6603(3)	0.2566(3)	0.04283(19)	0.0070(7)	1.0
N2/O2	32 <i>g</i>	0.7981(3)	0.2733(2)	0.12829(16)	0.0072(8)	0.86(3)/0.14(3)
N3	32 <i>g</i>	0.6724(3)	0.1035(3)	0.11819(15)	0.0069(7)	1.0
N4	32 <i>g</i>	0.5260(3)	0.0931(3)	0.03859(18)	0.0061(7)	1.0
N5/O5	32 <i>g</i>	0.8376(3)	0.1259(3)	0.04907(15)	0.0106(9)	0.76(4)/0.24(4)
N6/O6	16 <i>d</i>	1/2	1/4	-0.0330(2)	0.0103(13)	0.76(7)/0.24(7)
O7	32 <i>g</i>	0.6717(2)	-0.0534(2)	0.04400(14)	0.0106(6)	1.0

[a] Standard deviations are given in parentheses.

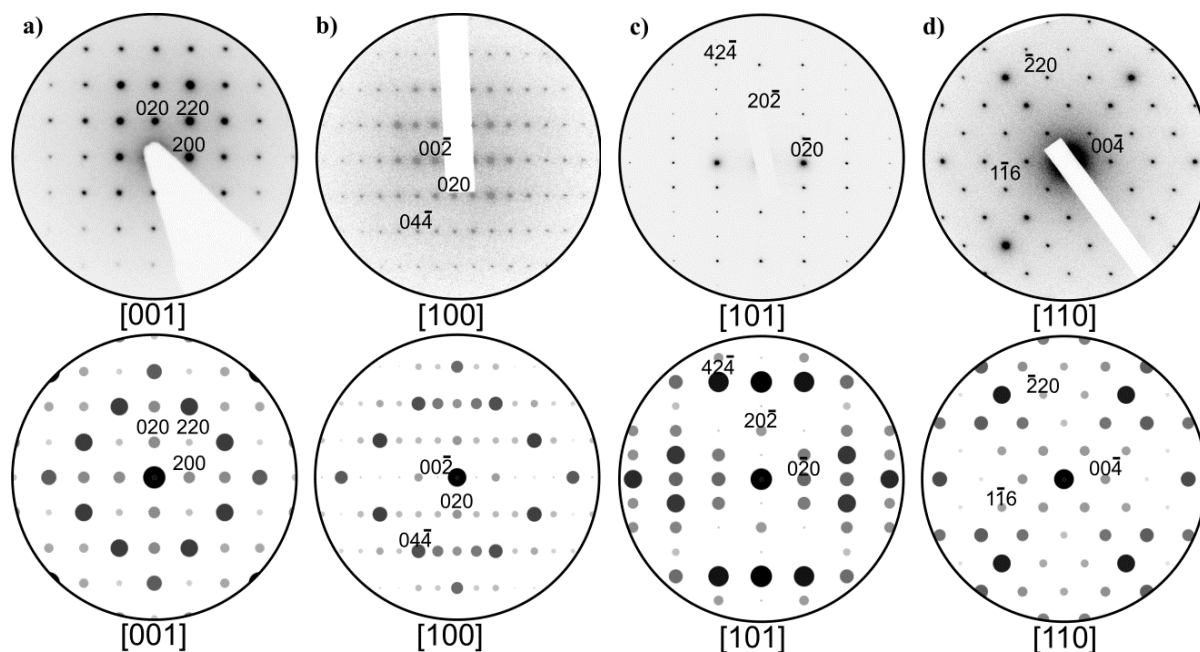


Figure 2. Experimental (top) SAED patterns with corresponding simulations (bottom, based on the single-crystal X-ray diffraction data) for $\text{CaMg}_2\text{P}_6\text{O}_3\text{N}_{10}$ obtained from different crystallites; exemplary reflections in the selected zero plains are labeled with indices.

Significant features in the HRTEM image simulations match well the experimental data (Figure 3) and thus corroborate the structure model of $\text{CaMg}_2\text{P}_6\text{O}_3\text{N}_{10}$. In a structure projection along $[713]$ the Ca atom positions appear as rows that strongly influence the image contrast. This is strongly affected by the Ca2 site (oblate displacement ellipsoid, see below). There are no indications of superstructures and there is no characteristic mismatch. Significant contrast changes (in simulations and experiments) occur when the defocus values are altered by more than around 3 nm or when the thickness changes by more than around 5 nm, but also when the Ca atom positions are shifted by more than around 0.05 Å.

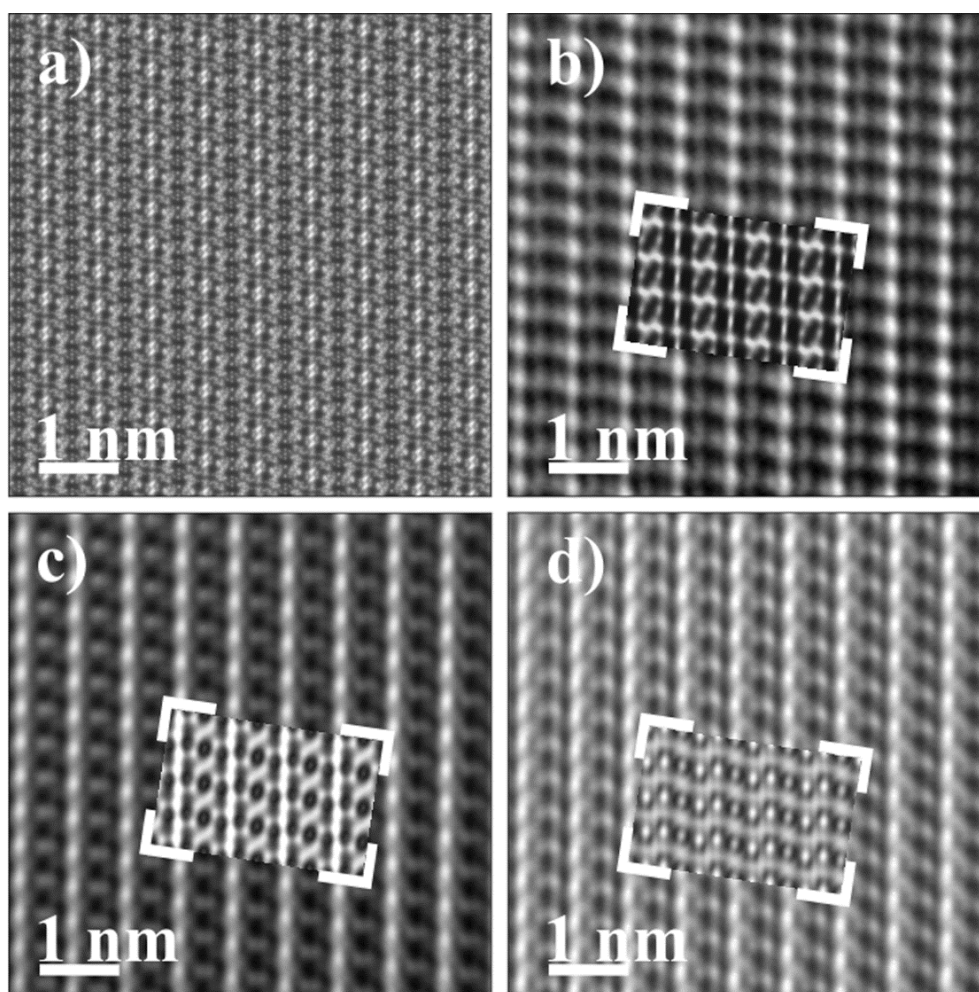


Figure 3. a) Projected potential and b–d) HRTEM images of $\text{CaMg}_2\text{P}_6\text{O}_3\text{N}_{10}$ along the $\langle 713 \rangle$ zone axis with image simulations (accelerating voltage: 300 keV, $C_s = 0.6$ mm, spread of focus: 3.6 nm, beam semiconvergence: 17 mrad, layer thickness two unit cells). Insets: defocus values: b) -70 , c) -43 , and d) -28 nm.

The Rietveld refinement of the powder X-ray data confirmed the presence of a single-phase product corresponding to the crystal structure of $\text{CaMg}_2\text{P}_6\text{O}_3\text{N}_{10}$, as determined from the single-crystal data (see Figure 4); traces of cubic boron nitride (c-BN, 6 %) correspond to residual amounts of the boron nitride capsule. Detailed information on the crystallographic data of the Rietveld refinement of $\text{CaMg}_2\text{P}_6\text{O}_3\text{N}_{10}$ can be found in Tables S1 and S2 in the Supporting Information.

The absence of N–H groups in the title compound was confirmed by FTIR spectroscopy (see Figure S1 in the Supporting Information). The chemical composition of the product was confirmed by energy-dispersive X-ray (EDX) spectroscopy; no elements other than Ca, Mg, P, O, and N were detected. The determined atomic ratio of Ca/O/P is in good agreement with the stoichiometric formula $\text{CaMg}_2\text{P}_6\text{O}_3\text{N}_{10}$ (see Table S3), and although the determination of N and P is less reliable, it is in the correct range.

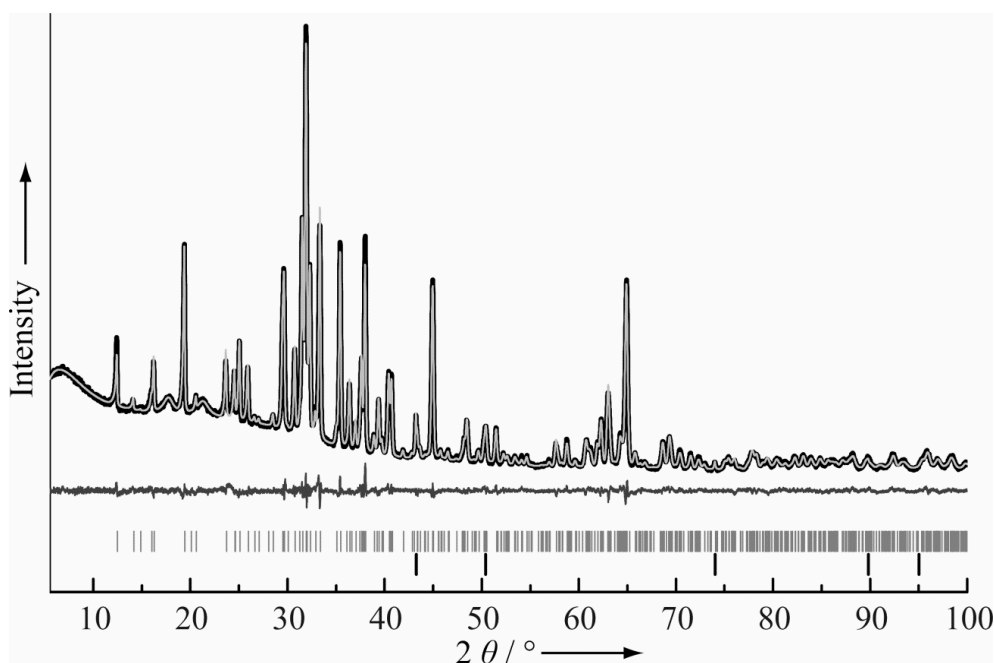


Figure 4. Observed (black line) and calculated (light-gray line) X-ray powder diffraction pattern, positions of Bragg reflections ($\text{CaMg}_2\text{P}_6\text{O}_3\text{N}_{10}$: vertical gray bars; c-BN: vertical bold bars), and difference profile for the Rietveld refinement of $\text{CaMg}_2\text{P}_6\text{O}_3\text{N}_{10}$ (dark-gray line).

3.2.2.3 Structure description

The crystal structure of $\text{CaMg}_2\text{P}_6\text{O}_3\text{N}_{10}$ consists of a three-dimensional network of vertex-sharing Q^4 - and Q^3 -type $\text{P}(\text{O},\text{N})_4$ tetrahedra in the ratio $\text{Q}^4/\text{Q}^3 = 3:1$, leading to a degree of condensation $\kappa = n(\text{P})/n(\text{O},\text{N}) = 0.46$ for the $[\text{P}_6\text{O}_3\text{N}_{10}]^{6-}$ substructure. The Q^3 -type $\text{P}(\text{O},\text{N})_4$ tetrahedra are composed of two singly bridging N^2 atoms, one singly bridging $(\text{O},\text{N})^2$ atom, and one terminal O^1 atom.

Figure 5 (a) shows the unit cell of $\text{CaMg}_2\text{P}_6\text{O}_3\text{N}_{10}$, one polyhedral building unit (PBU, light-gray tetrahedra) is highlighted. It contains all the P, N, and O positions and is thus well suited to describing the whole structure. The interconnected PBUs form a three-dimensional network (Figure 5, b). As shown in Figure 6, the PBU consists of vertex-sharing $\text{P}(\text{O},\text{N})_4$ tetrahedra forming condensed *dreier* and *sechser* rings, each *dreier* ring unit containing one Q^3 -type $\text{P}(\text{O},\text{N})_4$ tetrahedron with one terminal O^1 atom. This condensation results, in turn, in a truncated tetrahedron, with the centers of the $\text{P}(\text{O},\text{N})_4$ tetrahedra located at the vertices.

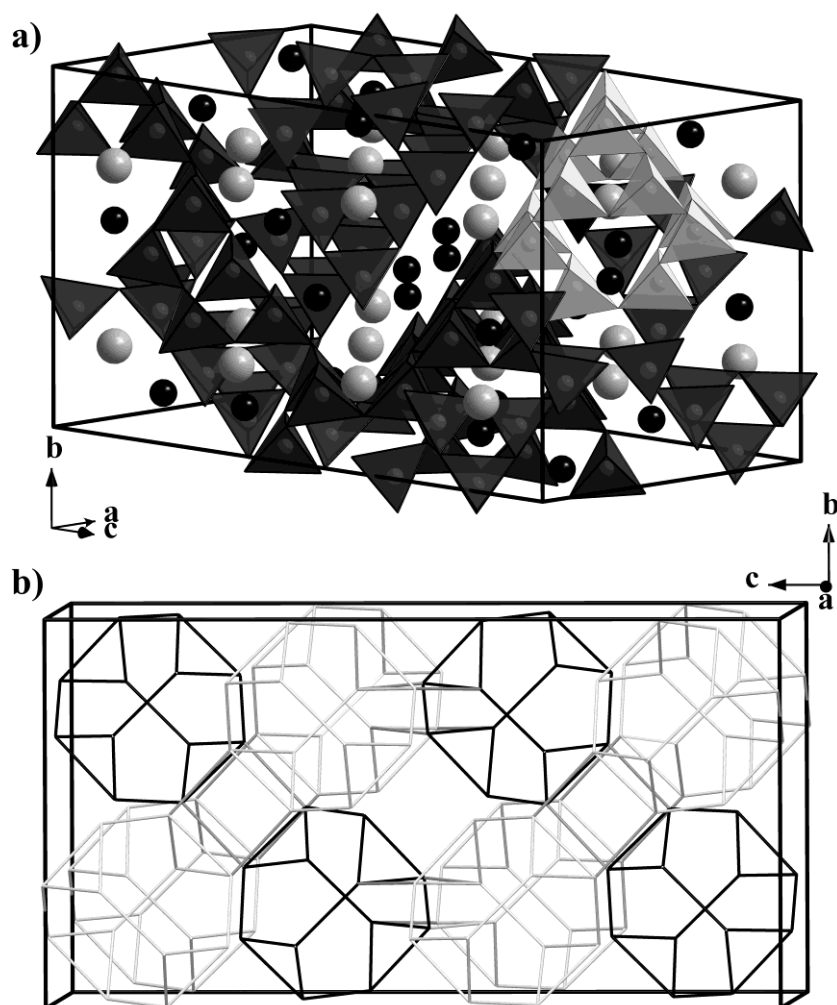


Figure 5. a) Crystal structure of $\text{CaMg}_2\text{P}_6\text{O}_3\text{N}_{10}$ viewed along $[-9,2,17]$. Ca atoms are gray, Mg atoms are black, the $\text{P}(\text{O},\text{N})_4$ tetrahedra are dark gray, and the characteristic building block is shown in light gray. b) Topological representation of the unit cell. Dark PBUs in unit cell, light gray PBUs partially outside unit cell along $[100]$. Each connecting line represents a P–N–P bond, cf. Figure 6.

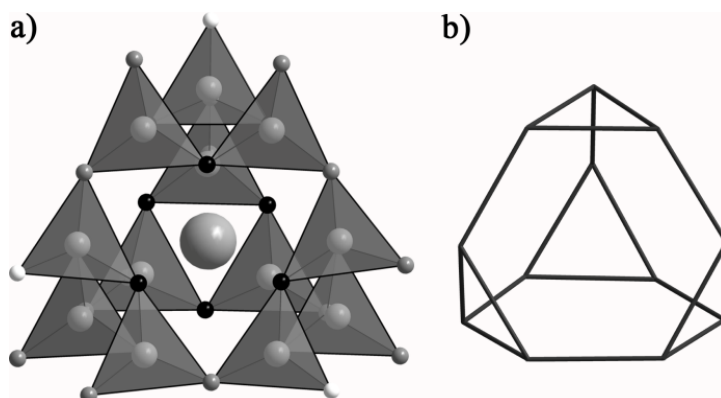


Figure 6. a) PBU of the structure of $\text{CaMg}_2\text{P}_6\text{O}_3\text{N}_{10}$ consisting of $\text{P}(\text{O},\text{N})_4$ tetrahedra (gray: Ca atom; black: N atoms; dark gray: N/O atoms; white: O atoms). b) Topological representation of the characteristic building unit. Each connecting line represents a P–N–P bond.

The center of the PBU is occupied by a Ca1 atom. This PBU is connected to other PBUs through two singly bridging (N/O) atoms in each *dreier* ring to form a *vierer* ring (see Figure 7). Thus, a three-dimensional network structure containing channels filled with Ca and Mg atoms is formed (see Figure 5). The topology of this network, determined by the TOPOS software,²¹ is represented by the point symbol $\{3.4.5.6^2.8\}_2\{3.6^2\}$ and has not been found in any other known compound so far.

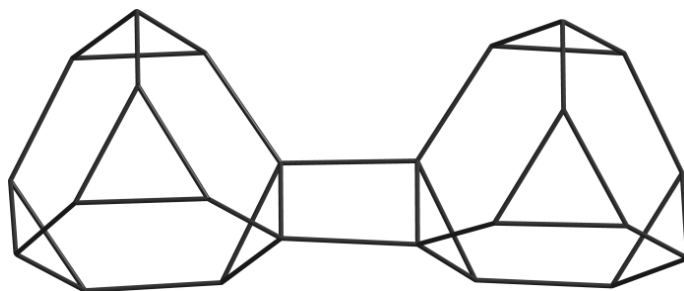


Figure 7. Topological representation of two interconnected characteristic building blocks. Each connecting line represents a P–N–P bond.

The bond lengths P–(O,N) range between 1.541(3) and 1.652(4) Å, and are in the range of those usually observed in other oxonitridophosphates.^{9–14} As expected, the P–(O,N)² bond lengths [1.601(3)–1.631(4) Å] within a Q⁴-type P(O,N)₄ tetrahedron involving a singly bridging O² are significantly longer than the P–O¹ bond lengths [1.541(3) Å] in Q³-type P(O,N)₄ tetrahedra. The (O,N)–P–(O,N) angles vary between 106.1(2) and 114.1(2)°, and thus differ slightly from the regular tetrahedral angle. The range of P–(O,N)–P angles [114.9(2)–124.0(2)°] is typical of oxonitridophosphate networks. Selected bond lengths and angles are given in Table 2.

The crystal structure contains two independent crystallographic Ca and one Mg position, the coordination spheres of which are shown in Figure 8. The two Ca positions exhibit remarkably different coordination polyhedra. The Ca1 position is coordinated by 12 N atoms that form a slightly distorted cuboctahedron (see Figure 8, left). Thus, $\text{CaMg}_2\text{P}_6\text{O}_3\text{N}_{10}$ is, to the best of our knowledge, the first compound with Ca atoms coordinated directly by such a large number of N atoms. The Ca–N distances in this cuboctahedron vary between 2.797(4) and 2.856(4) Å and are in good agreement with Ca–N distances in other known compounds as well as with the sum of the ionic radii.^{22–24} The Ca2 position is coordinated by six O/N atoms at distances of 2.184(5)–2.541(4) Å in a distorted octahedral arrangement. These distorted Ca(O,N)₆ octahedra are not connected to any other metal-atom-centered polyhedra. Figure 8 (right) shows that the displacement ellipsoid Ca2 is rather oblate. This follows from significantly different Ca–(O/N) distances in the Ca(O,N)₆ octahedron. Although the Ca–(N6/O6) distances [2.184(5) Å] in the axial positions are very short, the Ca–(N2/O2) distances in the equatorial positions [2.541(3) Å] correspond to those in other known calcium compounds (2.365–3.001 Å).^{22–25} Thus, the very short Ca2–N6/O6 distance [2.184(5) Å], based on the sum of the ionic radii (Ca–O: 2.35 Å; Ca–N: 2.46 Å),²² is not real, but results from the average position of a disordered

Ca2 atom that is randomly displaced from the center of the distorted octahedron. In the second coordination sphere, the Ca2 atom is coordinated by four N5/O5 atoms in a slightly distorted square-planar arrangement with a distance of 3.126(4) Å.

Table 2. Selected bond lengths and angles in the crystal structure of $\text{CaMg}_2\text{P}_6\text{O}_3\text{N}_{10}$.^[a]

P1–	N2/O2	1.622(4)	O7–	P1–	N2/O2	111.7(2)
	N3	1.638(4)			N3	112.0(2)
	N4	1.642(4)			N3	109.2(2)
	O7	1.541(3)			N4	108.6(2)
P2–	N1	1.651(4)	N2/O2–	P1–	N4	108.4(2)
	N2/O2	1.631(4)			N4	106.8(2)
	N3	1.631(3)			N3	108.9(2)
	N5/O5	1.634(4)			N5/O5	110.3(2)
P3–	N1	1.652(4)	N3–	P2–	N5/O5	108.6(2)
	N4	1.644(4)			N1	108.8(2)
	N6/O6	1.601(3)			N1	106.2(2)
	N5/O5	1.630(4)			N1	114.1(2)
			N6/O6–	P3–	N5/O5	106.1(2)
			N6/O6–	P3–	N4	107.4(2)
			N5/O5–	P3–	N4	112.5(2)
			N6/O6–	P3–	N1	111.8(2)
			N5/O5–	P3–	N1	112.3(2)
			N4–	P3–	N1	106.7(2)

[a] Standard deviations are given in parentheses.

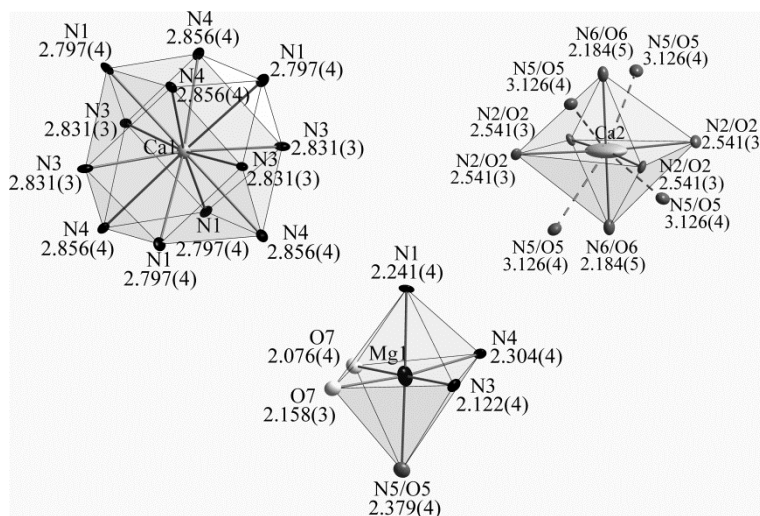


Figure 8. Coordination polyhedra and corresponding bond lengths [Å] of the Ca1 position (left), the Ca2 position (right), and the Mg1 position (bottom); ellipsoids are drawn with a probability factor of 70 %.

The Mg1 position is hexacoordinated by one O5/N5 atom, two terminal O¹ atoms, and three N atoms in a slightly distorted octahedron (see Figure 8, bottom). The Mg–(O,N) distances range between 2.076(4) and 2.379(4) Å, and correspond to those in other magnesium compounds as well as to the sum of the ionic radii.^{22,23,26,27} Two $\text{Mg}(\text{O},\text{N})_6$ octahedra are interconnected by two terminal O¹ atoms through a common edge to form $\text{Mg}_2(\text{O},\text{N})_{10}$ octahedron pairs. These pairs, in turn, interconnect with the CaN_{12} cuboctahedra through half of the latter's triangular faces (see Figure 9).

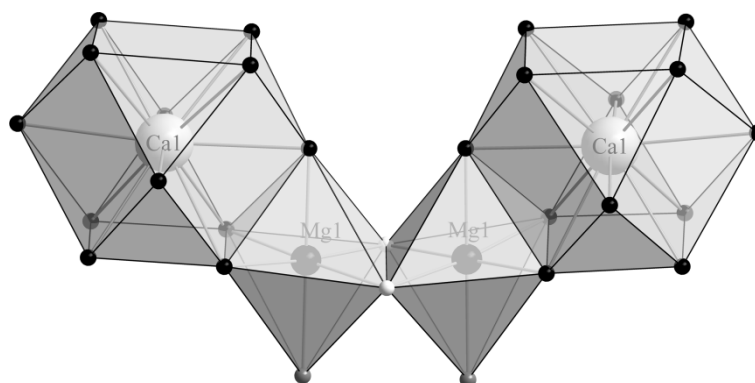


Figure 9. Representation of edge-sharing $\text{Mg}(\text{O},\text{N})_6$ octahedra that share faces with CaN_{12} cuboctahedra.

3.2.2.4 Bond-valence sum calculations

The structure model of $\text{CaMg}_2\text{P}_6\text{O}_3\text{N}_{10}$ and, in particular, the local displacements of Ca2 can be confirmed by bond-valence sum (BVS) calculations (see Table 3).²⁸ The deviations between the bond-valence sum and the oxidation state are in the range of 5 %, with the exception of the average Ca2 position and N6/O6 (occupied by 86 % N and 14 % O), which is at a very short distance from it. At this distance, Ca2 would have a BVS of 3.1, and the values calculated for both N6 (3.54) and O6 (2.64) are also higher than their formal charge. This unfavorable situation is avoided by a displacement of Ca2 from the average position. This leads to longer interatomic distances and thus lower and more reasonable BVS values, and thus explains the oblate displacement ellipsoid (see Figure 8).

Table 4: Bond-valence sums for $\text{CaMg}_2\text{P}_6\text{O}_3\text{N}_{10}$.

Atom	Ca1	Ca2	Mg	P1	P2	P3	N1	N3
BVS	1.9	3.1	1.95	4.84	4.73	4.78	2.81	2.89
oxidation state	2	2	2	5	5	5	3	3
Atom	N4	N2	O2	N5	O5	N6	O6	O1
BVS	2.83	2.83	2.18	2.74	2.12	3.54	2.64	1.86
oxidation state	3	3	2	3	2	3	2	2

3.2.2.5 Lattice-energy calculations (MAPLE)

Taking into account exclusively electrostatic interactions in an ionic crystal, which depend on the charge, distance, and coordination spheres of the constituting ions, the Madelung part of the lattice energy (MAPLE) was calculated (Table 4).^{22,29-31} The overall MAPLE value of $\text{CaMg}_2\text{P}_6\text{O}_3\text{N}_{10}$ ($166621 \text{ kJ mol}^{-1}$) is in good agreement with the sum of those of the binary compounds that formally constitute the quinary compound ($\text{CaO}^{32} + 2\text{MgO}^{33} + 2\text{P}_3\text{N}_5^{34}$, overall MAPLE value $166917 \text{ kJ mol}^{-1}$). The negligible deviation of 0.2 % confirms the electrostatic consistency of the refined crystal structure despite the expectedly rather different partial MAPLE values of the Ca1 and Ca2 positions. The difference between the partial MAPLE values of the Ca1 and Ca2 positions reflects the same discrepancy for Ca2 as its BVS value. The partial MAPLE values of the Mg, P, and O^1 atoms are congruent with reference values, whereas those of the N^2 atoms are slightly larger. As expected, the partial MAPLE values of the mixed O^2/N^2 positions range between those of the N^2 and O^1 sites.

Table 5: Partial MAPLE values and MAPLE sums [kJ/mol] of $\text{CaMg}_2\text{P}_6\text{O}_3\text{N}_{10}$.

$\text{CaMg}_2\text{P}_6\text{O}_3\text{N}_{10}$ [a]		Model	
Ca1	1969	+1	CaO^{32}
Ca2	2515	+2	MgO^{33}
Mg1	2639	+2	$\text{P}_3\text{N}_5^{34}$
P1	14708		
P2	14589		
P3	14571		
N1	6338		
N2/O2	5456		
N3	6339		
N4	6235		
N5/O5	5429		
N6/O6	5470		
O7	2572		
$\Sigma = 166621$		$\Sigma = 166917$	
		$\Delta = 0.2 \%$	

[a] Typical partial MAPLE values [kJ mol^{-1}]: Ca: 1700–2200;^{3,24} Mg: 2263–2640;^{23,35} P: 14422–15580; N^2 : 4600–6000; O^1 : 2000–2800.^{3,19,36}

3.2.3 Conclusion

CaMg₂P₆O₃N₁₀ represents a novel oxonitridophosphate with an unprecedented network of tetrahedra. It is the first known compound with a twelve-fold N coordination of Ca atoms. Single crystals of CaMg₂P₆O₃N₁₀ were obtained and isolated by adding catalytic amounts of NH₄Cl to the starting mixture. The high-pressure/high-temperature synthesis appears to be a very promising route for the synthesis of new oxonitridophosphates with interesting structural properties. Moreover, single crystals of oxonitridophosphates, obtained by this route, may significantly accelerate structural investigations in the future.

3.2.4 Experimental section

Preparations of starting materials

Ca(N₃)₂ was synthesized by stirring a suspension of ammonium azide with Ca(OH)₂ (Merck, p.a.). Caution: Special care is necessary when handling even dilute solutions of HN₃ because it is potentially explosive and the vapor is highly poisonous upon inhalation. Precautions have to be made that no volatile pure (boiling point 60 °C) or highly concentrated HN₃ can condense onto cool surfaces. After filtration, the solvent was evaporated under reduced pressure (90 mbar, 70 °C).³⁷ Finally, the colorless solid of Ca(N₃)₂ was recrystallized from acetone and dried in vacuum over P₄O₁₀.³⁸ The final product was stored under the exclusion of moisture and oxygen. NH₄N₃ was synthesized by treating equimolar amounts of NH₄NO₃ (Grössing, reinst) and NaN₃ (Acros Organics, 99 %) in a Schlenk tube with one open end located outside the furnace and slowly heating (50 °C/h) the mixture to 200 °C.³⁹ P₃N₅ was prepared starting from (PNCl₂)₃ (Merck, p.s.) in a corundum boat in a continuous flow of dried NH₃ (Messer, Griesheim, 3.8), as described in the literature.⁴⁰⁻⁴² PON was synthesized by heating a mixture of one part PO(NH₂)₃ and three parts NH₄Cl in a continuous flow of nitrogen at 680 °C. The process is detailed in the literature.⁹

Synthesis

CaMg₂P₆O₃N₁₀ was synthesized by using a modified Walker-type multi-anvil apparatus¹⁸ starting from stoichiometric amounts of Ca(N₃)₂, Mg₃N₂, P₃N₅, and PON with catalytic amounts of NH₄Cl (20.0 mg) as mineralizer. All manipulations were carried out under the exclusion of oxygen and moisture in an argon-filled glove-box (Unilab, Mbraun, Garching, O₂ < 1 ppm, H₂O < 0.1 ppm). The mixture of starting materials was thoroughly ground and tightly packed into a cylindrical capsule made of hexagonal boron nitride (Henze, Kempten) and sealed with a hexagonal boron nitride cap.

By using two MgO spacers (TechniKer, Küps, Germany), the capsule was centered in the middle of a Cr₂O₃-doped MgO octahedron (edge length 18 mm, Ceramic Substrates & Components Ltd, Isle of Wight), which served as a pressure medium. This MgO octahedron was equipped with a ZrO₂ tube (Cesima Ceramics, Wust-Fischbach, Germany) as thermal insulator as well as graphite tubes, which were used as electrical resistance furnaces. To achieve good electrical contact between the graphite tubes and tungsten carbide cubes, two plates of molybdenum were used. The octahedron was then placed at the center of an assembly of eight truncated tungsten carbide cubes (truncation edge lengths 11 mm, Hawedia, Marklkofen, Germany), which were separated with pyrophyllite gaskets. Detailed information on the construction of the described multi-anvil assembly can be found in literature.¹⁸ The sample was compressed up to 8 GPa at room temperature. Then it was heated up to 1100 °C within 60 min. This temperature was held constant for 60 min and subsequently the sample was cooled to room temperature. After slow decompression (10 h), the sample was isolated as a light-gray solid, which was not sensitive to air and moisture. NH₄Cl was removed from the product by washing it with water and ethanol.

Single-crystal X-ray diffraction

Single-crystal diffraction data were collected with a STOE IPDS I diffractometer (Mo-K_α radiation, graphite monochromator). A semi-empirical absorption correction was applied by using the XPREP program.⁴³ The crystal structure was solved by direct methods with SHELXS.⁴⁴ The structure was refined by the full-matrix least-squares method by using SHELXL.⁴⁴ Crystal data for CaMg₂P₆O₃N₁₀ are presented in Table 5. Further details of the crystal structure investigations can be obtained from the Fachinformationszentrum Karlsruhe, 76344 Eggenstein-Leopoldshafen, Germany (Fax: +49-7247-808-666; E-Mail: crysdata@fiz-karlsruhe.de); Please quote the depository number CSD-427175.

Table 5. Crystallographic data for the single-crystal structure determination of $\text{CaMg}_2\text{P}_6\text{O}_3\text{N}_{10}$.

Formula	$\text{CaMg}_2\text{P}_6\text{O}_3\text{N}_{10}$
Crystal system / space group	tetragonal / $I4_1/acd$ (no. 142)
Lattice parameters / Å	$a = 12.494(1)$, $c = 23.747(2)$
Cell volume / Å ³	3707.0(5)
Formula units per unit cell	16
Density / g · cm ⁻³	3.316
μ / mm ⁻¹	1.888
Radiation	Mo-K α ($\lambda = 0.71073$ Å)
Temperature / K	295
F(000)	3648.0
2θ range	$2.87^\circ \leq \theta \leq 27.50^\circ$
Total no. of reflections	9483
Independent reflections	1068 [$R(\text{int}) = 0.0674$]
Refined parameters	104
Goodness of fit	0.904
R_1 (all data); $R_1 (F^2 > 2\sigma(F^2))$	0.0736, 0.0381
wR_2 (all data); $wR_2 (F^2 > 2\sigma(F^2))$	0.0727, 0.0659
$\Delta\rho_{\text{max}}$, $\Delta\rho_{\text{min}}$ (e · Å ⁻³)	1.463, -1.126

Transmission electron microscopy

Ground samples were dispersed in absolute ethanol and drop-cast onto copper grids coated with a holey carbon film (S166–2, Plano GmbH, Germany). The grids were fixed on a double-tilt holder. SAED, HRTEM, and EDX measurements were taken with a Titan 80–300 (FEI, USA) with a field emission gun operated at 300 kV, equipped with a TEM TOPS 30 EDX spectrometer (EDAX, Germany). Images were recorded by using an UltraScan 1000 camera (Gatan, USA, resolution: 2k × 2k). In addition, SAED and EDX measurements were taken with a JEOL 2010 instrument (JEOL, Germany) with a thermal emitter operated at 200 keV, equipped with a EDAX Apollo XLT EDX detector (EDAX Germany). Images were recorded by using a TemCam F216 camera (TVIPS, Germany, resolution: 2k × 2k). HRTEM and SAED data were evaluated by using the Digital Micrograph,⁴⁵ Process Diffraction 7⁴⁶ and JEMS programs,⁴⁷ and EDX data were processed with ES Vision⁴⁸ and EDAX TEAM.⁴⁹

Powder X-ray diffraction

Powder diffraction data were collected with a HUBER G670 diffractometer [Cu-K α_1 radiation, Ge(111) monochromator] in Guinier geometry. Simulations of Bragg data were performed by using the

WINXPOW program package⁵⁰ on the basis of the single-crystal structural data. Rietveld refinement was carried out by using the TOPAS-Academic package.⁵¹

FTIR spectroscopy

The FTIR spectrum of CaMg₂P₆O₃N₁₀ was recorded in a KBr pellet with a Spectrum BX II spectrometer (Perkin–Elmer, Waltham MA, USA).

Scanning electron microscopy and energy-dispersive X-ray spectroscopy

SEM images and EDX spectra were acquired by using a JEOL JSM-6500F field emission scanning electron microscope (SEM) operated at 15 kV, equipped with a Si/Li EDX detector 7418 (Oxford Instruments). To provide electrical conductivity on the sample surface, it was coated with carbon using an electron beam evaporator (BAL-TEC MED 020, Bal Tec AG).

3.2.5 References

- 1 F. Liebau, *Structural Chemistry of Silicates: Structure, Bonding, and Classification*, Springer, Berlin, **1985**.
- 2 A. K. Cheetham, G. Férey, T. Loiseau, *Angew. Chem.* **1999**, *111*, 3466; *Angew. Chem. Int. Ed.* **1999**, *38*, 3268.
- 3 M. Zeuner, S. Pagano, W. Schnick, *Angew. Chem.* **2011**, *123*, 7898; *Angew. Chem. Int. Ed.* **2011**, *50*, 7754.
- 4 a) H. A. Höppe, *Angew. Chem.* **2009**, *121*, 3626; *Angew. Chem. Int. Ed.* **2009**, *48*, 3572;
b) W. Schnick, *Phys. Status Solidi RRL* **2009**, *3*, A113.
- 5 W. Schnick, *Angew. Chem.* **1993**, *105*, 846; *Angew. Chem. Int. Ed. Engl.* **1993**, *32*, 806.
- 6 H. Huppertz, W. Schnick, *Angew. Chem.* **1996**, *108*, 2115; *Angew. Chem. Int. Ed. Engl.* **1996**, *35*, 1983.
- 7 F. Karau, W. Schnick, *Angew. Chem.* **2006**, *118*, 4617; *Angew. Chem. Int. Ed.* **2006**, *45*, 4505.
- 8 M. Pouchard, *Nature* **2006**, *442*, 878.
- 9 S. J. Sedlmaier, J. Schmedt auf der Günne, W. Schnick, *Dalton Trans.* **2009**, 2081.
- 10 S. J. Sedlmaier, D. Weber, W. Schnick, *Z. Kristallogr. NCS* **2012**, *227*, 1.
- 11 R. Conanec, W. Feldmann, R. Marchand, Y. Laurent, *J. Solid. State Chem.* **1996**, *121*, 418.
- 12 W. Feldmann, *Z. Chem.* **1987**, *27*, 100.
- 13 W. Feldmann, P. L'Haridon, R. Marchand, *J. Solid. State Chem.* **2000**, *153*, 185.
- 14 S. J. Sedlmaier, E. Mugnaioli, O. Oeckler, U. Kolb, W. Schnick, *Chem. Eur. J.* **2011**, *17*, 11258.
- 15 a) S. Correll, O. Oeckler, N. Stock, W. Schnick, *Angew. Chem.* **2003**, *115*, 3674; *Angew. Chem. Int. Ed.* **2003**, *42*, 3549;
b) S. Correll, N. Stock, O. Oeckler, J. Senker, T. Nilges, W. Schnick, *Z. Anorg. Allg. Chem.* **2004**, *630*, 2205.

- 16 S. J. Sedlmaier, M. Döblinger, O. Oeckler, J. Weber, J. Schmedt auf der Günne, W. Schnick, *J. Am. Chem. Soc.* **2011**, *133*, 12069.
- 17 R. Marchand, W. Schnick, N. Stock, *Adv. Inorg. Chem.* **2000**, *50*, 193.
- 18 a) N. Kawai, S. Endo, *Rev. Sci. Instrum.* **1970**, *41*, 1178;
b) D. Walker, M. A. Carpenter, C. M. Hitch, *Am. Mineral.* **1990**, *75*, 1020;
c) D. Walker, *Am. Mineral.* **1991**, *76*, 1092;
d) D. C. Rubie, *Phase Transitions* **1999**, *68*, 431;
e) H. Huppertz, *Z. Kristallogr.* **2004**, *219*, 330-338.
- 19 F. W. Karau, L. Seyfarth, O. Oeckler, J. Senker, K. Landskron, W. Schnick, *Chem. Eur. J.* **2007**, *13*, 6841.
- 20 A. Marchuk, F. J. Pucher, F. W. Karau, W. Schnick, *Angew. Chem.* **2014**, *126*, 2501;
Angew. Chem. Int. Ed. **2014**, *53*, 2469.
- 21 a) V. A. Blatov, M. O'Keeffe, D. M. Proserpio, *CrystEngComm* **2010**, *12*, 44;
b) V. A. Blatov, *IUCr CompComm Newsletter* **2006**, *7*, 4.
- 22 R. D. Shannon, *Acta Crystallogr. Sect. A: Found. Crystallogr.* **1976**, *32*, 751.
- 23 V. Schultz-Coulon, W. Schnick, *Z. Anorg. Allg. Chem.* **1997**, *623*, 69.
- 24 F. Karau, W. Schnick, *Z. Anorg. Allg. Chem.* **2006**, *632*, 231.
- 25 M. Y. Chern, D. A. Vennos, F. J. DiSalvo, *J. Solid. State. Chem.* **1992**, *96*, 415.
- 26 S. R. Römer, W. Schnick, *Z. Anorg. Allg. Chem.* **2005**, *631*, 31.
- 27 F. Hinze, N. W. Johnson, M. Seibald, D. Muir, A. Moewes, W. Schnick, *Chem. Mater.* **2013**, *25*, 4044.
- 28 A. S. Wills, *VaList*, 4.0.7, UCL London **2010**.
- 29 R. Hoppe, *Angew. Chem. Int. Ed. Engl.* **1970**, *9*, 25.
- 30 R. Hoppe, R. Homann, *Z. Anorg. Allg. Chem.* **1970**, *379*, 193.
- 31 R. Hübenthal, MAPLE, Version 4, Programm zur Berechnung des Madelunganteils der Gitterenergie, University of Gießen, Germany, **1993**.
- 32 W. Primak, H. Kaufman, R. Ward, *J. Am. Chem. Soc.* **1948**, *70*, 2043.
- 33 D. Sun, H. Enoki, F. Gingi, E. Akiba, *J. Alloys. Compd.* **1999**, *285*, 279.
- 34 P. Kroll, W. Schnick, *Chem. Eur. J.* **2002**, *8*, 3530.
- 35 A. G. Petukhov, W. R. L. Lambrecht, B. Segall, *Phys. Rev. B: Condens. Matter* **1994**, *49*, 4549.
- 36 L. Boukbir, R. Marchand, Y. Laurent, P. Bacher, *Ann. Chim.* **1989**, *14*, 475.
- 37 F. Karau, *Dissertation*, Ludwig-Maximilians-Universität München (Germany) **1994**.
- 38 H. D. Fair, R. F. Walker, *Energetic Materials Vol.1: Physics and Chemistry of the Inorganic Azides*; Plenum Press: New York **1977**.
- 39 W. J. Frierson, *Inorg. Synth.* **1946**, *8*, 146.
- 40 J. Lücke, *Dissertation*, Rheinische Friedrich-Wilhelm-Universität Bonn (Germany) **1994**.
- 41 W. Schnick, J. Lücke, F. Kumeich, *Chem. Mater.* **1996**, *8*, 281.
- 42 S. Horstmann, E. Irran, W. Schnick, *Angew. Chem.* **1997**, *109*, 2085; *Angew. Chem. Int. Ed. Engl.* **1997**, *36*, 1873.
- 43 G. M. Sheldrick, XPREP, Data Preparation & Reciprocal Space Exploration, **1996**, v6.12, Siemens Analytical X-ray Instruments.

- 44 G. M. Sheldrick, *Acta Crystallogr., Sect. A: Found. Crystallogr.* **2008**, 64, 112.
- 45 Digital Micrograph 3.6.1, Gatan Software, Pleasanton, USA, **1999**.
Gatan Software Team, DigitalMicrograph, 3.6.1 **1999**.
- 46 J. L. Lábár, *Ultramicroscopy* **2005**, 103, 237.
- 47 P. A. Stadelmann, *JEMS*, 3.3425 **2008**.
- 48 ES Vision, 4.0.164, Emispec Systems Inc., Tempe, USA, **1994–2002**.
- 49 EDAX, TEAM, 3.4.1 **2013**.
- 50 Stoe & Cie GmbH, *WINXPOW* - Program for powder data handling, v2.21, Darmstadt, Germany, **2007**.
- 51 A. Coelho, *TOPAS - Academic*, Coelho Software, Brisbane, **2007**.

3.2.6 Supporting Information

A) Rietveld refinement of $\text{CaMg}_2\text{P}_6\text{O}_3\text{N}_{10}$

Rietveld refinement was carried out using TOPAS Academic 4.1, employing the fundamental parameter approach (convolution of source emission profiles, axial instrument contributions and crystalline microstructure effects). Preferred orientation of the crystallites in the powder was described using a spherical harmonics function of fourth order. All atomic positions of $\text{CaMg}_2\text{P}_6\text{O}_3\text{N}_{10}$ as well as isotropic thermal displacement parameters of Ca, Mg and P atom positions were refined freely. A common isotropic displacement parameter for the N, O and mixed occupied N/O atom positions was refined. The O/N ratio of all bridging atom positions, determined from the single-crystal data, were held constant.

Table S1. Crystallographic data of Rietveld refinement of $\text{CaMg}_2\text{P}_6\text{O}_3\text{N}_{10}$.

Formula	$\text{CaMg}_2\text{P}_6\text{O}_3\text{N}_{10}$
Crystal system	tetragonal
Space group	$I4_1/acd$ (no. 142)
Lattice parameters / Å	$a = 12.4939(1)$, $c = 23.7468(3)$
Cell volume / Å³	3706.84(9)
Formula units per unit cell	16
Density / g · cm⁻³	3.316
Diffractometer	Huber G670
Radiation	Cu-K α_1 ($\lambda = 1.54056$ Å)
2θ range	$5.5 \leq 2\theta \leq 99.9$
Data points	9449
Total number of reflections	487
Refined parameters	86
Background function	Shifted Chebyshev (18 parameters)
Goodness of fit	1.753
R_p, R_{wp}	0.0171, 0.0229

Table S2. Atomic coordinates, isotropic displacement parameters (\AA^2) and occupation of crystallographic positions from the Rietveld refinement of $\text{CaMg}_2\text{P}_6\text{O}_3\text{N}_{10}$; standard deviations in parentheses.

Atom	Wyckoff position	x	y	z	$U_{eq}/\text{\AA}^2$	Occupancy
Ca1	8a	1/2	1/4	1/8	0.0055(10)	1.0
Ca2	8b	1	3/4	3/8	0.0773(16)	1.0
Mg1	32g	0.3439(2)	0.0624(2)	0.0427(1)	0.0292(12)	1.0
P1	32g	0.6012(2)	0.0204(2)	0.0796(1)	0.0152(8)	1.0
P2	32g	0.7432(2)	0.1898(2)	0.0836(1)	0.0129(8)	1.0
P3	32g	0.5884(2)	0.1817(2)	0.0001(1)	0.0202(9)	1.0
N1	32g	0.6585(5)	0.2559(4)	0.0418(4)	0.0053(6)	1.0
N2/O2	32g	0.7976(4)	0.2745(3)	0.1267(3)	0.0053(6)	0.86/0.14
N3	32g	0.6736(4)	0.1021(5)	0.1188(2)	0.0053(6)	1.0
N4	32g	0.5223(4)	0.0921(5)	0.0391(3)	0.0053(6)	1.0
N5/O5	32g	0.8390(4)	0.1230(4)	0.0490(2)	0.0053(6)	0.76/0.24
N6/O6	16d	1/2	1/4	-0.0308(3)	0.0053(6)	0.76/0.24
O7	32g	0.6702(4)	-0.0548(4)	0.0440(2)	0.0053(6)	1.0

B) Energy dispersive X-ray (EDX) analysis of $\text{CaMg}_2\text{P}_6\text{O}_3\text{N}_{10}$ **Table S3.** Results of EDX measurements (left part SEM, right part TEMs) for various crystals of $\text{CaMg}_2\text{P}_6\text{O}_3\text{N}_{10}$ in atom-%; the absolute values for light atoms depend on the systematic errors associated with different experimental setups (electron microscope, EDX detector, software, see Experimental section) was used, the average composition agrees with the compound $\text{CaMg}_2\text{P}_6\text{O}_3\text{N}_{10}$.

Crystal	1	2	3	\emptyset SEM	1	2	3	\emptyset TEM1	calc.
N	57.6	51.9	55.8	55.1(29)	47.1	42.1	43.9	44.4(21)	45.5
O	14.5	14.5	11.4	13.5(18)	10.2	10.9	10.0	10.4(4)	13.6
Mg	7.0	7.5	7.8	7.4(4)	8.2	7.6	8.3	8.0(3)	9.1
P	18.4	22.6	21.8	20.9(23)	30.5	33.8	31.9	32.1(14)	27.3
Ca	2.5	3.5	3.2	3.1(5)	4.0	5.6	5.9	5.2(8)	4.5
Ca/P	0.14	0.15	0.15	0.15	0.13	0.17	0.18	0.16	0.16
Crystal	1	2	3	4	5	6		\emptyset TEM2	calc.
N	37.0	47.0	39.5	37.9	36.8	41.1		39.9(35)	45.5
O	14.0	9.1	11.2	10.8	11.3	13.8		11.7(17)	13.6
Mg	13.5	13.9	15.0	15.6	16.6	14.8		14.9(10)	9.1
P	31.2	27.5	31.5	32.8	32.4	27.5		30.5(21)	27.3
Ca	4.2	2.5	2.9	2.9	2.9	2.8		3.0(5)	4.5
Ca/P	0.13	0.09	0.09	0.09	0.09	0.10		0.10	0.16

C) FTIR spectrum of $\text{CaMg}_2\text{P}_6\text{O}_3\text{N}_{10}$

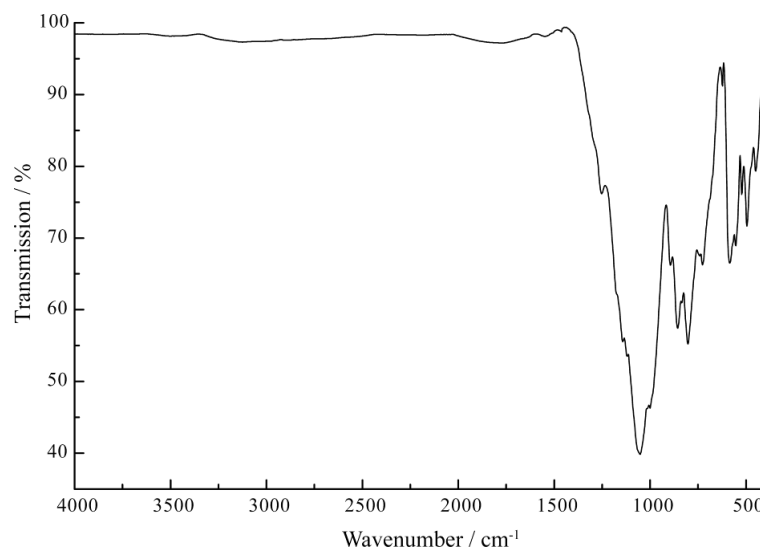


Figure S1. FTIR spectrum of $\text{CaMg}_2\text{P}_6\text{O}_3\text{N}_{10}$, measured using the KBr pellet method.

D) Enlarged HRTEM defocus series

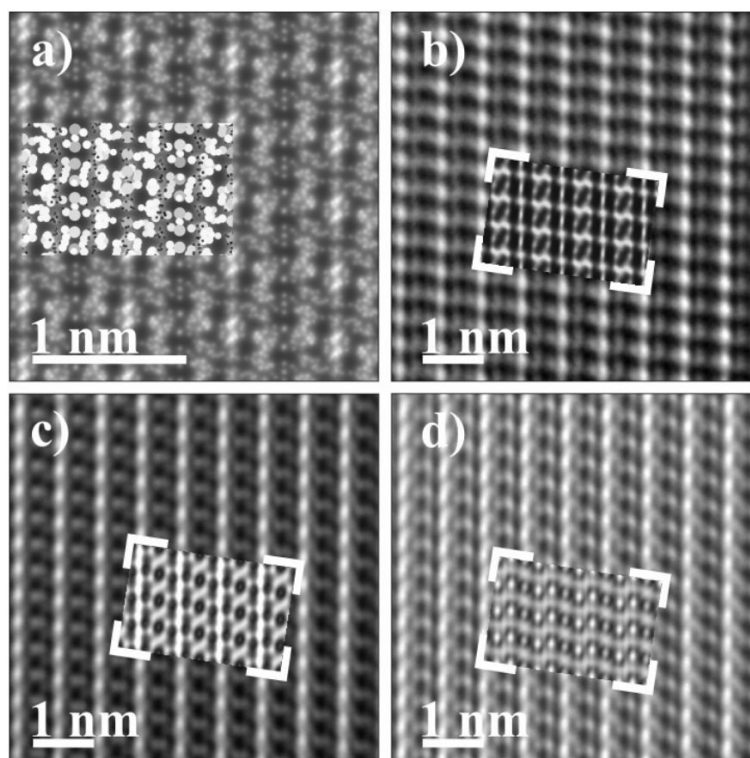


Figure S2. Projected potential (a) with structure projection inserted (a left; the heavier the element the larger and brighter the spheres) and HRTEM images (b-d) of $\text{CaMg}_2\text{P}_6\text{O}_3\text{N}_{10}$ along the $\langle 713 \rangle$ zone axis with image simulations (accelerating voltage = 300 keV, $C_s = 0.6$ mm, spread of focus = 3.6 nm, beam semi-convergence = 17 mrad, layer thickness two unit cells), inserted: defocus values -70 nm (b), -43 nm (c) and -28 nm (d).

3.3 Puzzling Intergrowth in Cerium Nitridophosphate Unraveled by Joint Venture of Aberration-Corrected Scanning Transmission Electron Microscopy and Synchrotron Diffraction

Simon D. Kloß, Lukas Neudert, Markus Döblinger, Markus Nentwig, Oliver Oeckler, Wolfgang Schnick

J. Am. Chem. Soc. **2017**, *139*, 12724.

Reprinted with permission from *Journal of the American Chemical Society*. Copyright 2017 ASC Publications.

Abstract

Thorough investigation of nitridophosphates has rapidly accelerated through development of new synthesis strategies. Here we used the recently developed high-pressure metathesis to prepare the first rare-earth metal nitridophosphate, $\text{Ce}_4\text{Li}_3\text{P}_{18}\text{N}_{35}$, with a high degree of condensation $> 1/2$. $\text{Ce}_4\text{Li}_3\text{P}_{18}\text{N}_{35}$ consists of an unprecedented hexagonal framework of PN_4 tetrahedra and exhibits blue luminescence peaking at 455 nm. Transmission electron microscopy (TEM) revealed two intergrown domains with slight structural and compositional variations. One domain type shows extremely weak superstructure phenomena revealed by atomic-resolution scanning TEM (STEM) and single-crystal diffraction using synchrotron radiation. The corresponding superstructure involves a modulated displacement of Ce atoms in channels of tetrahedra 6-rings. The displacement model was refined in a supercell as well as in an equivalent commensurate (3+2)-dimensional description in superspace group $P6_3(\alpha, \beta, 0)0(-\alpha-\beta, \alpha, 0)0$. In the second domain type, STEM revealed disordered vacancies of the same Ce atoms that were modulated in the first domain type, leading to sum formula $\text{Ce}_{4-0.5x}\text{Li}_3\text{P}_{18}\text{N}_{35-1.5x}\text{O}_{1.5x}$ ($x \approx 0.72$) of the average structure. The examination of these structural intricacies may indicate the detection limit of synchrotron diffraction and TEM. We discuss the occurrence of either Ce displacements or Ce vacancies that induce the incorporation of O as necessary stabilization of the crystal structure.

3.3.1 Introduction

It is ambitious to challenge the structural and compositional diversity of oxosilicates with a purely synthetic class of materials. The exploration of oxosilicates engaged and still engages a multitude of geologists, mineralogists, chemists, and materials scientists. Versatile interconnection patterns of SiO_4 tetrahedra combined with cations from almost all metals of the periodic table render oxosilicates one of the most diverse classes of materials.¹⁻³

Their fields of application range from construction materials, that is, components of concrete and ceramics, to functional materials like ion-exchange zeolites, catalysts, molecular sieves, and optical materials.

The yet little explored nitridophosphates, however, which are derived from silicates by isoelectronic substitution of Si-O by P-N bonds, have shown promising developments. Thorough investigation of first and second main group element nitridophosphates revealed several dozens of structures, some as straightforward as the single-chain comprising Ca_2PN_3 , and some complex as zeolitic $\text{Ba}_3\text{P}_5\text{N}_{10}\text{Br}:\text{Eu}^{2+}$ and nitride imide clathrate $\text{P}_4\text{N}_4(\text{NH})_4(\text{NH}_3)$.⁴⁻⁶ The last two were discussed for their potential application as a warm-white emitting phosphor for solid-state lighting and as a gas storage material, respectively.^{5,7} Moreover, distinct structural building blocks such as triply bridging N atoms, edge-sharing tetrahedra, and pentacoordinated P prove that structural diversity is, in theory, no impediment in rivaling silicates.⁸⁻¹⁰ Still, a sincere competition for diversity necessitates a comparable number of structure types and size of composition space. Recently, the latter was extended by accessing rare-earth nitridophosphates through an adaptive high-pressure metathesis route.¹¹ In high-pressure metathesis rare-earth halides are reacted with alkali-metal-containing nitridophosphates such as LiPN_2 to yield the desired rare-earth nitridophosphate and an alkali metal halide under pressures of several gigapascal (GPa).¹¹ It effectively circumvents the use of thermodynamically stable and unreactive starting materials like rare-earth nitrides and prevents the formation of phosphides, which can result from the reductive environment created by nitride ions. LiNdP_4N_8 , two $\text{Ln}_2\text{P}_3\text{N}_7$ polymorphs, and the nitridophosphateoxide $\text{Ho}_3[\text{PN}_4]\text{O}$ were already identified, all crystallizing in silicate-analogous structures.¹¹⁻¹³

Formal oxidation states limit the attainable degree of condensation, κ (ratio of tetrahedra centers to tetrahedra corners per sum formula), of a material family; while the minimum κ in all tetrahedra-based structures is 1/4, oxosilicates have a maximum κ of 1/2 (SiO_2) and nitridophosphates one of 3/5 (P_3N_5).¹⁴ High-pressure metathesis reliably produced rare-earth metal nitridophosphates with $\kappa = 1/4$ – $1/2$, while higher condensed structures have remained unobserved.^{12,13} The latter also have never been realized in oxosilicates because they would lead to cationic SiO_2 frameworks. In nitridophosphates higher condensed frameworks intrigue with structural motifs like triply bridging N and edge-sharing tetrahedra. Currently, the alkali metal nitridophosphates MP_4N_7 and $\text{M}_3\text{P}_6\text{N}_{11}$ (M = Na–Cs) are the only reported cases of such frameworks comprising metal ions.¹⁵⁻¹⁸ Hence, closing the gap between $\kappa = 1/2$ and 3/5 in rare-earth nitridophosphates is likely to uncover unprecedented tetrahedra networks. Such compounds feature rigid frameworks of all-side vertex-sharing tetrahedra, making them, for example, promising candidates as host lattices for inorganic solid-state lighting.¹⁹ The diversity of three-dimensional frameworks is, in theory, infinite,²⁰ and a general task of modern synthetic chemistry is to combine new structural motifs and complex elemental compositions in

order to realize increasingly sophisticated materials. But as the materials become more numerous, structure elucidation frequently encounters various challenges including microcrystalline heterogeneous samples, pseudosymmetry, and weak superstructures.^{21–23} Through technological advances, methods for solving these latter problems like aberration-corrected transmission electron microscopy (TEM), application of third generation synchrotrons, and refractive X-ray lenses producing microfocused beams for X-ray diffraction became available.^{24–27} Atomic resolution Z-contrast scanning TEM (STEM) now enables the direct observation of vacancies or superstructures to derive atom positions and first structure models.^{28–31}

Pushing TEM and synchrotron diffraction to their detection limits became necessary in the structure determination of here presented $\text{Ce}_4\text{Li}_3\text{P}_{18}\text{N}_{35}$, which is the first higher condensed ($\kappa = 0.514$) rare-earth metal nitridophosphate. $\text{Ce}_4\text{Li}_3\text{P}_{18}\text{N}_{35}$, which consists of a framework of all-side vertex-sharing PN_4 tetrahedra, was prepared following the high-pressure metathesis route. The microstructure of $\text{Ce}_4\text{Li}_3\text{P}_{18}\text{N}_{35}$ consists of two slightly different types of domains, one with randomly distributed Ce vacancies and one in which the Ce atoms enter a long-range ordered superstructure correlated to decreased O content. The elucidation of this superstructure was achieved by combined efforts of atomic-resolution STEM and synchrotron diffraction with a PILATUS pixel detector.^{32–34} Owing to the Ce vacancies, the average structure has the sum formula $\text{Ce}_{4-0.5x}\text{Li}_3\text{P}_{18}\text{N}_{35-1.5x}\text{O}_{1.5x}$ ($x \approx 0.72$). Curiously, the compound encompasses blue Ce^{3+} luminescence and paramagnetism as determined with superconducting quantum interference device (SQUID) magnetometry.

3.3.2 Experimental Details

Preparation of P_3N_5

The binary starting material P_3N_5 was prepared by an adapted synthesis route according to Grüneberg.³⁵ Phosphorus pentasulfide, P_4S_{10} (Sigma-Aldrich, 99.99 %), was reacted with constantly flowing NH_3 gas (Air Liquide, 5.0). A tube furnace equipped with a fused silica tube was dried together with a fused silica boat at 1000 °C for 4 h under reduced pressure of 10^{-3} mbar to exclude moisture and O_2 . The fused silica boat was loaded in an Ar counter flow with a limited amount of P_4S_{10} to prevent clogging of the tube by subliming byproducts. The tubing and the P_4S_{10} were saturated by a constant flow of ammonia over the course of 4 h after which the material was fired at 850 °C for additional 4 h. Temperature ramps for heat-up and cool-down were set to 5 °C/min. P_3N_5 was obtained as an orange-brown powder, which was successively washed with water/ethanol/acetone and characterized with powder X-ray diffraction (PXRD) and Fourier transform infrared spectroscopy (FTIR).

Preparation of LiPN₂

Lithium nitridophosphate LiPN₂, was prepared by solid state reaction of P₃N₅ with a 1.2-fold excess of Li₃N (Rockwood Lithium, 94 %).³⁶ Starting materials were mixed and thoroughly ground under the inert conditions of an Ar-filled glovebox (Unilab, MBraun, Garching, Germany) with partial pressures of O₂/H₂O < 1 ppm and then placed in a Ta crucible. The crucible was transferred to a dried fused silica tube under N₂ atmosphere, and the ampoule was sealed and fired at 800 °C with 96 h dwell and 5 °C/min ramp times. The obtained light-brown powder was successively washed with diluted hydrochloric acid/water/ethanol and characterized by means of PXRD and FTIR spectroscopy.

Preparation of Ce_{4-0.5x}Li₃P₁₈N_{35-1.5x}O_{1.5x} (x ≈ 0.72)

Ce_{4-0.5x}Li₃P₁₈N_{35-1.5x}O_{1.5x} (x ≈ 0.72) was prepared by high-pressure metathesis, following Eq 1 (see below). CeF₃ (Alfa Aesar, 99.99 %) and 4 equiv of LiPN₂ were reacted for 5 h at 1300 °C under a pressure of 5 GPa achieved with a 1000 ton hydraulic press (Voggenreiter, Mainleus, Germany) using a Walker-type module and the multianvil technique. A cylindrical and thick-walled hexagonal boron nitride (h-BN) crucible (Henze, Kempten, Germany) with outer diameter $d_{\text{outer}} = 3.67$ mm, inner diameter $d_{\text{inner}} = 2.00$ mm, outer length $l_{\text{outer}} = 6$ mm, inner length $l_{\text{inner}} = 5$, total volume $V_{\text{all}} = 63$ mm³, and sample volume $V_{\text{sample}} = 15$ mm³ was used and closed with a 1.5 mm thick h-BN lid. The temperature ramps were set to 120 min heat-up and cool-down. Starting materials were mixed and thoroughly ground in the Ar-filled glovebox. The sample-filled crucible was placed inside a Cr₂O₃-doped (6 %) MgO octahedron with 18 mm edge-length (Ceramic Substrates & Components, Isle of Wight, U.K.). Co-doped (7 %) tungsten carbide cubes (Hawedia, Marklkofen, Germany) with truncated edges (11 mm) were used as anvils to ensure quasi-hydrostatic pressure conditions. Additional information about the high-pressure multianvil technique can be found in literature.³⁷⁻⁴¹ The product was obtained in the form of small colorless and transparent crystals. The sample was washed with H₂O to remove byproduct LiF.

Spectroscopic Analysis

Morphology and elemental composition were examined with a JEOL JSM 6500F scanning electron microscope (SEM) equipped with a field-emission electron source and an Oxford Instruments 7418 Si/Li energy dispersive X-ray (EDX) detector. The sample was coated (BAL-TEC MED 020, BalTec AG) with carbon to reduce electrical charging of the insulating material. Details of the results of the analysis can be found in the article and the Supporting Information. FTIR spectra were recorded on a Spectrum BX II spectrometer (PerkinElmer, Waltham MA, USA) with ATR setup in the range of 600–4000 cm⁻¹. Details of the results of the analysis can be found in the article.

Inductively coupled plasma optical emission spectroscopy (ICP-OES) was carried out with a Varian Vista RL instrument for Ce, P, and Li. Details of the results of the analysis can be found in the article.

Magnetometry

Magnetic measurements were performed with a MPM-XL SQUID magnetometer (Quantum Design, San Diego, USA). Magnetic susceptibility was measured at a constant magnetic field of $M = 20$ kOe, in the range of 1.8 to 300 K. The sample was placed inside gelatin capsules of known diamagnetic properties.

Powder X-ray Diffraction

PXRD was recorded on powdered $\text{Ce}_{4-0.5x}\text{Li}_3\text{P}_{18}\text{N}_{35-1.5x}\text{O}_{1.5x}$ ($x \approx 0.72$) samples using a Stadi P diffractometer (Stoe & Cie GmbH, Darmstadt, Germany) in modified Debye-Scherrer geometry equipped with a MYTHEN 1K silicon strip detector (Dectris, Baden, Switzerland; angular range $\Delta 2\theta = 12.5^\circ$) and Mo- $\text{K}\alpha_1$ radiation ($\lambda = 0.7093$ Å, Ge(111) monochromator). The samples were filled into glass capillaries with 0.5 mm diameter and ~ 0.01 mm wall thickness. Data were collected in the range of $2^\circ \leq 2\theta \leq 76^\circ$ and the average structural model of $\text{Ce}_{4-0.5x}\text{Li}_3\text{P}_{18}\text{N}_{35-1.5x}\text{O}_{1.5x}$ ($x \approx 0.72$) obtained from single-crystal diffraction was used to fit the data with the Rietveld method.⁴² The peak shape was modeled using the fundamental parameters approach, which is a convolution of source emission profiles, axial instrument contributions, crystallite size, and microstrain effects. The background was modeled with a shifted Chebychev function and preferred orientation was treated with spherical harmonics of fourth order. Cylindrical absorption correction was performed taking into account capillary diameter and linear absorption coefficients of all phases present in the sample.

A Stoe Stadi P diffractometer (Stoe & Cie GmbH, Darmstadt, Germany) equipped with a graphite furnace and image plate position sensitive detector was used for temperature dependent PXRD. Samples were filled into fused silica capillaries with 0.5 mm diameter. Data were collected at constant temperature with 20 °C/step intervals up to 1000 °C and a 20 min collection time per step.

Single-Crystal X-ray Diffraction

High-intensity X-ray diffraction data of a $\text{Ce}_{4-0.5x}\text{Li}_3\text{P}_{18}\text{N}_{35-1.5x}\text{O}_{1.5x}$ ($x \approx 0.72$) single-crystal were obtained at the Swiss-Norwegian Beamline (SNBL), ESRF, Grenoble on the multipurpose PILATUS@SNBL diffractometer ($\lambda = 0.68010$ Å) with a Dectris Pilatus 2M detector.³² Data of multiple runs were summed up and binned with the SNBL toolbox. Integration was done with CrysAlis Pro⁴³ and semiempirical absorption correction with SADABS.⁴⁴ Solution and refinement of the average structure was done with SHELX-97.^{45,46} Further details on the crystal structure analysis can be obtained from the Fachinformationszentrum Karlsruhe, 76344 Eggenstein-Leopoldshafen, Germany

(fax: +49-7247-808-666; e-mail: crysdata@fiz-karlsruhe.de) on quoting the depository number CSD-433141. Refinements of the superstructure and the commensurately modulated model in (3+2)D superspace was carried out with JANA2006.⁴⁷ Crystal structures were visualized with VESTA and Diamond.^{48,49}

Transmission Electron Microscopy

For sample preparation, crystals of $\text{Ce}_{4-0.5x}\text{Li}_3\text{P}_{18}\text{N}_{35-1.5x}\text{O}_{1.5x}$ ($x \approx 0.72$) were ground in absolute ethanol and drop-cast on copper grids covered with holey carbon film (S166-2, Plano GmbH, Germany). For STEM and electron energy loss spectroscopy (EELS), the samples were plasma cleaned for 20 s. The grids were mounted on a double-tilt holder and transferred into a Cs DCOR probe corrected Titan Themis 300 (FEI, USA) TEM equipped with a X-FEG, a postcolumn filter (Enfinium ER-799), a US1000XP/FT camera system (Gatan, Germany) and a windowless, 4-quadrant Super-X energy dispersive X-ray (EDX) detector. TEM images were recorded using a 4k×4k FEI Ceta CMOS camera. The microscope was operated at 300 kV accelerating voltage for selected area electron diffraction (SAED), STEM-HAADF (with a camera length between 60 and 100 mm) and EELS. For drift corrected EDX mapping with atomic resolution, the microscope was operated at 120 kV accelerating voltage. For the evaluation of the TEM data, the following software was used: Digital Micrograph (Fourier filtering of STEM images, EELS spectra), ProcessDiffraction7 (geometric calculations for SAED), JEMS (SAED simulations), and ES Vision (EDX spectra).^{50–54}

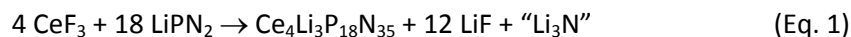
Optical Properties

Images of luminescent single-crystals mounted in glass capillaries were obtained on a Horiba Fluorimax4 spectrofluorimeter system attached to an Olympus BX51 microscope via fiber optics. Photoluminescence was determined on powdered samples with an in-house-built system based on a 5.3 in integrating sphere and a spectrofluorimeter equipped with a 150 W Xe lamp, two 500 mm Czerny-Turner monochromators, 1800 1/mm lattices and 250/500 nm lamps, with a spectral range from 230 to 820 nm.

3.3.3 Results and Discussion

3.3.3.1 Preparation and Chemical Analysis

The reaction of a molar ratio 1:4.5 of CeF_3 and LiPN_2 aimed to synthesize $\text{Ce}_4\text{Li}_3\text{P}_{18}\text{N}_{35}$ (see Experimental section) as the ratio P/N in LiPN_2 is close to the required atomic ratio of 18:35; following Eq. 1, Li_3N could be eliminated for a stoichiometric reaction.



As will be shown later, the actual sum formula is $\text{Ce}_{4-0.5x}\text{Li}_3\text{P}_{18}\text{N}_{35-1.5x}\text{O}_{1.5x}$ ($x \approx 0.72$) due to Ce vacancies. The presence of O probably stems from the crucible material since h-BN slowly decomposes in air to boric acid and B_2O_3 .⁵⁵ The crucible used in the experiment had a small sample to h-BN volume ratio (see Experimental section), allowing the diffusion of sufficient amounts of O into the sample. $\text{Ce}_{4-0.5x}\text{Li}_3\text{P}_{18}\text{N}_{35-1.5x}\text{O}_{1.5x}$ ($x \approx 0.72$) crystallizes in block-like colorless and transparent crystals up to $\approx 100 \mu\text{m}$ in size. The latter emit blue light upon excitation with UV or near-UV radiation (Fig. 1a, see Optical Properties). Morphology and elemental composition were determined by means of SEM (Fig. 1b) and EDX. The EDX values are in accordance with the theoretical sum formula ($\text{Ce}_{4.3}\text{P}_{16.1}\text{N}_{36.9}\text{O}_{1.2} / \text{Ce}_4\text{P}_{18}\text{N}_{33.92}\text{O}_{1.08}$, measured/calculated without taking Li into account). IR spectroscopy indicated the absence of N–H or O–H bonds; only the typical fingerprint region of nitridophosphates was observed (Figure S1). Temperature dependent powder diffraction showed that the phase is stable in air up to at least 1000°C (Figure S2). Rietveld refinement (Figure 2, Table S1) carried out on powder X-ray diffraction data confirms the average-structure model. Residual LiPN_2 is expected since the ratio 1:4 of the starting materials is nonstoichiometric with respect to sum formula $\text{Ce}_4\text{Li}_3\text{P}_{18}\text{N}_{35}$; h-BN stems from the crucible.^{36,56}

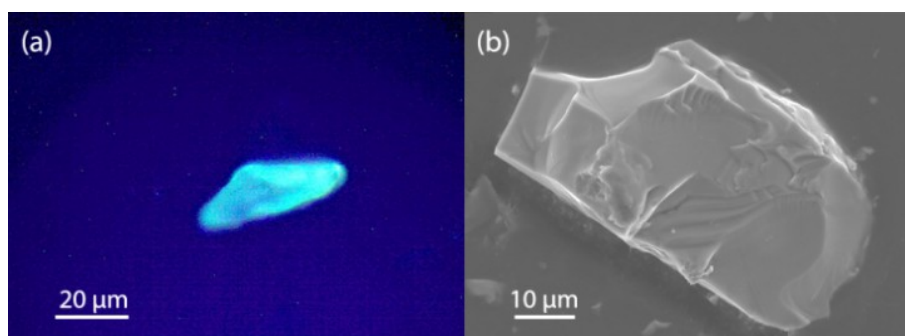


Figure 1. (a) Single-crystal of $\text{Ce}_{4-0.5x}\text{Li}_3\text{P}_{18}\text{N}_{35-1.5x}\text{O}_{1.5x}$ under excitation with 390 nm UV light, emitting blue light. (b) SEM micrograph of a $\text{Ce}_{4-0.5x}\text{Li}_3\text{P}_{18}\text{N}_{35-1.5x}\text{O}_{1.5x}$ single-crystal.

In thin-walled crucibles, $\text{Ce}_{4-0.5x}\text{Li}_3\text{P}_{18}\text{N}_{35-1.5x}\text{O}_{1.5x}$ could be prepared as the major constituent of the sample after introducing an O source in the form of amorphous PON.⁵⁷ Oxygen, therefore, seems to either to facilitate the formation of the compound or to stabilize it as it induces Ce vacancies. Such vacancy-stabilization is reminiscent of yttria-stabilized zirconia, in which the larger Y^{3+} cations stabilize the CaF_2 -type high-temperature phase.⁵⁸

3.3.3.2 Determination of the Average Structure

$\text{Ce}_{4-0.5x}\text{Li}_3\text{P}_{18}\text{N}_{35-1.5x}\text{O}_{1.5x}$ crystallizes in a hexagonal lattice with parameters $a = 13.9318(1)$ and $c = 8.1355(1)$ Å. The unit cell metrics and the average structure model were confirmed by TEM as discussed in the corresponding section. Space group $P6_3/m$ (no. 176) was assigned by analysis of systematically absent reflections in XPREP⁵⁹ and with superiority over $P6_3$ (no. 173), as refinement revealed. The structure was solved by direct methods,⁴⁶ yielding the positions of all heavy atoms. The positions of the light atoms Li and N were determined from difference Fourier maps. All atoms were refined anisotropically, taking into account dispersion correction terms for X-rays with $\lambda = 0.6801$ Å. Table 1 contains the crystallographic data and Table 2 the atom parameters. Anisotropic displacement parameters as well as bond lengths and angles can be found in Tables S2–S4. The site occupancy of position Ce2 is 0.635(2), and the atom has a prolate displacement ellipsoid elongated along [001]. At full occupation, the sum formula $\text{Ce}_4\text{Li}_3\text{P}_{18}\text{N}_{35}$ would be charge-balanced, but a Ce deficit necessitates O for N substitution, as inferred from EDX (see above), in order to maintain charge neutrality.

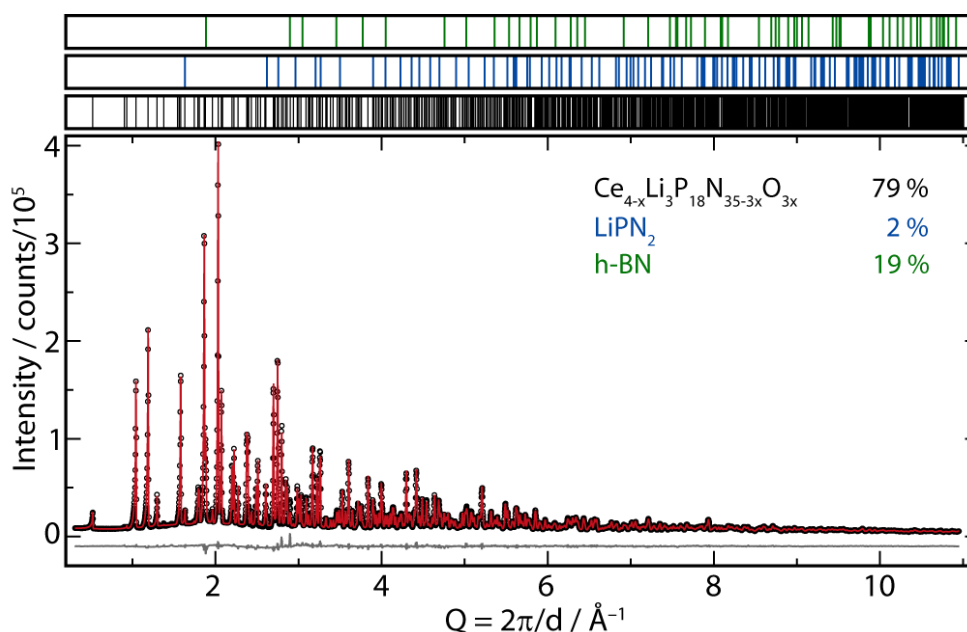


Figure 2. Rietveld refinement for a sample with $\text{Ce}_{4-0.5x}\text{Li}_3\text{P}_{18}\text{N}_{35-1.5x}\text{O}_{1.5x}$ as the main component and LiPN_2 and h-BN as side phases;^{36,56} observed pattern displayed with black circles, calculated pattern as a red line, difference plot as a gray line, positions of Bragg reflections above.

Table 1. Crystallographic data for the average structure of $\text{Ce}_{4-0.5x}\text{Li}_3\text{P}_{18}\text{N}_{35-1.5x}\text{O}_{1.5x}$.

Crystal Data	
formula	$\text{Ce}_{4-0.5x}\text{Li}_3\text{P}_{18}\text{N}_{35-1.5x}\text{O}_{1.5x}$ ($x \approx 0.72$)
formula mass, g mol^{-1}	1580.11
cryst syst	hexagonal
space group	$P6_3/m$ (no. 176)
cell param, Å	$a = 13.9318(1)$ $c = 8.1355(1)$
cell vol, Å ³	1367.51(3)
formula units per unit cell, Z	2
$F(000)$	1472
calc density, ρ , g cm^{-3}	3.837
abs. coeff, μ , mm^{-1}	6.235
Data Collection	
radiation	synchrotron, $\lambda = 0.68010$ Å
temp, K	293(2)
θ range, deg.	$1.615 \leq \theta \leq 31.971$
total no. of reflns	11325
independent reflns	1795
absorption correction	semiempirical ⁴⁴
R_{int} , R_{sigma}	0.019, 0.007
Refinement	
extinction coeff	0.0053(5)
refined params	101
GOF	1.233
$R1$ (all data), $R1 [F^2 > 2\sigma(F^2)]$	0.019, 0.019
$wR2$ (all data), $wR2 [F^2 > 2\sigma(F^2)]$	0.047, 0.047
$\Delta\rho_{\text{max}}$, $\Delta\rho_{\text{min}}$, e Å^{-3}	1.008, -2.025

Since X-rays cannot differentiate between N and O, the distribution of O atoms was derived from electrostatic calculations employing the Madelung part of lattice energy (MAPLE). Accordingly, the N4 position has the smallest partial MAPLE value, and bond valence sum (BVS) calculations also indicate an O share on the N4 position (Tables S5-7).⁶⁰ As MAPLE and BVS depend strongly on the atomic positions and considering that N4 belongs to the first coordination sphere of Ce2 with its prolate displacement ellipsoid, this is only conjecture. O atoms in close proximity to Ce2, however, are reasonable as they are required for charge compensation. The N4 position was therefore mixed with a fixed amount of 0.36O, yielding the sum formula $\text{Ce}_{4-0.5x}\text{Li}_3\text{P}_{18}\text{N}_{35-1.5x}\text{O}_{1.5x}$ with $x \approx 0.72$.

The atom sites N6, N7 and N8 (Figures 3 and 4) exhibit prolate displacement ellipsoids, which are likely a consequence of the Ce2 displacement discussed later in the section “Superstructure Determined from Synchrotron Data”. A possible lower symmetry, in which the afflicted N atoms are not mapped onto themselves by the horizontal mirror plane of space group $P6_3/m$, was ruled out by refinement in $P6_3$ (Figures S3 and S4 for more information), which did not yield any improvement.

Other models of twinning and associated symmetry reduction were ruled out by a refinement in $P1$ including all appropriate twin laws that would lead to Laue symmetry $6/m$.

3.3.3.3 Description of the Average Structure

The structure of $\text{Ce}_{4-0.5x}\text{Li}_3\text{P}_{18}\text{N}_{35-1.5x}\text{O}_{1.5x}$ consists of a framework built up from all-side vertex-sharing PN_4 tetrahedra (Figure 3). Their interconnection pattern is a combination of stacks of 6-rings and triangular columns running along $[001]$ (Figure 3, 4). This formal decomposition emerges from comparison with the oxonitridophosphates $\text{Ba}_6\text{P}_{12}\text{N}_{17}\text{O}_9\text{Br}_3$ and $\text{SrP}_3\text{N}_5\text{O}$; both comprise similar triangular columns.^{61,62} While the columns in $\text{Ba}_6\text{P}_{12}\text{N}_{17}\text{O}_9\text{Br}_3$ are not interconnected and therefore only periodic in one direction, they are interconnected via 2/3 of the triangles' vertices in $\text{SrP}_3\text{N}_5\text{O}$, forming layered anions with periodicity in two directions.⁶³

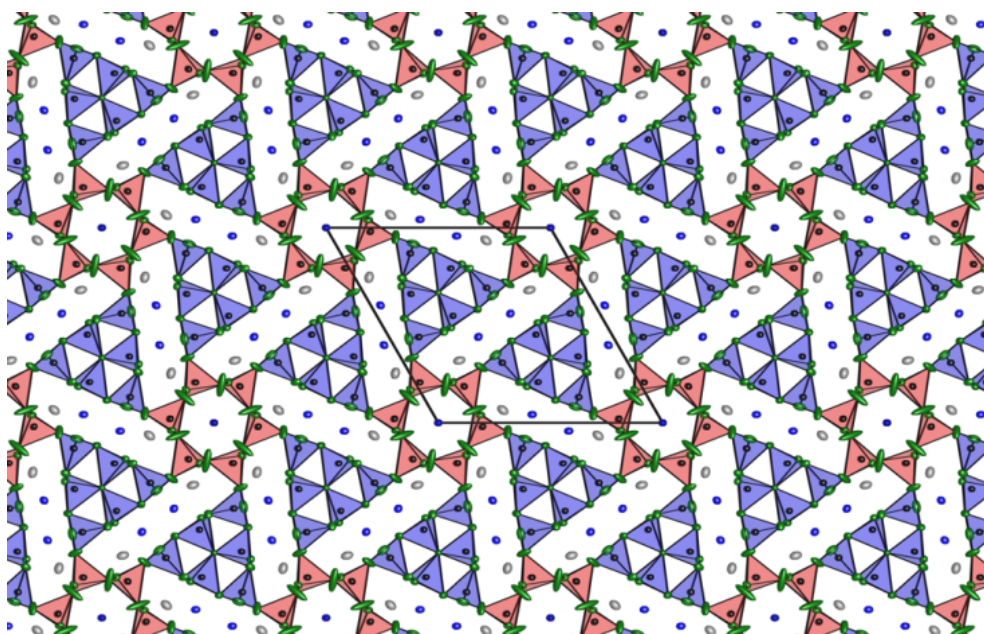


Figure 3. Crystal structure of $\text{Ce}_{4-0.5x}\text{Li}_3\text{P}_{18}\text{N}_{35-1.5x}\text{O}_{1.5x}$ in projection along $[001]$. The 6-ring-stacks and triangular columns are highlighted by red and blue tetrahedra, respectively. Atoms are displayed as their displacement ellipsoid at 90 % probability level, Ce in blue, Li in gray, P in black, and N in green.

In $\text{Ce}_{4-0.5x}\text{Li}_3\text{P}_{18}\text{N}_{35-1.5x}\text{O}_{1.5x}$, the triangular columns are interconnected via stacks of 6-rings and vice versa. Hence, an extended three-dimensional anionic framework with a molar ratio 1:2 of 6-ring stacks and triangular columns is formed. The triangular columns ${}^1_{\infty}[(\text{P}_{12}^{[4]}\text{N}_2^{[3]}\text{N}_{24}^{[2]})^{18-}]$, displayed in Figure 4a, comprise triply-bridging $\text{N}^{[3]}$ atoms, which are the reason for $\kappa = 0.514$. The 6-rings form stacks by sharing tetrahedra vertices, which alternately point up and down (Figure 4b).

The P–P connection pattern represents the framework of the structure (Figure 5, top left) and is referred to as the net topology. The P–P net is subsumed by point symbol⁶⁴ $(3.6^5)(3^3.4^4.5^3)(6^6)$, which

enumerates the shortest cycles originating from P-vertex angles (calculated by TOPOS⁶⁵). The analysis of point and vertex symbols (for the latter see Supporting Information) revealed that this net topology has been neither experimentally realized nor theoretically predicted.

For an intuitive understanding of $\text{Ce}_{4-0.5x}\text{Li}_3\text{P}_{18}\text{N}_{35-1.5x}\text{O}_{1.5x}$'s topology, the three-dimensional *natural tiling* in its maximum symmetry embedding was derived from the P–P connection pattern (Figure 5, top right and bottom).^{66,67} The 3D tiles' faces consist of *locally strong rings* (built up from P–P adjacencies) so that the *natural tiling* retains the full symmetry of the net it carries and the tiles represent chemically meaningful cavities in the structure.⁶⁷ The *natural tiling* consists of six tiles subsumed with signature $3[6^3]+[3^2.4^3]+3[3^2.4.6^2]+[6^5]+3[6^5.10^2]+[3^8.6^3]$ (face symbols) and transitivity symbol 3796 (number of symmetry inequivalent vertices, edges, faces, and tiles, in that order). The cations Ce1 and Li1 reside in the large $[6^5.10^2]$ cage ($V = 148 \text{ \AA}^3$, volume in crystal structure), and Ce2 resides in the $[6^5]$ cage ($V = 62 \text{ \AA}^3$, volume in crystal structure). A detailed description and view of the tiles can be found in the Supporting Information.

The maximum symmetry embedding of the tiling is in $P6_3/mmc$ (no. 194), which is also the maximum symmetry of a theoretical archetype (Figure 5). In $\text{Ce}_{4-0.5x}\text{Li}_3\text{P}_{18}\text{N}_{35-1.5x}\text{O}_{1.5x}$, the mirror plane perpendicular to $\langle 100 \rangle$ is absent due to a rotational twist of the 6-ring with respect to the triangular columns causing the interconnecting P–N–P angles to be 139.4° instead of 180° . Hence, the structure has symmetry $P6_3/m$, which is a subgroup of $P6_3/mmc$ by t_2 transition.

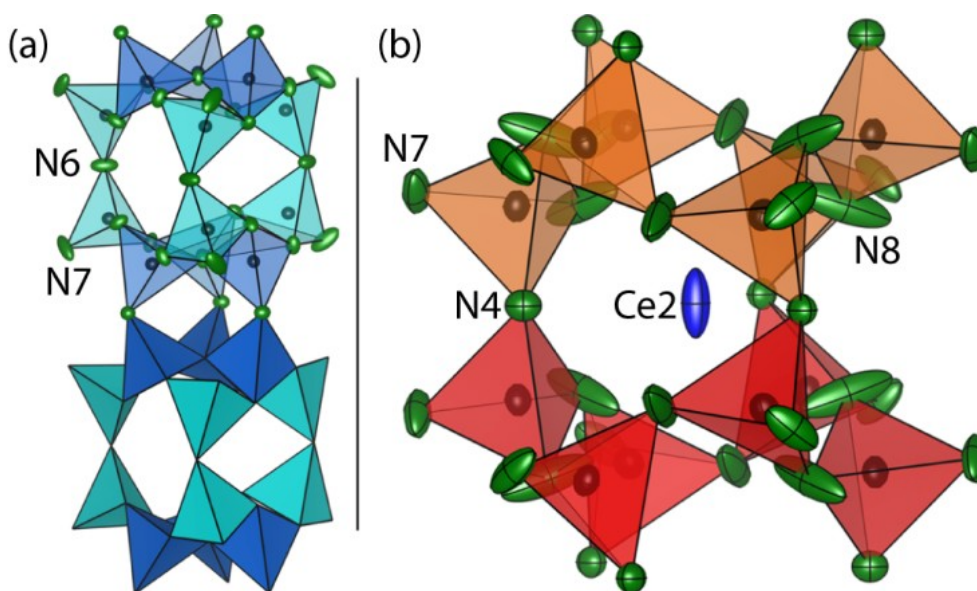


Figure 4. (a) Side-view of the triangular columns running perpendicular to $[001]$, tetrahedra bridged by N^[3] highlighted in royal blue. (b) One repetition unit of the 6-ring stacks. Ellipsoids are displayed at 90 % probability level.

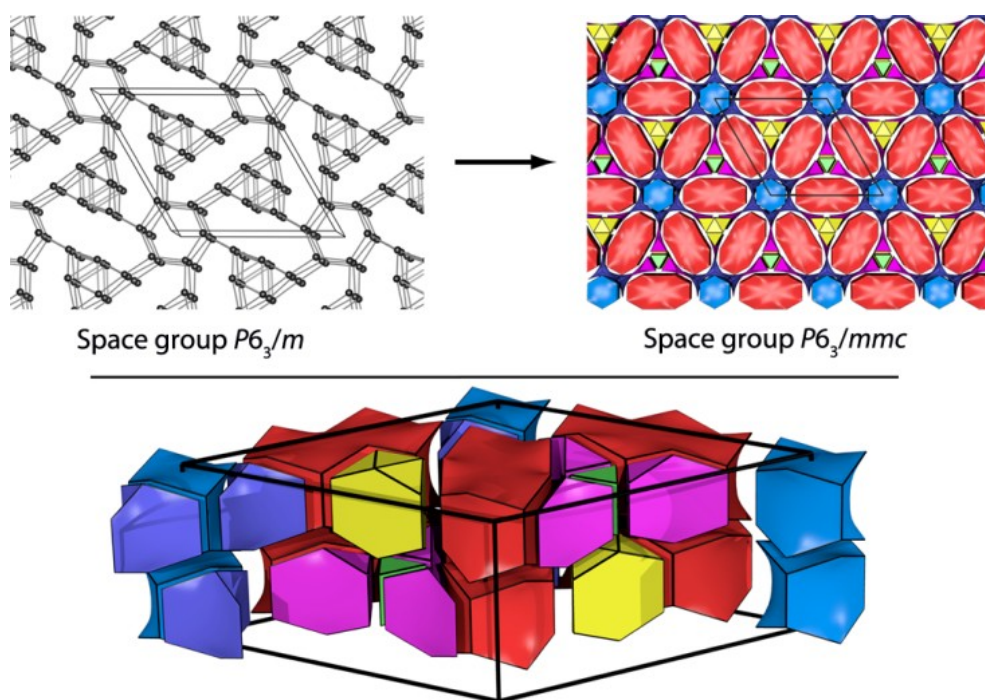


Figure 5. (top, left) P–P connection pattern; (top, right) *natural tiling* in projection along [001], consisting of six individual tiles. (bottom) Cross section through one unit cell of the tiling. Tiles are light blue [6^5], dark blue [6^3], yellow [$3^8.6^3$], pink [$3^2.4.6^2$], green [$3^2.4^3$], and red [$6^5.10^2$].⁶⁶

Table 2. Atom Sites of $\text{Ce}_{4-0.5x}\text{Li}_3\text{P}_{18}\text{N}_{35-1.5x}\text{O}_{1.5x}$.

	Wyckoff position	site symmetry	x	y	z	$U_{eq} / \text{\AA}^3$	occupancy
Ce1	6h	$m..$	0.44029(2)	0.04225(2)	1/4	0.00866(6)	1
Ce2	2a	$\bar{6}$	0	0	1/4	0.02020(17)	0.635(2)
P1	12i	1	0.02032(4)	0.20721(4)	0.06775(6)	0.00775(9)	1
P2	12i	1	0.33965(4)	0.54801(4)	0.07504(6)	0.00607(9)	1
P3	12i	1	0.43947(4)	0.30795(4)	0.06620(6)	0.00643(9)	1
N1	4f	$3..$	1/3	2/3	0.0750(4)	0.0066(4)	1
N2	6h	$m..$	0.2995(2)	0.48706(19)	1/4	0.0080(4)	1
N3	12i	1	0.46921(14)	0.20913(13)	0.0692(2)	0.0095(3)	1
N4	6h	$m..$	0.2080(2)	0.03965(19)	1/4	0.0113(4)	0.64
O4	6h	$m..$	0.2080(2)	0.03965(19)	1/4	0.0113(4)	0.36
N5	12i	1	0.11661(13)	0.53492(13)	0.0319(2)	0.0096(3)	1
N6	6h	$m..$	0.4296(2)	0.3469(2)	1/4	0.0140(5)	1
N7	12i	1	0.04775(19)	0.33260(16)	0.0406(3)	0.0185(4)	1
N8	12i	1	0.1293(2)	0.1946(3)	0.0725(3)	0.0377(8)	1
Li1	6h	$m..$	0.2540(5)	0.3193(5)	1/4	0.0208(12)	1

The coordination polyhedra surrounding the metal ions are displayed in Figure 6. Li1 is coordinated by six N atoms forming a distorted pentagonal pyramid (Johnson solid J_2), Ce1 by nine N atoms in an irregular polyhedron, and Ce2 by nine N atoms arranged in a distorted triaugmented triangular prism (Johnson solid J_{51}).⁶⁸ To approximate the magnitude of distortion, the polyhedra were compared to their holohedral counterparts as described in the Supporting Information (section Coordination Polyhedra). The bond lengths in these polyhedra (Figure 6) are typical for N coordination. They are comparable to those found in NdLiP_4N_8 [$d(\text{Li-N}) = 1.96$ to 2.17 Å], $\text{LiCa}_4[\text{BN}_2]_3$ [$d(\text{Li-N}) = 2.22$ Å], and $\text{Ba}_2\text{Cu}[\text{Si}_2\text{O}_7]$ -type $\text{Ce}_2\text{P}_3\text{N}_7$ [$d(\text{Ce-N}) = 2.44$ – 2.75 Å].^{11,13,69}

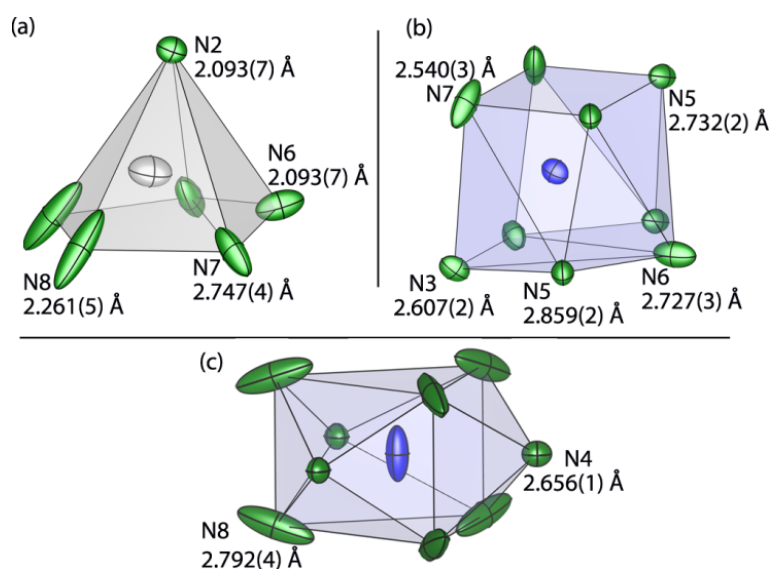


Figure 6. Coordination polyhedra around the sites of Li (a), Ce1 (b), and Ce2 (c); two coordination polyhedra are shown for Ce2, as they appear in stacks along [001] in the structure. Ce–N and Li–N distances are given for all independent N positions; the ellipsoids are displayed with 90 % probability.

In the average structure model discussed above, vacancies are present on the Ce2 site and as can be seen from Figure 6, Ce2 and certain N displacement ellipsoids are elongated. A similar case was reported for $\text{Ba}_{0.85}\text{Ca}_{2.15}\text{In}_6\text{O}_{12}$ ($P6_3/m$, no. 176), in which Ba atoms residing in analogous 6-ring channels entered a long-range periodic order resulting in a (3+1)D incommensurate modulation.⁷⁰ In the following sections, the causes and effects of the Ce2 vacancies and displacements are analyzed.

3.3.3.4 Transmission Electron Microscopy

$\text{Ce}_{4-0.5x}\text{Li}_3\text{P}_{18}\text{N}_{35-1.5x}\text{O}_{1.5x}$ was investigated by TEM to gain information about the Ce2 position. SAED patterns along zone axes [100] and [001] exhibit symmetry $2mm$ and 6, respectively, and correspond to reciprocal lattice sections reconstructed from single-crystal X-ray data, confirming hexagonal symmetry (Figures S6 and S7). Z-Contrast HAADF-STEM images and drift-corrected EDX mappings differentiate between Ce and P atoms; maxima coincide with the heavy-atom positions of the

average structure model (Figure 7, enlarged in Figure S8). In the Fourier filtered micrographs the intensities of the different Ce atom columns match the theoretical atom ratios along the different projections in consideration of the average structure model and the under-occupancy of Ce2.

Further EDX and SAED combined with high resolution STEM-HAADF suggested two different types of domains in $\text{Ce}_{4-0.5x}\text{Li}_3\text{P}_{18}\text{N}_{35-1.5x}\text{O}_{1.5x}$. The first revealed a lower O content, relative to the second, and additionally showed diffraction spots suggesting a superstructure (Figure 8). Since the quantification of little amounts of O by TEM EDX is difficult, several different crystallites were analyzed corroborating the suggested trend (Table S9). In the unfiltered STEM images of the second domain type with increased O content, the contrast of the Ce2 atom columns viewed along [001] varies significantly. In a wedge-shaped edge of a crystal some Ce2 atom columns are missing completely (Figure 9, larger and thinner region represented in Figure S9). This direct observation of the Ce atom columns confirms a random distribution of Ce2 vacancies as suggested by the average structure model.

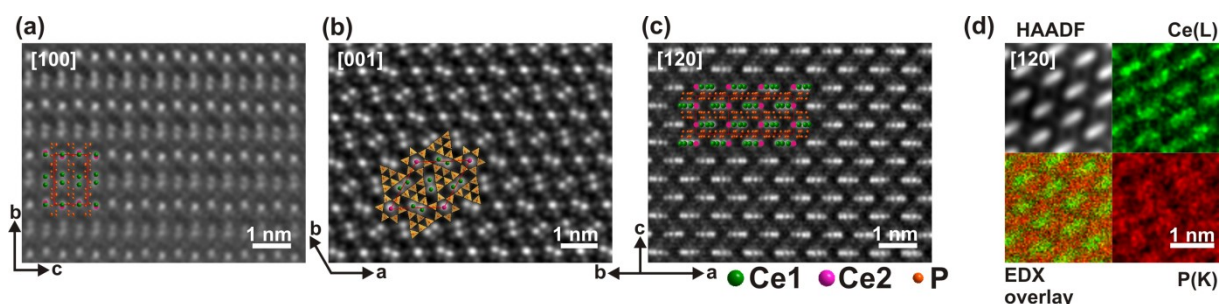


Figure 7. (a-c) Aberration-corrected STEM-HAADF Fourier filtered images along zone axes [100], [001] and [120]. Brighter contrast corresponds to Ce1 (green) and Ce2 (light green) atom columns, darker contrast to P columns (orange). The unit cells of the average structure in corresponding projections were overlaid in red. (d) Drift corrected EDX mappings along [120] in juxtaposition to a HAADF image of the same section. An enlarged version of this figure is Figure S8.

In the superstructure domains, the additional reflections hinted at hexagonal metrics with $a = 24.08$, $c = 8.1 \text{ \AA}$ as later determined by synchrotron diffraction on single crystals (see below). Superstructure reflections are most pronounced in SAED patterns along zone axes [120] of the average structure (Figures 10a and S10). Z-Contrast STEM images along this direction revealed a displacement of Ce2 atoms in [001] direction. Three different locked-in positions (nondynamic displacement) of the Ce2 atoms are directly discernible; one atom resides below (A), one atom above (C), and one atom (B) roughly at the Ce2 position of the average structure model. The distance between atoms at height A and C was measured to be roughly $0.3(1) \text{ \AA}$ based on 10 measurement points (details in Supporting Information). The Fourier transform of the STEM image (Figure S10) shows small additional peaks indicating a periodicity of the Ce2 displacement within the boundaries of the obtained image.

As the displacement is repetitive, they are likely the cause for the superstructure reflections observed in the SAEDs. Since EDX and SAED showed that the superstructure domains with very low O content are only a fraction of the crystal volume (Figure 8), the superstructure reflections of macroscopic single crystals are expected to have extremely weak intensity. A model of the superstructure will therefore be derived in the next section from synchrotron diffraction data. The Ce2 positions appear less bright than other Ce1 positions, which might indicate the presence of vacancies in the superstructure domains. Though such vacancies cannot be ruled out based on O contents due to the lacking accuracy of TEM EDX (Table S9), they appear to be less frequent than in domains without superstructure. The [120] zone-axis images of domains without superstructure even indicate completely missing Ce2 atom columns (Figure S10). The Fourier transform of those images do not suggest the presence of a further periodic ordering of Ce2 in accordance with the above - mentioned SAEDs. In order to balance the charge difference caused by the Ce2 vacancies, the presence of Ce^{4+} is conceivable. Therefore, EELS was performed to gain information about the formal oxidation states of the Ce atoms. EELS quantification of domains with a lower O content determined an atomic ratio Ce/P/N of 1:3.2:8.8 close to the ratio of 1:4.5:8.8 based on the sum formula of the average structure. In the examined domains no Li and O could be quantified with EELS. Off-axis EELS spectra do not indicate the presence of Ce^{4+} (Figure S11). They show the Ce-M₅ and Ce-M₄ edges at 882.0 and 899.5 eV energy loss, respectively, very close to typical values for Ce^{3+} (M₅ at 882.0 eV, M₄ at 899.7 eV) in $\text{Ce}_2\text{Zr}_2\text{O}_8$ or CeO_2 doped with lanthanides.^{71,72} A M₅ to M₄ ratio near to one and more asymmetrically shaped M₄ edge compared to the M₅ edge are characteristic for Ce^{3+} .⁷³

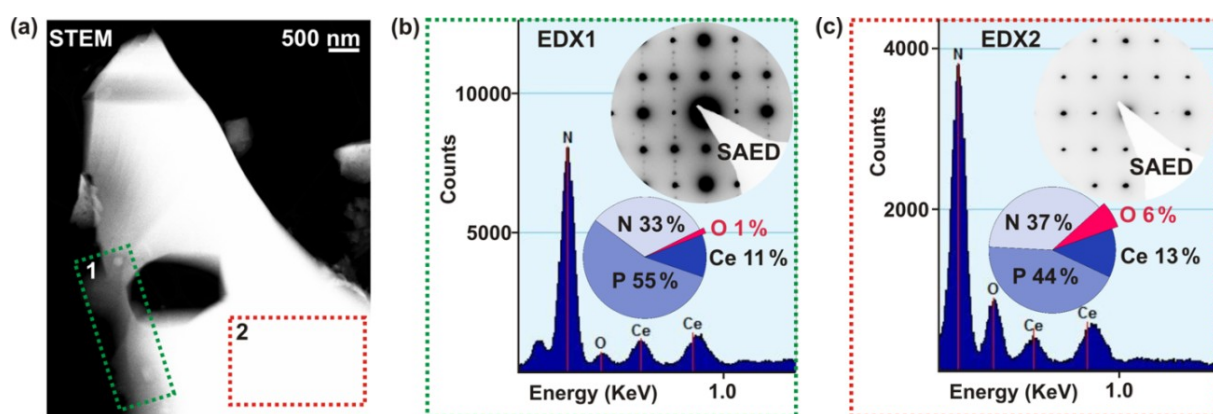


Figure 8. (a) Dark-field STEM micrograph of a representative crystallite of ground powder of $\text{Ce}_{4-0.5x}\text{Li}_3\text{P}_{18}\text{N}_{35-1.5x}\text{O}_{1.5x}$. The area in which the superstructure was observed is highlighted in green, the area without superstructure highlighted in red. (b, c) SAED along the [120] zone axis and EDX for the highlighted regions in panel a. EDX element ratios shown here were obtained from highlighted regions. The dark area is a hole in the crystal.

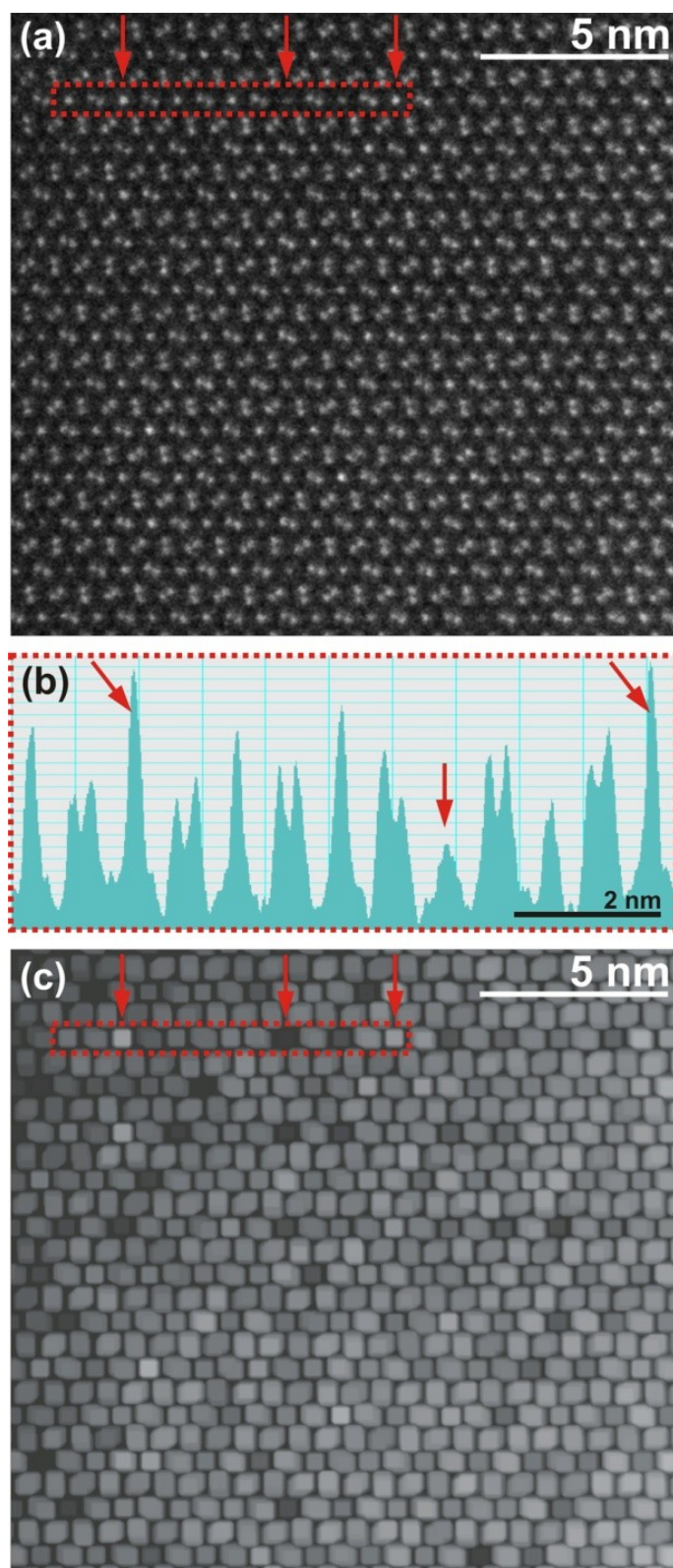


Figure 9. (a) Experimental STEM-HAADF image along [001] of a domain with increased O content showing Ce atom columns. Region of intensity line scan (b) highlighted in red in panel a and c. (c) Intensity map of panel a enhanced by interpolation of brightness over 4 pixels followed by augmenting the bright areas for 9 pixels. The intensity contrast represents the number of Ce atoms in the columns, highlighting a random distribution of Ce₂ vacancies in accordance with the average structure.

3.3.3.5 Superstructure Determined from Synchrotron Data

Synchrotron diffraction data were collected in sufficient quality for analysis of the superstructure suggested by SAED (for a detailed description of X-ray data analysis, the reader is referred to the Supporting Information). From the reciprocal lattice section $hk0$ shown schematically in Figure 11 (experimental patterns are shown in Figure S12), it is apparent that the superstructure is commensurate. The reciprocal lattice of the supercell as defined by vectors $a'^* = 2/3 a^* - 1/3 b^*$, $b'^* = 1/3 a^* + 1/3 b^*$ and $c'^* = c^*$ allows indexing of the whole diffraction pattern. These vectors span a hexagonal ($\sqrt{3} \times \sqrt{3}$)R30° supercell ($a' = 24.1306(1)$, $c' = 8.1335(1)$ Å) with three times the volume of the basic cell.

An initial supercell model for tentative structure refinement was obtained by $i3$ subgroup transformation of the basic structure model according to

$$\begin{pmatrix} a' \\ b' \\ c' \end{pmatrix} = \begin{pmatrix} a \\ b \\ c \end{pmatrix} \begin{pmatrix} 1 & -1 & 0 \\ 1 & 2 & 0 \\ 0 & 0 & 1 \end{pmatrix}$$

Due to pronounced parameter correlation, a conventional refinement of the superstructure in space groups $P6_3/m$ and its subgroup $P6_3$ failed, no significant deviation from the average model could be obtained. This failure is due to the extreme difference in intensity and counting statistics between basic and superstructure reflection (intensity to sigma ratio of the basic structure reflections and the ratio of the superstructure reflections: $I_b/\sigma = 23.7$ to $I_s/\sigma = 1.8$, Figure S12). Moreover, the space group of the superstructure could not be determined unequivocally from the diffraction pattern since the satellite reflections are only observed in hkl planes with $l = 2n$ and $n \neq 0$ (Figure S13).

Note that SAED patterns (Figure 10a) show superstructure reflections in all planes, most likely due to multiple diffraction. Assuming that mainly Ce2 atoms contribute to the superstructure, the reflections in the hkl with $l = \text{odd}$ planes are expected to be weak or absent since the Ce2 atoms in the average structure can be described by a smaller unit cell with $1/2 c$ translation. The unobserved reflections in the $hk0$ plane indicate that the Ce2 atoms are displaced solely along $[001]$, which is reasonable considering their coordination in a triaugmented triangular prism (Figure 6c). To resolve these issues, only the z coordinates of the Ce2 atoms in the supercell were refined⁴⁷ in $P1$ using the superstructure reflections, while all other atom parameters, which were already well-established by the average structure, remained fixed. Ce2 displaced from its average position (Figure S14) and hence corroborated the STEM findings. However, the z coordinates and thus the amplitude of the displacement cannot be determined since they are strongly correlated with the scale factor of the superstructure reflections, whose true value is unknown since the superstructure exists only in domains that correspond to an unknown fraction of the crystal.

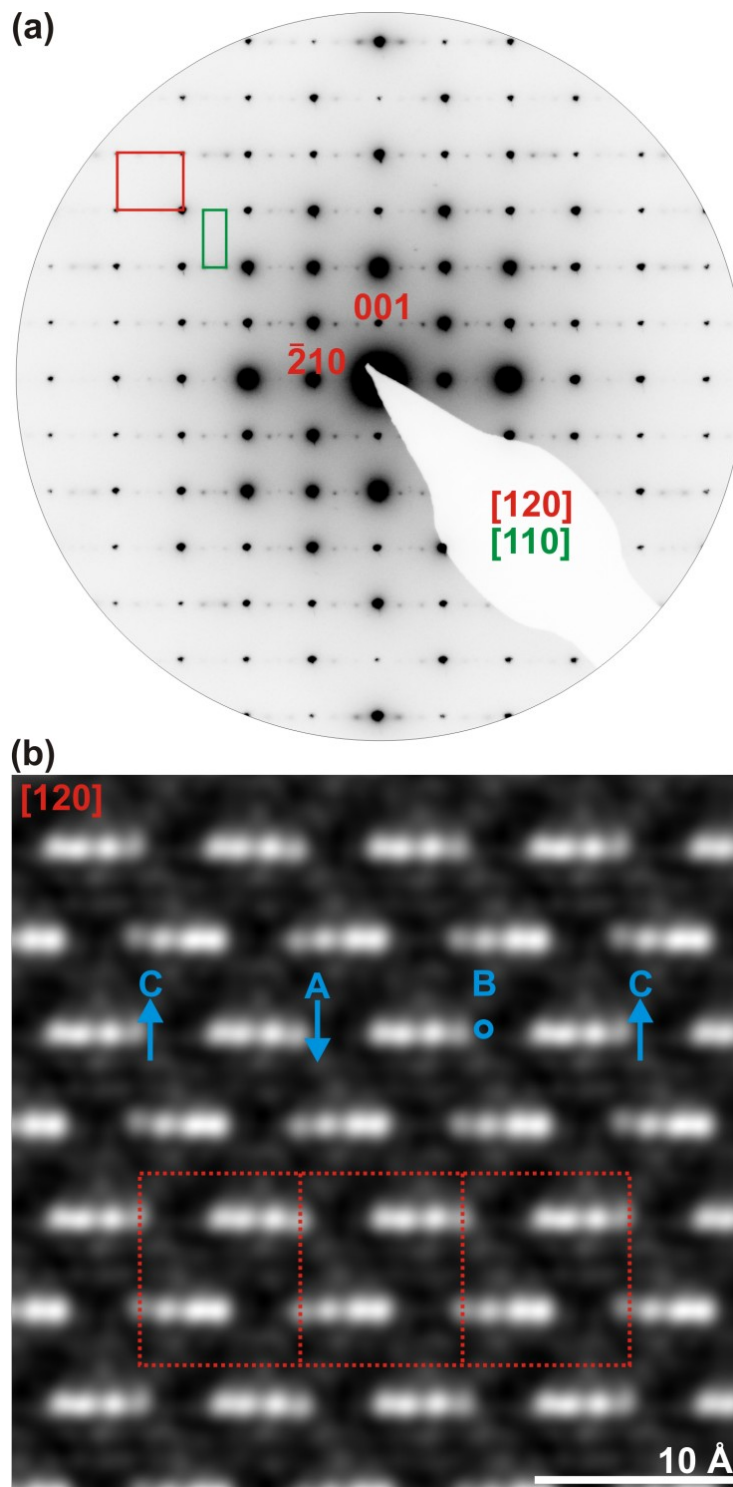


Figure 10. (a) SAED pattern of a superstructure domain along the [120] zone axis of the average structure (red indices and cell outlines); this corresponds to the [110] zone axis of the supercell (green, note the 30° rotation). (b) STEM-HAADF image along this direction showing a displacement of certain Ce2 atoms. Three different locked-in positions of Ce2 atoms along [001] are highlighted with arrows: A (displaced downwards), B (roughly in the middle), C (displaced upward); maximum distance between A and C $\approx 0.3(1)$ Å.

The diffraction pattern was indexed based on the basic cell with two modulation vectors $\mathbf{q}_1 = (1/3, 1/3, 0)$ and $\mathbf{q}_2 = (-2/3, 1/3, 0)$ (Figure 11) resulting in diffraction vectors $\mathbf{h} = h\mathbf{a}^* + k\mathbf{b}^* + l\mathbf{c}^* + m\mathbf{q}_1 + n\mathbf{q}_2$. Since the superstructure is commensurate, the indexing is ambiguous as one satellite is shared by three basic structure reflections. This might be regarded as merohedry in 5D but does not impede structure refinement as the reflections were treated as overlapped.⁷⁴ We are aware that an equivalent description in (3+1)D superspace could be possible due to the commensurate modulation vectors, which allow a description in the higher symmetric commensurate Bravais class $P6/mmm(1/3, 1/3, 0)$.⁷⁵ Because this is more difficult to implement in the refinement and because a commensurate description would not be applicable to possible related structures with incommensurate modulations, we favor the (3+2)D description. The (3+1)D case, however, is discussed in the Supporting Information and a commensurate (3+1)D superspace group is deduced there.

A displacive modulation in superspace is an arbitrarily shaped wave running parallel to the higher dimensional basis vectors, which projected onto physical space are the modulation vectors. Transferred to the superstructure domains of $\text{Ce}_4\text{Li}_3\text{P}_{18}\text{N}_{35}$, the modulation vectors \mathbf{q}_1 , \mathbf{q}_2 and their linear combination $\mathbf{q}_1 + \mathbf{q}_2$ give direction and wavelength of the modulation waves (Figure 11). Since Ce2 was shown to displace along [001], the modulated description necessitates a set of three purely z-polarized plane waves. Those modulation waves are expanded in sine and cosine functions, whose amplitudes are determined in the refinement. Since the waves are related by symmetry and the satellite order is one, only two amplitudes of one wave had to be determined. The refinement (Supporting Information for details) yielded the qualitative displacements of Ce2 atoms, corroborating the supercell description. The superstructure can be conceived as the superposition of three z-polarized plane waves with directions \mathbf{q}_{1d} , \mathbf{q}_{2d} , and $\mathbf{q}_{1d} + \mathbf{q}_{2d}$, wavelength $\lambda_m = 3a$ and mutual origin (Figure 12a). Ce2 atoms occur in three unique positions, one below, one above, and one approximately at the average z-coordinate (Figure 12b). Since the \mathbf{q} -vectors are commensurate, the supercell contains all structural variations but the long-range order of a domain can intuitively be grasped with the modulation-description.

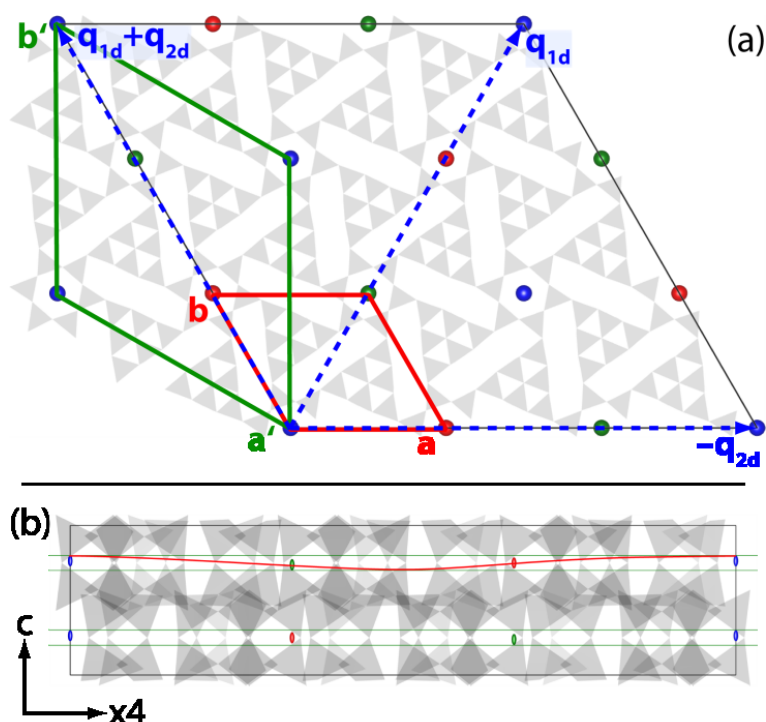


Figure 12. (a) Projection of the (3+2)D superstructure model onto 3D space along [001] direction in a section corresponding to a $3 \times 3 \times 1$ multiple (black) of the basic cell (red). The $(\sqrt{3} \times \sqrt{3})R30^\circ$ supercell is given in green, and the modulation waves are indicated by dashed blue vectors. Atoms of equivalent displacement are marked with color (red, green, blue). (b) Ce2 displacement along [001] and along the additional direction of (3+2)D superspace $x4$, atoms related by symmetry are marked with color.

3.3.3.7 Superstructure Discussion

Presumably, the Ce2 displacement causes the elongated N6, N7, and N8 ellipsoids observed in the basic structure (Figures 3, 4, and 6). The N8 atoms evade the nearing Ce2 atoms by rotating further from the 6-ring center; a displacement that in turn induced a twisting of N6 and N7, which are in close proximity to the 6-rings (Fig. 4a, b). However, the P atoms are unaffected by the Ce2 disposition, as indicated by regular displacement ellipsoids, and can be interpreted as centers of rotation for the N atoms. Since the P atoms are indifferent to the 6-ring conformation and no intratetrahedra N–P–N angles distort, this N-induced distortion seems to have a low energetic barrier. A displacive modulation of the N atoms, however, cannot be refined from the synchrotron data because the reflections in the $hk0$ plane that would carry such information are not observed even with the combination of PILATUS detector and third generation synchrotron. Displacement of heavy atoms in channel-like coordination environments has been reported before; a stabilization of Ba through modulation was suggested as the driving force in $\text{Ba}_{0.85}\text{Ca}_{2.15}\text{In}_6\text{O}_{12}$.⁷⁰ Similarly, the Ce2

displacement might be driven by electrostatics. By moving up and down the channels, Ce2 leaves the Ce2N₉ coordination sphere and enters a distorted octahedral coordination (Figure 6c), also evading the trigonal planar surrounding of N4 atoms. The octahedral coordination mimics the bonding situation in CeN and thus might be the driving force for the displacement.⁷⁶ A long-range modulation can arise since the framework is condensed with all-side vertex-sharing tetrahedra, conducting the displacement information from one 6-ring channel to the other via the bridging triangular columns. The strength of this long-range ordering, however, is small as can be inferred from the small displacement ellipsoids of all atoms except N6, N7, N8, and Ce2. Thus, an accumulation of Ce2 vacancies might interrupt the transfer of information on the modulation and create the nonmodulated domains.

3.3.3.8 Optical Properties

The emission spectrum of Ce_{4-0.5x}Li₃P₁₈N_{35-1.5x}O_{1.5x} (Figure 13) reveals optical emission in the range of 410 nm (detector start) to 526 nm with a maximum at 455 nm corresponding to a full width at half-maximum of 71 nm (3520 cm⁻¹). The peak shape is anisotropic and cannot be modeled by one Gaussian function. Owing to Ce³⁺'s electron configuration of [Xe]4f¹, the electronic ground state is split in two states of similar energy, ²F_{5/2}^o and ²F_{7/2}^o, which usually results in a broadening of the Ce³⁺ emission. Moreover, in the near-UV region, re-excitation might occur due to the small Stokes shift, explaining the anisotropy. As the Ce2 position is modulated, so is the coordination environment around the corresponding atom. This could also take effect on peak broadening. Usually, luminescence is observed from Ce³⁺-doped inorganic host frameworks since pure Ce-containing compounds tend to exhibit concentration quenching (although exceptions like the UV or blue luminescence of several Ce salts are known).⁷⁷ The suggested mechanism for concentration quenching involves a transfer of excitation energy between active ions in close spatial proximity, which increases the chance of a nonradiative decay of the excited state.^{78,79} The Ce-Ce distances might be too large for concentration quenching (d(Ce1-Ce1) = 4.760, d(Ce2-Ce2) = 4.068, d(Ce1-Ce2) = 5.862 Å) as the Ce atoms are separated by a rigid tetrahedra framework. Moreover, the Ce2 vacancies increase the interatomic distance between adjacent Ce2 atoms, which might facilitate luminescence. The UV-vis reflectance spectrum (Figure 13, black line) follows the inverse trend of the excitation spectrum, low reflectivity at high excitation and vice versa.

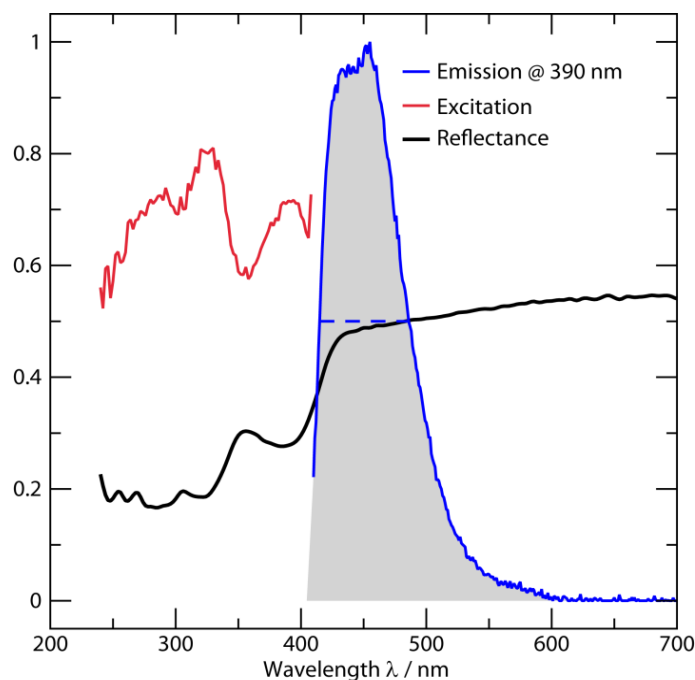


Figure 13. $\text{Ce}_{4-0.5x}\text{Li}_3\text{P}_{18}\text{N}_{35-1.5x}\text{O}_{1.5x}$ emission spectrum (blue) in the range 410–700 nm, excitation spectrum (red) in the range 240–400 nm, and reflectance (black) in the range of 240–700 nm.

3.3.3.9 Magnetic Properties

The predicted effective magnetic moment, μ_{eff} , of Ce^{3+} in electronic ground state $^2F_{5/2}^0$ is $\mu_{\text{eff}} = 2.54 \mu_{\text{B}}$ according to Hund's laws and Russel-Saunders' spin-orbit-coupling approximation. The effective magnetic moment of $\text{Ce}_{4-0.5x}\text{Li}_3\text{P}_{18}\text{N}_{35-1.5x}\text{O}_{1.5x}$ was determined with SQUID magnetometry by measuring the temperature dependent susceptibility at a constant magnetic field of 20 kOe (1 kOe = $7.96 \times 10^4 \text{ A} \cdot \text{m}^{-1}$). Because of the nonstoichiometric reaction of $\text{Ce}_{4-0.5x}\text{Li}_3\text{P}_{18}\text{N}_{35-1.5x}\text{O}_{1.5x}$, the total Ce content of the sample (0.5495 mmol/g) was determined with ICP-OES. A linear regression fit to the χ_{m}^{-1} data in the range of 50 to 200 K (Figure 14) yielded a $\mu_{\text{eff,exp}} = 2.71(1) \mu_{\text{B}}$, which is slightly larger than the theoretical value, and a Curie temperature of $\theta = -2.9(2) \text{ K}$. The 7 % deviation in theoretical and experimental μ_{eff} might be due to a slight under-determination of the sample's Ce content, which was solved with aqua regia at 200 °C. The electronic state of $\text{Ce}_{4-0.5x}\text{Li}_3\text{P}_{18}\text{N}_{35-1.5x}\text{O}_{1.5x}$ is paramagnetic.

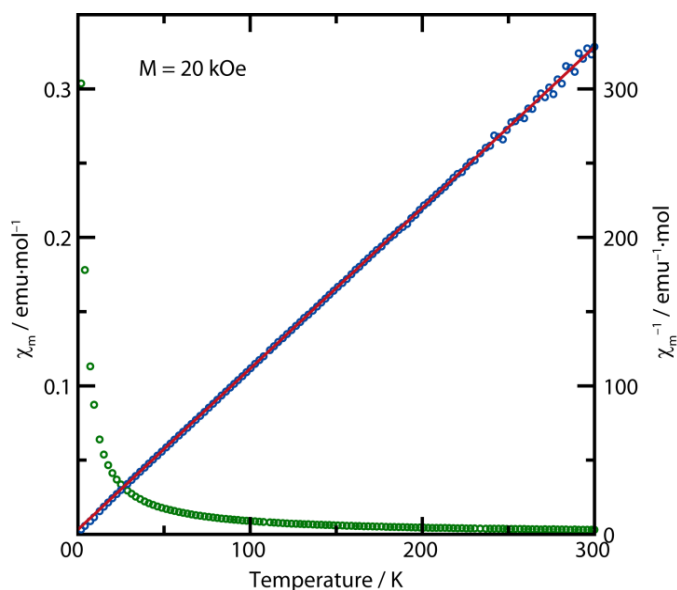


Figure 14. Molar magnetic susceptibility of $\text{Ce}_{4-0.5x}\text{Li}_3\text{P}_{18}\text{N}_{35-1.5x}\text{O}_{1.5x}$ determined at 20 kOe in the range of 1.85–300 K. Green circles χ_m vs. T , blue circles χ_m^{-1} vs. T , and a Curie-Weiss fit displayed as a red line.

3.3.4 Conclusion

Nitridophosphates with a degree of condensation larger than 1/2 are scarcely known. $\text{Ce}_{4-0.5x}\text{Li}_3\text{P}_{18}\text{N}_{35-1.5x}\text{O}_{1.5x}$ ($x \approx 0.72$) is the first nonalkali earth nitridophosphate comprising a framework with $\kappa > 1/2$; an example showing that high-pressure metathesis gives access to a large unexplored structure space. In retrospect to the here observed blue light emission, these expectedly rigid structures could lead to a new class of host frameworks for inorganic solid state lighting.

The joint venture of aberration-corrected STEM and synchrotron diffraction showed that $\text{Ce}_{4-0.5x}\text{Li}_3\text{P}_{18}\text{N}_{35-1.5x}\text{O}_{1.5x}$ ($x \approx 0.72$) contains two different domains, one with a higher and one with a lower O content, which we correlated to the amount of Ce2 vacancies. In the domains of low O content, the Ce2 atoms enter a long-range periodic order. Due to this Ce2 deficiency, the average structure has the sum formula $\text{Ce}_{4-0.5x}\text{Li}_3\text{P}_{18}\text{N}_{35-1.5x}\text{O}_{1.5x}$ ($x \approx 0.72$). In the superstructure domains TEM EDX revealed only negligible amounts of O, which could also stem from surface hydrolysis. Therefore, Ce2 vacancies cannot be ruled out but to our conjecture some domains exhibit full Ce2 occupation and sum formula $\text{Ce}_4\text{Li}_3\text{P}_{18}\text{N}_{35}$. Seemingly, the structure is stabilized either by forming a superstructure or by introducing vacancies on the Ce2 position.

Both supercell and superspace refinements yielded the same, due to the domains qualitative, superstructure model. With STEM we directly observed the Ce2 displacement and measured a distance of ca. 0.3(1) Å between lowest and highest atom. The small variation between the two domains necessitated an investigation at the detection limit of state of the art analysis methods that may indicate the frontier of structure analysis.

3.3.5 References

- 1 F. H. Allen, *Crystallographic Databases*; Bergerhoff, G., Brown, I. D. Eds.; International Union of Crystallography: Chester, **1987**.
- 2 Liebau, F. *Structural Chemistry of Silicates: Structure, Bonding, and Classification*; Springer: Berlin, Germany, **1985**.
- 3 A. Belsky, M. Hellenbrandt, V. L. Karen, P. Luksch, *Acta Crystallogr., Sect. B: Struct. Sci.* **2002**, 58, 364.
- 4 W. Schnick, V. Schultz-Coulon, *Angew. Chem.* **1993**, 105, 308; *Angew. Chem., Int. Ed. Engl.* **1993**, 32, 280.
- 5 A. Marchuk, W. Schnick, *Angew. Chem.* **2015**, 127, 2413; *Angew. Chem., Int. Ed.* **2015**, 54, 2383.
- 6 F. Karau, W. Schnick, *Angew. Chem.* **2006**, 118, 4617; *Angew. Chem., Int. Ed.* **2006**, 45, 4505.
- 7 M. Pouchard, *Nature* **2006**, 442, 878.
- 8 K. Landskron, H. Huppertz, J. Senker, W. Schnick, *Angew. Chem.* **2001**, 113, 2713; *Angew. Chem., Int. Ed.* **2001**, 40, 2643.
- 9 S. Horstmann, E. Irran, W. Schnick, *Angew. Chem.* **1997**, 109, 2085; *Angew. Chem., Int. Ed. Engl.* **1997**, 36, 1992.
- 10 D. Baumann, W. Schnick, *Angew. Chem.* **2014**, 126, 14718; *Angew. Chem., Int. Ed.* **2014**, 53, 14490.
- 11 S. D. Kloß, W. Schnick, *Angew. Chem.* **2015**, 127, 11402; *Angew. Chem., Int. Ed.* **2015**, 54, 11250.
- 12 S. D. Kloß, N. Weidmann, W. Schnick, *Eur. J. Inorg. Chem.* **2017**, 1930.
- 13 S. D. Kloß, N. Weidmann, R. Niklaus, W. Schnick, *Inorg. Chem.* **2016**, 55, 9400.
- 14 S. Horstmann, E. Irran, W. Schnick, *Angew. Chem.* **1997**, 109, 2085; *Angew. Chem., Int. Ed. Engl.* **1997**, 36, 1992.
- 15 K. Landskron, E. Irran, W. Schnick, *Chem. - Eur. J.* **1999**, 5, 2548.
- 16 H. Jacobs, R. Nymwegen, *Z. Anorg. Allg. Chem.* **1997**, 623, 429.
- 17 A. Vitola, J. Ronis, T. Millers, *Latv. PSR Zinat. Akad. Vestis, Kim. Ser.* **1990**, 90, 299.
- 18 K. Landskron, W. Schnick, *J. Solid State Chem.* **2001**, 156, 390.
- 19 K. A. Denault, J. Brgoch, S. D. Kloß, M. W. Gaultois, J. Siewenie, K. Page, R. Seshadri, *ACS Appl. Mater. Interfaces* **2015**, 7, 7264.
- 20 O. Delgado-Friedrichs, A. W. M. Dress, D. H. Huson, J. Klinowski, A. L. Mackay, *Nature* **1999**, 400, 644.
- 21 D. Durach, L. Neudert, P. J. Schmidt, O. Oeckler, W. Schnick, *Chem. Mater.* **2015**, 27, 4832.
- 22 F. Gramm, C. Baerlocher, L. B. McCusker, S. J. Warrender, P. A. Wright, B. Han, S. B. Hong, Z. Liu, T. Ohsuna, O. Terasaki, *Nature* **2006**, 444, 79.
- 23 D. Batuk, M. Batuk, A. M. Abakumov, J. Hadermann, *Acta Crystallogr., Sect. B: Struct. Sci., Cryst. Eng. Mater.* **2015**, 71, 127.
- 24 S. Hovmöller, X. Zou, *Cryst. Res. Technol.* **2011**, 46, 535.
- 25 W. Zhou, H. F. Greer, *Eur. J. Inorg. Chem.* **2016**, 2016, 941.
- 26 J. Sun, Z. He, S. Hovmöller, X. Zou, F. Gramm, C. Baerlocher, L. B. McCusker, *Z. Kristallogr. – Cryst. Mater.* **2010**, 225, 77.

- 27 F. Fahrnbauer, T. Rosenthal, T. Schmutzler, G. Wagner, G. B. M. Vaughan, J. P. Wright, O. Oeckler, *Angew. Chem.* **2015**, *127*, 10158; *Angew. Chem., Int. Ed.* **2015**, *54*, 10020.
- 28 F. Azough, R. Freer, *J. Am. Ceram. Soc.* **2010**, *93*, 1237.
- 29 R. Huang, T. Mizoguchi, K. Sugiura, H. Ohta, K. Koumoto, T. Hirayama, *Appl. Phys. Lett.* **2008**, *93*, 181907.
- 30 F. Yang, D. R. Coughlin, P. J. Phillips, Y. Yang, A. Devaraj, L. Kovarik, R. D. Noebe, M. J. Mills, , *Acta Mater.* **2013**, *61*, 3335.
- 31 K. Z. Baba-Kishi, *J. Appl. Crystallogr.* **2011**, *44*, 111.
- 32 V. Dyadkin, P. Pattison, V. Dmitriev, D. J. Chernyshov, *Synchrotron Radiat.* **2016**, *23*, 825.
- 33 B. Henrich, A. Bergamaschi, C. Broennimann, R. Dinapoli, E. F. Eikenberry, I. Johnson, M. Kobas, P. Kraft, A. Mozzanica, B. Schmitt, *Nucl. Instrum. Methods Phys. Res., Sect. A* **2009**, *607*, 247.
- 34 E. F. Eikenberry, C. Brönnimann, G. Hülsen, H. Toyokawa, R. Horisberger, B. Schmitt, C. Schulze-Bries, T. Tomizaki, *Nucl. Instrum. Methods Phys. Res., Sect. A* **2003**, *501*, 260.
- 35 A. Stock, H. Grüneberg, *Ber. Dtsch. Chem. Ges.* **1907**, *40*, 2573.
- 36 W. Schnick, J. Lücke, *Z. Anorg. Allg. Chem.* **1990**, *588*, 19.
- 37 N. Kawai, S. Endo, *Rev. Sci. Instrum.* **1970**, *41*, 1178.
- 38 H. Huppertz, *Z. Kristallogr.* **2004**, *219*, 330.
- 39 D. Walker, *Am. Mineral.* **1991**, *76*, 1092.
- 40 D. Walker, M. A. Carpenter, C. M. Hitch, *Am. Mineral.* **1990**, *75*, 1020.
- 41 D. Rubie, *C. Phase Transitions* **1999**, *68*, 431.
- 42 A. A. Coelho, *TOPAS-Academic V4.1*, Coelho Software, Brisbane, Australia, **2007**.
- 43 Agilent Technologies, *CrysAlis Pro*, Yarnton, Oxfordshire, England, **2011**.
- 44 Bruker AXS, Inc., *SADABS*, Madison, Wisconsin, USA, **2001**.
- 45 G. M. Sheldrick, *Acta Crystallogr., Sect. A: Found. Crystallogr.* **2008**, *64*, 112.
- 46 G. M. Sheldrick, *SHELXS – A Programm for Crystal structure Solution*, University of Göttingen, Germany, **1997**.
- 47 V. Petríček, M. Dušek, L. Palatinus, *Z. Kristallogr. – Cryst. Mater.* **2014**, *229*, 345.
- 48 K. Momma, F. Izumi, *J. Appl. Crystallogr.* **2011**, *44*, 1272.
- 49 K. Brandenburg, *Diamond; Crystal Impact GbR*, Bonn, Germany **2014**.
- 50 Gatan, Inc., *Digital Micrograph*, Pleasanton, California, USA, **1999**.
- 51 Lábár, J. L. *Ultramicroscopy* **2005**, *103*, 237.
- 52 Stadelmann, P. A. *JEMS; CIME-EPFL*, Saas-Fee, Switzerland **2008**.
- 53 Emispec Systems, Inc. *ES Vision*, Tempe, Arizona, USA, **2002**.
- 54 EDAX AMETEK, *TEAM*, Wiesbaden, Germany **2013**.
- 55 C. G. Cofer, J. Economy, *Carbon* **1995**, *33*, 389.
- 56 O. Hassel, *Nor. Geol. Tidsskr.* **1927**, *9*, 266.
- 57 R. Klement, O. Koch, *Chem. Ber.* **1954**, *87*, 333.
- 58 J. Goff, W. Hayes, S. Hull, M. Hutchings, K. Clausen, *Phys. Rev. B* **1999**, *59*, 14202.
- 59 Bruker AXS, Inc., *XPREP*, Karlsruhe, Germany, **2001**.

- 60 Hübenthal, R. *MAPLE, Programm zur Berechnung des Madelunganteils der Gitterenergie*, Vers. 4, University of Giessen, **1993**.
- 61 E. Mugnaioli, S. J. Sedlmaier, O. Oeckler, U. Kolb, W. Schnick, *Eur. J. Inorg. Chem.* **2012**, 2012, 121.
- 62 S. J. Sedlmaier, E. Mugnaioli, O. Oeckler, U. Kolb, W. Schnick, *Chem. Eur. J.* **2011**, 17, 11258.
- 63 O. Delgado-Friedrichs, M. O’Keeffe, *J. Solid State Chem.* **2005**, 178, 2480.
- 64 V. A. Blatov, M. O’Keeffe, D. M. Proserpio, *CrystEngComm* **2010**, 12, 44.
- 65 V. A. Blatov, A. P. Shevchenko, D. M. Proserpio, *Cryst. Growth Des.* **2014**, 14, 3576.
- 66 O. Delgado-Friedrichs, *3dt*, <http://www.gavrog.org/>, **2013**.
- 67 V. A. Blatov, O. Delgado-Friedrichs, M. O’Keeffe, D. M. Proserpio, *Acta Crystallogr., Sect. A: Found. Crystallogr.* **2007**, 63, 418.
- 68 N. W. Johnson, *Can. J. Math.* **1966**, 18, 169.
- 69 M. Somer, U. Herterich, J. Curda, K. Peters, H. G. von Schnering, *Z. Kristallogr.* **1994**, 209, 182.
- 70 G. Baldinozzi, F. Goutenoire, M. Hervieu, E. Suard, D. Grebille, *Acta Crystallogr. Sect. B: Struct. Sci.* **1996**, 52, 780.
- 71 L. A. J. Garvie, P. R. Buseck, *J. Phys. Chem. Solids* **1999**, 60, 1943.
- 72 S. Arai, S. Muto, J. Murai, T. Sasaki, Y. Ukyo, K. Kuroda, H. Saka, *Mater. Trans.* **2004**, 45, 2951.
- 73 A. M. D’Angelo, A. C. Y. Liu, A. L. Chaffee, *J. Phys. Chem. C* **2016**, 120, 14382.
- 74 L. Bindi, P. Bonazzi, M. Dušek, V. Petříček, G. Chapuis, *Acta Crystallogr., Sect. B: Struct. Sci.* **2001**, 57, 739.
- 75 S. Van Smaalen, *Acta Crystallogr., Sect. A: Found. Crystallogr.* **1987**, 43, 202.
- 76 W. Klemm, G. Winkelmann, *Z. Anorg. Allg. Chem.* **1956**, 288, 87.
- 77 F. A. Kröger, J. Bakker, *Physica* **1941**, 8, 628.
- 78 D. L. Dexter, J. H. Schulman, *J. Chem. Phys.* **1954**, 22, 1063.
- 79 F. Benz, H. P. Strunk, *AIP Adv.* **2012**, 2, 2.

3.3.6 Supporting Information

IR

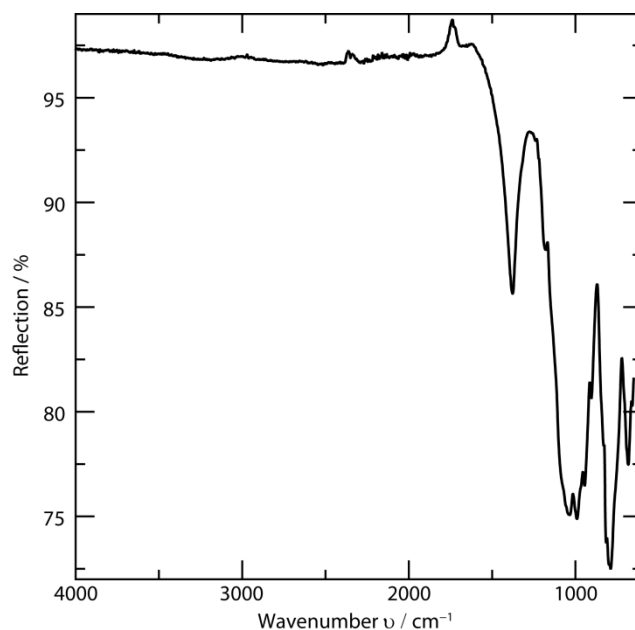


Figure S1: FTIR spectrum of $\text{Ce}_{4-0.5x}\text{Li}_3\text{P}_{18}\text{N}_{35-1.5x}\text{O}_{1.5x}$.

High-Temperature Powder XRD

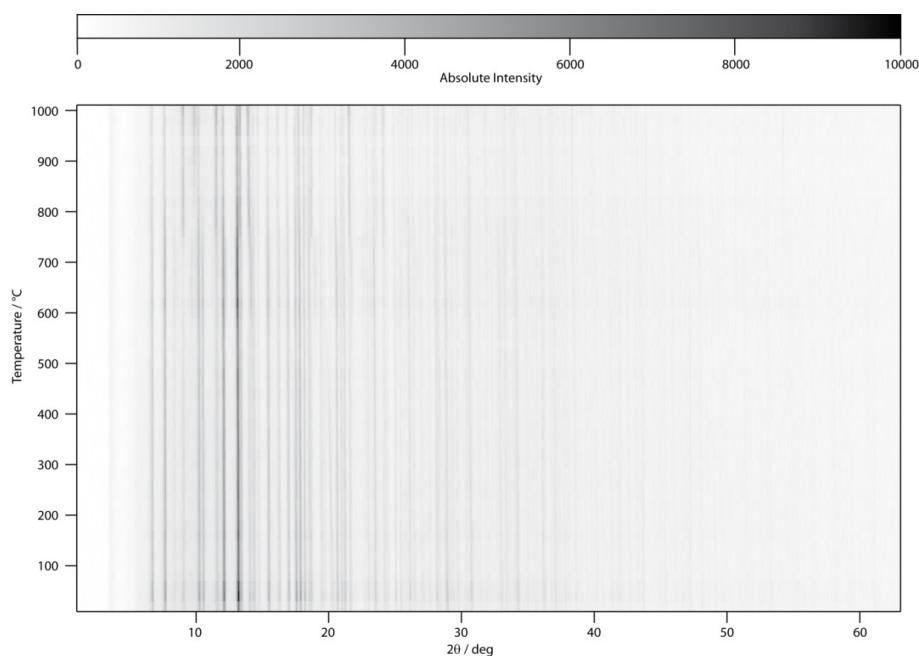


Figure S2: Top view of high-temperature powder X-ray diffraction patterns of $\text{Ce}_{4-0.5x}\text{Li}_3\text{P}_{18}\text{N}_{35-x}\text{O}_{1.5x}$. LiPN_2 was present as a side phase (main reflection at $2\theta = 10.5^\circ$ marked by an arrow), which decomposed at around 800 °C.

Details of Rietveld Refinement

Table S1: Crystallographic data for the Rietveld refinement of $\text{Ce}_{4-0.5x}\text{Li}_3\text{P}_{18}\text{N}_{35-1.5x}\text{O}_{1.5x}$ ($x \approx 0.72$).

Crystal Data	
Formula	$\text{Ce}_{4-0.5x}\text{Li}_3\text{P}_{18}\text{N}_{35-1.5x}\text{O}_{1.5x}$ ($x \approx 0.72$)
Crystal system, space group	hexagonal, $P6_3/m$ (no. 173)
Lattice parameters / Å	$a = 13.92153(9)$ $c = 8.12855(6)$
Cell volume / Å³	1364.32(2)
Formula units per cell Z	2
Data Collection	
Radiation	Mo-K α_1 ($\lambda = 0.7093$ Å)
Monochromator	Ge(111)
Diffractometer	Stoe StadiP
Detector	MYTHEN 1K
2θ-range / °	2–76
Temperature / K	297(2)
Data points	4958
Number of observed reflections	2706
Refinement	
Number of parameters	108
Constraints	0
Program used	TOPAS Academic V4.1
Structure refinement	Rietveld-Method
Profile function	fundamental parameters model
Background function	shifted Chebychev polynomial with 14 terms
R_{wp}	0.041
R_{exp}	0.008
R_p	0.028
R_{Bragg}	0.015

Additional Crystallographic data for $\text{Ce}_{4-0.5x}\text{Li}_3\text{P}_{18}\text{N}_{35-1.5x}\text{O}_{1.5x}$ ($x \approx 0.72$).

Table S2: Anisotropic displacement parameters of $\text{Ce}_{4-0.5x}\text{Li}_3\text{P}_{18}\text{N}_{35-1.5x}\text{O}_{1.5x}$ ($x \approx 0.72$), standard deviations in parentheses, based on single crystal analysis.

Atom	$U_{11} / \text{\AA}^2$	$U_{22} / \text{\AA}^2$	$U_{33} / \text{\AA}^2$	$U_{12} / \text{\AA}^2$	$U_{13} / \text{\AA}^2$	$U_{23} / \text{\AA}^2$
Ce1	0.01017(8)	0.00809(8)	0.00726(8)	0	0	0.00421(5)
Ce2	0.00781(16)	0.00781(16)	0.0450(4)	0	0	0.00391(8)
P1	0.00742(18)	0.00627(18)	0.0091(2)	0.00069(15)	0.00075(15)	0.00311(15)
P2	0.00599(18)	0.00650(18)	0.00609(19)	-0.00031(14)	-0.00003(14)	0.00339(15)
P3	0.00678(18)	0.00669(18)	0.00579(19)	0.00005(14)	0.00007(14)	0.00334(15)
N1	0.0053(6)	0.0053(6)	0.0092(11)	0	0	0.0026(3)
N2	0.0095(9)	0.0074(9)	0.0066(9)	0	0	0.0038(7)
N3	0.0120(7)	0.0087(6)	0.0084(7)	0.0012(5)	0.0036(5)	0.0058(5)
N4	0.0129(10)	0.0092(9)	0.0107(9)	0	0	0.0048(8)
O4	0.0129(10)	0.0092(9)	0.0107(9)	0	0	0.0048(8)
N5	0.0076(6)	0.0073(6)	0.0132(7)	-0.0026(5)	0.0003(5)	0.0032(5)
N6	0.0259(13)	0.0160(11)	0.0069(10)	0	0	0.0157(10)
N7	0.0283(10)	0.0102(7)	0.0204(9)	0.0072(7)	0.0141(8)	0.0120(7)
N8	0.0403(14)	0.084(2)	0.0196(10)	0.0256(13)	0.0169(10)	0.0546(16)
Li1	0.020(3)	0.011(2)	0.033(3)	0	0	0.008(2)

Table S3: Bond lengths (\AA) in $\text{Ce}_{4-0.5x}\text{Li}_3\text{P}_{18}\text{N}_{35-1.5x}\text{O}_{1.5x}$, standard deviations in parentheses.

Ce1		P1	
Ce1–N7	2.5394(19)	P1–N7	1.6059(19)
Ce1–N3	2.6069(17)	P1–N8	1.614(2)
Ce1–N6	2.727(3)	P1–N8	1.615(2)
Ce1–N5	2.7315(17)	P1–N4	1.6544(12)
Ce1–N5	2.8592(18)	P2	
Ce1–P2	3.3358(5)	P2–N5	1.6053(17)
Ce1–P3	3.3784(5)	P2–N2	1.6078(12)
Ce2		P2–N3	1.6103(18)
Ce2–N4	2.665(2)	P2–N1	1.6988(5)
Ce2–N8	2.792(3)	P3	
Li1		P3–N7	1.611(2)
Li1–N2	2.093(6)	P3–N6	1.6197(11)
Li1–N6	2.279(7)	P3–N3	1.6243(17)
Li1–N8	2.260(6)	P3–N5	1.6509(17)

Table S4: Selected bond angles (in °) in $\text{Ce}_{4-0.5x}\text{Li}_3\text{P}_{18}\text{N}_{35-1.5x}\text{O}_{1.5x}$, standard deviations in parentheses.

N–P1–N		N–P2–N		N–P3–N		P–N–P	
N7–P1–N8	109.15(16)	N5–P2–N2	112.84(11)	N7–P3–N6	109.89(13)	P2–N1–P2	120
N7–P1–N8	113.38(15)	N5–P2–N3	108.54(9)	N7–P3–N3	116.14(10)	P2–N2–P2	124.58(15)
N8–P1–N8	111.2(2)	N2–P2–N3	110.23(10)	N6–P3–N3	111.74(11)	P2–N3–P3	117.30(10)
N7–P1–N4	106.59(11)	N5–P2–N1	107.09(7)	N7–P3–N5	99.14(9)	P1–N4–P1	127.33(15)
N8–P1–N4	109.34(11)	N2–P2–N1	109.91(12)	N6–P3–N5	107.36(12)	P2–N5–P3	129.06(11)
N8–P1–N4	106.96(12)	N3–P2–N1	108.07(10)	N3–P3–N5	111.62(9)	P3–N6–P3	134.80(17)
						P1–N7–P3	138.41(13)
						P1–N8–P1	133.67(16)

MAPLE and BVS

Madelung part of the lattice energy (MAPLE) calculations were carried out with MAPLE based on an idealized structure model of $\text{Ce}_4\text{Li}_3\text{P}_{18}\text{N}_{35}$, as not fully occupied atom positions cannot be taken into account. To evaluate the calculated values, $\text{Ce}_4\text{Li}_3\text{P}_{18}\text{N}_{35}$ was formally decomposed into 4 CeN, 3 LiPN_2 , and 5 $\gamma\text{-P}_3\text{N}_5$.^{1–3}

Table S5: MAPLE calculations for $\text{Ce}_4\text{Li}_3\text{P}_{18}\text{N}_{35}$.

Compound	Multiplicator	MAPLE / $\text{kJ}\cdot\text{mol}^{-1}$	MAPLE · Multiplicator / $\text{kJ}\cdot\text{mol}^{-1}$
CeN	4	8686.1263	34744.5052
LiPN_2	3	28084.5637	84253.6911
P_3N_5	5	76829.8841	384149.421
Σ			503147.617
$\text{Ce}_4\text{Li}_3\text{P}_{18}\text{N}_{35}$	1	508459.308	508840.538
Deviation / %			1.13 %

Table S6: Partial MAPLE values for $\text{Ce}_4\text{Li}_3\text{P}_{18}\text{N}_{35}$. Typical values: N^{3-} 5000–6000 kJ/mol^{-1} , O^{2-} 2000–2800 kJ/mol^{-1} .

Atom	Partial MAPLE / $\text{kJ}\cdot\text{mol}^{-1}$
Ce1	4473
Ce2	3318
P1	15533
P2	14458
P3	15434
N1	7674
N2	6384
N3	6227
N4	5851
N5	6151
N6	5948
N7	5931
N8	6206
Li1	881

Table S7. Bond-valence sums for $\text{Ce}_{4-0.5x}\text{Li}_3\text{P}_{18}\text{N}_{35-1.5x}\text{O}_{1.5x}$.

Atom	Ce1	Ce2	Li1	P1	P2	P3	N1
BVS	2.44	1.93	0.86	5.0	4.93	4.94	3.09
Occupancy	1	0.64	1	1	1	1	1

Atom	N2	N3	N4	O4	N5	N6	N7
BVS	2.83	2.86	2.57	2.13	2.87	2.88	3.01
Occupancy	1	1	0.44	0.56	1	1	1

Difference Fourier Maps

Atom sites N6, N7 and N8 have strongly (Figure 3, 4 and 6) prolate displacement parameters, potentially caused by symmetry elements of the space group $P6_3/m$, which do not apply for the local structure. The ellipsoids might be explained by two independent N atoms that have slightly different x and y coordinates and are mapped onto each other by the mirror plane perpendicular to c . To falsify this suggested lower symmetry for the average long-range ordered structure, the structure refinement was repeated by systematically removing symmetry elements down to space group $P1$ under consideration of all relevant twin laws.

Omission of the inversion center and the mirror plane perpendicular to [001] (in the t_2 subgroup $P6_3$, no. 173) theoretically suffices for crystallographic splitting of the N8 site. Difference Fourier maps calculated in $P6_3$ revealed a mirror- and centrosymmetric electron density (Figure S3, S4), indicating that the N8 position is best described with $P6_3/m$ symmetry.

Difference Fourier maps in $P6_3$

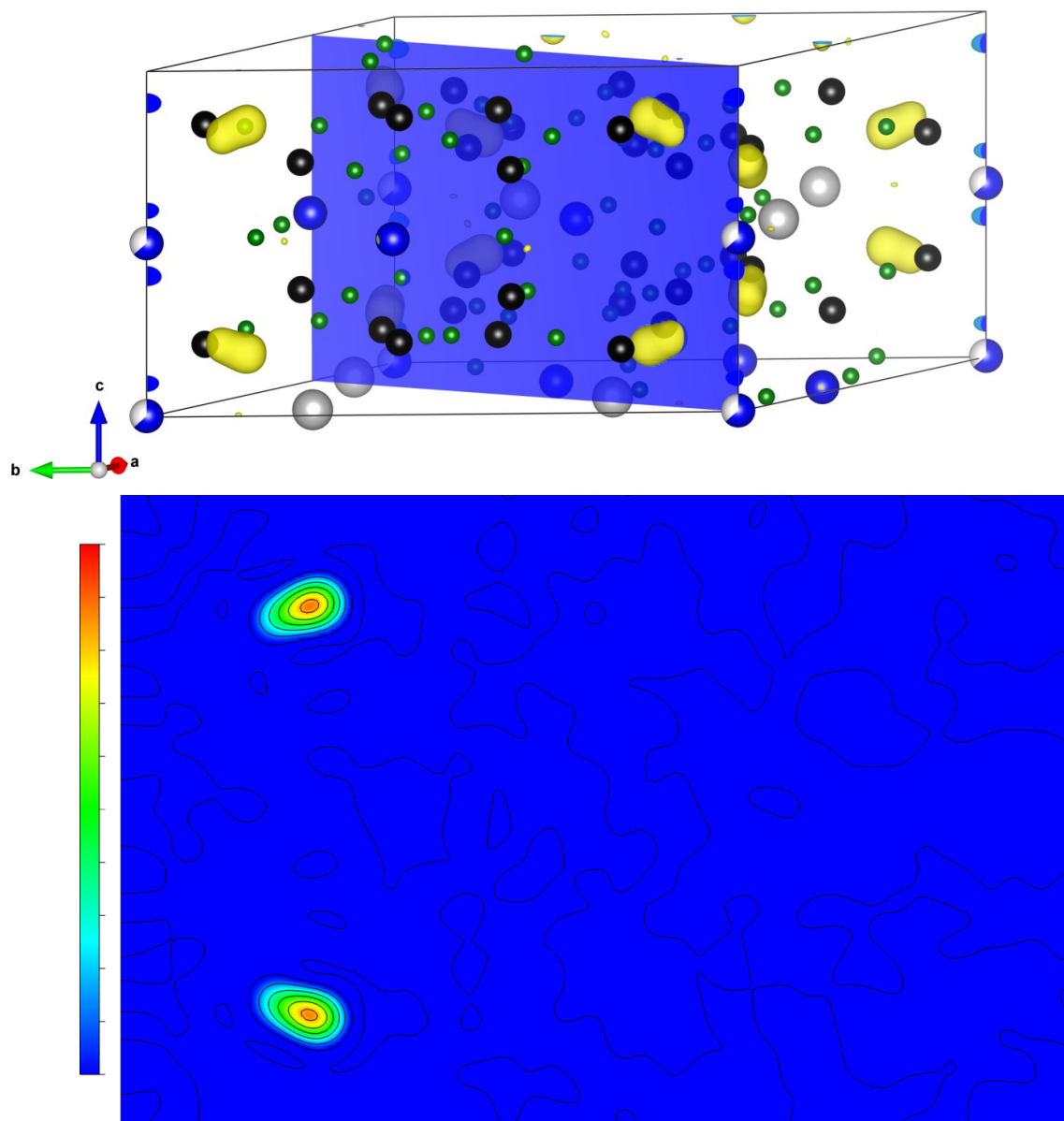


Figure S3: Difference Fourier maps ($F_{\text{obs}} - F_{\text{calc}}$) calculated for a structure model in space group $P6_3$, in which the atom positions of the 6-ring inter-tetrahedra bridging N were deleted. The top image shows the $F_{\text{obs}} - F_{\text{calc}}$ map of the unit cell, positive electron density in yellow, negative in blue. A plane $(-1.5 \ 1 \ 0)$ is highlighted in blue. The 2D contour $F_{\text{obs}} - F_{\text{calc}}$ plot through this plane is presented in the bottom part. It runs through the N8 atom positions. $F_{\text{obs}} - F_{\text{calc}}$ maps were calculated with VESTA.⁵

Difference Fourier maps in $P6_3/m$

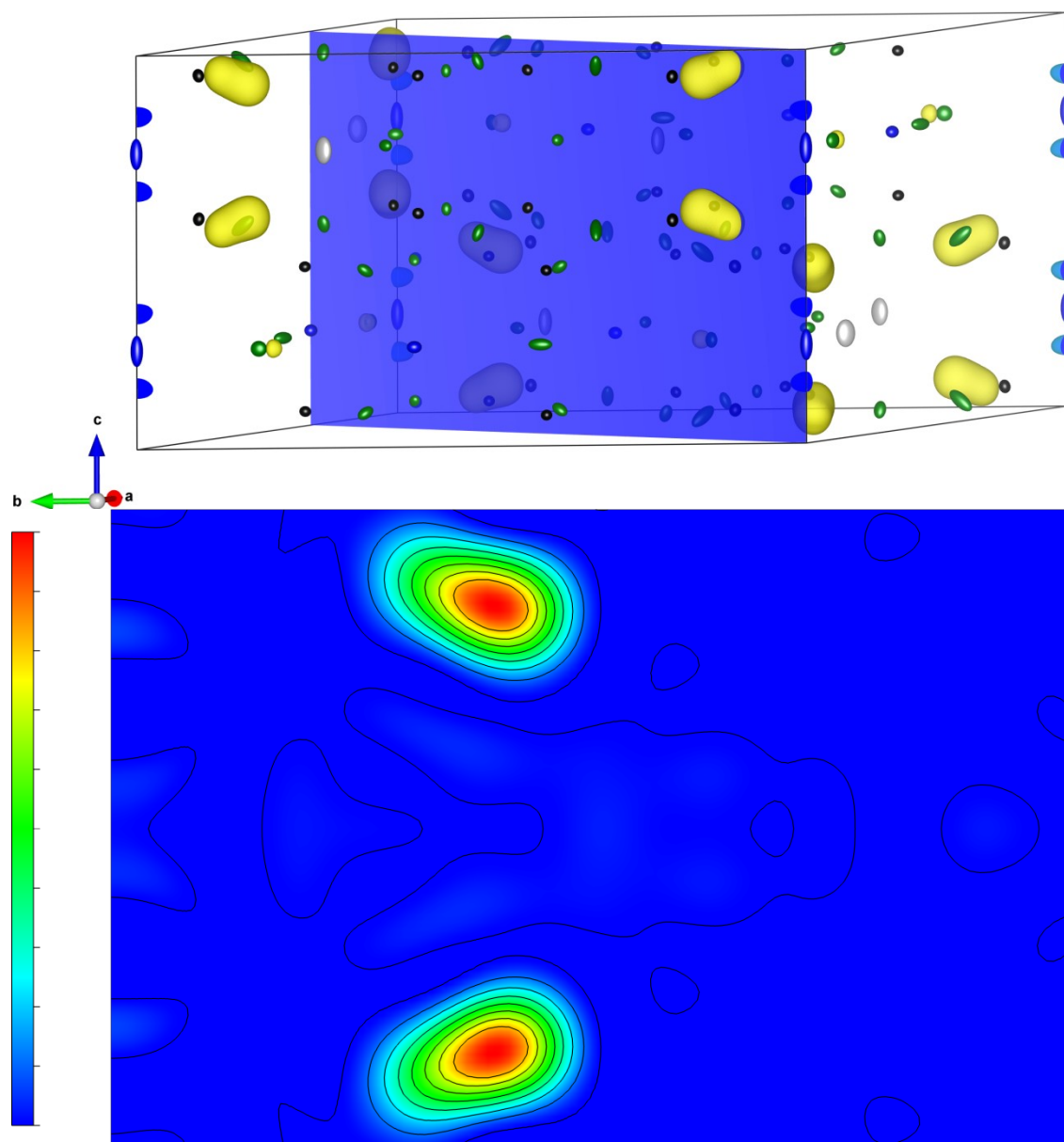


Figure S4: Difference Fourier maps ($F_{\text{obs}} - F_{\text{calc}}$) calculated for a structure model in space group $P6_3/m$, in which the atom positions of the 6-ring inter-tetrahedra bridging N were deleted. The top image shows the $F_{\text{obs}} - F_{\text{calc}}$ map of the unit cell, positive electron density in yellow, negative in blue. A plane $(-1.5 \ 1 \ 0)$ is highlighted in blue. The 2D contour $F_{\text{obs}} - F_{\text{calc}}$ plot through this plane is presented in the bottom part. It runs through the N8 atom positions. $F_{\text{obs}} - F_{\text{calc}}$ maps were calculated with VESTA.⁵

Network Topology

Vertex Symbol

The vertex symbol of the PN net of $\text{Ce}_{4-0.5x}\text{Li}_3\text{P}_{18}\text{N}_{35-1.5x}\text{O}_{1.5x}$ was calculated with TOPOS with ring sizes up to 12, larger ring sizes were neglected and the corresponding angle marked with an asterisk.⁵

P1: (6.6₂.6.6₂.6₂.6₂)

P2: (3.3.3.4.4.6.6.6.*.*)

P3: (3.6₂.6.6.6.6)

The framework's fundamental building units are essential rings of size 3 to 6, and no 10-ring are listed in the point as might contrarily be suggested by the structure's projection along [001] (Figure 3); vertex symbols only list the shortest rings and their number contained in the respective angle.⁶

Tiling

All six tiles occurring in the maximum symmetry embedding of the PN net of $\text{Ce}_{4-0.5x}\text{Li}_3\text{P}_{18}\text{N}_{35-1.5x}\text{O}_{1.5x}$ are presented along with their wireframe representation and face symbol as well as their volume occupation in the real crystal structure. Data calculated with TOPOS, tiles drawn with *3dt*.^{6,7}

Table S8: Face symbols and volume of the tiles shown in Figure S5.

Tile	Face Symbol	Volume /Å ³
a	[6 ⁵ .10 ²]	147.9
b	[3 ² .4 ³]	10.6
c	[6 ³]	17.0
d	[6 ⁵]	62.1
e	[3 ² .4.6 ²]	17.8
f	[3 ⁸ .6 ³]	59.6

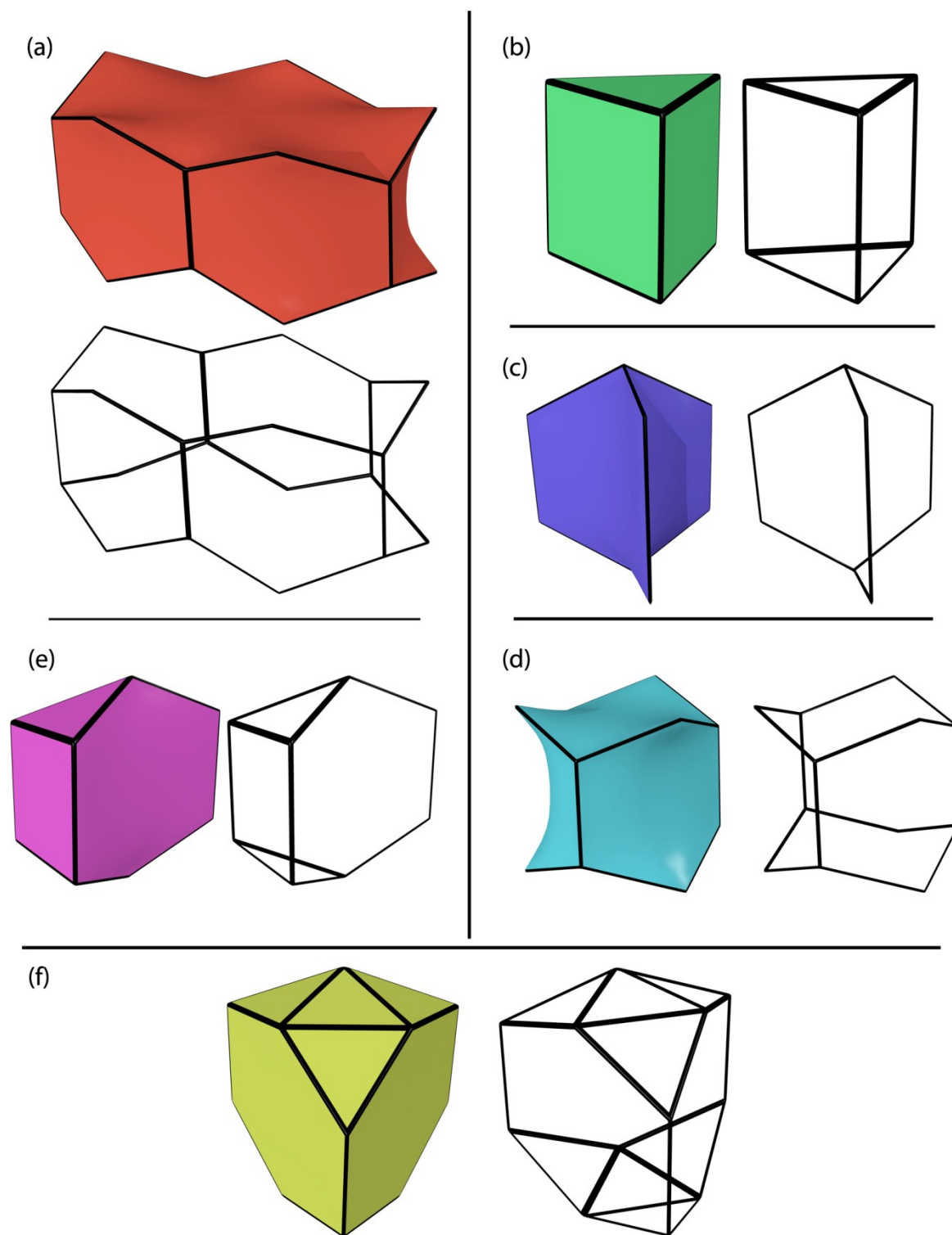


Figure S5: Tiles occurring in $\text{Ce}_{4-0.5x}\text{Li}_3\text{P}_{18}\text{N}_{35-1.5x}\text{O}_{1.5x}$, face symbols and volume given in Table S8.

Coordination Polyhedra

Li2 coordination

The pentagonal pyramid belongs to the class of Johnson solids, polyhedra that are not transitive on its faces, edges and vertices but constitute regular polygons.⁸ It is classified as Johnson solid J_2 with vertex symbol $(3^2.5)_5(3^5)$ and C_{5v} symmetry in Schönflies notation. According to site symmetry $m..$ of the Li1 position, distortions in the LiN_6 polyhedron removed the five-fold rotation axis, which is in any case non-crystallographic, but maintained one vertical mirror plane. Common Li–N bond lengths range from 2.0 to 2.4 Å (e. g. $NdLiP_4N_8$ $d(Li-N) = 1.96$ to 2.17 Å, $B_3Ca_4LiN_6$ $d(Li-N) = 2.22$ Å).^{9,10} The values found here reveal a large distance variation ($d(Li-N) = 2.09$ – 2.80 , $d_{\text{av}}(Li-N) = 2.41$ Å) leading to an effective coordination number of 3.6. Hence, the coordination might better be represented by a tetrahedron. However, the prolate Li atom displacement, which shows a displacement towards the remote N7 ($d(Li-N7) = 2.747(4)$), is illustrated by the distortion of the pentagonal pyramid.

Ce1 coordination

Ce1 resides inside the 10-ring channels and is coordinated in an irregular CeN_9 polyhedron, which is not one of the Johnson solids. A mathematically devised holohedral polygon with regular polygon faces, therefore, cannot be constructed. Through determination of faces based on shortest N–N distances, the face symbol could be $[3^7.4^2.5]$, describing the polyhedron as an arrangement of 4 N below and 5 N above Ce1 (depicted in Figure 6b). The corresponding vertex symbol is $(3^3.4)_2(3^2.4^2)_2(3.4.5)_2(3^3.5)_3$. The Ce1–N distances in the range of $d(Ce1-N) = 2.54$ – 2.93 Å coincide well with values of $Ba_2Cu[Si_2O_7]$ -type $Ce_2P_3N_7$ with $d(Ce-N) = 2.44$ – 2.75 Å.¹¹ The coordination number in $Ce_2P_3N_7$ is CN = 8, hence the bond lengths are slightly shorter.

Ce2 coordination

Ce2, which is not fully occupied (*s.o.f.* = 0.635), resides in the 6-ring channels and is coordinated by nine N atoms arranged after Johnson solid J_{51} , a triaugmented triangular prism (Figure 6c).⁸ J_{51} belongs to the class of deltahedra, polyhedra constructed solely by equilateral triangles. Its vertex symbol is therefore $(3^4)_3(3^5)_6$ and its holohedral symmetry group is D_{3h} , which is a crystallographic point group denoted $\bar{6}m2$ in Hermann-Mauguin notation. While space group $P6_3/mmc$, the maximal symmetry group of the net, features a $\bar{6}m2$ Wyckoff position, its $t2$ subgroup $P6_3/m$ does not and Ce2 is located on a $\bar{6}m2$ -fold symmetry axis in $P6_3/m$. Hence, symmetry of the triaugmented triangular prism surrounding Ce2 is reduced. Though two equilateral triangles comprise the triangular prism, which preserve the horizontal mirror plane and inversion center, the capping N4 atoms are not centered above the rectangular faces of the prism, thus eliminating the mirror plane

and 2-fold rotation perpendicular to the main rotation axis. The symmetry group is thus C_{3h} in Schönflies notation. Two Ce2–N bond distances are found, $d(\text{Ce2–N4}) = 2.656 \text{ \AA}$ and $d(\text{Ce2–N8}) = 2.792 \text{ \AA}$.

TEM

Table S9. TEM EDX of $\text{Ce}_{4-0.5x}\text{Li}_3\text{P}_{18}\text{N}_{35-1.5x}\text{O}_{1.5x}$ ($x \approx 0.72$) in atom% (standard deviations), mean values based on 9 measurement points each. All experiments showed more O than theoretically predicted. This might be due to hydrolysis of the surface. The experimental values, however, are to be understood in relation between the two domains.

	average value from model	mean value of domains with low O content	mean value of domains with higher O content
N (K)	60.9	53(4)	52(1)
O (K)	1.0	2(1)	5(1)
P (K)	31.8	39(5)	36(3)
Ce (L)	6.4	6(1)	7(2)

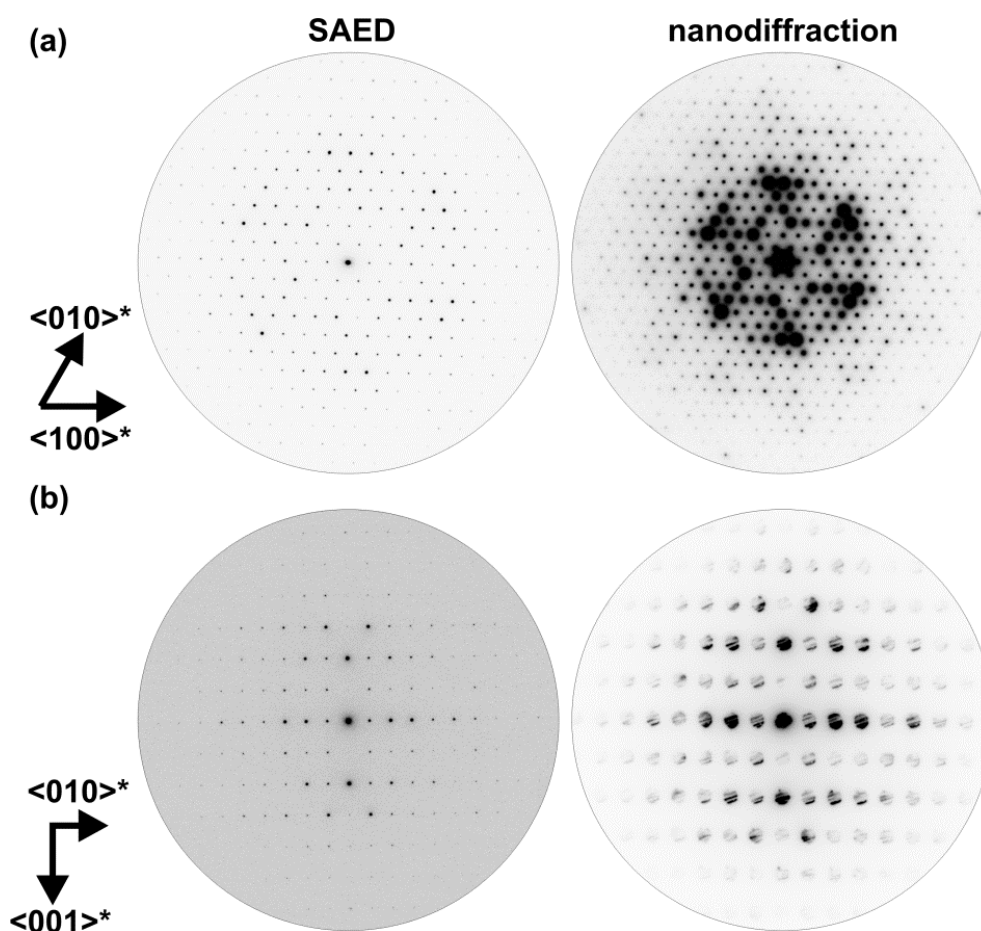


Figure S6. Electron diffraction along [001] (a) and [100] (b), both SAED (left) and nanodiffraction (right) whole pattern symmetry in accordance to space group $P6_3/m$ derived from X-ray data.

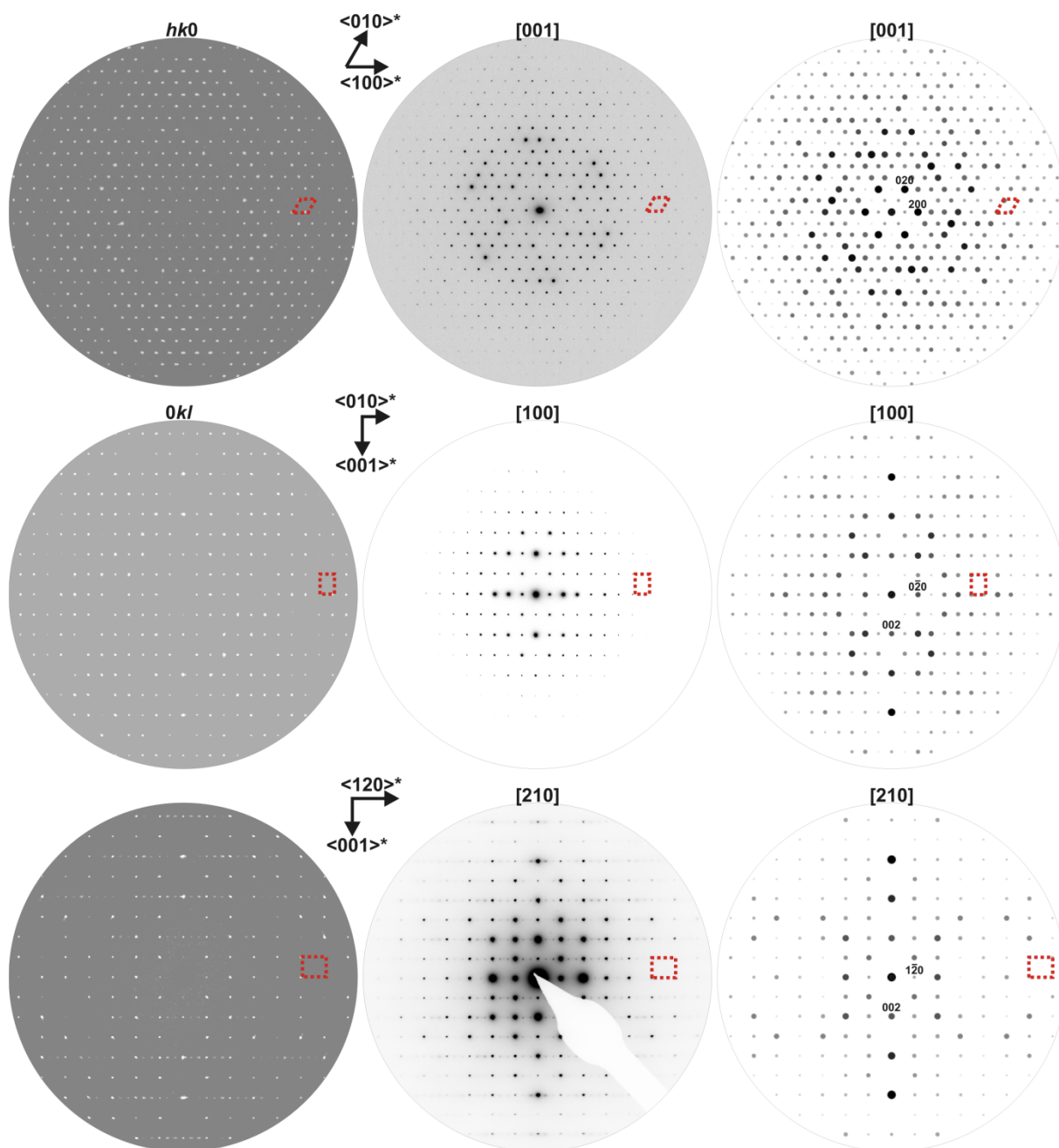


Figure S7. Reciprocal lattice sections (see also Figure S12, S13) reconstructed from single crystal X-ray diffraction data (left) compared to SAED patterns along special directions from different crystallites (middle) with corresponding simulations (right) based on single crystal X-ray data, all each unit cell highlighted in red.

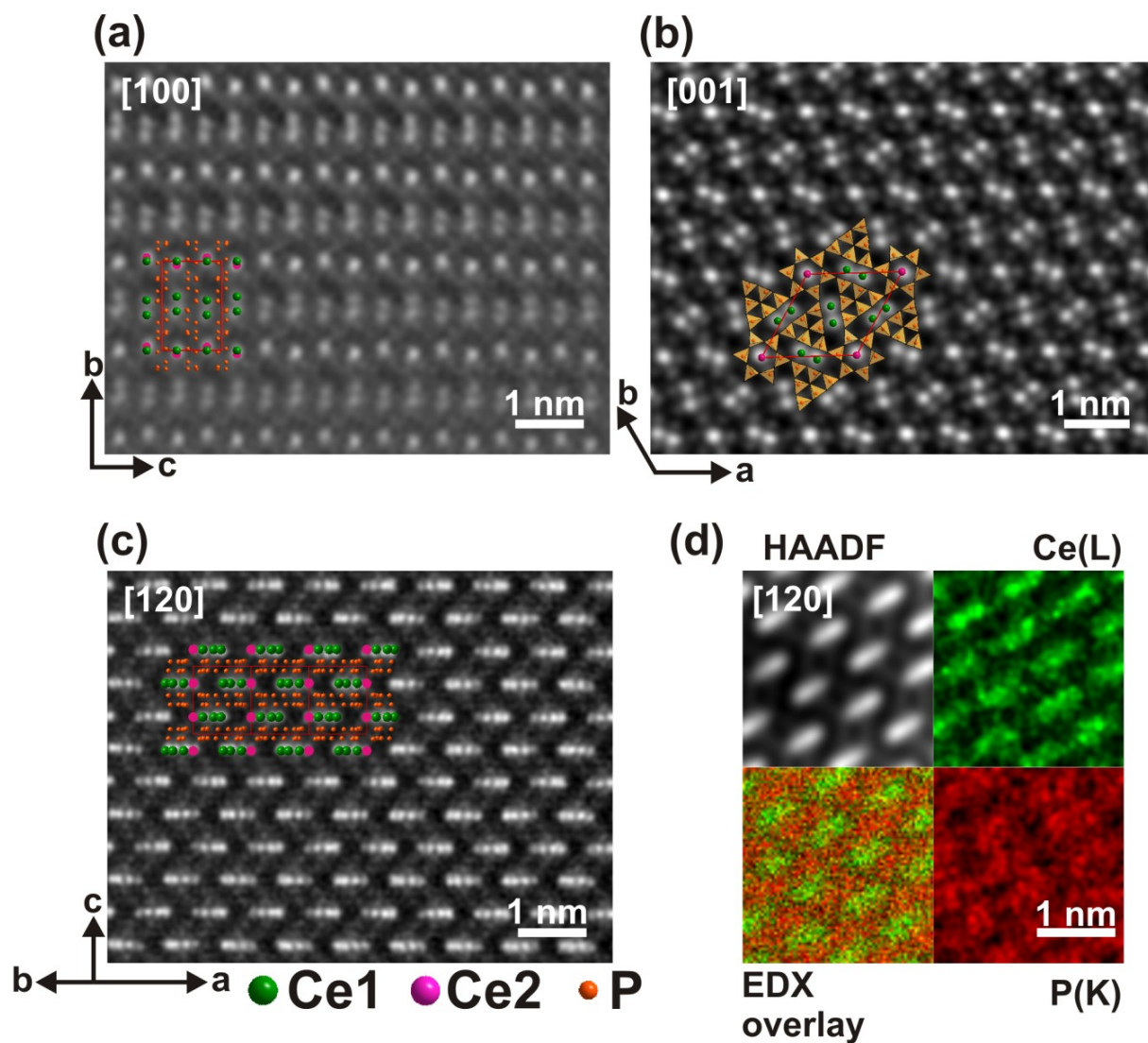


Figure S8. Fourier filtered STEM-HAADF images (a-c) including structure projection as overlay (P atoms in orange, Ce1 atoms in green, Ce2 atoms in light green) and drift corrected EDX mappings (d) both with atomic resolution viewed along zone axis [100], [001] and [120], bright contrasts correspond to Ce, darker ones to P.

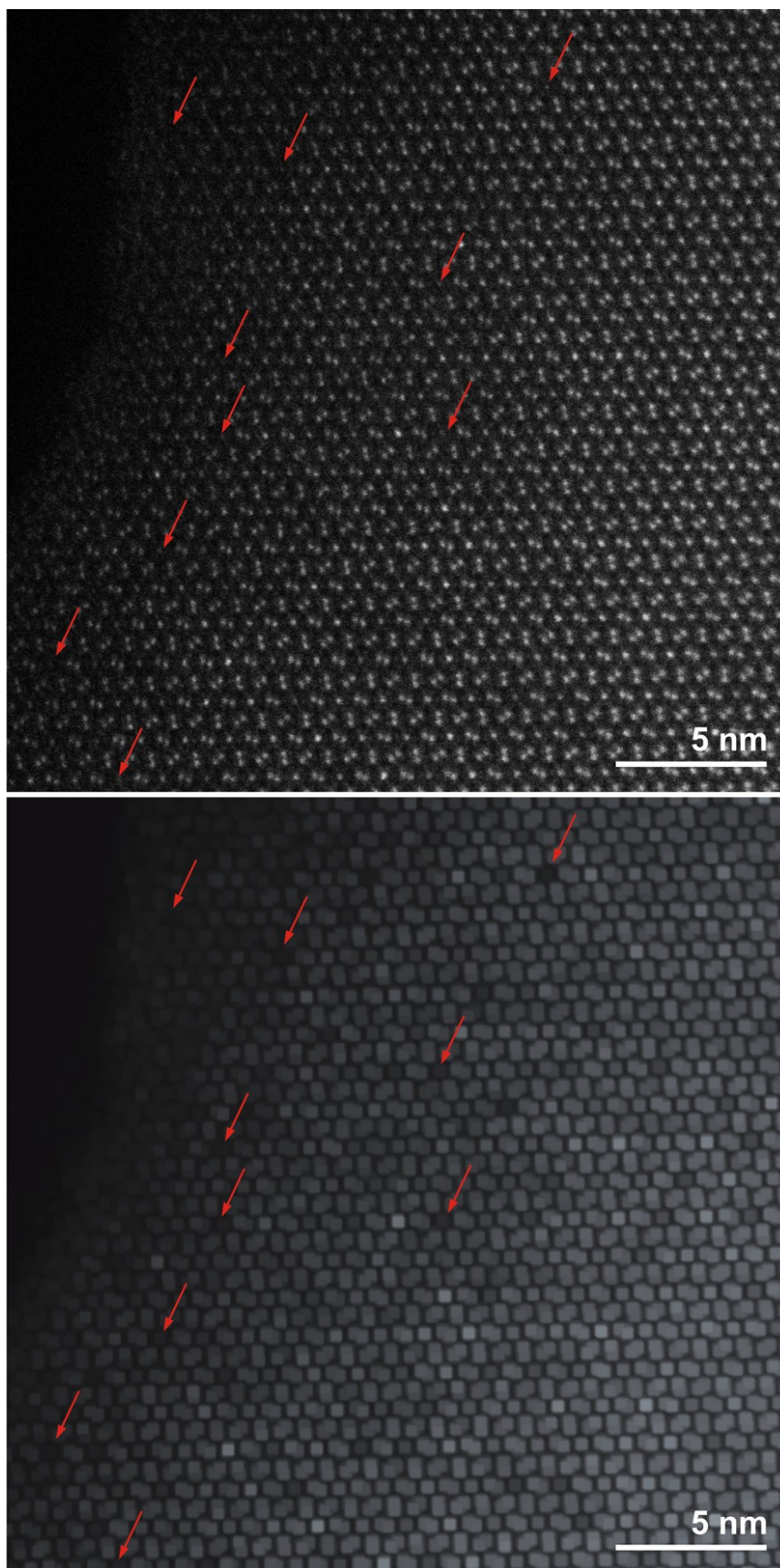


Figure S9. Top: Experimental unfiltered STEM-HAADF image along [001] showing Ce₂ atom columns with varying intensity (some marked by red arrows). Bottom: Same figure, visually enhanced by interpolating brightness over four pixels, followed by extrapolation of bright areas over nine pixels (with Photoshop).

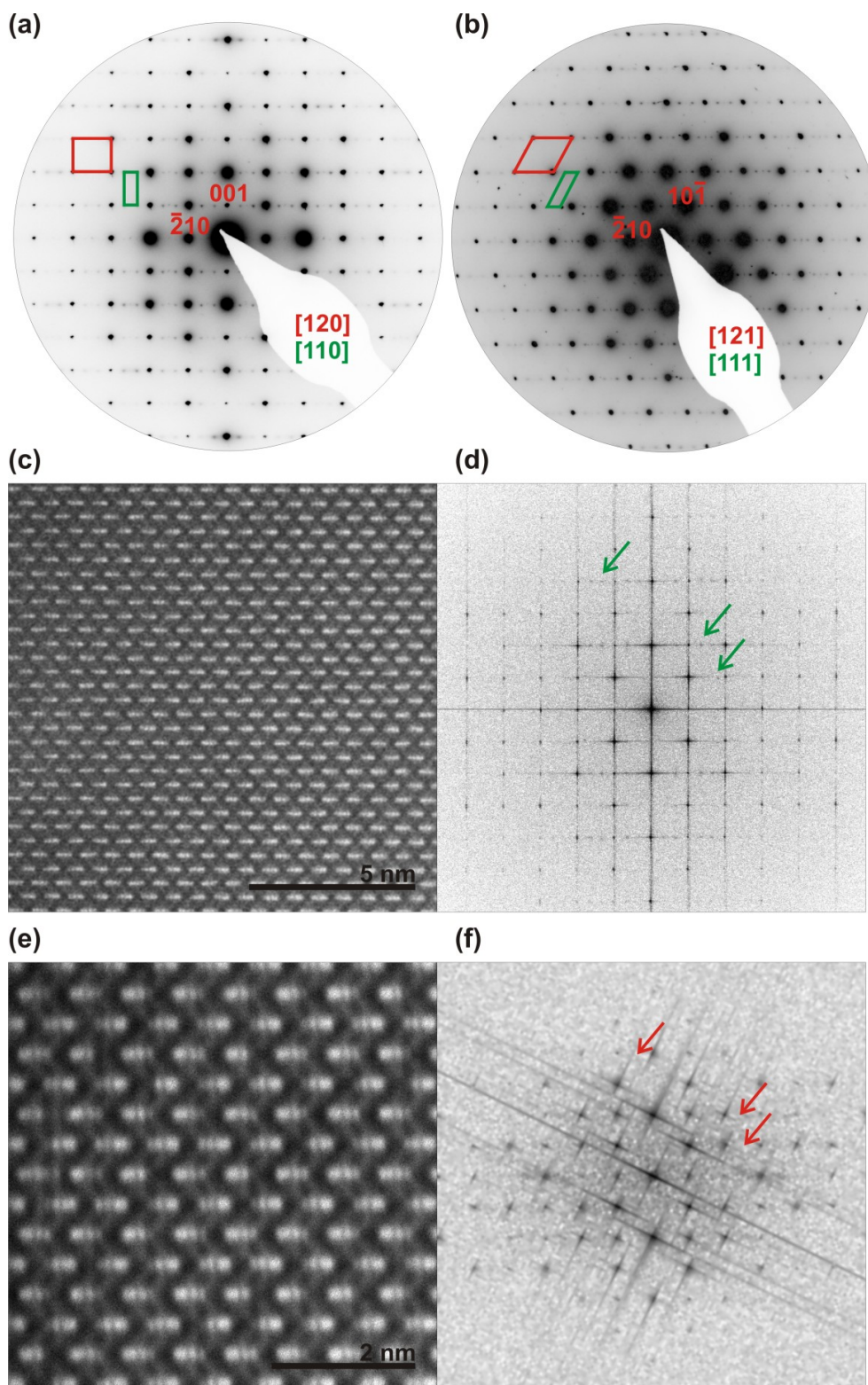


Figure S10. SAED patterns along [120] (a) and [121] (b) zone axis containing superstructure reflections, pattern indexed with the average structure model (red), supercell highlighted in green. Unfiltered STEM-HAADF image (c) along [120] with corresponding Fourier transform (d) showing superstructure reflections (green arrows) similar to those in SAED above based on different Ce2 positions. STEM-HAADF image (e) along [120] with corresponding Fourier transform (e) of a domain without superstructure, superstructure reflections are missing (red arrows) and no different Ce2 positions can be observed.

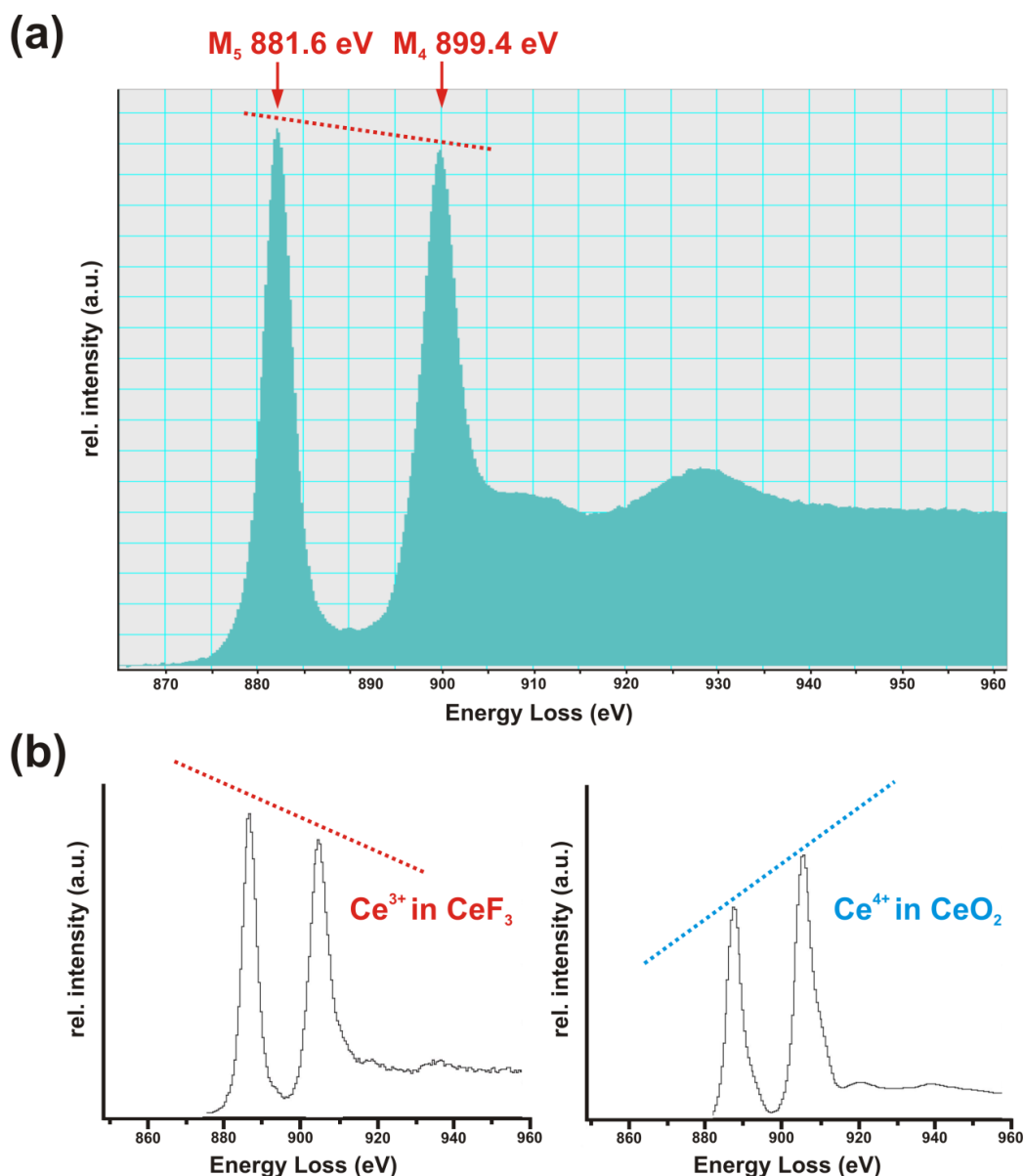


Figure S11. (a) EELS spectrum of $\text{Ce}_{4-0.5x}\text{Li}_3\text{P}_{18}\text{N}_{35-1.5x}\text{O}_{1.5x}$ ($x \approx 0.72$), red arrows represent positions of the Ce^{3+} - M_5 and Ce^{3+} - M_4 edges. (b) Reference EELS spectra of CeF_3 and CeO_2 from Arai et al.¹² Blue and red dotted lines illustrate different M_5/M_4 ratios in correspondence to Ce^{3+} and Ce^{4+} .

Off-axis EELS spectra do not suggest the presence of Ce^{4+} in $\text{Ce}_{4-0.5x}\text{Li}_3\text{P}_{18}\text{N}_{35-1.5x}\text{O}_{1.5x}$ (Figure S10). They show relative to the zero loss peak the Ce- M_5 and Ce- M_4 edges at 881.6 eV and 899.4 eV energy loss, respectively. These positions of the Ce signals are very close to typical values for Ce^{3+} (M_5 at 882.0 eV, M_4 at 899.7 eV) in $\text{Ce}_2\text{Zr}_2\text{O}_8$ or CeO_2 . The Ce^{4+} peaks occur at lightly increased energy loss. The M_5 to M_4 ratio is nearly one with the M_5 edge showing more intensity than the M_4 edge. This is in accordance with the higher M_5/M_4 ratio of Ce^{3+} compared to the lower M_5/M_4 ratio of Ce^{4+} known from the literature. The more asymmetrically shaped M_4 edge compared to the M_5 is also characteristic for Ce^{3+} .^{12,13,14}

Ce2 Displacement Measurement

Position deviation of the Ce2 atoms along [001] of 0.3(1) Å is the mean value of 10 directly measured distances from a representative STEM-HAADF micrograph (cf. Figure 10). In order to determine the maximum distance between two deflected Ce2 atoms (atoms A and C in Figure 10), in a first step the centers of gravity of the Ce2 atoms and a horizontal neutral axis perpendicular to [001] were defined. The distance of 0.3(1) Å is then the sum of the deviations of the centers of gravities of two Ce2 atoms (one above and one below) from the neutral axis in [001] direction.

Synchrotron Data

Supercell model refinement procedure

Data were integrated (see Experimental section) with the supercell parameters and absorption corrected with SADABS in Laue class 6/*m*.¹⁵ Two *hkl*-files were manually generated for the use with two scale factors; one *hkl*-file contained the average structure reflections and one contained the superstructure reflections ($-h+k = 3n$ are average structure reflections).

Initially, only the *z* coordinates of all Ce2 atoms within the supercell model were refined (with JANA2006)¹⁶ on the superstructure reflections, neglecting all symmetry restrictions (*P*1 symmetry). The other atom sites were kept fixed, which is feasible because the superstructure reflections carry information on the Ce2 distortion only and because the average structure is already well-established. The average structure scale factor was refined prior to including the satellite reflections and was kept constant for the following refinement steps since both scale factors were highly correlated. The scale factor of the superstructure reflections was set to the average structure scale factor and kept constant since it is to 100 % correlated to the Ce2 atom dislocation. The refinement converged in an *R*-value of ≈ 30 %. The refined Ce2 displacement of 0.1 Å corresponds to the minimal value since in this scenario the whole crystal would be modulated. The satellite reflection scale factor scales linearly with the displacement parameters; as the satellite reflection scale factor decreased to a fraction of the average structure scale factor the displacement gets larger (≈ 0.1 Å at same scale factor, ≈ 0.3 Å at one third of the average structure scale factor). Since the real superstructure reflection scale factor is unknown the accurate displacement cannot be determined.

A subsequent refinement was carried out in which all atoms were refined, but symmetry restrictions were applied. Those restrained the symmetry to *P*6₃/*m* for all non-Ce2 atoms and additional translational symmetry was added to treat the unit cell enlargement.

Reconstructed reciprocal lattice planes

The following reciprocal lattice planes are once shown as originally calculated (with linear intensity scaling) with the program Crystalis¹⁷ and once visually enhanced by conversion to gray-scale and optimization of the tonal correction with Adobe Photoshop.

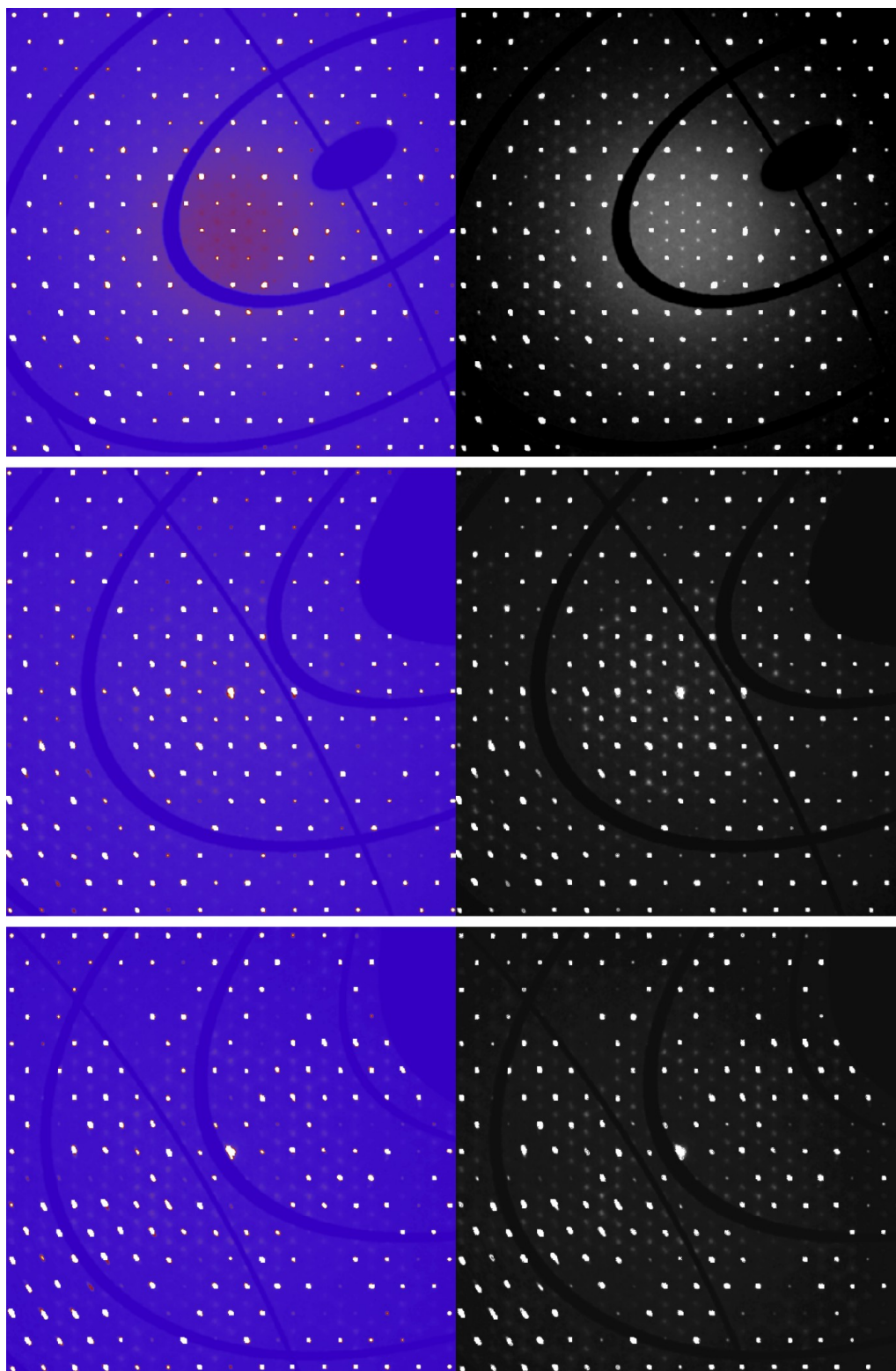


Figure S12. Top to bottom: hk_2 , hk_4 and hk_6 planes.

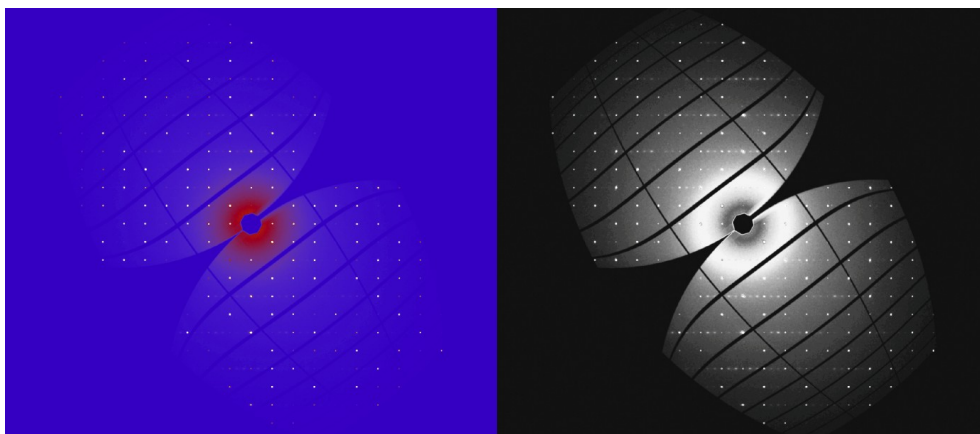


Figure S13. hhl plane. Visual enhancement (as stated above) reveals superstructure reflections for every lattice plane hkl with $l = 2n$, except for the $hk0$ plane.

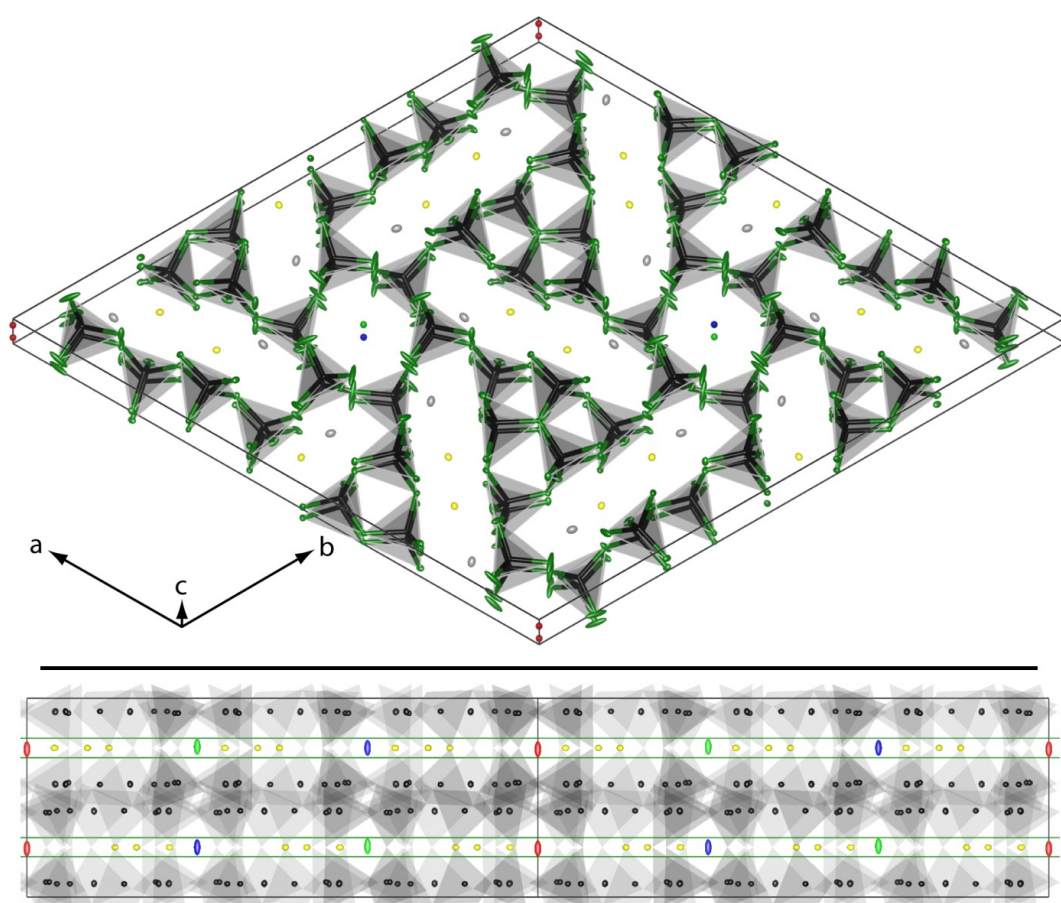


Figure S14. Results of the superstructure refinement: Ce2 atoms related by symmetry highlighted by the same color. Bottom: viewed along $\langle 110 \rangle$, Ce2 displacement is highlighted by green lines perpendicular $[001]$, N and Li atoms were not displayed for clarity.

Structure Description in (3+2)D superspace

Lattice, symmetry and modulation vectors

Since the superstructure refinement revealed $P6_3$ symmetry for the displaced Ce2 atoms, the superspace group $P6_3(\alpha, \beta, 0)0(-\alpha-\beta, \alpha, 0)0$ was chosen for the (3+2)D modulation description. The diffraction pattern was indexed based on the basic cell with two modulation vectors $q_1 = (1/3, 1/3, 0)$ and $q_2 = (-2/3, 1/3, 0)$ (Figure 11). The diffraction vector then is:

$$h = ha^* + kb^* + lc^* + mq_1 + nq_2$$

It is apparent that due to the commensurateness of the superstructure an unambiguous indexing is not possible as one satellite is shared by three basic structure reflections. This might be regarded as merohedry in 5D but does not impede structure refinement as the reflections were treated as overlapped.¹⁸ Hence, a set of three symmetry-equivalent modulation waves is obtained with directions q_1 , q_2 and the linear combination $q_1 + q_2$. Since the indexing is ambiguous, the maximum satellite order of the reflections $hklmn$ was set to $m = n = 1$. To retain the same satellite order for reflections of the symmetry equivalent direction $q_1 + q_2$, the order o is defined as

$$o = \frac{1}{2} (|m| + |n| + |n-m|)$$

Concluding from the superstructure refinement described above, a purely z-polarized modulation function $u^{\text{Ce2}}(x_4, x_5)$ is considered for the displacement of Ce2. Following Fourier's theorem, any wave-like function can be expanded in a basis of periodic sine and cosine functions.

$$u^{\text{Ce2}}(x_4, x_5) = \sum_m \sum_n [A_{mn} \cdot \sin(2\pi \cdot m \cdot x_4 + 2\pi \cdot n \cdot x_5) + B_{mn} \cdot \cos(2\pi \cdot m \cdot x_4 + 2\pi \cdot n \cdot x_5)]$$

Here, $x_4 = q \cdot r + t$ and $x_5 = q \cdot r + u$, in which r is the position of the Ce2 atom in unit cell $L = l_1x + l_2y + l_3z$ and phase shifts t and u denote the distance to physical space. Of the six amplitudes A_{10} , B_{10} , A_{01} , B_{01} , A_{11} , and B_{11} only two, e.g. A_{10} and B_{10} , have to be determined since the others are related by symmetry. The number of parameters to describe the commensurately modulated structure is two and therefore one less than in the supercell refinement.

Refinement

For the refinement in $P6_3(\alpha, \beta, 0)0(-\alpha-\beta, \alpha, 0)0$, the basic structure model was first transformed to $P6_3$. For all non-modulated atoms, however, the inversion center and mirror plane were manually reintroduced by setting local symmetry restrictions. All atomic positions and anisotropic displacement parameters were refined. The amplitudes A_{10} and B_{10} were refined to a significance of 0.004370(15) and 0.00223(3), respectively. The x_3 - x_4 and x_3 - x_5 F_{obs} Fourier maps are shown in

Figure S15. In this refinement, the scale factor of the average structure and the satellite reflection scale factor were assumed to be equal. Therefore, the resulting Ce2 displacement is the minimal value, as for the supercell refinement, since this assumes that the whole crystal is modulated. The site occupancy factors of Ce2 cannot be refined since they are also to 100 % correlated with the scale factor. From TEM EDX data (Table S10) we inferred that the superstructure domains contain very little oxygen that might just stem from surface hydrolysis. Hence, modulated domains with a fully occupied Ce2 are fathomable, in which local structure has sum formula $\text{Ce}_4\text{Li}_3\text{P}_{36}\text{N}_{70}$.

Superspace Symmetry Discussion

Both the supercell and superspace refinement yielded the same qualitative result and little uncertainty remains about the superstructure. However, in the superspace description, another interpretation of the modulation is possible, since the modulation vectors q_1 , q_2 , and q_1+q_2 are commensurate. In fact, the chosen Bravais class $P6/m(\alpha, \beta, 0)(-\alpha-\beta, \alpha, 0)$ does not contain the full symmetry of the observed lattice. Since $\alpha = \beta = 1/3$, the actual Bravais class should be $P6/mmm(\alpha, \alpha, 0)(-2\alpha, \alpha, 0)$. However, no incommensurate (3+2)D superspace group within this class is compatible with the superstructure.

The case that all components of the wave vectors in (3+2)D dimensions are commensurate can result in a (3+1)D modulation; for those special wave-vectors, *van Smaalen* derived additional commensurate (3+1)D Bravais-classes.¹⁹ Bravais-class $P6/mmm(1/3, 1/3, 0)$ fits the present problem and therefore the modulation could also be described in an adequate (3+1)D superspace group with $q = (1/3, 1/3, 0)$.

The commensurate (3+1)D superspace groups are not tabulated, but all space groups in 4D have been derived and are in principle accessible via the program CARAT (including 5D and 6D space groups).^{20–22} However, the deduction of (3+1)D spacegroups with the program is not straightforward so that we rather established it ourselves. Since the superstructure symmetry is known from previous analysis and a superspace group is determined by the arithmetic crystal class and translational components, one can formulate the commensurate (3+1)D superspace group $P6_3(1/3, 1/3, 0)0$ with non-lattice generator $(x_1-x_2, x_1, x_3+1/2, x_4)$. As can be verified by visual inspection of Figure 12 and S14, this superspace group describes the structure as well as the (3+2)D group. The (3+1)D group also resolves the indexing ambiguities since for satellite order $o = 1$, all reflections are then unique. The modulation is then described by one wave triplicated by space group symmetry.

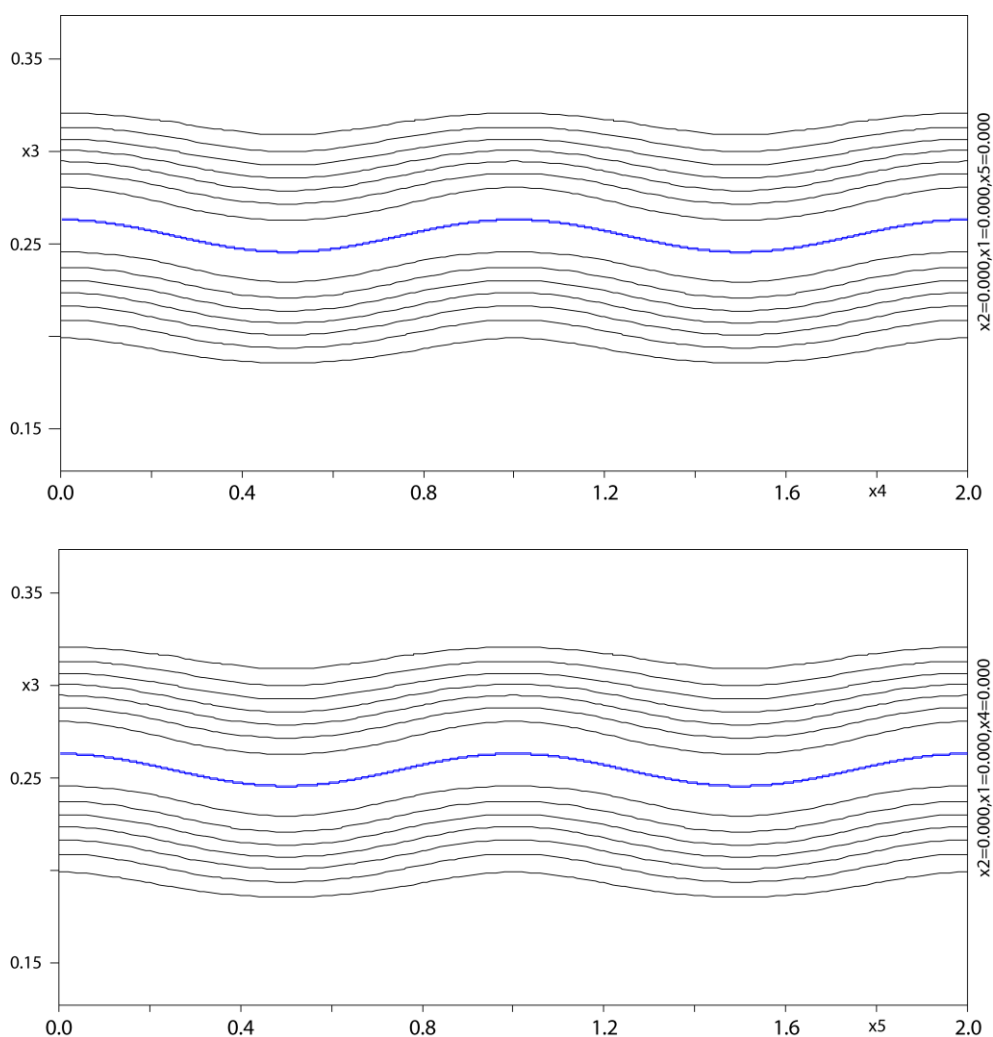


Figure S15. F_{obs} maps of the Ce2 position (blue line) in superspace. Top: x_3 vs. x_4 ; bottom: x_3 vs. x_5 map. Black lines indicate the electron density profile.

References

- 1 W. Klemm, G. Z. Winkelmann, *Anorg. Allg. Chem.* **1956**, 288, 87.
- 2 W. Schnick, J. Lücke, *Z. Anorg. Allg. Chem.* **1990**, 588, 19.
- 3 K. Landskron, H. Huppertz, J. Senker, W. Schnick, *Angew. Chem.* **2001**, 113, 2713; *Angew. Chem., Int. Ed.* **2001**, 40, 2643.
- 4 K. Köllisch, *Dissertation*, Ludwig-Maximilians-University, Munich, **2001**.
- 5 K. Momma, F. Izumi, *J. Appl. Crystallogr.* **2011**, 44, 1272.
- 6 V. A. Blatov, A. P. Shevchenko, D. M. Proserpio, *Cryst. Growth Des.* **2014**, 14, 3576.
- 7 O. Delgado-Friedrichs, *3dt*, <http://www.gavrog.org/>, **2013**.
- 8 N. W. Johnson, *Can. J. Math.* **1966**, 18, 169.
- 9 S. D. Klotz, W. Schnick, *Angew. Chem.* **2015**, 127, 11402; *Angew. Chem., Int. Ed.* **2015**, 54, 11250.
- 10 M. Somer, U. Herterich, J. Curda, K. Peters, H. G. von Schnering, *Z. Kristallogr.* **1994**, 209, 182.

- 11 S. D. Klotz, N. Weidmann, R. Niklaus, W. Schnick, *Inorg. Chem.* **2016**, 55, 9400.
- 12 S. Arai, S. Muto, J. Murai, T. Sasaki, Y. Ukyo, K. Kuroda, H. Saka, *Mater. Trans.* **2004**, 45, 2951.
- 13 L. A. J. Gravier, P. R. Buseck, *J. Phys. Chem. Solids* **1999**, 60, 1943.
- 14 A. M. D'Angelo, A. C. Y. Liu, A. L. Chaffee, *J. Phys. Chem. C* **2016**, 120, 14382.
- 15 Bruker AXS, Inc., SADABS, Madison, Wisconsin, USA, **2001**.
- 16 V. Petříček, M. Dušek, L. Palatinus, *Z. Kristallogr. – Cryst. Mater.* **2014**, 229, 345.
- 17 Agilent Technologies, *CrysAlis Pro*, Yarnton, Oxfordshire, England, **2011**.
- 18 L. Bindi, P. Bonazzi, M. Dušek, V. Petříček, G. Chapuis, *Acta Crystallogr., Sect. B: Struct. Sci.* **2001**, 57, 739.
- 19 S. Van Smaalen, *Acta Crystallogr., Sect. A: Found. Crystallogr.* **1987**, 43, 202.
- 20 W. Plesken, T. Schulz, *Exp. Math.* **2000**, 9, 407.
- 21 T. Janssen, A. Janner, E. Ascher, *Physica* **1969**, 42, 41.
- 22 G. Fast, T. Janssen, *J. Comput. Phys.* **1971**, 7, 1.

3.4 An unusual nitride network of aluminum-centered octahedra and phosphorus-centered tetrahedra and structure determination from microcrystalline samples

Lukas Neudert, Frank Heinke, Thomas Bräuniger, Florian J. Pucher, Gavin B. Vaughan, Oliver Oeckler and Wolfgang Schnick

Chem. Commun. **2017**, 53, 2709.

Reprinted with permission from *Chemical Communications*. Copyright 2017 RSC Publications.

Abstract

The new imidooxonitridophosphate $\text{AlP}_6\text{O}_{3x}(\text{NH})_{3-3x}\text{N}_9$ with $x \approx 0.33$ was synthesized under high-pressure high-temperature conditions. The crystal structure determination of the microcrystalline product involved a combination of electron microscopy, synchrotron X-ray diffraction and solid-state NMR. In the solid there are discrete AlN_6 octahedra that interconnect imidophosphate layers. The network topology is unprecedented but related to other nitride structures.

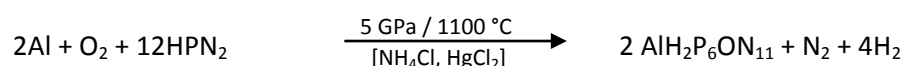
3.4.1 Introduction

Aluminum-containing nitrides are compounds of high interest¹ and even bulk or nanostructured AlN itself exhibits a variety of properties and applications: High electrical resistance and high thermal conductivity for thermal management, high toughness for armor material and structure-dependent electronic properties (band gap) for piezoelectric devices and nanoelectronic purposes.²⁻⁷ (Oxo-imido)nitridophosphates, which exhibit networks with a high degree of condensation, are discussed as high performance ceramics with good mechanical properties and high thermal and chemical stability. Recently discovered phosphorus nitrides are well suited to host lanthanide-based activator ions revealing strong luminescence.⁸⁻¹⁰ With regard to ion-exchange and ion-conductivity, nitridophosphates like $\text{Li}_{18}\text{P}_6\text{N}_{16}$, $\text{Li}_2\text{PO}_2\text{N}$, Li_7PN_4 represent candidates for energy storage materials.¹¹⁻¹³ The newly discovered layer-like $M\text{H}_4\text{P}_6\text{N}_{12}$ ($M = \text{Mg}, \text{Ca}$) may be a promising candidate for intercalation of metal ions and for exfoliation in order to obtain 2D nanomaterials.¹⁴ Subsequently, research for other robust nitrides with Al atoms as part of a network seems to be rewarding with respect to structure-property relations. Owing to the oxophilicity of aluminum, sixfold coordinated Al atoms have often been observed in oxides or hydrates. Thus, besides coordination compounds¹⁵ such as $\text{Al}(\text{EDA})_3 \cdot 3\text{BH}_4 \cdot \text{EDA}$ ¹⁶ only few crystal structures of nitrogen-containing compounds with sixfold coordinated aluminum have been elucidated so far in solid-state chemistry, e.g. those of $\text{Na}_3\text{AlP}_3\text{O}_9\text{N}$

(Fig. S1, ESI[†])^{17,18} and γ -ALON¹⁹ or $\text{Al}(\text{CN})_3$.²⁰ Shock-wave experiments that reach peak pressures between 15 and 43 GPa and temperatures around 1300 °C enabled the phase transition of AlN from the wurtzite to the rocksalt structure type,²¹⁻²⁴ with the latter containing AlN_6 octahedra stable at standard conditions. Tetrahedra-containing nitride networks show structural features similar to those of silicates. One can expect a broad structural diversity especially due to the presence of Al and P in one phase, because both elements are known for possible tetrahedral and octahedral coordination.²⁵ Yet, easily accessible methods for the synthesis of stable aluminum nitrides and related compounds such as oxonitrides or imido oxonitrides are lacking. This challenge has been overcome in terms of improving established high-pressure high-temperature synthesis at conditions up to 1500 °C and 15 GPa. Using reactive reactants like azides realizes a reductive N_2 atmosphere and enables routes to a wide range of metal containing nitrides.^{9,26-28} In favorable cases, addition of mineralizers like NH_4Cl also improves the growth of single crystals for structure determination. In the case of microcrystalline and possibly heterogeneous products, structure determination by powder X-ray diffraction or electron diffraction tomography may be an option, but it can be difficult and rather imprecise. In contrast, diffraction experiments with microfocused synchrotron X-ray radiation deliver accurate data of crystallites with volumes down to sub-micron size depending on chemical composition. Suitable microcrystals of new compounds can be discovered by transmission electron microscopy (TEM). Unit-cell dimension and chemical composition are accessible via selected area electron diffraction (SAED) and energy dispersive X-ray spectroscopy (EDX), respectively. Synchrotron X-ray data sets of these crystals can be obtained after re-locating them by X-ray fluorescence in combination with diffraction.^{29,30} This approach avoids the drawbacks of electron crystallography while exploiting its benefits. It is well suited for the investigation of small amounts of microcrystalline and possibly inhomogeneous samples obtained by high-pressure high-temperature synthesis and was successfully used to characterize the mixed network of $\text{AlP}_6\text{O}_{3x}(\text{NH})_{3-3x}\text{N}_9$ ($x \approx 0.33$), see Fig. 1.

3.4.2 Results and discussion

The compound was synthesized in a Walker-type multianvil press³¹ at 5 GPa and 1100 °C, starting from stoichiometric mixtures of amorphous HPN_2 ³² and Al powder (see paragraph S2, ESI[†]). NH_4Cl was added as mineralizer and HgCl_2 as activator for Al (formation of intermediate amalgams). The gray microcrystalline powder obtained is stable against air and moisture and contains micron- and submicron-sized crystallites (Fig. 1a-c). A tentative reaction equation may be written as:



The new imidooxonitridophosphate was identified by SAED (S3, ESI[†]) tilt series from selected microcrystals (Fig. 1d) which yielded a primitive monoclinic unit cell with $a = 4.7$, $b = 8.3$, $c = 10.6$ Å and $\beta = 101^\circ$. This corroborates the metrics determined by X-ray diffraction as seen by comparing SAED patterns with reciprocal lattice sections reconstructed from single-crystal X-ray diffraction data (see paragraph S4 and Fig. S8, ESI[†]). EDX spectra show no other elements than Al, P, O, N and confirmed the composition of $\text{AlH}_2\text{P}_6\text{ON}_{11}$ (Table S9, ESI[†]). In addition, electron energy-loss spectroscopy (EELS) on thin areas of crystallites also corroborates the presence of N as well as O (Fig. S10, ESI[†]).

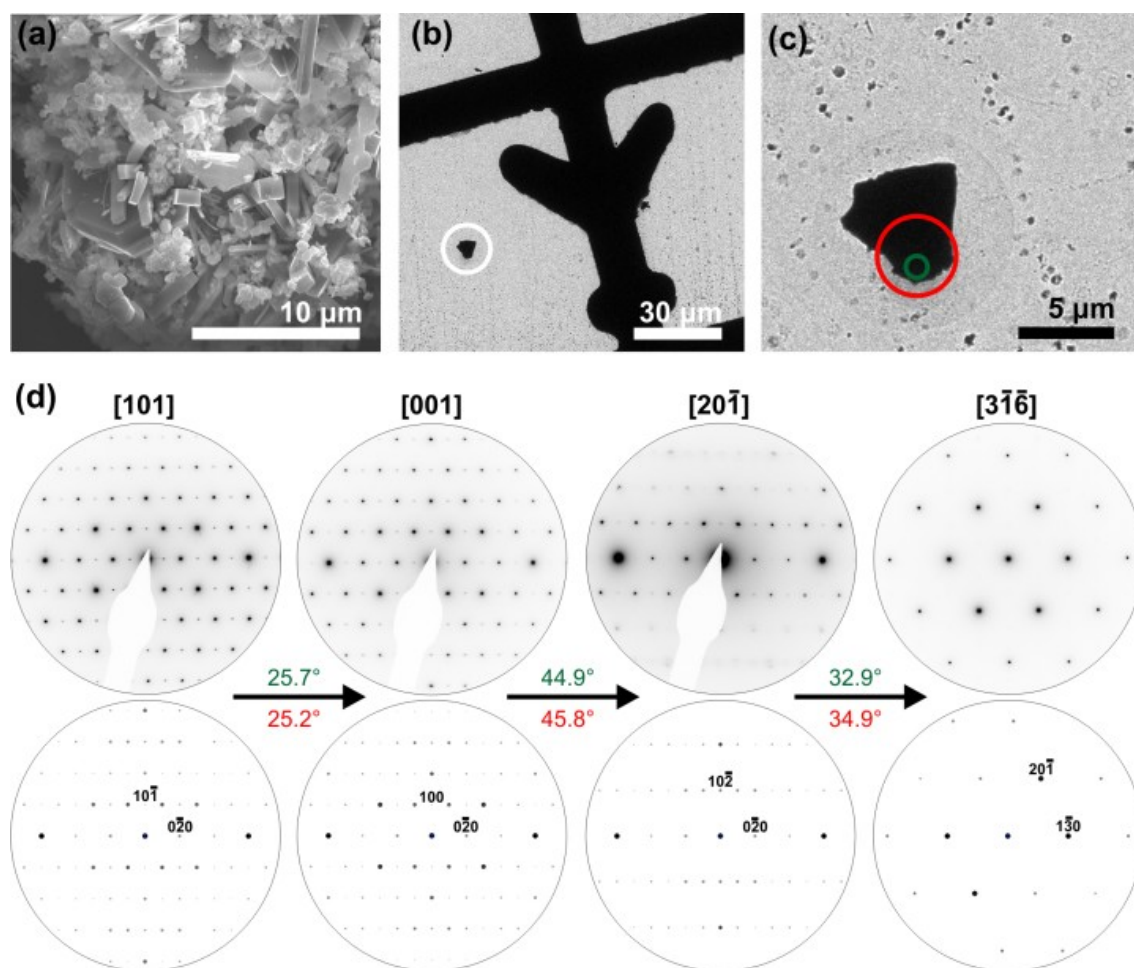


Fig. 1: SEM image (a) of microcrystals of $\text{AlP}_6\text{O}_{3x}(\text{NH})_{3-3x}\text{N}_9$ ($x \approx 0.33$) characterized by TEM (300 kV) and microfocused X-rays; (b) micro-crystal (marked by white circle) on a TEM finder grid; (c) area irradiated by SAED (green circle) and synchrotron radiation (red circle), (d) SAED tilt series with experimental patterns (top) and tilt angles (green) as well as simulated patterns and tilt angles (red) based on the refined structure model from X-ray data (bottom).

Attempts to determine the crystal structure from X-ray powder data did not yield an unequivocal structure model because of poor overall crystallinity, impurities, and reflection overlap of known (AlN and $\beta\text{-HPN}_2$)³² and further unknown byproducts.

However, after the structure had been elucidated (see below), Rietveld refinements confirmed that $\text{AlP}_6\text{O}_{3x}(\text{NH})_{3-3x}\text{N}_9$ is the main phase with a fraction of more than 90% (see Paragraph S5 Fig. S11 and Table S12, ESI[†]). High-temperature powder diffraction showed that $\text{AlP}_6\text{O}_{3x}(\text{NH})_{3-3x}\text{N}_9$ is stable up to 980 °C and decomposes into unidentified products at higher temperature (Fig. S13, ESI[†]).

The infrared spectrum (see paragraph S6 and Fig. S14, ESI[†]) shows strong absorption bands below 1500 cm^{-1} characteristic for imidonitridophosphate networks.^{33,34} The intense band at 434 cm^{-1} corresponds to Al—N bending vibrations, which is in good agreement with literature data for Al octahedrally coordinated by six N.²³ Additional significant absorption bands between 2600 - 3250 cm^{-1} can be attributed to N—H valence modes, that indicate presence of H in $\text{AlP}_6\text{O}_{3x}(\text{NH})_{3-3x}\text{N}_9$.^{14,35}

Further evidence for the presence of hydrogen in the structure comes from solid-state NMR spectroscopy (see paragraph S7, ESI[†]). The ^1H NMR spectrum (Fig. 2b) shows several components that are not completely resolved at 50 kHz MAS rate. The majority component at 7.2 ppm is most likely associated with NH_4^+ ions that may originate from the mineralizer NH_4Cl .^{14,36} The additional resonance at approximately 5 ppm probably originates from hydrogen in $\text{AlP}_6\text{O}_{3x}(\text{NH})_{3-3x}\text{N}_9$. More detailed information can be extracted from the ^{31}P NMR spectra shown in Fig. 2c. The chemical shifts of the two ^{31}P ($I=1/2$) resonance lines at 14.8 and -19.4 ppm are very similar to those observed in $\text{CaH}_4\text{P}_6\text{N}_{12}$.¹⁴ The number of ^{31}P resonances corroborates the pair-wise similarity of the four P atom sites in the structure model. The intensities of the two lines correspond to the multiplicities of the Wyckoff positions 4f and 2e. Part of the resonance at -19.4 ppm may, however, be due to the presence of $\beta\text{-HPN}_2$, as indicated by the superimposed spectrum in Fig. 2c (blue). In order to confirm the proximity of H to the P atoms in $\text{AlP}_6\text{O}_{3x}(\text{NH})_{3-3x}\text{N}_9$, magnetization was transferred from ^1H to ^{31}P in a cross-polarization (CP) experiment. As can be seen from Fig. 2c, both resonances are still present in the CP spectrum, which clearly shows the existence of hydrogen in the crystal structure. The resonance line of the central transition in the ^{27}Al (spin $I=5/2$) NMR spectrum (Fig. 2a) is broadened by quadrupolar interaction and centered around -7.7 ppm. Shifts in this range are typical for Al octahedrally coordinated by N,³⁷ which again is consistent with the structure model. Thus, in addition to rocksalt-type AlN ,²³ this compound is one of the rare examples where Al may actually be observed in such coordination in solid-state compounds.

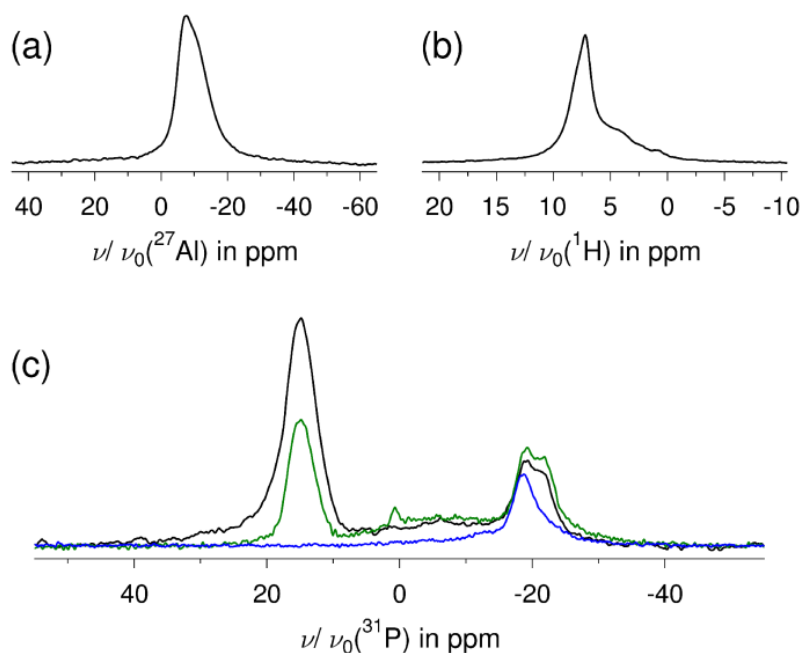


Fig. 2: Solid-state NMR spectra of $\text{AlP}_6\text{O}_{3x}(\text{NH})_{3-3x}\text{N}_9$ with $x \approx 0.33$ at 50 kHz MAS: (a) ^{27}Al , (b) ^1H and (c) ^{31}P - $\{^1\text{H}\}$ -cross-polarization spectrum (green line) superimposed with single-pulse excitation spectrum (black line) and the spectrum of $\beta\text{-HPN}_2$ (single-pulse excitation, blue line).

The synchrotron X-ray dataset (see paragraph S4, ESI[†]) of the pre-characterized crystal yielded a monoclinic crystal structure in space group $P2_1/m$ with lattice parameters $a = 4.7566(2)$, $b = 8.3266(3)$, $c = 10.6298(7)$ Å and $\beta = 101.601(4)^\circ$. Minor deviations from the lattice parameters from X-ray powder data (S3, Table S17, ESI[†]) may originate from chemical inhomogeneity of $\text{AlP}_6\text{O}_{3x}(\text{NH})_{3-3x}\text{N}_9$ with various values of x . All atoms except H were refined anisotropically, resulting in final residuals $R1(\text{obs}) = 0.0285$ and $wR2(\text{all}) = 0.0735$. The crystallographic data are summarized in the Supporting Information (Tables S15 - S17, ESI[†]). Further details on the structure analysis can be obtained from the Fachinformationszentrum Karlsruhe, 76344 Eggenstein-Leopoldshafen, Germany (fax: +49-7247-808-666; e-Mail: crysdata@fiz-karlsruhe.de) on quoting the depository number CSD-431557.

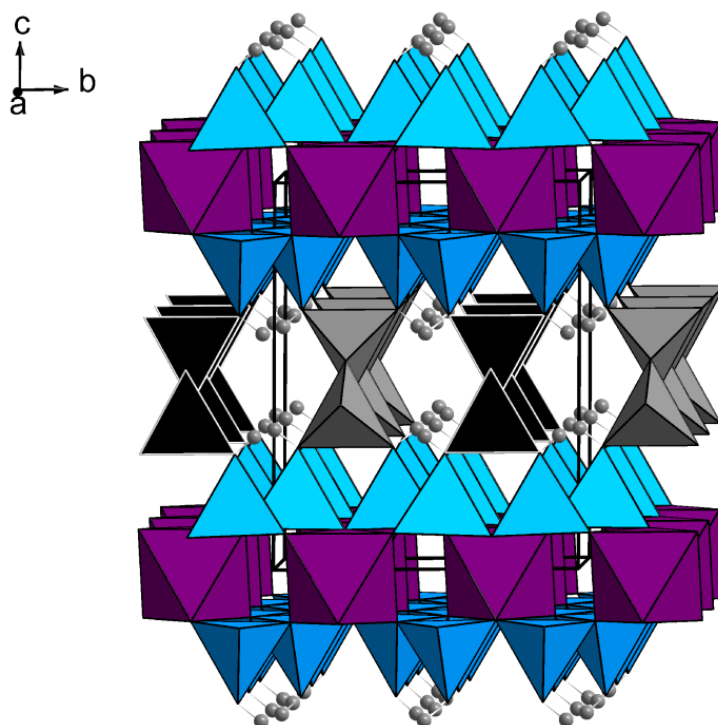


Fig. 3: Crystal structure of $\text{AlP}_6\text{O}_{3x}(\text{NH})_{3-3x}\text{N}_9$ with $x \approx 0.33$, view approximately along $[100]$, AlN_6 octahedra (violet), differently orientated $\text{P}(\text{N}/\text{N},\text{O})_4$ tetrahedra (gray and black, blue and light blue) and H atoms in gray.

The crystal structure of $\text{AlP}_6\text{O}_{3x}(\text{NH})_{3-3x}\text{N}_9$ (Fig. 3) is characterized by a stacking of imidoxonitridophosphate building blocks that extend parallel to (001) . These are built up from all-side vertex-sharing Q^4 -type $\text{P}(\text{N}/\text{O})_4$ tetrahedra and interconnected by slightly distorted AlN_6 octahedra (Fig. 4 left, there is only one Wyckoff site for Al) with a shorter axial Al-N bonds (2.033(2) - 2.047(2) Å) and longer equatorial Al-N bonds (2.105(2) - 2.107(2) Å). These are in good agreement with Al atoms coordinated by six N atoms in solids like $\text{Al}[\text{CN}]_3$ ²⁰ or NaCl-type AlN .²³ The driving force for the formation of unusual octahedrally coordinated Al atoms is most likely the high pressure applied during synthesis.³⁸ P-N bond lengths (Table S18, ESI†; 1.603(3) - 1.659(2) Å) correspond to typical bond lengths in (oxo)nitridophosphates.³⁹⁻⁴²

With regard to *Liebau*'s nomenclature,⁴³ the tetrahedra in the imidoxonitridophosphate layers form *sechser* rings oriented parallel to (001) , which are interconnected by zig-zag chains forming *dreier* rings (Fig. 4, right). Thus, these blocks between the AlN_6 octahedra formally correspond to an AB_2 structure formed by interconnected tetrahedra with A corresponding to P and N,NH,O corresponding to B. Ignoring Al atoms, the degree of condensation is $\kappa = n(\text{P}):n(\text{N}/\text{O}) = 0.5$. However, this substructure does not extend into a 3D framework. So far, this was considered typical for compounds with sterically demanding cations, e.g. hexagonal $\text{BaAl}_2\text{Si}_2\text{O}_8$ (hexacelsian), where Ba^{+2} ions are situated between *sechser* ring double layers of $(\text{Al}/\text{Si})\text{O}_4$ tetrahedra.^{44,45} Since Al^{3+} is rather small (53.5 pm),⁴⁶ ion size is, however, probably not a crucial factor in the present case.

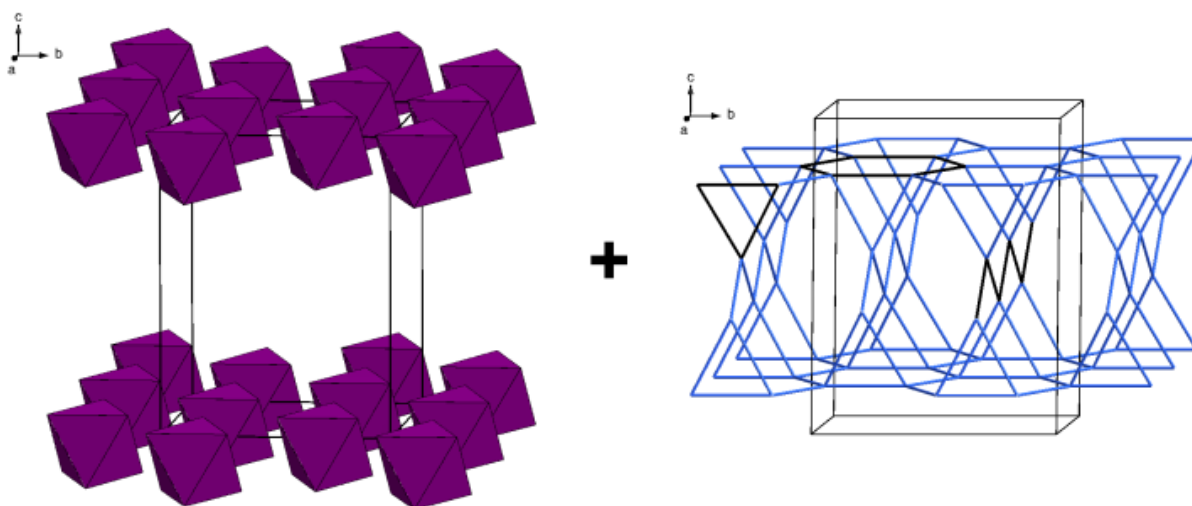


Fig. 4: Left: AlN_6 octahedra in $\text{AIP}_6\text{O}_{3x}(\text{NH})_{3-3x}\text{N}_9$, right: network topology, each line represents a P-N-P bond, zig-zag chains, *dreier* and *sechser* rings, according to nomenclature introduced by Liebau,⁴³ highlighted in black, unit cells outlined (both images with viewing direction along $\approx[100]$).

Due to similar X-ray scattering factors of O and N, bond valence sum calculations were used to assign trivalent N and divalent O or NH positions.⁴⁷ In conclusion, the anion positions of the *sechser* rings are occupied exclusively by N. Considering possible hydrogen bonds, every second position connecting these rings to the tetrahedra chains was assumed to be a NH group, whereas the positions within the tetrahedra chains in the middle of the building blocks have a mixed occupancy of N and O. This is in accordance with structure refinements based on X-ray data.

$\text{AIP}_6\text{O}_{3x}(\text{NH})_{3-3x}\text{N}_9$ is structurally related to the imidonitridophosphate $\text{CaH}_4\text{P}_6\text{N}_{12}$, which crystallizes in space group *Cmce*. Both structures exhibit the same point symbol^{14,48} $\{3.6^5\}$ because of an equal number of *dreier* and *sechser* rings and an equal linking in their networks. However, the network topologies are different, as are the unit-cell dimensions and space groups. The crystal structures of $\text{CaH}_4\text{P}_6\text{N}_{12}$ and $\text{AIP}_6\text{O}_{3x}(\text{NH})_{3-3x}\text{N}_9$ contain different arrangements of similar (yet not identical) structure motifs of six $\text{P}(\text{N},\text{O})_4$ tetrahedra as represented in Fig. 5a and Fig. 5b. Although both motifs exhibit the point symmetry *m* and the structures look quite similar at first glance, direct structural (e.g. group-subgroup) relations between the two compounds are not present due to differently orientated tetrahedra. The *sechser* ring layers in $\text{AIP}_6\text{O}_{3x}(\text{NH})_{3-3x}\text{N}_9$ (Fig. 5c and Fig. 5d, blue tetrahedra) and the interconnecting zig-zag tetrahedra chains (gray and black tetrahedra in Fig. 5c and Fig. 5d) within a building block of imidoxonitridophosphate layers between the Al^{3+} ions point in opposite directions (orientations represented by color variations in Fig. 5). This is different from the mutual orientation of the imidonitridophosphate layers and the zig-zag chains in $\text{CaH}_4\text{P}_6\text{N}_{12}$ (Fig. 5c), where both features point in the same direction within a building block between the Ca^{2+} ions.¹⁴

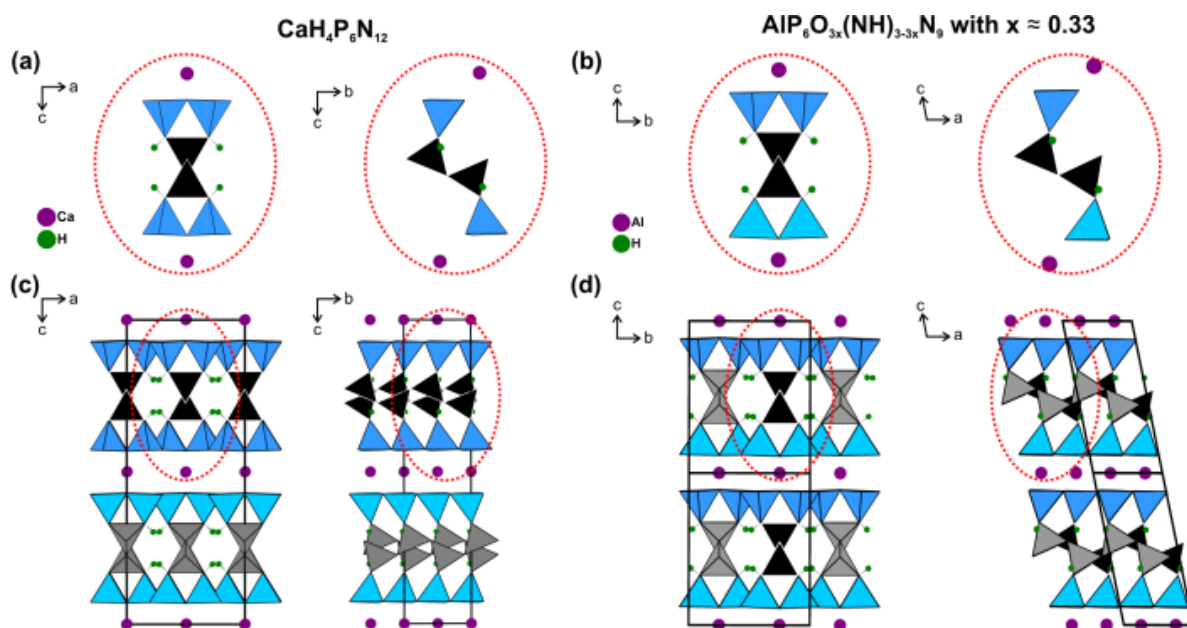


Fig. 5: Structure motifs of six tetrahedra of orthorhombic $\text{CaH}_4\text{P}_6\text{N}_{12}$ (a) and monoclinic $\text{AlP}_6\text{O}_{3x}(\text{NH})_{3-3x}\text{N}_9$ with $x \approx 0.33$ (b) present in the two different crystal structures (c and d); differently oriented tetrahedra chains (gray and black) and differently orientated tetrahedra in layers (blue and light blue) highlighted.

The orientation of the entire building blocks in $\text{CaH}_4\text{P}_6\text{N}_{12}$ alternate along [001], whereas the zig-zag chains (along [010]) between the *sechser* ring layers alternate within each building block in $\text{AlP}_6\text{O}_{3x}(\text{NH})_{3-3x}\text{N}_9$. The main similarity between both structures is the presence of imido(oxo)nitrido-phosphate building blocks with the same number of various ring sizes between the layers of octahedrally coordinated metal ions.

3.4.3 Conclusion

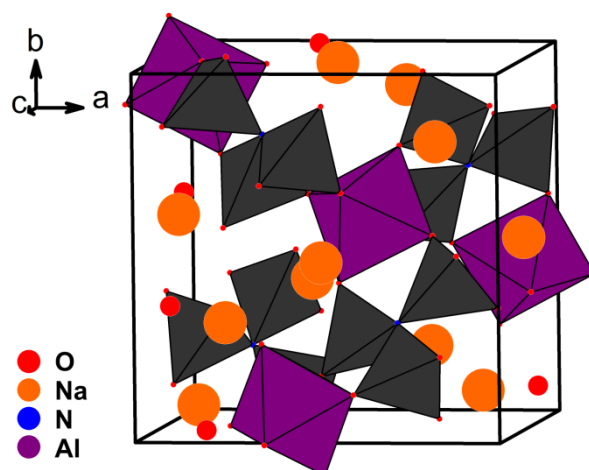
In conclusion, high-temperature and high-pressure conditions during synthesis appear to be essential in order to realize AlN_6 octahedra in stable compounds. Compared to rock salt type AlN ,²³ in this work less extreme conditions were sufficient to obtain AlN_6 octahedra in a imido(oxo)nitridophosphate network. With simultaneous presence of Al and P in one phase the light metal prefers octahedral coordination in contrast to P, which is tetrahedrally coordinated by N. Similarities and differences between the structures of $\text{AlP}_6\text{O}_{3x}(\text{NH})_{3-3x}\text{N}_9$ and $\text{CaH}_4\text{P}_6\text{N}_{12}$, respectively, become obvious by focusing on slightly different structure motifs. Both networks are built up from related structural motifs in different arrangements, pointing to possible rigid structures of imido(oxo)nitridophosphates. The characterization of $\text{AlP}_6\text{O}_{3x}(\text{NH})_{3-3x}\text{N}_9$ bridges the gap between imidonitridophosphates and oxonitridophosphates and can initiate a discussion about additional properties like high thermal stability, hardness, luminescence or optoelectronic properties and their structural requirements.

3.4.4 References

- 1 R. J. Xie, H. T. Hintzen, *J. Am. Ceram. Soc.* **2013**, *96*, 665.
- 2 G. A. Sack, R. A. Tanzilli, R. O. Pohl, J. W. Vandersande, *J. Phys. Chem. Solids.* **1987**, *48*, 641.
- 3 P. Boch, J. C. Glandus, J. Jarrige, J. P. Lecompte, J. Mexmain, *Ceram. Int.* **1982**, *8*, 34.
- 4 T. Koppe, H. Hofsäss, U. Vetter, *J. Lumin.* **2016**, *178*, 267.
- 5 H. M. Lee, K. Bharathi, D. K. Kim, *Adv. Eng. Mater.* **2014**, *16*, 655.
- 6 D. de Faoite, D. J. Browne, F. R. Chang-Díaz, K. T. Stanton, *J. Mater Sci.* **2012**, *47*, 4211.
- 7 K. Yong, S. F. Yu, *J. Mater Sci.* **2012**, *47*, 5341.
- 8 A. Marchuk, S. Wendl, N. Imamovic, F. Tambornino, D. Wiechert, P. J. Schmidt, W. Schnick, *Chem. Mater.* **2015**, *27*, 6432.
- 9 A. Marchuk, P. Schultz, C. Hoch, O. Oeckler, W. Schnick, *Inorg. Chem.* **2016**, *55*, 974.
- 10 F. J. Pucher, A. Marchuk, P. J. Schmidt, D. Wiechert, W. Schnick, *Chem. Eur. J.* **2015**, *21*, 6443.
- 11 M. Debbischi, S. Lebégue, *Phys. Rev. B* **2015**, *92*, 085127.
- 12 W. Schnick, J. Luecke, *Solid State Ionics* **1990**, *38*, 271.
- 13 K. Senevirathne, C. S. Day, M. D. Gross, A. Lachgar, N. A. W. Holzwarth, *Solid State Ionics* **2013**, *233*, 95.
- 14 A. Marchuk, V. Celinski, J. Schmedt auf der Günne, W. Schnick, *Chem. Eur. J.* **2015**, *21*, 5836.
- 15 R. A. Yokel, *Coordin. Chem. Rev.* **2002**, *228*, 97.
- 16 Q. Gu, Z. Wang, Y. Filinchuk, J. A. Kimpton, H. E. A. Brand, Q. Li, X. Yu, *J. Phys. Chem. C* **2016**, *120*, 10192.
- 17 J. Ronis, B. Y. Bondars, A. A. Vitola, T. Miller, *Latv. Kim. Z.* **1993**, *1*, 662.
- 18 R. Conanec, P. L'Haridon, W. Feldmann, R. Marchand, Y. Laurent, *Eur. J. Solid State Inorg. Chem.* **1994**, *31*, 13.
- 19 B. Tu, H. Wang, X. Liu, W. Wang, Z. Fu, *J. Am. Ceram. Soc.* **2013**, *96*, 1937.
- 20 D. Williams, B. Pleune, K. Leinenweber, J. Kouvetakis, *J. Solid State Chem.*, **2001**, *159*, 244.
- 21 K. Kondo, A. Sawaoka, K. Sato, M. Ando, *AIP Conf. Proc.* **1982**, *78*, 325.
- 22 K. Keller, T. Schlothauer, M. Schwarz, G. Heide, E. Kroke, *High Pressure Res.* **2012**, *32*, 23.
- 23 K. Keller, E. Brendler, S. Schmerler, C. Röder, G. Heide, J. Kortus, E. Kroke, *J. Phys. Chem. C* **2015**, *119*, 12581.
- 24 N. E. Christensen, I. Gorczyca, *Phys. Rev. B* **1994**, *50*, 4397.
- 25 P. Kroll, W. Schnick, *Chem. Eur. J.* **2002**, *8*, 3530.
- 26 T. G. Müller, F. Karau, W. Schnick, F. Kraus, *Angew. Chem.* **2014**, *126*, 13913 *Angew. Int. Ed.* **2014**, *53*, 13695.
- 27 N. Hirosaki, T. Takeda, S. Funahashi, R.-J. Xie, *Chem. Mater.* **2014**, *26*, 4280.
- 28 F. J. Pucher, A. Marchuk, P. J. Schmidt, D. Wiechert, W. Schnick, *Chem. Eur. J.* **2015**, *21*, 6443.
- 29 F. Fahrnbauer, T. Rosenthal, T. Schmutzler, G. Wagner, G. B. M. Vaughan, J. P. Wright, O. Oeckler, *Angew. Chem.* **2015**, *127*, 10158; *Angew. Chem. Int. Ed.*, **2015**, *54*, 10020.
- 30 F. Heinke, R. Meyer, G. Wagner, O. Oeckler, *Z. Anorg. Allg. Chem.* **2015**, *641*, 192.
- 31 H. Huppertz, *Z. Kristallogr.* **2004**, *219*, 330.

- 32 W. Schnick, J. Lücke, *Z. Anorg. Allg. Chem.* **1992**, 610, 121.
- 33 S. J. Sedlmaier, M. Eberspächer, W. Schnick, *Z. Anorg. Allg. Chem.* **2010**, 637, 362.
- 34 F. Karau, O. Oeckler, F. Schäfers, R. Niewa, W. Schnick, *Z. Anorg. Allg. Chem.* **2007**, 633, 1333.
- 35 K. Landskron, H. Huppertz, J. Senker, W. Schnick, *Z. Anorg. Allg. Chem.* **2002**, 628, 1465.
- 36 F. Taulelle, T. Loiseau, J. Maquet, J. Livage, G. Ferey, *J. Solid State Chem.* **1993**, 105, 191.
- 37 T. Bräuniger, M. Jansen, *Z. Anorg. Allg. Chem.* **2013**, 639, 857.
- 38 A. Neuhaus, E. Hinze, *Berich. Bunsen Gesell.* **1966**, 70, 1073.
- 39 L. Boukbir, R. Marchand, Y. Laurent, P. Bacher, G. Roult, *Ann. Chim.* **1989**, 14, 475.
- 40 W. Schnick, U. Berger, *Angew. Chem. Int. Ed. Engl.* **1991**, 30, 830.
- 41 F. W. Karau, W. Schnick, *J. Solid State Chem.* **2005**, 178, 135.
- 42 K. Landskron, W. Schnick, *J. Solid State Chem.* **2001**, 156, 390.
- 43 F. Liebau, *Structural Chemistry of Silicates: Structure, Bonding and Classification*; Springer, Berlin, Germany, **1985**.
- 44 Y. Takeuchi, *Mineral. J.* **1958**, 2, 311.
- 45 A. A. Kashaev, *Dokl. Akad. Nauk. SSSR* **1966**, 169, 201.
- 46 R. D. Shannon, *Acta. Crystallogr. Sect. A* **1976**, 32, 751.
- 47 A. S. Wills, *Valist, version 4.0.7*, University College London, UK, **2010**.
- 48 V. A. Blatov, A. P. Shevchenko, D. M. Prosperio, *Cryst. Growth Des.* **2014**, 14, 3576.

3.4.5 Supporting Information



S1: Crystal structure of cubic $\text{Na}_3\text{AlP}_3\text{O}_9\text{N}$, $\text{P}(\text{O},\text{N})_4$ tetrahedra in gray and AlO_6 octahedra highlighted in violet.^{1,2}

S2: Synthesis of $\text{AlP}_6\text{O}_{3x}(\text{NH})_{3-3x}\text{N}_9$ ($x \approx 0.33$)

Al powder (7.3 mg, 0.27 mmol, Grüssing, 99.99% metal content), amorphous HPN_2 (97.2 mg, 1.62 mmol, synthesized according to Lücke, ref. 3), HgCl_2 (0.7 mg, 1 mol% in relation to Al; as activator, i.e. for the amalgamation of Al) and NH_4Cl (1.0 mg, 1 mol% in relation to Al; as mineralizer) were ground in a ball mill (Specamill GS06000 with agate capsule and agate balls, Specac) with 2 balls (3x 3min). Oxygen impurities in starting materials could not be excluded completely. The mixture was tightly packed in a crucible of hexagonal boron nitride (Henze, Kempten) and closed with a cap of the same material. The reaction was carried out in a Walker-type multianvil assembly as described in ref. 4 and 5. The material was compressed to 5 GPa at room temperature and then heated to 1100 °C in 30 minutes. This temperature was held for 60 minutes and then cooled down in 120 minutes. After slow decompression (12 h), $\text{AlP}_6\text{O}_{3x}(\text{NH})_{3-3x}\text{N}_9$ ($x \approx 0.33$) was obtained as a microcrystalline gray powder, stable against air and moisture.

S3: Electron Microscopy

Scanning electron microscopy (SEM) was done with a Jeol JSM 6500F (Jeol, Germany) equipped with energy dispersive X-ray (EDX) detector (model 7418, Oxford Instruments, Great Britain). The sample was fixed on electrically conductive tabs (G3347, Plano GmbH, Germany). For transmission electron microscopy (TEM), microcrystals of $\text{AlP}_6\text{O}_{3x}(\text{NH})_{3-3x}\text{N}_9$ were ground in absolute ethanol and drop-cast on copper finder grids with a continuous carbon film (S160NH2, Plano GmbH, Germany) before transferring them into the TEM on a double-tilt holder. A Jeol 2010 (Jeol, Germany) with a LaB_6 emitter operated at 200 kV acceleration voltage combined with a TEM Cam F216 camera (TVIPS, Germany, resolution 2k x 2k) and an EDAX Apollo XLT EDX detector (EDAX, Germany) was used for

preliminary studies. In addition, a Titan 80-300 (FEI, USA) with a field emitter operated at 300 kV or 120 kV acceleration voltage combined with an UltraScan 1000 Camera (Gatan, USA, resolution 2k x 2k) and a TEM TOPS 30 EDX spectrometer (Gatan, Germany) was used. Electron energy loss spectroscopy (EELS) was done on the Titan 80-300 in STEM mode at 300 kV acceleration voltage with a post-column filter (GIF Tridiem 893, Gatan, Germany). For EELS measurements, the sample was plasma-cleaned for 20 s. The product is moderately electron-beam sensitive at acceleration voltages of 120-300 kV. For the evaluation of the TEM data, the following software was used: Digital Micrograph (EELS spectra), ProcessDiffraction7 (geometric calculations for selected area electron diffraction, SAED) and JEMS (SAED simulations), ES Vision and EDAX TEAM (EDX spectra).⁶⁻¹⁰

S4: Synchrotron Measurements and Crystal Structure Analysis

All single-crystal experiments were done at beamlineID11 of the ESRF (Grenoble, France) at a wavelength of 0.3351 Å (Si(111) double-crystal monochromator). The TEM grid containing the precharacterized microcrystals was fixed on a glass fiber on a goniometer head. The alignment of the crystal in the focused X-ray beam (ca. 4 x 6 µm) was done by an optical telescope, followed by more accurate centering via collecting single diffraction patterns while slightly shifting the sample. The data was recorded using a Frelon2k CCD detector and indexed as well as integrated with Crystals.¹¹ Parasitic scattering from Cu TEM grid was discarded. Further correction of the incident-angle-dependent detector absorption¹² and scaling as well as semi-empirical absorption correction was done.¹³ Further details on the structure analysis can be obtained from the Fachinformationszentrum Karlsruhe, 76344 Eggenstein-Leopoldshafen, Germany (fax: +49-7247-808-666; e-Mail: crysdata@fiz-karlsruhe.de) on quoting the depository number CSD-431557.

S5: Powder X-Ray Diffraction

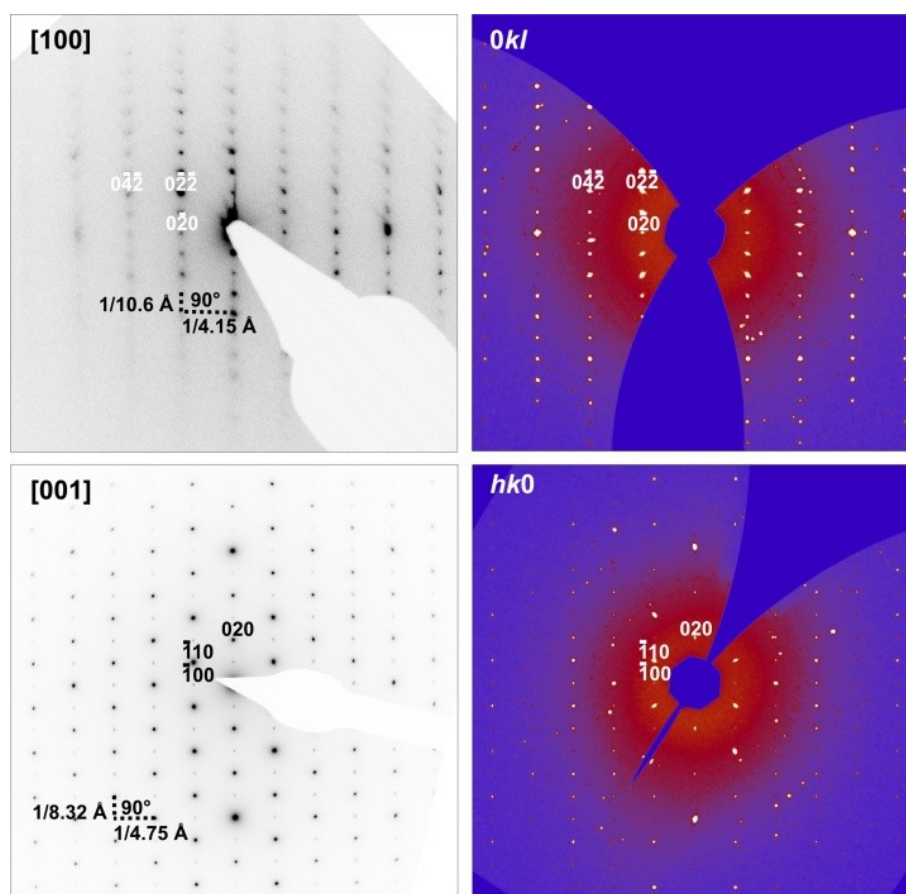
Powder diffraction patterns (samples filled in 0.3 mm in diameter glass capillaries under Ar; for temperature dependant measurements quartz glass capillaries of 0.3 mm in diameter were used) were collected at room temperature with a StoeStadiP (Cu K_{α1} radiation, modified Debye-Scherrer geometry, Ge(111) monochromator) and a Mythen 1K silicon stripe detector. Temperature dependant powder diffraction patterns were collected with a StoeStadiP (Mo K_{α1} radiation, modified Debye-Scherrer geometry, Ge(111) monochromator) and a Mythen 1K silicon stripe detector in 20 K steps to a maximum of 1000 °C. Data were collected at constant temperature. Rietveld refinements were done with TopasAcademic¹⁴ employing the fundamental parameters approach^{13,15} and using spherical harmonics of fourth order for modeling preferred orientation.¹⁶

S6: FTIR spectroscopy

The FTIR spectra of $\text{AlP}_6\text{O}_{3x}(\text{NH})_{3-3x}\text{N}_9$ ($x \approx 0.33$) were recorded with a Perkin-Elmer Spectrum BX II spectrometer using KBr pellets. The FTIR spectrum shows weak and broad absorption bands in the range from $3250 - 2600 \text{ cm}^{-1}$ corresponding to N-H valence modes. The strong absorption bands between 1500 and 800 cm^{-1} are characteristic for (imidooxo)nitridophosphate networks.¹⁷⁻²⁰

S7: Solid-state nuclear magnetic resonance (NMR) spectroscopy

Solid-state NMR spectra were acquired on a BrukerAvance-III spectrometer with an 11.7 T magnet, operating at a ^1H frequency of 500.25 MHz, using a commercial 1.3 mm double-resonance MAS probe. For all measurements, the ^1H resonance of 1% $\text{Si}(\text{CH}_3)_4$ in CDCl_3 was used as an external secondary reference.



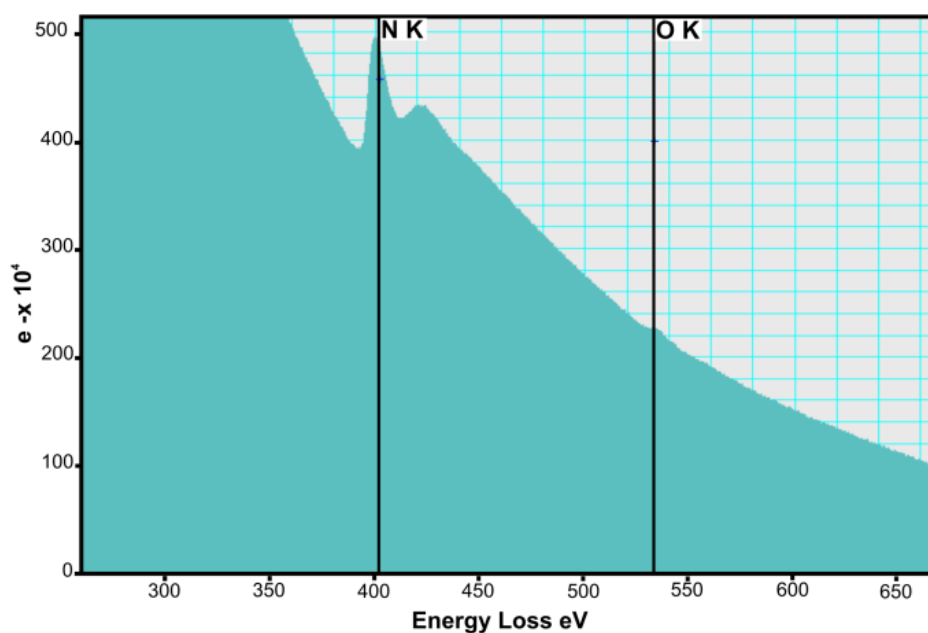
S8: SAED patterns (300 kV) from different crystallites (left, including directly measured unit cell parameters) compared to reciprocal lattice sections reconstructed from single crystal X-ray diffraction data (right).

The comparison between reciprocal lattice sections reconstructed from single-crystal X-ray diffraction data and SAED patterns in accordance to the monoclinic metrics. Neither in SAED patterns (S10, left) nor in the reciprocal lattice sections (S10, right) there is additional intensity between

reflections along [001]. This would be expected for an enlargement of the unit cell regarding the related compounds $MH_4P_6N_{12}$ with $M = Ca, Mg$.

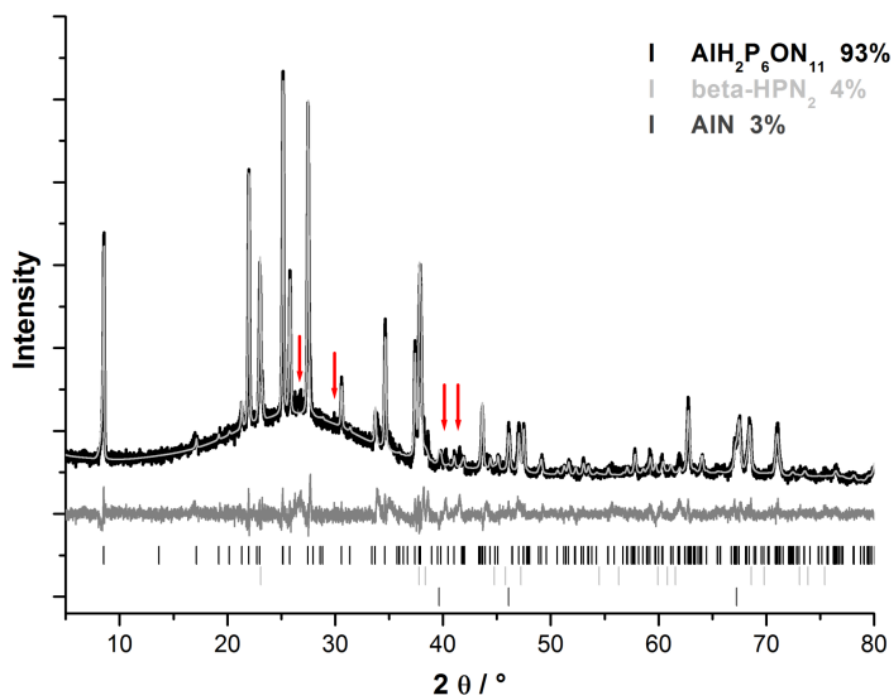
S9: TEM EDX measurements (300 kV) of $AlP_6O_{3x}(NH)_{3-3x}N_9$ in atom% (standard deviation).

	Al (K)	P (K)	N (K)	O (K)
K1	5.7	29.2	60.2	4.8
K2	6.0	32.8	58.3	2.9
K3	6.5	34.6	56.2	2.7
K4	5.6	30.7	56.9	6.8
K5	5.4	34.1	57.9	2.5
K6	6.4	34.7	56.6	2.3
K7	6.2	33.0	53.7	7.2
K8	6.0	35.2	52.5	5.7
K9	6.2	34.6	53.0	6.2
mean value	6.1(4)	33.2(20)	56.1(26)	4.6(20)
ideal value	5.3	31.6	57.9	5.3



S10: EELS spectrum (300 kV) of $AlP_6O_{3x}(NH)_{3-3x}N_9$, black lines represent positions of N-K and O-K edges.

The EELS spectrum shows the N-K edge at 401 eV energy loss as well as the O-K edge at 532 eV energy loss. The ratio of N:O based on EELS measurements is with 9:1 close to the ratio of 11:1 for $AlP_6O_{3x}(NH)_{3-3x}N_9$.

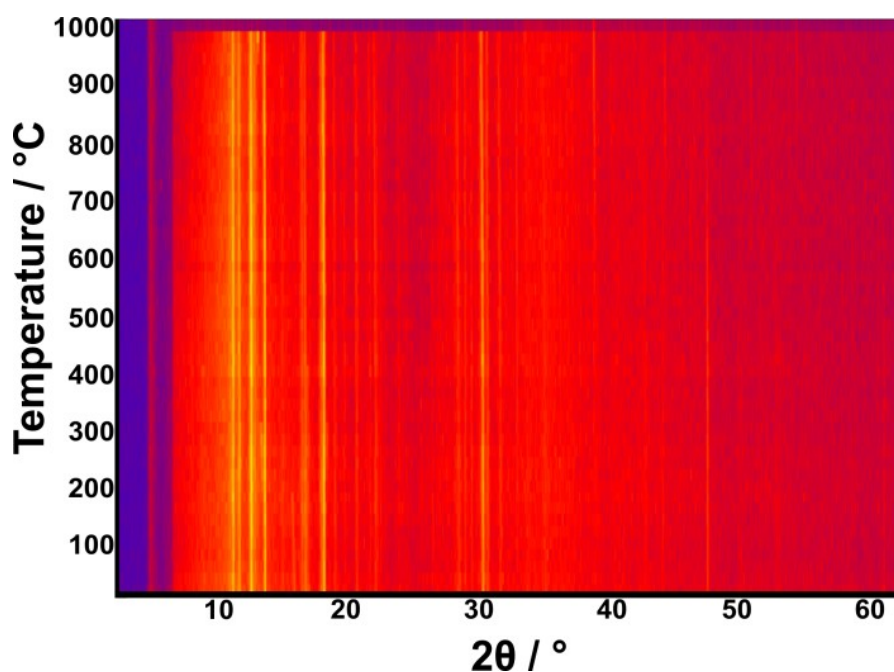


S11: Rietveld refinement of $\text{AlP}_6\text{O}_{3x}(\text{NH})_{3-3x}\text{N}_9$, observed (thick black line) and calculated (thin light gray line) powder diffraction patterns as well as difference plot (dark gray line) and positions of Bragg reflections (black: $\text{AlP}_6\text{O}_{3x}(\text{NH})_{3-3x}\text{N}_9$, light gray: $\beta\text{-HPN}_2$, dark grey: AlN).

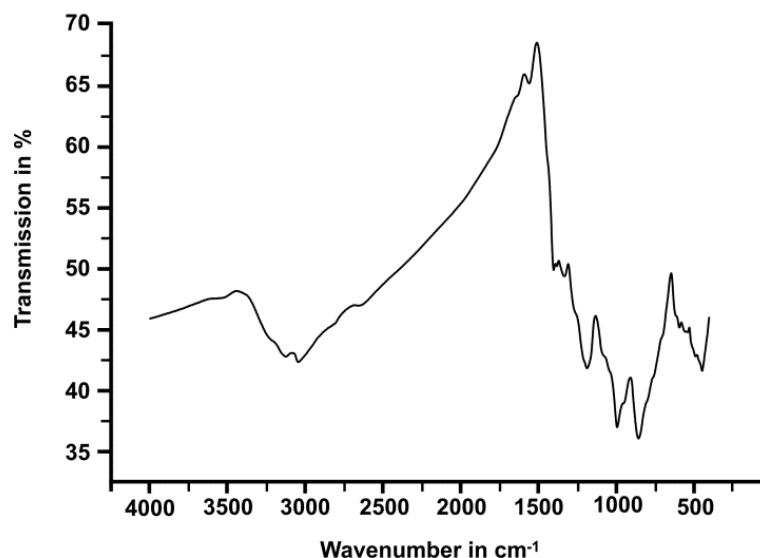
Additional unexplained reflections (red arrows in Fig. S11) belong to an unknown side phase. The structure determination of that side phase was not possible because no matching crystals for the combination of TEM and microfocused synchrotron diffraction could be found. The lattice parameters of $\text{AlP}_6\text{O}_{3x}(\text{NH})_{3-3x}\text{N}_9$ obtained by the Rietveld refinement show a small deviation (volume difference of 0.9 %) from those obtained by single-crystal measurements. This is probably caused by chemical variations in $\text{AlP}_6\text{O}_{3x}(\text{NH})_{3-3x}\text{N}_9$, represented by x .

S12: Crystallographic data of Rietveld refinement of $\text{AlP}_6\text{O}_{3x}(\text{NH})_{3-3x}\text{N}_9$ with $x \approx 0.33$ and with standard deviation in parentheses.

	$\text{AlH}_2\text{P}_6\text{ON}_{11}$	beta-HPN ₂	AlN
molar weight (in g/mol)	384.892	33.116	40.988
space group (no.)	$P2_1/m$ (11)	$I\bar{4}2d$ (122)	$Fm\bar{3}m$ (225)
unit cell parameters	$a = 4.7416(2)$	$a = 4.749(5)$	$a = 3.9373(4)$
(in Å / °)	$b = 8.3250(3)$ $c = 10.623(6)$ $\beta = 102.88(1)$	$c = 6.55(1)$	
cell volume (in Å ³)	408.79(4)	147.9(4)	61.03(2)
x-ray density (in g/cm ³)	3.1271(3)	2.694(7)	4.461(1)
absorption μ (in mm ⁻¹)	13.611(1)	11.48(3)	15.748(5)
number of reflections	277	17	3
spherical harmonics	4	0	0
R_{Bragg}	0.0348	0.0391	0.0667
independent parameters		53	
background parameters		18	
R_p / R_{wp}		0.0601 / 0.0797	
GooF		1.570	



S13: Temperature-dependant X-ray powder diffraction pattern of $\text{AlP}_6\text{O}_{3x}(\text{NH})_{3-3x}\text{N}_9$.



S14: FTIR spectrum of $\text{AlP}_6\text{O}_{3x}(\text{NH})_{3-3x}\text{N}_9$.

S15: Crystallographic data and details of the structure refinement of $\text{AlP}_6\text{O}_{3x}(\text{NH})_{3-3x}\text{N}_9$ with $x \approx 0.33$ and with standard deviation in parentheses.

formula	$\text{AlP}_6\text{O}(\text{NH})_2\text{N}_9$
molar weight (in g/mol)	384.892
crystal system / space group (no.)	monoclinic / $P2_1/m$ (no. 11)
lattice parameters (in Å, °)	$a = 4.7566(2)$, $b = 8.3266(3)$, $c = 10.6298(7)$, $\beta = 101.601(4)$
cell volume (in Å ³)	412.41(4)
density (in g·cm ⁻³)	3.100
formula units per unit cell	2
F(000)	380
θ range (in °)	$2.061 \leq \theta \leq 13.846$
wavelength (in Å)	0.3351
total no. of reflections / independent reflections	1285 / 1103
refined parameters / restraints	105 / 0
R-values(all data)	$R1 = 0.0351$, $wR2 = 0.0735$
R-values ($F^2 > 2\sigma(F^2)$)	$R1 = 0.0285$, $wR2 = 0.0702$
goodness of fit	1.046
absorption coefficient (in mm ⁻¹)	0.196
weight	$w = 1/[\sigma^2(F_o^2) + (0.0205P)^2 + 0.1217P]^*$
$\Delta\rho_{\text{max}}$, $\Delta\rho_{\text{min}}$ (in e Å ⁻³)	+0.63, -0.51

* $P = [2F_c^2 + \text{Max}(F_o^2, 0)]/3$

3.4 An unusual nitride network of aluminum-centered octahedra and phosphorus-centered tetrahedra and structure determination from microcrystalline samples

S16: Atom coordinates and equivalent isotropic displacement parameters (in Å²) of AlP₆O_{3x}(NH)_{3-3x}N₉ with standard deviation in parentheses.

atom	Wyckoff site	x	y	z	U_{eq}	s. o. f.
P1	4f	0.16554(8)	0.08551(4)	0.32927(5)	0.00890(12)	1
P2	4f	0.33412(8)	0.08486(4)	0.67156(5)	0.00893(12)	1
P3	2e	0.10774(12)	1/4	0.08409(7)	0.01196(14)	1
P4	2e	0.53473(12)	1/4	0.91759(7)	0.01218(15)	1
Al5	2e	0.75102(12)	1/4	0.50031(7)	0.00978(16)	1
N1/O1	2e	0.4273(4)	1/4	0.0511(2)	0.0218(5)	0.48(3)/0.52(3)
N2/O2	2e	0.8816(4)	1/4	0.9501(2)	0.0225(5)	0.52(3)/0.48(3)
N3	4f	0.0177(3)	0.57434(15)	0.37888(16)	0.0098(3)	1
N4	4f	0.5186(3)	0.07479(15)	0.37899(16)	0.0100(3)	1
N5	4f	0.0718(3)	0.09399(16)	0.17310(17)	0.0119(3)	1
N6	4f	0.5837(3)	0.59393(16)	0.17146(17)	0.0126(3)	1
N7	2e	0.0518(4)	1/4	0.3889(2)	0.0093(3)	1
N8	2e	0.4556(4)	1/4	0.6163(2)	0.0094(4)	1
H5	4f	0.02(2)	0.029(15)	0.129(15)	0.11(3)*	0.5
H6	4f	0.60(2)	0.517(17)	0.126(14)	0.11(3)*	0.5

* For both H atoms the same displacement parameter was used.

S17: Anisotropic displacement parameters (in Å²) of AlP₆O_{3x}(NH)_{3-3x}N₉ with standard deviation in parentheses.

Atom	U_{11}	U_{22}	U_{33}	U_{12}	U_{13}	U_{23}
P1	0.00643(18)	0.00652(19)	0.0141(3)	-0.00008(13)	0.00287(14)	-0.00016(11)
P2	0.00664(19)	0.00627(19)	0.0142(3)	0.00001(13)	0.00288(14)	-0.00004(11)
P3	0.0097(2)	0.0133(3)	0.0132(3)	0	0.00299(19)	0
P4	0.0102(2)	0.0123(3)	0.0139(3)	0	0.0021(2)	0
Al5	0.0083(3)	0.0089(3)	0.0128(4)	0	0.0036(3)	0
N1/O1	0.0118(8)	0.0343(12)	0.0200(13)	0	0.0049(7)	0
N2/O2	0.0125(8)	0.0361(12)	0.0189(13)	0	0.0031(7)	0
N3	0.0071(5)	0.0079(5)	0.0146(8)	-0.0011(5)	0.0023(5)	0.0002(4)
N4	0.0072(5)	0.0075(5)	0.0152(8)	-0.0010(5)	0.0023(5)	0.0003(4)
N5	0.0122(6)	0.0098(6)	0.0137(8)	-0.0002(5)	0.0026(5)	-0.0010(4)
N6	0.0149(6)	0.0103(6)	0.0122(8)	0.0000(5)	0.0016(5)	0.0020(5)
N7	0.0078(7)	0.0069(7)	0.0137(11)	0	0.0036(6)	0
N8	0.0080(7)	0.0071(7)	0.0134(11)	0	0.0033(6)	0

S18: Bond lengths in $\text{AlP}_6\text{O}_{3x}(\text{NH})_{3-3x}\text{N}_9$ with standard deviation in parentheses.

bond	length (in Å)	bond	length (in Å)
P1-N3	1.6413(14)	P3-N5	1.6361(15)
P1-N4	1.6585(15)	P4-N1/O1	1.6022(24)
P1-N5	1.6315(18)	P4-N2/O2	1.6164(21)
P1-N7	1.6454(11)	P4-N6	1.6394(16)
P2-N3	1.6535(15)	Al5-N3	2.1050(15)
P2-N4	1.6426(14)	Al5-N4	2.1071(15)
P2-N6	1.6373(18)	Al5-N7	2.0329(20)
P2-N8	1.6453(11)	Al5-N8	2.0470(20)
P3-N1/O1	1.6273(19)	N5-H5	0.73(14)
P3-N2/O2	1.6030(25)	N6-H6	0.81(15)

Taking only X-ray data into account, the assignment of light-atom sites in $\text{AlP}_6\text{O}_{3x}(\text{NH})_{3-3x}\text{N}_9$ is not unequivocal. Miscellaneous refinements with small differences in the occupancy of the light atoms yielded various models of the occupancy of H, N and O sites in the zig-zag tetrahedra chains but showed not significant differences in their figures of merit (*R*-values, GooF, interatomic distances, residual electron density). H positions are assigned to residual electron density and NMR investigations, N-H bond lengths refined. Bond-valence sum calculations²¹ were considered and the final model yielded suitable values for all cations (difference of P^{5+} and $\text{Al}^{3+} < 7\%$) and helped with the assignment of N vs. O/NH on the anion sites. The result is that Al is surrounded only by N atoms (N3, N4, N7, N8; difference $< 5\%$). Both N-H groups and N/O mixed occupied sites are located in the zig-zag chains because the N1/N2 BVS values for only N on this sites were too small (up to 11%) and the corresponding O1/O2 values for only O were too high (up to 24%). In the final refinement, the compositely occupied positions N1/O1 and N2/O2 showed the same ratio of O and N.

References

- 1 J. Ronis, B. Y. Bondars, A. A. Vitola, T. Miller, *Latv. Kim. Z.* **1993**, *1*, 662.
- 2 R. Conanec, P. L'Haridon, W. Feldmann, R. Marchand, Y. Laurent, *Eur. J. Solid State Inorg. Chem.* **1994**, *31*, 13.
- 3 W. Schnick, J. Lücke, *Z. Anorg. Allg. Chem.* **1992**, *610*, 121.
- 4 a) N. Kawai, S. Endo, *Rev. Sci. Instrum.* **1970**, *41*, 1178; b) D. Walker, M. A. Carpenter, C. M. Hitch, *Am. Mineral*, **1990**, *75*, 1020; c) D. Walker, *Am. Mineral.* **1991**, *76*, 1092; d) D. C. Rubie, *Phase Transitions* **1999**, *68*, 431; e) H. Huppertz, *Z. Kristallogr.* **2004**, *219*, 330.
- 5 A. Marchuk, L. Neudert, O. Oeckler, W. Schnick, *Eur. J. Inorg. Chem.* **2014**, *21*, 3427.

- 6 Digital Micrograph, version 3.6.1, Gatan Software Team, USA, **1999**.
- 7 J. L. Lábár, *Ultramicroscopy*, **2005**, 103, 237.
- 8 P. A. Stadelmann, *JEMS*, version 3.3425, CIME-EPFL, Switzerland, **2008**.
- 9 ES Vision, version 4.0.164, Emispec Systems Inc., USA, **2002**.
- 10 TEAM, version 3.4.1, EDAX AMETEK, Wiesbaden, Germany, **2013**.
- 11 CrysAlisPro 1.171.38.41, Rigaku Oxford Diffraction, Great Britain, **2015**.
- 12 G. Wu, B. L. Rodrigues, P. Coppens, *J. Appl. Crystallogr.* **2002**, 35, 356.
- 13 J. Bergmann, R. Kleeberg, A. Haase, B. Breidenstein, *Mater. Sci. Forum* **2000**, 347-349, 303.
- 14 A. Coelho, Topas-Academic, 4.1, Coelho Software, Australia **2007**.
- 15 R. W. Cheary, A. Coelho, J. P. Cline, *J. Res. Natl. Inst. Stand. Technol.* **2004**, 109, 1.
- 16 J. M. Jarvinen, *J. Appl. Crystallogr.* **1993**, 26, 525.
- 17 S. J. Sedlmaier, M. Eberspächer, W. Schnick, *Z. Anorg. Allg. Chem.* **2010**, 637, 362.
- 18 F. Karau, O. Oeckler, F. Schäfers, R. Niewa, W. Schnick, *Z. Anorg. Allg. Chem.* **2007**, 633, 1333.
- 19 K. Landskron, H. Huppertz, J. Senker, W. Schnick, *Z. Anorg. Allg. Chem.* **2001**, 628, 1465.
- 20 A. Marchuk, V. Celinski, J. Schmedt auf der Günne, W. Schnick, *Chem. Eur. J.* **2015**, 21, 5836.
- 21 A. S. Wills, *VaList*, version 4.0.7, University College London, UK, **2010**.

4 Structure-property relations of tin and indium containing tellurides

4.1 Overview

Tellurides are an important class of materials because of their high suitability for daily applications. Since tellurides have been discovered as phase change materials, as possible superconductors and as thermoelectrics, they became integral parts in modern materials science.¹⁻⁵ The change between crystalline and amorphous state of $\text{Ge}_2\text{Sb}_2\text{Te}_5$ and related materials encodes the binary code for optical storage (e.g. DVD-RW, blue ray) or phase change random access memory.⁶⁻⁸ With respect to energy materials, layered iron-containing selenides and tellurides are discussed as 2D superconductors.⁹⁻¹¹ Moreover, germanium antimony tellurides (GST materials) play a promising role as thermoelectric coolers and thermoelectric generators based on Peltier and Seebeck effects, respectively.¹² The major advantage of thermoelectric power generators without moving parts is their reliability. Thermoelectric generators consist of couples of p- and n-doped semiconductors and with applied temperature gradient, heat is converted directly into electrical power (see Fig. 1).¹³⁻¹⁵ The efficiency of this process is determined by the dimensionless figure of merit $ZT = S^2\sigma T / \kappa$, where S is the Seebeck coefficient (in $\mu\text{V/K}$), T the absolute temperature (in K), σ the electrical conductivity (in $\Omega^{-1}\text{m}^{-1}$) and κ the total thermal conductivity (in $\text{WK}^{-1}\text{m}^{-1}$). The latter is the sum of the electronic (κ_e ; heat transferred through electrons and holes) and phononic part (κ_{ph} ; heat transferred through lattice vibrations). κ_e is associated to σ by the Wiedemann-Franz law. The thermal conductivity depends inter alia on the real structure.¹⁶ The thermal diffusivity and thus κ_{ph} are influenced by the concentration and distribution of defects. The industry requests, with reference to commercially competitive power generators, ZT values of about four with a Carnot efficiency of $\sim 30\%$.¹⁷ Those, however, have not been reached yet, but thermoelectric generators still play an important role in the utilization of wasted heat.

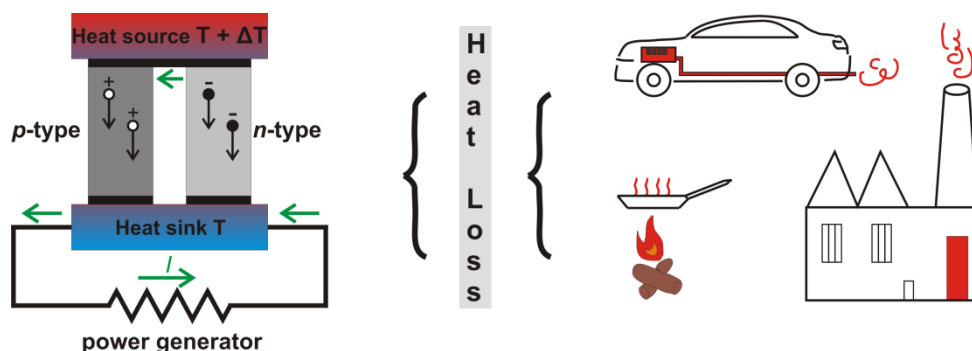


Fig. 1. A schematic of p- and n-type thermocouple (left) and some typical applications for generating electrical power with thermoelectric devices using wasted heat (right, highlighted in red).

In order to optimize the thermoelectric properties in a targeted manner, different approaches are possible. For reasons of manageable diversity of thermoelectric materials, the focus within this thesis is on tellurides, especially on substitution variants of GST materials. The Seebeck effect as material parameter is directly linked to the chemical composition, which can be changed by substitution of Ge, Sb or Te by various elements like Bi, Cd, In, Sn, Se. Furthermore, the ratios of the elements to each other can be adjusted, e.g. with the GeTe content.¹⁸ Substitution of Ge^{2+} by Ag^+ can modify the vacancy concentration, which is correlated to real-structure effects. Local mass fluctuations or nanostructuring, like nanoprecipitates in a matrix with a different composition, yield enhanced ZT values significantly larger than one.^{19,20} The concept of phonon-glass electron-crystal implies materials with crystal structures that allow efficient transmission of charge carriers while largely blocking the flow of heat by the lattice, as it is the case of glasses. As this concept arose, it changed the way of thinking about thermoelectric materials and enhanced ZT values were conceptually available.²¹⁻²³ Various thermal treatments (e.g. temper temperatures, heating and cooling rates) offer further possibilities for nanostructuring.^{24,25} In dependence of thermal treatment GST materials can be obtained in an amorphous phase, cubic high-temperature phase, stable trigonal phase and metastable pseudocubic phase. Substitutions mentioned above being able to shift the existence ranges of the modifications. The high-temperature phase crystallizes in the rocksalt type with Te^{2-} on the anion position and cation positions occupied with Sb^{3+} , Ge^{2+} and substituting elements and vacancies, respectively. Quenching the cubic high-temperature phase leads to a metastable pseudocubic modification with short-range ordered and defect layers, all of which being oriented orthogonal to the “cubic” $\langle 111 \rangle$. This phase can be described as an intermediate state between the cubic HT phase and the trigonal phase. Annealing below the stability range of the cubic high-temperature phase, results in the formation of thermodynamically stable layered structures similar to the *tetradymite* or GeTe type. Instead of locally ordered defect planes, van der Waals gaps are formed in the *fcc*-anion arrangement, which separate resulting blocks with a distorted rocksalt structure. The thickness of the individual building blocks is determined by the GeTe content.²⁶⁻²⁸ Structure models of the different tellurides can be based on powder X-ray diffraction combined with TEM and in ideal cases single crystal X-ray diffraction, when single crystals can be obtained from chemical transport. If elements with similar *Z* are present in one phase, diffraction experiments using anomalous dispersion are needed to refine the corresponding occupancy factors. From the methodical point of view, the detection of real-structure phenomena in tellurides is frequently done with TEM using electron diffraction, HRTEM and STEM.²⁹⁻³¹ TEM can record chemical and structural changes at scales below the coherence lengths of X-rays, making it the method of choice.

References

- 1 S. Raoux, W. Welnic, D. Ielmini, *Chem. Rev.* **2010**, *110*, 240.
- 2 S. Raoux, *Annu. Rev. Mater. Res.* **2009**, *39*, 25.
- 3 S. B. Riffat, X. Ma, *Appl. Therm. Eng.* **2003**, *23*, 913.
- 4 M. Zebarjadi, K. Esfarjani, M. S. Dresselhaus, Z. F. Ren, G. Chen, *Energ. Environ. Sci.* **2012**, *5*, 5147.
- 5 S. Perumal, S. Roychowdhury, K. Biswas, *J. Mater. Chem. C* **2016**, *4*, 7520.
- 6 M. Wuttig, N. Yamada, *Nat. Mater.* **2007**, *6*, 824.
- 7 D. Loke, T. H. Lee, W. J. Wang, L. P. Shi, R. Zhao, Y. C. Yeo, T. C. Chong, S. R. Elliott, *Science* **2012**, *336*, 1566.
- 8 V. Giraud, J. Cluzel, V. Sousa, A. Jacquot, A. Dauscher, B. Lenoir, H. Scherrer, S. Romer, *J. Appl. Phys.* **2005**, *98*, 013520.
- 9 Y. Mizuguchi, Y. Takano, *J. Phys. Soc. Jpn.* **2010**, *79*, 102001.
- 10 K. D. Oyler, X. Ke, I. T. Sines, P. Schiffer, R. E. Schaak, *Chem. Mater.* **2009**, *21*, 3655.
- 11 Q. Li, W. Si, I. K. Dimitrov, *Rep. Prog. Phys.* **2011**, *74*, 124510.
- 12 W. He, G. Zhang, X. Zhang, J. Ji, G. Li, X. Zhao, *Appl. Energ.* **2015**, *143*, 1.
- 13 L. E. Bell, *Science* **2008**, *321*, 1457.
- 14 J. R. Sootsman, D. Y. Chung, M. G. Kanatzidis, *Angew. Chem. Int. Ed.* **2009**, *48*, 8616.
- 15 L. -D. Zhao, V. P. Dravid, M. G. Kanatzidis, *Energy Environ. Sci.* **2014**, *7*, 251.
- 16 G. J. Snyder, E. S. Toberer, *Nat. Mater.* **2008**, *7*, 105.
- 17 F. J. DiSalvo, *Science* **1999**, *285*, 703.
- 18 T. Rosenthal, Dissertation, Ludwig-Maximilians-University, Munich, **2014**.
- 19 T. Rosenthal, M. N. Schneider, C. Stiewe, M. Doeblinger, O. Oeckler, *Chem. Mater.* **2011**, *23*, 4349.
- 20 F. Fahrnbauer, D. Souchay, G. Wagner, O. Oeckler, *J. Am. Chem. Soc.* **2015**, *137*, 12633.
- 21 M. Beekman, D. T. Morelli, G. S. Nolas, *Nat. Mater.* **2015** *14*, 1182.
- 22 T. M. Tritt, *Ann. Rev. Mater. Res.* **2011**, *41*, 433.
- 23 C. Xiao, J. Xu, B. Cao, K. Li, M. Kong, Y. Xie, *J. Am. Chem. Soc.* **2012**, *134*, 7971.
- 24 T. Schröder, T. Rosenthal, N. Giesbrecht, M. Nentwig, S. Maier, H. Wang, G. J. Snyder, O. Oeckler, *Inorg. Chem.* **2014**, *53*, 7722.
- 25 T. Schröder, T. Rosenthal, N. Giesbrecht, S. Maier, E.-W. Scheidt, W. Scherer, G. J. Snyder, W. Schnick, O. Oeckler, *J. Mater. Chem. A* **2014**, *2*, 6384.
- 26 M. N. Schneider, M. Seibald, P. Lagally, O. Oeckler, *J. Appl. Crystallogr.* **2010**, *43*, 1012.
- 27 M. N. Schneider, T. Rosenthal, C. Stiewe, O. Oeckler, *Z. Kristallogr.* **2010**, *225*, 463.
- 28 G. -S. Park, J. -H. Kwong, M. Kim, H. R. Yoon, W. Jo, T. K. Kim, J. -M. Zuo, Y. Khang, *J. Appl. Phys.* **2007**, *102*, 013524.
- 29 W. Zhou, H. F. Greer, *Eur. J. Inorg. Chem.* **2016**, 941.
- 30 U. Schürmann, V. Duppel, S. Buller, W. Bensch, L. Kienle, *Cryst. Res. Technol.* **2011**, *46*, 561.
- 31 S. Welzmler, T. Rosenthal, P. Ganter, L. Neudert, F. Fahrnbauer, P. Urban, C. Stiewe, J. de Boor, O. Oeckler, *Dalton Trans.* **2014**, *43*, 10529.

4.2 Structural variations in indium tin tellurides and their thermoelectric properties

Lukas Neudert, Stefan Schwarzmüller, Silvia Schmitzer, Wolfgang Schnick and Oliver Oeckler

J. Solid State Chem. **2018**, 258, 289.

Reprinted with permission from *Journal of Solid State Chemistry*. Copyright 2018 Elsevier.

Abstract

Indium-doped tin tellurides are promising and thoroughly investigated thermoelectric materials. Due to the low solubility of In_2Te_3 in SnTe and vice versa, samples with the nominal composition $(\text{SnTe})_{3-3x}(\text{In}_2\text{Te}_3)_x$ with $0.136 \leq x \leq 0.75$ consist of a defect-rocksalt-type Sn-rich and a defect-sphalerite-type In-rich phase which are endotaxially intergrown and form nanoscale heterostructures. Such nanostructures are kinetically inert and become more pronounced with increasing overall In content. The vacancies often show short-range ordering. These phenomena are investigated by temperature-dependent X-ray diffraction and HRTEM as well as STEM with element mapping by X-ray spectroscopy. The combination of real-structure effects leads to very low lattice thermal conductivity from room temperature up to 500 °C. Thermoelectric figures of merit ZT of heterostructured materials with $x = 0.136$ reach ZT values up to 0.55 at 400 °C.

4.2.1 Introduction

Concerning sustainable power generation, research for optimized thermoelectric materials plays an important role in materials science.¹ Such materials can reversibly interconvert thermal and electrical energy. The efficiency of this energy conversion is quantified by the dimensionless figure of merit $ZT = S^2\sigma T/(\kappa_{\text{ph}} + \kappa_{\text{e}})$, where S is the Seebeck coefficient, σ the electrical conductivity, T the temperature and κ_{ph} and κ_{e} the phononic and the electronic thermal conductivities, respectively. The latter two are coupled by the Wiedemann-Franz law and cannot be individually optimized in typical semiconductors. The same applies for S and σ which are both coupled to the charge-carrier concentration and effective mass. High Seebeck coefficients are found for semiconductors or insulators with low carrier concentrations whereas electrical conductivity is high for metals with high charge-carrier concentrations and mobilities.² Enhanced thermoelectric properties at certain temperatures would involve an improvement of S and σ with a simultaneous and more or less independent reduction of κ_{ph} . One promising approach combines chemical and structural variations, e.g. partial cation ordering, differently pronounced superstructures or partial long-periodic order as well as heterostructuring.^{3–6}

Vacancies and disorder often increase phonon scattering and lower κ_{ph} .^{7,8} Concerning doping and substitution, the associated change of the electronic structure, of course, also influence the thermoelectric properties.^{9,10}

Tellurides are prominent thermoelectric materials due to their broad structural variety, their suitable electronic properties and various ways of nanostructuring.^{11,12} For example, structure-property relations of prominent tellurides like PbTe, Bi₂Te₃, (GeTe)_x(AgSbTe₂)_{100-x} (TAGS materials) or phases of the system Ge/Sb/Te (GST materials) and their substitution variants were investigated extensively.^{13–17} There are only few studies about thermoelectric properties of indium tellurides. Tetragonal InTe, better written as In⁺In³⁺Te₂, shows very low thermal conductivity (ca. 0.4 Wm⁻¹K⁻¹ at \approx 330 °C).¹⁸ Electronic structure calculations for β -In₂Te₃ by discrete variational X-alpha cluster models based on LCAO and HFS approximations suggest that this defect sphalerite structure is a good thermoelectric material.¹⁹ Material optimization of In₂Te₃ was done, for instance, by combination with other thermoelectric materials like GeTe, Bi₂Te₃, InSb and Al-doped In/Sn/Te alloys. Heterostructuring can play a crucial role concerning enhanced thermoelectric properties.^{20–24}

In contrast, SnTe with rocksalt-type structure has limited thermoelectric efficiency. This is due to its rather low Seebeck coefficient (maximum S of 150 μ V/K at 600 °C) and relatively high thermal conductivity (9 – 3 W/mK between 25 – 500 °C). For the enhancement of thermoelectric properties at ambient pressure, recent work focuses on various p - and n -doping experiments with Bi, Sb, Mg, Ca, Sr, Mn, Fe, Cd, Hg.^{25–31} Sb doping leads to vacancies, possibly involving layer-like short-range order.³² In-doped variants reach figures of merit up to $ZT = 0.9$ at 900 K for Sn_{0.96}In_{0.027}Te, which can be further increased to $ZT = 1.1$ by adding iodine (Sn_{0.954}In_{0.027}I_{0.06}Te).³³ At the solubility limit of 6 mol% In₂Te₃ in SnTe, the vacancy concentration on the cation position amounts to 3.3 at%. The influence of larger amounts of SnTe in In₂Te₃ is so far unexplored. Yet, it is intriguing as SnTe and In₂Te₃ are stable over a broad temperature range. They crystallize in cubic structures with differently filled voids owing to the different ionic radii and valence electron concentrations.³⁴ SnTe is a rocksalt-type phase whereas In₂Te₃ adopts a defect-sphalerite type, which can be disordered or form superstructures.³⁵ Due to similar lattice parameters (SnTe³⁶: 6.300 Å, In₂Te₃³⁷: 6.170 Å) and the same basic fcc arrangement of Te atoms, endotaxial heterostructures of both structures in indium tin tellurides promise improved thermoelectric properties, at least in certain temperature ranges. Here we report on real-structure effects and the associated thermoelectric properties of such systems, taking into account two different cooling rates of samples.

4.2.2 Experimental Section

Synthesis

Samples of $(\text{SnTe})_{3-3x}(\text{In}_2\text{Te}_3)_x$ with $0.136 \leq x \leq 0.75$ were prepared by fusing stoichiometric mixtures of the elements (tin 99.999%, Inconex Kft. Fémipari, Budapest; indium 99.999%, Smart Elements; tellurium, 99.999%, Sigma Aldrich) in silica glass ampoules under Ar atmosphere at 860 °C for one day. Then they were quenched in water and subsequently annealed at 575 °C for up to 4 days, followed by slow cooling at air. Further samples were quenched in water after initial fusing. For thermoelectric characterization, disk-shaped samples with diameters of up to 20 mm were prepared like the slowly cooled ones in flat-bottom silica glass ampoules (but quenched at air after initial fusing). The ingots were polished to a thickness of 2 – 3 mm and cut into appropriate pieces. In order to simulate possible structural changes during thermoelectric measurements, pieces of the samples with $x \leq 0.3$ were heated up to 450 °C under Ar atmosphere for 1 h and then slowly cooled by switching off the furnace. All products were obtained as metallic gray ingots.

Analytical methods

The phase composition was analyzed by powder X-ray diffraction (PXRD). Samples were ground in an agate mortar and fixed between Mylar foils with traces of Lithelen vacuum grease. Data were recorded with a Guinier camera (G670, Huber, Germany; Cu- $K\alpha_1$ radiation, $\lambda = 1.54051 \text{ \AA}$, Ge(111) monochromator) equipped with an oscillating sample holder and a fixed image plate detector (15 min acquisition time and 15 read-outs). Temperature-programmed PXRD patterns were collected in steps of 20 K (30 min acquisition time each) from RT to 750 °C and back to RT (5 K/min rate) on a diffractometer with modified Debye-Scherrer geometry (StadiP, Stoe&Cie. GmbH, Germany; Mo- $K\alpha_1$ radiation, $\lambda = 0.7093 \text{ \AA}$, Ge(111) monochromator) equipped with a moving Mythen 1 K silicon stripe detector and a graphite furnace. Powdered samples were filled into silica glass capillaries (0.3 mm diameter) under Ar atmosphere. Rietveld refinements were carried out with TOPAS-Academic,³⁸ where reflection profiles were described by a fundamental parameter approach, anisotropic microstrain and crystal size effects. Slight preferred orientation was taken into account by 4th order spherical harmonics. For all refinements, the same set of parameters was used. Common displacement parameters for cations and anions, respectively, were assumed. Site occupancies were derived from energy-dispersive X-ray spectroscopy (EDX, see below), taking into account charge neutrality, overall composition and phase fractions. They were not refined due to similar X-ray scattering factors of In and Sn.

Chemical compositions were determined by EDX on polished parts of ingots (Dimple Grinder 650, Gatan, USA) using a Dualbeam Helios Nanolab G3UC (FEI, USA) scanning electron microscope (SEM)

with field emission gun (FEG) and X-Max80 SDD EDX-detector (Oxford Instruments, Great Britain) at 20 kV acceleration voltage. EDX spectra were collected until $5 \cdot 10^5$ counts were reached.

Transmission electron microscopy (TEM) was performed on a Titan Themis 60–300 (FEI, USA, 300 kV acceleration voltage) equipped with X-FEG, monochromator, C_s probe corrector and windowless 4-quadrant Super-X EDX detector (acquisition time per spectrum 45 s). Images were recorded using a 4k×4k Ceta CMOS camera (FEI, USA). Small amounts of the samples were ground in absolute ethanol, drop-cast on copper grids with holey carbon film (S166-2, Plano GmbH, Germany) and transferred into the microscope on a double-tilt holder. TEM data were evaluated using Digital Micrograph,³⁹ JEMS⁴⁰ and ProcessDiffraction7⁴¹ for indexing and simulation of SAED patterns and ES Vision⁴² for quantifying EDX spectra.

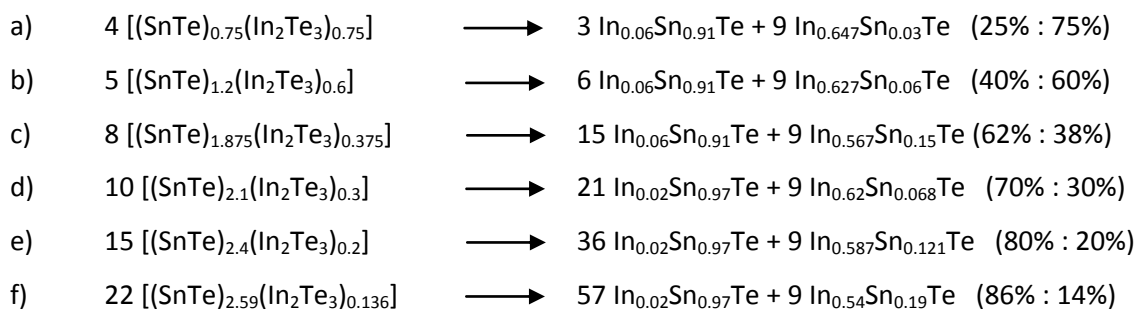
Physical property measurements

Thermoelectric measurements comprised 3 heating/cooling cycles up to 475 °C (heating/cooling rate 10 K/min, 3 data points per temperature) under He atmosphere. Seebeck coefficients and electrical conductivities were measured by a four-point setup⁴³ from cuboid samples ($\sim 6 \text{ mm} \times 2 \text{ mm} \times 1.5 \text{ mm}$) with a LSR-3 instrument (Linseis, Germany) equipped with NiCr/Ni thermocouples and Ni electrodes (measurement current: 100 mA). Thermal diffusivity D_{th} was measured applying the laser-flash method with an LFA1000 instrument (Linseis, Germany) equipped with Nd-YAG-Laser (350 V and 2 ms pulse) and InSb detector on disk-like samples (diameter 4–10 mm and 1–2 mm thickness) with same temperature program as for electrical transport measurements and 5 measurement points per temperature step. Simultaneous heat loss and finite pulse corrections were applied using Dusza's model.⁴⁴ Thermal conductivity was calculated according to $\kappa = C_p \cdot \rho \cdot D_{th}$ using densities ρ determined according to Archimedes' principle with a precision of 0.03 g/cm³. Heat capacities C_p were calculated according to the Dulong-Petit approximation.⁴⁵ According to experimental values for SnTe⁴⁶ and In₂Te₃,⁴⁷ C_p of these materials is about 10% higher than the Dulong-Petit value of 0.20 Jg⁻¹ K⁻¹ in the temperature range between RT and 500 °C; this probably adds this uncertainty to the values of κ and thus ZT, which may be slightly higher and lower, respectively.

4.2.3 Results and Discussion

4.2.3.1 Composition and average structure of quenched and slowly cooled phases

The present investigation focuses on heterogeneous samples $(\text{SnTe})_{3-3x}(\text{In}_2\text{Te}_3)_x$ with $0.136 \leq x \leq 0.3$; samples with In contents up to $x = 0.75$ are considered for comparison in order to confirm general trends (concerning homogeneous samples with lower In contents see Ref. 33). Quenching samples with In_2Te_3 contents $x > 0.167$ predominantly leads to inhomogeneous mixtures, which are probably not in equilibrium; traces of side phases were not elucidated in detail. According to PXRD and EDX, homogeneous rocksalt-type products with $x = 0.167$ and $x = 0.136$ could be obtained by quenching as shown by SEM-EDX and Rietveld refinements (cf. Table S1, Fig. S2 and crystallographic data in Tables S3 and S4; S abbreviates Supporting Information). In contrast, annealed ones reported in the literature were inhomogeneous showing nanoscale precipitates; thus, samples with $x > 0.06$ can form heterostructures.³³ For annealed samples with $x > 0.136$, PXRD and EDX show two cubic structures with different composition. Corresponding Rietveld fits are shown in Fig. 1 and Fig. S7, crystallographic data are given in Tables 1 and 2, S7 and S8 and EDX results are listed in Tables S5 and S6. For overall compositions corresponding to SnIn_2Te_4 (a), $\text{Sn}_2\text{In}_2\text{Te}_5$ (b), $\text{Sn}_5\text{In}_2\text{Te}_8$ (c), $\text{Sn}_7\text{In}_2\text{Te}_{10}$ (d), $\text{Sn}_{12}\text{In}_2\text{Te}_{15}$ (e) and $\text{Sn}_{19}\text{In}_2\text{Te}_{22}$ (f), the formal decomposition can be described by the following tentative equations which take into account approximate EDX results (uncertainties due to intergrown phases) and phase fractions from Rietveld refinements (biased by compositional uncertainties and the similar electron counts of In, Sn and Te); molar phase fractions are given after each equation.



The chemical compositions of the decomposition product correspond to In-doped SnTe in rocksalt structure type as main phase and defect-sphalerite-type Sn-doped In_2Te_3 with partially filled vacancies. As expected, the phase fraction of Sn-doped In_2Te_3 increases with increasing In content.

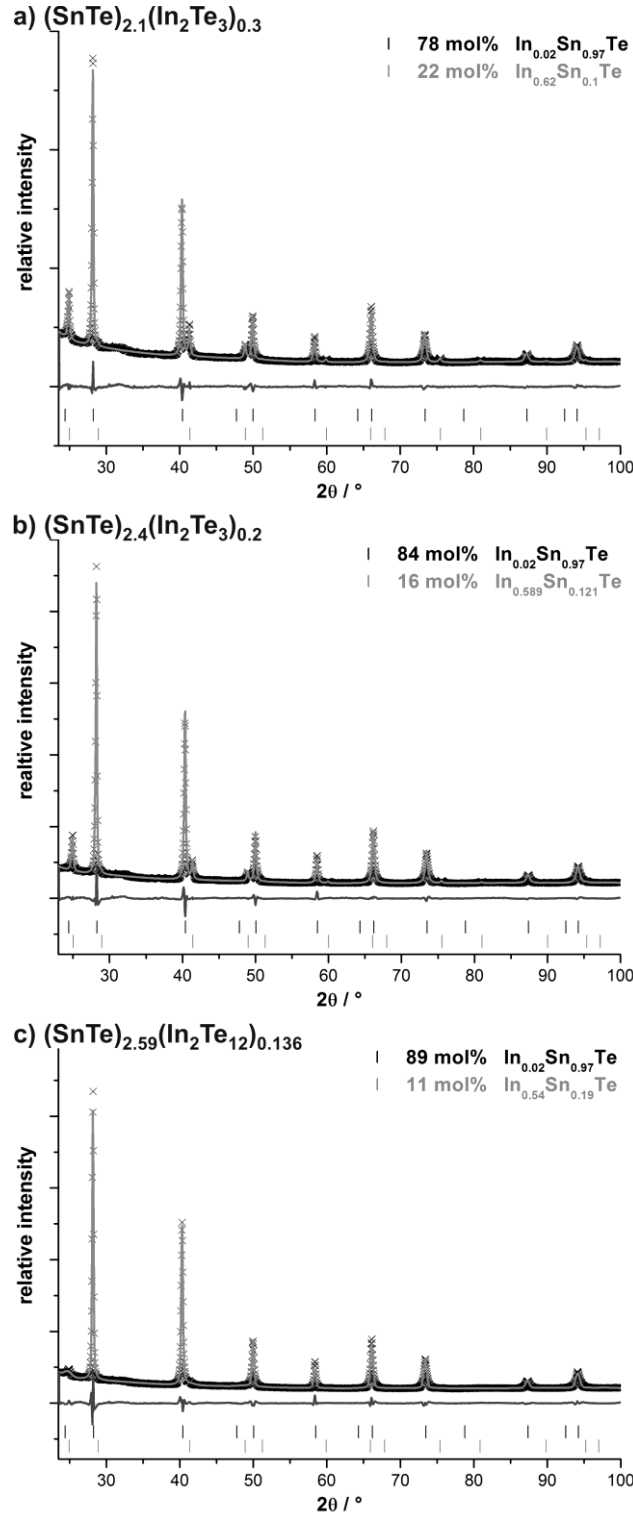


Figure 1. Rietveld fits of samples (annealed at 500 °C) with nominal compositions $(\text{SnTe})_{2.1}(\text{In}_2\text{Te}_3)_{0.3}$ (a), $(\text{SnTe})_{2.4}(\text{In}_2\text{Te}_3)_{0.2}$ (b) and $(\text{SnTe})_{2.59}(\text{In}_2\text{Te}_3)_{0.136}$ (c); experimental data (black), calculated pattern (light gray), difference plot (dark gray) and calculated reflection positions of different phases (vertical lines, black for rocksalt structure type and gray for defect-sphalerite structure type); phase fractions based on Rietveld refinement.

Table 1. Details of the Rietveld refinements of slowly cooled samples with the nominal compositions (SnTe)_{2.1}(In₂Te₃)_{0.3} (left) and (SnTe)_{2.4}(In₂Te₃)_{0.2} (middle) and (SnTe)_{2.59}(In₂Te₃)_{0.136} (right) and its decomposition products based on the decomposition reaction equations and EDX.

nominal composition	(SnTe) _{2.1} (In ₂ Te ₃) _{0.3}		(SnTe) _{2.4} (In ₂ Te ₃) _{0.2}		(SnTe) _{2.59} (In ₂ Te ₃) _{0.136}	
phase composition	In _{0.02} Sn _{0.97} Te	In _{0.62} Sn _{0.086} Te	In _{0.02} Sn _{0.97} Te	In _{0.587} Sn _{0.121} Te	In _{0.02} Sn _{0.97} Te	In _{0.54} Sn _{0.19} Te
M / g mol ⁻¹	245.045	208.996	245.045	209.362	245.045	209.245
space group (no.)	<i>Fm</i> 3 <i>m</i> (225)	<i>F</i> 43 <i>m</i> (216)	<i>Fm</i> 3 <i>m</i> (225)	<i>F</i> 43 <i>m</i> (216)	<i>Fm</i> 3 <i>m</i> (225)	<i>F</i> 43 <i>m</i> (216)
phase fraction / mol%	77.5(4)	22.5(4)	83.6(6)	16.2(6)	89.1(8)	10.9(8)
formula per unit cell	4	4	4	4	4	4
lattice parameter / Å	6.3141(2)	6.1644(3)	6.3071(2)	6.1607(4)	6.3072(2)	6.174(6)
cell volume / Å ³	251.72(2)	234.24(4)	250.89(2)	233.82(5)	250.90(2)	235.3(6)
X-ray density / g cm ⁻³	6.4659(6)	5.9735(9)	6.4873(5)	5.954(1)	6.4871(5)	5.99(2)
μ / mm ⁻¹	166.59(1)	152.80(2)	167.14(1)	152.43(3)	167.14(1)	153.4(4)
reflections	13	13	13	13	13	13
parameters / thereof background	23 / 12		26 / 12		23 / 12	
R _p / R _{wp} / Goof	0.0187 / 0.0264 / 3.082		0.0249 / 0.0360 / 4.381		0.0241 / 0.0366 / 4.347	
R _{Bragg}	0.0156		0.0127		0.0100	
	0.0136		0.0070		0.0354	

Table 2. Atom coordinates, site occupancies and isotropic displacement parameters for nominal compositions (SnTe)_{2.1}(In₂Te₃)_{0.3} (top), (SnTe)_{2.4}(In₂Te₃)_{0.2} (middle) and (SnTe)_{2.59}(In₂Te₃)_{0.136} (bottom), based on the decomposition reaction equations and EDX.

phase (structure type)	atom position	x y z	Wyckoff position	s.o.f.	B _{iso}
In _{0.02} Sn _{0.97} Te (NaCl)	In/Sn	½ ½ ½	4 <i>b</i>	0.02/0.97	0.44(3)
	Te	0 0 0	4 <i>a</i>	1	= B(iso) cation
In _{0.62} Sn _{0.086} Te (sphalerite)	In/Sn/□	¼ ¼ ¼	4 <i>c</i>	0.62/0.086/0.294	1.5(2)
	Te	0 0 0	4 <i>a</i>	1	= B(iso) cation
In _{0.02} Sn _{0.97} Te (NaCl)	In/Sn	½ ½ ½	4 <i>b</i>	0.02/0.97	0.62(3)
	Te	0 0 0	4 <i>a</i>	1	= B(iso) cation
In _{0.587} Sn _{0.121} Te (sphalerite)	In/Sn/□	¼ ¼ ¼	4 <i>c</i>	0.587/0.121/0.292	2.7(4)
	Te	0 0 0	4 <i>a</i>	1	= B(iso) cation
In _{0.02} Sn _{0.97} Te (NaCl)	In/Sn	½ ½ ½	4 <i>b</i>	0.02/0.97	1.00(3)
	Te	0 0 0	4 <i>a</i>	1	= B(iso) cation
In _{0.54} Sn _{0.19} Te (sphalerite)	In/Sn/□	¼ ¼ ¼	4 <i>c</i>	0.54/0.19/0.27	1.8(9)
	Te	0 0 0	4 <i>a</i>	1	= B(iso) cation

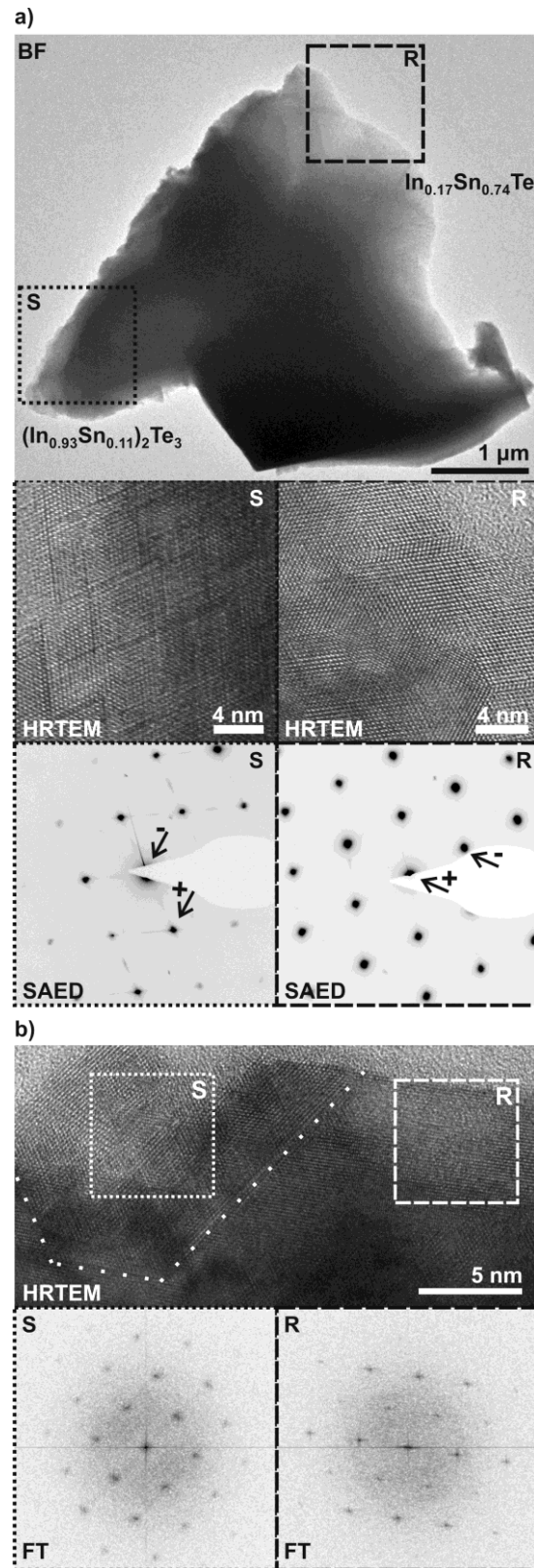


Figure 4. a) Bright-field image (top) of a quenched $(\text{SnTe})_{2.1}(\text{In}_2\text{Te}_3)_{0.3}$ crystal showing two different phases (bottom) distinguishable by HRTEM and SAED along [110], different reflection intensities are highlighted with + and -; b) HRTEM image of slowly cooled $(\text{SnTe})_{2.1}(\text{In}_2\text{Te}_3)_{0.3}$ along [110] and corresponding Fourier transforms (from highlighted square areas) of two intergrown domains. R and S denote rocksalt-type and sphalerite-type phases, respectively.

4.2.3.2 Thermal behavior of quenched phases

Temperature-dependent PXRD up to 700 °C (Fig. 2) shows structural changes and melting points of $(\text{SnTe})_{3-3x}(\text{In}_2\text{Te}_3)_x$ with $0.136 \leq x \leq 0.3$. Additional data for $0.375 \leq x \leq 0.75$ show the same trends concerning the influence of chemical composition on temperature-dependent changes in a more pronounced way (Fig. S10). At low temperatures, the samples contain two phases. At ca. 420–580 °C (Table S11, cf. line T1 in Figs. 2 and S10), the reflections of the In-rich sphalerite-type phase vanish. Since the melting points of In_2Te_3 ($T_{\text{melt}} = 667$ °C) and SnTe ($T_{\text{melt}} = 790$ °C) are relatively high, this most likely corresponds to their dissolution in the In-doped SnTe main phase. This dissolution is also corroborated by the temperature-dependent change of the lattice parameter of the In-doped SnTe main phase (Fig. 3). The lattice parameter of the Sn-rich phases increases with increasing temperature up to a plateau between ~300 °C and ~550 °C, where the dissolution of the In-rich phase starts. As it introduces up to 10% of vacancies on the cation site, lattice parameters of the rocksalt-type phases even decrease slightly upon heating before they increase again above ~600 °C. At ca. 700 °C (Table S11), the single crystalline phase melts (cf. line T2 in Figs. 2 and S10).

4.2.3.3 Influence of the composition on the nanostructure

In accordance with PXRD, TEM investigations show the decomposition of $(\text{SnTe})_{2.1}(\text{In}_2\text{Te}_3)_{0.3}$ into two phases with different In content, independent of the thermal treatment. Fig. 4a depicts different areas in a quenched crystal matching either the Sn-rich rocksalt-type phase (EDX: measured $\text{In}_{0.17}\text{Sn}_{0.74}\text{Te}$, calculated $\text{In}_{0.02}\text{Sn}_{0.97}\text{Te}$) or the In-rich defect-sphalerite-type phase (EDX: measured $\text{In}_{0.62}\text{Sn}_{0.073}\text{Te}$, calculated $\text{In}_{0.62}\text{Sn}_{0.086}\text{Te}$). The assignment of the phases is obvious from d values that differ by ~5% in HRTEM micrographs and SAED patterns and in particular from the different intensity distribution of Bragg peaks in SAED and Fourier transforms (Figs. 4 and 5, which also confirms the cubic metrics). The In-rich phase shows short-range layer-like defect ordering in planes perpendicular to $\langle 111 \rangle$, similar to the situation in disordered Ga_2Te_3 .^{48,49} Occasionally, the typical superstructures of In_2Te_3 ^{35,50} were also observed (Fig. S12), especially in In-rich precipitates, i.e. less pronounced in samples with the composition $(\text{SnTe})_{2.4}(\text{In}_2\text{Te}_3)_{0.2}$. Around the defect layers, the stacking of Te-atom layers remains a cubic ABC one as in the NaCl type as long as defects are not long-range ordered. This can be directly observed by HRTEM, even in slowly cooled $(\text{SnTe})_{2.4}(\text{In}_2\text{Te}_3)_{0.2}$ (Fig. S13). Sn incorporation reduces the number cation vacancies in the defect-sphalerite-type structure.

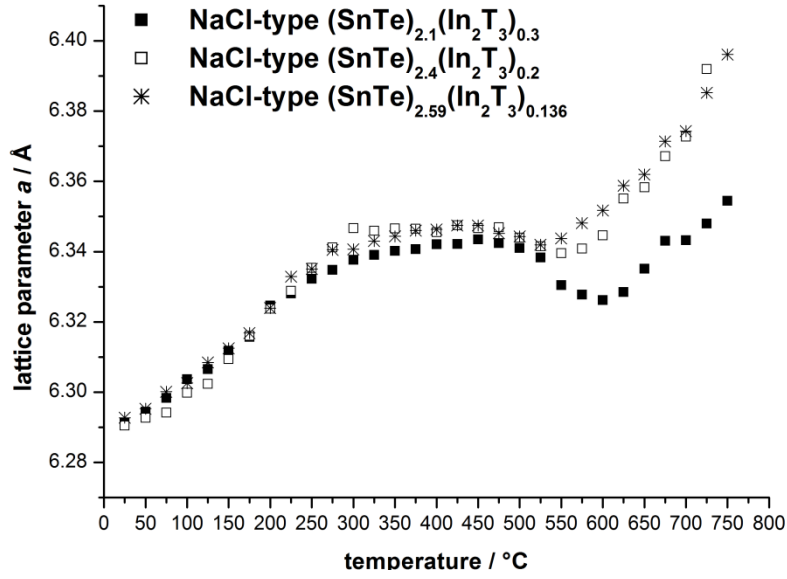


Figure 3. Temperature dependent behavior of the lattice parameters of rocksalt-type In-doped SnTe, starting from heterogeneous samples with an In-rich side phase (see text).

In contrast, the low In content of the rocksalt-type phase involves vacancy concentrations of ≈ 1 at%. HRTEM images of the SnTe-like phase thus show less pronounced defect ordering. At phase boundaries (Fig. 4b), the relative orientations of two phases indicate endotaxial intergrowth. This is also corroborated by Fig. S14, which indicates the superposition of two cubic diffraction patterns by reflection splitting at high angles. Depending on composition and thermal treatment, different degrees of defect ordering can be observed (Fig. 5). Heterogeneous phase composition has been observed for all slowly cooled samples.³³ In contrast to $x = 0.3$, sphalerite-type precipitates in samples with $x = 0.136$ and 0.2 were only detected after annealing or slow cooling. Thermal treatment thus has a stronger influence for compositions closer to the solubility limit of In_2Te_3 in SnTe. Scanning transmission electron microscopy (STEM) and STEM-EDX mapping highlight the In-rich precipitates (Fig. S15). Their size lies between 5 and 100 nm.

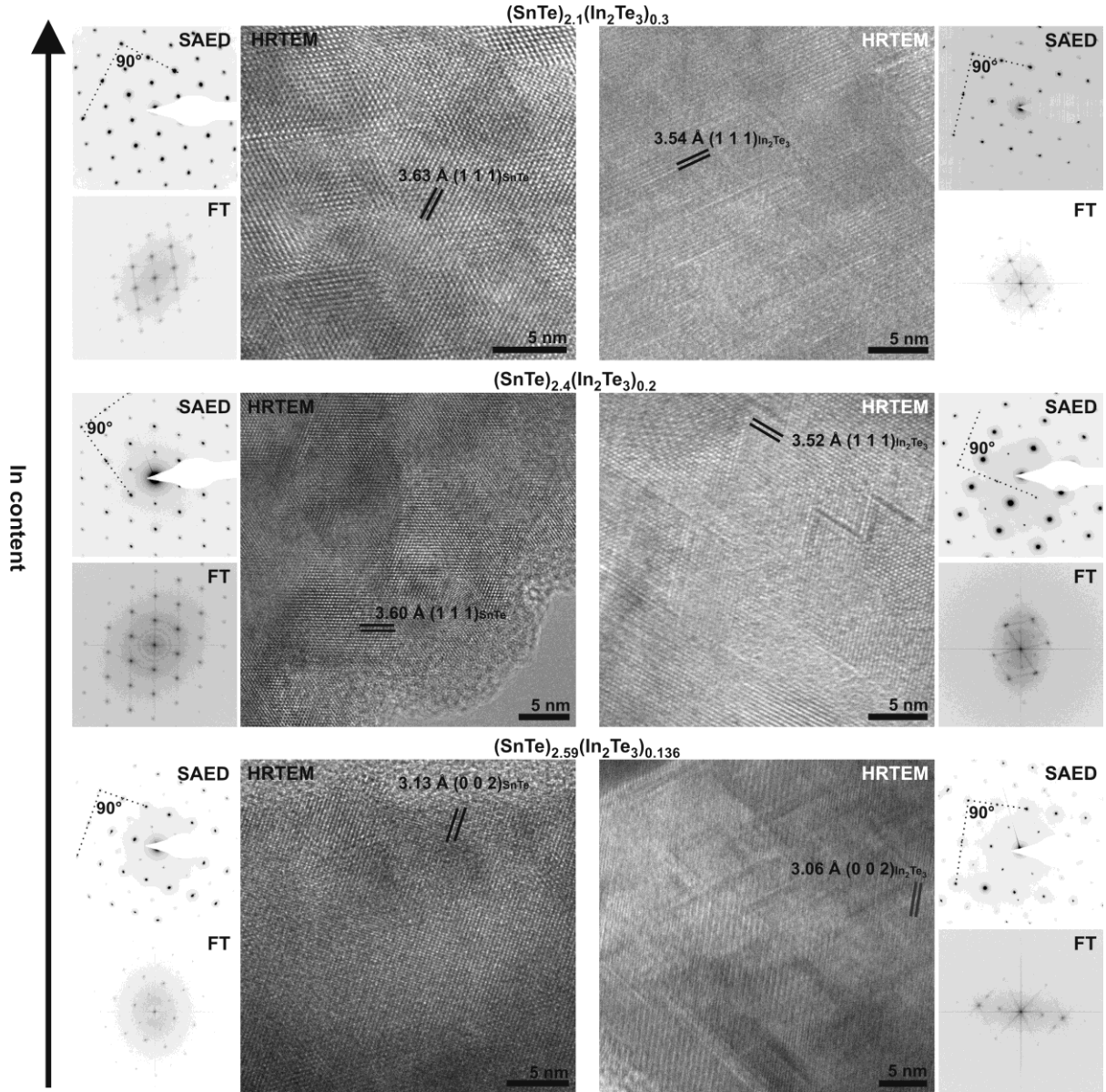


Figure 5. HRTEM images of quenched (left) and slowly cooled (right) $(\text{SnTe})_{3-3x}(\text{In}_2\text{Te}_3)_x$ with $0.136 \leq x \leq 0.3$ along the cubic $\langle 110 \rangle$ direction with corresponding Fourier transforms and SAED patterns, which show angles of $90^\circ \pm 0.1^\circ$ between the directions $[110]^*$ and $[001]^*$. The HRTEM images show rocksalt-type (left) and defect-sphalerite-type areas (right). Different lattice spacings corresponding to d_{111} and d_{002} were measured for both phases (highlighted in black).

4.2.3.4 Thermoelectric properties

As the high degree of covalent bonding in In_2Te_3 and variants thereof leads to unfavorable thermoelectric properties, only samples of $(\text{SnTe})_{3-3x}(\text{In}_2\text{Te}_3)_x$ with $x \leq 0.3$ were investigated (Fig. 6, cf. Fig. S16 for a direct comparison of the averaged properties). With the exception of the first heating of quenched samples, subsequent heating and cooling curves do not differ within experimental error. Slow cooling enhances the thermoelectric properties of all samples, probably due to the formation or coarsening of the precipitates. In subsequent cycles, no irreversible processes were observed.

Seebeck coefficients S of In-containing samples are significantly enhanced compared to pristine SnTe, both for the samples in this study as well as those with lower In content.³³ Positive S indicates p-type conduction. Band gaps estimated according to the Goldsmid-Sharp relationship^{51,52} are smaller than 0.18 eV for SnTe⁵³ at 300 K: 0.138 eV for $x = 0.3$, 0.143 eV for $x = 0.2$, 0.157 eV for $x = 0.136$ (Scheme S17). The rather high electrical conductivity σ of pristine SnTe decreases with increasing In_2Te_3 content, but its temperature dependence becomes less pronounced, the absolute values for $0.136 \leq x \leq 0.3$ are in the range of those for $x < 0.033$,³³ but lead to a non-linear behavior (maxima at $\approx 350^\circ\text{C}$) of S , σ and the power factor as a function of temperature.³³ Temperature dependent PXRD (Figs. 2 and 3) reveals that the discontinuities are that this is due to dissolution of In_2Te_3 .

Compared to In-doped SnTe with $x < 0.1$, the thermal conductivity κ for $x > 0.136$ lies in the same range with values $< 3.2 \text{ W m}^{-1} \text{ K}^{-1}$ and typically is lower. In doping in SnTe and the associated vacancies increase cation mass fluctuations yielding low values for the phononic part κ_{ph} ($< 2.0 \text{ W m}^{-1} \text{ K}^{-1}$ at RT), possibly enhanced by the segregation of the precipitates. In slowly cooled samples, they are larger and thus fewer, leading to increased κ_{ph} : the minimum $\kappa_{\text{ph}} = 0.6 \text{ W m}^{-1} \text{ K}^{-1}$ of $(\text{SnTe})_{2.88}(\text{In}_2\text{Te}_3)_{0.04}$ ³³ contrasts to $\kappa_{\text{ph}} \approx 0.15 \text{ W m}^{-1} \text{ K}^{-1}$ of $(\text{SnTe})_{2.59}(\text{In}_2\text{Te}_3)_{0.136}$ (both at 475°C) even though this value bears a relatively high systematic uncertainty.

ZT values of slowly cooled samples are higher than those of quenched ones (different heating curves in Fig. 6) since Sn-doped In_2Te_3 probably does not precipitate completely during quenching. For $x = 0.136$, samples with precipitates reach maximal ZT = 0.55 at 400°C .

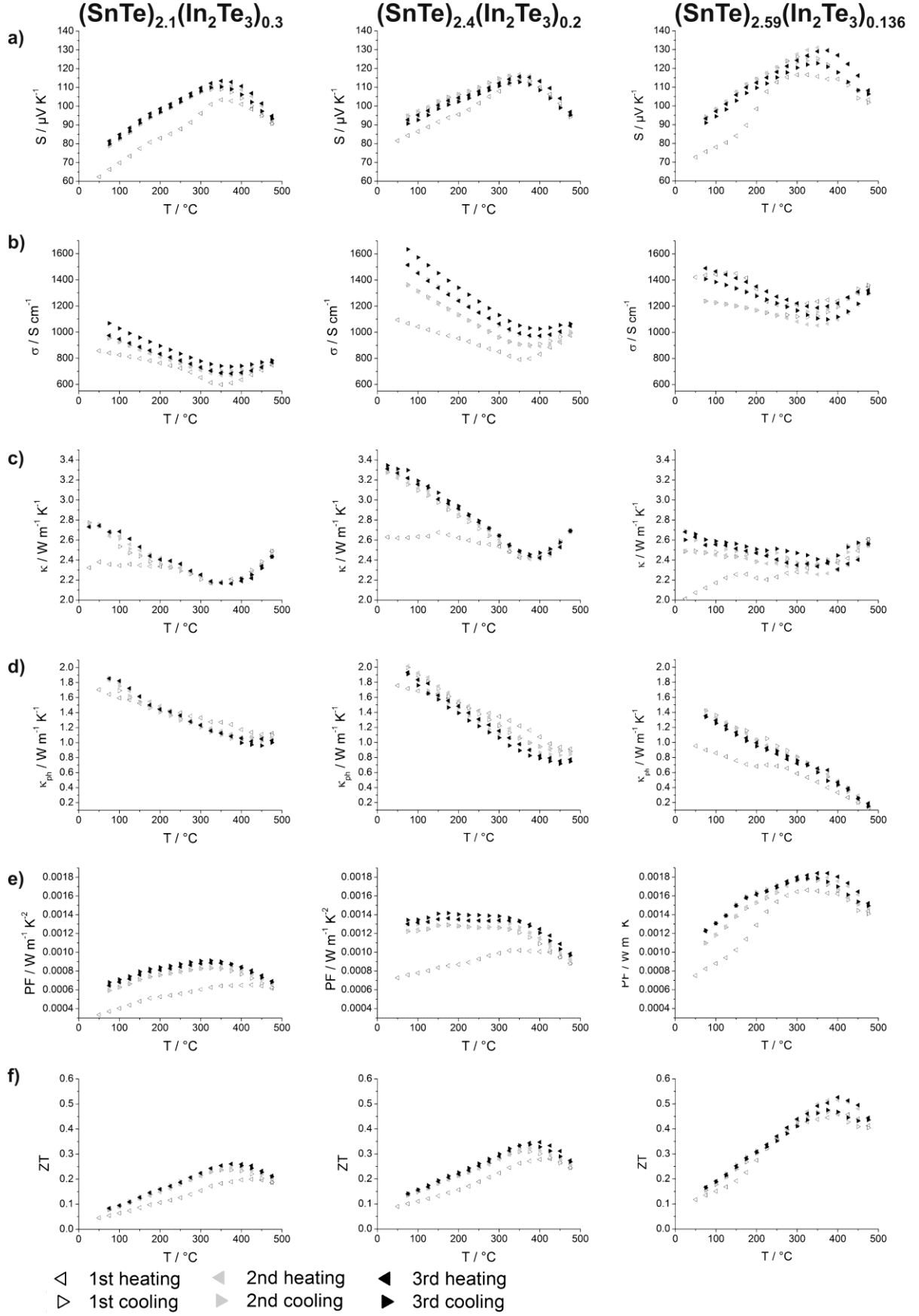


Figure 6. Thermoelectric properties of $(\text{SnTe})_{3-3x}(\text{In}_2\text{Te}_3)_x$ with $0.136 \leq x \leq 0.3$, different triangles represent different cycles of measurements: (a) Seebeck coefficient, (b) electrical conductivity, (c) total and (d) lattice thermal conductivity, (e) power factor and (f) thermoelectric figure of merit ZT.

4.2.4 Conclusion

In contrast to SnTe doped with low concentrations of In_2Te_3 (solid solutions with $x < 0.1$), higher concentrations may be expected to be comparable germanium-indium or tin-antimony tellurides with similar Sn or In concentrations. However, PXRD and TEM revealed the formation In-rich precipitates with defect-sphalerite-type structure and pronounced short-range defect ordering or long-range ordered superstructures at the highest In concentrations, where the precipitates are close to In_2Te_3 itself. The precipitates are endotaxially intergrown in a Sn-rich rocksalt-type matrix. Nanoscale heterostructures are little influenced by heat treatment. Both the heterostructuring as well as the defects explain the very low phononic parts of thermal conductivity over the whole temperature range. In terms of overall thermoelectric properties, no very high ZT values have been reached so far. Still, heterostructured phases containing SnTe and In_2Te_3 certainly have potential for further optimization. Co-doping with Se or Al may be a promising approach to combine the low κ with higher S and σ , similar to related studies on SnTe and SnSe.^{54,55} Heterostructures with In_4Se_3 ⁵⁶ may be another option.

4.2.5 References

- 1 W. He, G. Zhang, X. Zhang, J. Ji, G. Li, X. Zhao, *Appl. Energ.* **2015**, *143*, 1.
- 2 J. G. Snyder, E. S. Toberer, *Nat. Mater.* **2008**, *7*, 105.
- 3 J. R. Sootsman, D. Y. Chung, M. G. Kanatzidis, *Angew. Chem.* **2009**, *121*, 8768; *Angew. Chem. Int. Ed.* **2009**, *48*, 8616.
- 4 K. S. Siegert, F. R. L. Lange, E. R. Sittner, H. Volker, C. Schlockermann, T. Siegrist, M. Wuttig, *Rep. Prog. Phys.* **2015**, *78*, 013001.
- 5 W. G. Zeier, A. Zevalkink, Z. M. Gibbs, G. Hautier, M. G. Kanatzidis, G. J. Snyder, *Angew. Chem.* **2016**, *128*, 6938; *Angew. Chem. Int. Ed.* **2016**, *55*, 6826.
- 6 G. Chen, M. S. Dresselhaus, G. Dresselhaus, J. -P. Fleurial, T. Caillat, *Int. Mater. Rev.* **2003**, *48*, 45.
- 7 K. Woonchul, *J. Mater. Chem. C* **2015** *3*, 10336.
- 8 T. Rosenthal, M. N. Schneider, C. Stiewe, M. Döblinger, O. Oeckler, *Chem. Mater.* **2011**, *23* 4349.
- 9 R. Tuley, K. Simpson, *Materials* **2017**, *10*, 309.
- 10 M. Zhou, Z.M. Gibbs, H. Wang, Y. Han, C. Xin, L. Li, G. J. Snyder, *Phys. Chem. Chem. Phys.* **2014**, *16*, 20741.
- 11 Y. Pei, H. Wang, G. J. Snyder, *Adv. Mater.* **2012**, *24*, 6125.
- 12 M. G. Kanatzidis, *Chem. Mater.* **2010**, *22*, 648.
- 13 G. Tan, L. -D. Zhao, M. G. Kanatzidis, *Chem. Rev.* **2016**, *116*, 12123.
- 14 C. Gayner, K. K. Kar, *Prog. Mater. Sci.* **2016**, *83*, 330.

- 15 S. Perumal, S. Roychowdhury, K. Biswas, *J. Mater. Chem. C* **2016**, 4, 7520.
- 16 S. Welzmler, T. Rosenthal, P. Ganter, L. Neudert, F. Fahrnbauer, P. Urban, C. Stiewe, J. de Boor, O. Oeckler, *Dalton Trans.* **2014**, 43, 10529.
- 17 T. Rosenthal, S. Welzmler, L. Neudert, P. Urban, A. Fitch, O. Oeckler, *J. Solid State Chem.* **2014**, 219, 108.
- 18 M. K. Jana, K. Pal, U.V. Waghmare, K. Biswas, *Angew. Chem.* **2016**, 128, 7723; *Angew. Chem. Int. Ed.* **2016**, 55, 7792.
- 19 A. Vora-ud, C. Thanachayanont, S. Jugsujinda, V. Amornkitbamrung, T. Seetawana, *Proc. Eng.* **2011**, 8, 2.
- 20 H. Sun, X. Lu, H. Chi, D. T. Morelli, C. Uher, *Phys. Chem. Chem. Phys.* **2014** 16, 15570.
- 21 D. Lui, X. Li, R. Schmechel, M. Rettenmayr, *J. Electron. Mater.* **2016**, 45, 1654.
- 22 N. A. Heinz, T. Ikeda, G. J. Snyder, *Acta Mater.* 2012, 60, 4461.
- 23 Y. Pei, D.T. Morelli, *Appl. Phys. Lett.*, **2009**, 94, 122112.
- 24 H. Fu, P. Ying, J. Cui, Y. Yan, X. Zhang, *J. Electron. Mater.* **2011**, 40, 937.
- 25 D. Freik, S. Mudryi, I. Gorichok, V. Prokopiv, O. Matkivsky, I. Arsenjuk, O. Krynytsky, V. Bojchyk, *Ukr. J. Phys.* **2016**, 61, 155.
- 26 Z. Zhou, J. Yang, Q. Jiang, Y. Luo, D. Zhang, Y. Ren, X. He, J. Xin, *J. Mater. Chem. A* **2016**, 4, 13171.
- 27 R. A. R. A. Orabi, N.A. Mecholsky, J. Hwang, W. Kim, J. S. Rhyee, D. Wee, M. Fornari, *Chem. Mater.* **2016**, 28, 376.
- 28 X. J. Tan, H. Z. Shao, J. He, G. Q. Liu, J. T. Xu, J. Jiang, H. C. Jiang, *Phys. Chem. Chem. Phys.* **2016**, 181, 7141.
- 29 G. Tan, F. Shi, J. W. Doak, H. Sun, L. D. Zhao, P. Wang, C. Uher, C. Wolverton, V. P. Dravid, M. G. Kanatzidis, *Energy Environ. Sci.* **2015**, 8, 267.
- 30 M. M. Asadov, M. A. Alidzhanov, M. F. Mamedov, G. I. Kelbaliev, *Inorg. Mater.* **1998**, 34, 442.
- 31 L. D. Zhao, X. Zhang, H. Wu, G. Tan, Y. Pei, Y. Xiao, C. Chang, D. Wu, H. Chi, L. Zheng, S. Gong, C. Uher, J. He, M. G. Kanatzidis, *J. Am. Chem. Soc.* **2016**, 138, 2366.
- 32 A. Banik, B. Vishal, S. Perumal, R. Datta, K. Biswas, *Energy Environ. Sci.* **2016**, 9, 2011.
- 33 G. Tan, W. G. Zeier, F. Shi, P. Wang, J.G. Snyder, V. P. Dravid, M.G. Kanatzidis, *Chem. Mater.* **2015**, 27, 7801.
- 34 R. D. Shannon, *Acta Crystallogr. Sect. A* **1976**, 32, 751.
- 35 R. R. Desai, D. Lakshminarayana, P. B. Patel, P. K. Patel, C. J. Panchal, *Mater. Chem. Phys.* **2005**, 94, 308.
- 36 H. Krebs, K. Grün, D. Kallen, *Z. Anorg. Allg. Chem.* **1961**, 312, 307.
- 37 J. C. Woolley, B. A. Smith, *Proc. Phys. Soc.* **1958**, 72, 867.
- 38 A. Coello, TOPAS Academic, v. 4.1, Coelho Software, Brisbane, Australia, **2007**.
- 39 Gatan Software Team, Digital Micrograph, v. 3.6.1, **1999**.
- 40 P. A. Stadelmann, JEMS, v. 3.3425, **2008**.
- 41 J. L. Lábár, Process Diffraction, v. 7.3.2 Q, **2005**.
- 42 Emispec Systems Inc., ESVision, v. 4.0.164, **2002**.
- 43 L. J. Van der Pauw, *Philips Res. Rep.* **1958**, 13, 1.

- 44 L. Dusza, *High Temp. - High. Press.* **1995/1996**, 27/28, 467.
- 45 K. A. Borup, J. de Boor, H. Wang, F. Drymiotis, F. Gascoin, X. Shi, L. Chen, M. I. Fedorov, E. Müller, B. B. Iversen, G. J. Snyder, *Energy Environ. Sci.*, **2015**, 8, 423.
- 46 A. Pashinkin, A. Malkova, M. Mikhailova, *Russ. J. Phys. Chem.* **2006**, 80, 1342.
- 47 V. P. Zlomanov, M. S. Sheiman, V. N. Demin, B. Legendre, *J. Phase Equilib.* **2001**, 22, 339.
- 48 L. Kienle, V. Duppel, A. Simon, H. J. Deiseroth, *Z. Anorg. Allg. Chem.* **2003**, 629, 1412.
- 49 L. Kienle, O. Oeckler, H. J. Mattausch, V. Duppel, A. Simon, C. Reiner, M. Schlosser, K. Xhaxhiu, H. J. Deiseroth, *Mater. Sci. Semicond. Process.* **2003**, 6, 393.
- 50 G. L. Bleris, T. Karakostas, J. Stoemenos, N. A. Economou, *Phys. Stat. Sol. A* **1976**, 34, 243.
- 51 H. J. Goldsmid, J. W. Sharp, *J. Electron. Mater.* **1999**, 28, 869.
- 52 Z. M. Gibbs, H.-S. Kim, H. Wang, G. J. Snyder, *Appl. Phys. Lett.* **2015**, 106, 022112.
- 53 J. O. Dimmock, I. Melngail, A. Strauss, *Phys. Rev. Lett.* **1966**, 16, 1193.
- 54 L. -D. Zhao, G. Tan, S. Hao, J. He, Y. Pei, H. Chi, H. Wang, S. Gong, H. Xu, V.P. Dravid, C. Uher, G. J. Snyder, C. Wolverton, M.G. Kanatzidis, *Science* **2016**, 351, 141.
- 55 H. Fu, P. Ying, J. Cui, Y. Yan, X. Zhang, *J. Electron. Mater.* **2011**, 40, 937.
- 56 J. -S. Rhyee, K. H. Lee, S. M. Lee, E. Cho, S. I. Kim, E. Lee, Y. S. Kwon, J. H. Shim, G. Kotilar, *Nature* **2009**, 459, 965.

4.2.6 Supporting Information

Table S1: TEM-EDX results (in atom%) of quenched $(\text{SnTe})_{3-3x}(\text{In}_2\text{Te}_3)_x$ with $x = 0.136$ ($\text{Sn}_{19}\text{In}_2\text{Te}_{22}$) and $x = 0.2$ ($\text{Sn}_{12}\text{In}_2\text{Te}_{15}$), based on averaging 5 and 4 measurement points, respectively; calculated values for nominal composition are for comparison.

	$(\text{SnTe})_{2.4}(\text{In}_2\text{Te}_3)_{0.2}$	calc.	$(\text{SnTe})_{2.59}(\text{In}_2\text{Te}_3)_{0.136}$	calc.
In	7(2)	6.9	5.3(2)	4.7
Sn	39(2)	41.4	40.0(3)	44.2
Te	54(1)	51.7	54.7(4)	51.2

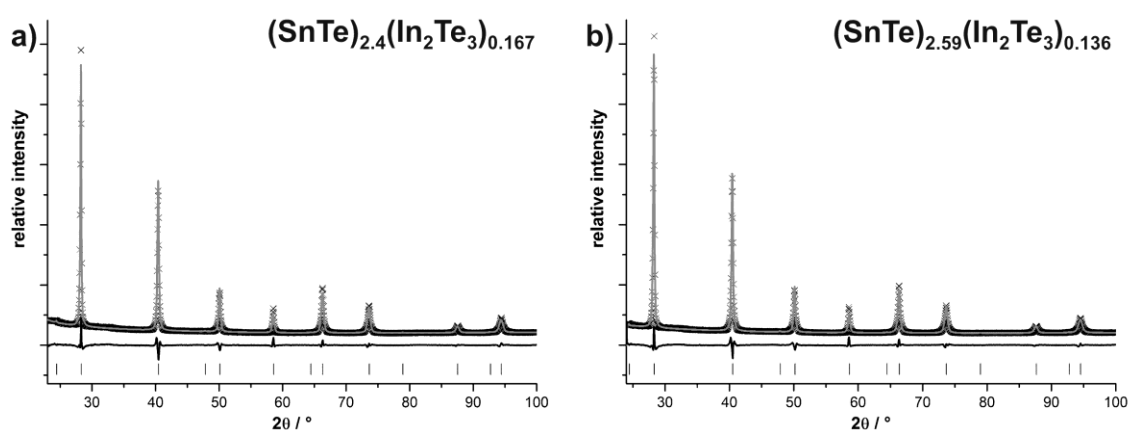


Figure S2: Rietveld fits of quenched $(\text{SnTe})_{2.4}(\text{In}_2\text{Te}_3)_{0.2}$ (a) and $(\text{SnTe})_{2.59}(\text{In}_2\text{Te}_3)_{0.136}$ (b): experimental data (black), calculated pattern (light gray), difference plot (dark gray, below), and calculated reflection positions (vertical lines, bottom).

Table S3: Details of the Rietveld refinements for quenched $(\text{SnTe})_{2.4}(\text{In}_2\text{Te}_3)_{0.2}$ and $(\text{SnTe})_{2.59}(\text{In}_2\text{Te}_3)_{0.136}$.

nominal composition	$(\text{SnTe})_{2.4}(\text{In}_2\text{Te}_3)_{0.2}$	$(\text{SnTe})_{2.59}(\text{In}_2\text{Te}_3)_{0.136}$
$M / \text{g mol}^{-1}$	238.759	240.024
space group (no.)	$Fm\bar{3}m$ (225)	$Fm\bar{3}m$ (225)
formula per unit cell	4	4
lattice parameter / Å	6.2968(2)	6.2925(2)
cell volume / Å ³	249.66(2)	249.15(2)
X-ray density / gcm ⁻³	6.3521(5)	6.3989(5)
$\mu / \text{in mm}^{-1}$	163.53(1)	164.77(1)
reflections	13	13
parameters / thereof background	23 / 12	14 / 6
R_p / R_{wp}	0.0226 / 0.0362	0.0234 / 0.0364
R_{Bragg}	0.0217	0.0082

Table S4: Atomic coordinates, site occupancies and isotropic displacement parameters of quenched $(\text{SnTe})_{2.4}(\text{In}_2\text{Te}_3)_{0.2}$ and $(\text{SnTe})_{2.59}(\text{In}_2\text{Te}_3)_{0.136}$.

phase	atom position	Wyckoff position	$x y z$	s.o.f.	B_{iso}
$(\text{SnTe})_{2.4}(\text{In}_2\text{Te}_3)_{0.2}$	In/Sn/□	4b	$\frac{1}{2} \frac{1}{2} \frac{1}{2}$	0.11/0.83/0.06	1.02(9)
(NaCl type)	Te	4a	0 0 0	1	0.52(9)
$(\text{SnTe})_{2.59}(\text{In}_2\text{Te}_3)_{0.136}$	In/Sn/□	4b	$\frac{1}{2} \frac{1}{2} \frac{1}{2}$	0.09/0.86/0.05	1.14(9)
(NaCl type)	Te	4a	0 0 0	1	0.56(8)

Table S5: TEM-EDX results (in atom%) of slowly cooled $(\text{SnTe})_{3-3x}(\text{In}_2\text{Te}_3)_{3x}$ with $0.136 \leq x \leq 0.3$, averaged from 4 - 6 measurement points each for both the Sn-rich and the In-rich phases; calculated values for nominal composition are for comparison.

	$(\text{SnTe})_{2.1}(\text{In}_2\text{Te}_3)_{0.3}$			$(\text{SnTe})_{2.4}(\text{In}_2\text{Te}_3)_{0.2}$			$(\text{SnTe})_{2.59}(\text{In}_2\text{Te}_3)_{0.136}$		
	Sn rich	In rich	calc.	Sn rich	In rich	calc.	Sn rich	In rich	calc.
In	5(1)	34(1)	10.5	5(1)	32(4)	6.9	3.8(8)	7.7(6)	4.7
Sn	40(1)	7(1)	36.8	40(1)	11(4)	41.4	41(2)	40.2(8)	44.2
Te	56(1)	58(2)	52.6	54(1)	57(1)	51.7	55(1)	52.2(9)	51.2

Note that uncertainties may be due to the dimensions of SEM-EDX measurement points that may to some extent be averaged measurements of both phases (e.g. nanoprecipitates in matrix with other composition).

Table S6: SEM-EDX results (in atom%) of quenched $(\text{SnTe})_{3-3x}(\text{In}_2\text{Te}_3)_{3x}$ with $0.375 \leq x \leq 0.75$, averaged from 5 - 8 measurement points each for both the Sn-rich and the In-rich phase; calculated values for nominal composition are for comparison.

	$(\text{SnTe})_{0.75}(\text{In}_2\text{Te}_3)_{0.75}$			$(\text{SnTe})_{1.2}(\text{In}_2\text{Te}_3)_{0.6}$			$(\text{SnTe})_{1.875}(\text{In}_2\text{Te}_3)_{0.375}$		
	Sn rich	In rich	calc.	Sn rich	In rich	calc.	Sn rich	In rich	calc.
In	20.8(6)	31.1(9)	28.6	21.5(3)	23.3(2)	22.2	6.8(8)	30(6)	13.3
Sn	24.9(8)	11.0(9)	14.3	23.9(1)	20.7(1)	22.2	43(2)	6(3)	33.3
Te	54.2(2)	57.9(3)	57.1	54.5(2)	56.0(2)	55.6	50(1)	66(5)	53.3

Note that uncertainties may be due to the dimensions of SEM-EDX measurement points that may to some extent be averaged measurements of both phases (e.g. nanoprecipitates in matrix with other composition).

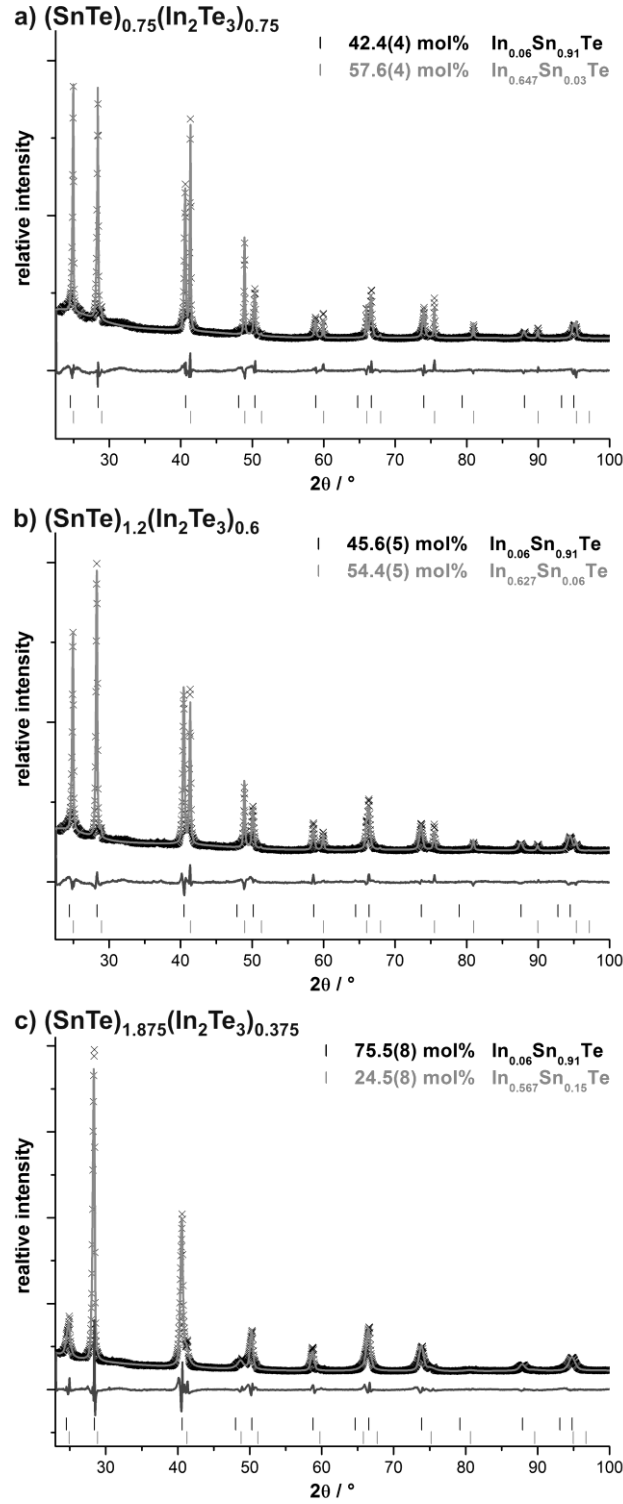


Figure S7: Tentative Rietveld refinement results for quenched samples with nominal composition $(\text{SnTe})_{0.75}(\text{In}_2\text{Te}_3)_{0.75}$ (a), $(\text{SnTe})_{1.2}(\text{In}_2\text{Te}_3)_{0.6}$ (b) and $(\text{SnTe})_{1.875}(\text{In}_2\text{Te}_3)_{0.375}$ (c); experimental data (black), calculated pattern (light gray), difference plot (dark gray, below) and calculated reflection positions of the different phases (thin black and gray vertical lines, bottom); phase fractions determined by Rietveld refinement are given in mol% (note that Rietveld programs initially yield weight%). Note that the quantification was not calibrated and also depends on the compositions assumed for the individual phases – it is therefore just a rough estimate.

Table S8: Details of the Rietveld refinements for quenched samples with nominal composition $(\text{SnTe})_{0.75}(\text{In}_2\text{Te}_3)_{0.75}$, $(\text{SnTe})_{1.2}(\text{In}_2\text{Te}_3)_{0.6}$ and $(\text{SnTe})_{1.875}(\text{In}_2\text{Te}_3)_{0.375}$. Phase compositions were estimated from EDX and take into account charge neutrality and overall sample composition.

nominal composition	$(\text{SnTe})_{0.75}(\text{In}_2\text{Te}_3)_{0.75}$		$(\text{SnTe})_{1.2}(\text{In}_2\text{Te}_3)_{0.6}$		$(\text{SnTe})_{1.875}(\text{In}_2\text{Te}_3)_{0.375}$	
phase composition	$\text{In}_{0.27}\text{Sn}_{0.6}\text{Te}$	$\text{In}_{0.573}\text{Sn}_{0.133}\text{Te}$	$\text{In}_{0.167}\text{Sn}_{0.75}\text{Te}$	$\text{In}_{0.555}\text{Sn}_{0.167}\text{Te}$	$\text{In}_{0.033}\text{Sn}_{0.95}\text{Te}$	$\text{In}_{0.612}\text{Sn}_{0.083}\text{Te}$
M / g mol ⁻¹	242.515	205.450	242.515	206.715	242.515	210.509
space group (no.)	$Fm\bar{3}m$ (225)	$F\bar{4}3m$ (216)	$Fm\bar{3}m$ (225)	$F\bar{4}3m$ (216)	$Fm\bar{3}m$ (225)	$F\bar{4}3m$ (216)
phase fraction / mol%	42.4(4)	57.6(4)	45.6(5)	54.4(5)	75.5(8)	24.5(8)
formula per unit cell	4	4	4	4	4	4
lattice parameter / Å	6.2684(2)	6.1631(2)	6.2936(2)	6.1632(2)	6.2784(4)	6.185(1)
cell volume / Å ³	246.30(2)	234.10(2)	249.28(2)	234.11(2)	247.48(5)	236.6(1)
X-ray density / g cm ⁻³	6.5400(6)	5.8292(4)	6.4619(6)	5.8650(6)	6.5509(1)	5.909(4)
μ / mm ⁻¹	168.44(2)	149.14(1)	166.42(2)	150.10(1)	167.63(3)	1451.35(9)
reflections	13	13	13	13	13	13
parameters / thereof background	26 / 12		26 / 12		27 / 12	
R_p / R_{wp} / GooF	0.0232 / 0.0319 / 3.706		0.0218 / 0.0300 / 3.371		0.0317 / 0.0512 / 6.370	
R_{Bragg}	0.0206	0.0183	0.0149	0.0225	0.0093	0.0133

Table S9: Atomic coordinates, site occupancies based on the decomposition reaction equations (charge neutrality, EDX, overall composition) and isotropic displacement parameters for nominal compositions $(\text{SnTe})_{0.75}(\text{In}_2\text{Te}_3)_{0.75}$ (top), $(\text{SnTe})_{1.2}(\text{In}_2\text{Te}_3)_{0.6}$ (middle) and $(\text{SnTe})_{1.875}(\text{In}_2\text{Te}_3)_{0.375}$ (bottom).

phase (structure type)	atom position	x y z	Wyckoff position	s.o.f.	B_{iso}
$\text{In}_{0.27}\text{Sn}_{0.6}\text{Te}$ (NaCl)	In/Sn/ \square Te	$\frac{1}{2} \frac{1}{2} \frac{1}{2}$ 0 0 0	4b 4a	0.06/0.91/0.03 1	0.76(6) = B_{iso} (cation)
$\text{In}_{0.573}\text{Sn}_{0.133}\text{Te}$ (sphalerite)	In/Sn/ \square Te	$\frac{1}{4} \frac{1}{4} \frac{1}{4}$ 0 0 0	4c 4a	0.647/0.03/0.323 1	2.7(1) = B_{iso} (cation)
$\text{In}_{0.167}\text{Sn}_{0.75}\text{Te}$ (NaCl)	In/Sn/ \square Te	$\frac{1}{2} \frac{1}{2} \frac{1}{2}$ 0 0 0	4b 4a	0.06/0.91/0.03 1	0.78(6) = B_{iso} (cation)
$\text{In}_{0.555}\text{Sn}_{0.167}\text{Te}$ (sphalerite)	In/Sn/ \square Te	$\frac{1}{4} \frac{1}{4} \frac{1}{4}$ 0 0 0	4c 4a	0.627/0.06/0.313 1	2.6(1) = B_{iso} (cation)
$\text{In}_{0.033}\text{Sn}_{0.95}\text{Te}$ (NaCl)	In/Sn/ \square Te	$\frac{1}{2} \frac{1}{2} \frac{1}{2}$ 0 0 0	4b 4a	0.06/0.91/0.03 1	0.90(9) = B_{iso} (cation)
$\text{In}_{0.612}\text{Sn}_{0.083}\text{Te}$ (sphalerite)	In/Sn/ \square Te	$\frac{1}{4} \frac{1}{4} \frac{1}{4}$ 0 0 0	4c 4a	0.567/0.15/0.283 1	0.9(4) = B_{iso} (cation)

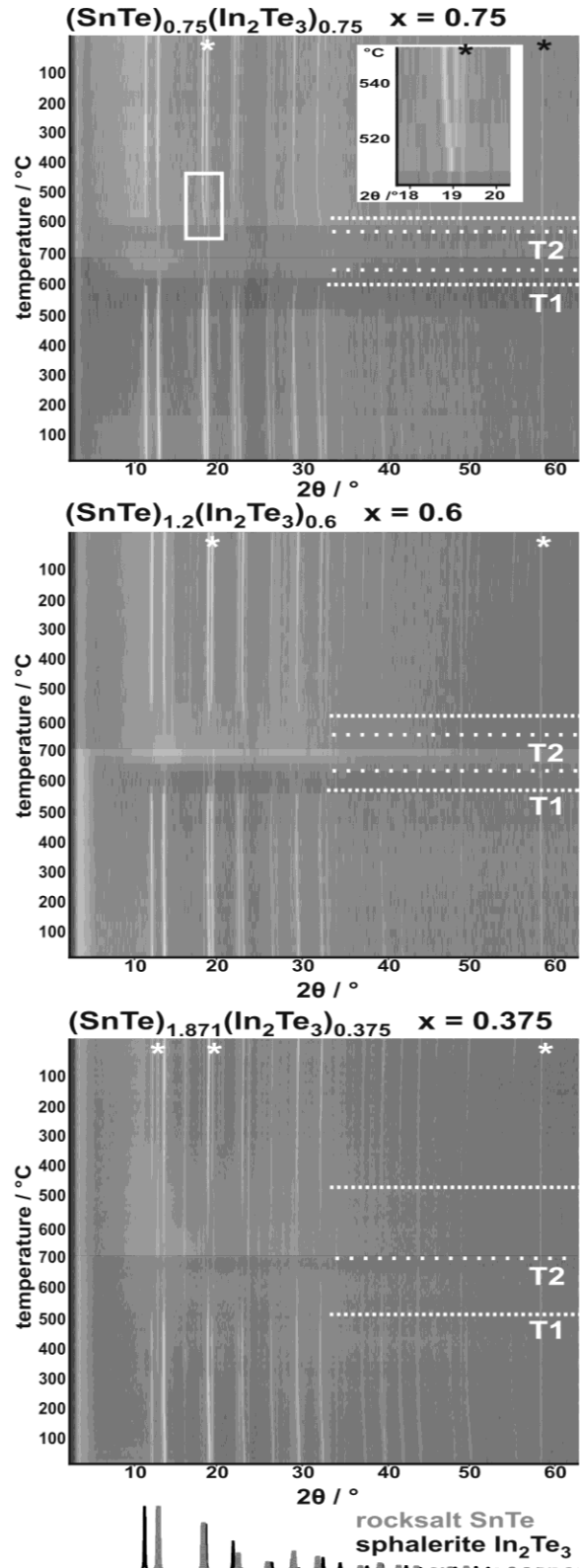


Figure S10: Temperature-dependent PXRD patterns (asterisks mark reflections caused by the furnace) of quenched $(\text{SnTe})_{0.75}(\text{In}_2\text{Te}_3)_{0.75}$ (top), $(\text{SnTe})_{1.2}(\text{In}_2\text{Te}_3)_{0.6}$ (middle) and $(\text{SnTe})_{1.875}(\text{In}_2\text{Te}_3)_{0.375}$ (bottom); heating and cooling (from bottom to middle and middle to top, respectively, in each image), the horizontal line as T1 marks the dissolution of the In-rich sphalerite-type phase in the main phase, the line at T2 marks the melting point; reduced number of intensities of certain reflections during cooling results from preferred orientation after recrystallization in small capillaries.

Table S11: Approximate temperatures where reflections matching the different structure types disappear as a consequence of dissolution (or exsolution during cooling) of the In-rich sphalerite-type phase or because of melting of the whole sample. Temperatures can be correlated with T1 and T2 in Figures 2 and S10.

nominal composition	T2 (melting point)	T1 dissolution / exsolution of the In-rich phase
$(\text{SnTe})_{0.75}(\text{In}_2\text{Te}_3)_{0.75}$	650 °C	580 °C
$(\text{SnTe})_{1.2}(\text{In}_2\text{Te}_3)_{0.6}$	680 °C	580 °C
$(\text{SnTe})_{1.875}(\text{In}_2\text{Te}_3)_{0.375}$	700 °C	540 °C
$(\text{SnTe})_{2.1}(\text{In}_2\text{Te}_3)_{0.3}$	700 °C	560 °C
$(\text{SnTe})_{2.4}(\text{In}_2\text{Te}_3)_{0.2}$	> 700 °C *	500 °C
$(\text{SnTe})_{2.59}(\text{In}_2\text{Te}_3)_{0.136}$	> 700 °C *	420 °C

* experiment carried out up to 700 °C, where the melting point was not yet reached.

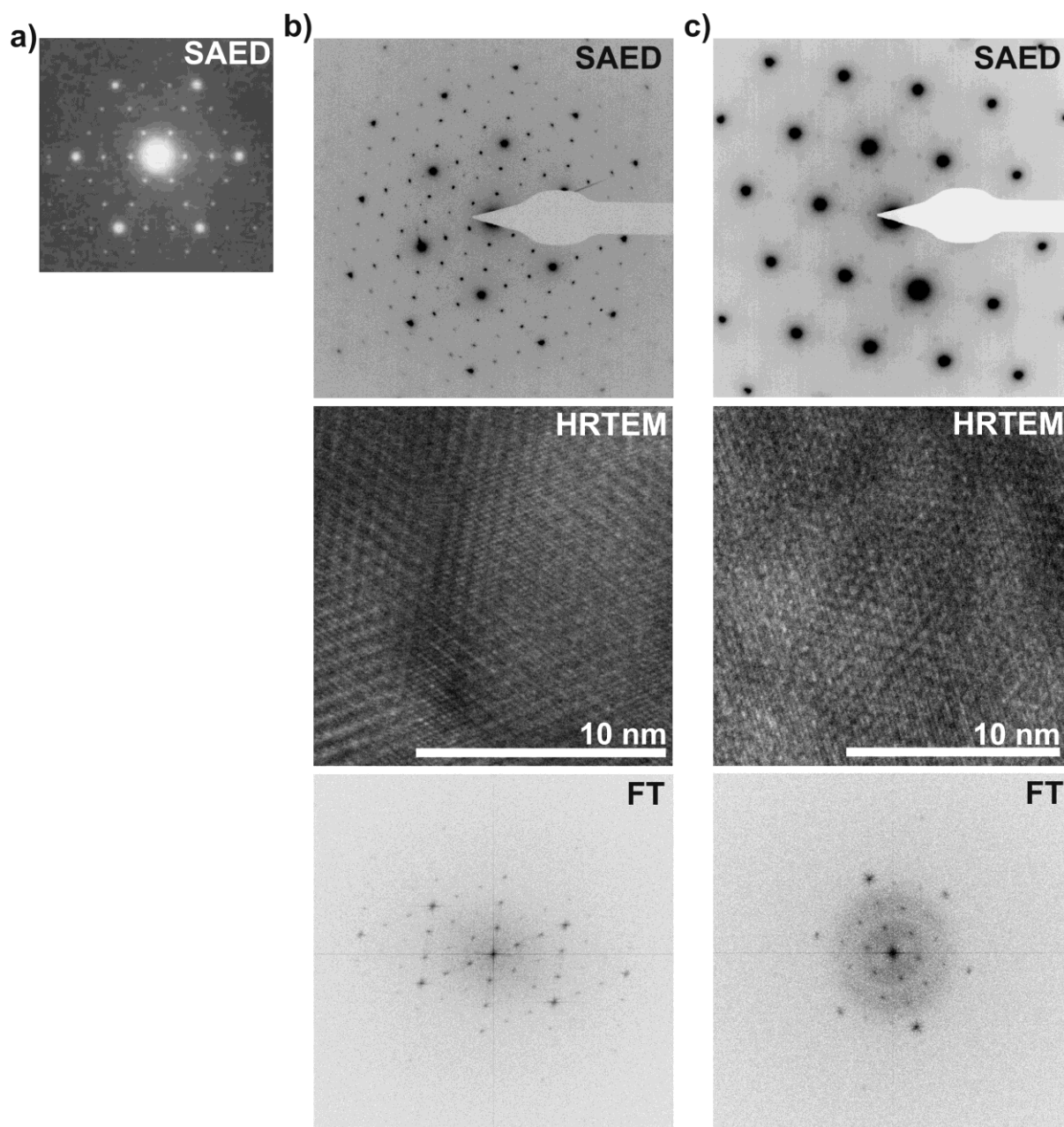


Figure S12: a) Electron diffraction pattern of “hypo-stoichiometric” cubic α -In₂Te₃-II (space group $F\bar{4}3m$, $a = 18.50$ Å, taken from G. L. Bleris, T. Karakostas, J. Stoemenos, N. A. Economou, *Phys. Stat. Sol. A* **1976**, 34, 243, a superstructure of defect sphalerite-type β -In₂Te₃ (R. R. Desai, D. Lakshminarayana, P. B. Patel, P. K. Patel, C. J. Panchal, *Mater. Chem. Phys.* **2005**, 94, 308; b) SAED and HRTEM images of In-rich precipitates in (SnTe)_{2.1}(In₂Te₃)_{0.3} along [111] with corresponding Fourier transforms, showing superstructure reflections similar to those of α -In₂Te₃-II; c) SAED and HRTEM images of precipitates with lower In content in (SnTe)_{2.4}(In₂Te₃)_{0.2} along [111] with corresponding Fourier transforms, showing very weak superstructure reflections whose positions correspond to those of α -In₂Te₃-II.

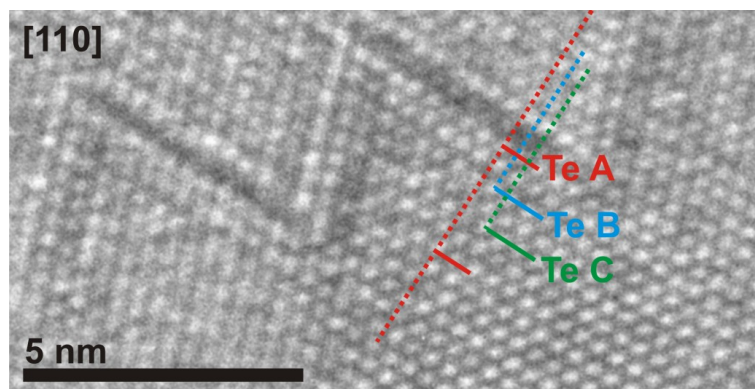


Figure S13: HRTEM image along [110] showing cubic ABC stacking sequence (highlighted by red, green and blue) of the Te-atom in slowly cooled $(\text{SnTe})_{2.4}(\text{In}_2\text{Te}_3)_{0.2}$.

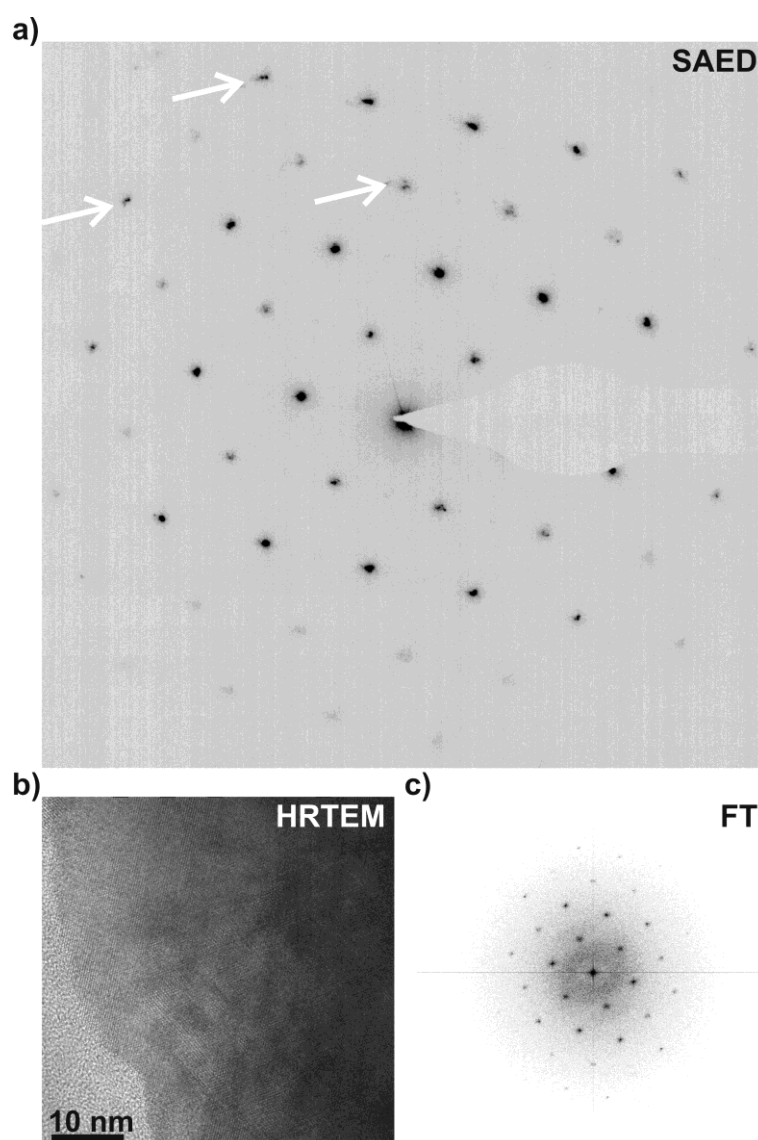


Figure S14: Slowly cooled $(\text{SnTe})_{2.1}(\text{In}_2\text{Te}_3)_{0.3}$ viewed along [110]: a) SAED pattern of a region with two intergrown domains showing reflection splitting at higher diffraction angles (highlighted with white arrows). b) HRTEM micrograph of same region with c) corresponding Fourier transform showing broad reflections due to simultaneous presence of rocksalt-type and sphalerite-type phases.

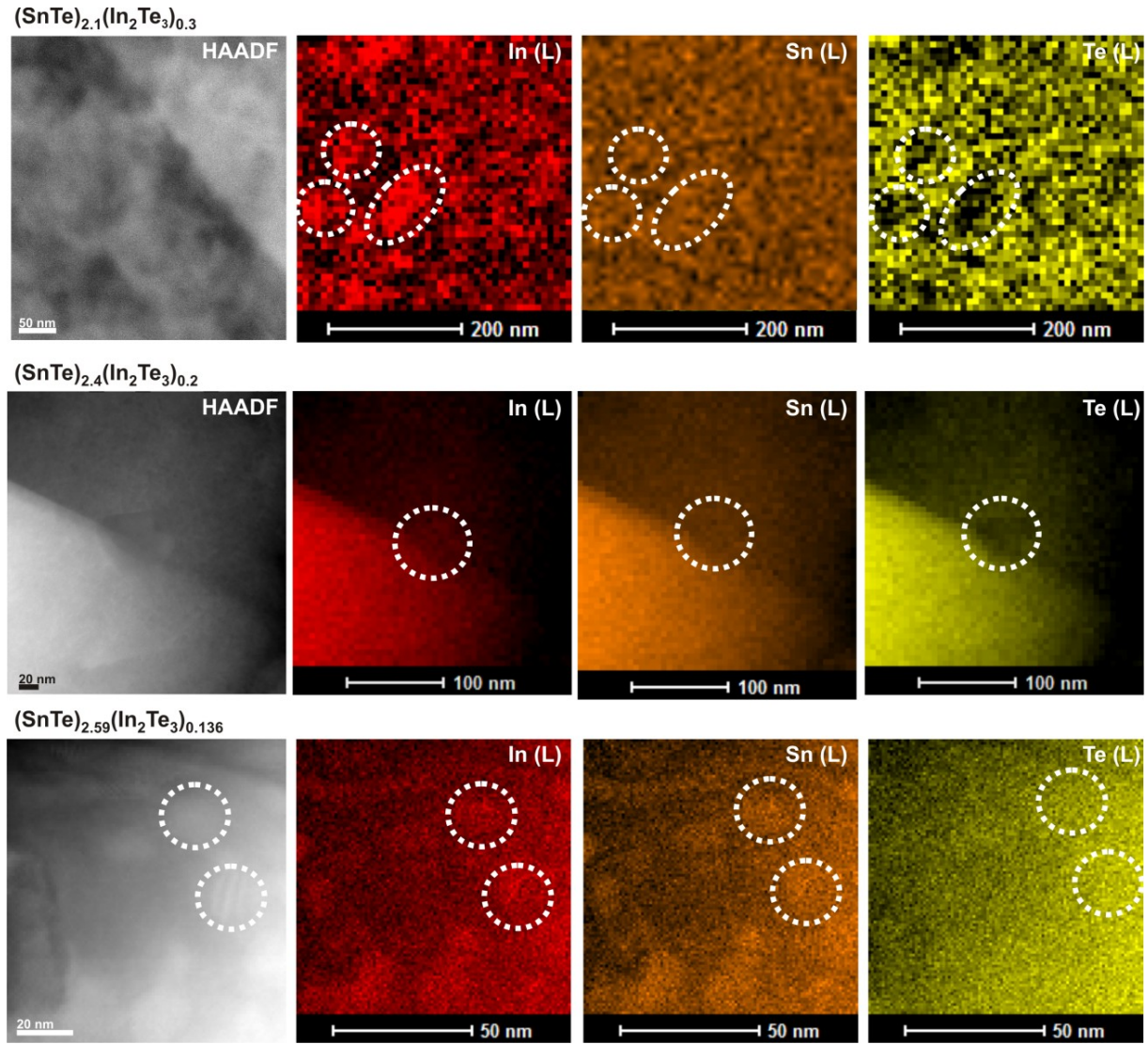


Figure S15: STEM-EDX mapping of representative crystals in slowly cooled $(\text{SnTe})_{3-3x}(\text{In}_2\text{Te}_3)_x$ with $0.136 \leq x \leq 0.3$; from the left to the right: HAADF image, In(L), Sn(L) and Te(L) EDX maps. Dotted circles are in the same place in all images for easier comparison.

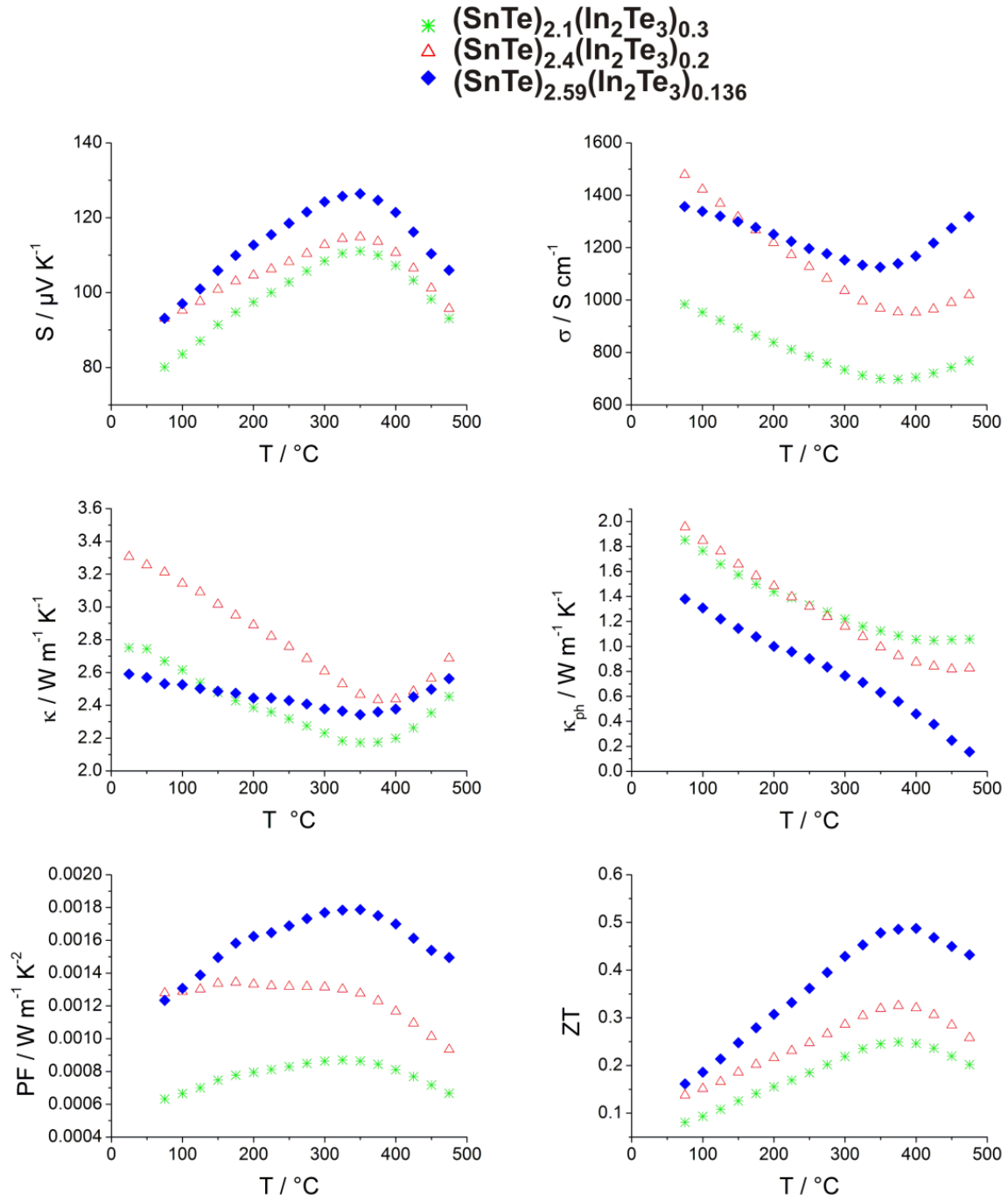


Figure S16: Averaged thermoelectric properties (without first heating curve) of $(\text{SnTe})_{3-3x}(\text{In}_2\text{Te}_3)_x$ with $0.136 \leq x \leq 0.3$.

Scheme S17: Calculations for the band gap estimation based on Goldsmid-Sharp relation:

- $E_g = 2eS_{\text{max}}T_{\text{max}} = 2 \cdot e \cdot 111.1 \mu\text{V K}^{-1} \cdot ((350 + 273.15) \text{ K}) = 0.138 \text{ eV}$ for $(\text{SnTe})_{2.1}(\text{In}_2\text{Te}_3)_{0.3}$
- $E_g = 2eS_{\text{max}}T_{\text{max}} = 2 \cdot e \cdot 114.8 \mu\text{V K}^{-1} \cdot ((350 + 273.15) \text{ K}) = 0.143 \text{ eV}$ for $(\text{SnTe})_{2.4}(\text{In}_2\text{Te}_3)_{0.2}$
- $E_g = 2eS_{\text{max}}T_{\text{max}} = 2 \cdot e \cdot 126.4 \mu\text{V K}^{-1} \cdot ((350 + 273.15) \text{ K}) = 0.157 \text{ eV}$ for $(\text{SnTe})_{2.59}(\text{In}_2\text{Te}_3)_{0.136}$

4.3 Structural Complexity and Thermoelectric Properties of Quaternary and Quinary Tellurides (Ge_xSn_{1-x})_{0.8}(In_ySb_{1-y})_{0.13}Te with 0 ≤ x, y ≤ 1

Lukas Neudert, Stefan Schwarzmüller, Manuel Scheel, Simon Welzmler and Oliver Oeckler

Z. Allg. Anorg. Chem. **2017**, 643, 1962.

Reprinted with permission from *Zeitschrift für anorganische und allgemeine Chemie*. Copyright 2017 Wiley Online Library.

Abstract

Starting from stoichiometric mixtures of the elements, quaternary and quinary solid solutions (Ge_xSn_{1-x})_{0.8}(In_ySb_{1-y})_{0.13}Te were obtained. Concerning the ratio Ge/Sn and Sb/In, respectively, lattice parameters of the metastable phases with rocksalt-type average structures approximately obey Vegard's law. Stable phases correspond to a disordered rocksalt type at high temperature and to trigonal layered structures with van der Waal gaps at lower temperature as shown by temperature-dependent powder X-ray diffraction combined with TEM, which reveals layer-like vacancy ordering, whose extent depends on composition and thermal treatment. In the long-periodically ordered model compounds 21R-Ge_{0.5}Sn_{0.5}InSbTe₄ and 9P-GeSnInSbTe₅ studied by resonant scattering data at K-absorption edges, Sb and Sn concentrate near the van der Waals gaps. Compared to Ge_{0.8}Sb_{0.13}Te and Sn_{0.8}Sb_{0.13}Te, the simultaneous presence of In and Sn combines increased electrical conductivity with low thermal conductivity and enhanced thermoelectric properties in certain temperature ranges. Phase transitions correlate with changes of the thermoelectric properties.

4.3.1 Introduction

Multinary tellurides exhibit various properties that lead to intriguing applications. The rapid transformation between amorphous and polycrystalline states enables information storage in phase-change RAM and optical storage media.¹⁻³ Such tellurides are semiconductors with small bandgaps, similar to thermoelectric materials that are known for the conversion of heat into electrical energy.⁴ The efficiency of thermoelectric materials can be quantified by the dimensionless Figure of merit $ZT = S^2\sigma T / (\kappa_{ph} + \kappa_e)$, where S is the Seebeck coefficient, σ is the electrical conductivity, T is the absolute temperature, and κ_{ph} and κ_e are the phononic (lattice) and electronic thermal conductivities, respectively. Since σ is correlated with κ_e via the Wiedemann-Franz law, these physical properties cannot be changed independently in order to optimize the ZT value. Simple binary chalcogenides like SnSe, PbTe, Bi₂Te₃, or copper selenides as well as complex compounds like clathrates,

$(\text{AgSbTe}_2)_x(\text{GeTe})_{1-x}$ (TAGS) or nanostructured tellurides such as $\text{AgPb}_m\text{SbTe}_{2+m}$ (LAST) exhibit good thermoelectric performance.⁵⁻¹² Structural complexity in compounds with simple basic structures may therefore be attractive concerning the targeted improvement of thermoelectric materials.¹³ Starting from the binary compounds GeTe , SnTe , In_2Te_3 , and Sb_2Te_3 , each possessing its individual advantages, combinations of them yield a wide range of possible thermoelectric materials with different levels of structural complexity.¹⁴⁻²⁰ As structure-property relations of germanium antimony tellurides (GST materials) have been investigated in much detail,^{18,21,22} the latter can serve as a ternary reference system. Figure 1 outlines examples for possible quaternary and quinary compounds of Ge, In, Sb, and Sn applied to a fixed cation to Te ratio. This selection ensures comparability to previous studies of Sn- or In-containing tellurides.^{23,24}

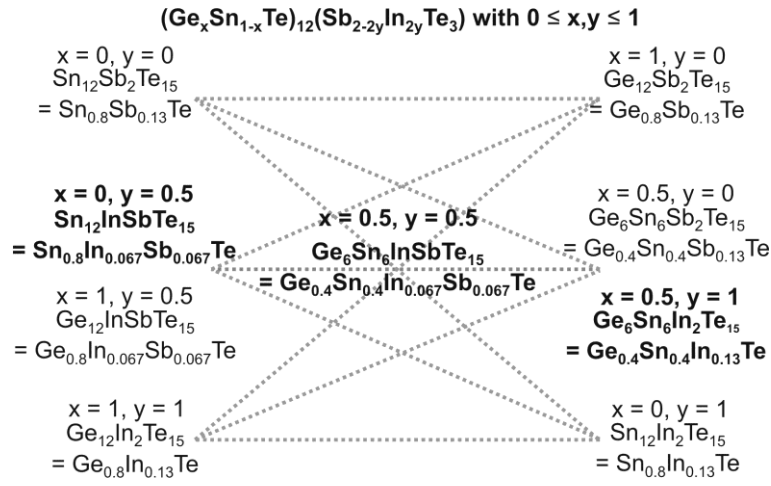


Figure 1. Scheme of a set of possible quaternary and quinary tellurides of Ge, In, Sb, and Sn with the same molar Te content based on the general formula $(\text{Ge}_x\text{Sn}_{1-x})_{0.8}(\text{In}_y\text{Sb}_{1-y})_{0.13}\text{Te}$. Phases investigated in this contribution are highlighted in bold typeface, the others are known from literature. As all samples in this contribution exhibit rocksalt-type structures, the general sum formula $(\text{Ge}_x\text{Sn}_{1-x}\text{Te})_{12}(\text{In}_{2y}\text{Sb}_{2-2y}\text{Te}_3)$ is normalized to $(\text{Ge}_x\text{Sn}_{1-x})_{0.8}(\text{In}_y\text{Sb}_{1-y})_{0.13}\text{Te}$, both with $0 \leq x, y \leq 1$.

he different charges of Ge^{2+} and Sb^{3+} lead to vacancies on the cation position. Quenching the disordered rocksalt-type high-temperature (HT) phase of GST materials leads to a metastable pseudo-cubic phase with short-range vacancy ordering. Depending on temperature, stable trigonal structures, e.g. In_3Te_4 -type ones with van der Waals gaps, are slowly formed from the pseudocubic phases.^{25,26} In addition, distorted variants of the rocksalt type have been described.^{3,27} Both composition and thermal treatment influence the thermoelectric properties of these tellurides. There are three approaches towards their optimization: (1) substitution (alloying) or co-doping,^{24,28,29} (2) inducing pronounced real structures based on vacancy ordering by “partial” diffusion-controlled phase transitions^{18,30} and (3) heterostructuring by segregation of precipitates with different composition in a GST matrix.³¹ Compared to $\text{Ge}_{0.8}\text{Sb}_{0.13}\text{Te}$, the compounds $\text{Ge}_{0.8}\text{In}_{0.067}\text{Sb}_{0.067}\text{Te}$ and

$\text{Ge}_{0.8}\text{In}_{0.13}\text{Te}$ (where vacancy ordering is little influenced by the In content) show that the substitution of Sb by In correlates with an increased Seebeck coefficient, improving ZT at temperatures below 250 °C.²⁴ On the other hand, Sn-containing GST materials such as $\text{Ge}_{0.4}\text{Sn}_{0.4}\text{Sb}_{0.13}\text{Te}$ and $\text{Sn}_{0.8}\text{Sb}_{0.13}\text{Te}$ show higher electrical conductivity and more pronounced vacancy ordering than pristine GST phases.²³ For $\text{Ge}_{3.25}\text{Sn}_{1.1}\text{Sb}_{1.1}\text{Te}_6$, a superstructure of the rocksalt type was observed.³² In contrast, samples with the composition $\text{Sn}_{0.8}\text{In}_{0.13}\text{Te}$ consist of an In-doped SnTe matrix and In-rich precipitates; they are characterized by low thermal conductivity ($2.5 \text{ W m}^{-1} \text{ K}^{-1}$ at ca. 400 °C).³³ Syntheses of quinary samples like $\text{Ge}_{0.4}\text{Sn}_{0.4}\text{In}_{0.067}\text{Sb}_{0.067}\text{Te}$ (normalized to Te_1) address the question how higher complexity correlates with structural effects and changes of thermoelectric properties; and they promise to afford intriguing samples for transmission electron microscopy (TEM). Due to the lacking scattering contrast of Sn, In, and Sb in conventional diffraction experiments, resonant X-ray scattering is required in order to elucidate the element distribution.³⁴ This can be applied to long-range ordered layered compounds. From such results, it is possible to draw conclusions regarding the element distribution around vacancy layers in disordered compounds. Therefore, the elemental distribution in the long-periodically ordered layered phases GeSnInSbTe_5 and $\text{Ge}_{0.5}\text{Sn}_{0.5}\text{InSbTe}_4$ was elucidated. This contribution focuses on structure-property relations of quaternary and quinary tellurides with the general composition $(\text{Ge}_x\text{Sn}_{1-x})_{0.8}(\text{In}_y\text{Sb}_{1-y})_{0.13}\text{Te}$. For comparison, quinary phases with higher vacancy concentration are also evaluated ($\text{Ge}_{0.286}\text{Sn}_{0.286}\text{In}_{0.143}\text{Sb}_{0.143}\text{Te}$ and $\text{Ge}_{0.35}\text{Sn}_{0.35}\text{In}_{0.1}\text{Sb}_{0.1}\text{Te}$).

4.3.2 Results and Discussion

4.3.2.1 Sample characterization and average crystal structures

All metallic gray products discussed in this contribution were obtained in quantitative yield and powder X-ray diffraction (PXRD) patterns confirm homogeneity. Energy-dispersive X-ray spectroscopy (EDX, cf. Table S1, Supporting Information) is consistent with the composition of the stoichiometric mixtures of starting materials. Rietveld refinements confirm a rocksalt-type average structure (at RT) for air-cooled samples of $\text{Ge}_{0.4}\text{Sn}_{0.4}\text{In}_{0.13}\text{Te}$, $\text{Sn}_{0.8}\text{In}_{0.067}\text{Sb}_{0.067}\text{Te}$, and $\text{Ge}_{0.4}\text{Sn}_{0.4}\text{In}_{0.067}\text{Sb}_{0.067}\text{Te}$ (Figure 2, Tables S2 and S3, Supporting Information). Rietveld refinements for further cubic samples (see below) are shown in Figure S4, Table S5, and Table S6 (Supporting Information). The predominantly Lorentz-shaped reflections are affected by anisotropic microstrain. For solid solution series $(\text{Ge}_x\text{Sn}_{1-x})_{0.8}(\text{In}_y\text{Sb}_{1-y})_{0.13}\text{Te}$, cubic lattice parameters a change approximately in accordance with Vegard's law (Figure S7, Supporting Information). With increasing Sn content, a increases while with increasing In content it decreases, however, less pronounced due to the relatively small difference in ionic radii (In^{3+} vs. Sb^{3+}) and low total In/Sb content.³⁵

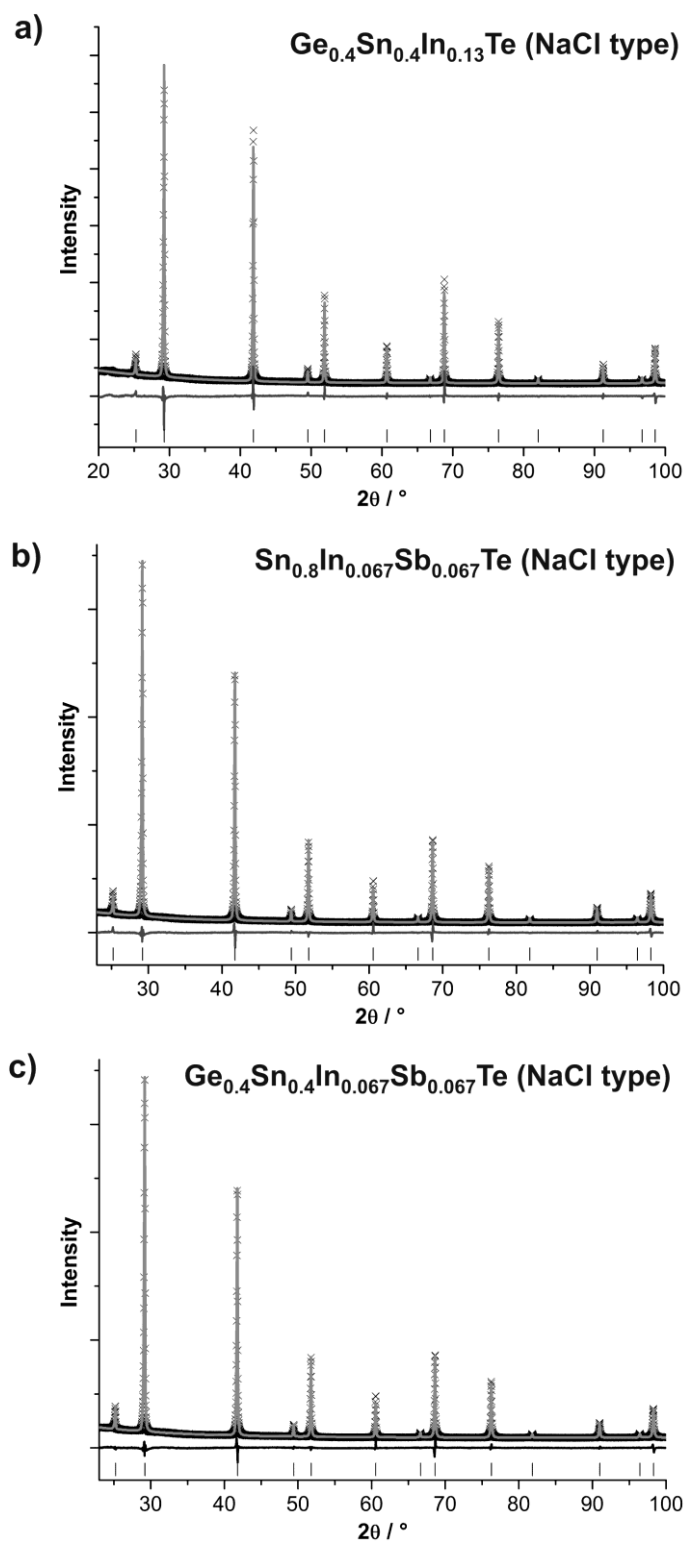


Figure 2. Profile fits of the Rietveld refinements based on X-ray diffraction patterns of $\text{Ge}_{0.4}\text{Sn}_{0.4}\text{In}_{0.13}\text{Te}$ (a), $\text{Sn}_{0.8}\text{In}_{0.067}\text{Sb}_{0.067}\text{Te}$ (b), and $\text{Ge}_{0.4}\text{Sn}_{0.4}\text{In}_{0.067}\text{Sb}_{0.067}\text{Te}$ (c) cooled to air; experimental data (black), calculated pattern (light gray), difference plot (dark gray), and calculated reflection positions (black vertical lines).

Pronounced layer-like defect ordering and a tendency towards superstructures becomes evident with increasing vacancy concentrations as illustrated for $\text{Ge}_{0.35}\text{Sn}_{0.35}\text{In}_{0.1}\text{Sb}_{0.1}\text{Te}$ and more clearly on

$\text{Ge}_{0.286}\text{Sn}_{0.286}\text{In}_{0.143}\text{Sb}_{0.143}\text{Te}$ by selected area electron diffraction (SAED) and high resolution transmission electron microscopy (HRTEM). “Comet-like” diffuse streaks observed in SAED patterns and Fourier transforms of HRTEM micrographs (Figure S8, Supporting Information) of quenched $\text{Ge}_{0.35}\text{Sn}_{0.35}\text{In}_{0.1}\text{Sb}_{0.1}\text{Te}$ can be explained by a pseudocubic domain structure with a non equidistant arrangement of finite vacancy layers.³⁶ HRTEM images of quenched $\text{Ge}_{0.286}\text{Sn}_{0.286}\text{In}_{0.143}\text{Sb}_{0.143}\text{Te}$ reveal some layered domains (size < 100 nm) with vacancy ordering (Figure 3). Occasionally, this corresponds to a fivefold superstructure of the rocksalt type along one of its $\langle 111 \rangle$ directions comparable to those of $\text{Ge}_3\text{MnSb}_2\text{Te}_7$ ³⁷ and $\text{Ge}_{3.25}\text{Sn}_{1.1}\text{Sb}_{1.1}\text{Te}_6$,³² in this case with three slabs along the trigonal axis to reach identity. According to HRTEM images (Figure S9d, Supporting Information), Te atoms retain their “cubic” ABC stacking sequence. This corresponds to a rhombohedral lattice with $a \approx 4.268 \text{ \AA}$ and $c \approx 52.3 \text{ \AA}$ (for details and coordinates, cf. Figures S9 and S10, Supporting Information). In this structure, one slab consists of five anion and four cation layers separated by a vacancy layer, the space group is $R\bar{3}m$. A simulated SAED patterns assuming the superposition of twin domains corresponds to the experimental one. Yet, most ordered domains in $\text{Ge}_{0.286}\text{Sn}_{0.286}\text{In}_{0.143}\text{Sb}_{0.143}\text{Te}$ are very small, so that PXRD patterns exhibit only very weak reflections that can be attributed to the layered structure (Figure S11, Supporting Information).

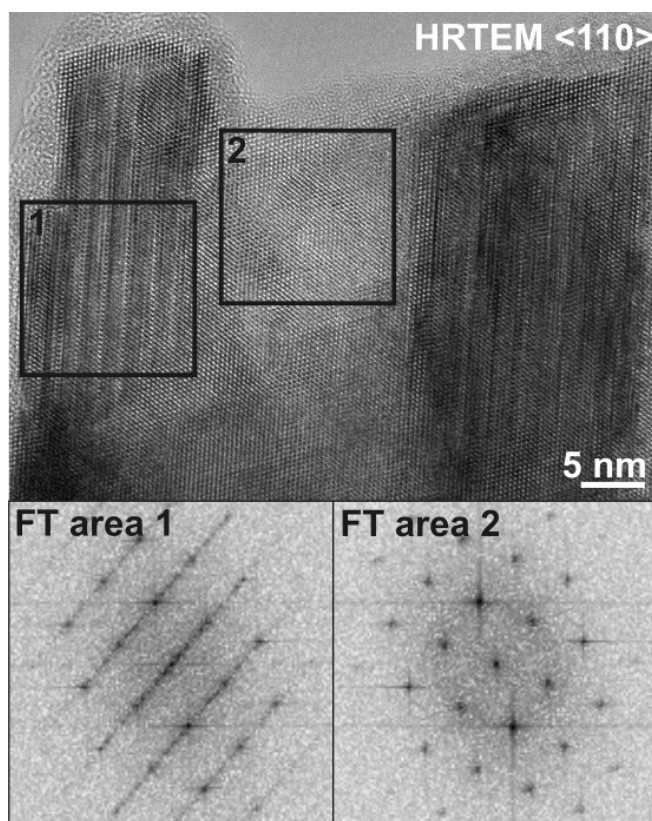


Figure 3. HRTEM image and corresponding Fourier transforms of the marked areas of quenched $\text{Ge}_{0.286}\text{Sn}_{0.286}\text{In}_{0.143}\text{Sb}_{0.143}\text{Te}$ along $\langle 110 \rangle$ zone axis (with respect to pseudocubic modification), areas with layered and rocksalt structures labelled with 1 and 2, respectively.

4.3.2.2 Element distribution in quinary phases with layered structures determined by resonant X-ray diffraction

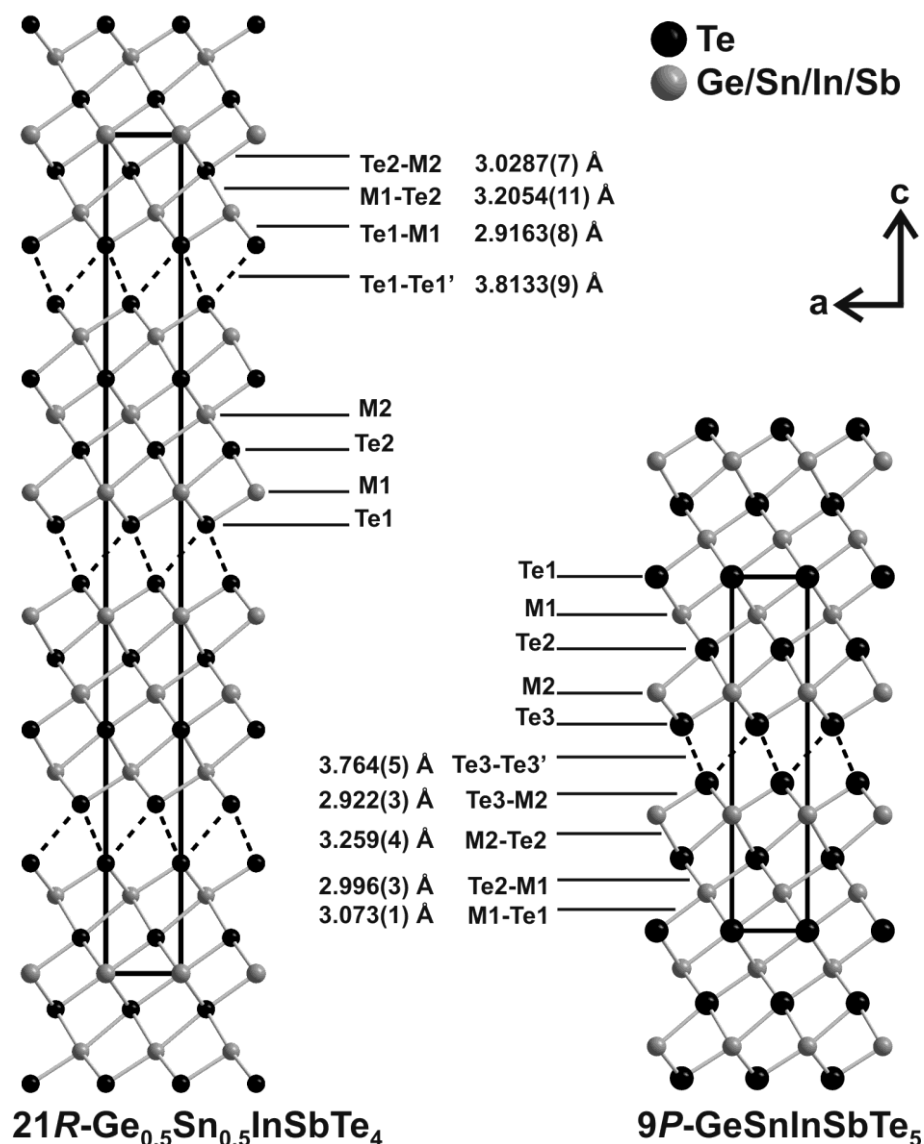


Figure 4. Crystal structures of $\text{Ge}_{0.5}\text{Sn}_{0.5}\text{InSbTe}_4$ and GeSnInSbTe_5 with selected interatomic distances.

Problems with low scattering contrast of In/Sn/Sb/Te were overcome by using anomalous dispersion in order to elucidate the cation distribution in the long-periodically ordered layered tellurides $\text{Ge}_{0.5}\text{Sn}_{0.5}\text{InSbTe}_4$ and GeSnInSbTe_5 . Powder data collected slightly at the low-energy side of the *K*-absorption edges of In, Sn, Sb, and Te were combined with an off-edge dataset in joint Rietveld refinements (cf. Experimental Section). No anti-site disorder was taken into account and for the anion positions full occupancy with Te was assumed. Results of the refinements are provided in Figure 4, Figures S12 and S13 (Supporting Information) as well as in Table 1, Table 2, Table 3, and Table S14 (Supporting Information). Further details of the structure determinations are available from Fachinformationszentrum Karlsruhe, D-76344 Eggenstein-Leopoldshafen (Germany), on quoting

the depository numbers CSD-433534 (21R-Ge_{0.5}Sn_{0.5}InSbTe₄) and CSD-433533 (9P-GeSnInSbTe₅) as well as the names of the authors and citation of the paper (E-mail: crysdata@fiz-karlsruhe.de).

Table 1. Crystallographic data and details of the joint Rietveld refinement (patterns recorded at different wavelengths near absorption edges) for annealed 21R- Ge_{0.5}Sn_{0.5}InSbTe₄.

21R-Ge _{0.5} Sn _{0.5} InSbTe ₄						
M / g mol⁻¹	842.650					
space group	$R\bar{3}m$ (no. 166)					
Z	3					
lattice parameters / Å	$a = 4.25141(11)$ $c = 41.2224(12)$					
cell volume / Å³	645.25(4)					
X-ray density / gcm⁻³	6.5055(4)					
F(000)	1047					
parameters / thereof background	189 / 120 (24 for each dataset)					
wavelength / Å	all data	0.354198(9) ^[a]	0.389706(1)	0.406596(1)	0.424565(1)	0.443690(1)
		off edge	Te-K edge	Sb-K edge	Sn-K edge	In-K edge
reflections	1786	344	366	350	359	367
μ / in mm⁻¹	-	1927.8(1)	2343.8(1)	1243.69(7)	1064.12(6)	1055.82(6)
R_p	0.0476	0.0471	0.0385	0.0508	0.0499	0.0505
R_{wp}	0.0678	0.0634	0.0571	0.0730	0.0702	0.0711
Goof	2.369	1.831	2.036	2.723	2.712	2.323
R_{Bragg}	-	0.0124	0.0151	0.0147	0.0140	0.0213

[a] e.s.d. from wavelength calibration

Table 2. Crystallographic data and details of the joint Rietveld refinement (patterns recorded at different wavelengths near absorption edges) for annealed 9P-GeSnInSbTe₅.

9P-GeSnInSbTe ₅						
M / g mol⁻¹	1065.920					
space group	$P\bar{3}m1$ (no. 164)					
Z	1					
lattice parameters / Å	$a = 4.26208(5)$ $c = 17.3730(2)$					
cell volume / Å³	273.305(7)					
X-ray density / gcm⁻³	6.4761(2)					
F(000)	442					
parameters / thereof background	215 / 120 (24 for each dataset)					
wavelength / Å	all data	0.354198(9) ^[a]	0.389807(8)	0.406685(6)	0.424694(6)	0.443820(6)
		off edge	Te-K edge	Sb-K edge	Sn-K edge	In-K edge
reflections	2350	435	469	443	462	469
μ / in mm⁻¹	-	1886.88(5)	1114.88(3)	965.08(2)	843.46(2)	723.64(2)
R_p	0.0639	0.0632	0.0600	0.0739	0.0599	0.0668
R_{wp}	0.0900	0.0935	0.0811	0.0995	0.0851	0.0937
Goof	2.019	2.338	1.445	1.853	2.473	1.833
R_{Bragg}	-	0.0228	0.0176	0.0226	0.0219	0.0188

[a] e.s.d. from wavelength calibration

Table 3. Cation site occupancy factors in 21R-Ge_{0.5}Sn_{0.5}InSbTe₄ and 9P-P-GeSnInSbTe₅; numbers without standard deviation result from sum-formula constraints (parameters not independent)

	site/ Wyck.	Ge	Sn	In	Sb
21R-	M1 / 6c	0.132(4)	0.239(9)	0.235(11)	*0.39
Ge_{0.5}Sn_{0.5}InSbTe₄	M2 / 3a	0.235	0.022	0.531	0.212
9P-	M1 / 2d	*0.37	0.09(1)	0.37(2)	0.164(8)
GeSnInSbTe₅	M2 / 2c	0.13	0.41	0.13	0.335

Ge_{0.5}Sn_{0.5}InSbTe₄ forms a 21R-In₃Te₄-type structure (space group $R\bar{3}m$) isostructural to GeSb₂Te₄, but the element distribution (Figure 4, Table 3) differs from (Ge_{1-x}Sn_x)Sb₂Te₄.³⁹ Ge²⁺ and In³⁺ predominantly concentrate in the center of the distorted rocksalt-type slabs (M2: 23.5 % Ge, and

53.1 % In), whereas Sn^{2+} and Sb^{3+} prefer the position near the van der Waals gaps (M1: 23.9 % Sn and 39.0 % Sb). The slabs are separated by van der Waals gaps with a Te–Te distance of 3.8133(9) Å, which deviates less than 3 % from the corresponding distance in isostructural tellurides.^{29,40,41} The coordination octahedron next to the van der Waals gap (M1) is strongly distorted with shorter bonds [2.9163(8) Å] to the unsaturated Te atoms and longer bonds [3.0287(7) Å] to the Te atoms within the slab. The distortion is corroborated by bond angles and lengths: Te1–M1–Te1: 93.59(3)°, M1–Te2: 3.2054(11). Bond lengths [Te2–M2: 3.0287(7) Å] and angles [Te2–M2–Te2: 89.14(2)°] of the M2 octahedrons within the slabs are more regular.

Similar to $(\text{Ge}_{1-x}\text{Sn}_x)_2\text{Sb}_2\text{Te}_5$, quinary GeSnInSbTe_5 crystallizes in the 9P-Pb₂Bi₂Se₅ structure type (space group $P\bar{3}m1$).^{39,42} The Te–Te distance at the van der Waals gaps is relatively short [3.764(5) Å], indicating typical partially covalent bonding. The distorted 3+3 coordination of M2 next to the van der Waals gap [M2–Te3 bonds 2.922(3) Å, M2–Te2 bonds 3.259(4) Å] is also typical and becomes more regular around M1 towards the middle of the slabs [M1–Te1: 3.073(1) Å]. Bond angles are a measure of the distortion of the octahedra: Te3–M2–Te3 93.64(9)°, Te2–M2–Te2 81.68(8) vs. Te2–M1–Te1 90.73(6)°, Te1–M1–Te1 87.81(3)°. Ge^{2+} and In^{3+} prefer positions inside the slabs (M2: 37 % Ge, 37 % In), whereas Sn^{2+} and Sb^{3+} concentrate near the van der Waal gap (M1: 41 % Sn, 33.5 % Sb). This element distribution might be explained by large lone-pair ions preferring the distorted octahedra.

4.3.2.3 TEM study of $(\text{Ge}_x\text{Sn}_{1-x})_{0.8}(\text{In}_y\text{Sb}_{1-y})_{0.13}\text{Te}$

amples with constant vacancy concentration (in contrast to the TEM studies above) enable to assess the influence of the various chemical compositions on real structures. Starting from ternary tellurides like GST materials, several TEM studies elucidated the influence of the chemical composition on the nanostructures. Here we address the new phases mentioned in Figure 1.^{23,24} TEM imaging on $\text{Sn}_{0.8}\text{In}_{0.067}\text{Sb}_{0.067}\text{Te}$, $\text{Ge}_{0.4}\text{Sn}_{0.4}\text{In}_{0.13}\text{Te}$, and quinary $\text{Ge}_{0.4}\text{Sn}_{0.4}\text{In}_{0.067}\text{Sb}_{0.067}\text{Te}$ shows many deviations from the average structure. Depending on the composition, nanostructures are more or less pronounced (Figure 5).

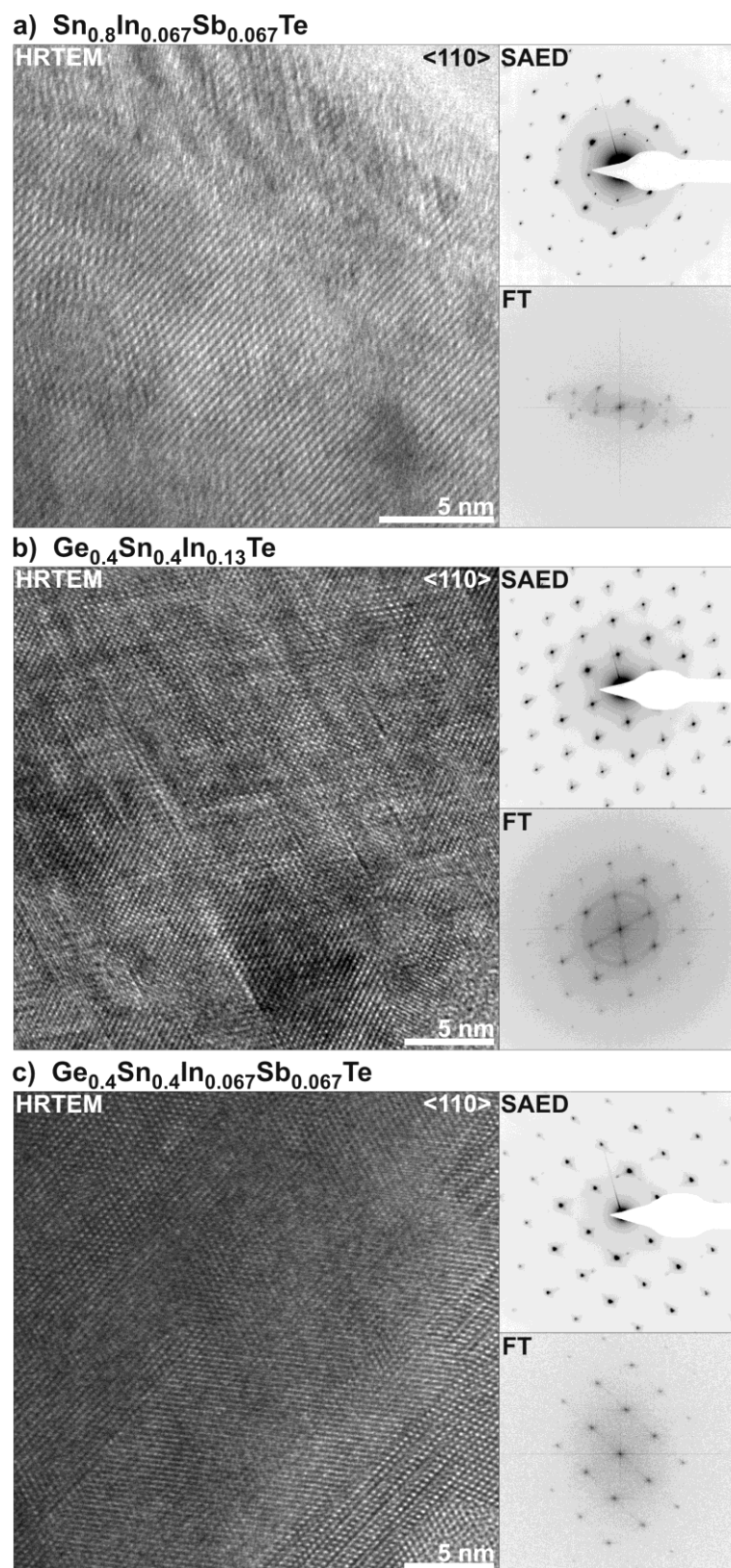


Figure 5. Representative HRTEM images of quenched (a) $\text{Sn}_{0.8}\text{In}_{0.067}\text{Sb}_{0.067}\text{Te}$, (b) $\text{Ge}_{0.4}\text{Sn}_{0.4}\text{In}_{0.13}\text{Te}$ and (c) $\text{Ge}_{0.4}\text{Sn}_{0.4}\text{In}_{0.067}\text{Sb}_{0.067}\text{Te}$ crystallites along the (pseudo)-cubic $\langle 110 \rangle$ direction with corresponding Fourier transforms and SAED patterns.

In the present element combination, high Sn content seems to impede extensive layer-like vacancy ordering, this is a certain similarity with In-doped SnTe. Vacancy layers were only locally observed in HRTEM images of $\text{Sn}_{0.8}\text{In}_{0.067}\text{Sb}_{0.067}\text{Te}$ (Figure 5a), comparable to $\text{Sn}_{0.8}\text{Sb}_{0.13}\text{Te}$ (Figure S15, Supporting Information) and $\text{Sn}_{0.8}\text{In}_{0.13}\text{Te}$,³³ diffraction patterns show almost no diffuse streaks. Similar to studies on $\text{Ge}_{0.4}\text{Sn}_{0.4}\text{Sb}_{0.13}\text{Te}$ or $\text{Ge}_{0.8}\text{In}_{0.13}\text{Te}$,^{23,24} the presence of Ge seems to facilitate the formation of irregularly spaced finite vacancy layers in $\text{Ge}_{0.4}\text{Sn}_{0.4}\text{In}_{0.13}\text{Te}$ and $\text{Ge}_{0.4}\text{Sn}_{0.4}\text{In}_{0.067}\text{Sb}_{0.067}\text{Te}$ indicated by typical “comet-shaped” diffuse streaks (Figure 5b, c). Thermal treatment also strongly influences nanostructures as exemplarily shown for $\text{Ge}_{0.4}\text{Sn}_{0.4}\text{In}_{0.067}\text{Sb}_{0.067}\text{Te}$ (Figure 6). A pronounced nanostructure is obtained after very slow cooling to room temperature (for 1 d). The observed herringbone-like arrangement of vacancy layers (Figure 6 top) is well known from $\text{Ge}_{0.8}\text{Sb}_{0.13}\text{Te}$ and $\text{Sn}_{0.8}\text{Sb}_{0.13}\text{Te}$.²³ Faster thermal treatment similar to that during thermoelectric measurements leads to less pronounced short-range defect ordering (Figure 6 bottom). Yet, PXRD patterns of differently treated samples (Figure S16, Supporting Information) are rather similar as they only represent average structures.

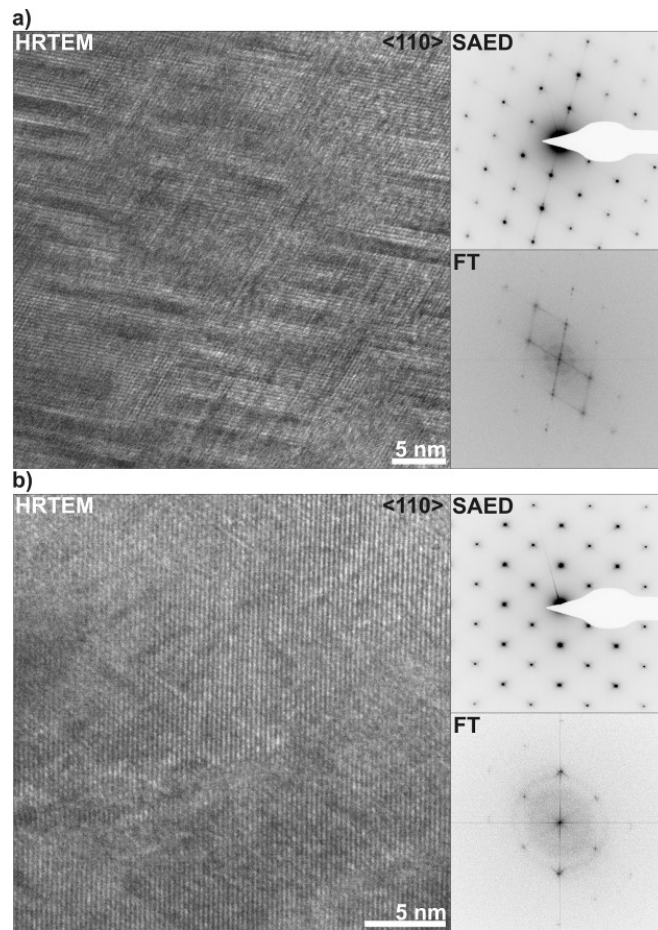


Figure 6. Representative HRTEM images with corresponding FT and SAED patterns of $\text{Ge}_{0.4}\text{Sn}_{0.4}\text{In}_{0.067}\text{Sb}_{0.067}\text{Te}$ cooled to RT within 1 d (a) and of $\text{Ge}_{0.4}\text{Sn}_{0.4}\text{In}_{0.067}\text{Sb}_{0.067}\text{Te}$ thermally treated as during thermoelectric measurements (b).

4.3.2.4 Temperature-dependent behavior and thermoelectric properties

Temperature-dependent PXRD was performed starting from quenched samples (Figure 7 bottom and Figure S17, Supporting Information). Similar to In-doped SnTe, $\text{Sn}_{0.8}\text{In}_{0.067}\text{Sb}_{0.067}\text{Te}$ exhibits no phase transitions between RT and 700 °C. In accordance with literature, phase transitions between cubic HT phases and trigonal stackings of distorted rocksalt-type slabs interconnected via van der Waals gaps were observed for the quinary phases discussed in this contribution, more pronounced for higher vacancy concentrations. A phase transition for $\text{Ge}_{0.286}\text{Sn}_{0.286}\text{In}_{0.143}\text{Sb}_{0.143}\text{Te}$ is indicated by reflection splitting, resembling the pattern of the $39R\text{-As}_2\text{Ge}_4\text{Te}_7$ structure type between 300 °C and 500 °C (Figure S18, Supporting Information). However, temperature-dependent PXRD patterns of $\text{Ge}_{0.4}\text{Sn}_{0.4}\text{In}_{0.13}\text{Te}$ and $\text{Ge}_{0.4}\text{Sn}_{0.4}\text{In}_{0.067}\text{Sb}_{0.067}\text{Te}$ show only moderate reflection broadening in the existence range of trigonal phases, suggesting only a slight trigonal distortion of the average cubic structure. Thermoelectric properties of some $(\text{Ge}_x\text{Sn}_{1-x})_{0.8}(\text{In}_y\text{Sb}_{1-y})_{0.13}\text{Te}$ phases and comparable ones are presented in Figure 7a–d. At temperatures of phase transitions, thermoelectric properties also change, visualized by temperature-dependent PXRD patterns (Figure 7e). Comparable to GST materials, temperature T1 marks the transition from the metastable pseudocubic to the trigonal layered modifications with van der Waals gaps that transform to the cubic HT phase at T2. During subsequent cooling/heating cycles, only the transition between the rocksalt-type HT phases and trigonal ones occur. In accordance with GST and Sn-containing GST,^{23,31} phase transitions have a stronger influence on thermoelectric properties at higher vacancy concentrations. Focusing on rocksalt-type structures of the quinary phases in this contribution, which exhibit more promising properties than layered ones, higher ZT values correlate with lower vacancy concentration because of the favored cubic structure. Further improvement is observed when Ge is completely substituted by Sn (Figure 7 left). The high electrical conductivity ($\sigma = 2300 \text{ S}\cdot\text{cm}^{-1}$ at 75 °C) of $\text{Sn}_{0.8}\text{In}_{0.067}\text{Sb}_{0.067}\text{Te}$ drops at HT, in contrast to nearly constant progression of σ for the other phases. With relative changes of S and κ similar to In-doped SnTe, $\text{Sn}_{0.8}\text{In}_{0.067}\text{Sb}_{0.067}\text{Te}$ shows a non-linear behavior of the ZT value with its maximum between 300 °C and 400 °C. The formation and dissolution of In-rich precipitates has been discussed in this context.³³ Regarding substitution of individual elements, the maximal Seebeck coefficient changes significantly (ca. $180 \mu\text{V}\cdot\text{K}^{-1}$ for $\text{Ge}_{0.8}\text{In}_{0.13}\text{Te}$, ca. $160 \mu\text{V}\cdot\text{K}^{-1}$ for $\text{Sn}_{0.8}\text{Sb}_{0.13}\text{Te}$, and ca. $100 \mu\text{V}\cdot\text{K}^{-1}$ for $\text{Ge}_{0.8}\text{In}_{0.067}\text{Sb}_{0.067}\text{Te}$). The low thermal conductivities of all the complex phases containing In appear promising, especially at temperatures < 300 °C. Like other cubic phases, $\text{Ge}_{0.4}\text{Sn}_{0.4}\text{In}_{0.13}\text{Te}$ and $\text{Ge}_{0.4}\text{Sn}_{0.4}\text{In}_{0.067}\text{Sb}_{0.067}\text{Te}$, show low minimal thermal conductivities of $\kappa_{\min} \approx 2.4 \text{ Wm}^{-1}\cdot\text{K}^{-1}$. For $\text{Ge}_{0.35}\text{Sn}_{0.35}\text{In}_{0.1}\text{Sb}_{0.1}\text{Te}$ and $\text{Ge}_{0.286}\text{Sn}_{0.286}\text{In}_{0.143}\text{Sb}_{0.143}\text{Te}$, a further improvement is observed. This may be due to more pronounced nanostructures. Yet, the complexity of a quinary system precludes general trends concerning the influence of a specific element on thermoelectric properties.

4.3 Structural Complexity and Thermoelectric Properties of Quaternary and Quinary Tellurides ($\text{Ge}_x\text{Sn}_{1-x}$)_{0.8}($\text{In}_y\text{Sb}_{1-y}$)_{0.13}Te with $0 \leq x, y \leq 1$

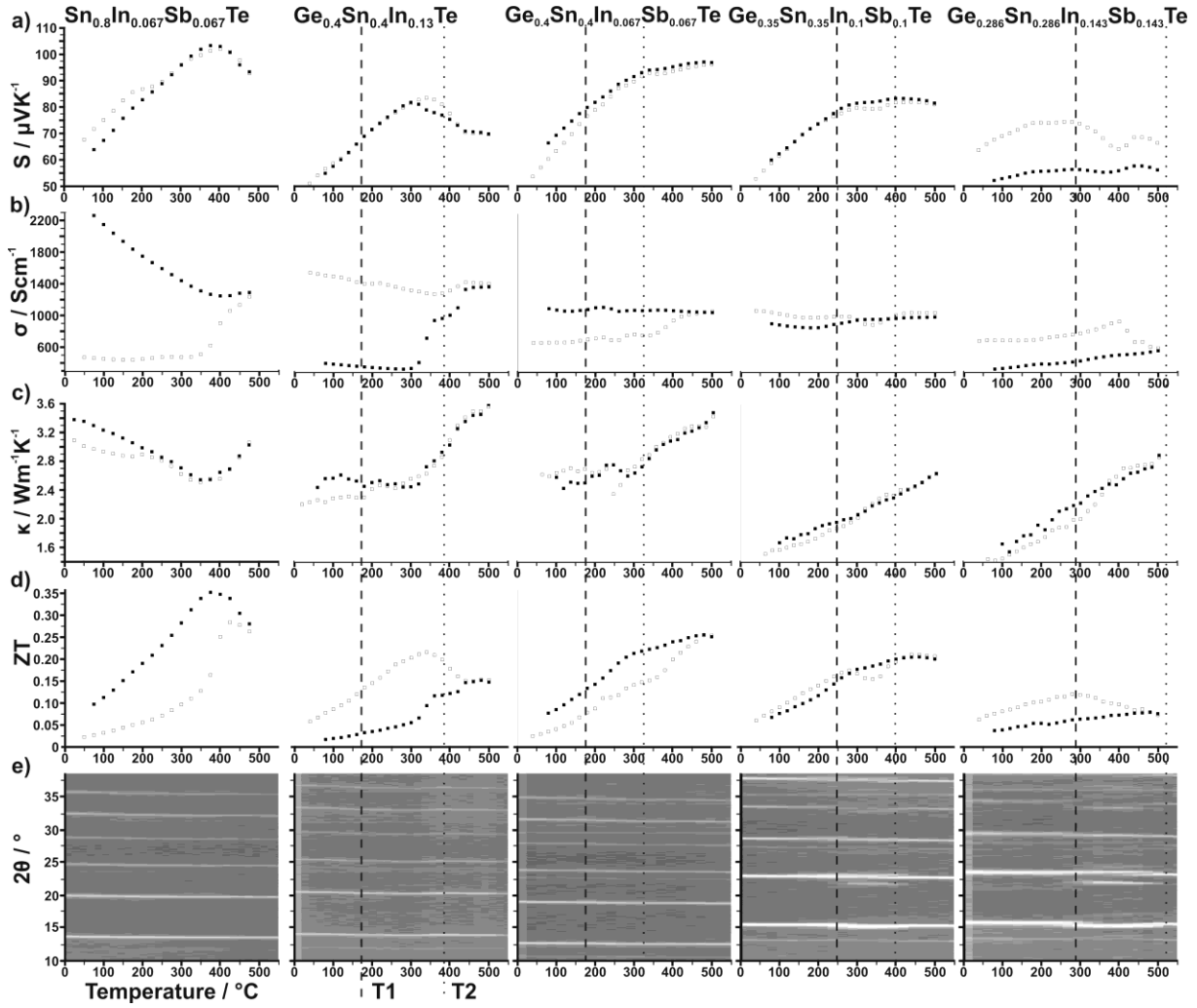


Figure 7. Thermoelectric properties, (a) Seebeck coefficient, (b) electrical conductivity, (c) thermal conductivity, and (d) ZT value of quaternary and quinary phases starting from air-quenched samples in relation to their thermal behavior; thermoelectric properties of the first heating illustrated with empty squares and averaged properties from reproducibly cycled measurements illustrated with filled black squares; (e) heating sections of the temperature-dependent PXRD data (complete temperature-dependent PXRD cf. Figure S17, Supporting Information), which correspond to the first heating curve of thermoelectric measurements; changes indicate phase transitions discussed in the text, they are marked by vertical black dashed (T1) and dotted lines (T2).

4.3.3 Conclusions

This study gives a comparison of quaternary and quinary tellurides with Ge, In, Sb, and Sn regarding their average and real structures as well as their thermoelectric properties. Phases ($\text{Ge}_x\text{Sn}_{1-x}$)_{0.8}($\text{In}_y\text{Sb}_{1-y}$)_{0.13}Te with $0 \leq x, y \leq 1$ crystallize in average rocksalt-type structures at HT and in quenched samples. TEM revealed the tendency of forming layered structures with increasing vacancy concentration. Thermal treatment similar to that applied during thermoelectric measurements enables only limited vacancy ordering at low temperatures. It results in a herringbone-like

arrangement of vacancy layers in the quinary compounds discussed. The distribution of Ge and In within the rocksalt-type slabs and of Sb and Sn near the van der Waals gaps in trigonal 21R- $\text{Ge}_{0.5}\text{Sn}_{0.5}\text{InSbTe}_4$ and 9P- GeSnInSbTe_5 structures as determined by resonant PXRD differs from the element distribution in related quaternary compounds. It is a model for the environment of finite vacancy layers in highly disordered phases. The influence of changes of the elemental ratios in quaternary and quinary phases outbalance differently pronounced nanostructures with individual distributions of vacancy layers. The simultaneous presence of In and Sn results in ZT values related to ones of In-containing GST materials. Quinary tellurides like $\text{Ge}_{0.4}\text{Sn}_{0.4}\text{In}_{0.067}\text{Sb}_{0.067}\text{Te}$ or $\text{Ge}_{0.35}\text{Sn}_{0.35}\text{In}_{0.1}\text{Sb}_{0.1}\text{Te}$ have the advantage of nearly constant electrical conductivity combined with very low thermal conductivity over a large temperature range. In order to increase the Seebeck coefficient of quinary phases, further changes in the element ratios may be a promising approach. This study, however, shows that individual aspects of material optimization cannot be simply combined in order to further improve ZT in an additive way.

4.3.4 Experimental Section

Synthesis

Samples of $(\text{Ge}_x\text{Sn}_{1-x})_{0.8}(\text{In}_y\text{Sb}_{1-y})_{0.13}\text{Te}$ were prepared by melting stoichiometric amounts of the elements (Ge: 99.99 %, Smart Elements; Sb: 99.99 %, Smart Elements; In: 99.999 %, Smart Elements; Te 99.999 %, Alpha Aesar; Sn: 99.999 %, Inconex Kft. Fémipari Budapest) in silica glass ampoules in an argon atmosphere at 900 °C for 24 h. All samples were then quenched at air, follow by annealing at 590 °C for 4 d and subsequently quenched at air for $(\text{Ge}_x\text{Sn}_{1-x})_{0.8}(\text{In}_y\text{Sb}_{1-y})_{0.13}\text{Te}$ with $0 \leq x, y \leq 1$ or in water ($\text{Ge}_{0.35}\text{Sn}_{0.35}\text{In}_{0.1}\text{Sb}_{0.1}\text{Te}$, $\text{Ge}_{0.286}\text{Sn}_{0.286}\text{In}_{0.143}\text{Sb}_{0.143}\text{Te}$). The same temperature treatment (with final quenching at air) was applied for the samples for thermoelectric characterization. The mass of the samples did not differ from that of the weighed starting materials by more than 3 wt %. In order to monitor structural changes depending on thermal treatment, parts of the samples of $\text{Ge}_{0.4}\text{Sn}_{0.4}\text{In}_{0.067}\text{Sb}_{0.067}\text{Te}$ were again heated in silica ampoules in an argon atmosphere, applying two different temperature programs: (a) heating up to 580 °C and subsequently cooling by switching off the furnace and (b) heating up to 450 °C in 1 h and subsequently cooling by switching off the furnace. In order to simulate the temperature treatment during thermoelectric measurements the last procedure was repeated two times. The layered phases $\text{Ge}_{0.5}\text{Sn}_{0.5}\text{InSbTe}_4$ and GeSnInSbTe_5 were obtained by fusing stoichiometric mixtures of the elements in silica glass ampoules under Ar atmosphere at 950 °C for 4 d and subsequently annealing for 6 d at 550 °C ($\text{Ge}_{0.5}\text{Sn}_{0.5}\text{InSbTe}_4$) or 350 °C (GeSnInSbTe_5) and finally quenched in water. All products were obtained as metallic gray ingots.

Powder X-ray diffraction

Samples were ground in an agate mortar and fixed between Mylar foils with traces of Lithelen vacuum grease. PXRD patterns were recorded with a Guinier camera [G670, Huber, Germany; Cu-K_{α1} radiation, λ = 1.54051 Å, Ge(111) monochromator] with 15 min acquisition time (10 read-outs). Temperature-dependent PXRD patterns were recorded with a diffractometer with modified Debye-Scherrer setup [StadiP, Stoe & Cie. GmbH, Germany; Mo-K_{α1} radiation, λ = 0.7093 Å, Ge(111) monochromator] equipped with a moving Mythen 1 K silicon stripe detector and a graphite furnace. Powdered samples were filled into silica glass capillaries (diameter 0.5 mm) in an argon atmosphere and heated with 5 K·min⁻¹ from RT to 750 °C and back to room temperature. Every 20 K, data were collected with 30 min acquisition time for each pattern. PXRD of Ge_{0.5}Sn_{0.5}InSbTe₄ and GeSnInSbTe₄ with synchrotron radiation was carried out at beamline ID31 of the ESRF (Grenoble, France) with a Debye-Scherrer setup [array of 9 point detectors with Si(111) analyzer crystals].⁴³ Samples in silica glass capillaries (0.2 mm diameter) were rotated during data acquisition. The off-edge wavelength 0.354198(9) Å was calibrated with a Si standard (NIST 670c).⁴⁴ The positions of the absorption edges were determined for each compound from energy-dependent fluorescence scans. The wavelengths for measurements were chosen slightly on the low-energy side of the K edges of the respective element (Sb-K edge: 30.4868 keV, 0.406698 Å; Te-K edge: 31.8087 keV, 0.389781 Å; In-K edge: 27.9403 keV, 0.443747 Å; Sn-K edge: 29.1966 keV, 0.424653 Å). Energy-dependent fluorescence yielded dispersion correction terms Δf'' and the corresponding Δf' using Kramers-Kronig transform⁴⁵ as provided by the program CHOOCH.⁴⁶

All Rietveld refinements were carried out with TOPAS-Academic, where reflection profiles were described by a fundamental parameter approach,⁴⁷ including anisotropic microstrain and spherical harmonics of the 4th order for preferred orientation. For the refinements with each type of data (laboratory X-rays or synchrotron radiation) the same set of parameters were used. For laboratory radiation, site occupancies were derived from the nominal composition, which was in accordance with EDX (see below). Common displacement parameters were refined for cations and Te, respectively. In case of resonant X-ray data, site occupancies were refined using individual displacement parameters for each Wyckoff position. These refinements were constrained to match the nominal compositions. Stephens' algorithm was used to describe anisotropic line-shape broadening.⁴⁸

Electron microscopy

The chemical composition was verified using EDX spectroscopy during scanning (SEM) and transmission (TEM) electron microscopy. SEM was performed on a JSM 6500F instrument (JEOL) operated at 30 keV accelerating voltage with a Si/Li EDX detector (Oxford Instruments, model 7418). For TEM sample preparation, small amounts of the samples were ground in absolute ethanol, drop-cast on copper grids with holey carbon film (S166–2, Plano GmbH, Germany) and transferred into the microscope on a double-tilt holder. TEM was done using a Titan Themis 60–300 (FEI, USA) operated at 300 kV acceleration voltage and equipped with X-FEG, monochromator, C_s corrector and windowless 4-quadrant Super-X EDX detector (acquisition time 45 s). Micrographs and diffraction patterns were recorded with a $4k \times 4k$ Ceta CMOS camera (FEI, USA) and evaluated using Digital Micrograph,⁴⁹ JEMS⁵⁰ and ProcessDiffraction7⁵¹ for indexing and simulation of SAED patterns. EDX spectra were quantified using ES Vision.⁵²

Thermoelectric Characterization

Electrical conductivities and Seebeck coefficients were measured on cuboid samples (ca. $6 \times 2 \times 1.5$ mm³) in a helium atmosphere with a four-point setup,⁵³ on an LSR-3 instrument (Linseis, Germany) with NiCr/Ni thermocouples and a continuous reverse of the polarity of the thermocouples. Measurements comprised 3 heating/cooling cycles 50 – 475 – 75 °C with 25 K steps at 10 K·min^{−1} heating rate and 3 data points per temperature. Thermal diffusivity (D_{th}) measurements were performed in a helium atmosphere applying the laser-flash method with an LFA1000 instrument (Linseis, Germany) equipped with Nd-YAG-Laser (350 V and 2 ms pulse) and InSb detector on disk-shaped samples (diameter 4–10 mm and 1–2 mm thickness). Corrections for simultaneous heat loss were considered using Dusza's model.⁵⁴ Heat capacities c_p were estimated according to the Dulong-Petit approximation⁵⁵ and densities ρ were determined using Archimedes' principle with a precision of 0.03 g·cm^{−3}. The thermal conductivity was obtained as $\kappa = c_p \cdot \rho \cdot D_{th}$. The calculated c_p values used in this contribution (0.214–0.22 J·g^{−1}·K^{−1} at 300 K) are in the range of measured c_p values of related binary and ternary compounds ($\text{Ge}_{0.8}\text{Sb}_{0.13}\text{Te}$: 0.23 J·g^{−1}·K^{−1},²³ SnTe: 0.19 J·g^{−1}·K^{−1},⁵⁶ Sb₂Te₃: 0.205 J·g^{−1}·K^{−1},⁵⁷ In₂Te₃: 0.22 J·g^{−1}·K^{−1},⁵⁸ all at 300 K; temperature-dependent changes < 10%). The combined uncertainty of the measurements is ~ 15% for the ZT value.

4.3.5 References

- 1 K. S. Siegert, F. R. L. Lange, E. R. Sittner, H. Volker, C. Schlockermann, T. Siegrist, M. Wuttig, *Rep. Prog. Phys.* **2015**, 78, 013001.
- 2 M. Wuttig, N. Yamada, *Nat. Mater.* **2007**, 6, 824.
- 3 T. Matsunaga, H. Morita, R. Kojima, N. Yamada, K. Kifune, Y. Kubota, Y. Tabata, J. J. Kim, M. Kobata, E. Ikenaga, K. Kobayashi, *J. Appl. Phys.* **2008**, 103, 093511.
- 4 M. N. Schneider, T. Rosenthal, C. Stiewe, O. Oeckler, *Z. Kristallogr.* **2010**, 224, 463.
- 5 H. J. Goldsmid, *Materials* **2014**, 7, 2577.
- 6 T. Zhu, Y. Liu, C. Fu, J. P. Heremans, J. G. Snyder, X. Zhao, *Adv. Mater.* **2017**, 29, 1605884.
- 7 C. Han, Q. Sun, Z. Li, S. X. Dou, *Adv. Energy Mater.* **2016**, 6, 1600498.
- 8 W. Liu, X. Yan, G. Chen, Z. Ren, *Nano Energy* **2012**, 1, 42.
- 9 J.-A. Dolyniuk, B. Owens-Baird, J. Wang, J. V. Zaikina, K. Kovnir, *Mat. Sci. Eng.* **2016**, 108, 1.
- 10 G. Tan, L.-D. Zhao, M. G. Kanatzidis, *Chem. Rev.* **2016**, 116, 12123.
- 11 K. F. Hsu, S. Loo, F. Guo, W. Chen, J. S. Dyck, C. Uher, T. Hogan, E. K. Polychroniadis, M. G. Kanatzidis, *Science* **2004**, 303, 818.
- 12 B. A. Cook, M. J. Kramer, X. Wie, J. L. Harringa, E. M. Levin, *J. Appl. Phys.* **2007**, 101, 053715.
- 13 J. R. Sootsman, D. Y. Chung, M. G. Kanatzidis, *Angew. Chem.* **2009**, 121, 8768; *Angew. Chem. Int. Ed.* **2009**, 48, 8616.
- 14 E. M. Levin, M. F. Besser, R. Hanus, *J. Appl. Phys.* **2013**, 114, 083713.
- 15 P. Bauer Pereira, I. Sergueev, S. Gorsse, J. Dadda, E. Müller, R. P. Herman, *Phys. Status Solidi B* **2013**, 250, 1300.
- 16 H. Sun, X. Lu, H. Chi, D. T. Morelli, C. Uher, *Phys. Chem. Chem. Phys.* **2014**, 16, 15570.
- 17 Y. Z. Pei, D. T. Morelli, *Appl. Phys. Lett.* **2009**, 94, 122112.
- 18 T. Rosenthal, M. N. Schneider, C. Stiewe, M. Döblinger, O. Oeckler, *Chem. Mater.* **2011**, 23, 4349.
- 19 A. Banik, B. Vishal, S. Perumal, R. Datta, K. Biswas, *Energy Environ. Sci.* **2016**, 9, 2011.
- 20 G. J. Snyder, E. S. Toberer, *Nat. Mater.* **2008**, 7, 105.
- 21 F. Fahrnbauer, P. Urban, S. Welzmler, T. Schröder, T. Rosenthal, O. Oeckler, *J. Solid State Sci.* **2013**, 208, 20.
- 22 M. N. Schneider, X. Biquard, C. Stiewe, T. Schröder, P. Urban, O. Oeckler, *Chem. Commun.* **2012**, 48, 2192.
- 23 T. Rosenthal, L. Neudert, P. Ganter, J. de Boor, C. Stiewe, O. Oeckler, *J. Solid State Chem.* **2014**, 215, 231.
- 24 T. Rosenthal, S. Welzmler, O. Oeckler, *Solid State Sci.* **2013**, 25, 118.
- 25 M. N. Schneider, O. Oeckler, *Z. Anorg. Allg. Chem.* **2008**, 634, 2557.
- 26 P. Urban, M. N. Schneider, O. Oeckler, *J. Solid State Chem.* **2015**, 227, 223.
- 27 M. N. Schneider, P. Urban, A. Leineweber, M. Döblinger, O. Oeckler, *Phys. Rev. B* **2010**, 81, 184102.
- 28 S. Perumal, S. Roychowdhury, K. Biswas, *J. Mater. Chem. C* **2016**, 4, 7520.

- 29 S. Welzmler, F. Fahrnbauer, F. Hennersdorf, S. Dittmann, M. Liebau, C. Fraunhofer, W. G. Zeier, G. J. Snyder, O. Oeckler, *Adv. Electron. Mater.* **2015**, *1*, 1500266.
- 30 R. Sankar, D. P. Wong, C. S. Chi, W. L. Chien, J. S. Hwang, F. C. Chou, L. C. Chen, K. H. Chen, *Cryst. Eng. Comm.* **2015**, *17*, 3440.
- 31 F. Fahrnbauer, D. Souchay, G. Wagner, O. Oeckler, *J. Am. Chem. Soc.* **2015**, *137*, 12633.
- 32 T. Rosenthal, S. Welzmler, L. Neudert, P. Urban, A. Fitch, O. Oeckler, *J. Solid. State Chem.* **2014**, *219*, 108.
- 33 L. Neudert, S. Schwarzmüller, S. Schmitzer, W. Schnick, O. Oeckler, *J. Solid. State Chem.* **2018**, *258*, 289.
- 34 S. Welzmler, P. Urban, F. Fahrnbauer, L. Erra, O. Oeckler, *J. Appl. Crystallogr.* **2013**, *46*, 769.
- 35 R. D. Shannon, *Acta Crystallogr. Sect. A* **1976**, *32*, 751.
- 36 P. Urban, M. N. Schneider, M. Seemann, J. P. Wright, O. Oeckler, *Z. Kristallogr.* **2015**, *230*, 369.
- 37 S. Welzmler, F. Heinke, P. Huth, G. Bothmann, E. -W. Scheidt, G. Wagner, W. Scherer, A. Pöpl, O. Oeckler, *J. Alloys Compd.* **2015**, *652*, 74.
- 38 L. E. Shelimova, O. G. Karpinskii, T. E. Svechnikova, I. Y. Nikhezina, E. S. Avilov, M. A. Kretova, V. S. Zemskov, *Inorg. Mater.* **2008**, *44*, 371.
- 39 S. Welzmler, T. Rosenthal, P. Ganter, L. Neudert, F. Fahrnbauer, P. Urban, C. Stiewe, J. de Boor, O. Oeckler, *Dalton Trans.* **2014**, *43*, 10529.
- 40 O. Oeckler, M. N. Schneider, F. Fahrnbauer, G. Vaughan, *Solid State Sci.* **2011**, *13*, 1157.
- 41 L. E. Shelimova, O. G. Karpinskii, T. E. Svechnikova, E. S. Avilov, M. A. Kretova, V. S. Zemskov, *Inorg. Mater.* **2004**, *40*, 1264.
- 42 O. G. Karpinsky, L. E. Shelimova, M. A. Kretova, J. -P. Fleurial, *J. Alloys Compd.* **1998**, *268*, 112.
- 43 J. -L. Hodeau, P. Bordet, M. Anne, A. Prat, A. N. Fitch, E. Dooryhee, G. Vaughan, A. Freund, *Proc. SPIE* **1998**, *3448*, 353.
- 44 J. P. Wright, G. B. M. Vaughan, A. N. Fitch, *IUCr Computing Commission Newsletter* **2003**, *1*, 92.
- 45 R. de Kronig, *J. Opt. Soc. Am.* **1926**, *12*, 547.
- 46 G. Evans, R. F. Pettifer, *J. Appl. Crystallogr.* **2001**, *34*, 82.
- 47 A. Coelho, TOPAS-Academic, v. 4.1, **2007**.
- 48 P. W. Stephens, *J. Appl. Crystallogr.* **1999**, *32*, 281.
- 49 Gatan Software Team, Digital Micrograph, v. 3.6.1, **1999**.
- 50 P. A. Stadelmann, JEMS, v. 3.3425, **2008**.
- 51 J. L. Lábár, Process Diffraction, v. 7.3.2 Q, **2005**.
- 52 Emispec Systems Inc., ESVision, v. 4.0.164, **2002**.
- 53 L. J. Van der Pauw, *Philips Res. Rep.* **1958**, *13*, 1.
- 54 L. Dusza, *High Temp. - High Pressures* **1995/1996**, *27/28*, 467.
- 55 K. A. Borup, J. de Boor, H. Wang, F. Drymiotis, F. Gascoin, X. Shi, L. Chen, M. I. Fedorov, E. Müller, B. B. Iversen, G. J. Snyder, *Energy Environ. Sci.* **2015**, *8*, 423.
- 56 A. S. Pashinkin, A. S. Malkova, M. S. Mikhailova, *Russ. J. Phys. Ch.* **2006**, *80*, 1522.
- 57 A. S. Pashinkin, A. S. Malkova, M. S. Mikhailova, *Russ. J. Phys. Ch.* **2008**, *82*, 999.
- 58 V. P. Zlomanov, M. S. Sheiman, V. N. Demin, B. Legendre, *J. Phase Equilibria*, **2001**, *22*, 339.

4.3.6 Supporting Information

Table S1. Results of EDX analyses (of at least 3 individual measurements) in atom%: measured (with standard uncertainties estimated from variance) / calculated (from nominal composition).

	Ge	Sn	In	Sb	Te
Ge_{0.4}Sn_{0.4}In_{0.13}Te *	21.9(7) / 20.7	19.8(3) / 20.7	7.1(2) / 6.9	-	51.2(2) / 51.7
Sn_{0.8}In_{0.067}Sb_{0.067}Te	-	43.1(7) / 41.4	4.0(4) / 3.4	2.3(4) / 3.4	50.6(6) / 51.7
Ge_{0.4}Sn_{0.4}In_{0.067}Sb_{0.067}Te	18.8(8) / 20.7	21.8(2) / 20.7	3.9(3) / 3.4	2.5(3) / 3.4	53.0(8) / 51.7
Ge_{0.4}Sn_{0.4}Sb_{0.13}Te *	19(3) / 20.7	21.8(4) / 20.7	-	7(1) / 6.9	52(3) / 51.7
Ge_{0.8}In_{0.067}Sb_{0.067}Te *	40(4) / 41.4	-	3.5(5) / 3.4	3.8(5) / 3.4	52(3) / 51.7
Ge_{0.72}Sn_{0.08}In_{0.067}Sb_{0.067}Te *	34(1) / 37.2	5.3(4) / 4.1	3.3(9) / 3.4	3.6(8) / 3.4	54.3(9) / 51.7
Ge_{0.24}Sn_{0.56}In_{0.067}Sb_{0.067}Te *	12.3(3) / 12.4	30.0(6) / 29.0	3.4(7) / 3.4	2.3(3) / 3.4	52.0(2) / 51.7
Ge_{0.08}Sn_{0.72}In_{0.067}Sb_{0.067}Te *	5.9(9) / 4.1	3.9(1) / 3.4	38(2) / 37.2	1.2(2) / 3.4	51(1) / 51.7
Ge_{0.35}Sn_{0.35}In_{0.1}Sb_{0.1}Te *	18.1(6) / 18.4	19.4(4) / 18.4	5.3(2) / 5.3	5.0(4) / 5.3	52.2(8) / 52.6
Ge_{0.286}Sn_{0.286}In_{0.143}Sb_{0.143}Te	14(2) / 15.4	16.2(2) / 15.4	8.4(4) / 7.7	7.4(4) / 7.7	54(2) / 53.8
Ge_{0.5}Sn_{0.5}InSbTe₄	6.1(4) / 7.1	6.9(5) / 7.1	15.0(5) / 14.3	16.0(6) / 14.3	56.1(8) / 57.1
GeSnInSbTe₅	9.4(6) / 11.1	11.3(5) / 11.1	12.2(6) / 11.1	12.8(6) / 11.1	54.2(7) / 55.5

* analyses from TEM-EDX, all others from SEM-EDX

Table S2. Crystallographic data from the Rietveld refinements for Ge_{0.4}Sn_{0.4}In_{0.13}Te, Sn_{0.8}In_{0.067}Sb_{0.067}Te and Ge_{0.4}Sn_{0.4}In_{0.067}Sb_{0.067}Te cooled at air.

	Ge _{0.4} Sn _{0.4} In _{0.13} Te	Sn _{0.8} In _{0.067} Sb _{0.067} Te	Ge _{0.4} Sn _{0.4} In _{0.067} Sb _{0.067} Te
M / g mol⁻¹	219.062	237.519	219.991
space group		$Fm\bar{3}m$ (no. 225)	
Z		4	
lattice parameter <i>a</i> / Å	6.09689(3)	6.27036(4)	6.11014(3)
cell volume / Å³	226.634(4)	246.534(5)	228.114(4)
density, X-ray / g cm⁻³	6.4200(1)	6.422(1)	6.4032(1)
μ / in mm⁻¹	150.542(3)	165.76(3)	150.714(2)
reflections	13	13	13
parameters / thereof background	15 / 6	17 * / 6	15 / 6
R_p / R_{wp}	0.0240 / 0.0382	0.0198 / 0.0290	0.0218 / 0.033
R_{Bragg}	0.0367	0.0157	0.0099

* different number of parameters due to more parameters for crystallite size and microstrain

Table S3. Atom coordinates, site occupancies and isotropic displacement parameters for $\text{Ge}_{0.4}\text{Sn}_{0.4}\text{In}_{0.13}\text{Te}$, $\text{Sn}_{0.8}\text{In}_{0.067}\text{Sb}_{0.067}\text{Te}$ and $\text{Ge}_{0.4}\text{Sn}_{0.4}\text{In}_{0.067}\text{Sb}_{0.067}\text{Te}$; due to similar scattering factors of In, Sb and Sn, their occupancies were calculated from the nominal composition, the deviation of site-specific sums from 1 corresponds to the number of vacancies.

	Te position (fully occupied)	$x y z$	B_{iso}	cations / vacancies	$x y z$	occupancy	B_{iso}
$\text{Ge}_{0.4}\text{Sn}_{0.4}\text{In}_{0.13}\text{Te}$	$4a$	0 0 0	0.76(3)	$4b$	$\frac{1}{2} \frac{1}{2} \frac{1}{2}$	0.4 Ge 0.4 Sn 0.13 In	2.01(4)
$\text{Sn}_{0.8}\text{In}_{0.067}\text{Sb}_{0.067}\text{Te}$	$4a$	0 0 0	0.51(3)	$4b$	$\frac{1}{2} \frac{1}{2} \frac{1}{2}$	0.8 Sn 0.067 In 0.067 Sb	1.53(4)
$\text{Ge}_{0.4}\text{Sn}_{0.4}\text{In}_{0.067}\text{Sb}_{0.067}\text{Te}$	$4a$	0 0 0	1.13(3)	$4b$	$\frac{1}{2} \frac{1}{2} \frac{1}{2}$	0.4 Ge 0.4 Sn 0.067 In 0.067 Sb	2.49(3)

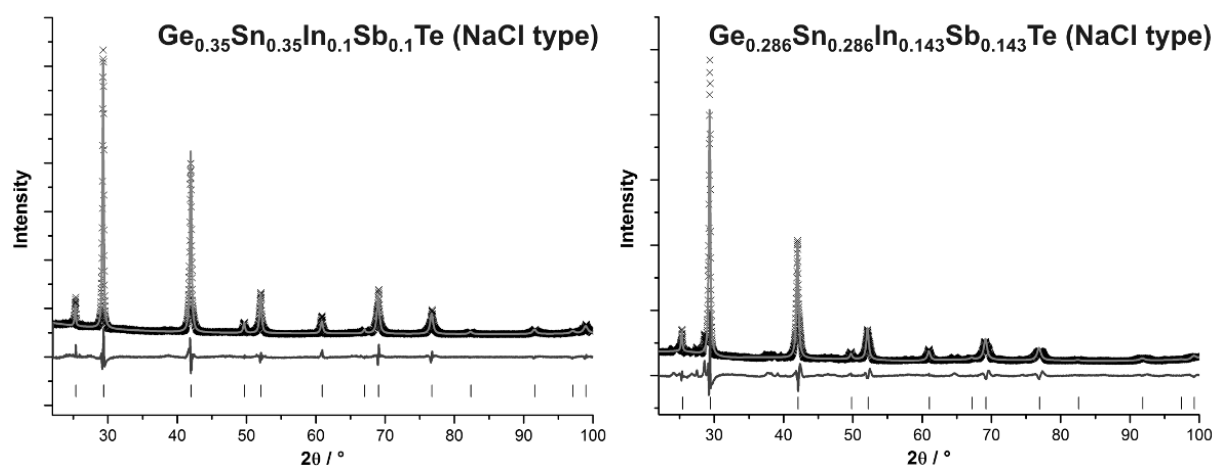


Figure S4. Profile fits of Rietveld refinements for air-cooled samples with the nominal compositions (which are in accordance with EDX, Table S1) $\text{Ge}_{0.286}\text{Sn}_{0.286}\text{In}_{0.143}\text{Sb}_{0.143}\text{Te}$ (left) and $\text{Ge}_{0.35}\text{Sn}_{0.235}\text{In}_{0.1}\text{Sb}_{0.1}\text{Te}$ (right); experimental data (black), calculated pattern (light gray), difference plot (dark gray) and calculated reflection positions (black vertical lines). These profile fits represent a rough approximation of the average crystal structures of these samples, reflection broadening corresponds to rhombohedral distortions in small domains (similar to Fig. 3). Traces of a trigonal superstructure of the rocksalt type in $\text{Ge}_{0.286}\text{Sn}_{0.286}\text{In}_{0.143}\text{Sb}_{0.143}\text{Te}$ (note the weak unexplained reflections) were further characterized by TEM (cf. Fig. S8 - S10).

Table S5. Crystal data and details of the Rietveld refinements for $\text{Ge}_{0.35}\text{Sn}_{0.35}\text{In}_{0.1}\text{Sb}_{0.1}\text{Te}$ and $\text{Ge}_{0.286}\text{Sn}_{0.286}\text{In}_{0.143}\text{Sb}_{0.143}\text{Te}$.

	$\text{Ge}_{0.35}\text{Sn}_{0.35}\text{In}_{0.1}\text{Sb}_{0.1}\text{Te}$	$\text{Ge}_{0.286}\text{Sn}_{0.286}\text{In}_{0.143}\text{Sb}_{0.143}\text{Te}$
M / g mol⁻¹	218.230	216.157
space group	$Fm\bar{3}m$ (no. 225)	
Z	4	
lattice parameter / Å	$a = 6.0785(2)$	$a = 6.0647(5)$
cell volume / Å³	224.59(2)	223.06(5)
density, X-ray / g cm⁻³	6.4539(6)	6.436(1)
μ / in mm⁻¹	153.80(2)	155.85(4)
reflection	13	13
parameters / thereof background	19 / 6	19 / 6
R_p / R_{wp}	0.0236 / 0.0368	0.0465 / 0.0697
R_{Bragg}	0.0076	0.0129

Table S6. Atom coordinates, refined site occupancies and displacement parameters from the Rietveld refinements for $\text{Ge}_{0.35}\text{Sn}_{0.35}\text{In}_{0.1}\text{Sb}_{0.1}\text{Te}$ and $\text{Ge}_{0.286}\text{Sn}_{0.286}\text{In}_{0.143}\text{Sb}_{0.143}\text{Te}$ (cf. Table S5).

	Te position (fully occupied)	x y z	B_{iso}	cations / vacancies	x y z	occupancy	B_{iso}
rocksalt-type $\text{Ge}_{0.35}\text{Sn}_{0.35}\text{In}_{0.1}\text{Sb}_{0.1}\text{Te}$	$4a$	0 0 0	1.73(8)	$4b$	$\frac{1}{2} \frac{1}{2} \frac{1}{2}$	0.35 Ge 0.35 Sn 0.1 In 0.1 Sb	3.99(8)
rocksalt-type $\text{Ge}_{0.286}\text{Sn}_{0.286}\text{In}_{0.143}\text{Sb}_{0.143}\text{Te}$	$4a$	0 0 0	2.9(2)	$4b$	$\frac{1}{2} \frac{1}{2} \frac{1}{2}$	0.286 Ge 0.286 Sn 0.143 In 0.143 Sb	4.4(1)

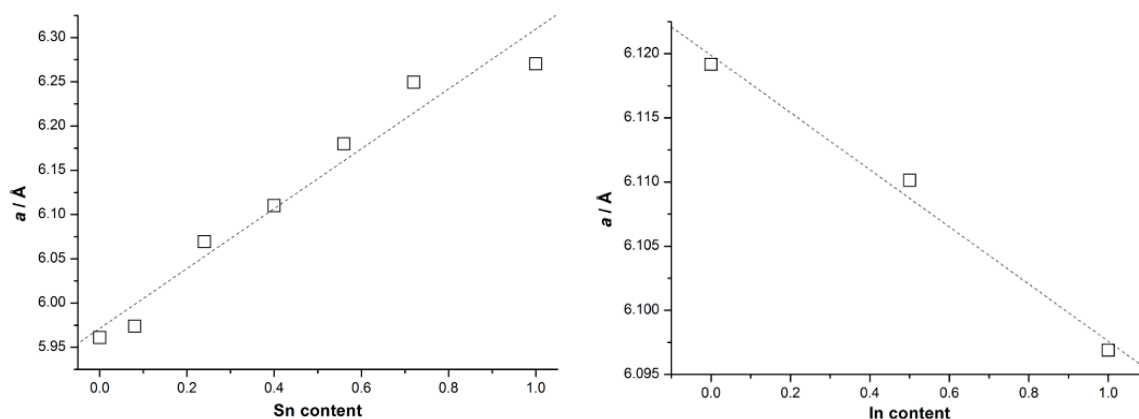


Figure S7. Vegard plots for $(\text{Ge}_x\text{Sn}_{1-x})_{0.8}\text{In}_{0.067}\text{Sb}_{0.067}\text{Te}$ with $0 \leq x \leq 1$ (left) and for $\text{Ge}_{0.4}\text{Sn}_{0.4}(\text{In}_y\text{Sb}_{1-y})_{0.13}\text{Te}$ with $0 \leq y \leq 1$ (right): samples quenched at air, cubic lattice parameter a vs. Sn and In content, respectively. Least-squares standard deviations of lattice parameters are in the range of 10^{-4} Å, but exact values of a depend on the cooling rate and are thus not reproducible within the numerical standard deviation.

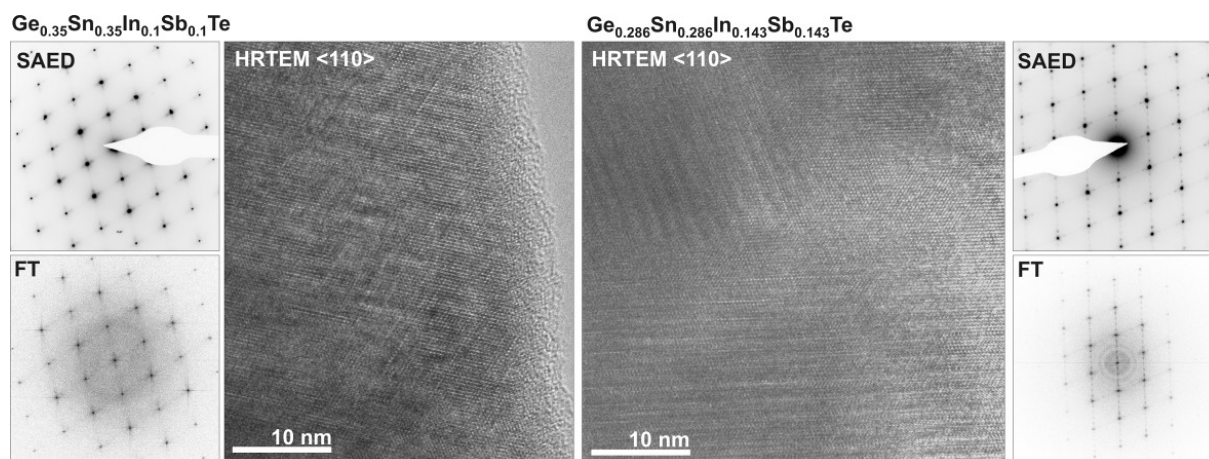


Figure S8. HRTEM images of $\text{Ge}_{0.35}\text{Sn}_{0.35}\text{In}_{0.1}\text{Sb}_{0.1}\text{Te}$ (left) and $\text{Ge}_{0.286}\text{Sn}_{0.286}\text{In}_{0.143}\text{Sb}_{0.143}\text{Te}$ (right), both samples annealed in existence range of cubic high-temperature phase and subsequently quenched in water; viewed along the cubic $\langle 110 \rangle$ direction, with corresponding Fourier transforms and SAED patterns. Areas with pronounced real-structure phenomena were chosen as evidenced by diffuse streaks that indicate an irregular distribution of spacings of the vacancy layers, especially in $\text{Ge}_{0.35}\text{Sn}_{0.35}\text{In}_{0.1}\text{Sb}_{0.1}\text{Te}$.

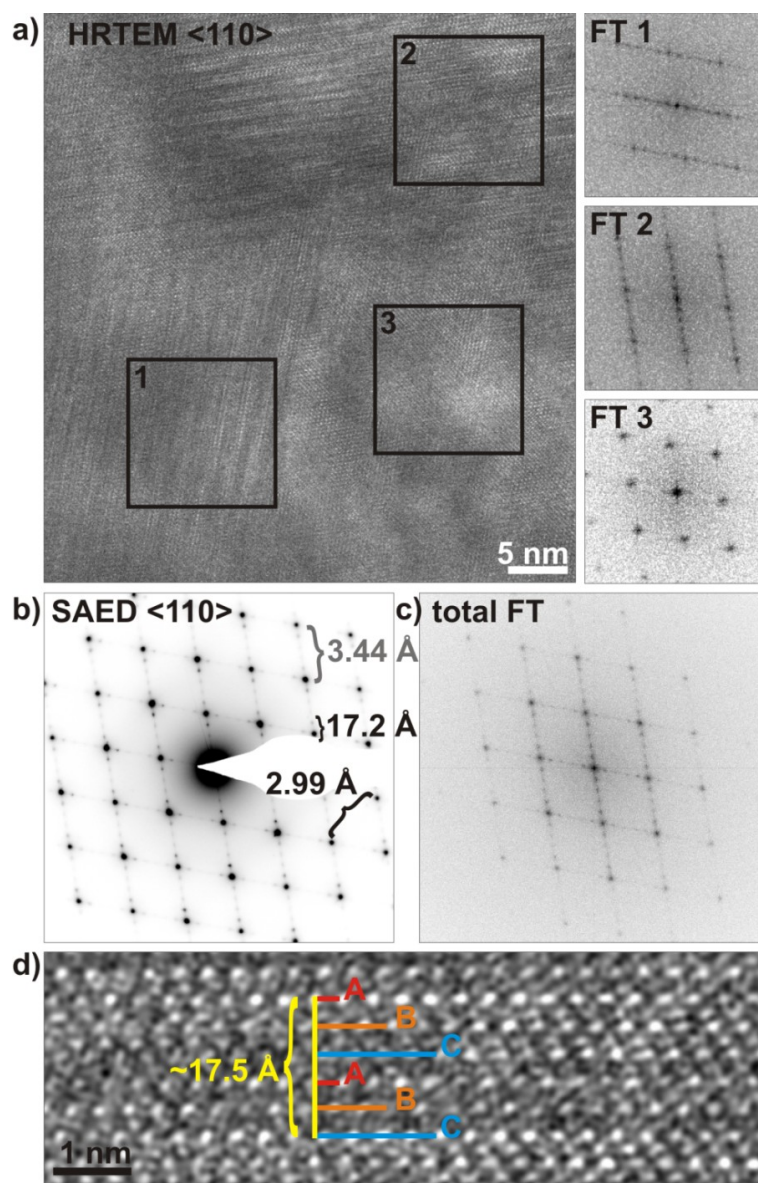


Figure S9. SAED and HRTEM of water-quenched $\text{Ge}_{0.286}\text{Sn}_{0.286}\text{In}_{0.143}\text{Sb}_{0.143}\text{Te}$ showing a superstructure of the rocksalt type comparable to those found in samples of $\text{Ge}_{3.25}\text{Sn}_{1.1}\text{Sb}_{1.1}\text{Te}_6$ (T. Rosenthal, S. Welzmler, L. Neudert, P. Urban, A. Fitch, O. Oeckler, *J. Solid. State Chem.* **2014**, 219, 108) and $\text{Ge}_3\text{MnSb}_2\text{Te}_7$ (S. Welzmler, F. Heinke, P. Huth, G. Bothmann, E. -W. Scheidt, G. Wagner, W. Scherer, A. Pöpl, O. Oeckler, *J. Alloys Compd.* **2015**, 652, 74): (a) HRTEM image (left) with corresponding Fourier transforms of different regions (right) indicating the possible superposition of three (or more likely, four) different regions corresponding to individual twin domains: 1. long-range ordered layer-like atom arrangement with a periodicity of ca. $3 \cdot 17.2 \text{ \AA} = 51.6 \text{ \AA}$, 2. similar to 1. but differently oriented and 3. without additional reflections in the ZOLZ (but most likely in other directions); (b) SAED pattern along the pseudocubic $\langle 110 \rangle$ direction (with respect to a cF lattice with $a \approx 6.0 \text{ \AA}$) with four additional reflections along $\langle 111 \rangle$ [and additional ones in Fig. S10]. This suggests trigonal metrics with $a_{\text{trigonal}} = a/\sqrt{2} = 2d_{002}/\sqrt{2} = (2 \cdot 2.99 \text{ \AA})/\sqrt{2} = 4.23 \text{ \AA}$ and $c_{\text{trigonal}} = 15 \cdot d_{111} = 15 \cdot 3.44 \text{ \AA} = 51.6 \text{ \AA}$ [transformation matrix $(1 \ 1 \ 0 \mid 1 \ \bar{1} \ 0 \mid 15 \ \bar{15} \ 15)$ from the cF cell]. The total Fourier transform of the HRTEM image (c) matches the SAED pattern (b). The Fourier-filtered HRTEM image (d) shows the ABC stacking of Te atoms around a vacancy layer (highlighted in color).

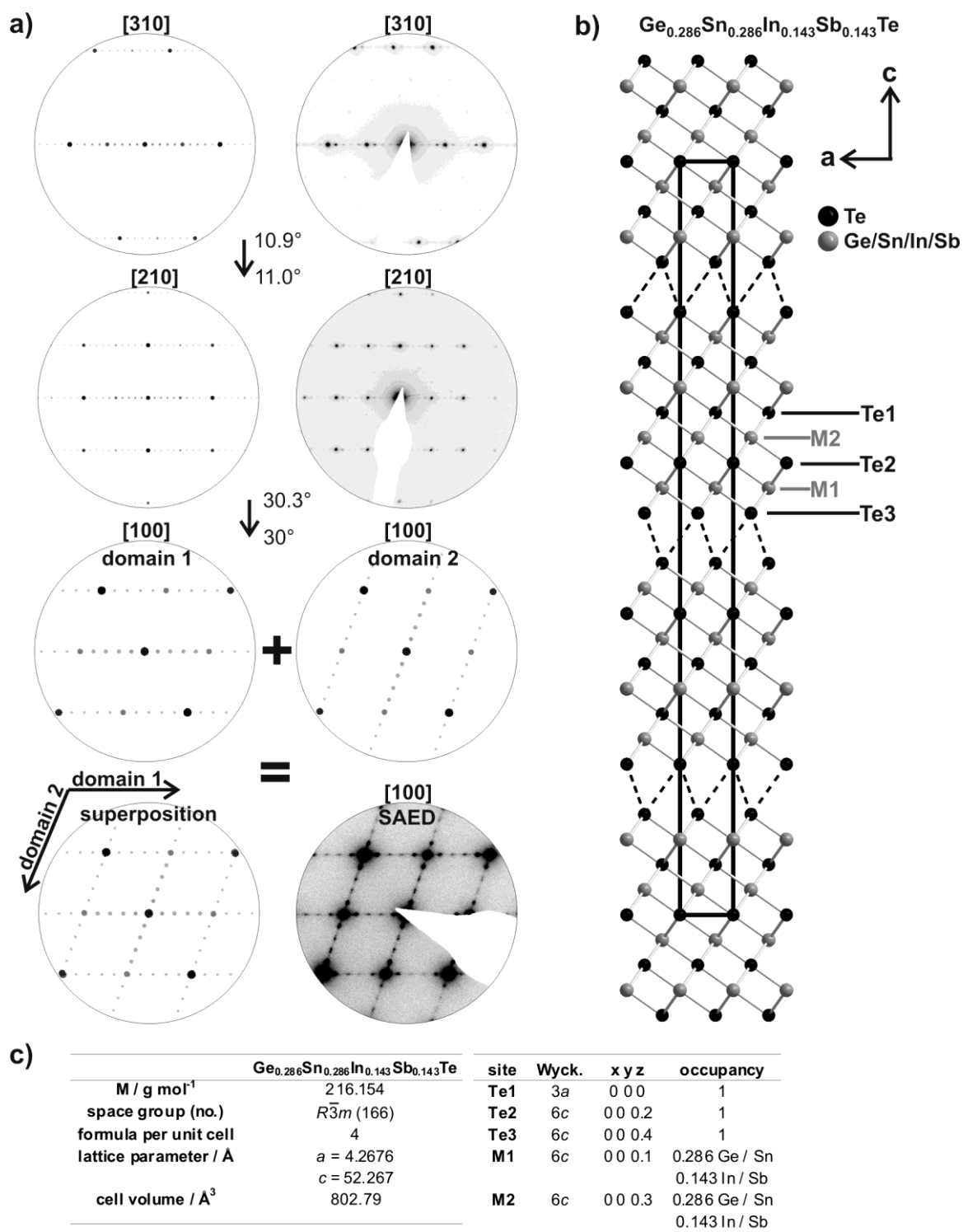


Figure S10. a): SAED tilting series of quenched $\text{Ge}_{0.286}\text{Sn}_{0.286}\text{In}_{0.143}\text{Sb}_{0.143}\text{Te}$ with corresponding simulations and indexing based on a long-range ordered superstructure model in space group $R\bar{3}m$ with a stacking of 27 atom layers along trigonal [001] (refers to one of the rocksalt type lattice's $\langle 111 \rangle$ directions). The patterns at the bottom are a twin-like superposition of the domains 1 and 2 that result from vacancy ordering in layers perpendicular to their individual [001] (indicated by black arrows). b): view of the constructed superstructure (cf. manuscript) and c) crystallographic data of the superstructure model (lattice parameters adapted to fit the PXRD pattern).

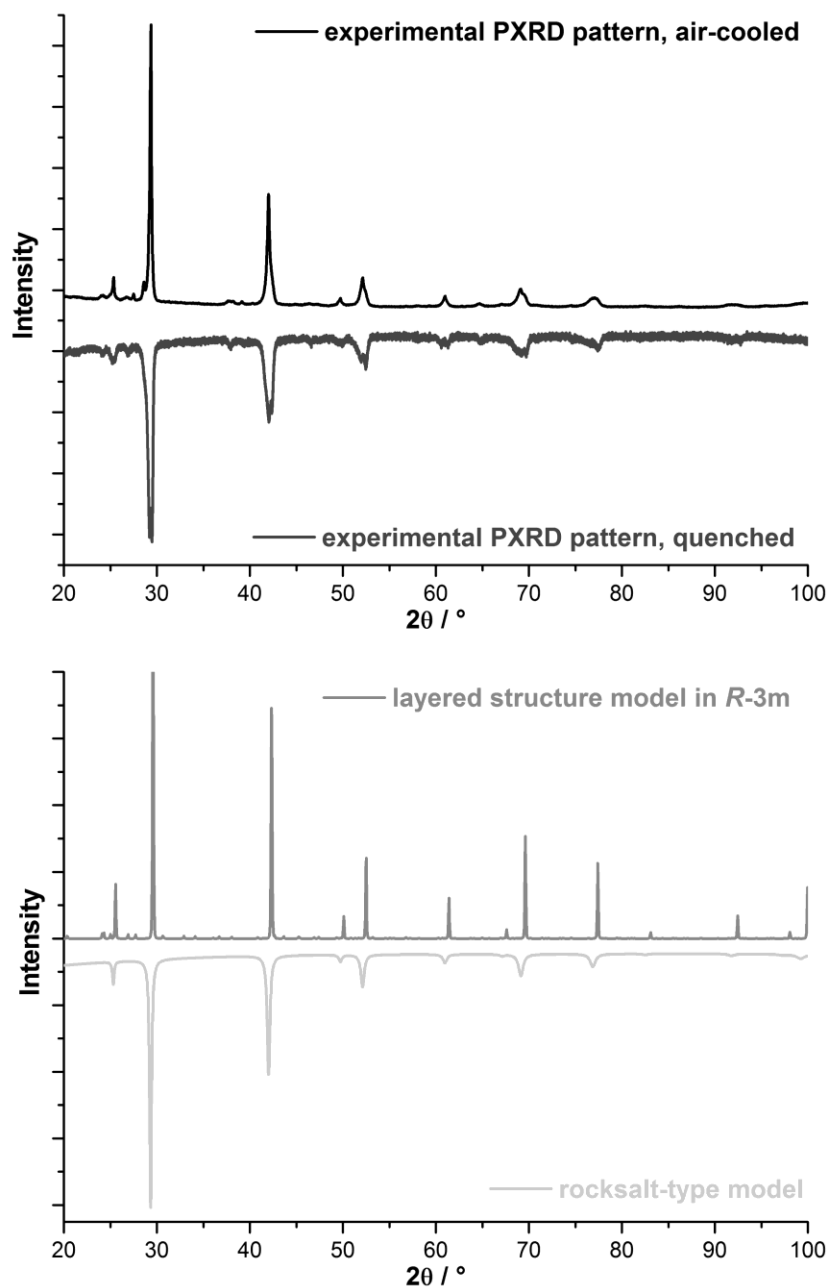


Figure S11. PXRD patterns of $\text{Ge}_{0.286}\text{Sn}_{0.286}\text{In}_{0.143}\text{Sb}_{0.143}\text{Te}$: water-quenched sample vs. sample cooled at air (top, dark gray and black, respectively). Both may be explained as a superposition of a phase with average NaCl-type structure and a layered structure model in $R\bar{3}m$ as shown in Fig. S10 (bottom, gray and light gray, respectively).

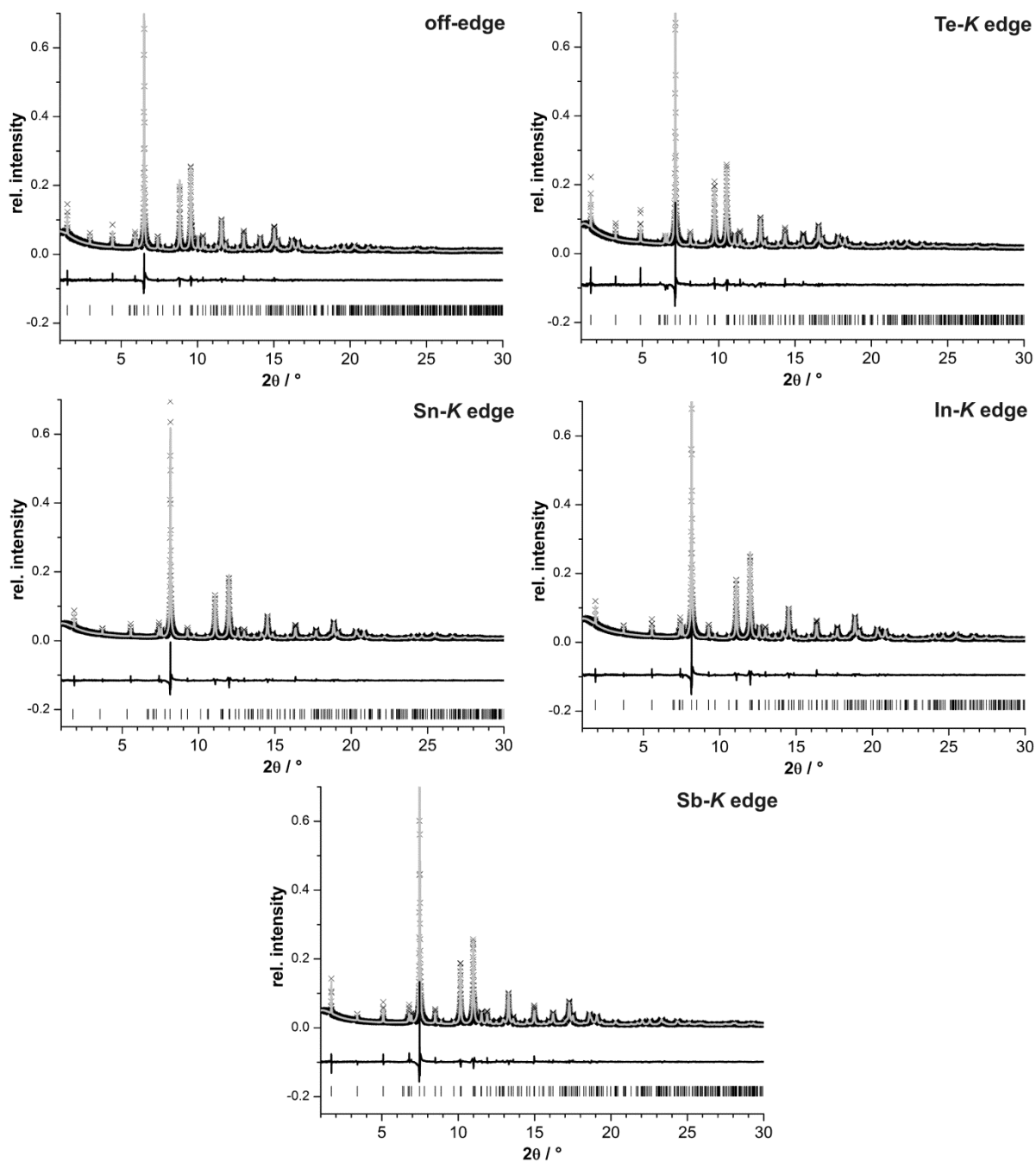


Figure S12. Profile fits of the Rietveld refinements for quenched 21R-Ge_{0.5}Sn_{0.5}InSbTe₄ based on diffraction patterns with synchrotron radiation (the strongest reflection is cut off) measured at different wavelengths; experimental data (black), calculated pattern (light gray), difference plot (dark gray) and calculated reflection positions (black vertical lines).

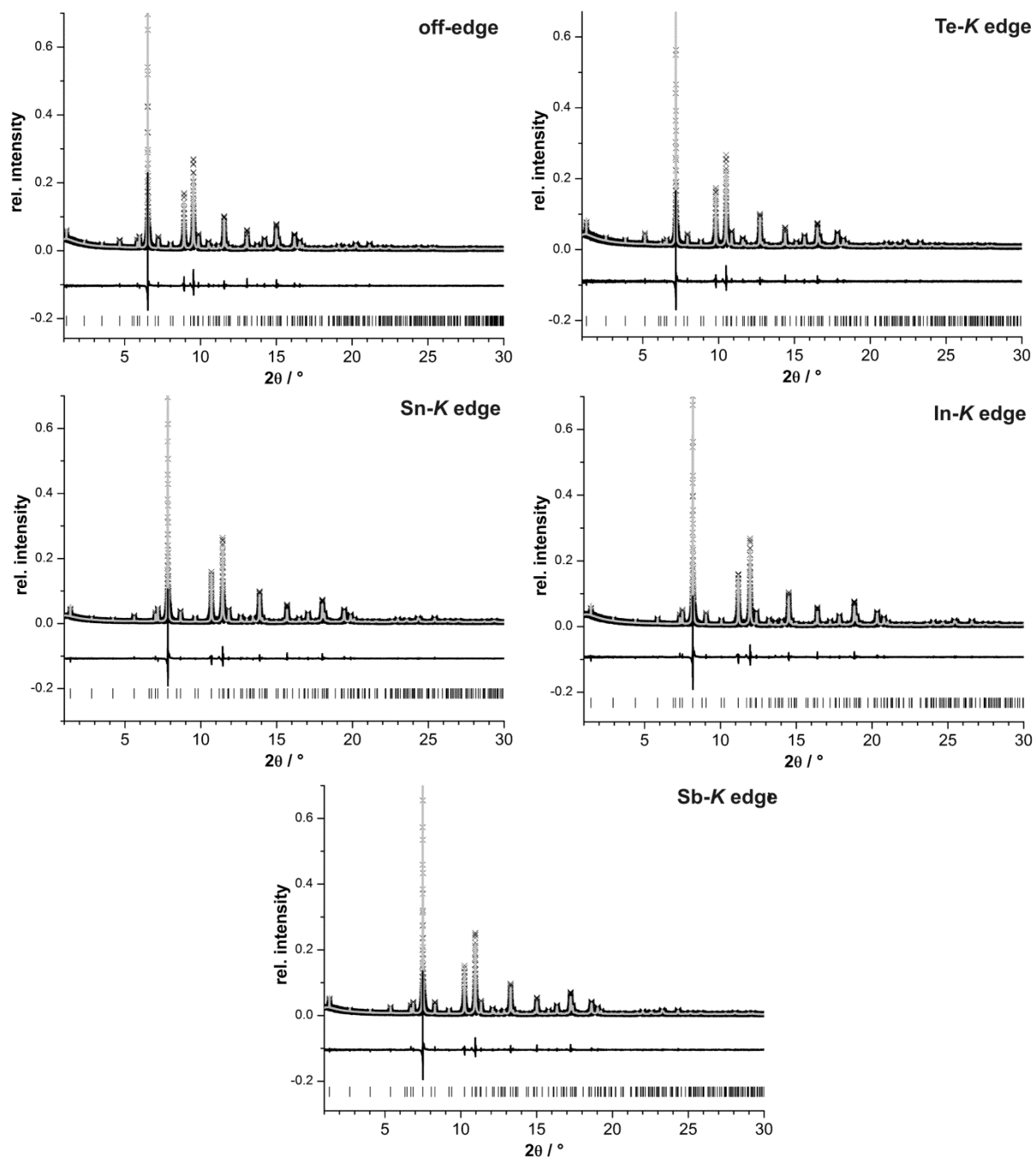


Figure S13. Profile fits of the Rietveld refinements for quenched $9P\text{-GeSnInSbTe}_5$ based on diffraction patterns with synchrotron radiation (the strongest reflection is cut off) measured at different wavelengths; experimental data (black), calculated pattern (light gray), difference plot (dark gray) and calculated reflection positions (black vertical lines).

Table S14. Atom coordinates, site occupancies and isotropic displacement parameters for 21R- $\text{Ge}_{0.5}\text{Sn}_{0.5}\text{InSbTe}_4$ and 9P- GeSnInSbTe_5 ; Te positions assumed to be fully occupied, occupancies without standard deviations are calculated from refined ones via constraints (cf. manuscript).

	Te positions	$x y z$	B_{iso}	cation positions	$x y z$	occupancy	B_{iso}
21R-$\text{Ge}_{0.5}\text{Sn}_{0.5}\text{InSbTe}_4$	$6c^{[a]}$	0 0 0.29029(3)	1.32(3)	6c	0 0 0.42638(3)	0.132(4) Ge 0.239(9) Sn 0.235(11) In 0.39 Sb	1.50(4)
	$6c^{[a]}$	0 0 0.13127(2)	1.08(3)	3a	0 0 0	0.235 Ge 0.022 Sn 0.531 In 0.212 Sb	0.31(5)
9P-GeSnInSbTe_5	$1a^{[a]}$	0 0 0	1.22(4)	2d	$\frac{1}{2} \frac{1}{2} 0.10590(12)$	0.37 Ge 0.09(1) Sn 0.37(2) In 0.164(8) Sb	1.02(2)
	$2d^{[a]}$	$\frac{1}{2} \frac{1}{2} 0.2043(1)$	0.90(3)	2c	0 0 0.32729(8)	0.13 Ge 0.41 Sn 0.13 In 0.335 Sb	1.63(4)
	$2d^{[a]}$	$\frac{1}{2} \frac{1}{2} 0.4175(1)$	1.67(4)				

[a] Te position fully occupied

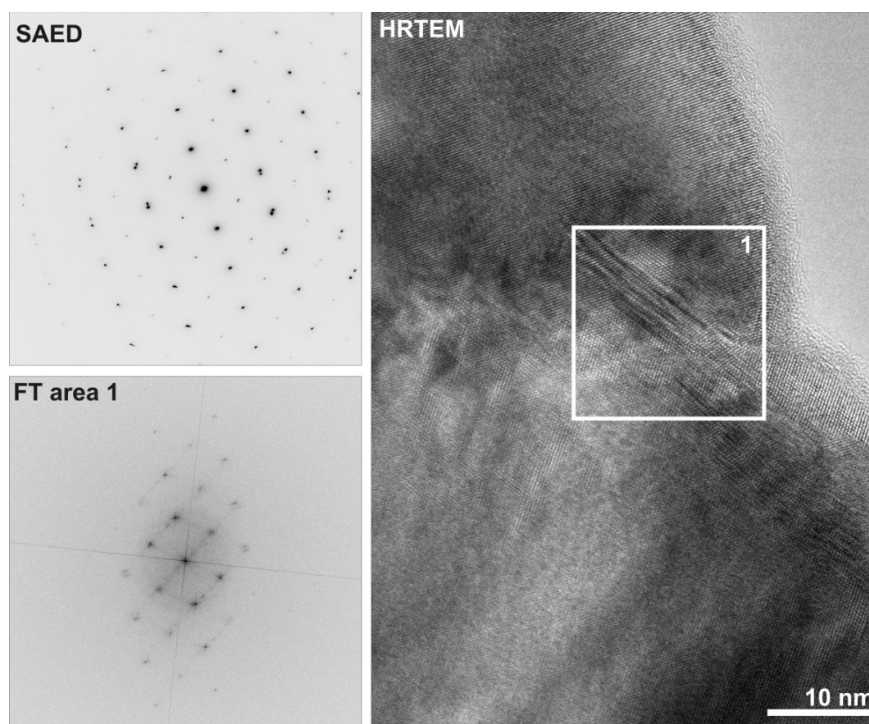


Figure S15. HRTEM image (right) of a crystallite in quenched $\text{Sn}_{0.8}\text{Sb}_{0.13}\text{Te}$ along the pseudocubic $\langle 110 \rangle$ direction with corresponding Fourier transform and SAED pattern. Short range ordering of the vacancies to layers is observed in some areas and corresponds to diffuse intensities between Bragg positions in Fourier transforms of selected areas (bottom left). This ordering occurs only in small domains, therefore the diffuse intensities are very weak (and almost invisible) in the SAED pattern (top left) of the whole crystallite.

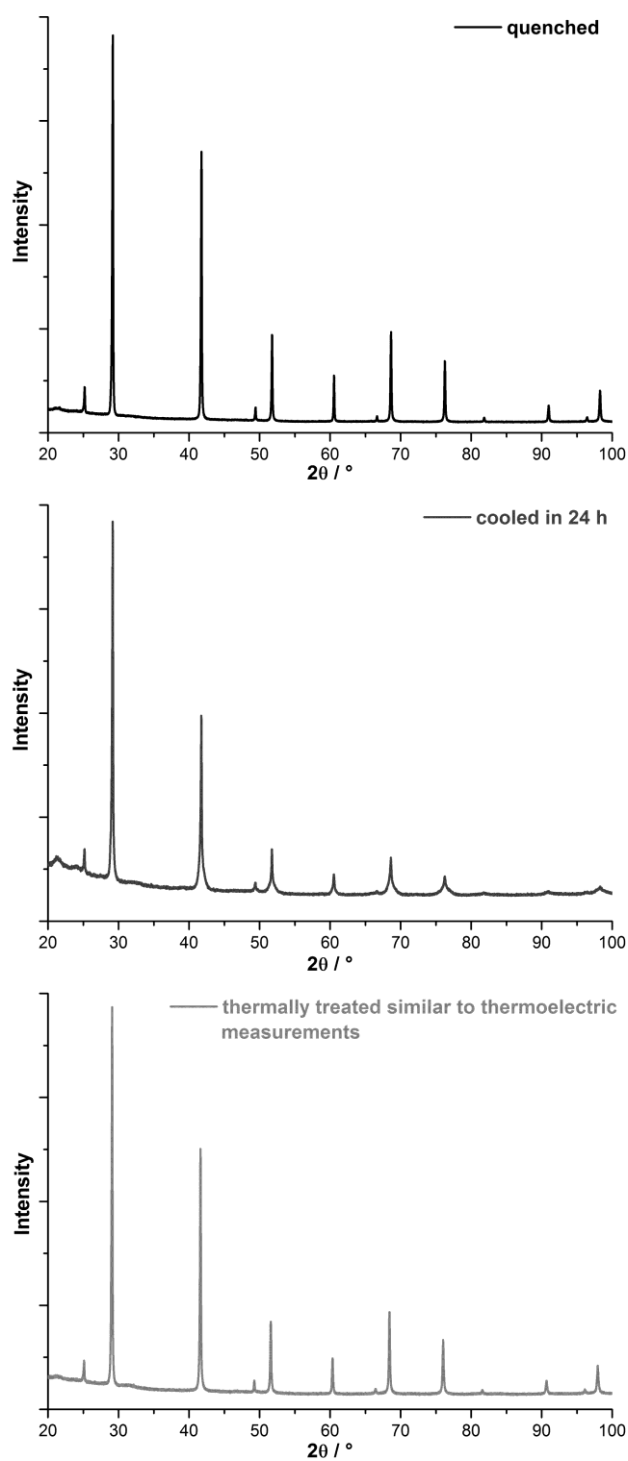


Figure S16. PXRD patterns of $\text{Ge}_{0.4}\text{Sn}_{0.4}\text{In}_{0.067}\text{Sb}_{0.067}\text{Te}$ with different thermal treatments, they are very similar.

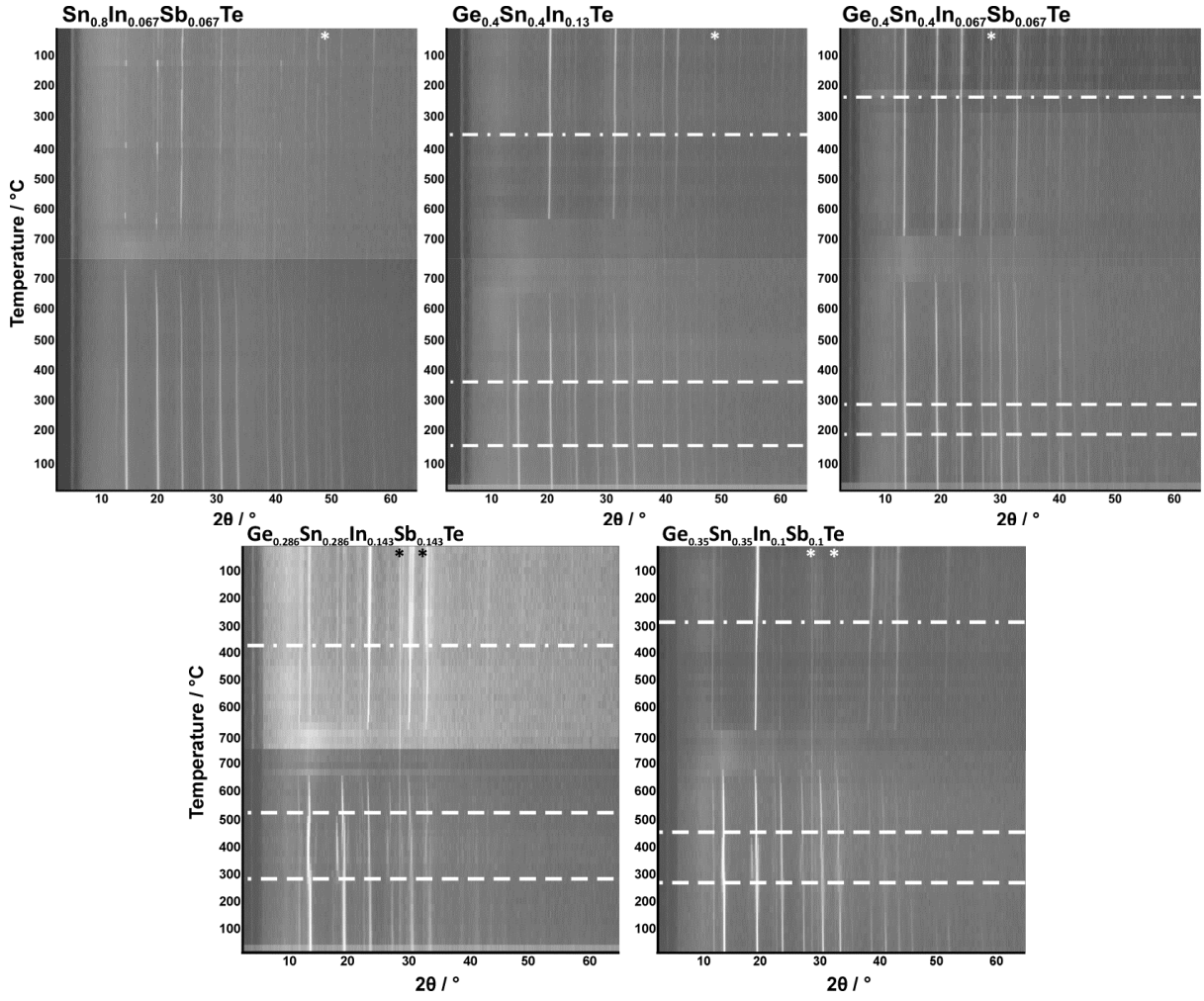


Figure S17. Temperature-dependent PXRD patterns of water-quenched $\text{Sn}_{0.8}\text{In}_{0.067}\text{Sb}_{0.067}\text{Te}$ (top left), $\text{Ge}_{0.4}\text{Sn}_{0.4}\text{In}_{0.13}\text{Te}$ (top middle), $\text{Ge}_{0.4}\text{Sn}_{0.4}\text{In}_{0.067}\text{Sb}_{0.067}\text{Te}$ (top right), $\text{Ge}_{0.286}\text{Sn}_{0.286}\text{In}_{0.143}\text{Sb}_{0.143}\text{Te}$ (bottom left) and $\text{Ge}_{0.35}\text{Sn}_{0.35}\text{In}_{0.1}\text{Sb}_{0.1}\text{Te}$ (bottom right); patterns during heating and cooling (from bottom to middle and middle to top, respectively, in each image), horizontal lines mark phase transitions (dashed lines mark the existence range of the layered trigonal modification during heating, dashed-dotted lines mark the transition temperature from cubic high-temperature phase to the trigonal phase during cooling), asterisks mark reflections caused by the furnace, reduced number of intensities of certain reflections during cooling result from preferred orientation caused by recrystallization of melts in capillaries.

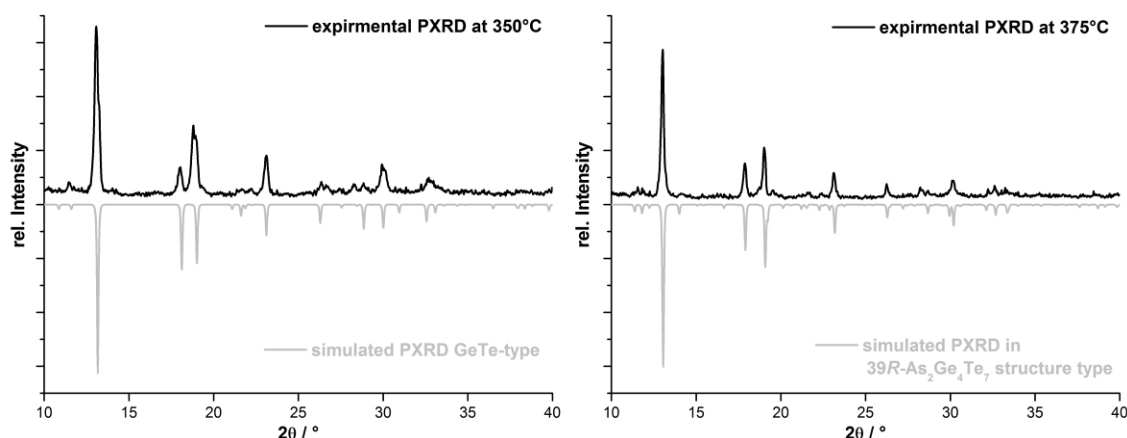


Figure S18. PXRD pattern of $\text{Ge}_{0.35}\text{Sn}_{0.35}\text{In}_{0.1}\text{Sb}_{0.1}\text{Te}$ collected at 350 °C (left) with a simulation corresponding to an average structure with the GeTe structure type; Differences between experimental and calculated pattern may be due to the presence of remaining pseudocubic (quenched, cf. manuscript) phase. PXRD pattern of $\text{Ge}_{0.286}\text{Sn}_{0.286}\text{In}_{0.143}\text{Sb}_{0.143}\text{Te}$ collected at 375 °C (right, black) with a simulation corresponding to the 39R- $\text{As}_2\text{Ge}_4\text{Te}_7$ structure type. Black lines represent experimental PXRD patterns and light gray lines PXRD simulation with site occupancies according to the nominal composition of the quinary compounds. (compare with references: M. N. Schneider, O. Oeckler, *Z. Anorg. Allg. Chem.* **2008**, 634, 2557 and M. N. Schneider, P. Urban, A. Leineweber, M. Döblinger, O. Oeckler, *Phys. Rev. B* **2010**, 81, 184102).

5 Using electron microscopy for the elucidation of new crystal structures

5.1 Intergrowth of luminescent oxonitridosilicates with complex crystal structures

Lukas Neudert, Dajana Durach, Peter Schultz, Wolfgang Schnick, Oliver Oeckler

unpublished results

As previously discussed in Chapter 2, high-temperature synthesis of metal hydrides with metal fluorides at simultaneous presence of metal amides and silcondiimide allows easy access to new (oxo)nitridosilicates. If O is present in the product, it stems usually from impurities of commercial chemicals. When dopants like CeF_3 or EuF_2 are added to the starting materials, the activator ions partly occupy the metal sites and luminescence can be observed. In order to obtain phase-pure products, such a broad synthetic approach can be unfavorable due to the likely formation of competing products with similar structures and similar chemical composition. This also applies for the reaction of $\text{La}(\text{NH}_2)_3$, LaF_3 and BaH_2 with “ $\text{Si}_2(\text{NH})_3 \cdot 6 \text{NH}_4\text{Cl}$ ” at 1600 °C in a radio-frequency furnace, which leads to an heterogeneous microcrystalline product (see Fig. 1). Yellow (Eu^{2+} -doping) or green (Ce^{3+} -doping) luminescence of the majority of the product can be correlated to new oxonitridosilicates because the emission of rare-earth doped $\text{BaSi}_7\text{N}_{10}$ is significantly shifted towards blue emission.¹

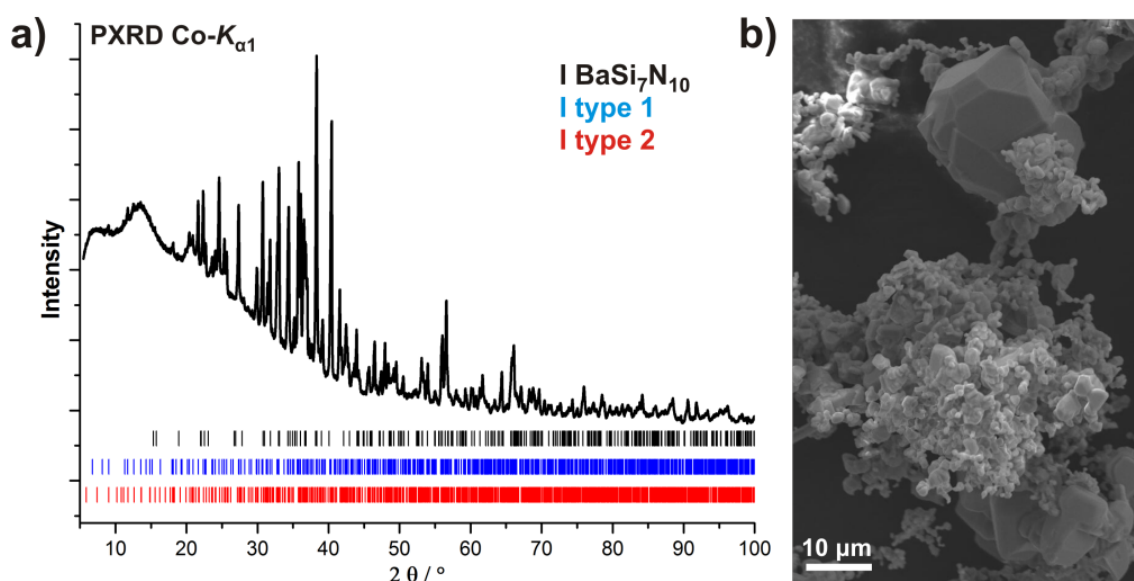


Fig. 1: (a) Powder X-ray diffraction pattern of heterogeneous sample with side phase $\text{BaSi}_7\text{N}_{10}$ (black tick marks). The majority of the reflections belong to unit cell parameters of new oxonitridosilicates identified by TEM (red and blue tick marks). (b) SE image of heterogeneous product containing large $\text{BaSi}_7\text{N}_{10}$ crystals besides new microcrystalline and related phases type 1 and 2.

The structure determination of the new phases using common laboratory methods was limited, because of reflection overlap in powder diffraction patterns and small size of the crystals $< 10 \mu\text{m}$. Following the method combination discussed in Chapter 2, the combined analysis of SAED patterns as part of TEM pre-characterization and reciprocal lattice sections obtained from synchrotron X-ray data showed that systematic absences were incompatible with any space group. It was likely that the vast majority of the crystals were intergrown on the micrometer scale. With further electron-diffraction experiments, two sets of lattice parameters were found (type 1: hP $a = 17.5 \text{ \AA}$, $c = 22.7 \text{ \AA}$, type 2: hP $a = 20.2 \text{ \AA}$, $c = 22.7 \text{ \AA}$, see Fig. 2). The $2mm$ and 6 symmetry of the SAED patterns along zone axis $<100>$ and $[001]$, respectively, match the hexagonal P lattices and suggest Laue class $6/m$. The same c parameter and relations $a_2 = \sqrt{3} a_1/2$ and $3V_2 = 4V_1$ associate the two unit cells. As the viewing directions with respect to the two different unit cells were derived (e.g. along zone axis $[110]$ and $[120]$), superposition of SAED patterns of type 1 and type 2, explain the experimental diffraction patterns of intergrown crystals (see Fig. 2 a). Reflection positions match those of the simulated ones. EDX revealed the two oriented intergrown phases as barium-lanthanum oxonitridosilicates with different Ba:La:Si ratios (type 1 $\approx 1:2:4$ and type 2 $\approx 1:3:6$). Subsequently, individual non-intergrown single crystals with dimensions of maximum $1.5 \times 10 \times 1 \mu\text{m}^3$ of both types were identified on TEM grids. Comparable TEM investigations on a product using SrH_2 instead of BaH_2 as starting material revealed a third new phase with similar hexagonal metrics to type 2 but Sr instead of Ba ($a = 19.6 \text{ \AA}$, $c = 21.9 \text{ \AA}$). For the structure models of the two related oxonitridosilicate frameworks sub-micron synchrotron X-ray diffraction data were collected (ID11, ESRF, Grenoble). The pre-characterized microcrystals were re-located using X-ray fluorescence scans.

Because of the complexity of the interrupted, centrosymmetric 3D frameworks of vertex- and edge-sharing $\text{Si}(\text{O},\text{N})_4$ tetrahedra, a tentative structure model of type 1 can be described most properly assuming two different slab-like building blocks, stacked parallel to $<001>$ (see Fig. 3a: A light green and B green). The pronounced tendency towards intergrowth is due to very similar building blocks in both structures. Model one shows an equal top and bottom tetrahedra building block, represented by A in Fig. 3. It is built up from *achter* ring cages and in their centers distorted trigonal OLa_5 bipyramids (see Fig. 3b light green and 3e structural elements I in pink). Building block B (see Fig. 3 c-d) is the reason for the difference between the two structure models. For the structure of type 1 the building block B (see Fig. 3 c) consists of pairs of branched *vierer* rings (structural motif II green), *dreier* rings (structural motif III orange) and pairs of tetrahedra (structural motif IV blue). Although the structure model of type 2 is not finally refined, great similarity between the structure models are apparent because some structural motifs are present in both structures.

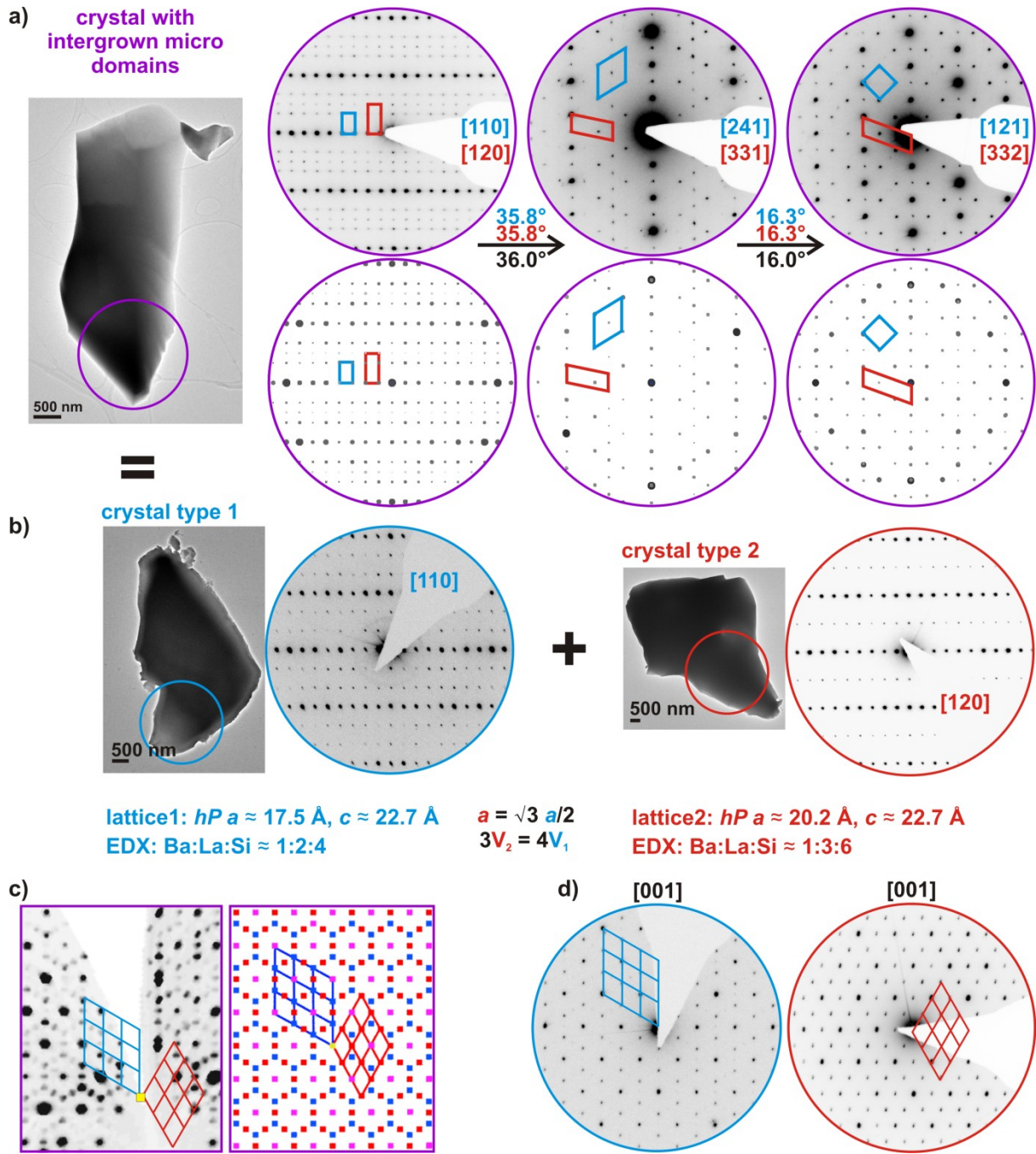


Fig. 2: BF image and SAED tilting series of an intergrown crystallite (a top) and corresponding superposition of the SAED simulations of the lattice points (based on tentative structure models, derived from X-ray data, a bottom) with unit cells of two new and related hexagonal phases highlighted; type1 (blue) and type2 (red). Individual pre-characterized crystallites with unit cell parameters and EDX of the two new oxonitridosilicates, each a BF image and a representative SAED pattern (b). The superposition of type 1 and type 2 patterns results in the patterns of the intergrown crystal (highlighted in violet). Comparison of reciprocal lattice section of an intergrown crystal including a schematic pattern decomposition into the two lattice types (c) with SAED patterns of different individuals (d); all viewed along [001]; Dimensions of the lattice types highlighted in blue and red.

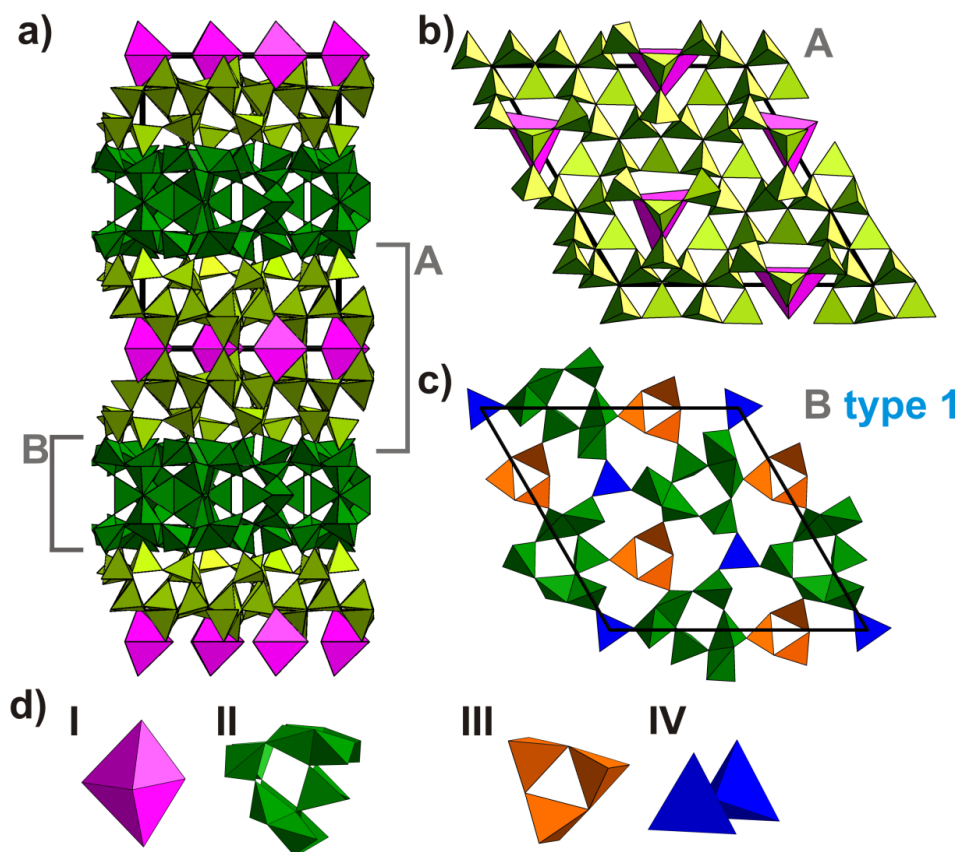


Fig. 3: Crystal structure of type 1 phase with building block A and B highlighted in green and light green (a). Substructure of the building blocks (b and c). Individual structural motifs I-IV (d).

STEM-HAADF at atomic resolution viewed along the special directions can support the structure refinement of type 2 (a, c, d). Z-contrast images along zone axis [100] showed similar heavy atom positions of the type 2 La/Ba and La/Sr oxonitridosilicates and suggest isotypic crystal structures (see Fig. 4 a, b). The distribution of elements with low scattering contrast such as the combinations N/O and Ba/La can be analyzed with bond-valence sum calculations. Similar to the approach described in chapter 2.2 and 5.1 green luminescence $\text{La}_{3-x}\text{Ba}_x\text{Si}_6\text{N}_{11-x}\text{O}_x\text{:Ce}^{3+}$ with $x \approx 0.1$ crystallizing in the $\text{La}_3\text{Si}_6\text{N}_{11}$ structure type^{2,3} was found and characterized.

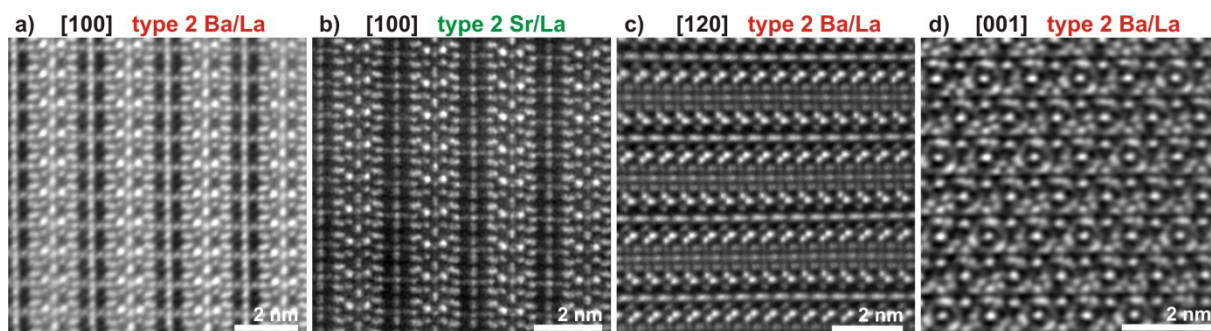


Fig. 5: Fourier-filtered Z-contrast STEM-HAADF images of Ba/La oxonitridosilicate type 2 along special directions showing the projection of the heavy atoms (a, c, d). The contrast distribution (metal cation positions) along [100] of (a) match the one of the isotypic La/Sr oxonitridosilicate (b).

5.2 Phase identification and unit-cell parameter of new oxonitridophosphates

Lukas Neudert, Dominik Bauman, Simon D. Kloß, Wolfgang Schnick, Oliver Oeckler

unpublished results

Rapidly growing databases like the Inorganic Crystal Structure Database with around 4000 additional entries per year underline the importance of structure determination on materials science. The most common method to elucidate the crystal structure of novel solids is single-crystal or powder X-ray diffraction. However, these methods are often limited by the size of the obtained single crystals or phase purity of powder samples. Other analytical methods or combinations thereof are more practical to overcome these challenges than the optimization of the synthesis conditions. As electron microscopy links imaging, diffraction and chemical analysis via BF, SAED and EDX, it is possible to identify different phases in heterogeneous microcrystalline samples. With the help of chemical composition and initial unit-cell parameters, it is possible to compare the product with databases or to identify the corresponding phases as new ones.

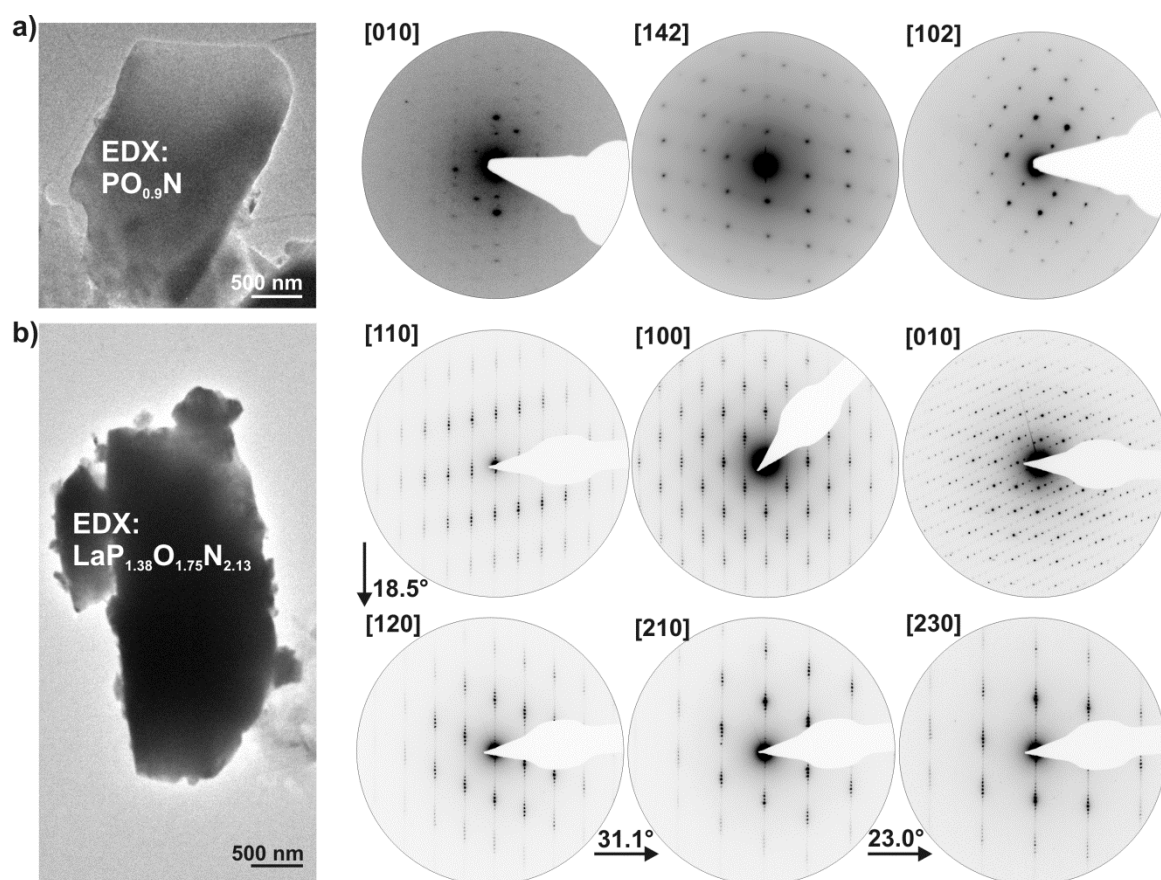


Fig. 1: New microcrystalline phases discovered by combination of SAED and EDX; a) BF image with averaged EDX, indexed SAED pattern of a monoclinic PON modification ($a = 26.6 \text{ \AA}$, $b = 4.8 \text{ \AA}$, $c = 21.4 \text{ \AA}$, $\beta = 123.3^\circ$). b) BF image with averaged EDX and SAED-tilting series of the first lanthanum oxonitridophosphate (monoclinic, $a = 14.0 \text{ \AA}$, $b = 7.1 \text{ \AA}$, $c = 41.4 \text{ \AA}$, $\beta = 97.7^\circ$).

The determination of the unit-cell parameters can be done manually with a SAED tilting series around one axis with a 90° angle. Such an approach was applied to identify two microcrystalline phases, obtained from high-pressure high-temperature synthesis. The first lanthanum oxonitridophosphate and a new monoclinic PON modification were found (see Fig. 1). Structure models were obtained using single-crystal datasets collected with sub-micron synchrotron beams (e.g. ID11, ESRF, Grenoble) of pre-characterized crystallites on TEM grids.⁴ HRTEM or STEM images could not be obtained at atomic resolution since the samples are beam sensitive.

5.3 Formation of Superstructures in Tellurides

Lukas Neudert, Juliane Stahl, Matthias Grotevent, Oliver Oeckler

unpublished results

TEM can be important for the elucidation of real-structure effects of many tellurides. In this context, a non-periodical stacking of layers along [001] or defect ordering and superstructure formation, seems to be likely for ferromagnetic $\text{Fe}_{2.3}\text{GeTe}$ crystallizing in the space group $P\bar{3}m1$. The structure of $\text{Fe}_{2.3}\text{GeTe}$ is related to that of Fe_3GeTe_2 and Fe_2Ge . Additional reflections in SAED pattern can be explained by double diffraction based on superimpose of laminar crystals. This effect causes Moiré patterns in HRTEM and additional reflections in the corresponding FT.⁵ No superstructure but a non-periodic stacking of building units along [001] in correspondence to diffuse intensity along [001]* was found in $\text{Fe}_{2.3}\text{GeTe}$ (see Fig. 1).⁶

Under ideal circumstances represented for example by simple or high symmetric crystal structures, atomic resolved STEM-HAADF can directly visualize atom positions, from which structure models can be derived or confirmed. STEM-HAADF is powerful especially if the samples are heterostructured or individual domains are only extended over a few nanometers.⁷⁻¹⁰ By SAED tilting series and STEM-HAADF images along the special projection [110] (see Fig. 2), the rocksalt structure type in quenched $\text{Ge}_{0.35}\text{Sn}_{0.37}\text{In}_{0.07}\text{Sb}_{0.11}\text{Te}$ is directly visible. The heavier Te atoms correspond to brighter contrast due to increased scattering power. Darker contrast corresponds to the mixed occupied site of Ge/Sn/In/Sb with vacancies. Furthermore, such quinary thermoelectrics show pronounced real structure effects after slow cooling.¹¹

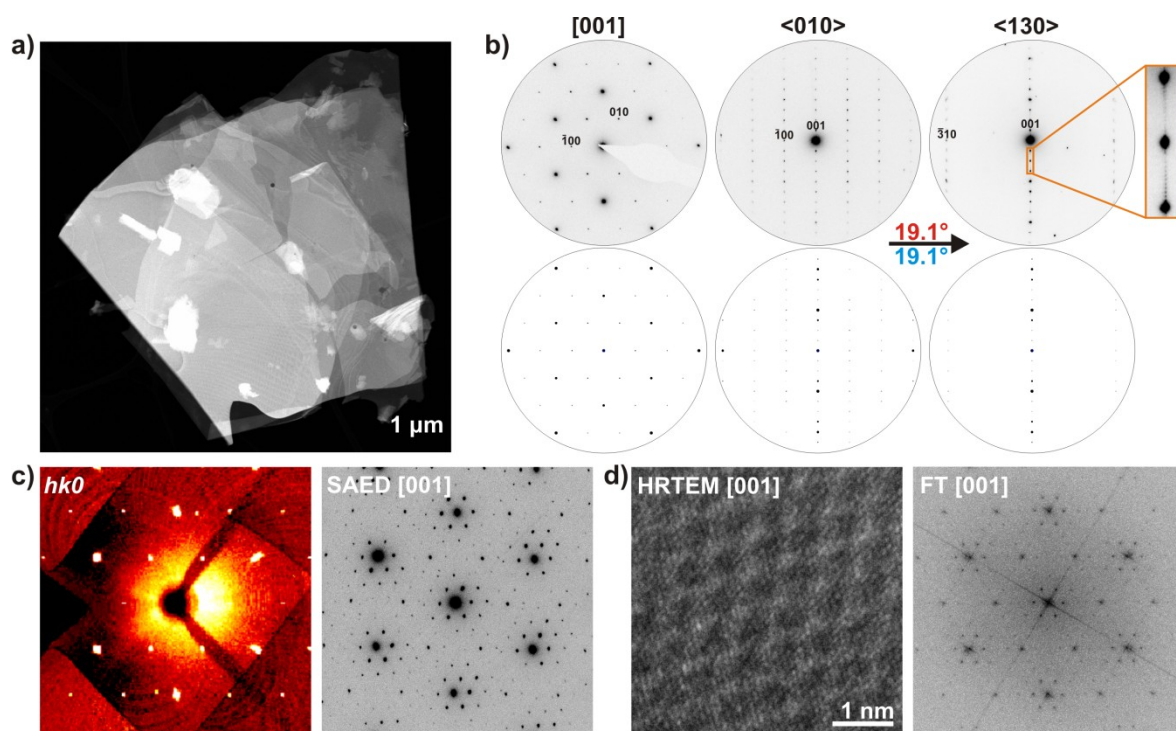


Fig. 1: TEM data of ferromagnetic $\text{Fe}_{2.3}\text{GeTe}$: Plate-like crystal shape observed in STEM dark-field image (a), SAED with corresponding simulations and tilting angles, diffuse intensity along $[001]^*$ (highlighted in orange) (b), SAED and reciprocal lattice section both viewed along $[001]$ (c), corresponding HRTEM and FT (d), both with additional reflections explained by double diffraction based on laminar crystals superimpose.



Fig. 2: Directly observed rocksalt structure in $\text{Ge}_{0.35}\text{Sn}_{0.37}\text{In}_{0.07}\text{Sb}_{0.11}\text{Te}$: STEM-HAADF micrographs viewed along $[110]$ zone axis (left). Z-contrast allows differentiation between Te atoms and mixed occupied cation sites. Enlargement (right) with structure projection of rocksalt-type with Te^{2-} in red and cations in green.

With the combination of electron diffraction and HRTEM a superstructure in $\text{Ge}_4\text{In}_2\text{Te}_7$ was elucidated qualitatively and a trigonal structure model was constructed (see Fig. 3). Additional reflections in SAED pattern and HRTEM images with pronounced vacancy ordering in different domains of quenched $\text{Ge}_{0.571}\text{In}_{0.286}\text{Te}$ ($\text{Ge}_4\text{In}_2\text{Te}_7$) revealed a fourfold superstructure of the rocksalt type along one of its $\langle 111 \rangle$ directions comparable to those of other tellurides like $\text{Ge}_3\text{MnSb}_2\text{Te}_7$ or $\text{Ge}_{3.25}\text{Sn}_{1.1}\text{Sb}_{1.1}\text{Te}_6$.¹²⁻¹⁴ As SAED provides the dimensions of the lattice parameters and HRTEM illustrates the remaining “cubic” ABC stacking sequence of the Te atoms, a rhombohedral structure model in space group $R\bar{3}m$ with $a \approx 4.23 \text{ \AA}$ and $c \approx 41.1 \text{ \AA}$ could be derived. The model consists of

three slabs each with four anion and three cation layers. The slabs are separated by vacancy layers (see Fig. 3g). Simulated and superimposed SAED patterns match the experimental diffraction pattern assuming the superposition of twin domains in $\text{Ge}_4\text{In}_2\text{Te}_7$ compared to similar observations described for $\text{Ge}_{0.286}\text{Sn}_{0.286}\text{In}_{0.143}\text{Sb}_{0.143}\text{Te}$.¹¹

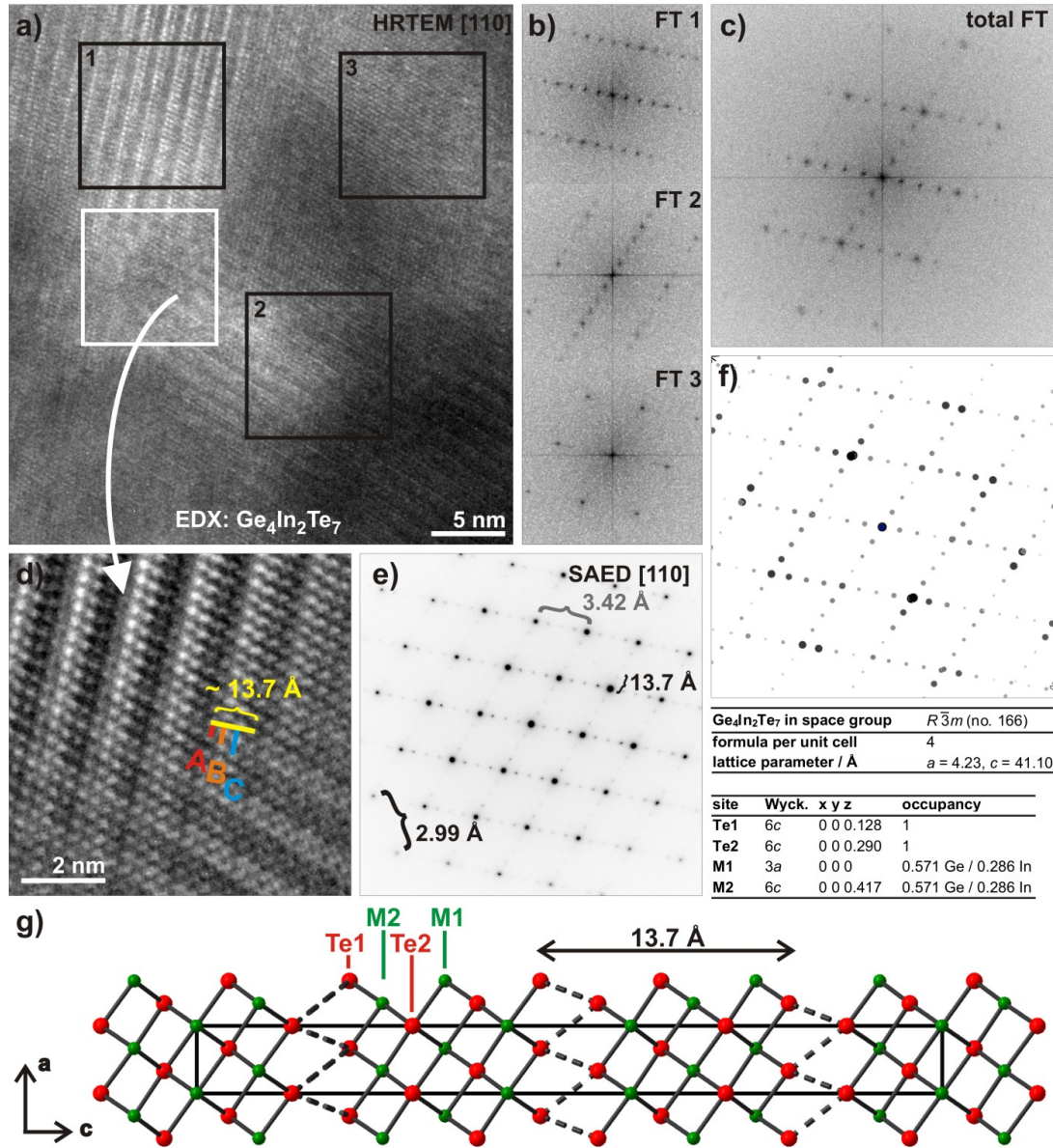


Fig. 3: Structure model of quenched $\text{Ge}_4\text{In}_2\text{Te}_7$ ($\text{Ge}_{0.571}\text{In}_{0.286}\text{Te}$) derived from TEM: trigonal superstructure of rocksalt type: HRTEM images (a) and corresponding Fourier transforms of different regions (b, d) and SAED pattern (e) indicating the possible superposition of three (or more likely, four) different regions corresponding to individual twin domains. Simulated SAED pattern as superposition of two domains (f) along trigonal [100] which refers to one of the rocksalt type lattice's $\langle 111 \rangle$ directions. Fourier filtered enlarged HRTEM image shows ABC stacking of the Te atoms around the vacancy layer (d). Combined with the periodicity of 13.7 Å taken from SAED a long-range ordered trigonal structure model in space group $R\bar{3}m$ is likely ($a_{\text{trigonal}} = a_{\text{cubic}}/\sqrt{2} = d_{002} \cdot 2/\sqrt{2} = (2.99 \text{ Å})/\sqrt{2} = 4.23 \text{ Å}$ and $c_{\text{trigonal}} = 3 \cdot 4 \cdot d_{\text{cubic}111} = 12 \cdot 3.42 \text{ Å} = 3 \cdot 13.70 \text{ Å} = 41.10 \text{ Å}$). Projection and crystallographic data of the constructed superstructure model of $\text{Ge}_4\text{In}_2\text{Te}_7$ (g).

Reference

- 1 Y. Q. Li, A. C. A. Delsing, R. Metslaar, G. de With, H. T. Hintzen, *J. Alloys. Comp.* **2009**, 487, 28.
- 2 T. Seto, N. Kijima, N. Hirotsaki, *ECS Transactions* **2009**, 9, 247.
- 3 M. Woike, W. Jeitschko, *Inorg. Chem.* **1995**, 34, 5105.
- 4 F. Fahrnbauer, T. Rosenthal, T. Schmutzler, G. Wagner, G. B. M. Vaughan, J. P. Wright, O. Oeckler, *Angew. Chem.* **2015**, 127, 10158; *Angew. Chem. Int. Ed.* **2015**, 54, 10020.
- 5 H. -J. Deiseroth, K. Aleksandrov, C. Reiner, L. Kienle, R. K. Kremer, *Eur. J. Inorg. Chem.* **2006**, 8, 1561.
- 6 J. Stahl, L. Neudert, O. Oeckler, D. Johrendt, *Z. Anorg. Allg. Chem.* **2016**, 426, 1064.
- 7 A. Mayoral, T. Carey, P. A. Anderson, I. Diaz, *Micropor. Mesopor. Mat.* **2013**, 166, 117.
- 8 L. Lazzarini, E. Rotunno, *Mat. Sci. Semicon. Proc.* **2017**, 65, 77.
- 9 P. Donnadieu, Y. Shao, F. De Geuser, G. A. Botton, S. Lazar, M. Cheynet, M. de Boissieu, A. Deschamps, *Acta Mater.* **2011**, 59, 462.
- 10 C. M. Wang, V. Shutthanandan, Y. Zhang, S. Thevuthasan, G. Duscher, *J. Am. Ceram. Soc.* **2005**, 88, 3184.
- 11 L. Neudert, S. Schwarzmüller, M. Scheel, S. Welzmler, O. Oeckler, *Z. Allg. Anorg. Chem.* **2017**, 643, 1962.
- 12 S. Welzmler, F. Heinke, P. Huth, G. Bothmann, E. -W. Scheidt, G. Wagner, W. Scherer, A. Pöpl, O. Oeckler, *J. Alloys Compd.* **2015**, 652, 74.
- 13 T. Matsunaga, N. Yamada, *Phys. Rev. B* **2004**, 69, 104111.
- 14 T. Rosenthal, S. Welzmler, L. Neudert, P. Urban, A. Fitch, O. Oeckler, *J. Solid State Chem.* **2014**, 219, 108.

6 Conclusion and Outlook

6.1 Complex oxonitridosilicate and oxonitridophosphate frameworks

In this thesis, diffraction and imaging techniques using X-rays and electrons were adopted synergistically to handle challenging cases of structure determinations of nitride networks. With the efficient combination of SAED, STEM, EDX and microfocused synchrotron X-ray diffraction, microcrystalline and heterogeneous samples no longer prevent the structural elucidation of new compounds. The drawbacks of a general high-temperature synthesis using reactive starting materials for (oxo)nitridosilicates were overcome by the efficient methodical combination. This also applies to the (oxo)nitridophosphates presented in this thesis which were obtained from high-temperature and high-pressure synthesis involving small amounts of product, occasionally of poor crystallinity.

During this work, TEM was the starting point for the discovery and structural characterization of several microcrystalline (oxo)nitridosilicates and (oxo)nitridophosphates. In addition, it was important for supporting structure refinements and structure confirmation. Even for intergrown microdomains of structurally related phases, TEM investigations yielded the unit cell parameters, provided further symmetry information, and disclosed sum formulas of recently identified compounds. Subsequently, microfocused X-ray synchrotron radiation enabled the collection of accurate structural data, which allows precise, state-of-the-art structure determination of chemically and structurally complex nitrides. When isotypic Ba/La and Sr/La oxonitridosilicates are found, the unequivocal assignment of Sr and La the subsequent transfer to the assignment of Ba and La positions is possible. In principle, the joint characterization of TEM and microfocused X-ray diffraction allows all steps of phase identification, structure determination as well as its confirmation on only one microcrystal coming from a powder sample. For chemists, this approach can be a powerful opportunity to identify and characterize new compounds with less laborious synthesis, even in cases of adverse product quality. This method can be considered as further development of the single-particle-diagnosis approach¹ extended to crystallites with small scattering volume $< 1 \mu\text{m}^3$. The small scattering volume of the $\text{La}_{24}\text{Sr}_{10.58}[\text{Si}_{36}\text{N}_{72}]\text{O}_{7.16}\text{F}_{6.84}$ needles required the use of intense synchrotron radiation. The latter might be substituted in the future by electron diffraction tomography as it has been shown for nanorods.² Although structure determinations based on powder X-ray or electron-diffraction tomography data have the advantage that no synchrotron with microfocused beam is needed, these methods frequently render less precise structure models. However, missing structural information can be compensated by using the rough structure model from electron data and combining them with additional information from Rietveld refinements or with theoretical

calculations.^{3,4} Precise 2D and 3D structure models can be obtained with the advancement of electron crystallography and its combination with DFT methods.⁵⁻⁷

The knowledge of crystal structures is the first step toward the derivation of syntheses for phase-pure products or structure-property relation for a systematic tuning of intriguing properties, like luminescence. The demonstration of a theory-experiment relation appears to be worthwhile purpose and was achieved by the synthesis and structural elucidation of $\text{La}_{24}\text{Sr}_{10.58}[\text{Si}_{36}\text{N}_{72}]\text{O}_{7.16}\text{F}_{6.84}$. Its highly symmetric AB_2 framework topology has been predicted theoretically, but it was now synthesized and characterized. For future synthesis in order to obtain prospective phosphors, this nitridosilicate oxide fluoride can act as a starting point for a broad structural and chemical plurality of metal containing rigid nitridosilicates with a structure related to the one of $\text{La}_{24}\text{Sr}_{10.58}[\text{Si}_{36}\text{N}_{72}]\text{O}_{7.16}\text{F}_{6.84}$. Further ion-exchange or substitution experiments, which can involve the rigid anionic network as well as the incorporated counter ions appears to be promising. The overall charge is adjustable by changing the O/F ratio. From several SiAlONs it is known that Si can be substituted by Al.⁸ Furthermore, $\text{La}^{3+} / \text{Sr}^{2+}$ can be exchanged by Na^+ , Ca^{2+} or other lanthanides including the doping of the activator ions Eu^{2+} and Ce^{3+} . Such chemical variations can be documented by Z-contrast imaging using STEM-HAADF. Thus, the position and the distribution of the different ions can be directly visualized. With the latter, conclusions about changed activator-ion concentration and distribution in relation to changed luminescence properties might be drawn.

In addition to the structural similarities of (oxo)nitridosilicates and (oxo)nitridophosphates, this thesis also shows similar challenges in their synthesis and structure determination. Thus, it is reasonable to apply comparable approaches to overcome obstacles on structure determination of (oxo)nitridophosphates. The combination of TEM and X-ray methods was examined on non-ideal samples of new nitridophosphates with complex structures. Starting from microcrystalline products from syntheses in the multianvil press the structural diversity of oxonitridophosphates is expanded by the identification and characterization of $\text{AlP}_6\text{O}_{3x}(\text{NH})_{3-3x}\text{N}_9$ ($x \approx 0.33$). This first aluminum imido-oxonitridophosphate bridges the gap between imidonitridophosphates and oxonitridophosphates. The motif of six corner sharing $\text{P}(\text{N/O/NH})_4$ tetrahedra in slightly different arrangements was observed in $\text{AlP}_6\text{O}_{3x}(\text{NH})_{3-3x}\text{N}_9$ as well as in $\text{CaH}_4\text{P}_6\text{N}_{12}$ and $\text{SrH}_4\text{P}_6\text{N}_{12}$. This allows the suggestion that the prioritized formation of this motif helps to stabilize rigid imido-(oxo)nitridophosphate frameworks. The knowledge about their structural relations may open a pathway to a higher condensed compound represented by $M^{\text{II}}\text{P}_8\text{N}_{14}$.

Structure models with unusual displacement parameters or models based on PXRD with very broad reflections or with several unknown side phases can give rise to doubts about the correctness of the structure determination. For such ambiguous cases like $\text{CaMg}_2\text{P}_6\text{O}_3\text{N}_{10}$, CaGaSiN_3 as well as air and moisture sensitive $\text{CaMg}_2\text{GaN}_3$ and $\text{CaMg}_2\text{Ga}_2\text{N}_4$, SAED-tilting series as well as HRTEM-defocus series

provide structurally relevant contributions for the final models. Thus, more crystal structures can be determined and analyzed leading to a better understanding of nitrides.

The methodical diversity of TEM was applied to comprehensive and targeted investigations on the first non-alkali earth nitridophosphate $\text{Ce}_4\text{Li}_3\text{P}_{18}\text{N}_{35}$ with a degree of condensation of $\kappa > \frac{1}{2}$. The linking of SAED, STEM-HAADF imaging, EDX and EELS allowed for an elucidation of different structural features even on the sub-angstrom scale in two different domain types in the blue luminescent nitridophosphate. As the detection of small structural variations from an average structure model requires either strong interaction between probe and material or high brilliance of the detecting beam combined with a large crystal volume, TEM facilitated a targeted search of a superstructure of $\text{Ce}_4\text{Li}_3\text{P}_{18}\text{N}_{35}$. STEM-HAADF enabled the direct observation of Ce^{3+} vacancies or Ce^{3+} displacements, leading to a long-range periodic order in $\text{Ce}_4\text{Li}_3\text{P}_{18}\text{N}_{35}$. Structure refinements in a supercell or with a superspace group based on synchrotron X-ray data yielded the same qualitative superstructure model as the one derived from STEM. The displacements of the Ce2 atoms in some domains are responsible for the unusual displacement parameters of the average structure model based on diffraction data of the whole crystal. The major conclusion is that the structure of $\text{Ce}_4\text{Li}_3\text{P}_{18}\text{N}_{35}$ is stabilized either by forming a superstructure or by introducing vacancies on one Ce2 site. Due to the vacancies the compound has the sum formula $\text{Ce}_{4-0.5x}\text{Li}_3\text{P}_{18}\text{N}_{35-1.5x}\text{O}_{1.5x}$ with $x \approx 0.72$. This comprehensive structure determination presents the combination of aberration-corrected (S)TEM^{9,10} and synchrotron diffraction driven to the edge of their state-of-the-art performance limits.

Such a synergistic and efficient combination of transmission electron microscopy and synchrotron X-ray diffraction for the structure determination of new nitrides, expands fundamental structural research significantly and pushes structure determination to a higher level of detail. This is all the more remarkable as the probed samples were not just model systems but rather novel complex compounds have been characterized. TEM presented in this thesis explains and displays structural phenomena of nitrides, where X-ray diffraction reaches its limits. The remark: “What I can see, I believe” can act as an overall conclusion for the TEM within this thesis. Trial and error approaches are being replaced by the ability to visualize crystal structures of nitrides directly at the atomic scale.

By means of such a combination of modern analytical instruments the understanding of intriguing properties known from nitrides, notably solid-state lighting, may be enabled. With the advancement and better accessibility of electron-diffraction tomography there is an additional method available in order to obtain precise structural data less elaborately, compared to synchrotron diffraction data.

6.2 Tin and indium containing tellurides

Although the synthesis of tellurides does not rival the complexity of the nitrides presented previously, structure and property changes of thermoelectric tellurides based on different chemical compositions or different thermal treatment are difficult to identify and are even more difficult to translate into distinct structure-property relations. Investigations on the systems $(\text{SnTe})_{3-3x}(\text{In}_2\text{Te}_3)_{3x}$ and $(\text{Ge}_x\text{Sn}_{1-x})_{0.8}(\text{In}_y\text{Sb}_{1-y})_{0.13}$ show the combination of laboratory and synchrotron X-ray methods with TEM in order to provide detailed structural analysis down to the angstrom scale. In addition to the knowledge of the average crystal structures, the description of real-structure phenomena is needed to understand their decisive influence on the thermoelectricity of the tellurides. As the chemical and structural complexity of ternary, quaternary or even quinary tellurides increases, diffraction as well as imaging techniques are required to illustrate different real-structure effects. The overall methodical link with measurements of physical properties allows an integral characterization. Thus, such combinations can help to optimize thermoelectric variables. In heterostructured thermoelectric materials, it is rewarding to characterize precipitates not only in their appearance, but also to determine their crystal structure. The results presented in this work are the basis for conclusions about successful material optimization.

The formation of Sn-doped In-rich precipitates similar to In_2Te_3 with defect-sphalerite-type structure and pronounced short-range defect ordering embedded in an In-doped SnTe matrix seem to have an effect of lowering the phononic contribution to the thermal conductivity over the whole temperature range between 25 and 500 °C. The precipitates, which are endotaxially intergrown with the Sn-rich rocksalt-type matrix, picture the degree of disorder on the nm and μm scale. The insertion of vacancies on the cation sites and their partial ordering invokes increased disorder on the atomic length scale. In addition, it can be concluded that the characteristics of these heterostructures are more influenced by changing the In content than by various heat treatments. The potential of optimized heterostructured phases containing SnTe and In_2Te_3 are better described based on the conclusions of this thesis. Further co-doping,^{11,12} to achieve higher Seebeck coefficients and higher electrical conductivity may open new and more application-oriented research on tellurides containing Sn and In. Furthermore, such comparative studies extend the understanding of solid-state reactions, when not only the initial and the final state are considered, but structural and chemical changes within various influences are documented. The extension of the starting materials SnTe and In_2Te_3 with GeTe and Sb_2Te_3 for the high-temperature synthesis leads to increased miscibility and homogenous quaternary and quinary tellurides with predominantly average rocksalt-type structure. SAED and HRTEM document the pathway of differently pronounced defect ordering over a herringbone-like arrangement of vacancy layers to layer-like trigonal superstructures of the rocksalt type. This underlines the importance of TEM to elucidate superstructures, when laboratory powder

X-ray methods are limited.¹³ Resonant X-ray diffraction on trigonal layer-like $21R\text{-Ge}_{0.5}\text{Sn}_{0.5}\text{SbInTe}_4$ and $9P\text{-GeSnSbInTe}_5$ revealed the cation distribution within the rocksalt-type slabs, separated by van der Waal gaps. Thus, the environment of finite vacancy layers in highly disordered phases is illustrated, resulting in an improved understanding of the formation of superstructures of the rocksalt type. Once more, the synergism of synchrotron X-ray diffraction, electron diffraction, HRTEM and spatially-resolved EDX turned out to be ideal combination for the investigation of such microscopic and nanoscopic effects.

With respect to the thermoelectric properties, a trend towards nearly constant electrical conductivity combined with very low thermal conductivity over a large temperature range has emerged when Sn and In are present. A significant improvement of the Seebeck coefficients of the current quaternary and quinary tellurides by further changes in the element ratios and defect concentrations, predict reaching properties that are more seminal.

References

- 1 N. Hirosaki, T. Takeda, S. Funahashi, R. -J. Xie, *Chem. Mater.* **2014**, 26, 4280.
- 2 A. Mayence, J. R. G. Navarro, Y. Ma, O. Terasaki, L. Bergström, P. Oleynikov, *Inorg. Chem.* **2014**, 53, 5067.
- 3 P. Guo, L. Liu, Y. Yun, J. Su, W. Wan, H. Gries, H. Zhang, F. -S. Xiao, X. Zou, *Dalton Trans.* **2014**, 43, 10593.
- 4 S. Wang, G. -D. Lee, S. Lee, E. Yoon, J. H. Warner, *ACS Nano* **2016**, 10, 5419.
- 5 M. Gemmi, P. Oleynikov, *Z. Kristallogr.* **2013**, 228, 51.
- 6 Z. Wang, Z. Zhang, W. Liu, Z. L. Wang, *Micron* **2017**, 95, 16.
- 7 H. Xu, Z. Shen, H. Konishi, G. Luo, *Am. Mineral* **2014**, 99, 2043.
- 8 M. Zeuner, S. Pagano, W. Schnick, *Angew. Chem.* **2011**, 123, 7898; *Angew. Chem. Int. Ed.* **2011**, 50, 7754.
- 9 P. E. Batson, N. Dellby, O. L. Krivanek, *Nature* **2002**, 418, 617.
- 10 S. J. Pennycook, *Ultramicroscopy* **2017**, 180, 22.
- 11 J. Q. Li, S. Huang, Z. P. Chen, Y. Li, S. H. Song, F. S. Liu, W. Q. Ao, *Phys. Chem. Chem. Phys.* **2017**, 19, 28749.
- 12 D. K. Bhat, S. Shenoy U, *J. Phys. Chem. C* **2017**, 121, 7123.
- 13 T. Rosenthal, S. Welzmler, L. Neudert, P. Urban, A. Fitch, O. Oeckler, *J. Solid State Chem.* **2014**, 219, 108.

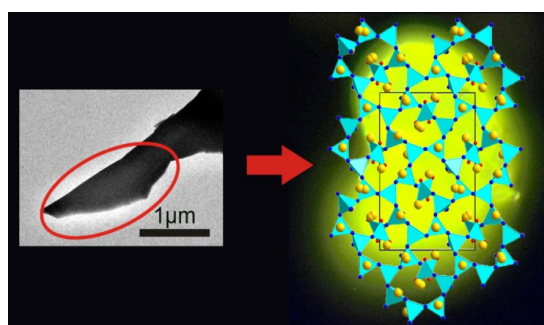
7 Summary

In this PhD thesis, various challenges occurring during the discovery and the structure determination of new nitrides as well as the characterization of structure-property relations have been solved by means of combined X-ray and electron microscopy methods. The focus is on diffraction data based on electron beams, laboratory and synchrotron X-ray radiation as well as on atomic resolved TEM methods of imaging, and spectroscopy to analyze (oxo)nitridosilicates, oxonitridophosphates and tellurides. These combinations of methods proved to be particularly successful.

Structure determination of nitride networks

(Oxo)nitridosilicates doped with rare earth elements are well known as luminescent materials, e.g. in phosphor-converted LEDs. New phosphors are required in order to realize inter alia higher efficiency and higher color rendering indices for commercial LEDs. As luminescence properties are widely dependent on the crystal structure, precise structure determination of such phosphors is crucial. The syntheses of the (oxo)nitridosilicates, mentioned in this thesis, involve high-temperature conditions ($T > 1500^{\circ}\text{C}$) of a radio-frequency furnace and utilize reactive nitrogen-rich materials in combination with metal hydrides and metal halogenides. This metathesis related approach yielded numerous products predominantly microcrystalline and heterogeneous. With the combination of SAED, STEM, EDX and powder X-ray diffraction it was possible to identify six new microcrystalline (oxo)nitridosilicates described in chapter two and five. Due to similarities between (oxo)nitride-silicate and (oxo)nitridophosphate tetrahedral networks, similar approaches for the characterization of both stable compound classes are reasonable and were applied.

$\text{La}_3\text{BaSi}_5\text{N}_9\text{O}_2\text{:Ce}^{3+}$ – A yellow phosphor with an unprecedented tetrahedra network; structure investigated by combination of electron microscopy and synchrotron X-ray diffraction

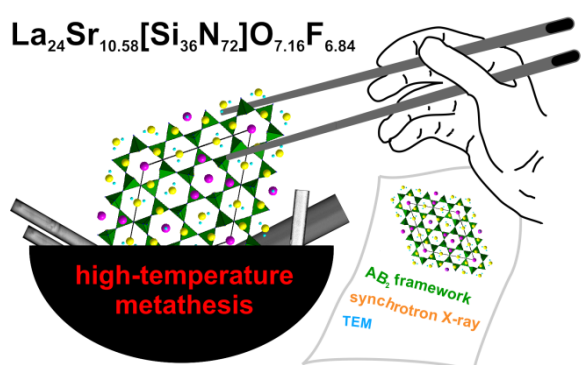


Starting from multiphase products obtained from high-temperature synthesis, the microcrystalline and luminescent compounds $\text{La}_3\text{BaSi}_5\text{N}_9\text{O}_2\text{:Ce}^{3+}$ were identified by the combination of EDX and SAED, yielding its sum formula and its metrics. This pre-characterization was the basis for the data collection

using microfocused synchrotron X-ray radiation and the subsequent structure determination of the orthorhombic oxonitridosilicate. $\text{La}_3\text{BaSi}_5\text{N}_9\text{O}_2\text{:Ce}^{3+}$ crystallizes in space group $Pmn2_1$ ($a = 9.5505(8)$,

$b = 19.0778(16)$, $c = 12.1134(9)$ Å and $Z = 8$) showing an interrupted framework that consists of vertex-sharing SiN_4 and SiN_2O_2 tetrahedra. One quarter of the cation sites are split positions. HRTEM and Z-contrast STEM images confirmed the structure model of $\text{La}_3\text{BaSi}_5\text{N}_9\text{O}_2:\text{Ce}^{3+}$ and highlighted anti-phase boundaries. Bond-valence sum calculations helped with the atom assignment. The high quality of this crystal structure determination is required in order to enable property tuning, as there is a sensitive correspondence between atomic environments and luminescence. The structure determination of $\text{La}_3\text{BaSi}_5\text{N}_9\text{O}_2:\text{Ce}^{3+}$ by the combination of TEM and microfocused synchrotron X-ray diffraction is the first example yielding highly accurate crystal-structure data for the case of the large amount of more than 150 atoms with greatly differing atomic weight in the unit cell.

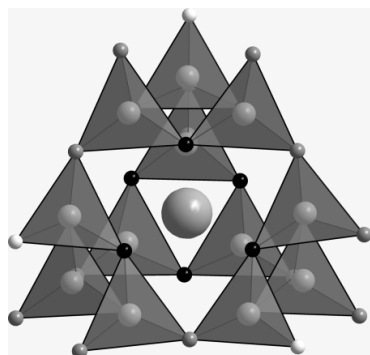
Highly Symmetric AB_2 Framework Related to Tridymite in the Disordered Nitridosilicate $\text{La}_{24}\text{Sr}_{14-7x}[\text{Si}_{36}\text{N}_{72}](\text{O}_{1-x}\text{F}_x)_{14}$ ($x = 0.849$)



The challenges of the structure determination of $\text{La}_{24}\text{Sr}_{10.58}[\text{Si}_{36}\text{N}_{72}]\text{O}_{7.16}\text{F}_{6.84}$ are based on two circumstances. On the one hand because of its microcrystalline needle-shaped crystals and on the other hand due to the presence of cation vacancies combined with the fact that the ratio of charge and electron count, i.e. scattering power, is the same

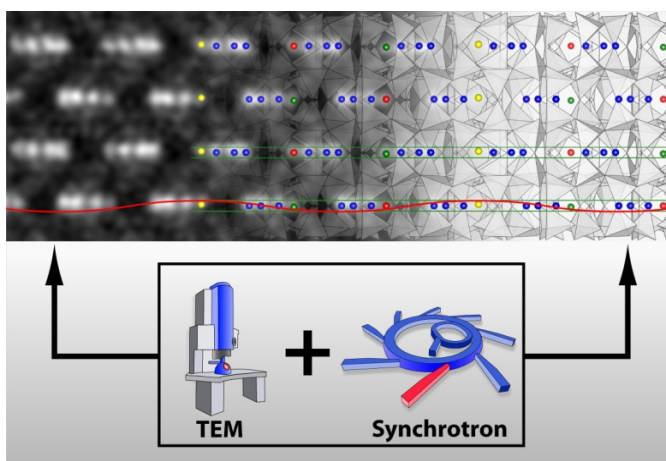
for La^{3+} and Sr^{2+} . The refinement of $\text{La}_{24}\text{Sr}_{10.58}[\text{Si}_{36}\text{N}_{72}]\text{O}_{7.16}\text{F}_{6.84}$ is precise despite the small scattering volume of the crystals and the complexity of the nitridosilicate oxide fluoride. The latter crystallizes in a predicted highly symmetric AB_2 framework (space group $P6_3/mmc$, $a = 16.2065(3)$, $c = 9.4165(1)$ Å, $Z = 1$) and the cavities of the hexagonal structure are filled with La^{3+} , Sr^{2+} as well as O^{2-} and F^- ions. The framework is related to that of tridymite but differs in the orientation of the SiN_4 tetrahedra. SAED confirms the hexagonal metrics, no superstructure reflections were detected. High-resolution Z-contrast STEM images yielded the projected heavy atom positions of $\text{La}_{24}\text{Sr}_{10.58}[\text{Si}_{36}\text{N}_{72}]\text{O}_{7.16}\text{F}_{6.84}$ for the confirmation of the structure model. The characterization of $\text{La}_{24}\text{Sr}_{10.58}[\text{Si}_{36}\text{N}_{72}]\text{O}_{7.16}\text{F}_{6.84}$ combines an advanced methodical approach with the structure determination represents theory-experiment relation.

CaMg₂P₆O₃N₁₀ – A Quinary Oxonitridophosphate with an Unprecedented Tetrahedra Network Structure type



CaMg₂P₆O₃N₁₀ was obtained from a combined high-temperature and high-pressure synthesis in the multianvil press. Unusual enlarged displacement ellipsoids and consequently anomalous interatomic distances may indicate an incorrect structure determination and justify a closer investigation with TEM. In the structure model of CaMg₂P₆O₃N₁₀ an unusually oblate Ca2 displacement ellipsoid was observed. SAED of CaMg₂P₆O₃N₁₀ confirmed its metrics, as determined by X-ray diffraction. HRTEM micrographs match the corresponding simulations based on the structure model, which lead to confirmation of the latter. The oblate Ca2 displacement ellipsoid was further explained by BVS. CaMg₂P₆O₃N₁₀ exhibits an interpenetrating network of two subnets build up by interconnected *Friauf* polyhedral, which are formed by twelve P(O/N)₄ tetrahedra. The results on CaMg₂P₆O₃N₁₀ show how exceptional atomic environments can be explained.

Puzzling Intergrowth in Cerium Nitridophosphate Unraveled by Joint Venture of Aberration-Corrected Scanning Transmission Electron Microscopy and Synchrotron Diffraction

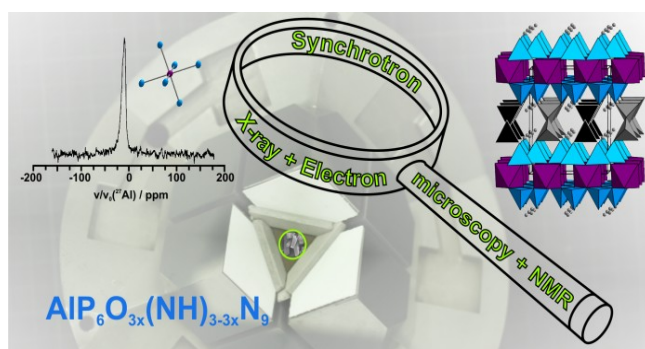


The first rare-earth metal nitridophosphate Ce₄Li₃P₁₈N₃₅ with a degree of condensation > 0.5 was synthesized by high-pressure metathesis starting from CeF₃ and LiPN₂. Ce₄Li₃P₁₈N₃₅ exhibits an unprecedented hexagonal structure (averaged model: space group *P*6₃/*m* with *a* = 13.9318(1) and *c* = 8.1355(1) Å, *Z* = 2). The cations Li⁺ and Ce³⁺ fill channels parallel [001] built up by

triangular columns of ${}^1_{\infty}[(\text{P}_{12}^{[4]}\text{N}_2^{[3]}\text{N}_{24}^{[2]})^{18-}]$ units and a stacking of *sechser* rings with alternating up and down orientation of the P(N/O)₄ tetrahedra. TEM revealed two intergrown domain types that differ slightly in composition and structure. In the first one, high resolution Z-contrast STEM micrographs directly revealed a distortion of ≈ 0.3 Å of the Ce2 atoms along [001] explaining a threefold superstructure. The corresponding supercell was derived from SAED. For the quantitative interpretation of these very weak reflections, synchrotron radiation was used. The superstructure

model was refined in a supercell as well as in an equivalent commensurate (3+2)-dimensional description in the superspace group $P6_3(\alpha, \beta, 0)0(-\alpha - \beta, \alpha, 0)0$. The second domain type with the sum formula $\text{Ce}_{4-0.5x}\text{Li}_3\text{P}_{18}\text{N}_{35-1.5x}\text{O}_{1.5x}$ ($x \approx 0.72$) shows slightly higher oxygen content, which correlates with Ce2 vacancies. The vacancies were directly observed in high resolution Z-contrast STEM micrographs, showing their random distribution. EDX was used to determine the different compositions of the domains and EELS confirmed the absence of Ce^{4+} . Apart from these special structural features, $\text{Ce}_4\text{Li}_3\text{P}_{18}\text{N}_{35}$ exhibits blue luminescence peaking at 455 nm and shows paramagnetic behavior. $\text{Ce}_4\text{Li}_3\text{P}_{18}\text{N}_{35}$ marks a outstanding example of how thorough investigations at the state-of-the-art limitation of TEM and X-ray diffraction can detect structural deviations on the sub-Å scale as well as extend the scope of nitridophosphates with desired properties like luminescence.

An unusual nitride network of aluminum-centered octahedra and phosphorus-centered tetrahedra and structure determination from microcrystalline samples



In contrast to (oxo)nitridosilicates, few oxo-nitridophosphates have been synthesized to date. This is due to fundamental difficulties concerning their synthesis and often the poor crystallinity of the reaction products. In terms of structural characterization and new structures, comparable questions arise.

Electron microscopy in combination with X-ray structure determination, identifies new phases and helps to uncover properties that are associated with special structural features. $\text{AlP}_6\text{O}_{3x}(\text{NH})_{3-3x}\text{N}_9$ with $x \approx 0.33$ was synthesized as a microcrystalline product under high-pressure and high-temperature conditions in the multianvil press. Electron microscopy yielded the monoclinic unit-cell parameters and the sum formula. EELS confirmed the N:O ratio. Microfocused synchrotron X-ray diffraction and solid-state NMR were applied to determine the crystal structure of $\text{AlP}_6\text{O}_{3x}(\text{NH})_{3-3x}\text{N}_9$ (space group $P2_1/m$ with $a = 4.7566(2)$, $b = 8.3266(3)$, $c = 10.6298(7)$ Å and $\beta = 101.601(4)^\circ$, $Z = 2$). The structure consists of discrete AlN_6 octahedra that interconnect imidophosphate layers. The network topology is unprecedented but related to that of $\text{MP}_6\text{H}_4\text{N}_{12}$ with $M = \text{Ca}, \text{Mg}$. The structural characterization of $\text{AlP}_6\text{O}_{3x}(\text{NH})_{3-3x}\text{N}_9$ by the synergism of high-pressure, high-temperature synthesis, TEM and microfocused synchrotron X-ray diffraction overcome the individual methodical shortcomings thus, an efficient approach towards new nitridophosphates and their characterization is presented.

Unpublished nitrides

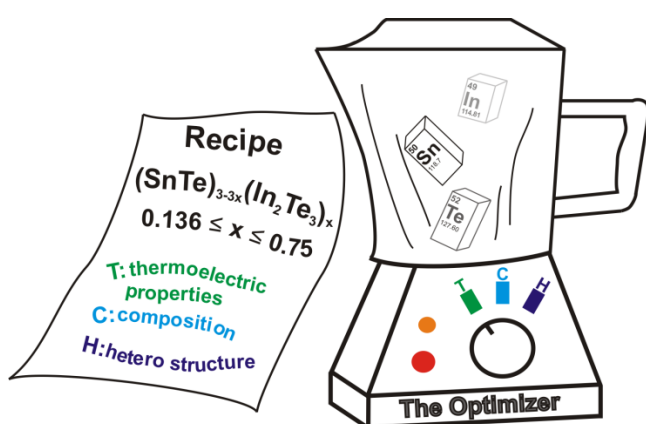
The combination of electron microscopy and microfocused synchrotron X-ray diffraction was applied for the identification of additional new nitrides. Two coherently intergrown barium lanthanum oxonitridosilicate oxides were identified and characterized with TEM. They both show hexagonal symmetry and exhibit nearly the same c lattice parameter and a 3:4 ratio between the unit cell volumes. Single-crystal data of other non-intergrown and pre-characterized crystallites were collected using sub-micron synchrotron beams. The two related crystal structures can be described as sandwich-like stacking of building blocks that contain vertex and corner sharing $\text{Si}(\text{O}/\text{N})_4$ tetrahedra, forming complex connection patterns. The cations of Ba, La and Sr, in the case of an isotopic compound also found by TEM, are located in the cavities of the framework. HRTEM and high resolution STEM-HAADF provide helpful data for the refinement and confirmation of the structure models. A fourth La/Ba oxonitridosilicates was identified and pre-characterized by TEM. Synchrotron X-ray data revealed that the green luminescent $\text{La}_{3-x}\text{Ba}_x\text{Si}_6\text{N}_{11-x}\text{O}_x:\text{Ce}^{3+}$ ($x \approx 0.1$) crystallizes in the $\text{La}_3\text{Si}_6\text{N}_{11}$ structure type. With regard to oxonitridophosphates, a new monoclinic PON modification and the first lanthanum oxonitridophosphate have been detected and described by means of electron diffraction and EDX.

Thermoelectric tellurides

One of the key motivations of the present research is to provide valuable contributions to energy-converting materials or energy savings in any form. Besides fundamental research on rigid nitride networks that may find applications, e.g. as phosphors, the optimization of thermoelectric materials is equally relevant for energy-saving materials. Prominent binary chalcogenides like PbTe, GeTe, SnTe, SnSe or In_2Te_3 and Bi_2Te_3 are ideal starting candidates to form different ternary, quaternary or quinary thermoelectrics with individual beneficial properties. The mutual dependence of thermoelectric properties and structural changes is the main subject of the investigations on tellurides in this thesis. Since GST materials and their substitution variants are promising and thoroughly investigated thermoelectric materials, they are an initial compound class for comparative material optimization with respect to the thermoelectric figure of merit. Substitution experiments on GST involve changing the vacancy concentration or ways of introducing disorder. GST-related compounds are examples that show differently pronounced real-structure phenomena like disorder leading to superstructures, short-range ordering of defects, or non-periodic stacking of building units, all of which effect thermoelectricity.

Experiences up to now have shown that the supplement of X-ray diffraction methods by TEM in relation to thermoelectric measurements, allows the correlation between variable thermoelectric properties and structural changes at the same time, illustrated by electron diffraction, HRTEM as well as spatially-resolved EDX. With this, TEM helps to document and understand structural changes of compounds in the system Ge/In/Sn/Sb/Te, even if no significant increase of the thermoelectric performance is observed.

Structural variations in indium tin tellurides and their thermoelectric properties

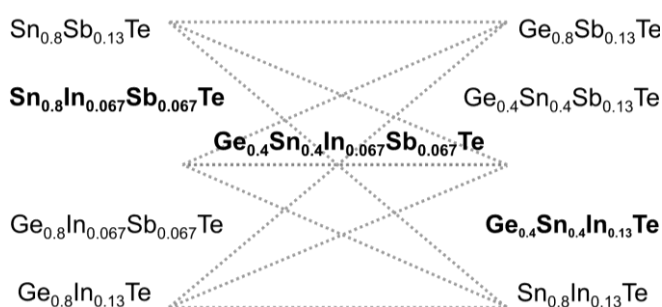


Ternary phases with the nominal composition $(\text{SnTe})_{3-3x}(\text{In}_2\text{Te}_3)_x$ with $0.136 \leq x \leq 0.75$ were obtained by fusing the elements. By means of TEM and PXRD a Sn-rich defect rocksalt type and an In-rich defect-sphalerite type phase were characterized. The relationship between the nominal composition and the observed phase fractions was elucidated. The

low solubility of In_2Te_3 in SnTe and vice versa leads to heterostructures with endotaxial intergrowth of the Sn-rich and the In-rich nanodomains or nanoscaled precipitates of In-rich phases in the Sn-rich matrix. HRTEM and STEM EDX mapping illustrates this result. In addition to various vacancy concentrations associated with the In content, quenching or slow cooling of the samples has a major influence on the characteristic and the pronunciation of the real-structure effects, shown by temperature-dependent PXRD, HRTEM, and STEM. Such wide-ranging investigations are an elegant way of quantitatively evaluating the heterostructuring and its influence on the properties of $(\text{SnTe})_{3-3x}(\text{In}_2\text{Te}_3)_x$. Randomly distributed defects or short-range ordered defects observed for quenched $(\text{SnTe})_{3-3x}(\text{In}_2\text{Te}_3)_x$ with $0.136 \leq x \leq 0.3$ can enhance phonon scattering and thus, very low thermal conductivities $\kappa_{\text{ph}} \ll 2.0 \text{ W m}^{-1} \text{ K}^{-1}$ are measured. Slow cooling instead of quenching of $(\text{SnTe})_{3-3x}(\text{In}_2\text{Te}_3)_x$ phases with band gaps $< 0.16 \text{ eV}$ enhances thermoelectric ZT values to a maximum of 0.55 for $x = 0.136$ below 450°C .

Structural Complexity and Thermoelectric Properties of Quaternary and Quinary Tellurides

$(\text{Ge}_x\text{Sn}_{1-x})_{0.8}(\text{In}_y\text{Sb}_{1-y})_{0.13}\text{Te}$ with $0 \leq x, y \leq 1$



In order to study the influence of combined Ge and Sb substitution by Sn and In on structure-property relations, various ternary, quaternary and quinary thermoelectric tellurides were investigated. Starting from In_2Te_3 , SnTe , GeTe and Sb_2Te_3 , p-type

semiconducting phases with the sum formula $(\text{Ge}_x\text{Sn}_{1-x})_{0.8}(\text{In}_y\text{Sb}_{1-y})_{0.13}\text{Te}$ with $0 \leq x, y \leq 1$ were obtained by fusing the elements in silica ampoules. Depending on the Ge/Sn and Sb/In ratios, the solid solutions of the metastable phases show defect rocksalt-type structure that obey Vegard's law. TEM and synchrotron X-ray diffraction revealed the tendency towards forming trigonal structures with increasing Te content. TEM showed the severe impact on various degrees of nanostructuring based on such substitutions as well as thermal treatment. For quenched $\text{Ge}_{0.286}\text{Sn}_{0.286}\text{In}_{0.143}\text{Sb}_{0.143}\text{Te}$, a long-range ordered superstructure of the rocksalt structure type (space group $R\bar{3}m$, $a = 4.2676 \text{ \AA}$, $c = 52.267 \text{ \AA}$) with a stacking of 27 atom layers including a twin-like superposition of differently orientated domains was derived from SAED, HRTEM and PXRD. Similar investigations on quenched $\text{Ge}_{0.571}\text{In}_{0.286}\text{Te}$ ($\text{Ge}_4\text{In}_2\text{Te}_7$) revealed a superstructure with 21 atom layers (space group $R\bar{3}m$, $a \approx 4.23 \text{ \AA}$ and $c \approx 41.1 \text{ \AA}$). Resonant X-ray diffraction data yielded structure models and the elemental distribution of $21R\text{-Ge}_{0.5}\text{Sn}_{0.5}\text{InSbTe}_4$ (space group $R\bar{3}m$, $a = 4.2454(2) \text{ \AA}$, $c = 41.162(2) \text{ \AA}$) and $9P\text{-GeSnInSbTe}_5$ (space group $P\bar{3}m1$, $a = 4.2624(1) \text{ \AA}$, $c = 17.3730(6) \text{ \AA}$). Ge^{2+} and In^{3+} concentrated in the center of the slab-like building blocks and Sn^{2+} and Sb^{3+} prefer the positions near to the van der Waal gaps, which separate the building blocks related to the rocksalt type. As they influence thermoelectric properties, differently pronounced nanostructures like randomly distributed or short-range ordered vacancies for $(\text{Ge}_x\text{Sn}_{1-x})_{0.8}(\text{In}_y\text{Sb}_{1-y})_{0.13}\text{Te}$ samples are illustrated by HRTEM. The combined presence of Sn and In significantly increases electrical conductivity while keeping thermal conductivity low. Lowering the phononic contribution to the thermal conductivity by introducing nanostructures like defect layers with limited lateral extension perpendicular to $\langle 111 \rangle_{\text{cubic}}$ is one approach for optimizing ZT as applied in $\text{Ge}_{0.4}\text{Sn}_{0.4}\text{In}_{0.067}\text{Sb}_{0.067}\text{Te}$. The combination of physical characterization, laboratory X-ray, and resonant X-ray diffraction as well as TEM, links different analytical methods and allow integral characterization of quaternary and quinary tellurides. These contributions constitute more than an overview of the variety of structural features of In and Sn containing tellurides, associated with their individual thermoelectric properties.

A Miscellaneous

A 1 List of Publications

A 1.1 Part of this thesis

- [1] $\text{La}_3\text{BaSi}_5\text{N}_9\text{O}_2\text{:Ce}^{3+}$ – A yellow phosphor with an unprecedented tetrahedra network; structure investigated by combination of electron microscopy and synchrotron X-ray diffraction**

Dajana Durach, Lukas Neudert, Peter J. Schmidt, Oliver Oeckler, Wolfgang Schnick
Chem. Mater. **2015**, 27, 4832-4838.

The synthesis of the samples, PXRD analysis, topological analysis, and writing of the major parts of the manuscript was performed by D. Durach. L. Neudert conducted the TEM investigations and evaluated TEM data. He identified $\text{La}_3\text{BaSi}_5\text{N}_9\text{O}_2\text{:Ce}^{3+}$ as new phase. L. Neudert prepared the TEM parts of the manuscript and helped to formulate the manuscript. O. Oeckler did the synchrotron measurements and the structure determination. The luminescence characterization was done by P. J. Schmidt. The whole project was directed and supervised by W. Schnick and O. Oeckler. All authors revised the manuscript.

- [2] Highly Symmetric AB_2 Framework Related to Tridymite in the Disordered Nitridosilicate $\text{La}_{24}\text{Sr}_{14-7x}[\text{Si}_{36}\text{N}_{72}](\text{O}_{1-x}\text{F}_x)_{14}$ ($x = 0.489$)**

Lukas Neudert, Dajana Durach, Felix Fahrenbauer, Gavin. B. M. Vaughan, Wolfgang Schnick, Oliver Oeckler
Inorg. Chem. **2017**, 56, 13070-13077.

L. Neudert wrote the manuscript performed the final structure refinement of the synchrotron diffraction data. He also analyzed the network topology, performed the BVS calculations and conducted the TEM investigations as well as the evaluation of the corresponding TEM data. D. Durach performed the synthesis and F. Fahrenbauer helped in the data collection at the synchrotron and the subsequent structure solution. The whole project was directed and supervised by W. Schnick and O. Oeckler. All authors revised the manuscript.

[3] $\text{CaMg}_2\text{P}_6\text{O}_3\text{N}_{10}$ – A Quinary Oxonitridophosphate with an Unprecedented Tetrahedra Network Structure type

Alexey Marchuk, Lukas Neudert, Oliver Oeckler, Wolfgang Schnick

Eur. J. Inorg. Chem. **2014**, 3427-3434.

M. Marchuk synthesized the samples, performed the Rietveld refinement, evaluated the spectroscopic data, analyzed the topology and prepared the major parts of the manuscript. He and O. Oeckler performed the structure determination from single-crystal diffraction data. L. Neudert conducted the TEM experiments and evaluated the TEM data. O. Oeckler supported the TEM data interpretation. L. Neudert also performed the bond-valence sum calculations and helped in creating graphical material and writing the manuscript. O. Oeckler and W. Schnick directed and supervised the work and all authors revised the manuscript.

[4] Aberration-corrected STEM and Synchrotron Diffraction Joint Venture to Elucidate a Microstructured Rare-Earth (Oxo)Nitridophosphate

Simon D. Klotz, Lukas Neudert, Markus Doeblinger, Markus Nentwig, Oliver Oeckler, Wolfgang Schnick

J. Am. Chem. Soc. **2017**, 139, 12724-12735.

S. Klotz synthesized $\text{Ce}_4\text{Li}_3\text{P}_{18}\text{N}_{35}$, wrote the major parts of the publication and performed the structure determination of the averaged and the superstructure models. L. Neudert wrote the TEM parts of the manuscript helped the formulation of the other parts and helped with the creation of the graphical material. L. Neudert conducted all TEM experiments. M. Doeblinger supported with data interpretation and assisted conducting the EDX mapping and EELS measurements. With the synchrotron X-ray data processed by M. Nentwig, S. Klotz refined the final superstructure model. The topological characterization and interpretation of the physical properties were done by S. Klotz. O. Oeckler and W. Schnick directed and supervised the work and all authors revised the manuscript.

[5] An unusual nitride network of aluminum-centered octahedra and phosphorus-centered tetrahedra and structure determination from microcrystalline samples

Lukas Neudert, Frank Heinke, Thomas Bräuniger, Florian J. Pucher, Gavin B. Vaughan, Oliver Oeckler, Wolfgang Schnick

Chem. Commun. **2017**, 53, 2709-2712.

L. Neudert wrote the publication. Using TEM methods he identified and pre-characterized $\text{AlP}_6\text{O}_{3x}(\text{NH})_{3-3x}\text{N}_9$ ($x \approx 0.33$) from a sample synthesized by F. J. Pucher. L. Neudert reproduced the synthesis and performed X-ray powder diffraction methods and bond-valance sum calculations. F. Heinke did the structure refinement based on synchrotron data. M. Doeblinger supervised the EELS investigations. NMR experiments were carried out by C. Minke and T. Bräuniger, who also did the NMR data evaluation and contributed the corresponding part of the manuscript. O. Oeckler directed and supervised the project. W. Schnick contributed to the discussion and all authors revised the manuscript.

[6] Thermoelectric materials in the system In/Sn/Te, variations in structures and properties

Lukas Neudert, Stefan Schwarzmüller, Silvia Schmitzer, Wolfgang Schnick, Oliver Oeckler

J. Solid State Chem. **2018**, 258, 289-297.

L. Neudert wrote the publication, conducted all X-ray, SEM and TEM experiments and evaluated all data. L. Neudert supervised and directed the synthesis and the preparation of the samples done by S. Schmitzer as part of her Bachelor thesis. S. Schwarzmüller performed the thermoelectric measurements and was involved in data interpretation and text writing. O. Oeckler directed and supervised the work. W. Schnick contributed to the discussion and all authors revised the manuscript.

[7] Structural Complexity and Thermoelectric Properties of Quaternary and Quinary Tellurides $(\text{Ge}_x\text{Sn}_{1-x})_{0.8}(\text{In}_y\text{Sb}_{1-y})_{0.13}\text{Te}$ with $0 \leq x, y \leq 1$

Lukas Neudert, Stefan Schwarzmüller, Manuel Scheel, Simon Welzmler, O. Oeckler

Z. Allg. Anorg. Chem. **2017**, 643, 1962-1970.

L. Neudert formulated the manuscript, performed all experiments of sample preparation and electron microscopy (TEM and SEM) and evaluated the corresponding data. M. Scheel helped him with the synthesis and the preparation of the samples and preliminary evaluation of all data as part of his Bachelor thesis. L. Neudert followed through with the refinement of the resonant powder diffraction data, begun by S. Welzmler. Thermoelectric characterization was performed by S. Schwarzmüller. O. Oeckler directed and supervised the work and all authors revised the manuscript.

A 1.2 Other Publications

- [1] **Layered Nitridomagnesogallates $\text{CaMg}_2\text{GaN}_3$ and $\text{CaMg}_2\text{Ga}_2\text{N}_4$**
C. Poesl, L. Neudert, W. Schnick
Eur. J. Inorg. Chem. **2017**, 1067-1074.
- [2] **Ammonothermal Synthesis of Novel Nitrides: Case Study on CaGaSiN_3**
J. Häusler, L. Neudert, M. Mallmann, R. Niklaus, A. -C. L. Kimmel, N. S. A. Alt, E. Schlücker, O. Oeckler, W. Schnick
Chem. Eur. J. **2017**, 23, 2583-2590.
- [3] **Komplexe Silicatstrukturen in Mikrodomänen von Lumineszenzmaterialien**
O. Oeckler, L. Neudert, P. Schultz, D. Durach, W. Schnick
Z. Anorg. Allg. Chem. **2016**, 426, 1013. (conference proceedings)
- [4] **Struktur-Eigenschafts-Beziehungen Struktur-Eigenschafts-Beziehungen von Verbindungen im System Ge/Sn/Sb/In/Te**
L. Neudert, M. Scheel, S. Schwarzmüller, O. Oeckler
Z. Anorg. Allg. Chem. **2016**, 426, 1048. (conference proceedings)
- [5] **$\text{Fe}_{2.3}\text{GeTe}$ - a new layered ferromagnetic telluride**
J. Stahl, L. Neudert, O. Oeckler, D. Johrendt
Z. Anorg. Allg. Chem. **2016**, 426, 1064. (conference proceedings)
- [6] **Nanostructured rocksalt-type solid solution series $(\text{Ge}_{1-x}\text{Sn}_x\text{Te})_n\text{Sb}_2\text{Te}_3$ ($n = 4, 7, 12$; $0 \leq x \leq 1$): Thermal behavior and thermoelectric properties**
T. Rosenthal, L. Neudert, P. Ganter, J. de Boor, C. Stiewe, O. Oeckler
J. Solid State Chem. **2014**, 215, 231-240.
- [7] **Layered germanium tin antimony tellurides: element distribution, nanostructures and thermoelectric properties**
S. Welzmler, T. Rosenthal, P. Ganter, L. Neudert, F. Fahrnbauer, P. Urban, C. Stiewe, J. de Boor, O. Oeckler
Dalton Trans. **2014**, 43, 10529-10540.

**[8] Novel superstructure of the rocksalt type and element distribution in
 germanium tin antimony tellurides**

T. Rosenthal, S. Welzmler, L. Neudert, P. Urban, A. Fitch, O. Oeckler

J. Solid State Chem. **2014**, 219, 108-117.

A 2 Conference contributions

[1] Post-Coesit-Modifikation von PON

S. Vogel, R. Niklaus, L. Neudert, O. Oeckler, W. Schnick

43. Hirschegg-Seminar für Festkörperchemie, Hirschegg (Austria) **2017**.

[2] Cer-Nitridophosphat mit Problemen

S. D. Kloß, L. Neudert, O. Oeckler, W. Schnick

43. Hirschegg-Seminar für Festkörperchemie, Hirschegg (Austria) **2017**.

[3] Struktur-Eigenschafts-Beziehungen von Verbindungen im System Ge/Sn/Sb/In/Te

L. Neudert, M. Scheel, S. Schwarzmüller, O. Oeckler

18. Vortragstagung Fachgruppe Festkörperchemie und Materialforschung der Gesellschaft Deutscher Chemiker, Innsbruck (Austria) **2016**.

[4] Komplexe Silicatstrukturen in Mikrodomänen von Lumineszenzmaterialien

O. Oeckler, L. Neudert, P. Schulz, D. Durach, W. Schnick

18. Vortragstagung Fachgruppe Festkörperchemie und Materialforschung der Gesellschaft Deutscher Chemiker, Innsbruck (Austria) **2016**.

[5] Fe_{2.3}GeTe – a new layered ferromagnetic telluride

J. Stahl, L. Neudert, O. Oeckler, D. Johrendt

18. Vortragstagung Fachgruppe Festkörperchemie und Materialforschung der Gesellschaft Deutscher Chemiker, Innsbruck (Austria) **2016**.

[6] Two new microcrystalline (oxo)nitridosilicates with complex crystal structures determined by combination of TEM and synchrotron micro diffraction

L. Neudert, P. Schulz, D. Durach, O. Oeckler, W. Schnick

16th European Microscopy Congress, Lyon (France) **2016**.

[7] Zwei neue Oxonitridosilicate mit komplexen Kristallstrukturen aus einer heterogenen mikrokristallinen Probe

P. Schulz, D. Durach, L. Neudert, W. Schnick, O. Oeckler

42. Hirschegg-Seminar für Festkörperchemie, Hirschegg (Austria) **2016**.

- [8] **Structure determination of microcrystalline oxonitridosilicates and oxonitrido-imidophosphates by combination of TEM and synchrotron methods**
L. Neudert, F. Pucher, D. Durach, O. Oeckler, W. Schnick
Microscopy Conference 2015, Göttingen (Germany) 2015.
- [9] **Structure determination of luminescent oxonitridosilicates by a combination of electron microscopy and microfocus synchrotron diffraction**
L. Neudert, D. Durach, O. Oeckler, W. Schnick
23th Annual Meeting of the German Crystallographic Society (DGK), Göttingen (Germany) 2015.
- [10] **Unusual Tetrahedra Network Structures of Lanthanum Barium Oxonitridosilicates**
D. Durach, F. Fahrnbauer, L. Neudert, O. Oeckler, W. Schnick
15th European Conference on Solid State Chemistry, Vienna (Austria) 2015.
- [11] **Neue Lanthannitridosilicate und ihr Potential als Leuchtstoff**
D. Durach, P. Schultz, L. Neudert, O. Oeckler, W. Schnick
Obergurgl-Seminar Festkörperchemie, Obergurgl (Austria) 2014.
- [12] **TEM und Synchrotron-Mikrodiffraction zur Strukturaufklärung neuer Oxonitridophosphate und-silicate**
P. Schultz, D. Durach, L. Neudert, A. Marchuk, T. Rosenthal, W. Schnick, O. Oeckler
Mitteldeutsches Anorganiker-Nachwuchssymposium, Freiberg (Germany) 2014.
- [13] **Structure determination of luminescent oxonitridosilicates by a combination of electron microscopy and microfocus synchrotron diffraction**
L. Neudert, D. Durach, O. Oeckler, W. Schnick
17th Wöhler-Tagung, Saarbrücken (Germany) 2014.
- [14] **Crystal structure of $\text{CaMg}_2\text{P}_6\text{O}_3\text{N}_{10}$**
L. Neudert, A. Marchuk, O. Oeckler, W. Schnick
22th Annual Meeting of the German Crystallographic Society (DGK), Berlin (Germany) 2014.

- [15] **Kombination von TEM und Synchrotron-Mikrofokussdiffraction**
L. Neudert, G. Wagner, F. Fahrnbauer, T. Rosenthal, A. Marchuk, P. Urban, T. Schmutzler, W. Schnick, O. Oeckler
39. Hirschegg-Seminar für Festkörperchemie, Hirschegg (Austria) 2013.
- [16] **Real-structure effects of quaternary and quinary germanium antimony telluride thermoelectrics caused by doping with silver and indium**
L. Neudert, T. Rosenthal, T. Schröder, M. Döblinger, O. Oeckler
Microscopy Conference 2013, Regensburg (Germany) 2013.
- [17] **Optimizing thermoelectric properties of germanium antimony tellurides in different temperature ranges by substitution**
S. Welzmler, T. Rosenthal, T. Schröder, F. Schleife, S. Schwarzmüller, L. Neudert, K. Nimmrich, P. Ganter, P. Huth, B. Kersting, O. Oeckler
11th European Conference on Thermoelectrics, Noordwijk (Netherlands) 2013.
- [18] **Tuning real-structure effects and physical properties of germanium antimony tellurides by substitution**
S. Welzmler, T. Rosenthal, T. Schröder, F. Schleife, S. Schwarzmüller, L. Neudert, P. Ganter, P. Huth, B. Kersting, O. Oeckler
14th European Conference on Solid State Chemistry, Bordeaux (France) 2013.
- [19] **Thermoelectric germanium antimony tellurides: Tuning nanostructures and properties by partial vacancy ordering and doping**
O. Oeckler, T. Rosenthal, S. Welzmler, T. Schröder, L. Neudert
2nd EuCheMS Inorganic Chemistry Congress, Jerusalem (Israel) 2013.
- [20] **Nanostructures of thermoelectric Ge/Sb/Te materials and the effect of Se, In and Sn substitution**
T. Rosenthal, S. Welzmler, L. Neudert, K. Nimmrich, P. Ganter, O. Oeckler
15th European Microscopy Congress, Manchester (England) 2012.

[21] Structure elucidation of germanium tin antimony tellurides by TEM and X-ray methods

T. Rosenthal, L. Neudert, S. Welzmler, O. Oeckler

20th Annual Meeting of the German Crystallographic Society (DGK), Munich (Germany) 2012.

[22] "Diffuses ABC" – Leerstellen-Ausordnung in Telluriden und "eingefrorene Zwischenzustände"

O. Oeckler, M. N. Schneider, T. Rosenthal, L. Neudert, P. Urban, J. Wight

Hemdsärmelkolloquium, Oldenburg (Germany) 2012.

[23] Struktur und Eigenschaften Sn- und In-substituierter GST-Materialien

S. Welzmler, T. Rosenthal, F. Fahrnbauer, P. Urban, P. Ganter, L. Neudert, L. Erra,

O. Oeckler

Hirschegg-Seminar für Festkörperchemie, Hirschegg (Austria) 2012.

B Deposited Crystallographic Data

Crystallographic data of the compounds characterized in this work were deposited at the Fachinformationszentrum (FIZ) Karlsruhe, Germany (fax: +49-7247-808-666, e-mail: crysdata@fiz-karlsruhe.de) and are available on quoting the following CSD depository numbers.

Compound	CSD-Number
$\text{La}_3\text{BaSi}_5\text{N}_9\text{O}_2$	429510
$\text{La}_{24}\text{Sr}_{10.58}\text{Si}_{36}\text{N}_{72}\text{O}_{7.16}\text{F}_{6.84}$	432688
$\text{CaMg}_2\text{P}_6\text{O}_3\text{N}_{10}$	427175
$\text{Ce}_{4-0.5x}\text{Li}_3\text{P}_{18}\text{N}_{35-1.5x}\text{O}_{1.5x}$ ($x \approx 0.72$)	433141
$\text{AlP}_6\text{O}_{3x}(\text{NH})_{3-3x}\text{N}_9$ ($x \approx 0.33$)	431557
$9P\text{-GeSnInSbTe}_5$	433533
$21R\text{-Ge}_{0.5}\text{Sn}_{0.5}\text{InSbTe}_4$	433534

C Curriculum Vitae

Personal Details

Name	Lukas Neudert
Date of Birth	15.03.1989
Place of Birth	Memmingen
Nationality	German

Education

10.2013 - 02.2018	Research assistant in the groups of Prof. Dr. Wolfgang Schnick (Department of Chemistry, <i>Ludwig-Maximilians-Universität München</i>) and of Prof. Dr. Oliver Oeckler (Institute for Material Science and Crystallography, Leipzig University, Leipzig) Doctoral thesis entitled: "Transmission Electron Microscopy and X-Ray Diffraction – Joint Characterization of Nitride Networks and Thermoelectric Tellurides"
02.2013 - 08.2013	Master thesis (Inorganic Chemistry) in the group of Prof. Dr. Wolfgang Schnick (Department of Chemistry, <i>Ludwig-Maximilians-Universität München</i>) Master thesis entitled: "Structure Elucidation of Multinary Tellurides and (Oxo)nitridophosphates by Combination of X-ray Methods and Transmission Electron Microscopy"
09.2011 - 02.2013	Master of Science (Chemistry) <i>Ludwig-Maximilians-Universität München</i>
04.2011 - 08.2011	Bachelor thesis (Inorganic Chemistry) at in the group of Prof. Dr. Thomas Klapötke (Department of Chemistry, <i>Ludwig-Maximilians-Universität München</i>) Bachelor thesis entitled: "Synthesis of New Oxidizers for Infrared Decoy Flares on the Basis of Halogenated Nitrogen Rich Heterocycles"
10.2008 - 04.2011	Bachelor of Science (Chemistry and Biochemistry) <i>Ludwig-Maximilians-Universität München</i>

06.2008	Allgemeine Hochschulreife
09.1999 - 06.2008	Secondary School Feodor-Lynen-Gymnasium, Munich and Friedrich-Ludwig-Jahn Gymnasium Greifswald
09.1995 - 07.1999	Primary School Edith-Stein-Grundschule, Memmingen, Fletcher-Maynard Elementary School, Boston, MA and St. Canius Grundschule, Munich